PERFORMANCE CHARACTERISATION OF DUPLEX STAINLESS STEEL IN NUCLEAR WASTE STORAGE ENVIRONMENT

A thesis submitted to
The University of Manchester for the degree of
Doctor of Philosophy (Ph.D.)
in the Faculty of Engineering and Physical Sciences

2015

Cem Örnek

School of Materials

List of Contents

Final word count: 113,088 words

List of Abbreviations

Ag/AgCl	Silver/silver chloride (reference electrode)
AFM	Atomic force microscope/microscopy
AISCC	Atmospheric-induced stress corrosion cracking
ASCC	Atmospheric stress corrosion cracking
BSD	Backscatter diffraction
BSE	Backscatter electron
CSL	Coincidence site lattice
DD	Deposition density
DRH	Deliquescence relative humidity
DSS	Duplex stainless steel
EAC	Environment-assisted cracking
EBSD	Electron backscatter diffraction
EDX	Energy-dispersive x-ray spectroscopy
Ecorr	Corrosion potential
Ecrev	Crevice potential
Epit	Pitting potential
FIB	Focus ion beam microscopy
GB	Grain boundary
HAGB	High-angle grain boundary
ILW	Intermediate-level radioactive waste
LAGB	Low-angle grain boundary
MFM	Magnetic force microscopy
NDA	Nuclear Decommissioning Authority
NHE	Normal/standard hydrogen electrode
OCP	Open-circuit potential
RH	Relative humidity
RT	Room temperature
SCC	Stress corrosion cracking
SCE	Saturated calomel electrode
SE	Secondary electron
SEM	Scanning electron microscopy/microscope
SKP	Scanning Kelvin probe
SKPFM	Scanning Kelvin probe force microscopy
TEM	Transmission electron microscopy/microscope
Vol.-%	Volume percent
WLI	White light interferometry/interferometer
Wt.-%	Weight percent
XRD	X-ray diffraction

Abstract

The majority of UK's intermediate level radioactive waste is currently stored in 316L and 304L austenitic stainless steel containers in interim storage facilities for permanent disposal until a geological disposal facility has become available. The structural integrity of stainless steel canisters is required to persevere against environmental degradation for up to 500 years to assure a safe storage and disposal scheme.

Hitherto existing severe localised corrosion observances on real waste storage containers after 10 years of exposure to an ambient atmosphere in an in-land warehouse in Culham at Oxfordshire, however, questioned the likelihood occurrence of stress corrosion cracking that may harm the canister's functionality during long-term storage. The more corrosion resistant duplex stainless steel grade 2205, therefore, has been started to be manufactured as a replacement for the austenitic grades.

Over decades, the threshold stress corrosion cracking temperature of austenitic stainless steels has been believed to be 50-60°C, but lab- and field-based research has shown that 304L and 316L may suffer from atmospheric stress corrosion cracking at ambient temperatures. Such an issue has not been reported to occur for the 2205 duplex steel, and its atmospheric stress corrosion cracking behaviour at low temperatures (40-50°C) has been sparsely studied which requires detailed investigations in this respect.

Low temperature atmospheric stress corrosion cracking investigations on 2205 duplex stainless steel formed the framework of this PhD thesis with respect to the waste storage context. Long-term surface magnesium chloride deposition exposures at 50°C and 30% relative humidity for up to 15 months exhibited the occurrence of stress corrosion cracks, showing stress corrosion susceptibility of 2205 duplex stainless steel at 50°C.

The amount of cold work increased the cracking susceptibility, with bending deformation being the most critical type of deformation mode among tensile and rolling type of cold work. The orientation of the microstructure deformation direction, i.e. whether the deformation occurred in transverse or rolling direction, played vital role in corrosion and cracking behaviour, as such that bending in transverse direction showed almost 3-times larger corrosion and stress corrosion cracking propensity.

Welding simulation treatments by ageing processes at 750°C and 475°C exhibited substantial influences on the corrosion properties. It was shown that sensitisation ageing at 750°C can render the material enhanced susceptible to stress corrosion cracking at even low chloride deposition densities of ≤145 µm/cm². However, it could be shown that short-term heat treatments at 475°C can decrease corrosion and stress corrosion cracking susceptibility which may be used to improve the materials performance. Mechanistic understanding of stress corrosion cracking phenomena in light of a comprehensive microstructure characterisation was the main focus of this thesis.

Declaration

No portion of the work referred to in this thesis has been submitted in support of an application for another degree or qualification of this, or any other university, or other institute of learning.

Manchester, in the August 2015

Copyright Statement

Candidates Background

I was born in Aalen, in the Swabian Eastern Alp, in Germany in 1984. I finished my first education at the school *Schillerschule Aalen* in 1999 and decided to become a car mechanic straight after.

I completed my apprenticeship in a local urban bus company in cooperation with the *Technical School of Aalen* in 3.5 years with distinction.

Further on, I carried forward my education at the *Technical School in Aalen* and completed my GCSE also with distinction. Subsequently, I went to the high school *Technische Oberschule* in Stuttgart and achieved my A-levels certificate which opened me the door to enter a university. Prior to my university life, I fulfilled my national civilian service obligation at a hospital in Stuttgart.

I studied surface and materials engineering at *Aalen University of Applied Science* and achieved my bachelor's degree in 2011 with distinction. The title of my final year project was "*Thermal Heat Treatments of Duplex Stainless Steels in the 400 to 550°C Temperature Range and their Influence on the Corrosion Properties"* and was in collaboration of *Aalen University* and the *University of Manchester*.

Later on, I joined the Corrosion and Protection Centre and Materials Performance Centre of the *University of Manchester* and enjoyed working with Dr Dirk L Engelberg, whom I am most grateful for, on the *Performance Characterisation of Duplex Stainless Steel in Nuclear Waste Storage Environments*.

Acknowledgement

I would like express my cordially thanks and respect to **Dr Dirk L Engelberg**, my academic supervisor, for his endless support, unpayable knowledge-share, and smooth communication during my doctoral education. I have been utmost appreciating his technical guidance but also his warm welcome and help in personal and family-related issues. I will keep his friendly nature always in good remembrance.

My deep appreciations are expressed to **Mr Paul Jordan** who was always supportive in technical problems. I also thank to **Dr John Walton**, senior experimental officer, for his support in atomic force microscopy and his willingness in fruitful scientific discussions. I would like to further thank to **Mr Micheal Faulkner**, **Mrs Xiangli (Shirley) Zhong**, **Mr Teruo Hashimoto**, **Mr Octavia Cuica**, **Mr Christopher Wilkins**, and **Mr Ali Gholinia** for their support in electron microscopy and related techniques. I am also grateful for **Mr Garry Harrison** for his endless support in x-ray diffraction stress measurements. I also thank to **Mr Hong Liu** for his support in white light interferometry. I owe much appreciation to **Mr Sam McDonald** and **Mr Fabien Leonard** who were extremely helpful in conducting computed x-ray tomography tests and data analysis.

I gratefully acknowledge **my colleagues** in the **Materials Performance Centre** and **Corrosion and Protection Centre** with whom I had fruitful relationship whether academic or in private. I wish them to successfully complete their project with best achievable mark. I thank **Prof M Grace Burke**, **Dr Nicholas Stevens**, **Dr Fabio Scenini**, **Prof Stuart B Lyon**, **Dr Anthony Cook**, **Dr Jonathan Duff**, and others for their support in different scientific area and related discussions.

My last but my greatest appreciations I would like to devote to are **my dear mum**, **my lovely wife,** and **my dear brother** who have been always caring for me, more than I did for myself! I am regretful for the time being away from them and appreciate their understanding and endless support.

There are feelings which cannot be expressed by words, and I am in a moment in which I cannot do more than expressing my thanks to **our Lord** who granted me health and opportunity to fulfil my dreams which I was dreaming many years ago.

Dedication

Devoted to my mum, wife, and brother…

1 Introduction

Radioactive nuclear waste (or radwaste) is the solid, liquid, or gaseous form of substances produced by nuclear power, and is categorised according to its amount and radioactive level. *Intermediate-level wastes (ILW) are heavily contaminated materials which became radioactive by time and form the majority of radioactive wastes, requiring proper shielding against radionuclide migration.*

The Radioactive Waste Management Directory (RWMD) of the Nuclear Decommissioning Authority (NDA) of the UK has developed a generic disposal concept which envisages the emplacement of ILW in a geologically-isolated environment. The waste form is immobilised and packaged in physical containments made from stainless steels to as-called waste packages (see Figure 1-1). All packages are stored aboveground on site of waste origin for up to 150 years in so-called interim storages, and will be transported to a suitable geological disposal facility (repository) to be emplaced in large purpose-built vaults excavated at depths between 300-1000 metres. The waste packages are envisaged to be geologically isolated after a storage period of up to 350 years before closure of the repository [1-3].

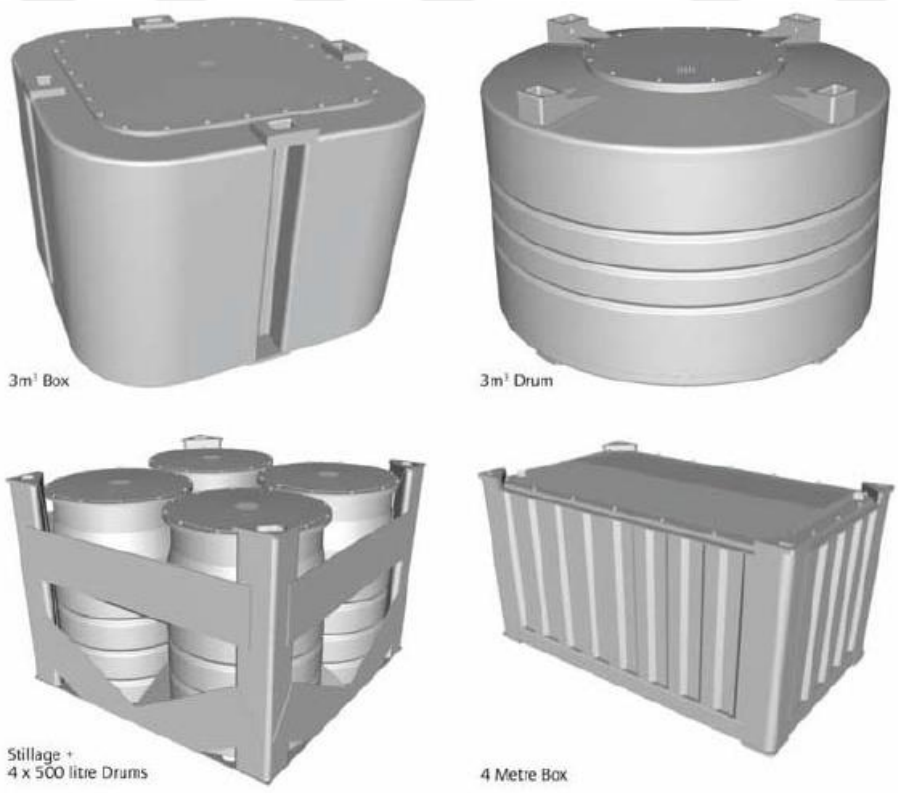

Figure 1-1: Standard waste containers for ILW [6]

Stainless steels have been decided as package material for ILW encapsulation which render sufficient performance in nuclear cross capture as shielding against radionuclide migration and good mechanical properties with high corrosion resistance. Thousands of waste containers made from 316L and 304L austenitic stainless steels have been manufactured, and so far 25,000 m³ ILW have been successfully encapsulated into 47,000 packages and emplaced in storage facilities.

The main potential harm to the structural integrity of stainless steel containers is corrosion and stress corrosion cracking. Some minor corrosion cases have been recently observed on in-use austenitic waste storage canisters in an in-land warehouse in Culham at Oxfordshire after a storage time of ten years as shown in Figure 1-2; therefore, the likelihood of stress corrosion cracking occurrence over long-term storage has remained [4, 5]. Duplex stainless steels have been recommended as a replacement option, and ILW containers have already been manufactured from grade 2205 duplex stainless steels within the last few years.

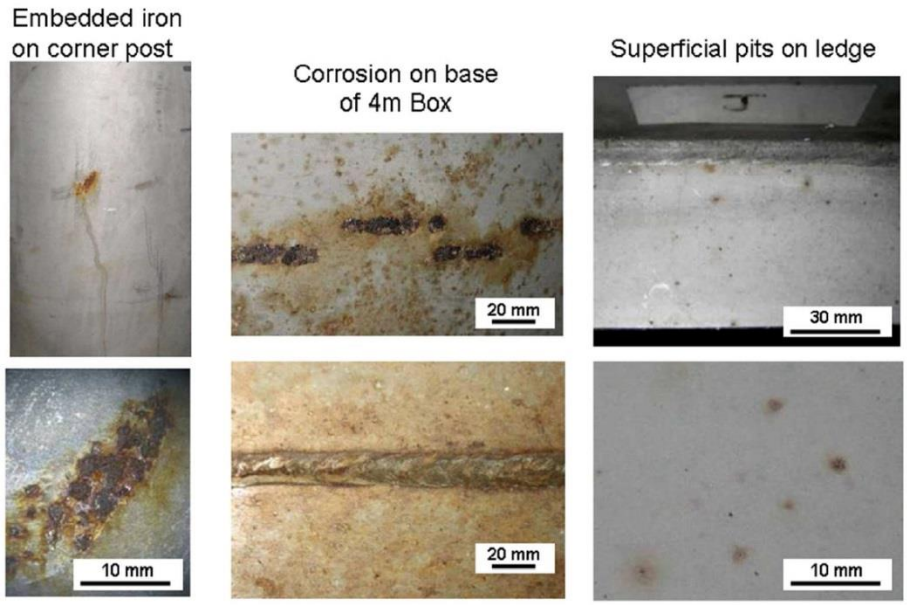

Figure 1-2: The surface of 304L prototype ILW-container after exposure to ~10 years in the inland warehouse in Culham, Oxfordshire; Both photographs in the middle show an area of embedded iron (contamination) and areas underneath the base of the container (including welds) which was exposed to high chloride contamination due to pick up of de-icing salt (in some measurements >100 µg/cm^2); photographs to the right show corrosion of horizontal ledges (chloride contamination ~10 µg/cm^2) [5].

The corrosive environment is set primarily by atmospheric contamination level, temperature, relative humidity and climatic fluctuations, container surface contamination, and deposited

impurities. There is an environmental and operational controlling approach to minimise or even block the effect of container corrosion. The relative humidity and temperature are key factors influencing corrosion processes. Therefore, the relative humidity (RH) is outlined by either keeping the amount of humidity well below the deliquescence point of any deposited salt or far above to dilute salt-laden deposits.

The first approach is preferred as this would ensure no corrosion over a long timeline. However, a relatively dry storage environment of <10% RH would need to be set which is practicable difficult to achieve. Therefore, the second approach reflects more suitable applicability where about 60% RH is set. The temperature of the storage facility is desired to be kept at ≤10°C which is below the critical pitting temperature of 304L stainless steel. The temperature of the containers during above-ground storage is unlikely to exceed 30ºC; however, there is a long-term target temperature of 50ºC in the repository [7].

The environmental and operational controlling approaches are corrosion mitigation measures only and are not sufficient to sustain the structural integrity of stainless steels containers. The container material in this respect has crucial importance and that is why high-alloyed stainless steels are required. The container materials corrosion is also set by the materials alloying chemistry and its microstructure. The effect of alloying elements on corrosion behaviour is well-known and do not require further studies in this respect. However, microstructure characterisation of duplex stainless steels has never been conducted in detail, and there is a lack of mechanistic understanding of corrosion and stress corrosion cracking processes at low temperatures (≤50°C).

Comprehensive studies about atmospheric stress corrosion cracking susceptibility with relevance to ILW storage and repository conditions exist for austenitic stainless steels, and it is known that 304L and 314L may be rendered susceptible to localised corrosion and stress corrosion cracking at and below 50°C. However, stress corrosion cracking susceptibility of duplex stainless steels has been less well characterised, and questions have been remained about the likelihood of stress corrosion cracking propensity in the ILW storage context, which will be handled in this thesis.

This thesis is structured in an alternative thesis format in which results and discussion sections are replaced by scientific journal papers which are categorised into three main chapters (see chapter 5). The first chapter (chapter 6) deals with microstructure

characterisation and the influence of strain and stress on the corrosion susceptibility of 2205 duplex stainless steel. Local Volta potential measurements have been correlated with strain heterogeneities induced by cold rolling in the microstructure, and the effect of different type of deformation modes have been discussed in light of stress corrosion cracking propensity.

The second chapter (chapter 7) handles environment-assisted cracking susceptibility in which hydrogen-assisted and chloride-induced stress corrosion cracking has been discussed. The propensity of 2205 duplex stainless steel to stress corrosion cracking in atmospheric environments in comparison to immersed conditions has been shown. It could be demonstrated that 2205 duplex stainless steel can be rendered susceptible to stress corrosion cracking under ILW storage-relevant conditions, and that the microstructure constituents; ferrite and austenite show different corrosion and cracking behaviour. It could be further demonstrated that electron microscopy is required to see fine-scale micro-cracks formed under low-surface chloride deposition density conditions which may not be observable by conventional optical microscopy. The importance therein lies in the fact that non-observed cracks may lead to false conclusions causing serious impacts on long-term performance assessments. Furthermore, it could be shown that not only the atmospheric corrosion incubation time but also the corrosion rate, which can change by time, has importance to assess long-term structural container performance.

In the last chapter (chapter 8), the effect of furnace-sensitised microstructure (heat treatment) will be discussed in detail. The effect of low-temperature embrittlement also known as '475°C Embrittlement' on the corrosion performance has been introduced. The reasons for the change in corrosion performance have been elucidated by introduction of a corrosion model, which is the first in this kind, and showed how this phenomenon could be used deliberately to improve container corrosion's performance. Sigma-phase embrittlement and associated loss of corrosion and stress corrosion cracking performance has been discussed. Comprehensive microstructure investigations of sensitised microstructure containing various secondary phases produced during ageing have been made in light of localised corrosion performance of 2205 duplex stainless steel.

2 Motivation and Aim of Research

This PhD project ***"Performance characterisation of duplex stainless steel in nuclear waste storage environment"*** was a part of a large-collaborated project with focus on *"In-situ time-dependent characterisation of corrosion processes in nuclear waste storage and geological disposal facility environments"*, in which University of Manchester was partnered with the University of Birmingham (Dr A. Davenport), University of Bristol (Dr T. Scott), and the Diamond Light Source (Prof T. Raymond). The project was funded by the EPSRC and NDA through research grant NDA/EPSRC (EP/I036397/1).

The motivation for the research was to gain in-depth knowledge about atmospheric stress corrosion cracking propensity of 2205 duplex stainless steel at low temperatures and mild corrosive conditions. The aim was to obtain a mechanistic understanding of the effect of annealed and sensitised microstructures, external load, and residual stress on the material corrosion performance.

ILW storage- and repository-relevant exposure conditions that are low-surface chloride deposition density levels at 50°C were chosen as testing environments. As-received, heat-treated, and cold-worked microstructures were investigated in detail. Comprehensive microstructure characterisation was carried out to develop mechanistic understanding of atmospheric corrosion and stress corrosion cracking processes.

3 Literature Review

In this chapter basic metallurgical and corrosion aspects are aimed to be delivered with a wider introduction into atmospheric corrosion and atmospheric-induced stress corrosion cracking.

3.1 Basic Metallurgical Aspects

Solids are formed from liquids by the process so-called solidification. In the liquid state, atoms are randomly mobile and become rigidly fixed after solidification. A rigid solid body is called crystal when atoms are regularly and periodically placed, otherwise the non-crystalline structure is amorphous. Crystalline solids consist of a repeating pattern of their components in three dimensions, the so-called crystal lattice. The smallest repeated unit of a crystal is a unit cell and contains all information about the entire three-dimensionally symmetrical crystal (Figure 3-1).

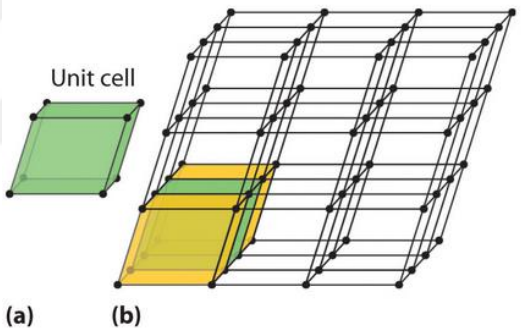

Figure 3-1: (a) A three-dimensional unit cell and (b) the resulting regular three-dimensional lattice [8]

There are seven fundamentally different kinds of unit cells which differ in size and geometry (Figure 3-2). The unit cell can be described by the relative length of two edges and the angle between them. In the cubic unit cell all sides have the same length and all angles are 90°. There are other cells with different side lengths and angles possible.

Iron crystallises with a body-centred cubic (BCC) crystal structure, but is allotropic i.e. it can appear in different crystal structures (Figure 3-3). Iron is alloyed with various elements to produce materials with desired properties. As long as iron is the base metal, the matrix will be

either BCC or FCC (face-centred cubic) structured depending on the chemical composition and processing history of the alloy.

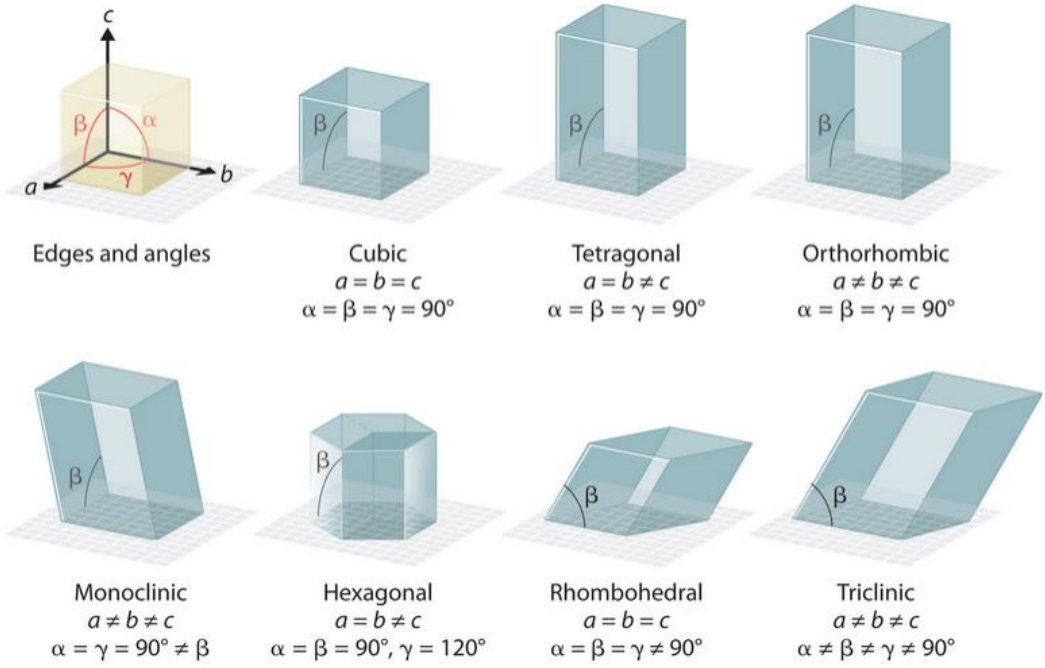

Figure 3-2: General features of the seven basic unit cells. The lengths of the edges of the unit cells are indicated by a, b, and c, and the angles are defined as: α, the angle between b and c; β, the angle between a and c; and γ, the angle between a and b [8]

The positions of the iron atoms define the crystal structure. In the BCC lattice one iron atom is located in the centre of the unit cell and eight other iron atoms are situated at the corners of the cubic cells by one eighth only (Figure 3-3). There are in total two atoms in the cubic cell filling 68% of the cube space. The atoms are in touch in the space diagonal where atomic motion along this line is mostly favoured. In contrast, there is one atom placed in the centre on each cube face in the FCC lattice belonging with the half volume of the atom to the unit cell with also eight further atoms situating on the edges forming all together 4 atoms in space, which is 74% of the cube (Figure 3-3). The atoms in the FCC lattice touch along the face diagonal and are closely-packed. The atoms are more mobile in the FCC lattice due to the higher packing density and more motion directions.

Alloying elements are either substitutional or interstitials depending on their atomic size, chemical nature (binding strength), and their positions in the lattice. Basically, all metals in the iron matrix replace the position of an iron atom in the lattice and are therefore substitutionals. Their atomic diameters do not differ so much than light and small elements

such as carbon and nitrogen, which are interstitials, and are located in interstitial vacancies in the lattice, as schematically illustrated in Figure 3-4 (lattice strain can be caused). However, in certain conditions chemical bonding between interstitials and substitutionals can be energetically favoured so that both can form a new lattice in which the interstitials can take the position of a lattice atom (such as in intermetallic or intermediary phases).

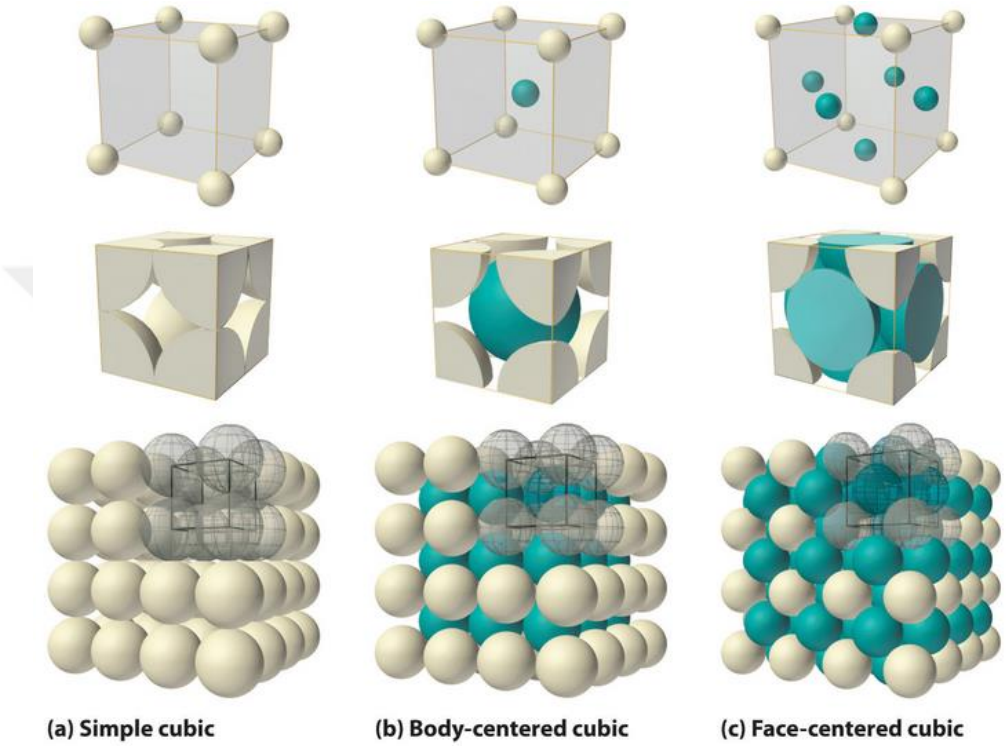

Figure 3-3: Three cubic unit cells: (a) simple cubic (b) body-centred cubic, (c) face-centred cubic. There are three representations for each: a ball-and-stick model (top), a space-filling cutaway model that shows the portion of each atom that lies within the unit cell (middle), and an aggregate of several unit cells (bottom) [8]

The BCC iron, in pure or as an alloy, has been known as ferrite and the FCC one as austenite. Both ferrite and austenite are distinct phases in an iron-based microstructure. A phase is a microscopically homogeneous region with distinct chemical and physical variances in the microstructure. In the metallurgy nomenclature, ferrite is known as alpha (α) or delta (δ) and austenite as gamma (γ). Depending on the chemical composition of iron alloys either ferrite or austenite is first formed during solidification. For example, if iron is alloyed by 5% nickel and 25% chromium, then ferrite is primarily formed during solidification and austenite is precipitated by the consumption of ferrite regions. Delta ferrite (δ) is therefore the matrix in the microstructure, and austenite can be precipitated in the ferrite matrix. Hence, the alloying chemistry determines the structure of the microstructure.

Iron is often alloyed by chromium and nickel. To make it stainless at least 10.5 wt.-% of chromium is needed. The alloying elements influence the existence fields of ferrite and austenite regions. Thermodynamically distinct phases can be shown in phase diagrams. In Figure 3-5 the Fe-Cr-Ni ternary phase diagram is shown. Distinct existence areas of ferrite and austenite regions can be seen in the dependency of temperature and chemical composition.

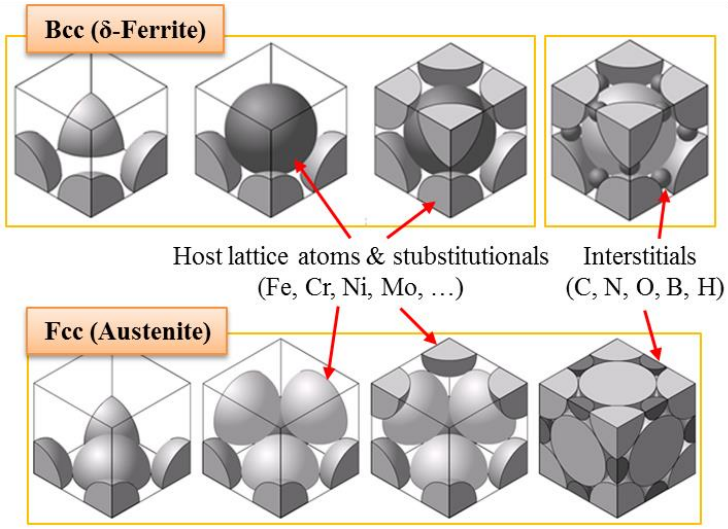

Figure 3-4: Crystal structures of ferrite and austenite showing the positions of alloying elements [9]

Iron is the matrix-forming element in stainless steels, therefore, both ferrite and austenite phases accommodate all alloying elements. Both phases; austenite and ferrite have characteristic properties which are important to know. Due to its atomic nature and crystallographic structure, ferrite is ferromagnetic and less closely-packed than austenite which is paramagnetic. Ferrite is less plastically deformable than austenite, but is harder and stiffer, and the thermal expansion coefficient of ferrite is lower than that of austenite [10].

Alloying elements are categorised into ferrite formers and austenite formers. It is the ferrite forming elements which increase the existence field of ferrite, and the austenite formers increasing that of austenite. In other words, ferrite formers limit or inhibit the formation of austenite, and austenite formers increase the level of austenite.

It is important to know the microstructure which highly determines material properties. The microstructure can be predicted using the constitution diagram introduced by *Schaeffler*

(Figure 3-6). Chromium and nickel are the most important alloying elements in stainless steels; therefore, all alloying elements have been quantified as Cr and Ni equivalents. The alloying elements contribute to Cr or Ni equivalents according to their strength as such:

Ni (eq) = Ni + (30 x %C) + (0.5 x %Mn) + (30 x %N)

Cr (eq) = %Cr + %Mo + (1.5 x %Si) + (0.5 x %Nb) + (5 x %V) + (3 x %Al)

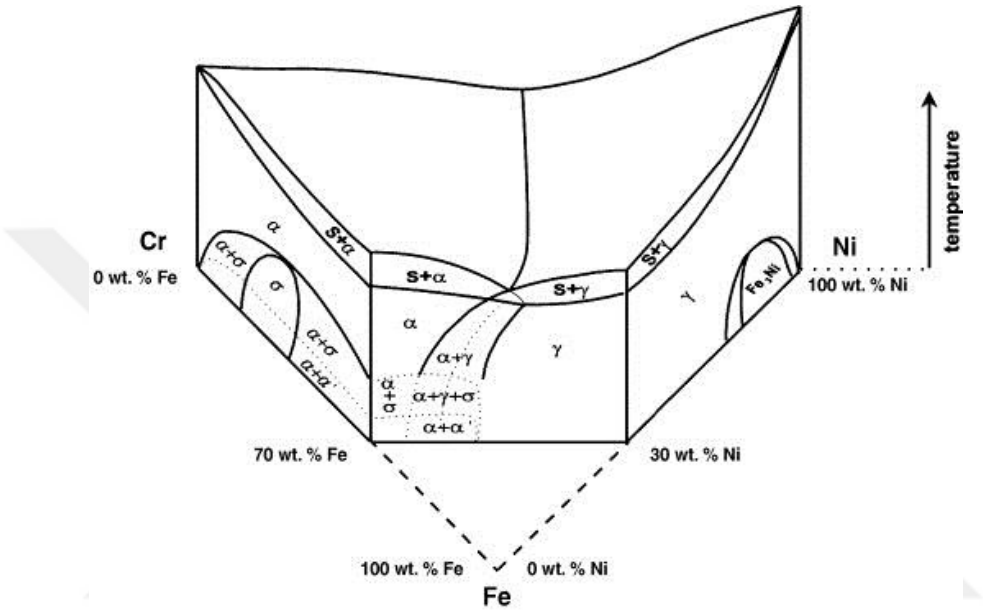

Figure 3-5: Fe-Cr-Ni phase diagram [11]

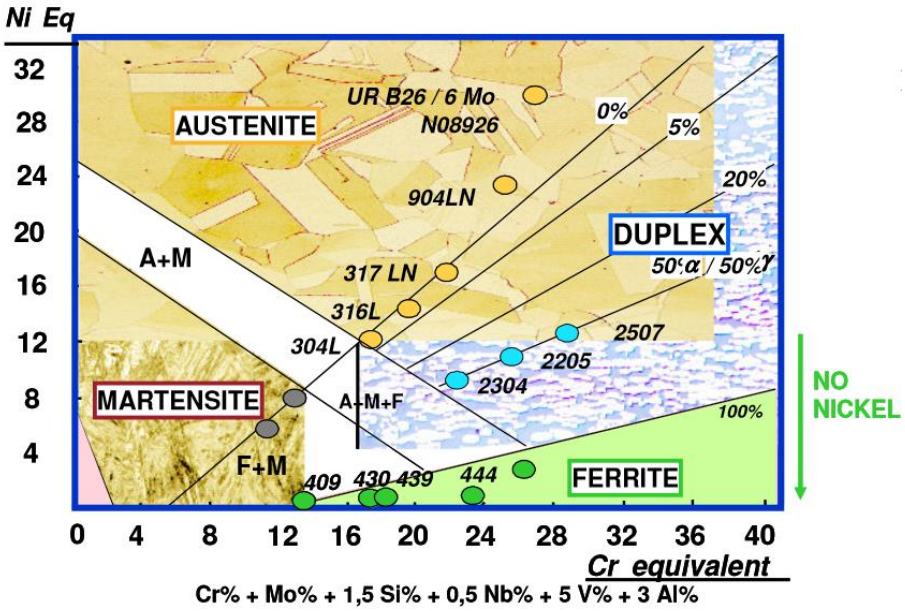

Figure 3-6: *Schaeffler* constitution diagram of stainless steel weld metal. Ni and Cr equivalents are given in wt.-% [12, 13].

The *Schaeffler* constitution diagram can be used to predict the microstructure levels from the chemical composition by comparing the effects of austenite and ferrite stabilising elements.

3.2 Basic Deformation Aspects

The crystal structure and the packing density determine the deformation behaviour of a metal. The ability to undergo permanent deformation is called ductility, and the amount of work necessary to break a material is called toughness. The principal deformation process in ferrite is slip in ⟨111⟩ directions at (110), (112), and (113) planes. The combination of slip direction and slip plane is the slip system. Dislocation movement is preferred on slip planes, and it is easier if the crystal have closest-packed slip systems. The austenite has the highest possible packing density with 4 {111} closest-packed slip planes and 3 ⟨111⟩ slip directions resulting in 12 closest-packed slip systems. Therefore, austenite has the best deformation capacity of all Bravais lattice types. All {111} slip planes of austenite are illustrated in Figure 3-7.

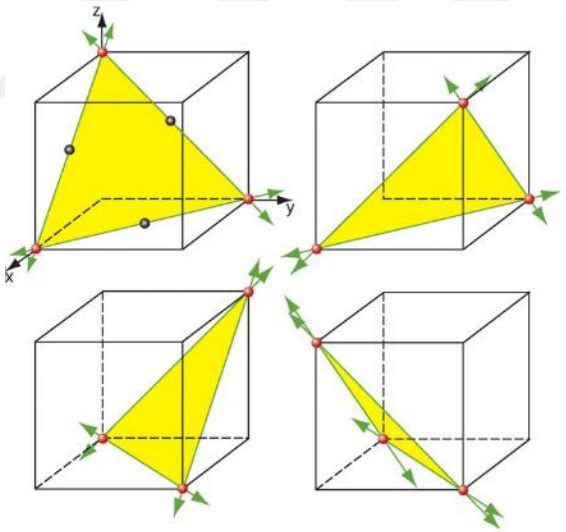

Figure 3-7: (111) slip planes of FCC (austenite) [14]

Due to their less packing densities bcc lattice structures (ferrite) miss closest-packed systems. Only ⟨111⟩ directions are closest-packed, and atoms can slip on these directions only. However, deformation processes involve edge dislocation movements for which slip planes need to be taken into account (not only slip direction). Ferrite is quite difficult to deform and

is, therefore, hard in nature. However, in the ferritic lattice relatively-closest-packed slip planes are formed which facilitate plastic deformation to some extent.

For the ferrite there are

- 6 {110} slip planes with 2 slip directions in ⟨111⟩ = 12 slip systems (Figure 3-8),
- 12 {111} slip planes with 1 slip direction in ⟨111⟩ = 12 slip systems (Figure 3-9),
- 24 {113} slip planes with 1 slip direction in ⟨111⟩ = 24 slip systems (Figure 3-10); hence, in total 48 relatively-closest-packed slip systems.

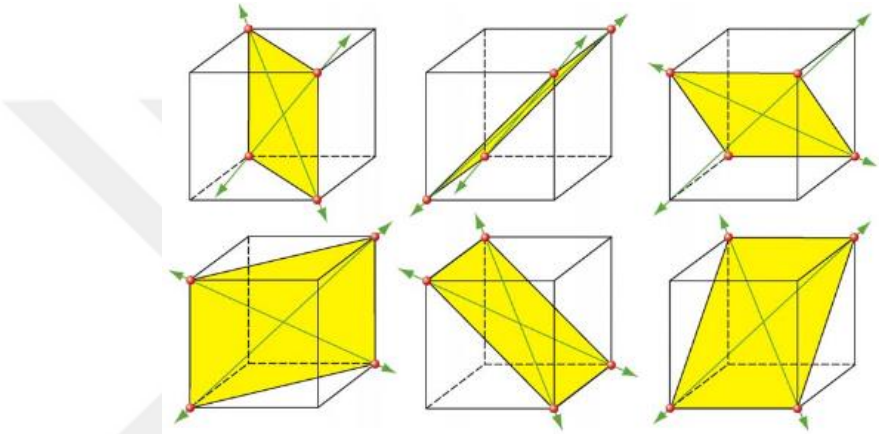

Figure 3-8: (110) slip planes of bcc [14]

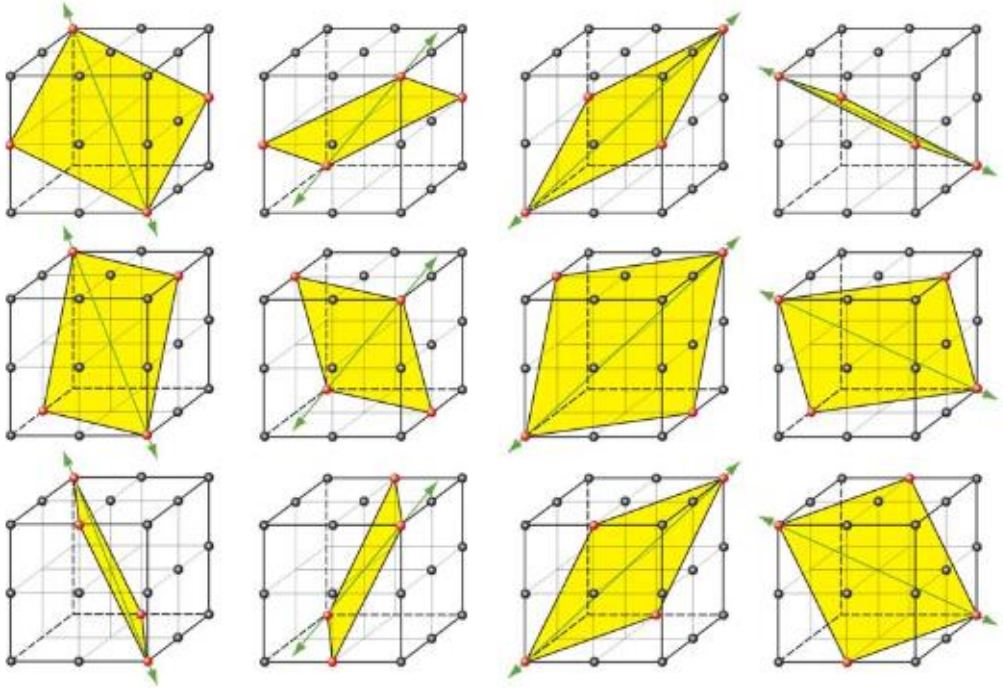

Figure 3-9: (112) slip planes of bcc [14]

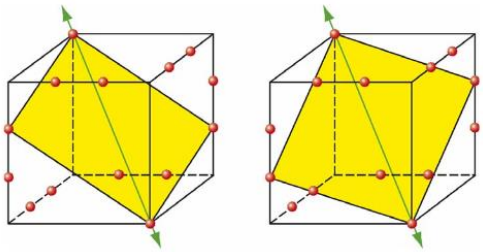

Figure 3-10: (123) slip planes of bcc [14]

All slip planes and directions for ferrite and austenite are summarised in Table 3-1.

Table 3-1: Sip systems [14, 15]

Lattice	Example	Unit cell	Slip plane			Slip direction	Total slip planes
			type	amount	Type		
FCC	Fe_{γ} Al Cu Ni	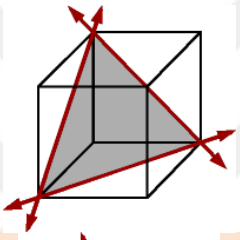	{111}	4	⟨110⟩	3	12
BCC	$Fe_{\alpha/\delta}$ Mo W Nb	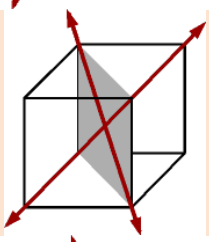	{110}	6	⟨111⟩	2	12
	$Fe_{\alpha/\delta}$ Mo W Nb	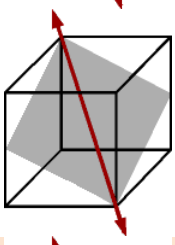	{112}	12	⟨111⟩	1	12
	$Fe_{\alpha/\delta}$ W_{α} Mo	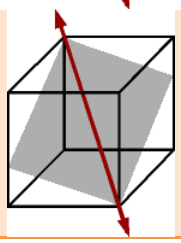	{123}	24	⟨111⟩	1	24

The consequence of lattice structure formation is the occurrence of stacking faults that are imperfections in the lattice sequence leading to an inconsistence stacking sequence of atomic planes. Stacking faults are like grain boundaries two-dimensional planar defects. Stacking faults disrupt slip planes and hinder slip processes. If an atomic plane is missing in the

stacking sequence, it results in an intrinsic stacking fault. If an atomic plane is inserted in the sequence, it results in an extrinsic stacking fault. If the atomic plane sequences reverses themselves in a mirror plane it results in a twinning fault [16]. Twinning mostly occurs in the austenite phase, but can also occur in the ferrite.

The stacking fault energies in the ferrite are higher than those in the austenite. Therefore the deformation process in ferrite is much more energy-consuming than in austenite. In austenite the deformation process can be slip on the $\{111\}\langle 111\rangle$ systems as well as by twinning, whereas the principal deformation process in ferrite is slip in the $\langle 111\rangle$ direction in the (110), (112), and (123) planes [17]. If twinning are formed in ferrite these are then (11-2) [11-1] systems. The twinning systems of ferrite and austenite are summarised in Table 3-2 [16].

Table 3-2: Twinning ferrite (BCC) and austenite (FCC) [16]

Crystal Structure	Twinning Planes	Twinning Directions
FCC	(111)	[11-2]
BCC	(112)	[11-1]

3.2.1 Cold deformation

Cold deformation is plastic deformation of a material at low temperatures (maximum 40% of the melting point). Cold deformation induces strain hardening in the lattice by increasing the dislocation density, and leads to changes in the material and corrosion properties. The deformation behaviour is determined by the crystal structure of the material, the deformation history i.e. the temperature at which the deformation was processed, and the strain rate. The type of deformation mode can also have influence on the microstructure development.

3.2.1.1 Cold Rolling

Materials are run through cold-rolling processes in order to achieve desired shapes with good dimensional accuracy and surface finish. The amount of strain introduced determines the hardness and other material properties. Usually, the hardness and strength are increased by the cost of a reduction of toughness and ductility. Cold rolling introduces compressive strains leading to a squeezed microstructure in the compression direction and elongated un-equiaxed grains in the rolling direction as illustrated in Figure 3-11.

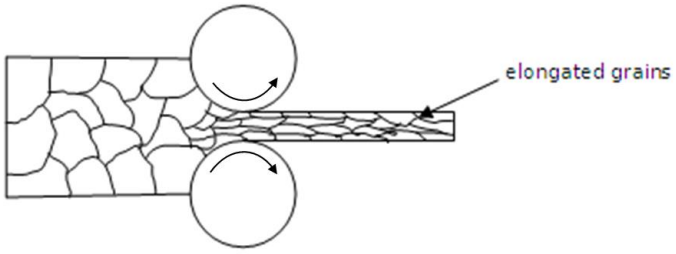

Figure 3-11: Cold-rolling process

3.2.1.2 Bending Deformation

Bending or flexure characterises the deformation behaviour of a structural element of which one dimension is, typically, 1/10 of the other structural dimensions. On the outer surface of the bent material, the beam, tensile stresses are formed, and on the inner radius compressive forces are acting on. There is no stress acting on the interface zone between both tensile and compressive regions, the neutral axis. A bent beam is illustrated schematically in Figure 3-12.

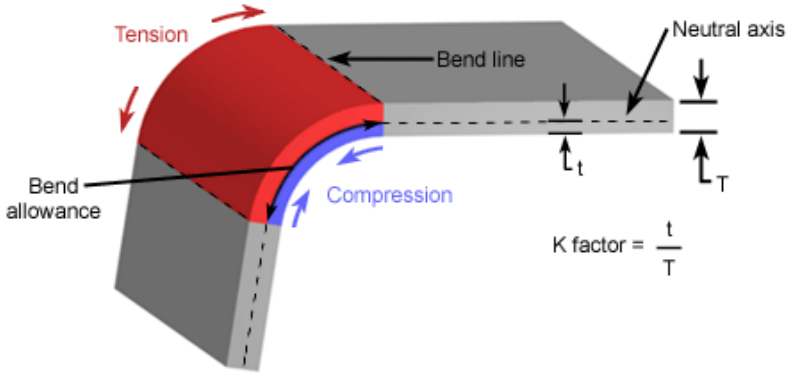

Figure 3-12: Bending deformation [18]

3.2.1.3 Tensile Deformation

Tensile deformation is the elongation of the material with typical uniaxial path of load. Tensile strain is usually used to express an increase in length. A reduction in length would be compressive strain. Strain is a measure of deformation and is dimensionless. It represents the displacement of segments or units in a material relative to a reference length.

3.3 Stainless Steels

Stainless steels contain ≥10.5 wt.-% chromium in which the chromium atoms are statistically-inordinately dispersed in the microstructure, with low amounts of carbon typically ≤0.03 wt.-% and further interstitial and substitutional alloying elements. 'Stainless' is the capability of steels staying chemically inert against corrosion in non-aggressive environments [15, 20-23]. Under high oxygen, low salinity, and good circulation environments stainless steels do not readily corrode, rust, or stain with water.

Stainless steels are highly alloyed and contain a multi-component microstructure. The Fe-Cr-Ni ternary phase system determines mainly the number and types of phases that are present, the composition of each phase, and the microstructures that exist. However, further alloying elements shift the existence fields of equilibrium phases (solubility boundaries), and the resulting phase diagram can be highly complicated. The majority of stainless steels contain 11-30% Cr, and ~1-25% Ni, and other alloying elements such as N, Mo, Mn, etc. The ternary system of Fe-Cr-Ni was earlier introduced in Figure 3-5.

The metallurgical fabrication of modern stainless steels is well-defined and the microstructure, therefore, does not contain any impurities, which are un-desired chemical traces in the microstructure. Modern alloys can be engineered with ppb precision in order to achieve optimised material metallurgy. Chemical composition and microstructure specifications are highly-controlled and adjusted for desired applications.

Stainless steels are classified according to their microstructure, as shown in Figure 3-13.

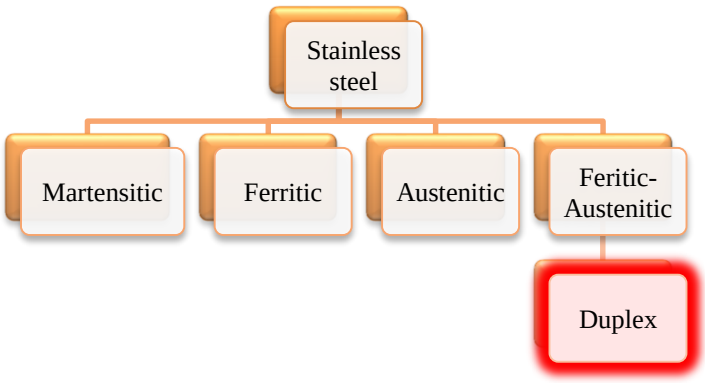

Figure 3-13: Classification of stainless steels

The microstructure is set by the chemical composition and heat treatments followed by rapid quenching. In following all stainless steel types will be shortly introduced.

3.3.1 Martensitic Stainless Steels

Martensite is in nature a hard phase. Stainless steels containing 11-13% Cr can show martensitic structure (α') which is transformed after proper heat treatment in the ferrite-austenite region with subsequent quenching (γ → α'). Martensitic stainless steels combine high strength with good fracture toughness, and are corrosion resistant. The microstructure of this alloy group is not fully martensitic. Martensite is the strengthening factor and shares with ferrite and austenite certain proportions of the microstructure. Martensitic stainless steels are not considered as ILW container materials due to their lower corrosion resistance and brittleness.

3.3.2 Ferritic Stainless Steels

Ferritic stainless steels contain in general 13-17% Cr and show a fully ferritic microstructure. A typical microstructure of ferritic stainless steels is representatively shown in Figure 3-14(c). Ferrite grains show typically wavy grain boundary structures with convex or concave form. The grains can be irregularly shaped with varying grain sizes. Ferritic stainless steels are not considered as ILW container materials due to their low toughness and formability, susceptibility to embrittlement, notch sensitivity, and poor weldability. Ferritic stainless steels are highly susceptible to hydrogen-induced stress corrosion cracking due to the high diffusivity of interstitial elements in the BCC lattice structure and very low solubility. Reactive hydrogen atoms can penetrate easily into the ferritic microstructure and block or hinder dislocation movements. Moreover, at higher lattice defect sites, such as grain boundaries, reactive hydrogen atoms can recombine to hydrogen molecules and induce cracks.

3.3.3 Austenitic Stainless Steels

Austenitic stainless steels have austenite as primary phase which contain Ni, Cr, Mn and N as main alloying elements. A typical microstructure of austenitic stainless steels is shown in Figure 3-14(a). The grain boundaries of austenite grains are typically straight and not waved.

The shape of the grains appears more discretely than ferrite grains. Large fractions of twin boundaries are present within the grains, usually 10-30%.

High Cr and Ni contents suppress the transformation from austenite to ferrite during cooling and keep the microstructure (almost) fully austenitic. This is attributed mainly to nickel which maintains the austenite phase on cooling, and chromium which slows the transformation kinetics down. Austenite stabilisers; N and Mn contribute to the phase stability of the austenite more than nickel.

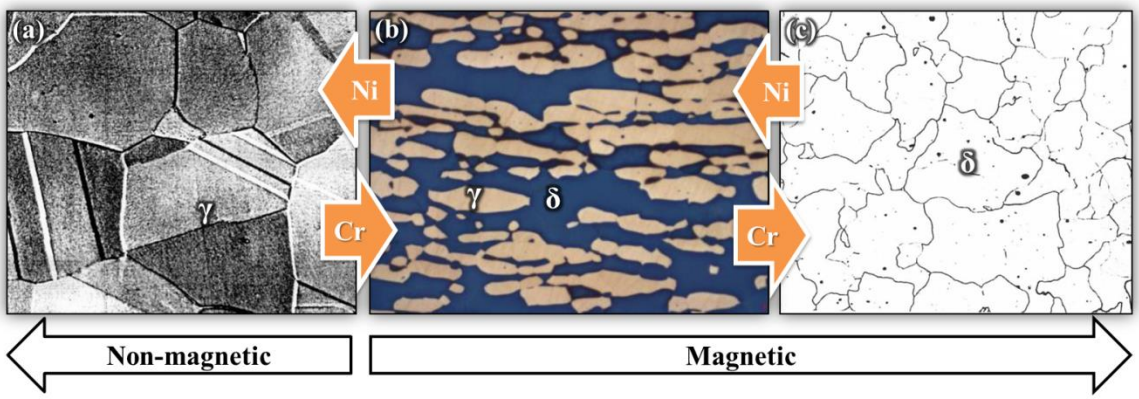

Figure 3-14: Microstructure of (a) austenitic [28], (b) austenitic-ferritic (duplex), and (c) ferritic [28] stainless steels. Note the distinguishable grain boundary characters of ferrite and austenite phases. The average grain sizes of forged stainless steels are typically in the range of 5-30 µm.

Austenitic stainless steels have high ductility and low yield stress in comparison to other types of stainless steels. Their good toughness stems from the FCC structure which provides more planes for the flow of edge dislocations. Hardness enhancement can be achieved through mixed crystal strengthening or cold-working only, and not by heat treatment.

The microstructure can contain remaining ferrite (δ) up to 10 vol.-% which increases the hardness and chloride stress corrosion cracking resistance, and is therefore desired in the microstructure.

Austenitic stainless steels can contain up to 0.08 wt.-% carbon which makes this type of steel highly prone to metallic carbide precipitation at grain boundaries causing sensitisation. Sensitisation is the enhanced localised corrosion susceptibility due to evolution of often chromium depletion zones at and adjacent to precipitates formed, which are often situated at grain boundaries. Welding processes are integrated in the manufacture of ILW canisters

which can render susceptible the welded region and heat-affected zones to sensitisation and, hence, to localised or intergranular corrosion.

The most common austenitic stainless steels are widely known as the 300 series. Most ILW containers have been manufactured from 316L and 304L austenitic stainless steels. Grade 304 was introduced after the 1970's when argon oxygen decarburisation and vacuum oxygen decarburisation techniques were used to remove carbon from the bulk material. Later, lower carbon-containing type 304L, indicated with L (<0.03% C), was introduced which shows lesser sensitisation susceptibility. The more localised corrosion resistant alloy; 316L with 2-3% Mo adding was introduced for more critical applications.

Table 3-3: Material specifications of some stainless steels [24, 25]

	Alloy		Chemical Analysis (wt.-%)				PRE_N	Mechanical Properties		
Grade	UNS	EN	C	Cr	Ni	Mo		Proof Stress [MPa]	Tensile [MPa]	Elongation [%]
304L	S30403	1.4307	0.03	18.5	9	-	19	200	500-700	40
316L	S31603	1.4404	0.03	17	11.5	2.1	24	220	520-670	40

Austenitic grades have limitations in severe application cases. Austenitic stainless steels can experience stress corrosion cracking if used in atmospheric corrosive environment where the temperature, local chemistry (contamination), and residual stress interaction have sufficient severity [26].

3.3.4 Duplex Stainless Steels

Duplex stainless steels contain ≥11% Cr and consist of a bi-phase microstructure of ferrite (δ) and austenite (γ) in balanced amounts, typically in a 50:50 ratio. The phases are equally distributed and δδ-, δγ- and γγ-grain boundaries form the microstructure [21, 23, 27]. The ferrite is enriched in ferrite-former elements and the austenite is enriched in austenite formers. In Figure 3-14(b), a typical microstructure of a duplex stainless steel is shown. Alloying austenite with chromium leads to the development of ferrite. In contrary, alloying ferrite with nickel leads to the formation of austenite.

Duplex stainless steels are hot-rolled during processing for grain refinement which can be additionally cold-rolled to optimise material properties and material shape. Consequently, the grain structure is elongated along the rolling direction forming non-equiaxed ferrite and

austenite grains with varying sizes and morphologies leading to inhomogeneous and microstructure orientation-dependent physical and electrochemical properties.

Duplex alloys have superior corrosion and mechanical properties to most common austenitic grades, and often overwhelm the performance of their austenitic counterparts [21, 29, 30]. The ferritic structure confers high mechanical strength with high chloride corrosion and stress corrosion cracking resistance, while the austenite renders high toughness with good hydrogen stress corrosion cracking resistance [29]. The ferrite has a low solubility for interstitial elements, especially for hydrogen, resulting in high susceptibility to hydrogen stress corrosion cracking. The elemental diffusivity in ferritic phase is higher than in austenite (typically 100-times for e.g. carbon), causing precipitation, decomposition and phase transformation occurrence in or at ferritic grains with faster kinetics [31].

Austenite grains can dissolve more interstitial elements (~1000-times), such as N, H, C, and austenite former elements, such as Ni and Mn, whilst the ferrite is far more enriched with ferrite former elements (Cr, Mo, Si). Ferrite has a lower weldability than austenite, and is prone to low temperature embrittlement.

Duplex stainless steels are classified according to their chemical compositions as illustrated in Figure 3-15 [20, 21, 32, 33]. The pitting equivalent resistance number (PRE) is an empirical value which describes the corrosion resistance of a stainless steel in a corrosive environment. It is determined by the chemical composition of the alloy where the chemical elements Cr, Mo, and N are mainly counted [21, 34, 35].

If the corrosion behaviour of the stainless steel in the corrosive environment is unknown, the PRE_N can be taken as a “rule of thumb value” for estimation of material applicability. Chromium, nitrogen, molybdenum, and tungsten determine the PRE value of an alloy. If nitrogen is alloyed, this is denoted as PRE_N. However, there is an inconsistent use of these denotations. PRE_N and PRE are often used for the same purpose [21]. The higher the value the more corrosion resistant the alloy is against pitting corrosion. The elemental contribution to the PRE_N is different for each element and not consistent for all stainless steels [20, 21, 34]. However, as a typical guide, following mathematical formulas are sufficient for the most stainless steels:

$PRE_N = \%Cr + 3.3 \times \%Mo$ (Ferritic stainless steels)

$PRE_N = \%Cr + 3.3 \times \%Mo + 16 \times \%N$ (Austenitic stainless steels)

$PRE_N = \%Cr + 3.3 \times \%Mo + 30 \times \%N$ (Duplex stainless steels)

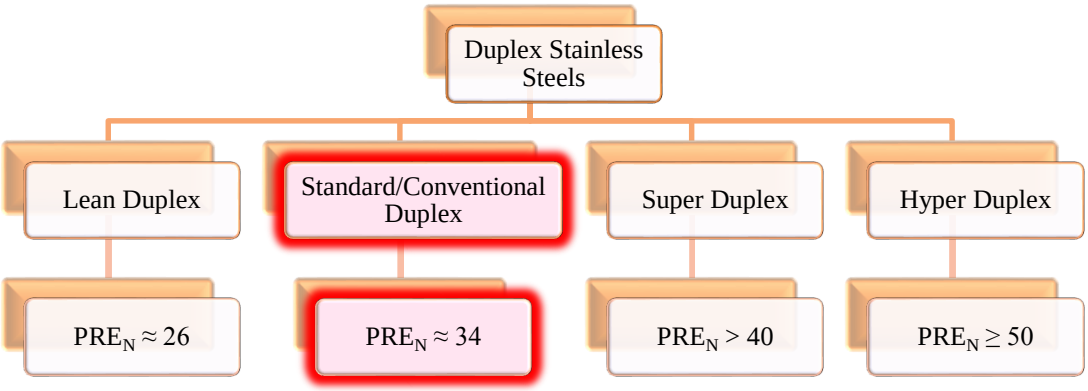

Figure 3-15: Categorisation of duplex stainless steels and their corresponding PRE_N value

According to the PRE_N values duplex alloys have higher pitting corrosion resistance than austenitic grades, thus these are more attractive materials for critical applications in corrosive environments.

3.3.4.1 Grade 2205 Duplex Stainless Steel

Grade 2205 duplex stainless steel is the most-commonly used and investigated duplex alloy. Usually, very low carbon (<0.03 wt.-%) is alloyed to impede sensitisation in the microstructure. "2205" is a trivial denotation and indicates the chromium and nickel composition, namely 22 wt.-% Cr and 5 wt.-% Ni. It has not become a trademark, and therefore inconsistent nomenclature can be found in the literature. For example, SAF 2205 is a Sandvik-owned trademark and derives from *S*andvik *A*ustenite *F*errite. DX 2205 and UR 2205 Mo is the same product manufactured by Arcelor Mittal. The Unified Numbering System (UNS) designation for alloy 2205 is S31803 and S32205; their difference is shown in Table 3-4.

The Euronorm denotation for 2205 is X2CrNiMoN22-5-3 and its number is EN 1.4462. Typical physical properties of 2205 are given in Table 3-5.

Table 3-4: Chemical composition of grade 2205 DSS [36]

Grade		C	Mn	Si	P	S	Cr	Mo	Ni	N
2205 (S31803)	Min	-	-	-	-	-	21.0	2.5	4.5	0.08
	Max	0.030	2.00	1.00	0.030	0.020	23.0	3.5	6.5	0.2
2205 (S32205)	Min	-	-	-	-	-	22.0	3.0	4.5	0.08
	Max	0.030	2.00	1.00	0.030	0.020	23.0	3.5	6.5	0.2

Table 3-5: Physical properties of grade 2205 DSS [36]

Elastic Modulus (GPa)	Yield Strength 0.2% Proof, min (MPa)	Tensile Strength, min (MPa)	Elongation (% in 50 mm)	Hardness (HB)
200	450	620	25	293 max

Grade 2205 provides superior pitting and crevice corrosion resistance to grade 316L in almost all corrosive environments. Its yield strength is twice higher than that of a 316L austenitic grade, and also provides a more profitable weight to cost ratio.

3.3.4.2 Grade 2507 Super Duplex Stainless Steel

Grade 2507 is a super duplex stainless steel containing 25% Cr and 7% Ni. Its chemical compositions can be taken from Table 3-6.

Table 3-6: Chemical composition of grade 2507 DSS [37]

Grade		C	Mn	Si	P	S	Cr	Mo	Ni	N
2507 (S32750)	Min	-	-	-	-	-	24.0	3.0	6.00	0.24
	Max	0.030	1.20	0.80	0.035	0.020	26.0	5.0	8.00	0.32

UNS number of 2507 is S32507. As this grade is higher alloyed superior corrosion and physical properties are achieved to the conventional duplex grade 2205. The Euronorm denotation for 2507 is undetermined, however most common 2507 duplex grade are known for 1.4507, 1.4410 and 1.4501.

Table 3-7: Mechanical properties of grade 2507 [37]

Yield Strength 0.2% Proof, min (MPa)	Tensile Strength, min (MPa)	Elongation A5 (%)	Hardness (HB)
550	750	15	310

3.4 Secondary Phases and Precipitates in Stainless Steels

Duplex stainless steels are highly-alloyed materials and can be, therefore, prone to numerous precipitation and phase transformations, which usually lead to sensitisation and embrittlement. There have been a large number of precipitations and phase reactions reported to occur in stainless steels [15, 20, 21, 27, 29, 35, 38-57]. Secondary phases are undesired due to their counter effects on corrosion and mechanical properties. The most important precipitates relevant for duplex stainless steels can be summarised and classified as

- Carbides;
- Nitrides;
- Chi/Sigma-Phase;

The composition and structure are exhaustively defined in the literature and listed in Table 3-8 [26].

Table 3-8: Possible precipitates formable in duplex stainless steels

Precipitate	Structure	Lattice Parameter [Å]	Composition*	Reference
$M_{23}C_6$	Face-centred-cubic	a = 10.57-10.68	$Cr_{16}Fe_5Mo_2C$	[26]
M_6C	Diamond cubic	a = 10.57-10.68	$(Fe,Cr)_{21}Mo_3C$; $(Fe,Cr)_5SiC$	[26]
MN	Cubic	a = 4.13-4.18	CrN	[26]
MN	Orthorhombic		CrN	
M_2N	Hexagonal	a = 2.8 c = 4.4	Cr_2N	[26]
Sigma	Hexagonal	a = 8.8 c = 4.54	(Fe,Ni,Cr,Mo]	[26]
Laves phase	Hexagonal	a = 4.73 c = 7.72	Fe_2Mo	[26]
Z phase	Tetragonal	a = 3.037 c = 7.391	CrNbN	[26]
Chi phase	Body-centred cubic	a = 8.807-8.878	$Fe_{36}Cr_{12}Mo_{10}$	[26]
G phase	Face-centred-cubic	a = 11.2	$Ni_{16}Nb_6Si_7$; $Ni_{15}Nb_6Si_7$	[26]
R phase	Hexagonal	a = b = 10.7 c = 19.87	FeCrNiMoSi	[58-60]

*Note that the composition is alloy-dependent

3.5 Basic Corrosion Aspects

Corrosion is the electrochemical reaction of a material with its environment and is a natural damaging process which can harm material structural integrity. The thermodynamic instability of metals is the reason for corrosion propensity which is expressed by the solubility potential of the metal in the corrosive environment. In nature, the metallic bonding is loose, and the material cohesion of metals is weak in contrast to covalent or ionic bonding. This phenomenon forces metals back to their thermodynamically more stable origin ionic bonding state; hydroxidic, carbonatic, sulphidic, or oxidic ores [15, 20, 61, 62]..

The aggressivity of reactive environments and the metal propensity to corrosion determine the extent of corrosion. The reactive environment is highly promoted if an electrolyte with aggressive ions (corrosion promoters) is present. Nowadays atmospheres contain aggressive compounds which can adsorb on metal surfaces and form with the presence of mist or moisture in the air corrosion-active electrolytes.

The electrolyte on the metal surface enables the formation of a so-called corrosion cell whereby sub-steps of corrosion reactions can occur on locally separated regions; the anode and cathode. The oxidation of a metal occurs on the anode, and its reduction on the cathode. Both have heterogeneous characters and happen at a metal/non-metal interface, and occur on the metal surface. Corrosion is a heterogeneous redox reaction at a metal/non-metal interface in which the metal is oxidised and the non-metal is reduced [15, 20, 61, 62].

3.5.1 Principles of Corrosion

All corrosion processes are based on two aspects; thermodynamics and kinetics. The thermodynamic aspect provides information about the possibility of corrosion reactions. This consideration formulates electrochemical equilibriums with the aim to find an assessment factor when an electrochemical reaction voluntarily takes place and when it happens with external forces only. The kinetics considers certain reaction retardations as a function of time of such possible reactions and makes a statement about reaction rates [15, 20, 61, 62].

3.5.1.1 Electrolytic Reduction-Oxidation of Metals (Redox)

In an electrochemical reaction electric charge is transported through the phase boundary layer metal/electrolyte (electrode) which is accompanied by a chemical exchange. In contact of a metal with an electrolytic solution (electrolyte), at the phase boundary metal atoms will oxidise and leave their atom sites of the metal matrix by migrating as positively charged ions (cation) into the solution, according to the following oxidation process:

$$M \rightarrow M^{z+} + ze^{-} \text{ (oxidation) (Eq. 1)}$$

This phenomenon is called oxidation and is illustrated in Figure 3-16(b). The driving force is the temperature (thermal movement), the solution force of the electrolyte (aggressivity), and the standard solubility/oxidation potential of the metal in the electrolyte. Some of the oxidised cations diffuse further towards the electrolyte and form with its anions ionic compounds while others stay at the metal/electrolyte interface and form with the remaining negatively charged metal matrix an electrolytic double layer which is schematically illustrated in Figure 3-16(c).

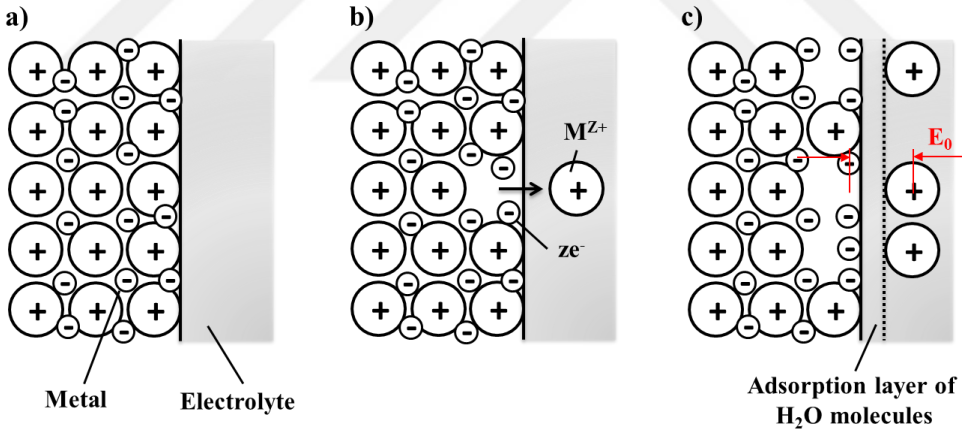

Figure 3-16: Schematic illustration of an electrolytic oxidation process occurring on the metal surface (re-drawn according to [15]): (a) showing immersion of a metal in an electrolyte (non-equilibrium), (b) showing electrolytic oxidation of metal ions M^{z+}, (c) showing interface metal/electrolyte with potential difference (equilibrium)

An electrostatic force, E_0 as pointed in Figure 3-16(c), arises by the reason of charge separation of the negatively-charged metal matrix and the positively-charged metal ions in solution and causes an arrangement of the cations very close at the interface. Thus, a dynamic equilibrium arises at which some oxidised cations will be reduced on the metal matrix according to the following reduction reaction, while other metal cations still further oxidise:

$$M^{z+} + ze^{-} \rightarrow M \text{ (reduction) (Eq. 2)}$$

The entire electrolytic oxidation process of metals is illustrated schematically in Figure 3-16. Corrosion involves *red*uction and *ox*idation reactions between at least two species which is typically abbreviated as *redox*.

The standard equilibrium redox potential, E_o, is characteristic for a metal and a measure for its chemical resistance under prevalent conditions. E_o is a function of temperature, type and concentration of electrolyte, and pressure. The standard equilibrium redox potentials or standard electrode potentials are measured against a standard hydrogen electrode (stable potential) and are available in the literature known as electrochemical series. Some electrochemical series are listed in Table 3-9. The influence of a slight variation in pH shows the electrode potential change of the half cell.

Table 3-9: Electrochemical series [20, 62]

Element (Ions)	Electrode reaction	E_o (V)	Potential (V) at		Corrosion behaviour
			pH = 6	pH = 7.5	
Au^{3+}	$Au^{3+} + 3e = Au$	+ 1.42	+ 0.3	+ 0.2	
Mn^{3+}	$Mn^{3+} + e = Mn^{2+}$	+ 1.51			noble
Cr^{6+}	$Cr_2O_7^{2-} + 14H^+ + 6e = 2Cr^{+3} + 7H_2O$	+ 1.33			
O_2	$O_2 + 4H^+ + 4e = 2H_2O$	+ 1.229			
Pt^{2+}	$Pt^{2+} + 2e = Pt$	ca. + 1.2			
Ag^+	$Ag^+ + e = Ag$	+ 0.800	+ 0.2	+ 0.15	
Fe^{3+}	$Fe^{3+} + e = Fe^{2+}$	+ 0.771			
$O_2 + 2H^+$	$O_2 + 2H^+ + 2e = H_2O_2$	+ 0.682			
Cu^+	$Cu^+ + e = Cu$	+ 0.521			
O_2	$O_2 + 2H_2O + 4e = 4OH^-$	+ 0.401			
Cu^{2+}	$Cu^{2+} + 2e = Cu$	+ 0.337	+ 0.2	+ 0.1	
H^+	$2H^+ + 2e = H_2$	± 0.000			
Sn^{2+}	$Sn^{2+} + 2e = Sn$	- 0.136	- 0.3	- 0.8	
Mo^{3+}	$Mo^{3+} + 3e = Mo$	ca. - 0.2			
Ni^{2+}	$Ni^{2+} + 2e = Ni$	- 0.23	+ 0.1	+ 0.04	
Cr^{3+}	$Cr^{3+} + 3e = Cr$	- 0.71	- 0.2	- 0.3	
Mn^{2+}	$Mn^{2+} + 2e = Mn$	- 1.18			
Ti^{2+}	$Ti^{2+} + 2e = Ti$	- 1.63			reactive
Al^{3+}	$Al^{3+} + 3e = Al$	- 1.66			

The electrochemical series is a useful database for rough estimation of the corrosion behaviour of a metal. It can be used as an implemental to understand and assess corrosion processes. However, since kinetics are not considered and corrosion processes can be localised and quite complicated, therefore, this list cannot be taken always as an evaluating reference.

3.5.1.2 Passivity

Some metals have the capability to form in the presence of oxygen ultra-thin layers of metal oxide, the passive layer, which covers the surface and have protective characteristics. The passive layer prevents the material from corrosion, and is highly dense in nature. Passive layers of stainless steels are typically conductive and show 1-3 nm thicknesses [63, 64].

Above the corrosion potential, metals are in an active state, and metal oxidation can occur. A protective oxide layer (passivity) can be formed by increasing the potential of the metal which decelerates corrosion reaction significantly. The metal surface is protected at the passive state as long as its integrity is maintained. However, metals do not need to get first active to get passive. Passivity occurs spontaneously and strengthens typically by time (thickness).

Passive films are stable over a wide potential range but can breakdown or rupture at higher noble potentials which can lead to an accelerated localised corrosion rate. This phenomenon is called transpassivity. The active, passive, and transpassive states are depicted in Figure 3-17.

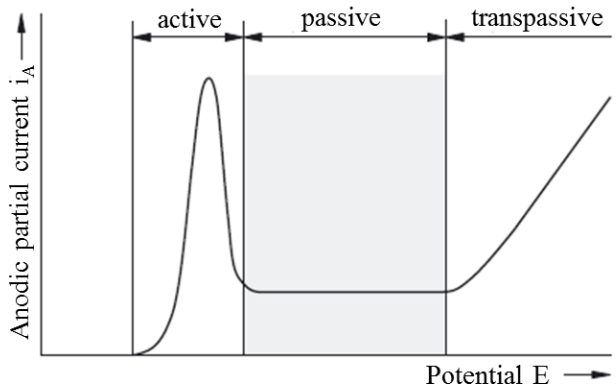

Figure 3-17: Anodic partial current curves of a passivating metal [20]

Stainless steels are corrosion resistant due to this phenomenon of passivity. Chromium forms a very dense and protective passive layer and is the main reason for passivity of stainless steels. Minimum 10.5 wt.-% Cr is required in iron alloys to become stainless and, hence, corrosion resistant. In the presence of nickel in the matrix, more chromium is necessary.

The passivity of 18-8 Cr-Ni stainless steels is similar to the passive behaviour of pure chromium [15, 20, 62]. In very low pH environments and in the presence of strong oxidisers

the chromium protective layer can oxidise rapidly. Such conditions can be prevalent under atmospheric corrosion environments, particularly in the presence of chloride ions and elevated temperatures.

3.5.1.3 Corrosion Reactions in Aqueous Solutions

The potential difference, the aggressivity of the electrolyte (i.e. the degree of dissociation), and the oxygen concentration determine the extent of corrosion. Reactive metals have higher electrolytic oxidation potentials (solution tension) than noble metals. The different oxidation potentials are the reason for corrosion. A reactive metal submerged into an electrolyte shows higher anodic partial currents than cathodic partial currents at the beginning which is apparent with a negative electrode potential at the reactive metal and a positive electrode potential at the noble metal. After a while the anodic and cathodic partial currents reach state of equilibrium, as illustrated schematically in Figure 3-18 and Figure 3-19 as an example on Zn (reactive) and Cu (noble).

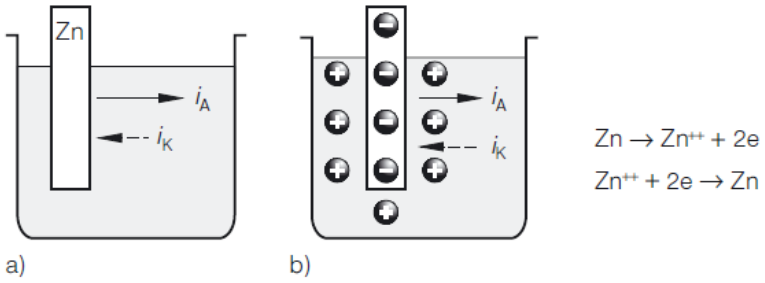

Figure 3-18: Half-cell of an reactive metal: (a) at the beginning of the reaction the anodic partial current i_A is higher than the cathodic partial current i_K and (b) state of equilibrium

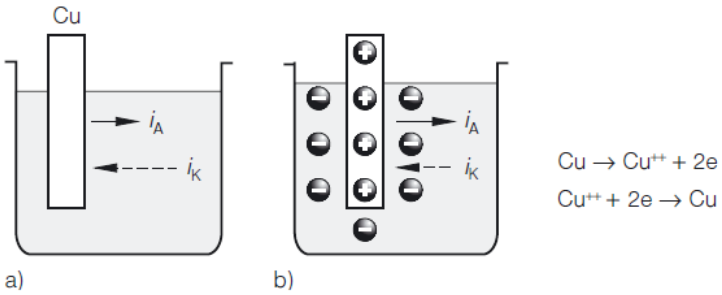

Figure 3-19: Half-cell of a noble metal: (a) at the beginning of the reaction the cathodic partial current i_K is higher than the anodic partial current i_A and (b) state of equilibrium

However, if two dissimilar metals with different half-cell potentials are brought into contact in an electrolyte, the reactive metal will become the anode and the noble one the cathode. In such cases the partial currents on each electrode will never equilibrate, and corrosion will proceed unless kinetic retardations occur. The anodic reaction is the metal oxidation and the cathodic reaction can be dependent on the electrolyte condition [65]:

(1) Hydrogen evolution $H^+ + e^- \rightarrow \frac{1}{2}H_2$ (Eq. 3)

(2) Oxygen reduction (acid solutions) $O_2 + 4H^+ + 4e^- \rightarrow 2H_2O$ (Eq. 4)

(3) Oxygen reduction (neutral/basic solutions) $O_2 + 2H_2O + 4e^- \rightarrow 4OH^-$ (Eq. 5)

(4) Metal ion reduction $M^{3+} + e^- \rightarrow M^{2+}$ (Eq. 6)

The type of cathodic reaction is dependent on the pH and the oxygen concentration of the electrolyte. In electrolytes with pH < 6, the predominant cathodic reaction is hydrogen evolution. However, oxygen reduction can occur simultaneously if oxygen is present and becomes the major cathodic reaction mechanism at pH > 6. Oxygen reduction can still be the dominating reaction at pH = 2 under atmospheric corrosion conditions which will be dealt later. In neutral and basic solutions hydroxyl ions are formed through oxygen reduction. Moreover, in the presence of strong oxidizers metal cations can be reduced from a higher oxidation state to a lower oxidation state which can promote the anodic metal oxidation significantly. In Figure 3-20 the corrosion scheme for aqueous corrosion is illustrated schematically and simplified on the example of the corrosion of iron.

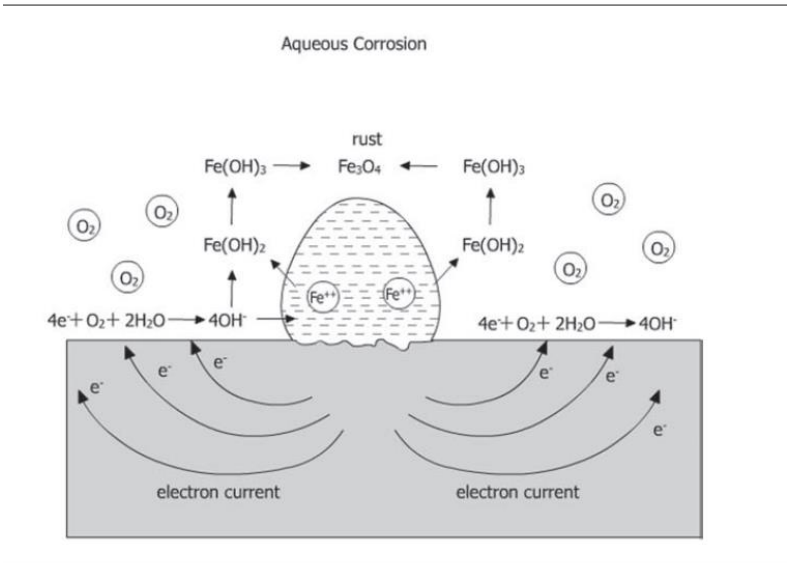

Figure 3-20: Aqueous corrosion of iron (simplified and schematic) [62]

Real corrosion mechanisms are quite complicated, and the reactions can be of large scale. *Graedel and Frankenthal* [66] described the corrosion chemistry of iron comprehensively. The environment determines prevalent corrosion mechanisms and corrosion products.

Iron gets first oxidised in the form of Fe^{2+} cations and can form a variety of corrosion products. Fe(II) can combine with hydroxyl ions and form the metastable product $Fe(OH)_2$, which can further oxidise to form $Fe(OH)_3$. Simultaneous hydrolysis reaction can occur at which Fe(II) and Fe(III) hydrolyse water to hydroxyl ions, according to the following reaction equations and decrease the pH:

$$Fe^{2+} + 2H_2O \rightarrow Fe^{2+} + 2H^+ + 2OH^- \rightarrow Fe(OH)_2 \text{ (alkaline)} \quad \text{(Eq. 7)}$$

$$Fe^{3+} + 3H_2O \rightarrow Fe^{3+} + 3H^+ + 3OH^- \rightarrow Fe(OH)_3 \text{ (pH} \approx 5) \quad \text{(Eq. 8)}$$

The higher the oxidation state of a cation the stronger is its hydrolysis effect. This is the reason for corrosion-promoting effects of Fe(III).

3.5.1.4 Anodic and Cathodic Partial Reactions

Anodic and cathodic reactions are necessary in corrosion processes. The corrosion process on a metal can only be developed if the remaining electrons in the metal matrix after oxidation of metal ions are consumed by cathodic reactions. Anodic and cathodic reactions are locally separated from each other.

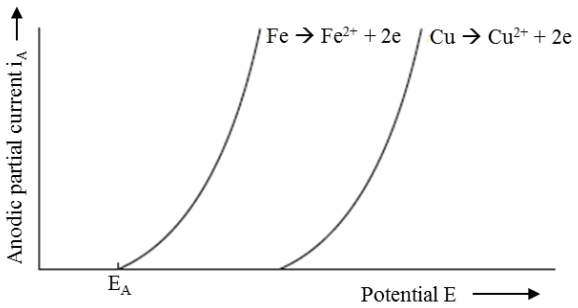

Figure 3-21: Anodic partial current curves i_A = f(E, Metal), E_A = anodic potential [20]

Both partial reactions take place in the metal/electrolyte interface. At the anode electrons are supplied by metal oxidation which is more favoured the less the nobility of the metal is. In

Figure 3-21, anode partial currents as a function of metal nobility expressed in potential is schematically shown on a reactive (Fe) and a noble metal (Cu).

There are two different types of cathodic reactions; acidic corrosion and oxygen corrosion. The pH and oxygen concentration of the electrolyte determine which type is prevalent.

3.5.1.5 Acidic/Hydrogen Corrosion

Metals with negative electrochemical standard potentials can be oxidised in non-oxidising and oxygen-free acidic electrolytes under the evolution of hydrogen gas, while noble metals are immune (noble, sluggish in reaction). Hydrogen corrosion is a dominating corrosion reaction occurring in acidic environments only (pH < 6). The lower the pH the higher is the potential for the cathodic partial current. The cathodic partial current during hydrogen evolution is logarithmically increased (note the negative current value) by increasing the cathodic potential which is schematically illustrated in Figure 3-22. The reaction equation for hydrogen corrosion i.e. cathodic hydrogen evolution is as following:

$$H^+ + e^- \rightarrow \frac{1}{2}H_2 \quad \text{(Eq. 3)}$$

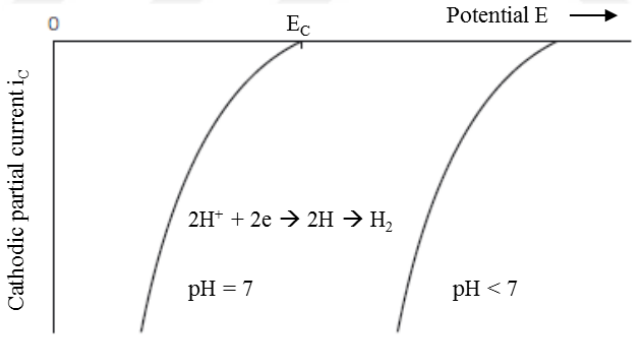

Figure 3-22: Cathodic partial current curves of hydrogen reduction; i_C = f(E,pH), E_C = cathodic potential [20]

Anodic and cathodic partial currents cannot be measured, but the sum current (= corrosion current of the corrosion cell) can be measured which is schematically shown in Figure 3-23.

The point where anodic and cathodic currents are equal is the equilibrium rest potential (also open circuit potential, OCP).

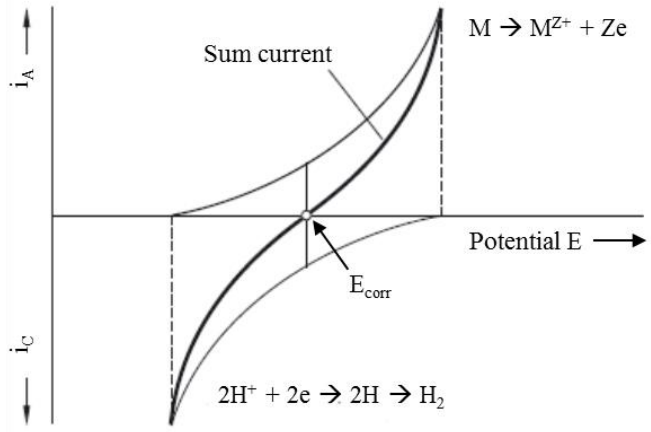

Figure 3-23: Sum current curve during hydrogen/acidic corrosion; E_{corr} = corrosion potential [20]

Metals with different corrosion potentials show different behaviour in oxygen-free acidic environments as shown schematically in Figure 3-24. Metals with lower corrosion potentials suffer from higher metal oxidation due to high partial currents (curve 1) while nobler metals corrode less (curve 2) as the partial currents are small. Some metals may stay immune in certain environments because no state of equilibrium is possible (curve 3).

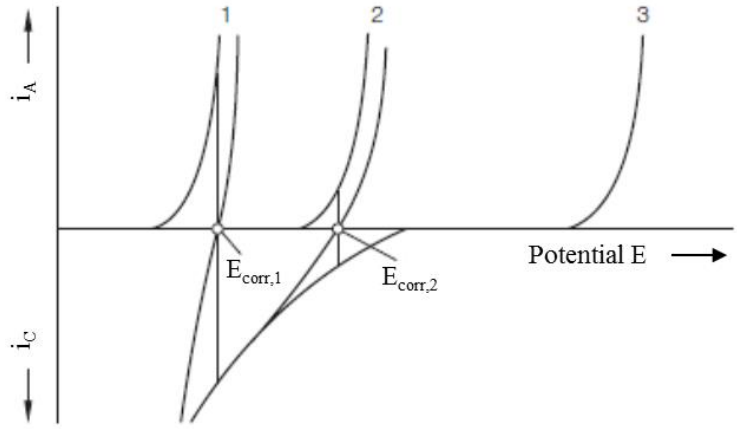

Figure 3-24: Corrosion behaviour of metals with different corrosion potentials [20]

3.5.1.6 Oxygen Corrosion

Oxygen can be abundantly present in the electrolyte, such as under atmospheric corrosion conditions, and lead to cathodic oxygen reduction:

(1) Oxygen reduction (acid solutions) $O_2 + 4H^+ + 4e^- \rightarrow 2H_2O$ (Eq. 4)

(2) Oxygen reduction (neutral/basic solutions) $O_2 + 2H_2O + 4e^- \rightarrow 4OH^-$ (Eq. 5)

This phenomenon has been known as oxygen corrosion and occurs with larger corrosion rates than hydrogen corrosion. The oxygen concentration in a corrosive medium can polarise cathodic potentials to very high values, forming high cathodic currents, so that even noble metals can corrode. This is schematically illustrated in Figure 3-25 where the severity of oxygen corrosion in comparison to hydrogen corrosion is pointed out. Cathodic partial currents in oxygen corrosion exist over a wide potential range where the corrosion initiation becomes a matter of time only. This has significant importance for the atmospheric corrosion propensity of grade 2205 duplex stainless steel which is a highly resistant alloy. In the abundance of oxygen which is the case for atmospheric conditions the initiation of corrosion is a matter of time only. This will be discussed later more in detail.

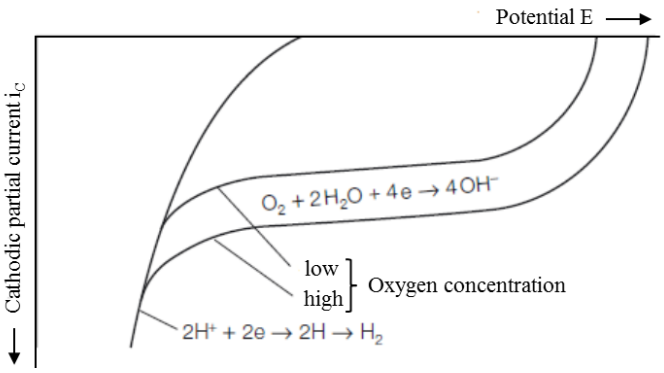

Figure 3-25: Cathodic partial current as function of oxygen concentration [20]

3.5.2 Corrosion Forms

The corrosion process that leads to material damage can stem from a uniform or local attack, or by the formation of a crack which is classified by visual observation. There are eight common corrosion forms. These are:

(1) Uniform, or general corrosion
(2) Galvanic, or two-metal corrosion
(3) Crevice corrosion
(4) Pitting corrosion
(5) Intergranular corrosion

(6) Selective leaching
(7) Erosion corrosion (beyond that also tribocorrosion)
(8) Stress corrosion

3.5.2.1 Uniform/General Corrosion

When the corrosion chemistry is very aggressive over a wider range on the materials surface, or the metal is for any reason not passive, the corrosion attack is homogeneously distributed over a large area of the surface and occurs uniformly. This is also called general corrosion. The metal oxidation is expressed by high anodic currents causing material thinning.

The operational safety is in general not endangered since the metal oxidation rate is low due to low current densities, and premature safety measures can be taken as extensive corrosion products can be monitored. However, due to different local electrochemical relations the corrosion process can proceed unequally ending with synclinal or trough-shaped attacks.

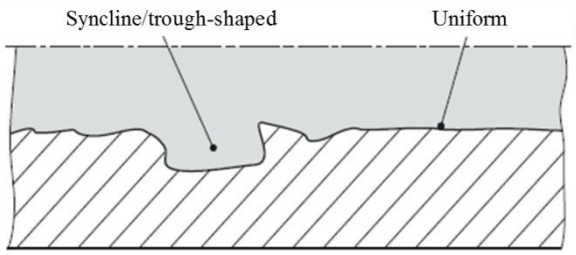

Figure 3-26: Uniform corrosion

3.5.2.2 Crevice Corrosion

Crevice corrosion is an intensified localised attack occurring within crevices or under shielded areas on metal surfaces with the presence of a corrosive. Crevice corrosion is associated with very small volumes in which electrolytes can penetrate, and in which stagnant conditions are prevalent.

The electrochemical conditions within the crevice can become much more severe than outside the crevice. At the initial stage, the electrolytic conditions in- and outside the crevice are the same. However, within the crevice the electrolyte is stagnant because of no convection, so a renewal of reducing species is limited.

In the case of oxygen reduction the rate determining factor is the cathodic reaction; oxygen is consumed within the crevice making the crevice net anodic, while the outside adjacent to the crevice becomes net cathodic. Due to a large cathode to anode area, metal oxidation within the crevices can accelerate and anions in the electrolyte, such as chlorides, can be attracted into the crevice. Corrosion products usually remain in the crevice and partially hydrolyse into an insoluble metal hydroxide and free acid:

$$M^+Cl^- + H_2O \rightarrow M^+OH^- + H^+Cl^- \quad \text{(Eq. 9)}$$

This hydrolysis effect leads to a decrease of the pH, locally, and an additional increase in metal removal inside the crevice is caused. The crevice corrosion mechanism is illustrated schematically in Figure 3-27.

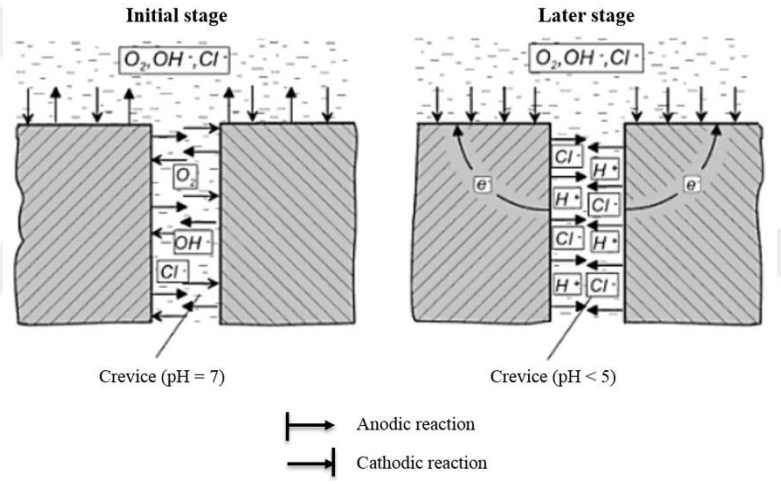

Figure 3-27: Mechanism of crevice corrosion [15]

3.5.2.3 Pitting Corrosion

Pitting corrosion is, also like crevice corrosion, a type of localised corrosion at which specific regions of a metal surface are locally attacked leading to small holes or pits (Figure 3-28).

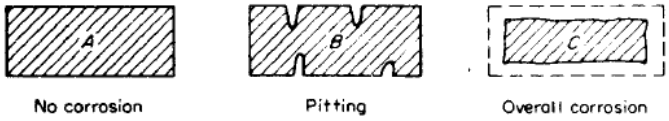

Figure 3-28: Represented scheme of pitting corrosion [65]

Pitting may be understood as the intermediate stage between uniform corrosion and fully corrosion resistant behaviour which depends on the corrosive environment and materials chemistry (Figure 3-28).

The attack can have various morphologies (Figure 3-29) depending on the material condition and local electrochemical nature. The diameter of a pit is either the same or less than the depth. Pits can occur isolated or close together and look like a rough surface. Pitting corrosion can be more damaging as it causes material perforation with a small percentage of weight loss.

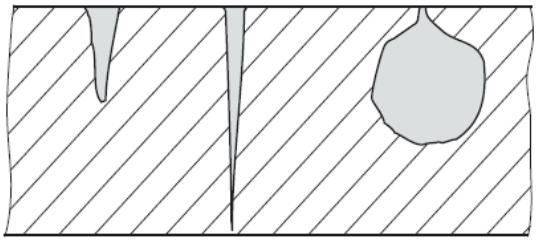

Figure 3-29: Pit morphologies [20]

The detection of corrosion pits is not trivial due to their small size and possible occlusion by corrosion products. It is also not easy to quantify pitting corrosion due to varying number of pits and different geometries (depth, form, and size). Pitting corrosion is a statistical phenomenon which makes prediction of pitting corrosion difficult.

Pitting incubation time can vary from days to years. This is quite critical for ILW storage conditions since such an attack could lead to a leak of radioactive matter after an unexpected and not foreseeable period of time. Once a pit has initiated, the metal oxidation rate will increase rapidly to an ever-increasing rate [65].

The mechanism for pitting corrosion is more or less similar to crevice corrosion. Pits are initiated at such sites where micro defects of passive layer are present, more aggressive corrosive species are accumulated, or other metallurgical or microstructural features that have low atomic cohesion enabling disruption and breakdown of the material's structural integrity. Pitting corrosion can show different appearances. Some can be like crater-shaped; some like a pinhole, and others undermined holes with a lacy cover. This is showcased schematically in Figure 3-29. Pitting corrosion can occur for stainless steels in the passive region only.

3.5.2.4 Galvanic Corrosion

Galvanic corrosion occurs if two dissimilar metals are brought into contact in a corrosive environment. The driving force for galvanic corrosion is their different electrochemical potential in the corrosive in which the less-resistant metal oxidises more rapidly while the more-resistant metal becomes more resistant. The less resistant metal becomes net anodic while the other becomes net cathodic since both metals can still corrode, but with different oxidation rates.

Galvanic corrosion can be intensified by environmental effects such as distance and metal area. Galvanic effects are largest on the interface of both anodic and cathodic metals, and decreases in extent with increasing distance. If a large cathode and a small anode are present, larger anodic oxidation occurs than the opposite due to higher current densities.

Galvanic corrosion is readily recognised by the localised attack near the metal junction. In the ILW storage concept galvanic corrosion in the macroscopic view has no importance since no other metals joint together. However, micro-galvanic effects between ferrite and austenite in the microstructure have vital importance because it determines the corrosion behaviour of the material. This will be discussed in the context of selective corrosion in the following sub-chapter.

3.5.2.5 Selective Corrosion/Leaching

Selective corrosion is also a form of localised attack and driven by micro-galvanic effects within the microstructure. Microstructural compounds such as phases, precipitates, grains, and sub-grains can have different local corrosion potentials which may trigger localised galvanic effects. The corrosion propensity of sensitised regions can trigger localised corrosion leading to preferred net anodic and net cathodic sites.

However, selective attack is not limited to sensitisation effects only. The ferrite phase in duplex stainless steels, typically, dissolves selectively in most neutral and chloride-bearing media. Ferrite forms the anode while austenite is the net cathode. The ferrite to austenite ratio can change the oxidation rates and even the corroding phase by changing the anode to cathode ratio (ferrite and austenite fractions). Small ferrite (austenite) grains can be surrounded by larger austenite (ferrite) grains and lead to micro-galvanic coupling which may increase or retard the oxidation rate of ferrite.

Ferrite in grade 2205 duplex stainless steel has often been reported to form the net anode, while the austenite is the net cathode in chloride environments [50, 67-69], but this has been seen to be the opposite in sulphuric acid medium [69]. The corrosion potential of ferrite is lower than that of austenite, despite of the higher Cr and Mo concentrations in the ferrite [70-72]. Austenite is probably more corrosion resistant due to higher Ni and N contents which improves its passivity and decrease its oxidation rate [73, 74].

Cold working can also lead to highly susceptible localised corrosion sites. There is a different load-sharing behaviour of ferrite and austenite during plastic deformation, and austenite usually stores the most plastic energy causing most severe structural alterations in the austenite, such as high rises in dislocation density and stacking faults [47, 75-77]. Austenite becomes then highly susceptible to localised corrosion which can even suppress the selective dissolution of the ferrite [47, 75-77].

Selective corrosion can also occur due to material-related or electrolyte-related differences which may lead to the formation of local corrosion cells which are in the first instance:

- Grains with different orientations
- Inner-grains and grain boundaries due to segregation effects
- Non-deformed and deformed material sections
- Slip-band-free and slip-band zones
- Pure and contaminated zones
- Regions with varying chemical compositions (segregation, phases)
- Regions with intact and disrupted passivity

Formation of local corrosion cells based upon electrolyte-related cases can arise from local electrochemical variations, such as concentration differences of oxygen, chloride, and other ionic species causing similar effects as described above.

3.5.2.6 Intergranular Corrosion

Intergranular corrosion is mostly encountered in sensitised microstructures. Sensitisation is the enhanced localised susceptibility to corrosion activity induced by the formation of primarily chromium-enriched precipitates (carbides), typically, occurring on grain boundaries. Sensitised grain boundaries become net anodic while the grain interiors form the

net cathode (Figure 3-30). Welding or ageing treatments are often the reason for sensitisation of stainless steels.

Chromium carbides are often seen in austenitic stainless steels. Duplex stainless steels are less prone to carbide formation due to little carbon contents. However, other secondary phases, such as sigma (σ), chi (χ), and nitrides (Cr_2N, CrN) can be precipitated and also cause intergranular corrosion.

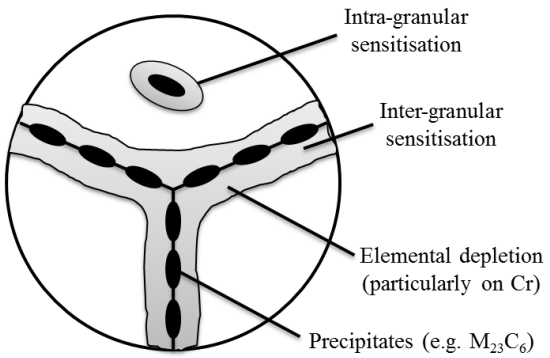

Figure 3-30: Grain boundary sensitisation

3.5.3 Stress Corrosion Cracking

Stress corrosion cracking is the synergistic interaction of corrosive species with mechanical load acting on a material causing the nucleation and growth of cracks which may lead to unexpected material failure. Stress corrosion cracking is the most dangerous form of manifestation of corrosion since cracks are typically not seen. Cracks are often nucleated from corrosion pits or crevices which act as stress concentrators (notch effect), and therefore, pits can presage cracks.

The mechanism of stress corrosion cracking is argued. However, the disruption of the passive layer leading to nucleation of corrosion pits with preferred growth along slip planes or grain boundaries is believed to form the initial crack incubates. Dislocation motion is then activated leading to enhanced dislocation mobility on adjacent slip bands and/or slip-band gliding causing crack growth (propagation). The mechanism is schematically illustrated in Figure 3-31.

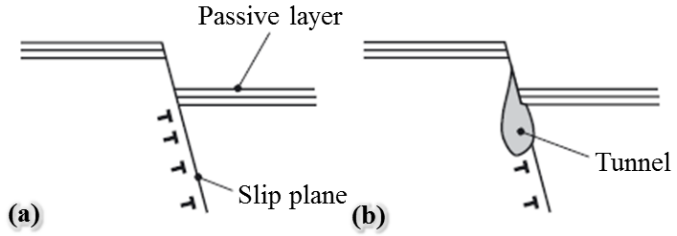

Figure 3-31: Stress corrosion cracking mechanism showing (a) disruption of the passive layer and (b) tunnel formation acting as a crack incubate [20]

The crack propagation has either intergranular or transgranular pathway. The intergranular type of stress corrosion cracking occurs if micro-galvanic effects between grain boundaries and the grain-matrix exist, while transgranular crack propagation occurs through grains. Intergranular and transgranular stress corrosion cracking is schematically illustrated in Figure 3-32.

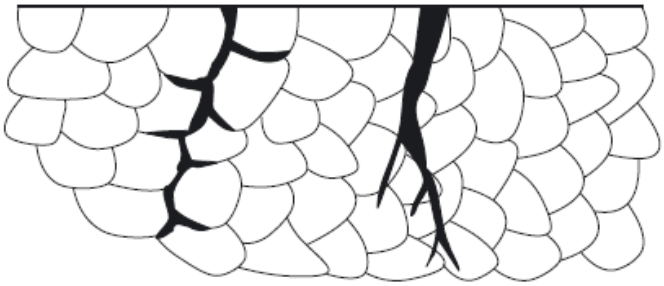

Figure 3-32: Intergranular (left) and transgranular (right) stress corrosion cracking [20]

3.5.4 Atmospheric Corrosion

Corrosion of materials exposed to air and its pollutants with the presence of humidity is called atmospheric corrosion. Pollutants and aerosols containing aggressive ionic species, such as chloride, sulphur, or microorganisms can adsorb on the metal surface and form with the presence of humid air thin film electrolytes, which can create aggressive chemistries. Usually, oxygen is abundant and unlimitedly supplied through the thin film liquids. Atmospheric corrosion is an interaction of the metal surface with thin-film electrolytes, hygroscopic species, and climatic cycles. It refers to the exposure situation of a metal. Atmospheric corrosion is of utmost concern for the storage of ILW [23, 65, 78-80].

3.5.4.1 Types of Atmosphere

Atmospheres are in general classified with respect to the pollution and their concentration into marine, industrial, urban, and rural. Local conditions determine the rate of corrosion; therefore, knowledge about exposure conditions has vital importance.

Rural – The atmosphere at rural sites contains, in general, fewer pollutants than other regions and possesses little corrosivity. There is little or no heavy manufacturing processes generating sulphur species at such places. Moisture, oxygen, and a lesser amount of carbon dioxide are typically major constituents.

Urban – Due to little industrial activity the atmosphere on urban sites contain SO_2 and NOx which are known as typical corrosion promoters.

Industrial – Heavy industrial manufacturing facilities generate high amounts of pollutants such as SO_2, NOx, chlorides, nitrates, etc.

Marine – The air in coastal or marine sites is contains high amount of chloride and organic pollutants arising from the evaporation of sea salt. Dependent on the wind direction, wind speed, temperature, and distance from the coast, contaminants can be swept towards the countryside to a significant amount. Marine environments contain the highest salinity and can cause severe corrosion.

The climatic conditions for each type of atmosphere can be different. The NDA considers storage of ILW containers in interim storage facilities at coastal sites (see Figure 3-33) for up to 150 years before the final disclosure in geological disposal repositories deep underground becomes available [1, 2, 81]. In the UK, key components of atmospheric pollutions are S, Cl, N, Mg, Ca, and Na which can deposit on the stainless steel surface (not by rain but by dry deposition).

Figure 3-33: Overview of ILW storage facilities in the UK considered in scope [81]

3.5.4.2 Stages of Atmospheric Corrosion

Atmospheric corrosion can be categorised into dry, damp, and wet stages. In the dry stage, no humid film is on the surface and the metal is purely oxidised. The corrosion damage caused at this stage can be virtually neglected.

Damp corrosion can occur if water from the (humid) air precipitates onto the metal surface forming with corrosive species microscopic “invisible” salt-laden moisture films, which is most severe when the humidity is close to the deliquescence point of the salt. The salt concentration is set by the humidity, and low amounts of dissolved contaminants can cause severe corrosion (high concentration) at the deliquescence relative humidity (DRH).

The wet atmospheric corrosion stage is associated with dew, ocean spray, rain water, water splashing, etc. and is similar to aqueous corrosion (immersed condition). Corrosion mechanisms of wet corrosion and corrosion in bulk solutions are practically the same. Wet-dry cycles manifested by climatic fluctuations can lead to enhanced corrosion activities [23, 64, 82-86].

3.5.4.3 Theory of Atmospheric Corrosion

Atmospheric corrosion processes require thin-film electrolytes to initiate electrochemical reactions on metal surfaces. Water precipitation is triggered by high relative humidities, and hygroscopic salt species adhering on the metal surface can absorb water at and above their critical relative humidities (deliquescence point).

Deliquescence of a salt is the capability to incorporate water and form micro droplets forming saturated salts at the DRH. The salt solution is diluted at higher humidity levels which can result in the growth of the electrolyte deposit. The principal formation of thin-film electrolytes by moisturising of precipitated hygroscopic salts is schematically shown in Figure 3-34. Atmospheric corrosion is highest at the deliquescence point for each salt contaminant.

$MgCl_2$ and $CaCl_2$ are responsible for the low DRH of sea salts and, hence, the most critical salts. Carnallite ($MgKOH \cdot 6H_2O$) is a common mineral that is generally considered to be one the most representative of seawater evaporates. In the presence of chlorides, $MgCl_2 \cdot 6H_2O$ is typically formed stays as the last evaporate onto the metal surface. The deliquescence point for $MgCl_2 \cdot 6H_2O$ is 33% RH at room temperature and 30% RH at 50°C [7]. 10-12 M of chloride has been reported to be formed at the deliquescence point for magnesium chloride which is more severe in contrast to NaCl which forms 5-6 M chloride at its DRH (78% RH) [83, 85, 86].

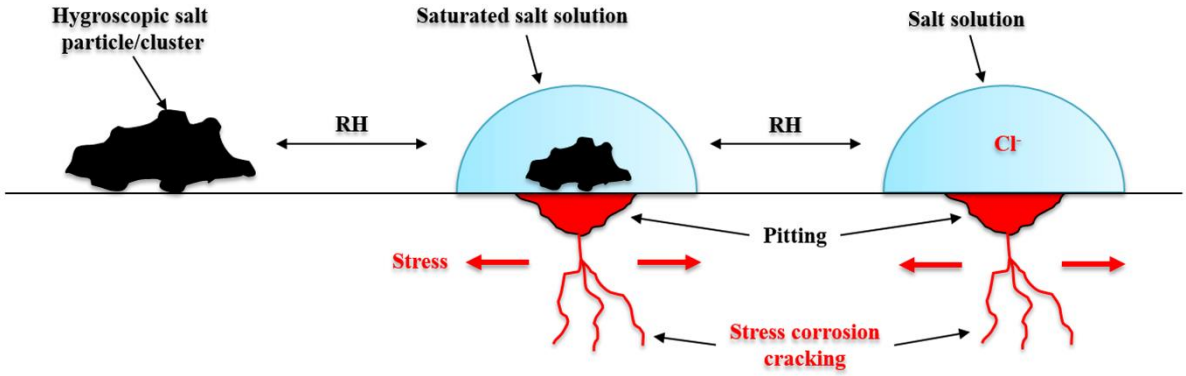

Figure 3-34: Principle of atmospheric corrosion and atmospheric stress corrosion cracking

The cathodic reaction is often neutral oxygen reduction. However, hydrogen evolution can be the prevailing mechanism if the pH is low (pH < 5). Two reaction steps may be involved, with hydrogen peroxide as an intermediate species:

$$O_2 + 2H_2O + 2e^- \rightarrow H_2O_2 + 2OH^- \quad \text{(Eq. 10)}$$

$$H_2O_2 + 2e^- \rightarrow 2OH^- \quad \text{(Eq. 11)}$$

Oxygen is often available in abundance and unlimitedly supplied in thin-film electrolytes. Corrosive concentrations can reach very high levels, particularly in conditions of alternate wetting and drying processes. *Evans et al.* [87] could show that Fe(III) oxides (rust) triggered a second cathodic reaction at wetting of a dry surface enhancing atmospheric corrosion rates. Temperature and RH fluctuations are common in interim storages and cannot be avoided [4, 5].

Pitting initiation during atmospheric corrosion is illustrated schematically in Figure 3-35.

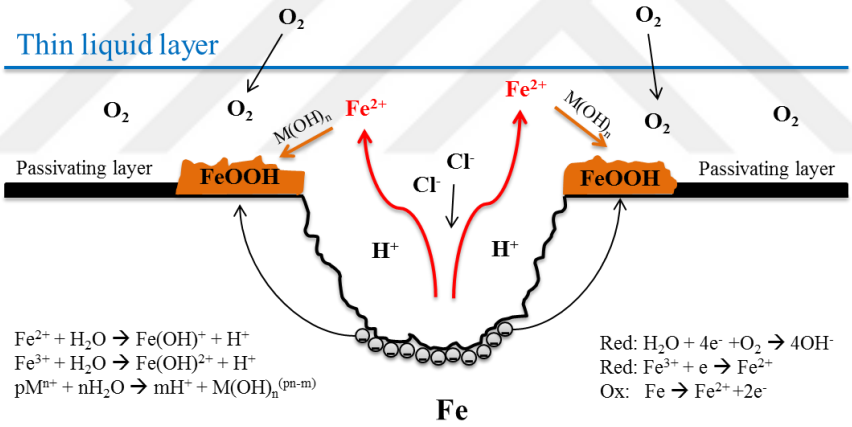

Figure 3-35: Corrosion initiation during atmospheric corrosion

3.5.4.4 Factors Affecting Atmospheric Corrosion

Atmospheric corrosion is an electrochemical process and requires an electrolyte on the surface. Atmospheric corrosion can be a discontinuous process when the liquid is dry. Corrosion takes place only during the time of wetness (t_w) which is the time period of electrolyte presence on the surface. The relative humidity, temperature, chemical and physical properties of the electrolyte, corrosion products, material's chemical composition, microstructure, and surface condition are the most important factors to be taken into consideration for ILW storage container corrosion.

3.5.4.4.1 Effect of Relative Humidity

Leygraf and Graedel [64] studied the interaction of relative humidity and monolayers adsorbed on metal surfaces. The metal surface exposed to extremely low relative humidities contained a monolayer of hydroxyl species firmly adhering on the passive layer with strong, probably cohesive forces. This layer had a high degree of ordering and was immobile (Figure 3-36).

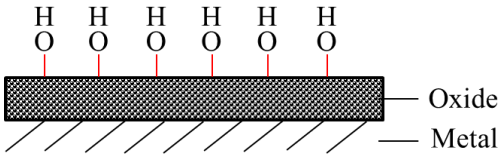

Figure 3-36: Schematic depiction of immobile surface hydroxyl layer on a metal surface [64]

Monolayers of water molecules adhered on the metal surface with the increase of relative humidity. The number of monolayers adhered was characteristic for a metal and changed as a function of time (Figure 3-37). The degree of ordering of the first layer was high and the mobility low. The monolayers became more randomly oriented and mobile with the increase of the humidity. The electrochemical properties of electrolytes containing more than three monolayers of water showed bulk solution-like behaviour.

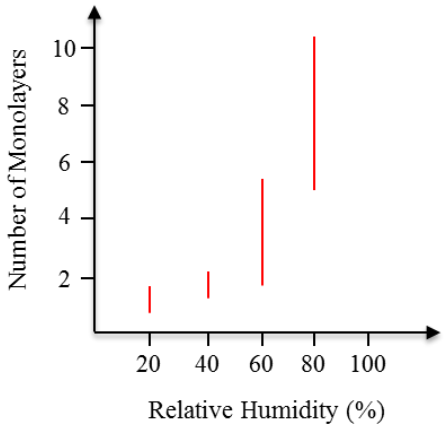

Figure 3-37: Interaction of absorbed monolayers of water on metals with relative humidity [64]

Tsutsumi et al. [86, 88] studied the effect of RH on chloride ion concentration of $MgCl_2$ deposits at room temperature on 304 austenitic stainless steel and showed that the critical

atmospheric-induced chloride concentration at which stable pitting corrosion occurs is around 6 M at 298 K corresponding to ~65% RH (Figure 3-38).

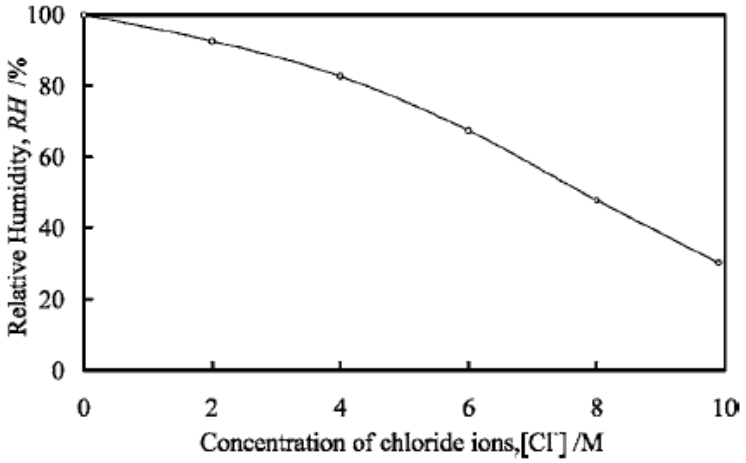

Figure 3-38: Effect of RH on chloride concentration in $MgCl_2$ solution at 300 K [86, 88]

This is in agreement of the hypothesis of *Newman and co-workers* who believed that 5-6 M bulk chloride ion concentration is required to sustain stable pit growth in this material [89, 90].

Tsutsumi et al. [86, 88] claimed that the critical RH for atmospheric pitting corrosion lies between 65% and 75% as after 100 hours exposure at 75% RH no pitting were observed. However, the incubation time for pitting might have been higher than 100 hours so no definite statement for a long-term pitting initiation possibility can be made with a short-term test. At atmospheric corrosion tests, it may not be possible to extract statements relevant for long-term applications with short-term corrosion tests. This is a common problem for all long-term prediction assessments.

Tsutsumi et al. [86, 88] further found that under thin-film electrolyte conditions pitting propagation was horizontally directed while under bulk solution conditions pit growth follows preferably a vertical direction. This was believed to be a matter of pH which was low and wider around atmospheric corrosion pits than pits nucleated in aqueous solutions where the pH drop is confined in the centre of the pit (pit bottom). The solution over the atmospheric pit area was immediately saturated with oxidised metal ions due to the low volume of electrolyte/water. The saturation might have reduced the metal oxidation rate in

the centre leading to more homogeneous pit propagation. Under atmospheric conditions, pit growth in thin-film electrolytes is less favoured in the vertical direction than in the horizontal direction in contrast to aqueous pitting corrosion. This has practical importance for ILW stainless steel storage containers since life-time modelling of these containers require data obtained from atmospheric corrosion measurements. Aqueous corrosion pitting rates may lead to false misinterpretations of the life-time of the ILW-container. However, microstructure processing orientation may still favour corrosion propagation in certain directions under atmospheric conditions. This will be discussed later.

Tsutsumi et al. [86, 88] further reported pH = 3 developing under saturated and diluted $MgCl_2$ containing droplets, which might be responsible for the uniform-like pitting corrosion. However, this might be due to local aggressiveness of the electrolyte which may have caused numerous pits to nucleate in high density appearing macroscopically in uniform-like corrosion morphology. Higher chloride concentrations are well-likely necessary to sustain stable pitting in 316L steel and in 2205 duplex stainless steel. At relative humidities at or close to the saturation point of $MgCl_2$, the onset of corrosion, even for duplex stainless steel, is highly speculated to be a matter of time which strongly depends on the environment temperature.

3.5.4.4.2 Effect of Thin-Film Droplet Size

The droplet size (diameter and thickness) forming onto the surface determines the cathode to anode ratio, hence the probability of occurrence and the extent of corrosion. $MgCl_2$ and NaCl form the main airborne salt constituent in the atmosphere. However, despite the abundance of NaCl in sea salt $MgCl_2$ evaporates can form more critical corrosion chemistries on stainless steel surfaces leading to higher concentrated salt solutions at low humidities (below ~78% RH).

Tsutsumi et al. [86, 88] concluded in their studies that an increase in droplet size (diameter and thickness) enhances chloride-induced pitting corrosion. Peripheral areas of a growing pit were seen to become net cathodic which became larger in size when the droplet was larger, leading to higher rates of metal oxidation.

The droplet forms with the metal and the atmosphere a three-phase-boundary which determines the corrosion characteristics. If the droplet thickness (X_d) is little, oxygen transfer

through migration is rapid from the gas phase into the liquid, and the rate-determining cathodic reaction is oxygen absorption (oxygen absorption rate). However, the diffusion process of oxygen through the solution (oxygen diffusion rate) may be a rate-determining step of the cathodic reaction for thicker droplets. There have been various studies conducted on the effect of droplet thickness and diameter on the corrosion propensity [83, 85, 86, 88]. All have in common that there are three distinguishable ranges of droplet thicknesses in which the cathodic diffusion-limited oxygen reduction current density shows different dependencies:

(i) *Very low electrolyte thickness (20-200 µm)*: Oxygen diffusion through the electrolyte layer is the rate determining step (RDS) for the cathodic reaction. Oxygen available in the electrolyte can react fast and deplete quickly when no further oxygen is supplied. The cathodic diffusion-limited oxygen reduction current density does not vary with droplet thickness.

(ii) *Intermediate electrolyte thickness (20-1000 µm)*: The cathodic diffusion-limited oxygen reduction current density is inversely proportional to the droplet thickness.

(iii) *Large electrolyte thickness (>1000 µm)*: Oxygen dissolution at the air/electrolyte interface is the RDS and the cathodic diffusion-limited oxygen reduction current density is independent from the droplet thickness.

Thus, the droplet size determines the occurrence of corrosion and its extent, and, therefore, the larger the droplet is, the higher is the probability of occurrence and extent of corrosion.

The thickness of the droplet strongly depends on the relative humidity. *Tsutsumi et al.* [86, 88] studied the effect of relative humidity on the droplet thickness using magnesium chloride electrolyte with varying concentrations. It became evident that the droplet thickness increased with relative humidity as shown in Figure 3-39. However, no explanation on this phenomenon was made. The increase of relative humidity has a dilution effect of the salt-laden droplets. Water activity increases with the relative humidity meaning that at higher humidity levels water coherency bonding might be greater than at lower levels leading to an increase of the contact angle (higher surface tension) resulting in a growth of the droplet thickness.

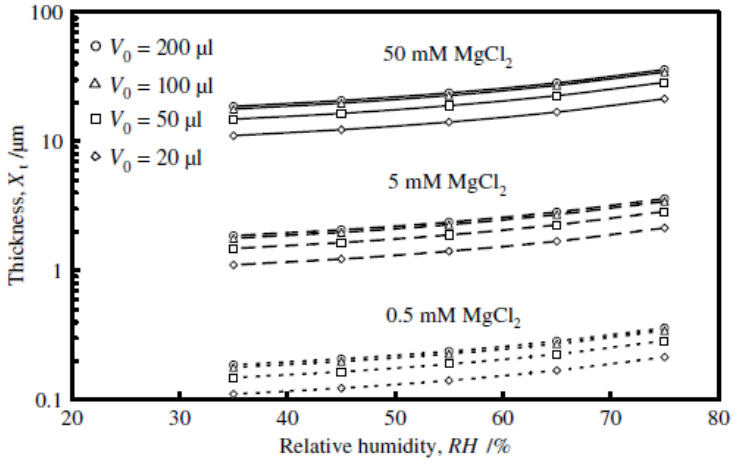

Figure 3-39: Effect of relative humidity on droplet thickness (calculated) with different initial droplet volumes (V_0) and concentrations [88]

The cathode to anode ratio is high in large droplets and, hence, the corrosion rate is high. The droplet size can be ambiguous since droplets can show similar diameter but different thickness; hence, a different corrosion behaviour. The oxygen content in thicker droplets is higher, therefore, high cathodic current densities can be generated leading to more severe corrosion reactions. This probably also influences the cathode to anode ratio, which is higher for larger but thinner droplets as schematically depicted in Figure 3-40.

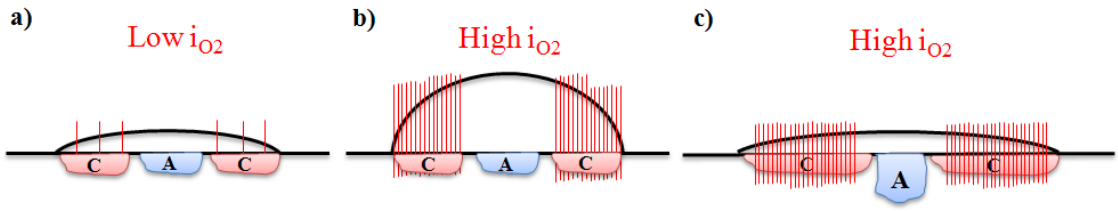

Figure 3-40: Effect of droplet size to cathodic current densities: (a) small droplet size (thickness and diameter) causes little corrosion due to low cathodic current densities, (b) larger droplet thickness but similar diameter/area causes higher corrosion rates due to higher cathodic current densities, and (c) larger droplet diameter but lower thickness causes higher corrosion rates due to larger cathodic areas

Too small droplets (in diameter and thickness) may not lead to corrosion since pitting initiation and growth can be suppressed due to very small effective cathode area, or due to the fact that the cathode and anode become practically inseparable. In this respect, *Hihara and Li* did meaningful study about the effect of droplet size on the corrosion behaviour of carbon steel and pure iron [91]. NaCl droplets formed by the deliquescence of pre-deposited NaCl

particles on steel were examined. They discovered that droplet sizes in the ranges of 45-93 µm (small droplets) and 96-338 µm (large droplets) showed similar open-circuit potential (OCP) behaviour within each range measured versus a saturated calomel electrode using micro-capillary technique (see Figure 3-41).

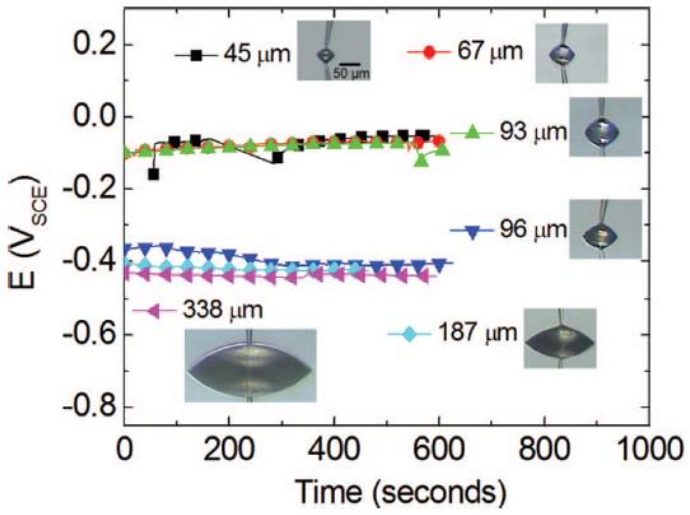

Figure 3-41: OCP measurements in different-sized droplets of NaCl electrolytes with inserts showing the live images of the droplets during OCP measurements. The 50 µm scale bar applies to all images [91].

The large droplets showed immediate corrosion after electrolyte formation, while the small droplets did not corrode even after six hours of exposure. The difference in the OCP behaviour between different NaCl droplets was believed to be due to the lack of corrosion under small droplets which is indicative of passivation, since passivation is accompanied by high OCP values. Prior to the tests, the samples were stored in a dry box (~1% RH) in order to allow surface oxide film formation on the carbon steel and pure iron. Therefore, the steel was protected against corrosion for small droplets.

Furthermore, in order to understand the relationship between OCP behaviour and the presence of the passivation layer on the steel, further OCP measurements were conducted on freshly polished samples that were pre-stored in a dry box (~1% RH) with varying storage time. The NaCl droplet, which was formed onto the freshly polished surface without pre-storage, showed the lowest OCP behaviour and corroded immediately. The surface was highly hydrophilic leading to a high wettability as can be seen in Figure 3-42(a). The droplet formed onto the sample that was pre-stored for 10 days had substantially higher OCP values,

but dropped abruptly down after a short while and adopted similar OCP values. This clearly concluded the existence of a surface passive layer which was beneficial, for a short time at least, retarding corrosion initiation of the steel. The wettability of that droplet was different. The surface became slightly hydrophobic, and the droplet had a larger thickness than the previous droplet.

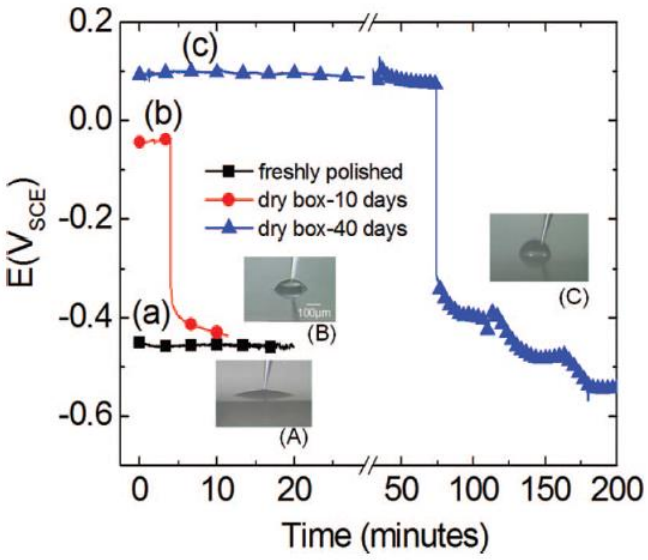

Figure 3-42: OCP measurements in NaCl droplets conducted on steel with different surface conditions. Images show the actual droplet shape during the measurement. The 100 μm scale bar applies to all images [91].

The thin electrolyte formed onto the sample pre-stored for 40 days had the highest OCP values and remained for a longer time passive. However, a larger drop in the OCP was seen yielding lower final OCP values than the previous droplets. It seemed that the aggressivity under that droplet was the largest despite the presence of the protective oxide layer. The authors did not comment on this phenomenon. It could be argued that the pre-storage surface treatment affected the droplet diameter and thickness due to different contact angles of the droplets. This may have changed the cathodic oxygen reduction currents, and possibly also the cathode to anode ratio. Initially, the surface oxide layer dissolved, probably more locally than homogeneously, and it was a matter of time to consume or break the passive layer, while in the meantime the metal was protected. When the surface oxide was dissolved, primarily locally, probably the attack on the metal was larger due to the fact either that a larger cathode to anode ratio was formed leading to more severe localised corrosion, and/or the oxygen

dissolved in the solution had supporting effects on the cathodic reaction due to the presence of abundant oxygen (more than the previous surfaces).

Hihara and Li [91] further investigated the anodic polarisation behaviour of a small (diameter, D = 42 µm) and a large droplet and found that under both droplets pitting corrosion occurred. The small droplet showed an OCP of -40 mV and was initially passive. During anodic polarisation it remained passive until the pitting potential (390 mV) was reached where one large pit was formed at the peripheral area of the droplet resembling "chicken eye" appearance, accompanied by an increase of the current density as shown in Figure 3-43.

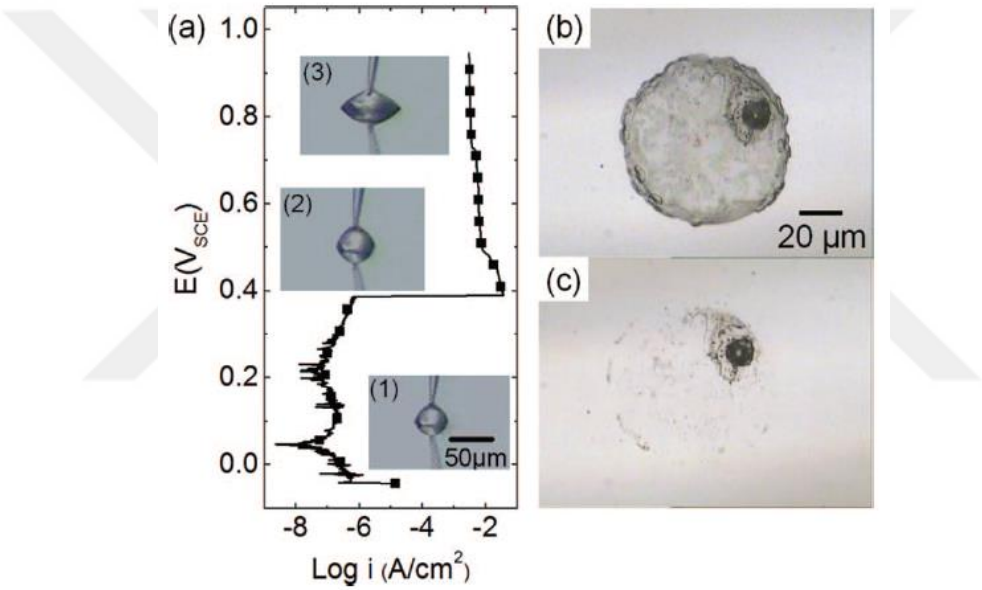

Figure 3-43: (a) Anodic polarisation curve obtained for a small NaCl droplet (D = 42 µm) with inserts showing the actual droplet shape during polarisation (the scale bar applies to all images); (b) an optical micrograph showing the droplet area after polarisation; (c) the droplet area after cleaning with pure water. Images (b) and (c) have the same scale bar [91].

The large droplet had an OCP of -70 mV and was also initially passive. The passivity range was shorter than the small droplet and pitting commenced earlier at 330 mV as shown in Figure 3-44(a). The current densities in the passive range were larger than those measured in the small droplet, showing clearly the effect of droplet size on the extent of corrosion. Thus, corrosion activity was favoured with the increase of droplet size which is often manifested by a decrease of the pitting potential (E_{pit}).

Hihara's examinations [91] showed that the peripheral area of the large droplet was unaffected which indicated that these regions were net cathodic while the centre of the droplet was net anodic as can be seen in Figure 3-44(b). Moreover, the corrosion morphology was different to that observed under the small droplet. While a single pit of ~20 µm was seen under the small droplet larger corrosion area occurring together with a corrosion pit in similar size, but located in the centre of the droplet as shown in Figure 3-44(c).

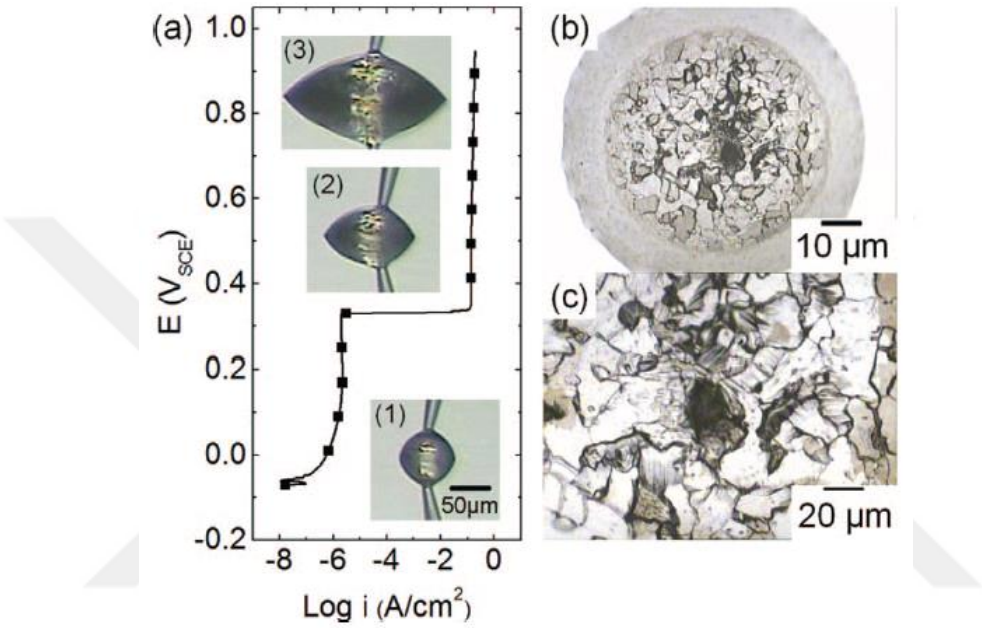

Figure 3-44: (a) Anodic polarisation curve obtained for a larger NaCl droplet (D = 74 µm) with inserts showing the actual droplet shape recorded during polarization (the scale bar applies to all images); (b) an optical micrograph showing the droplet area after polarisation; (c) the droplet area after cleaning with pure water [91].

Hihara and Li [91] did not discuss an important phenomenon, called secondary spreading, which occurred evidently during their polarisation tests. The droplet morphology changed during polarisation and caused an expansion of the droplets, which can be seen in the image inserts in Figure 3-43(a) and Figure 3-44(a). The droplet laterally expanded by ~3 µm with the increase of anodic potential, and further grew by ~26 µm after commencing of pitting yielding a total lateral growth of 29 µm. The large droplet, in contrast, showed a lateral growth of ~150 µm before pitting and a further growth of ~160 µm after pitting yielding a total lateral growth of ~310 µm. It is apparent that this growth was due to anodic polarisation which became more effective after the onset of pitting corrosion. The phenomenon of lateral

growth of the droplet is called secondary spreading and will be discussed in the following more in detail.

3.5.4.4.3 Secondary Spreading Effect

Secondary spreading is the expansion of a salt-laden thin-film electrolyte either by a direct lateral growth of the electrolyte (Figure 3-44), or by wetting and formation of micro-droplets at the peripheral regions of the primary droplet, with the coalescence of the micro-droplets with the main droplet (Figure 3-45). The effect of spreading can vary and depends on the surface state of a metal, kind of deposited salt, temperature, and the relative humidity at and above the deliquescence point of a salt-laden droplet. The corrosion chemistry of the initial deposit can be profoundly changed due to the fact that the exposed salt per unit area (deposition density) can change heterogeneously and cause the formation of different aeration cells. Prediction or simulation of atmospheric corrosion may, therefore, be highly difficult.

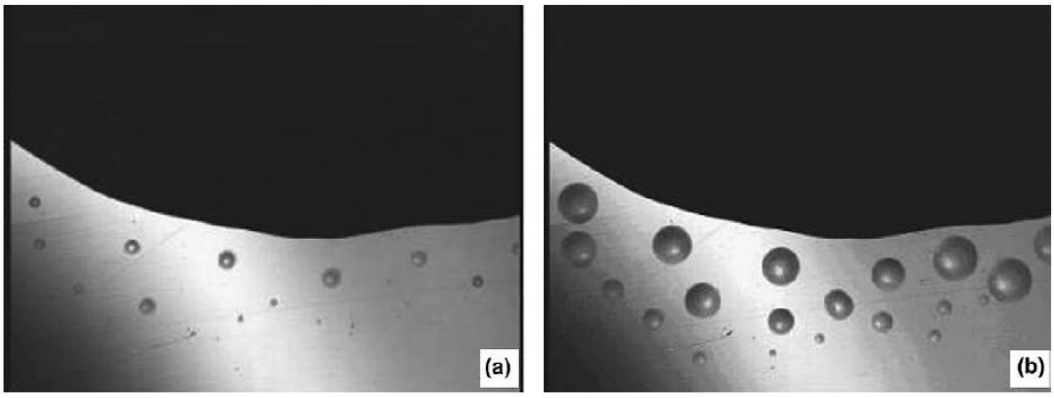

Figure 3-45: Visual representation of secondary spreading showing the formation of micro-droplets around the main droplet (black): (a) initial stage, (b) after 20 seconds of time elapse [92]

Secondary spreading has importance and has been discussed thoroughly elsewhere [83, 85, 86, 88, 92-94]. *Tsuru et al.* [85] and *Zhang et al.* [92] did meaningful work regarding to the characterisation and mechanism of micro-droplet formation. Both are in common that the formation of secondary spreading follows three steps:

1- Wetting of the peripheral area beyond the salt-laden thin-film electrolyte (droplet) due to hydroxylation by cathodic oxygen reduction, and the adsorption of water by attracting mechanism from the air

2- Formation of micro-droplets at cathodic sites adjacent to the primary droplet margin and their growth
3- Eventual and potential coalescence of formed micro-droplets with the main droplet

According to *Tsuru et al.* [85] and *Zhang et al.* [92] micro-droplet formation can only occur on materials with sufficient corrosion propensity in the given environment. Micro-droplet formation can be enhanced when the corrosive is more aggressive and when the metal is more prone to corrosion.

Zhang et al. [92] clearly demonstrated how a thin-film electrolyte containing NaCl expanded with time for various metal coupling pairs (Figure 3-46). Least secondary spreading was observed on the most corrosion resistant material (stainless steel). Secondary spreading can, therefore, be a qualitative measure for evaluation or assessment of corrosion behaviour of duplex stainless steel.

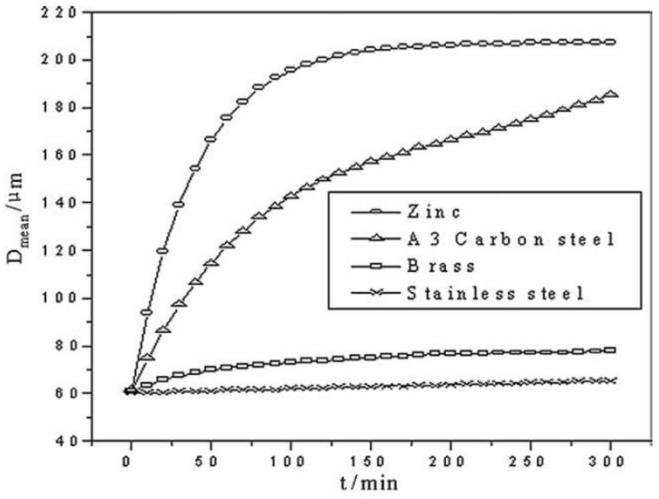

Figure 3-46: Effect of metal coupling on secondary spreading in NaCl containing thin-film electrolyte: showing the mean growth of the droplet diameter (D_{mean}) of the area covered with secondary micro-droplets as a function of time [92]

Both author groups used the scanning Kelvin probe (SKP) technique to analyse the effect of secondary spreading. Low potential values (referenced vs. NHE) i.e. anodic potentials were measured in the centre of the main droplet versus a stainless steel reference needle, whilst high potentials i.e. cathodic potentials were measured over peripheral areas where micro-droplets were formed indicating cathodic properties for the peripheral areas. Clear potential differences between the centre and the peripheral sites of the initial droplet were measured,

and it was the potential difference argued as the driving force for micro-droplet formation. An excerpt from their SKP results is depicted in Figure 3-47 [92].

Similar results were obtained by *Tsuru et al.* [85] who investigated the effect of Kelvin potential development under NaCl and $MgCl_2$ droplets in 80% RH. It was seen that the droplet centre formed the anode and the periphery the cathode. Lateral expansion (secondary spreading) of the droplet was also observed with a slight thickness increase indicating significant water uptake from air. It was also observed that the cathodic activity increased by area as well as by a potential increase and the anode became more discrete in confined regions resembling a C-shape which indicated higher corrosion activity.

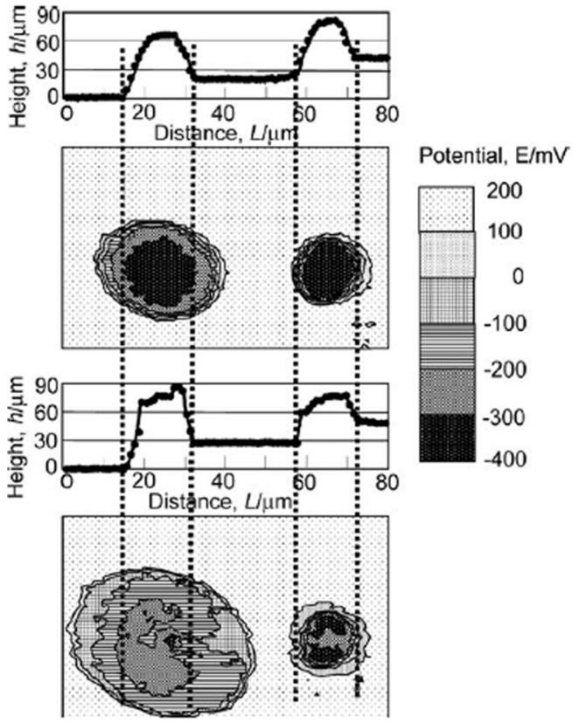

Figure 3-47: Secondary spreading assessments via scanning Kelvin probe measurements: Volta potentials maps and surface profiles around the primary droplets of 0.5 M NaCl (left) and 0.25 $MgCl_2$ (right), respectively deposited on carbon steel at 80% RH [85]. Note there is a certain time elapse between the top and bottom map.

Zhang et al. [92] validated their Kelvin probe potential data (Figure 3-48) by electrochemical polarisation studies. A NaCl containing droplet was placed onto a gap of two stainless steel electrodes which were isolated from each other but electrically connected through a

potentiostat. The droplet linked both steels, and a potential between both electrodes was applied. Micro-droplets were formed on the cathode only (Figure 3-49). Increase of the polarisation current caused an accelerating micro-droplet formation and wider spreading.

From these studies, it could be inferred that the corrosion current established by the (micro-) galvanic potential difference between the central and the marginal region of the droplet was the driving force to initiate and spread micro-droplet formation since no secondary spreading was observed occurring on the anode. The effect was more pronounced if the micro-galvanic potential was higher [92].

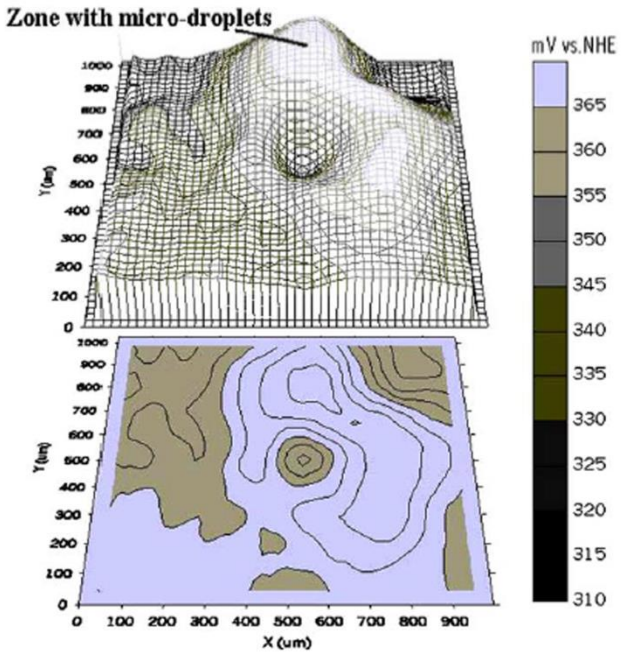

Figure 3-48: Secondary spreading assessments via the scanning Kelvin probe technique: Volta potential map of a droplet and its surrounding area including regions with micro-droplets is shown [92]

In addition, the polarisation current on the effect of micro-droplet formation was studied, and the results showed that the micro-droplet formation was increased with increasing current densities (Figure 3-50).

Zhang et al. [92] investigated the effect of RH on micro-droplet formation, and they found the micro-droplet formation was the largest when the RH was close to the DRH of the salt compound. No explanation for this was made. Highest corrosion activity might have been the reason since at the DRH the anionic concentration of any salt is at its highest. Hence, largest

potential difference between the anode and cathode could be established which could have led to high micro-droplet formation rates. No micro-droplet formation was observed when the RH was lower than or higher the DRH of the salt compound. Below the DRH, the salt compound was dry; therefore, no water activity existed. At higher RH than the DRH the main/primary droplet growth was faster than the micro-droplet formation.

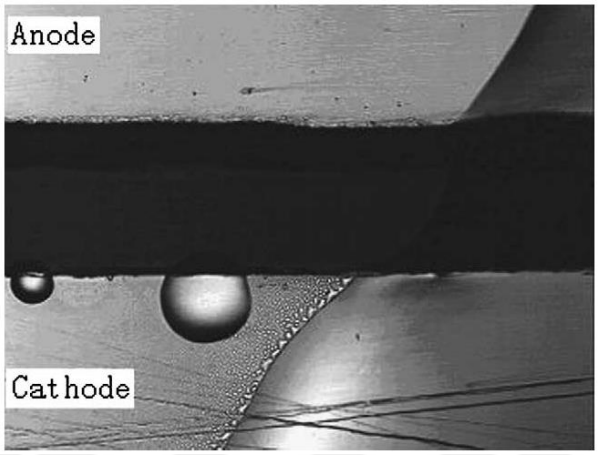

Figure 3-49: Micro-droplets formed only on the cathode of two stainless steel electrodes (optical images with 50x magnification) [92]

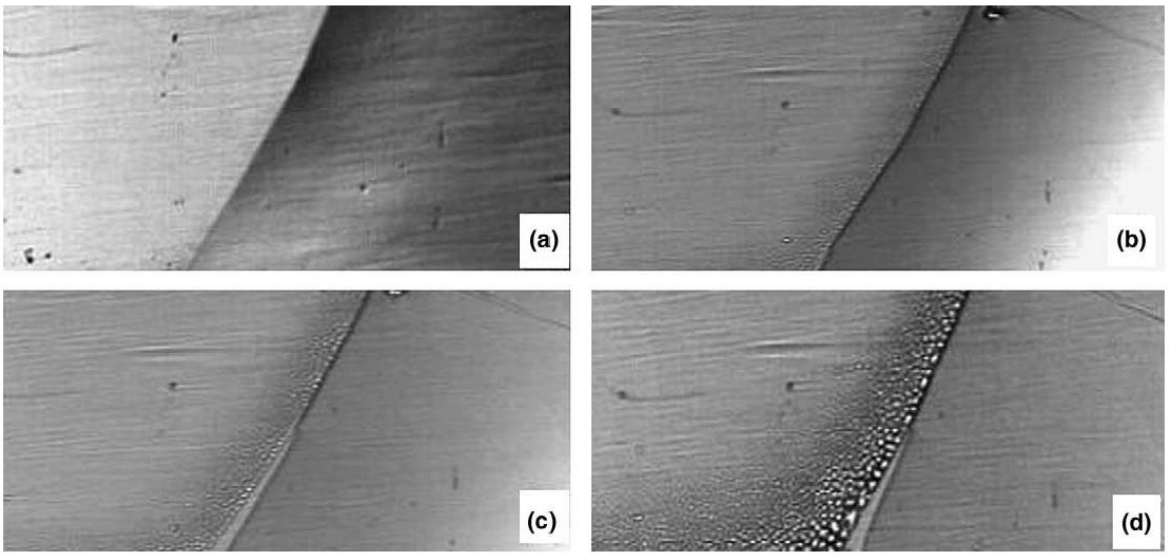

Figure 3-50: Effect of polarisation current on micro-droplet formation: showing increasing micro-droplet formation after polarisation at 100 mV for 10 s with different current densities: (a) i = 0 µA; (b) i = 5 µA; (c) i = 10 µA; (d) i = 20 µA [92]

Zhang et al. [92] classified $MgCl_2$ and $CaCl_2$ as "weak" corrosive salts at elevated relative humidities, and NaCl was speculated to be more corrosive under identical chloride

concentration due to the fact that larger secondary spreading of NaCl containing droplets occurred than $MgCl_2$ and $CaCl_2$ containing droplets. Tests performed with NaCl droplets on stainless steels showed large areas of micro-droplet formation, while for identical exposure conditions (90% RH at 20°C) with $MgCl_2$ secondary spreading was not observed for which no explanation was given. The fact that the solubility of $MgCl_2$ is greater than that of NaCl, and that higher chloride ion concentrations can be formed on the DRH (10-12 M for $MgCl_2$ while 6 M for NaCl) $MgCl_2$ should be a "stronger" corrosive salt at relative humidities lower than the DRH of NaCl (~78% RH). However, at and above the DRH of NaCl the effective chloride concentration under NaCl deposits is higher than that under $MgCl_2$; hence, NaCl can be considered as the more critical salt at higher relative humidities. The statement of *Zhang et al.* statement can be questioned since secondary spreading alone cannot be regarded as a measure for the atmospheric corrosion propensity.

The secondary spreading mechanism involves an increase of the number and volume of micro-droplets formed which can change by exposure time. Droplets can merge and form larger droplets [85, 92]. Micro-droplet formation is a function of salt type, material, RH, and temperature and can only be formed if the metal substrate forms anodic active regions where corrosion processes occur. *Tsuru et al.* [85] and *Zhang et al.* [92] showed that the size and location of the anode did not change while the cathode area expanded with time leading to enhanced corrosion activities. The rate of expansion strongly depended on the RH, and was enhanced by increasing the RH, suggesting that significant water uptake from the air occurred (Figure 3-51).

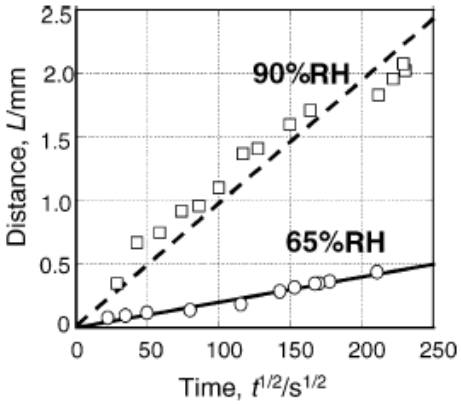

Figure 3-51: Effect of RH on secondary spreading of 0.5 M NaCl droplet [85]

Tsuru et al. [85] developed a model explaining the mechanism of secondary spreading (Figure 3-52) based upon Kelvin probe measurements and droplet spreading observations (lateral growth and micro-droplet formation). The development of cathodic potentials at the peripheral area of the droplet and anodic potentials in the centre showed a galvanic potential difference evolution which increased by time. Extensive cathodic oxygen reduction occurred on cathodic sites and led to a pH increase.

Local pH increase caused an electrical charge development between cathodic and anodic regions resulting in a cation migration towards the peripheral areas of the droplet to balance negative electrical charge. Metal hydroxides, $M^{x+}(OH)_x$ precipitated as discrete particles due to their low solubility and deposited onto the surface. Formation of $M^{x+}(OH)_x$ is accompanied by local depletion of water molecules which trigger water movement from the bulk droplet to the cathodic areas and also water uptake from air. The latter causes an increase of the droplet volume with lateral expansion and thickness growth of the droplet. Water and ionic species concentration balance, and water uptake from air is required to balance water activity in the droplet. The surface at high humidities contains certain amounts of monolayers of water depending on the surface nature of the metal and the relative humidity. Three layers of water molecules are enough to sustain bulk-solution-like water activity as shown by *Leygraf and Graedel* [64].

The expansion of the droplet is controlled by the movement of cations and water molecules through the water layer at the cathodic regions at the peripheral areas of the droplet. The cations can migrate outwards the droplet and attract oxygen and further water molecules and precipitate as $M^{x+}(OH)_x$. Discrete micro-droplets can be formed by absorbing water molecules and oxygen from air when the migration distance from the primary/main droplet is large, otherwise the water clusters formed are instantaneously linked to the primary droplet. Separate corrosion cells can be formed in single micro-droplets and cause corrosion.

The type of salt compound and the RH have large influence on the secondary spreading behaviour. *Tsuru et al.* [85] observed higher secondary spreading rates for NaCl containing droplets than for $MgCl_2$-laden electrolytes at 80% RH (Figure 3-52). Na^+ ions have smaller solvation diameters than Mg^{2+} ions, and therefore Na^+ ions have higher mobility. Furthermore, the hydroxides of group I metals are soluble (here Na) and group II metals are

very sparingly soluble (here Mg) causes faster secondary spreading of Na-containing electrolytes than those containing Mg.

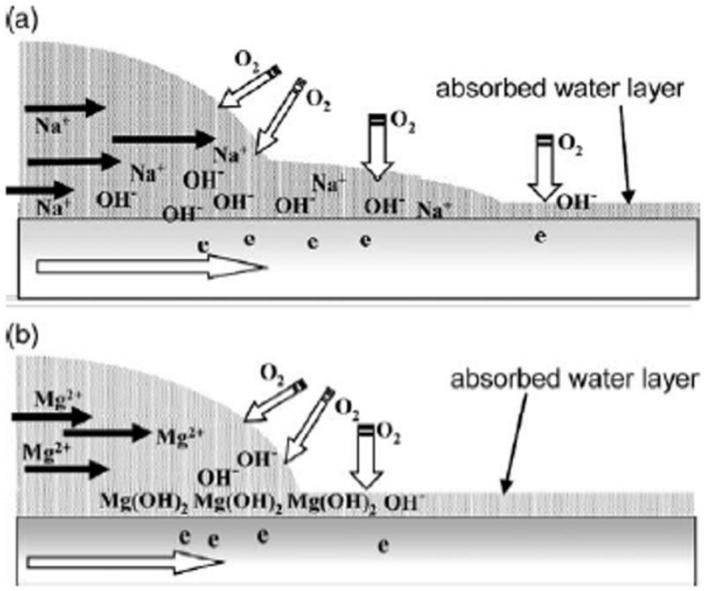

Figure 3-52: Mechanism of wetting and spreading at the rim of the droplet for (a) NaCl and (b) $MgCl_2$ solutions [85]

Micro-droplets tend to grow concentrically and coagulate to form larger droplets when they come into contact as observed by *Ebert et al.* [94] and *Neufeld et al.* [93].

The cathodic current is controlled by oxygen reduction which strongly depends on the rate of oxygen uptake from air, and the anodic activity is controlled by the rate of anodic metal dissolution. Secondary spreading increases the wetted area (larger corrosion cell), and hence causes larger corrosion rates due to the fact that a larger effective droplet has been formed.

Zhang et al. [92] reported that oxygen has a vital role in micro-droplet formation, who asserted that no micro-droplet formation would occur when oxygen in air is replaced by argon eliminating cathodic oxygen reduction. Hence, no corrosion cells can be formed and the corrosion process stops when oxygen is consumed. The phenomenon that corrosion processes can be retarded might be beneficial for the ILW storage context. The entire facility could be purged with Argon (or hutches with ILW storage containers?). However, the applicability may not be cost-effective, but can be regarded as a way of counter measure in the worst case when the structural integrity of stainless steel containers has become likely to fail.

3.5.4.4.4 Hygroscopic Behaviour of Salts

Salts in nature are hygroscopic and can absorb water from air and cause corrosion. The deliquescence point is always lower than the dew point; therefore, the electrolyte necessary for corrosion can almost only be formed by deliquescence of a salt compound upon the metal surface. Below the deliquescence point, water from air can still adsorb onto salt crystals to form a hydrated salt with crystal water bonding. The concentration of crystal water can increase with RH leading at the deliquescence point of the salt to a spontaneous liquidation of the salt and formation of a saturated solution.

Above the deliquescence point, the salt solution is diluted with the increase of RH. The process backwards does not necessarily lead to a fully dry salt at the deliquescence point. The salt solution crystallises at a much lower RH; at its efflorescence point [95, 96] as illustrated schematically in Figure 3-53. Therefore, in real ILW storage conditions where temperature and RH fluctuations are inevitable a shift of the deliquescence point of various salt compounds should always kept in mind. Hence, in real-storage cases the deliquescence point is dynamic and can be further influenced by organic matter.

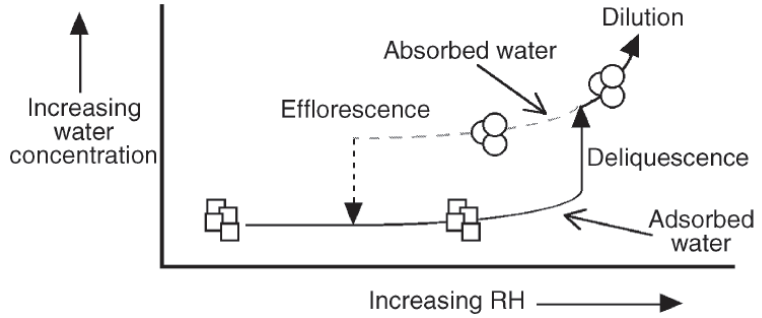

Figure 3-53: Relationship between salt water content, relative humidity, and deliquescence of salt crystals [95]

Deliquescence in such cases can be highly complicated which may have supporting effect of corrosion processes. Interim storage facilities are operated at 50-60% RH levels in order to keep pollutants containing $CaCl_2$ and $MgCl_2$ salt compounds highly diluted. However, the deliquescence point of these salts could be shifted to higher RH values, or the deliquescence point of NaCl, which is at 78% RH, could be lowered to lesser RH values and lead to higher concentrated solutions than expected which can cause atmospheric pitting corrosion [95, 96].

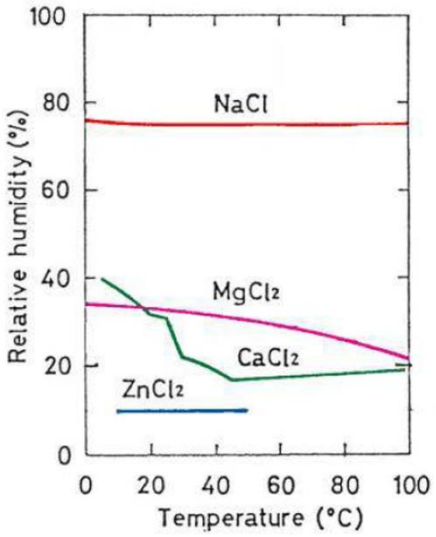

Figure 3-54: Temperature dependency of the deliquescence behaviour of different salts [97]

NaCl can be still wet below its DRH for a certain amount of time since water can adhere onto salt crystals. Questions remained whether corrosion can become likely even at lower relative humidities than the DRH? The temperature behaviour of the DRH in equilibrium of some salt compounds is shown in Figure 3-54.

3.6 Atmospheric-induced Stress Corrosion Cracking Propensity of DSS

The lifetime of ILW storage containers can be limited by corrosion mechanisms. Atmospheric pitting and/or crevice corrosion are possibly the most detrimental form of localised corrosion. However, in the presence of stress (residual or externally applied) in the microstructure, a more severe type of degradation, namely atmospheric stress corrosion cracking can reduce the lifetime to much shorter periods. Environmental parameters affecting corrosion and stress corrosion cracking propensity are the temperature, moisture, type and chemistry of contamination, gaseous atmosphere, metallurgical factors, residual stress, mechanical load, air flow rate, surface finish, and surface biological activities [98].

Residual or applied strain at the container material can support pitting or crevice corrosion initiation and lead to crack formation at corrosion sites. Atmospheric or atmospheric-induced stress corrosion cracking (ASCC) could therefore be the most critical failure mechanism of ILW containments [50, 64, 82, 88, 96, 97, 99-105].

Grade 2205 duplex stainless steel (DSS) has three advantages over 304L and 316L austenitic stainless steels as ILW container materials [68, 97]:

- Increased localised corrosion resistance
- Improved chloride-induced stress corrosion cracking resistance
- Higher threshold stress and temperature for stress corrosion cracking.

However, grade 2205 is susceptible to pitting corrosion at ≥35°C, and may be susceptible to stress corrosion cracking as well. For many years the threshold stress corrosion cracking temperature has been believed to be around 50-60°C for austenitic stainless steels [7, 68, 97, 106-108]. The atmospheric stress corrosion cracking propensity of duplex stainless steels has been by far less studied. Recent publications will be introduced and discussed in detail.

3.6.1 Studies of *Prosek et al.* (2009)

Prosek et al. carried out a systematic investigation of the effect of salt chemistry, temperature, and RH on atmospheric corrosion and atmospheric stress corrosion susceptibility of various austenitic and duplex stainless steels. U-bend specimens were prepared from sheet metals with specifications given in Table 3-10 and the surface exposed

with salt-laden droplets with 66 µl volume yielding 90 mm² coverage area in climatically-controlled environments at 15, 30, 50, and 70% relative humidities and at 20-50°C [68]. The U-bends were exposed with $MgCl_2$, $CaCl_2$, and NaCl salts solutions having 26000, 29000, and 14000 µg/cm² deposition densities, respectively for 4-22 weeks.

Table 3-10: Material specification of U-bends used in the study of *Prosek et al.* [68]

Stainless Steel Grade			Microstructure	Typical Chemical Composition (wt%)					Thickness	Total
ASTM	EN	UNS	(PRE)	Cr	Ni	Mo	N	Other	(mm)	Strain
304	1.4301	S30400	Austenite (18)	18	8.4	0.1	0.04		2.9	0.15
316L	1.4404	S31603	Austenite (24)	18	11.4	2.1	0.04		2.9	0.15
904L	1.4539	N08904	Austenite (30)	20	24.7	4.5	0.04	1.5% Cu	1.9	0.10
S31254	1.4547	S31254	Austenite (43)	20	18.0	6.1	0.20	Cu	2.0	0.10
S32101[(1)]	1.4162	S32101	Duplex (26)	22	1.5	0.3	0.23	5% Mn	1.4	0.07
2304	1.4362	S32304	Duplex (26)	22	4.8	0.3	0.09		2.0	0.10
2205	1.4462	S32205	Duplex (35)	22	5.5	3.0	0.12		2.0	0.10
2507	1.4410	S32750	Duplex (43)	25	7.7	4.0	0.29		3.0	0.15

(1) LDX 2101.

The aggressiveness of chloride salt deposits was assumed to be predominantly controlled by the activity of chloride ions in the salt water droplet, and it was argued that the equilibrium chloride concentration in the droplet in a certain RH determines the chloride stress corrosion susceptibility. The chloride concentration is the highest at the DRH of the salt and has a certain solubility limit at each temperature and RH (Figure 3-55). It was argued that the solubility limit of the salt shows the maximum corrosion susceptibility in that temperature and that the RH can only have a dilution effect of the solution (Figure 3-56). $CaCl_2$ showed the largest chloride concentration, therefore, highest driving force for corrosion. A chloride concentration of 12.4 M was calculated for $MgCl_2$ at 50°C.

Stress corrosion cracking was observed in a certain RH range on 304, 316, and 2304 stainless steels only, whilst the super austenitic and duplex stainless steels showed corrosion but no cracking after post-mortem observation of the corrosion morphologies using optical microscopy (Table 3-11). *Prosek et al.* [68] believed that these testing conditions in such a short time were representative for material applications relevant for swimming pools and concluded a safe application for non-cracked materials.

The fact that stress corrosion cracking of stainless steels occurs with very low rates, means that *Prosek et al.* may have misinterpreted the long-term applicability of, in particular, lean 2101 duplex stainless steel. The incubation time for stress corrosion cracking was alleged to

lie within the testing time although longer incubation times may be possible and probably alloy-dependent.

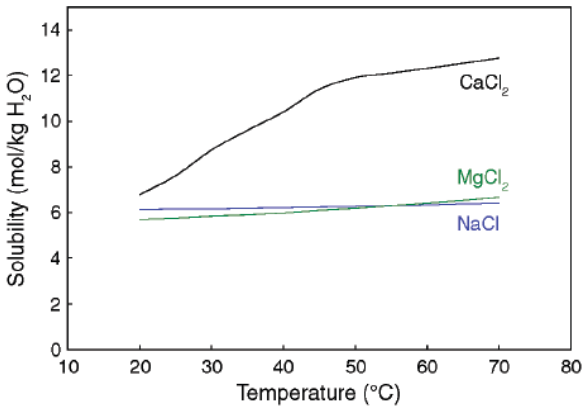

Figure 3-55: Solubility of chloride salts as a function of temperature [68]

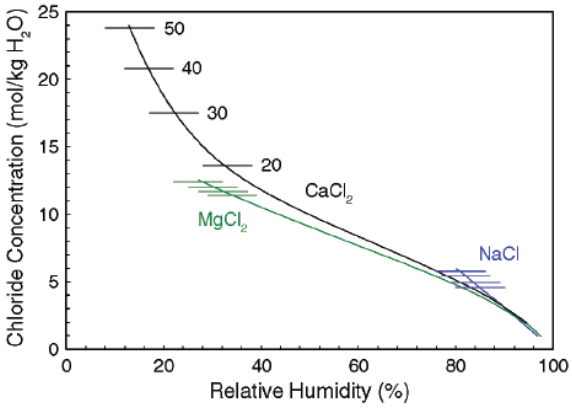

Figure 3-56: Calculated equilibrium chloride concentration in water solutions of different salts as a function of relative humidity. Horizontal lines indicate solubility limits at 50, 40, 30, and 20°C (from top to bottom) [68]

Table 3-11: Test results of U-bend specimens exposed with chloride deposits [68]

Exposure Conditions			Exposure	Stainless Steel Grade (UNS)							
Salt	T (°C)	RH	(weeks)	304	316L	904L	S31254	S32101	2304	2205	2507
$MgCl_2$	50	~30	4	SCC 6	SCC 6	PIT	PIT	PIT	PIT	PIT	PIT
$CaCl_2$	50	~15	4	SCC 3	SCC 2	ET	ET	PIT	ET	ET	ET
$MgCl_2$	50	~30	22	SCC 6	SCC 6	PIT	PIT	PIT	ET	PIT	PIT
$CaCl_2$	50	~15	22	SCC 5	SCC 4	PIT	PIT	PIT	PIT	PIT	PIT
$MgCl_2$	40	30	4	SCC 2	PIT	NO	NO	PIT	ET	ET	PIT +
$CaCl_2$	40	30	4	SCC 6	SCC 6	PIT	PIT	PIT	ET	ET	PIT +
$MgCl_2$	40	30	10	SCC 2	PIT	PIT	NO	ET	ET	ET	NO
$CaCl_2$	40	30	10	SCC 6	SCC 6	PIT	PIT	ET	ET	ET	PIT +
NaCl	40	30	10	NO	NO	NO	NO	NO	NO	NO	NO
$MgCl_2$	40	50	10	SCC 5	PIT	PIT	PIT	ET	PIT +	PIT	ET
$CaCl_2$	40	50	10	SCC 4	PIT	PIT	PIT	ET	PIT +	PIT	ET
NaCl	40	50	10	NO	NO	NO	NO	NO	NO	NO	NO
$MgCl_2$	40	70	10	ET	NO	NO	NO	ET	NO	NO	NO
$CaCl_2$	40	70	10	ET	NO	NO	NO	ET	NO	NO	NO
NaCl	40	70	10	NO	NO	×	NO	NO	×	NO	NO
$MgCl_2$	30	30	10	SCC 2	PIT	×	PIT	ET	×	ET	ET
$CaCl_2$	30	30	10	SCC 6	SCC 6	×	PIT	ET	×	PIT	ET
$MgCl_2$	30	50	10	PIT	NO	×	NO	PIT	×	PIT	ET
$CaCl_2$	30	50	10	PIT	PIT	×	ET	PIT +	×	PIT	ET
$MgCl_2$	30	70	10	ET	NO	×	NO	NO	×	NO	NO
$CaCl_2$	30	70	10	ET	NO	×	NO	ET	×	NO	NO
$MgCl_2$	20	30	10	PIT	PIT	×	PIT	ET	×	PIT	PIT
$CaCl_2$	20	30	10	PIT	PIT	×	PIT	ET	×	PIT	PIT
$MgCl_2$	20	50	10	PIT	PIT	×	NO	PIT +	×	ET	ET
$CaCl_2$	20	50	10	PIT	PIT	×	NO	PIT +	×	ET	ET

SCC #: stress corrosion cracks found in a given number of six contaminated zones
PIT: pitting
ET: surface etching
NO: no corrosion
×: not tested
+: tiny cracks

Furthermore, the spatial resolution of optical microscopy is limited to ~1 µm which render impossible to notice cracks in sizes of ≤1 µm. There could have been micro-cracks formed which may have not been noticed for which, actually, a scanning electron microscope would

be required. For example, a 1.4 mm long crack was denoted as ‘tiny’ (Figure 3-57). It will be shown later that what was called ‘tiny’ was in fact the largest crack observed in this work.

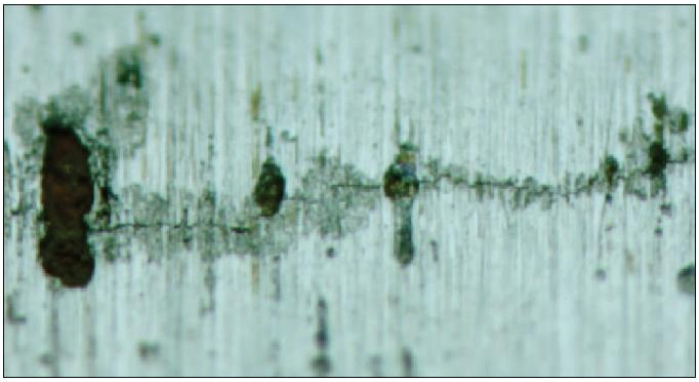

Figure 3-57: ‘Tiny’ crack on the surface of grade 2304 duplex stainless steel exposed with $MgCl_2$ at 40°C and at 50% RH for 10 weeks; width 1.4 mm [68]

The fact that vast deposition densities of chloride salts were used may also bring into question the relevance for ILW-container application, due to the fact that such a large amount of salt may never be expected to be formed above the stainless steel surface. Stress corrosion cracking can occur in certain potential regimes only, and using high chloride deposits and large droplet sizes increases the local corrosion potential so that general corrosion can occur where stress corrosion cracking evolution may become less likely, or the metal anodic dissolution rate may exceed the rate of stress corrosion cracking.

3.6.2 Studies of Prosek et al. (2013-2014)

Prosek et al. [107, 109] did comprehensive landmark investigations of atmospheric chloride-induced stress corrosion cracking susceptibility on various grades of duplex stainless steels. The effect of temperature, relative humidity, amount and type of chloride salt deposits was systematically investigated on welded plate materials. Salt-laden water droplets were deposited onto the surface of various hot-rolled plate (HRP) and cold-rolled coil (HRC) duplex stainless steels materials (see Table 3-12) in welding-induced stressed and unaffected regions (Figure 3-58) and exposed to different relative humidities and temperatures in a climatically controlled cabinet.

Table 3-12: Material specifications of materials used in the investigations of *Prosek et al.* [107, 109]

Material	Chemical Composition (wt%)									Ferrite Content (%)	Austenite Spacing (µm)	Grain Size (µm)	PRE[A]	CPT[B] (°C)
	C	Si	Mn	P	Cr	Ni	Mo	Cu	N					
2101/HRC	0.018	0.7	5.0	0.02	21.4	1.6	0.2	0.2	0.22	50±2	5.4	—	26	18
2202/HRP	0.017	0.4	1.3	0.02	23.0	2.5	0.3	—	0.21	53±6	6.1	—	27	37
2304/HRC	0.015	0.4	1.5	0.03	23.2	4.8	0.4	0.3	0.12	49±2	3.2	—	26	33
2304/HRP	0.018	0.4	1.3	0.03	22.7	4.3	0.3	—	0.15	46±2	6.2	—	26	30
2205/HRP	0.017	0.3	1.8	0.03	22.2	4.9	2.6	—	0.16	53±2	5.8	—	33	49
304L/HRC	0.019	0.3	1.6	0.03	18.2	8.1	—	0.5	0.07	—	—	16	19	<10
316L/HRC	0.022	0.5	1.3	0.03	16.9	10.1	2.1	0.4	0.05	—	—	23	25	15

[A] Pitting resistance equivalent, PRE = Cr + 3.3Mo + 16N.
[B] ASTM G150.

X-ray diffraction stress measurements revealed a compressive nature of ferrite and austenite in the unaffected regions, while the heat-affected zone was tensile stressed. Both phases were tensile stressed in the direction measured perpendicular (radial) to the circular weld while the ferrite remained compressive and austenite was tensile in the direction measured transverse (tangential) as can be seen in Figure 3-59. Apparently, larger tensile stresses were built up in the austenite in comparison to in the ferrite after the welding treatment.

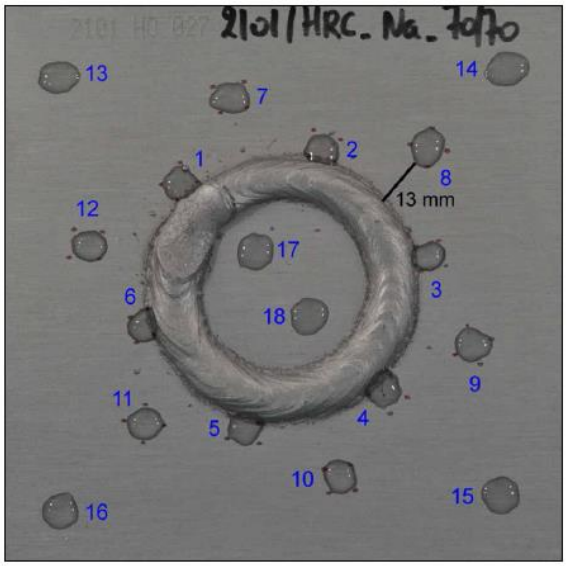

Figure 3-58: Photograph of a specimen (130 mm by 130 mm) showing a circular weld and deposited salt droplets (ø ≈ 8 mm); Drop 1-6 (Ring 1) is located on the heat-affected zone, drops 7-12 (Ring 2) is 13 mm offset to the heat-affected zone, drop 13-16 (corners) are on unaffected regions and drop 17 and 18 (centre) are within the circular weld [107, 109].

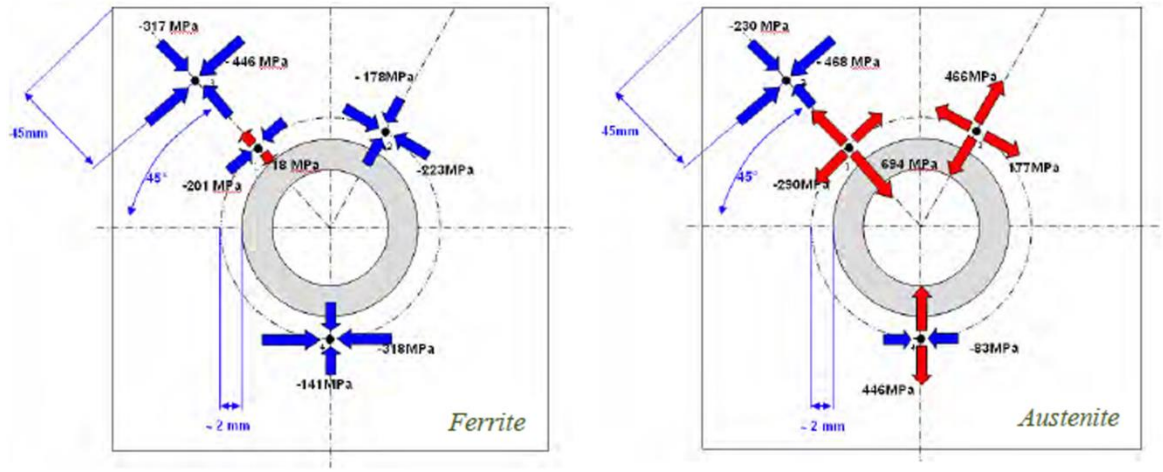

Figure 3-59: X-ray diffraction stress measurement results of welded 2205 duplex stainless steel. Blue arrows indicate compressive stress and red arrows indicate tensile stress [109].

Salt-laden droplets of $MgCl_2$, $CaCl_2$, and NaCl with deposition densities from 1.6-16000 µg/cm² were used. The investigations showed that $CaCl_2$ had the most severe effect on corrosion and stress corrosion cracking susceptibility, and it was believed that this salt determines the long-term corrosion performance of the material used. A summary of the corrosion tests using $CaCl_2$ deposits after exposure to 50°C and 30% RH for 8 weeks is given in Table 3-13.

Table 3-13: Summary of corrosion tests showing the corrosion morphology observed as a function of surface chloride coverage of $CaCl_2$ deposits after exposure to 50°C and at 30% RH for 8 weeks [107, 109]

Cl^- Coverage (g/m²)	2101/HRC	2202/HRP	2304/HRP	2205/HRP	304L/HRC	316L/HRC
0.016	NC	NC	NC	NC	NC	NC
0.16	Etching	Etching	Selective	Etching	Pitting	Pitting
1.6	Pitting	Pitting	Etching	Etching	SCC	SCC
16	Selective	Selective	Selective	Selective	SCC	SCC
160	Selective	Selective	Selective	Selective	SCC	SCC

Grade 2205 duplex stainless steel was the most corrosion resistant stainless steel among various other types of equivalent stainless steel grades. Selective corrosion of ferrite was observed occurring under chloride deposits with 1600 and 16000 µg/cm² of $CaCl_2$. Selective corrosion of ferrite was reported to be the main corrosion mechanism of all duplex grades used as can be seen in Figure 3-60. The extent of corrosion (depth and width) was larger on heat affected regions than on unaffected sites.

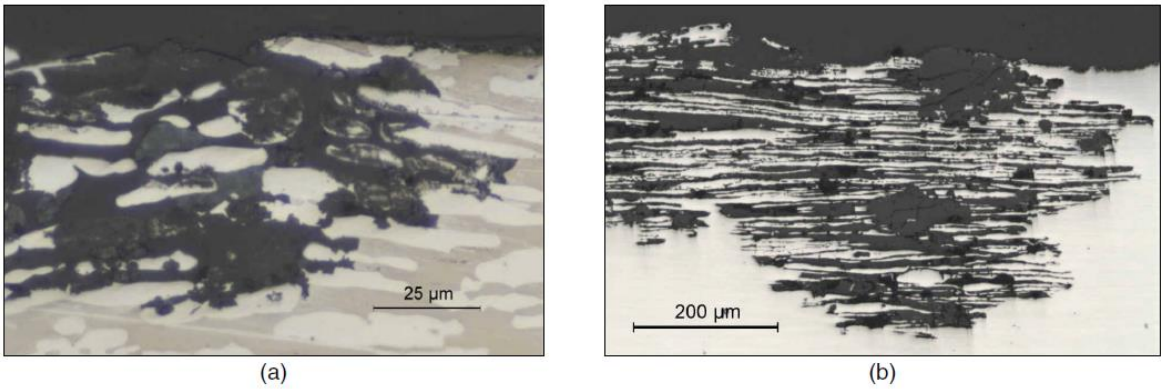

Figure 3-60: Cross-sectional optical micrographs of corroded samples showing selective corrosion of ferrite (a) of 2202/HRP under $CaCl_2$ deposits after exposure to 50°C and 50% RH (Ring 2), (b) of 2101/HRC under NaCl deposits after exposure to 50°C and 70% RH (Ring 2) [107, 109].

Pitting corrosion was seen to occur simultaneously with selective corrosion of ferrite on a macroscopic scale on the heat-affected microstructure (Figure 3-61). This may be attributed to sensitisation effects caused by the welding treatment.

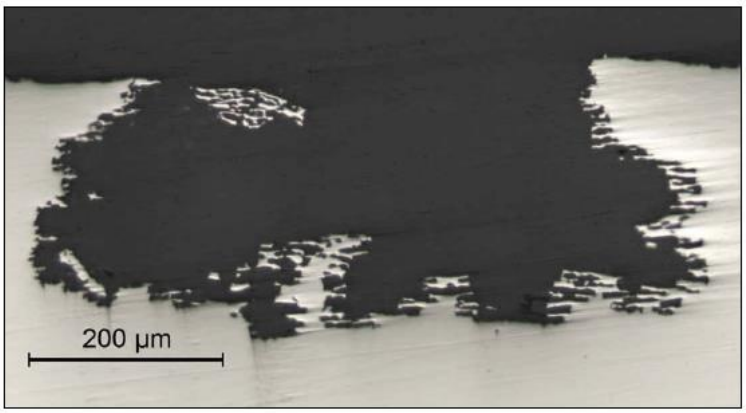

Figure 3-61: Cross-sectional optical micrographs showing pitting with selective corrosion of 2304/HRP after exposure to 70°C and 90% RH formed under salt droplet containing NaCl (Ring 1). Pit diameter is 980 µm [107, 109].

Prosek et al. did not observe stress corrosion cracking occurring at ≤50°C for 2205 duplex stainless steel under any type of salt droplet solution. However, they reported SCC occurrence at 70°C and 30% RH under $CaCl_2$ deposits after 8 weeks exposure (see Figure 3-62). Selective corrosion was observed on the surface, and cracks were seen propagating through the austenite and interphase boundaries only. The crack propagation path seemed to be slightly preferred along the rolling direction of the microstructure. The cracks observed

were typical for the passive type of stress corrosion cracking with branching character clearly indicating chloride-induced stress corrosion cracking mechanism.

Lean duplex grade 2202 was seen to suffer from stress corrosion cracking at temperatures as low as 30°C at 50% RH under $CaCl_2$ electrolyte within 8 weeks (Figure 3-63). This clearly demonstrated superior stress corrosion cracking resistance of 2205 duplex stainless steel to lower alloyed duplex grades.

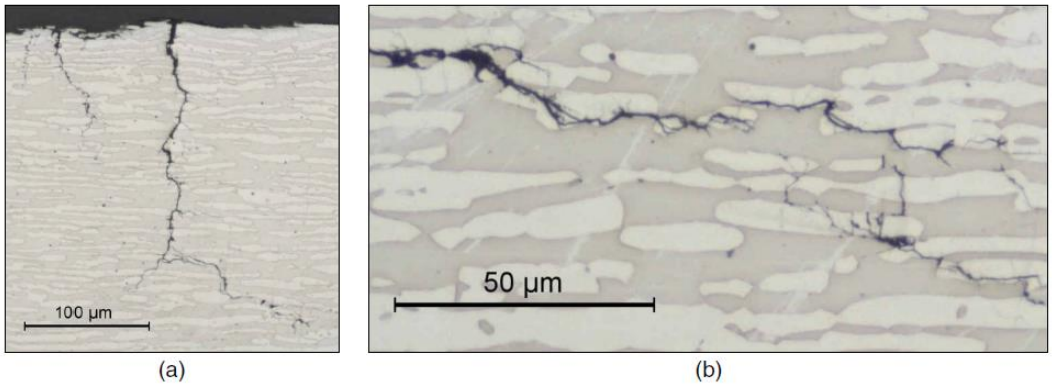

Figure 3-62: Cross-sectional optical micrographs of 2205/HRP after exposure to 70°C and 30% RH in Ring 1 showing (a) SCC occurred under a deposit containing $CaCl_2$, (b) SCC occurred under a deposit containing $MgCl_2$. Austenite is bright and ferrite dark [107, 109].

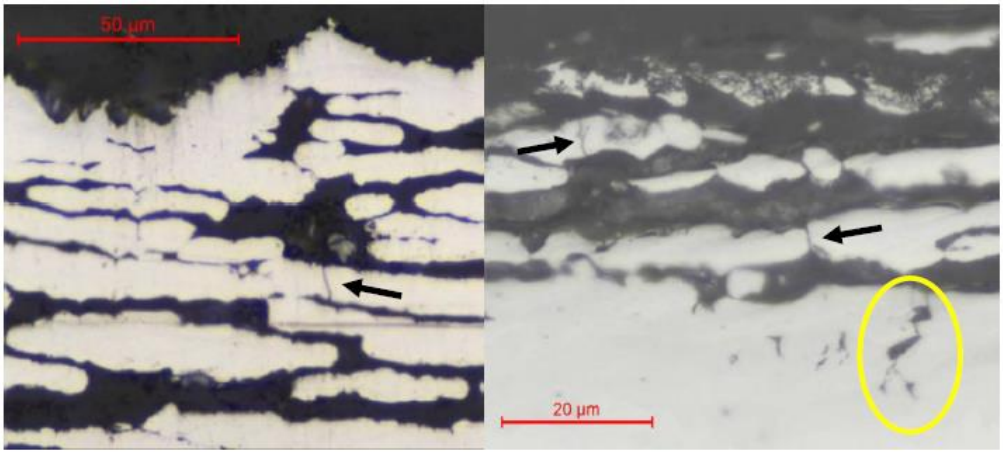

Figure 3-63: Cross-sectional optical micrographs showing micro-cracks formed in austenite (arrows) while selective corrosion occurred on ferrite in 2202/HRP after exposure to 30 °C and 50 % RH under a deposit containing $CaCl_2$. Exposure time was 8 week: (a) Ring 1 droplet 4, (b) ring 1 droplet 1 [109]

Large selective corrosion of ferrite was observed penetrating towards the bulk interior by leaving the surrounding austenite grains almost unaffected. Seemingly, austenite remained passive and suffered from cracking whilst ferrite actively dissolved. This indicated that austenite was more cathodic than ferrite since selective corrosion of ferrite clearly indicated

highre oxidation rates. Stress corrosion cracks initiated on interphase boundaries or directly on austenite grains and propagated, usually, transgranular through the grains. Cracks were seen to develop on highly tensile-stressed regions only, i.e. ring 1 sites apparently showing the need for large tensile stresses to render the material susceptible to stress corrosion cracking.

Similar corrosion morphology was also observed on 2101 lean duplex stainless steel. Selective corrosion of ferrite was the prevalent corrosion mechanism occurring jointly with stress corrosion cracking of austenite under $MgCl_2$ electrolyte after 8 weeks exposure to 20°C and at 50 % RH (Figure 3-64). Again cracking was observed occurring in regions with high tensile stresses only (ring 1). The authors concluded enhanced tendency for corrosion and stress corrosion cracking with increasing temperature and decreasing RH with most severe attack occurring on the DRH of the specific salt.

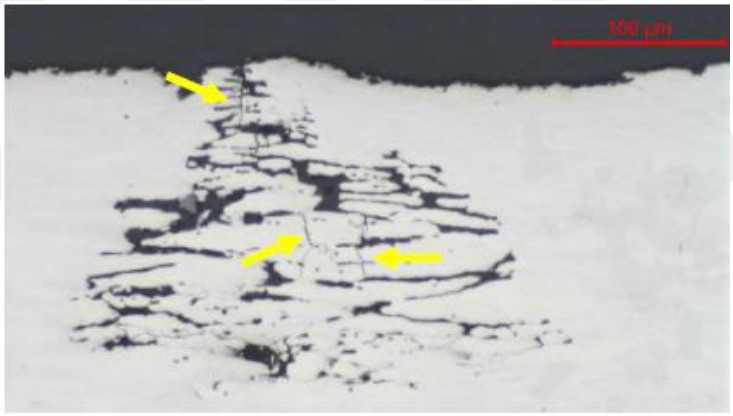

Figure 3-64: Cross-sectional optical micrograph showing micro-cracks formed in austenite (arrows) whilst selective corrosion occurred on ferrite in 2101/HRC after exposure to 20 °C and at 50 % RH under a deposit containing $MgCl_2$ for 8 weeks (Ring 1, droplet 1) [109]

Selective corrosion and stress corrosion cracking susceptibility regimes as a function of temperature and relative humidity were mapped in corrosion diagrams as shown in Figure 3-65. Maximum corrosion susceptibility can be seen occurring under $CaCl_2$ electrolytes followed by $MgCl_2$. No corrosion attack was observed under NaCl droplets at temperatures ≤60°C and shall be deemed to be harmless for real ILW storage container application of 2205 duplex stainless steel.

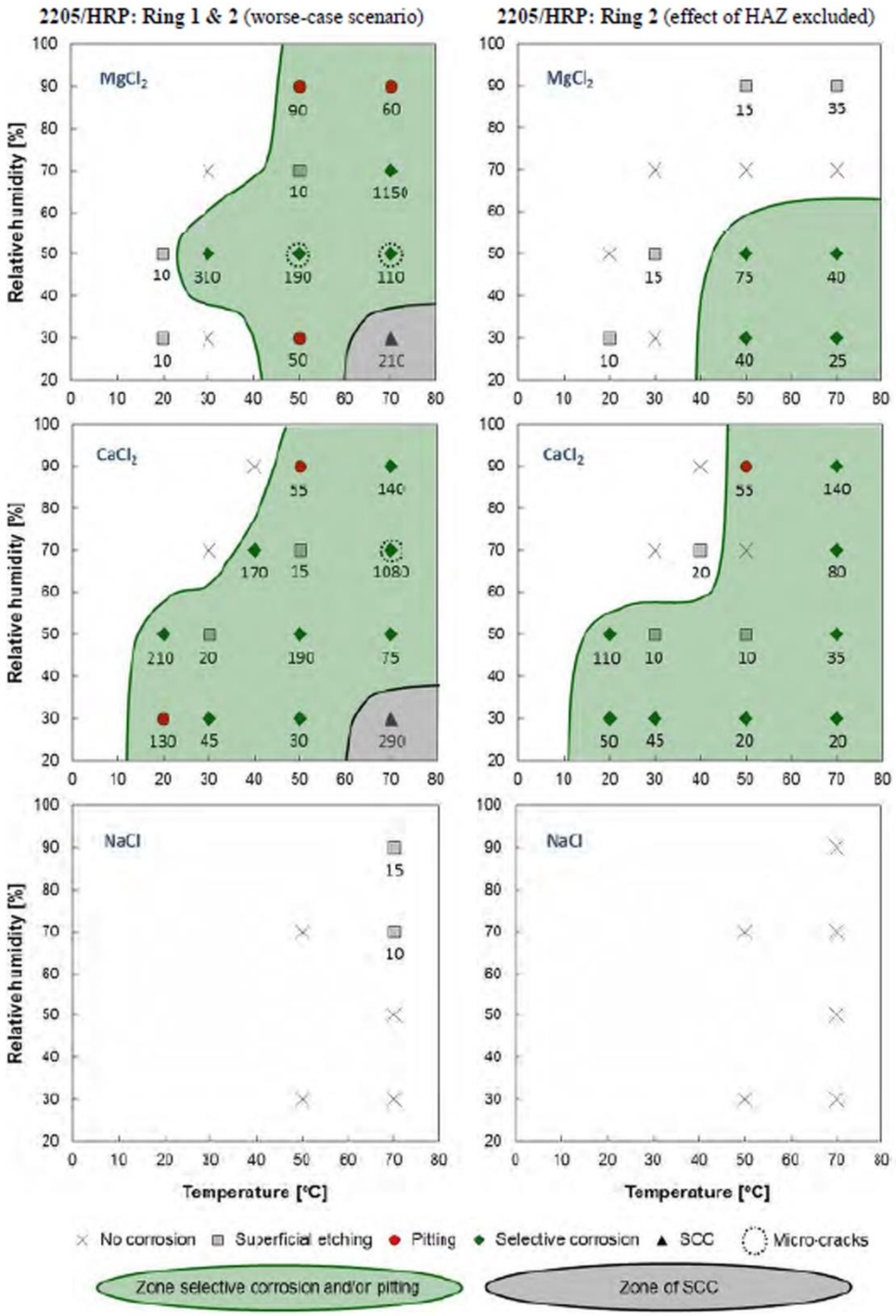

Figure 3-65: Morphology and depth of attack of 2205 duplex stainless steel. Numbers indicate the corrosion depth measured in µm [109]

Stress corrosion cracking was observed at 70°C only, and selective corrosion of ferrite was the prevalent corrosion mechanism at all regimes. However, the occurrence of selective corrosion and/or etching at temperatures as low as 20°C could still make possible the development of stress corrosion cracking after much longer exposure times although *Prosek*

et al. argued that stress corrosion cracking of 2205 duplex stainless steel is not possible at temperatures ≤50°C [107]. This was done based on the solubility limit of the salt chloride and the required critical chloride concentration to initiate stress corrosion cracking (see Table 3-14).

Table 3-14: Calculated threshold temperatures for the onset of stress corrosion cracking in the presence of saturated solutions of selected chloride salts with sufficient surface chloride coverage (in °C) [107]

Stainless Steel	$ZnCl_2$	$FeCl_3$	LiCl	$CaCl_2$	$MgCl_2$	$FeCl_2$	KCl	NaCl
304L/HRC	<20	<20	<20	<20	20	23	65	65
316L/HRC	<20	<20	<20	22	28	32	74	76
2205/HRP	<20	≈35	50	48	63	62	>80	>80

The threshold temperature for the onset of stress corrosion cracking under $MgCl_2$ deposits is 63°C; thus, cracking is not possible below that temperature. The calculated solubility limit for $MgCl_2$ at 50°C yields a maximum chloride concentration of 12.4 M and is lower than the equilibrium chloride concentration necessary to initiate SCC. Therefore, SCC is not possible for conditions with equilibrium chloride concentrations higher than the maximum chloride concentration at the solubility of the salt. In the presence of $CaCl_2$, however, SCC may still be possible at 48°C and at 35°C, if $FeCl_3$ is present. Figure 3-66 shows corrosion diagrams established by *Prosek et al.* showing SCC and selective/pitting corrosion regimes under various salt chloride solutions as a function of critical chloride concentration and temperature.

The diagrams and calculations from *Prosek et al.* are very useful but seem to be too simplistic since the authors did not consider metallurgical effects, the effect of the magnitude of tensile stress, the type of deformation (rolling, bending etc.), microstructural orientation effects (i.e. tensile direction along rolling or transverse direction), nor secondary spreading effects and the effect of droplet size. All these parameters can significantly influence stress corrosion cracking susceptibility.

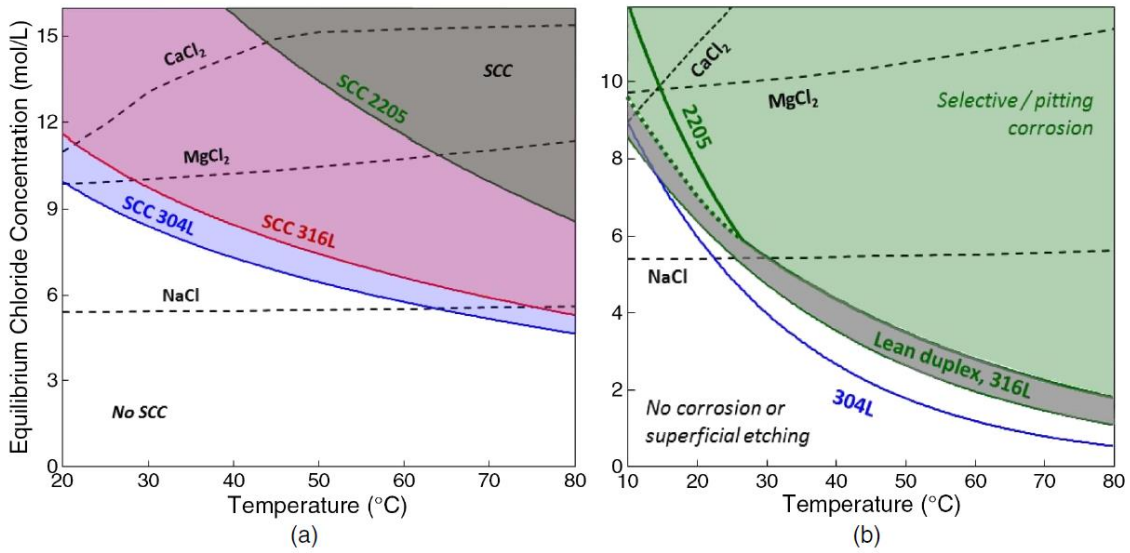

Figure 3-66: Corrosion diagrams of stainless steels showing (a) SCC regimes and (b) selective/pitting corrosion regimes under various salt chloride solutions as a function of critical chloride concentration and temperature. Full lines show the critical chloride concentration necessary to initiate SCC for each alloy. Dashed curves show solubility limits of $CaCl_2$, $MgCl_2$, and NaCl [107].

3.6.3 Studies of Arnold et al. (1997)

Arnold et al. studied atmospheric stress corrosion cracking susceptibility of grade 2205 duplex stainless steel and other stainless steels [110-112]. U-bend specimens with 10 mm bending radius were deposited with 500 µl of 30% $MgCl_2$ (droplet diameter 2.5-3 mm) and exposed to climatically-controlled environments at 40°C at 35% and 70% RH for up to 342 days. A deposition density of 3056 mg/cm² of $MgCl_2$ was calculated.

Stress corrosion cracking with crack length more than 100 µm accompanied by pitting corrosion and selective corrosion cracking of ferrite was observed after 42 days exposure at 40°C and 35% RH as can be seen in Figure 3-67(b). On the austenitic 316L stainless steel stress corrosion cracking was also observed to initiate from a corrosion pit as shown in Figure 3-67(b).

It should be noted that the deposition density used was extreme, and such a vast amount of salt deposits would never be expected to occur in real ILW storage facilities. However, these tests showed that grade 2205 duplex stainless steel may be rendered susceptible to stress corrosion cracking if extremely strong conditions can be prevailing.

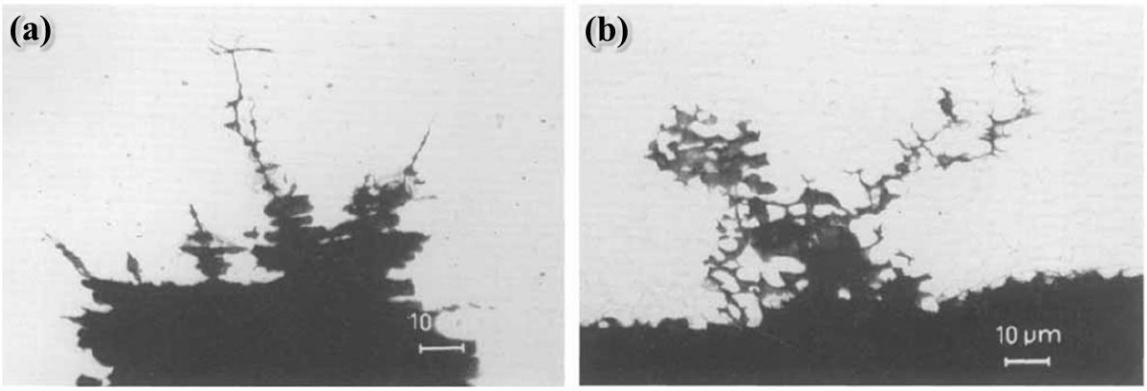

Figure 3-67: Atmospheric stress corrosion cracking: (a) 316L and (b) 2205 DSS [110]

3.6.4 Studies of Tani et al. (2008)

Tani et al. [113] studied atmospheric stress corrosion cracking propensity of 2507 super duplex stainless steel and 304 and 316 austenitic stainless steels using constant-load specimens deposited with exposed 1000 µg/cm² chloride wetted deposits under 35% RH at 80°C as a function of applied stress and time with maximum exposure times up to 1533 days (~64 months). The salt used was synthetic sea water containing mainly NaCl, $MgCl_2$, and Na_2SO_4.

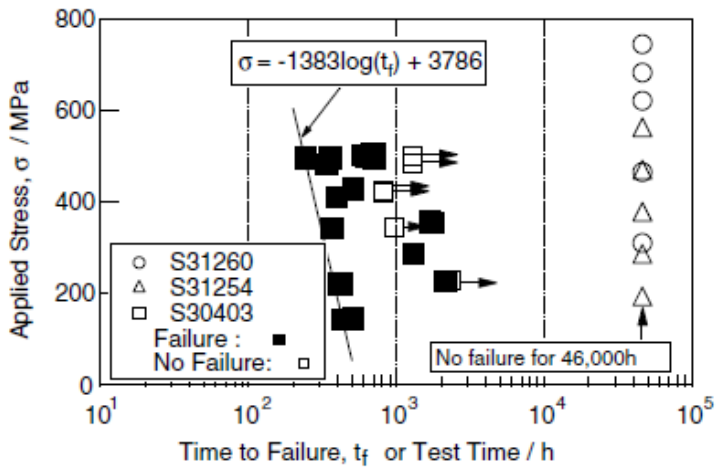

Figure 3-68: Atmospheric stress corrosion susceptibility of stainless steels using constant-load test setup with 1000 µg/cm² chloride surface deposits after exposure to 35% RH and 80°C [113]

The austenitic grades; 304 and 316 were seen to show stress corrosion cracking after 500 hours exposure while the super duplex grade 2507 (S31260) showed, even after 46000 hours exposure time, no stress corrosion cracking occurrence. Corrosion only was reported after

optical microscopy analysis, which was most-likely selective corrosion. Increase of applied stress decreased the time to failure for both austenitic grades, but did not affect the performance of grade 2507 duplex stainless steel (Figure 3-68). However, stress corrosion cracking may have occurred, but were not noticed by using optical microscopy. Scanning electron microscopy investigations might have made it possible to see micro-cracks. Therefore, no absolute conclusion can be drawn.

3.6.5 Summary

Stress corrosion cracking under atmospheric chloride deposits can be more severe in comparison to full aqueous immersion conditions and occur below the believed critical threshold temperature (~60°C) for stress corrosion cracking. It could be shown that the corrosion propensity is enhanced by the amount of salt chloride deposits and residual/applied stress on the material.

A critical aspect, which has not been discussed in the literature, is the concept of critical pitting temperature (CPT) and critical crevice temperature (CCT). The fact that stress corrosion cracking is favoured to initiate from existing pits and/or crevices may facilitate stress corrosion cracking evolution at temperatures below 50°C.

CPT and CCT values for most common stainless steels types in their solution-annealed conditions have been determined using various methods such as the ASTM G48 method with 6% $FeCl_3$ (Figure 3-69). The currently used austenitic grades 304L and 316L are evidently more prone to pitting and crevice corrosion, and, hence more susceptible to stress corrosion cracking. The CPT and CCT values of grade 2205 duplex stainless steel are lower than 50°C, and it is therefore possible, when the conditions can be made, that stress corrosion cracking can occur even at room temperature.

Furthermore, in the literature the effect of corrosion chemistry, alloy composition, and applied stress have been investigated on atmospheric stress corrosion cracking susceptibility. However, the effect of microstructure of the stress corrosion cracking performance has not been studied yet. Therefore, comprehensive microstructural characterisation in light of corrosion and stress corrosion cracking propensity was the main focus for this thesis. No consideration was given to statistical evaluation and computational modelling.

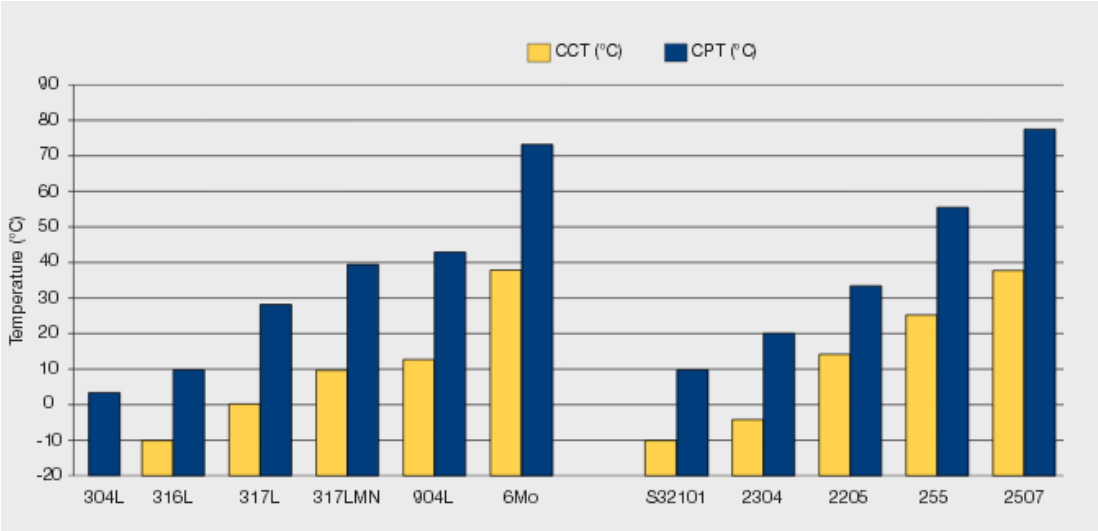

Figure 3-69: Critical pitting (CPT) and crevice (CCT) temperatures of solution-annealed duplex and austenitic grades in 6% ferric chloride medium according to ASTM G48 standard [114]

3.7 Metrology Techniques

Metrology techniques enable imaging and characterisation of the surface by means of a microscope. Microscopes are grouped depending on the type of interaction with the sample to generate an image of the surface. Interactions with the surface can be light or photons (optical microscope), electrons (electron microscope), or a probe (scanning probe microscope).

3.7.1 Optical Light Microscope (OLM)

An optical microscope uses visible light and a system of lenses to magnify the surface of a material. The image can be captured by a light-sensitive camera to generate a micrograph.

3.7.2 Scanning Electron Microscopy (SEM)

Scanning electron microscope (SEM) is used to reveal and characterise microstructural details with high resolution than an optical microscope. SEM's are often equipped with detectors for chemical analysis and crystallographic characterisation.

An electron beam is generated and directed to an (electrical conductive) surface. The interaction of the electron beam reveals a wide range of information which is collected with specially-designed detectors. Most interaction products of the electrons with the atoms at and near the sample surface are schematically illustrated in Figure 3-70.

Secondary electrons (SE) are generated from the inelastic scattering resulting from the interaction of incident electrons with the shell electrons of the atom. Secondary electrons are generally ejected with very low energies, up to 50 eV, from the nearest surface, up to 10 nm depth. The scattered electrons are collected by an SE-detector, and provide topographic information.

The ejection of a secondary electron produces a "hole" in the atom shell which puts the energy state of the atom to a higher level. An electron from the outer shell jumps into the hole of the inner shell by releasing a specific amount of energy and emanates a material-characteristic X-ray radiation. This energy has a characteristic wavelength specific for every atom. The characteristic X-ray radiation is used for elemental analysis. An energy-dispersive X-ray detector (EDX or EDS) is used to measure X-ray intensities by counting the photons generated. The EDX technique is semi-quantitative due to simultaneous occurrence of

undesired physical phenomena such as continuum X-ray and secondary X-ray absorption effects. Therefore, quantitative EDX results should never be stated more than one decimal after the comma.

If the primary electron interacts with the core of the atom and is bounced back, it loses its initial energy by inelastic scattering. This electron is then called backscattered electron and is collected by a backscattered electron detector (BSD).

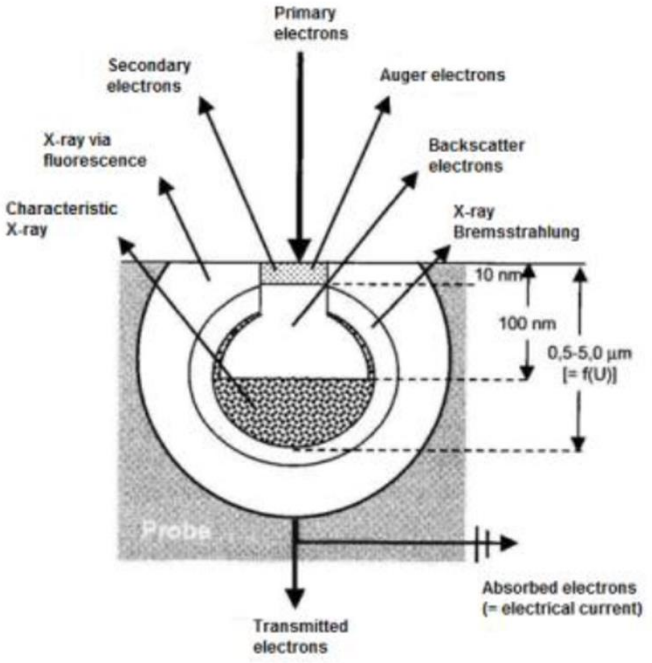

Figure 3-70: Products of all interactions between primary electrons with the material [115]

3.7.3 White Light Interferometry (WLI)

White light Interferometry (WLI) is a non-contact optical method to obtain surface topography information on 3D structures with sub-micron to Ångstrom resolution. Basically, the surface topography is scanned and mapped mathematically to a 2D or 3D image. All results are digital and quantitative, and can be post-processed. There are a few operation principles of WLI but in this thesis the Vertical Scanning Interferometry (VSI) method will be explained in detail only. In principal, the interferometer setup consists of a

- Light source,
- Condenser/collimating lens,

- Beam splitter,
- Reference mirror, and a
- CCD image sensor.

The light source is a laser which generates the light (white or green) with a high coherence path length. The light travels through an aperture which bundles the rays and focuses on the condenser lens. The condenser lens collimates the light and relays to a beam splitter. There, the light is separated into a reference and a measurement beam. While the reference beam is relayed to a very flat reference mirror with pre-set distance and is reflected back to the beam splitter, in the same time, the measurement beam is relayed to the surface where it is reflected or scattered from. Both beams interfere constructively or destructively at the beam splitter and are relayed to the CCD camera. They form an interference pattern of the test surface topography that is spatially resolved by the individual CCD pixels. The arrangement of the components is schematically shown in Figure 3-71. Scanning of the surface happens by changing the measurement beam path length relative to the reference beam (which is steadily constant) through an accurate piezo-controlled positioning stage.

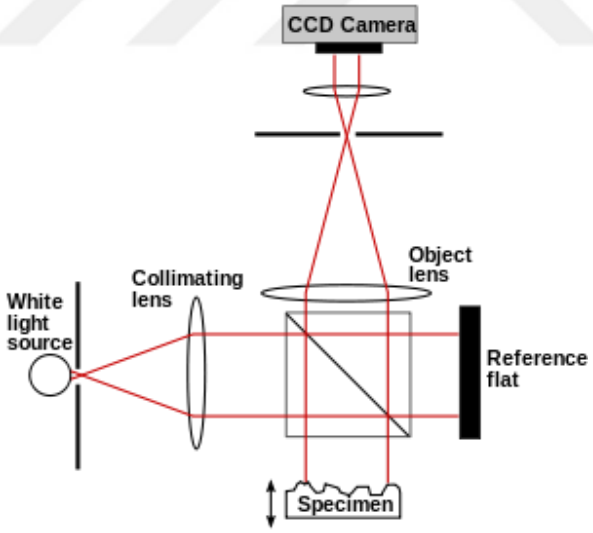

Figure 3-71: Basic interferometer setup

The CCD camera transmits all signals obtained to a CPU. The software enables data processing for 2D or 3D analysis and storing. The light source can either generate white or green light. White light has a more broaden wave length range (380-700 nm) than green light (520-570 nm) and is used for rougher surfaces and lower magnifications. Green light has a

more narrow spectral width than white light, so surface features with smaller different heights can be imaged with a much more accuracy as the phase pattern of the reflecting light from the surface matches more with the light reflecting from the reference mirror in the CCD image sensor plane.

In principal, topographic information obtained via WLI can provide data with sub-micron resolution in comparison to basic optical or electron microscopes. The measurement is done easily and quickly. Typical vertical resolution is 5 nm, and lateral resolution about 120 nm [116]. This non-contact measurement technique enables corrosion morphology (e.g. pit) studies with 3D imaging.

3.7.4 Atomic Force Microscopy (AFM)

Atomic Force Microscopy (AFM) is an imaging tool for real-space atomic-scales of surfaces spanning the realms of optical and electron microscopes. It is used for surface topography analysis with three-dimensional imaging and is both a profiler with unprecedented resolution characterising mechanical properties and a microscope characterising electrical and magnetic properties.

The principle of an AFM is schematically illustrated in the block diagram shown in Figure 3-72. The AFM consists of a conductive AFM probe, laser source and a position-sensitive detector, power supply, lock-in amplifier, and a feedback unit (servo controller). An AC voltage is applied on an AFM probe which vibrates above the sample surface with a known resonance frequency. The probe is rastered across the surface while a laser light is continuously emitting onto the back and reflecting to a position-sensitive photo detector allowing tracing vertical and horizontal motions of the probe. The probe consists of a sharp tip on a cantilever which is mounted on a holder (the entire is the probe or chip). A typical AFM probe is shown in Figure 3-73.

If the tip is scanned across the surface it follows the surface contour precisely. The force is kept constant with a feedback mechanism (for adjustments) which allows keeping the cantilever at a constant level while the tip follows the contour of the surface [117]. The cantilever is vibrated via the applied AC voltage at or near its resonance frequency by a small piezoelectric element. This vibration is used to shake the probe stack on the cantilever, which

interacts with the surface to obtain a mechanical response (surface topography) and further secondary response (either electric or magnetic) [117].

Any force gradient on the cantilever changes the resonance frequency of the cantilever. Attractive forces decrease the drive frequency and make the cantilever softer, and repulsive forces increase it and make the cantilever stiffer. So, the system is able to measure forces in a very high accuracy. The atomic forces are around 10^{-18} N in order of magnitude. A damping system is compulsory for eliminating other external vibration like the building frequency. Thermally induced vibrations of the cantilever at room temperature will limit the force sensitivity to 10^{-15} N, thus the temperature must be kept at a certain temperature level [117].

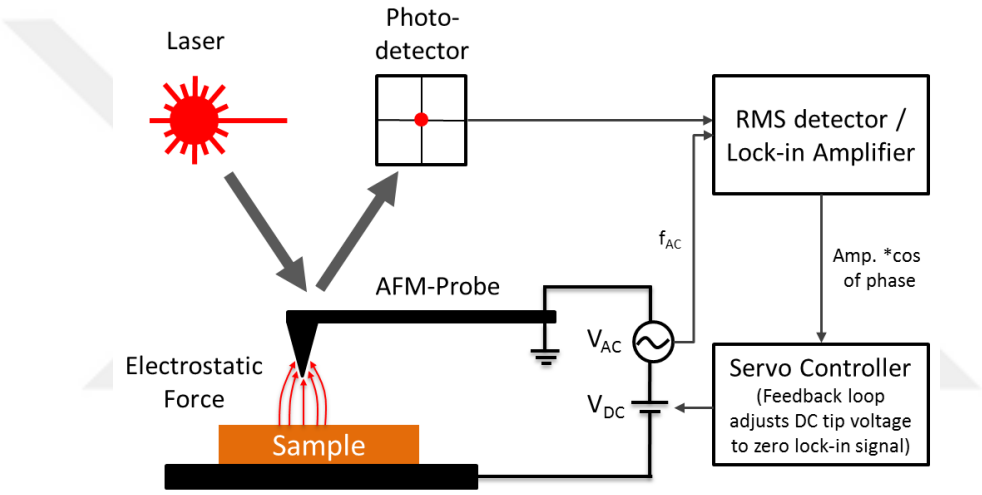

Figure 3-72: Block diagram showing the principle of atomic force microscopy

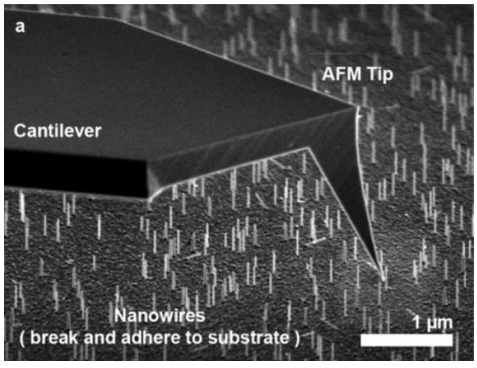

Figure 3-73: AFM probe

The AFM is designed for measuring any type of interaction such as interatomic, electromagnetic, and magnetic forces on atomic scale to investigate both conductors and insulators.

3.7.4.1 Scanning Kelvin Probe Force Microscopy (SKPFM)

Scanning Kelvin Probe Force Microscopy (SKPFM) is a non-destructive probing technique based on atomic force microscopy (AFM) which measures the contact potential difference (CPD) between the scanning probe used (mostly Pt-coated n-doped Si) and the sample surface [118-122]. This can be used to determine the electron work function (Φ) and Volta potential (ψ) of the metal to be investigated. The electron work function, Φ and Volta potential, ψ are characteristic properties of a metal surface. They belong to the only one potential which can be measured directly against a reference and are useful quantities for electrochemical characterisation of the microstructure of a metal.

The metal's work function or Volta potential is that it has "fingerprints" in all electrochemical processes. The potential measured SKPFM provides an indication of the practical nobility of the surface and enables the assessment of the likely corrosion behaviour of various alloy systems [22, 123-126]. However, this measured potential has not been discussed thoroughly, and questions regarding to its real nature and meaning in corrosion science have been remained. In the following, the nature and the meaning of measured potential by SKPFM will be discussed.

3.7.4.1.1 Definition of Potentials

If two different metals (Figure 3-74(a)) are brought into contact, a measurable contact potential is formed at their contact area due their different Fermi energy levels. The Fermi level (E_F) corresponds to the chemical potential (μ_i) of the bulk metal phase and is the work required to bring a mole of *i* particles from infinity into the bulk of an uncharged, dipole layer-free material. It considers all interaction forces without those of being of purely electrostatic nature (ion-ion, ion-solvent, and solvent-solvent interactions). Electrons of the metal with higher Fermi level (low chemical potential) will drift to the metal (Pt-probe) with lower Fermi level (high chemical potential) until equilibrium is formed. The metal, say iron, will be positively charged and the nobler metal, say platinum, negatively charged, as illustrated in Figure 3-74(b).

The contact potential exists physically at the interface at the contact area of both electrodes. An electrostatic force is exerted from the metal to the probe equal to the amount of energy of the work function difference (ΔΦ). The Φ describes the change of energy at a given

temperature and pressure when the electron drifts from a point just outside the surface to a point inside the metal [127, 128]. The force or potential derived is called the Volta potential and has a governing range from about 10 nm to 100 µm [128]. It defines the binding energy of the electron to the material which also defines the partial molar free energy of the electron [128]. Usually, the electron does not feel its image charge (no attraction forces) 10 nm above the surface [127, 128].

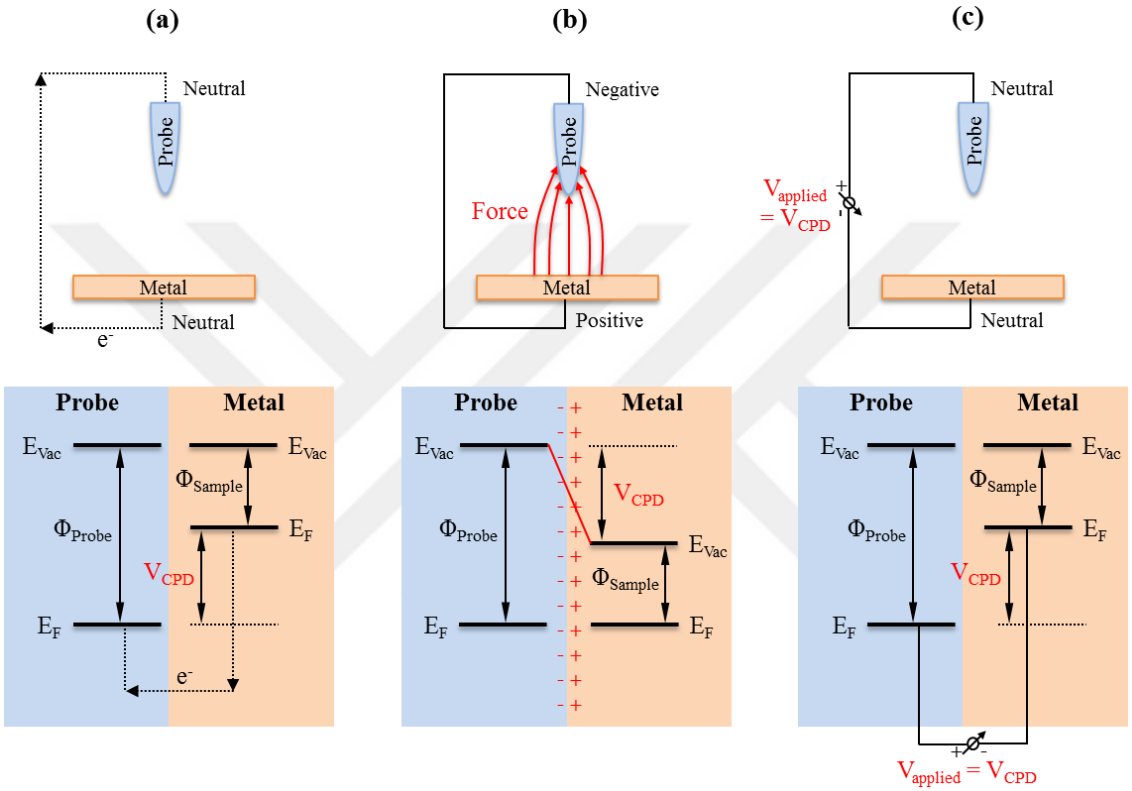

Figure 3-74: (a) Two metals (Pt and Fe) with two different Fermi levels (E_F) before in physical contact, (b) After contact both E_F are equalised, an electrical double layer and a contact potential difference (CPD) is formed, (c) An applied voltage between both metal substrates with identical amount but negative sign nullifies the exerted electrostatic force [122].

In the surface of a metal a charge separation causes an electrified interface, thus an electric dipole layer is formed which leads to a potential drop across the surface. This, in turn, affects the Volta potential of the metal. At the surface boundary valence electrons are trapped in potential wells, so energy is needed to "tunnel" the electrons from this energetically favourable state through the electric double layer. This potential drop across the surface is called the surface potential or dipole potential of the metal, χ_M.

The surface potential χ is the energy required to bring the electron from just outside the surface into the bulk metal phase and arises from the dipole layer. It describes short-range interaction forces and governs over a range up to about 10 nm from the surface. Hence, there is a potential difference across the interface which equals a potential barrier for an electron to overcome in charge transfer reactions. The potential structure of a metal surface is schematically illustrated in Figure 3-75.

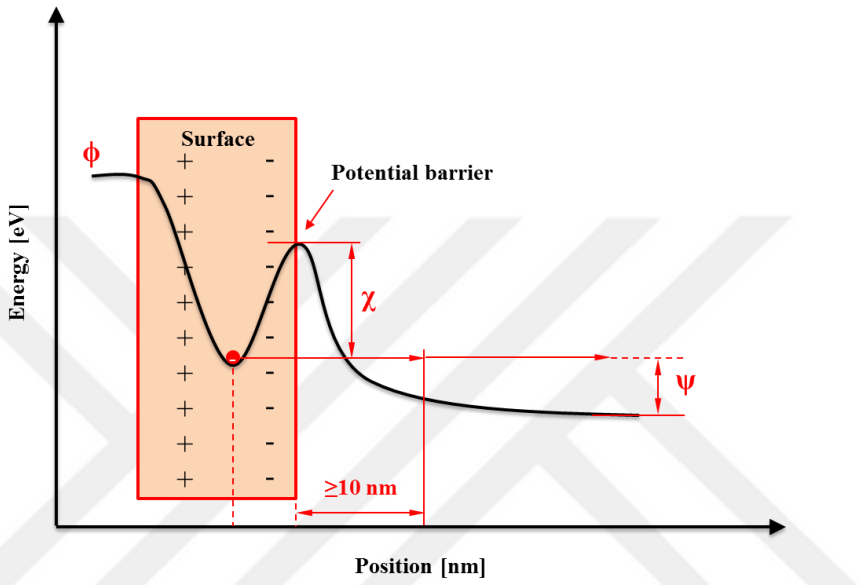

Figure 3-75: Potential structure of a metal surface [128-131]

When metals are exposed to air (due to their large affinity to oxygen), an oxide layer onto the surface is formed, which is an unequal adsorption of charges with opposite sign on the two sides of the interface. Moreover, hydroxyl bonding with an additional possible net preferential orientation can adhere and an additional surface or dipole potential may be formed, χ_{Ox}. This is schematically illustrated in Figure 3-77.

In air or humid environments the thickness and chemistry of the oxide layer can vary and water molecules can adhere onto the surface leading to a larger surface potential drop across the interface. Both surface potentials; $\chi_M + \chi_{Ox}$ lead to a drop of the exerted electrostatic field between the tip and the sample surface. Hence, the metal surface exposed to different environmental media can easily be altered electrochemically which changes the surface properties of the metal as schematically illustrated in Figure 3-76.

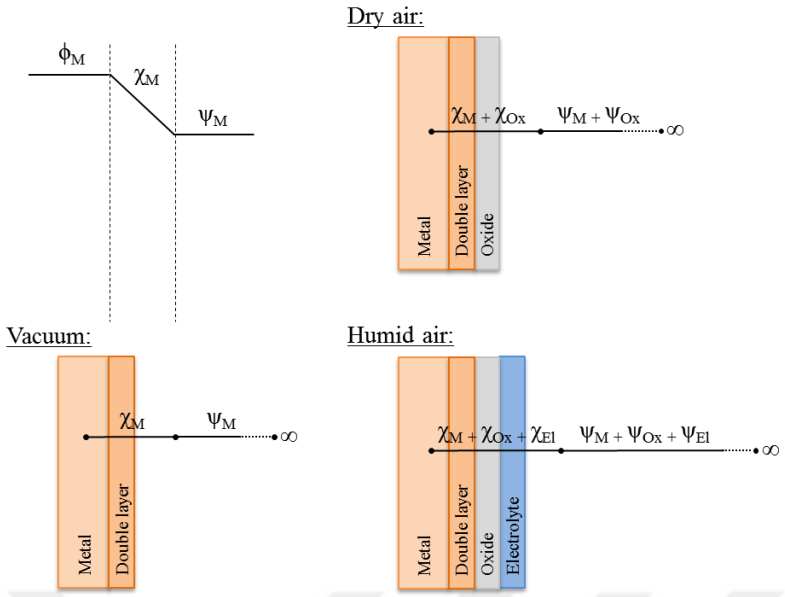

Figure 3-76: Schematic definition of electrostatic potentials of a metal (M) in vacuum, dry air (oxide) and humid air (electrolyte)

The electrostatic and chemical dipole layers reduce the E_F of the metal and make it quasi nobler. Corrosion is an electrochemical reaction with a net positive charge transfer (of electrons) from the (local) anode (metal) to a (local) cathode with chemical exchange. The driving force for corrosion is the difference between the chemical potential of all substances in a metal, the chemical potential (= Fermi level) of the electrolyte/solution (affinity ≠ 0), and the electrostatic potential difference (Galvani potential difference) between anode and cathode.

The chemical potential (Fermi level) describes the Gibbs free energy of a reversible metal potential which is the equilibrium point at which the rate of metal dissolution into ionic species and the rate of metal ion deposition is equal. The metal dissolution is a charge-transfer process that occurs across the interface between the metal and the electrolyte. The chemical differences and Galvani potential differences between the metal and the electrolyte determine the possibility and the extent of metal dissolution. It depends on the electrode potential which represents the energy levels of electrons (the Fermi level) in an electrode immersed in solution.

E_F is the total chemical potential of the electrons in the metal, and is the work needed to add one electron to the body. It relates to the voltage and current flow in an electronic circuit. The charge-transfer (electrons) in a metal dissolution reaction can be described via the electron

work function (Φ) and the Volta potential (ψ) of a metal. Work function Φ and Volta potential ψ are not the same and should not be confused with each other. The electron work function is the required work to be done to bring an electron from the bulk material (smeared E_F region) to just outside the metal surface (ψ regime). ψ is the energy needed to bring a charge from infinity to just above the surface where it does not feel its image charge, usually 10 nm distance to the surface [127, 128]. Both are characteristic for a material and depend on the surface state of the metal. The Φ has two contributions to move the electron from inside the metal to just outside the surface (ψ regime); the first part involves the energy needed to overcome short-range interaction forces of a chemical nature which is the chemical potential μ, and the second part is the energy required to tunnel the existing dipole layer (potential barrier) which is electrical in nature and is the surface potential, χ of the metal.

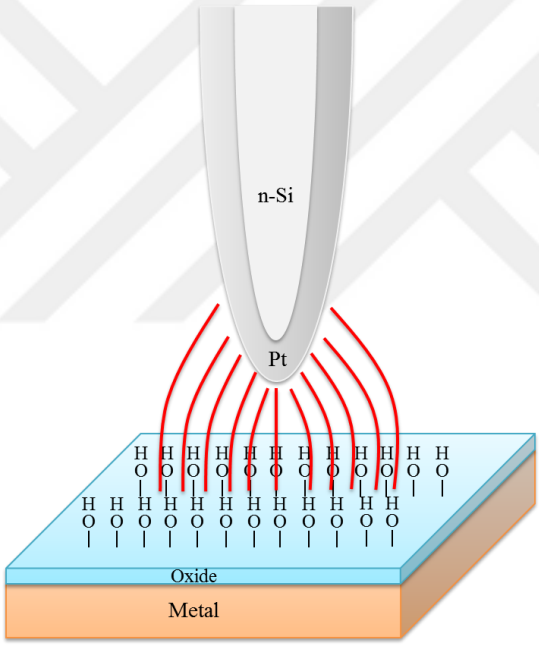

Figure 3-77: Formed oxide with hydroxyl bindings on the metal substrate (low humid atmospheric conditions) [64]

Following relationship between the electron work function, chemical potential, and surface potential exists:

$$\Phi = -\mu - zF\chi \quad \text{(Eq. 12)}$$

F is the Faraday constant and z the charge number of the metal particle, or if an electron is considered then

$$\Phi = -\mu + F\chi \quad \text{(Eq. 13)}$$

The total potential difference across the electrified interface is determined by the surface potential, χ and the Volta potential, ψ, also known as outer potential. Noble metals have higher ψ than reactive metals, as indicated in Figure 3-78 ($\psi_{Pt} > \psi_{Me}$). Volta and surface potentials form the inner potential ϕ, also called the Galvani potential, and describe the full electrostatic energy needed to bring a test charge from infinity into the metal interior:

$$\phi = \psi + \chi \quad \text{(Eq. 14)}$$

Both potentials are fully electrostatic in nature.

The $\Delta\Phi$ between the probe and the metal is the driving force of the electrostatic force exerted. It would equal to the chemical potential difference, $\Delta\mu$, between both metals, and would correspond to the potential measured by SKPFM under fully vacuum condition, if a potential gradient across the surface dipole layer could be neglected. However, in corrosion studies SKPFM is measured under dry or humid air conditions. So, the potential measured by SKPFM cannot be related purely to the $\Delta\Phi$:

$$\Delta V = CPD = \Delta\Phi - zF\Delta\chi = \Phi_M - \Phi_{Pt} - zF(\chi_M + \chi_{Pt}) \quad \text{(Eq. 15)}$$

The AFM-based SKPFM applies a voltage in order to nullify the generated force which corresponds to the CPD with negative sign, if the sample is grounded and a potential is applied to the probe (Figure 3-74(c)).

In other words it is the work function difference minus the surface potential difference of both metals. The CPD corresponds to the electron work function difference, $\Delta\Phi$, and surface potential difference, $\Delta\chi$, and the Volta potential difference, $\Delta\psi$, between both metals. The exerted electrostatic force is nullified, and the voltage required corresponds to CPD and $\Delta\psi$, as stated in the following equation:

$$\Delta V = CPD = \Delta\Phi - zF\Delta\chi = \Delta\psi = \psi_{Me} - \psi_{Pt} \quad \text{(Eq. 16)}$$

All metals have different chemical potentials which obviously accounts for different Φ values. The Φ is dependent upon the crystal face orientation due to the variation of dipole layers at polycrystalline materials with different surface geometry [128, 132]. Hence, the

potential measured in KPFM is affected by surface potential contributions of both metals which depend on the temperature, pressure, and humidity.

The potential values might also change by time due to surface reactions. Therefore, it is important to choose a proper AFM probe with high wear resistance and very low chemical affinity. Platinum coating (≥ 20 nm thickness) on n-doped silicon AFM-tips turned out to be very useful over long test times. Additionally, plateau-shaped tips are more useful and show more stable trace-retrace potential curves than sharp or curvature-shaped tips.

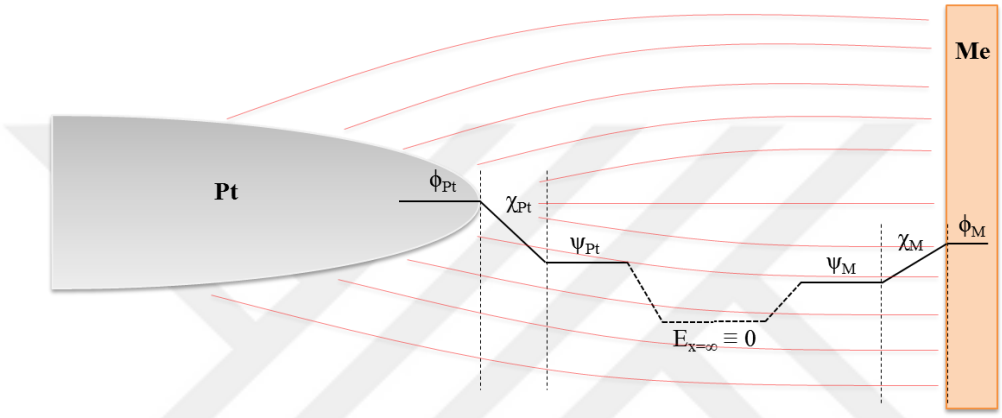

Figure 3-78: Schematic illustration of Galvani, Surface, and Volta potentials

Regions of decreased ψ and Φ can help to assess and possibly predict locations with higher risk of corrosion and cracking initiation and propagation [132]. *Nazarov et al.* [132] did meaningful work on the effect of surface defects and residual stress on SKP measured potentials to assess pitting corrosion and stress corrosion cracking propensity. They could show that regions with high stress localisation associated with lower corrosion potentials decreased the SKP measured potential and indicated corrosion occurrence. There is obviously a relationship between surface defects and local electrochemical potentials which characterises the ability of the metal's dissolution. However, there is a question if potential measured via SKP or KPFM in air can be used in order to predict local corrosion phenomena?

Both Kelvin probe techniques cannot be used under immersed conditions to easily cross-link to corrosion processes. However, the potential measured in air can give a hint of electrically more active sites of the microstructure. In air environments, regions with large local potential differences would indicate stronger driving forces for oxidation. However, KPFM could be

used to assess local corrosion phenomena if immersion-like conditions could be created. This can be done by manipulating the relative humidity (RH).

In dry air environment, the surface of a metal consists of a chemically bonded monolayer of hydroxyl bindings (see Figure 3-77) [64]. Monolayers of water molecules can adhere on the metal surface if the relative humidity is increased. Beyond 60% RH, more than three adhering water monolayers are formed on the surface. According to *Leygraf et al.* [64], in aqueous films thicker than three layers bulk solution-like conditions can prevail. Thus, KPFM measurements in humid air ≥ 60% RH could be used to correlate measured local Volta potentials with local electrochemical properties of the metal.

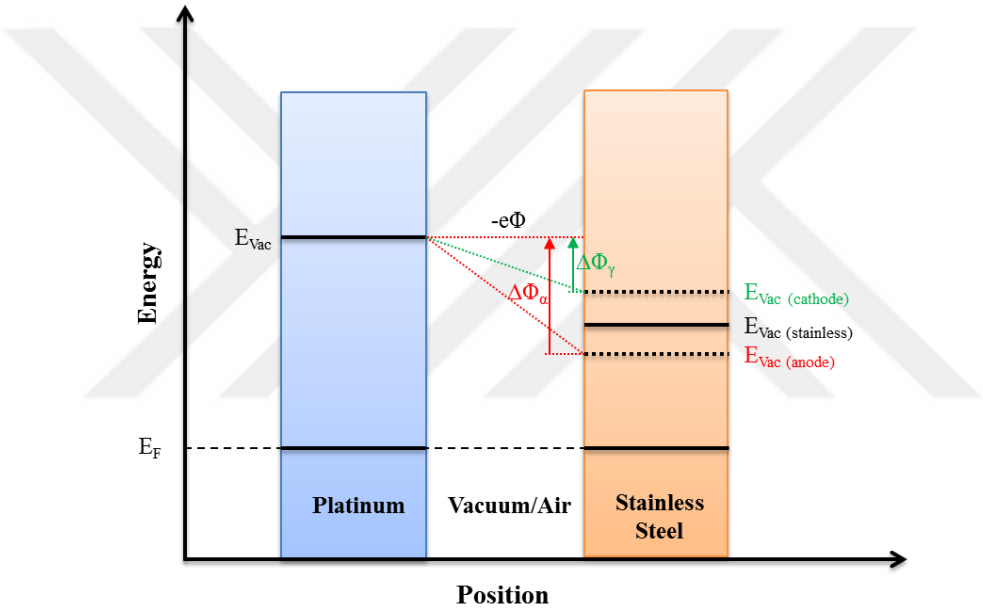

Figure 3-79: Electron work function difference (ΔΦ) between the AFM probe (Pt-coating) and the metal investigated, here as an example duplex stainless steel: Austenite is usually the cathode and ferrite the anode under OCP conditions.

However, this is valid for open-circuit conditions only (stationery states i.e. E_{corr}), and kinetic information such as corrosion rates cannot be derived. The pitting corrosion behaviour can also not be determined by SKPFM. Corrosion in an open system is a dynamic process; the potential of the metal can locally change. More active (anodic) regions can become by time less active or entirely noble (cathodic) which cannot be followed up by SKPFM technique.

SKPFM measurements made in vacuum or air cannot directly be taken for explaining corrosion or stress corrosion phenomena in aqueous solutions. However, the work function of

the metal under vacuum or immersed conditions will be identical; but the surface potential due to surface chemistry alterations and the contribution of the electrochemical double layer under immersed conditions will affect the potential values. Hence, under vacuum/air conditions the potential measured gives an indication for the surface reactivity; sites with higher work function differences (if with respect to Pt) could be assumed of sites with more favoured electronic activity (anodic character).

Pt has the highest work function and is a metal with high practical nobility. In duplex stainless steel, ferrite and austenite have different chemical potentials due their different chemical compositions; hence their work function is different. Often the austenite is nobler than the ferrite due to higher nitrogen and nickel content; therefore, the austenite is expected to show lower $\Delta\Phi$ measured via SKPFM (Figure 3-79). However, the preferential corrosion of the ferrite cannot be generalised since corrosion is not a material but a system property.

The preferential corrosion of ferrite under $MgCl_2$-bearing atmospheric corrosion conditions has been previously reported [50, 133]. It was shown that during atmospheric corrosion under the same salt-laden deposit ferrite and austenite can selectively corrode, dependent upon the region within the deposited area. *Aoki et al.* [70, 71, 134] could demonstrate that under certain conditions the preferential corrosion can flip over between either phases, or both phases corrode simultaneously, or all remain passive. *Lee et al.* [135] showed that ferrite and austenite have different corrosion potential, with ferrite being the first dissolving phase during anodic polarisation followed by the dissolution of austenite at higher anodic potentials. Selective corrosion of ferrite or austenite is dependent on the local electrochemical conditions determined by the type of electrolyte, its aggressiveness, and (externally applied) potential. So, absolute statements about localised corrosion through SKPFM cannot be made.

Nevertheless, the Kelvin probe technique can be a useful assessing tool in corrosion studies, allowing microstructure screening for potential corrosion-active sites. Regarding to the question which microstructure sites play vital roles in localised corrosion SKPFM can be very elucidative.

A linear correlation between the Volta potential differences of pure elements measured in air and their corrosion potential in different aqueous solution was reported by *Frankel et al.* [136]. This observation has awakened wide interest to implement the Kelvin probe technique in corrosion science. However, *Rohwerder et al.* [137] showed that this correlation is not

always true. They clearly showed on pure iron that the corrosion potential measured during immersion as a function of pH deviated from the existing correlative relationship with the Kelvin probe measured Volta potential in dry air obtained upon immersion. The meaning of the measured potentials needs therefore to be validated prior to corrosion assessments in order to avoid misinterpretations.

3.7.4.1.2 Principles of SKPFM

The principles of the operation of the SKFPM technique have been discussed thoroughly in the literature [120, 122, 138, 139]. The following is a concise outline only.

SKPFM measures the work function (φ) difference between the tip of an AFM-probe and the sample surface. In general, the work function gives information about the composition and electronic state of local structures on the metal surface. Work function is defined by the energy that is necessary to remove an electron from the Fermi level of a solid into vacuum far away from the surface [140, 141]. If two metals are brought into electrical contact their Fermi levels become equalised by electric current transfer from the higher Fermi level (here the sample) to the lower one (here the tip) as earlier shown in Figure 3-74(a). A measureable CPD is formed between the AFM-tip and the sample, being defined as:

$$V_{CPD} = \frac{\varphi_{sample}}{\mathrm{q}} - \frac{\varphi_{tip}}{\mathrm{q}} \equiv \frac{\Delta\varphi}{q} \quad \text{(Eq. 17)}$$

where V_{CPD} is the measureable potential/voltage by the AFM, φ_{sample} is the work function of the metal, φ_{tip}, is the work function of the tip, and q is the elementary charge.

Electrons are transferred from the less noble to the nobler metal upon which both materials (electrodes) become charged. This causes a change in their local vacuum levels (E_{Vac}). Charging is accompanied by the development of an electrostatic force field existing between the tip and the metal surface as shown in Figure 3-74(b). The idea of SKPFM is to nullify this force which has come across due to the CPD. It should be mentioned that a CPD is necessary for SKPFM. By applying an external voltage between the tip and sample the CPD can be nullified. The applied voltage is a DC-bias V_{DC} and an AC voltage $V_{AC}\cdot\sin(\omega t)$ of frequency ω. The voltage in summa between the tip and sample is then

$$V = (V_{DC} - V_{CPD}) + V_{AC} \cdot \sin(\omega t) \quad \text{(Eq. 18)}$$

Charge separation results in the exhibition of a capacitance between the tip and the sample surface, which can be described as

$$F = \frac{1}{2}\frac{\partial C}{\partial z}V^2 \quad \text{(Eq. 20)}$$

where C is the capacitance, z is the separation, and V is the voltage. Combining the latter two equations results in the following term:

$$F = F_{DC} + F_{\omega} + F_{2\omega} \quad \text{(Eq. 21)}$$

It has become evident that the electrostatic force has three contributing terms; F_{DC}, F_{ω}, and $F_{2\omega}$.

The DC-component has a contribution to the topographic signal, the ω-component at the characteristic frequency of ω has a contribution to the detection of the CPD, and the 2ω is used for capacitance microscopy. In SKPFM, the 2ω-term can be neglected. The three forces are described mathematically as following:

$$F_{DC} = \frac{\partial C}{\partial z}\left[\frac{1}{2}(V_{DC} - V_{CPD})^2 + \frac{1}{4}V_{AC}^2\right] \quad \text{(Eq. 22)}$$

$$F_{\omega} = \frac{\partial C}{\partial z}(V_{DC} - V_{CPD})V_{AC}\sin(\omega t) \quad \text{(Eq. 23)}$$

$$F_{2\omega} = -\frac{1}{4}\frac{\partial C}{\partial z}V_{AC}^2\cos(2\omega t) \quad \text{(Eq. 24)}$$

For CPD measurements a lock-in amplifier (also known as a phase-sensitive detector) detects the cantilever deflection of ω during the scan. A lock-in amplifier can extract signals from noisy environments through a complicated mathematical algorithm. During the scan V_{DC} is adjusted so that $V_{DC} - V_{CPD} = 0$. The applied voltage (V_{DC}) then corresponds to the contact potential difference at the measured resonant frequency ω with negative sign.

The applied voltage does not reflect the absolute Volta potential of the sample because it is measured against the tip, which is in most cases Pt or Pt-Ir. For an absolute value, the tip used has to be measured against a reference sample with known work function and then added to the applied voltage [118, 122, 124].

In principal, all variations in the Volta potential differences measured can be related to local practical nobility of the microstructure. SKPFM is a two pass technique in which at the first

pass topographic information is obtained by scanning the tip across the metal surface. There are different types of modes to scan the topography such as in permanent or intermittent contact of the tip with the surface (ContactMode™ and TappingMode™). The peculiarity of TappingMode™ is that the tip on the cantilever intermittently contacts the surface across a line (max. 100 µm) to record the topography of the surface without being damaged resulting from friction or adhesive forces. This is beneficent for good image quality as in ContactMode™ distorted data can be obtained.

After recording the surface profile, the cantilever is lifted up to a pre-determined height (25-100 nm) which is called LiftMode™ to allow for a second pass of the scanned profile. Both TappingMode™ and LiftMode™ are visualised in Figure 3-80.

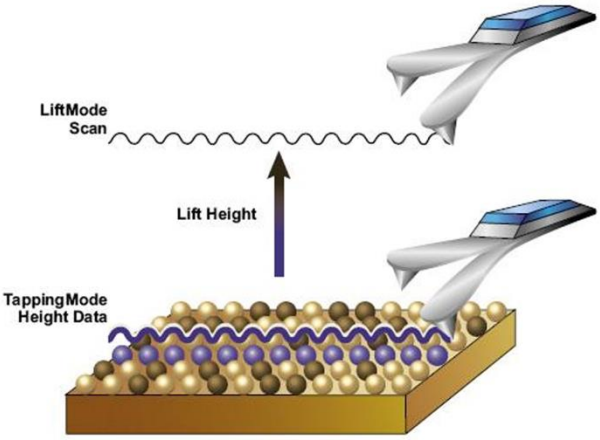

Figure 3-80: Illustration of TappingMode™ and LiftMode™ [142]

In LiftMode™, the system can retrace the scanned profile and follow simultaneously the recorded topographic data. LiftMode™ is not an imaging mode, but rather than a technique that enables other modes to be used such as measuring the Volta potential difference. In LiftMode™ first the topography is scanned, and in the following line, the "lift line" the tip traces the previously acquired topographic information back and adds a Z-offset, and the CPD ($\Delta\psi$) is measured. In Figure 3-81 the principal of the SKPFM technique is shown.

Spatial resolution of up 20 nm can be achieved with 1 mV potential sensitivity [122, 126]. The real obtainable spatial resolution depends on the user expertise and the tip used, not only to the device.

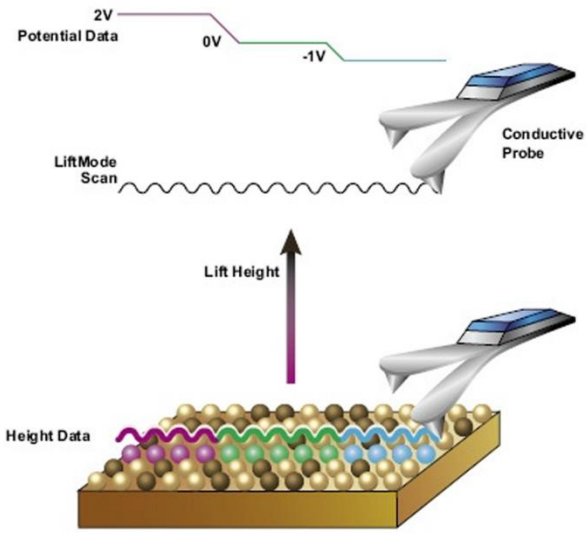

Figure 3-81: Principle of Scanning Kelvin Probe Force Microscopy [143]

3.7.4.2 Magnetic Force Microscopy (MFM)

MFM uses like SKPFM a combination of TappingMode™ and LiftMode™ to trace and record topographic information in the first scan, followed by a second scan by measuring magnetic properties. The tip used for MFM has to be magnetic. The principle of MFM is illustrated in Figure 3-82.

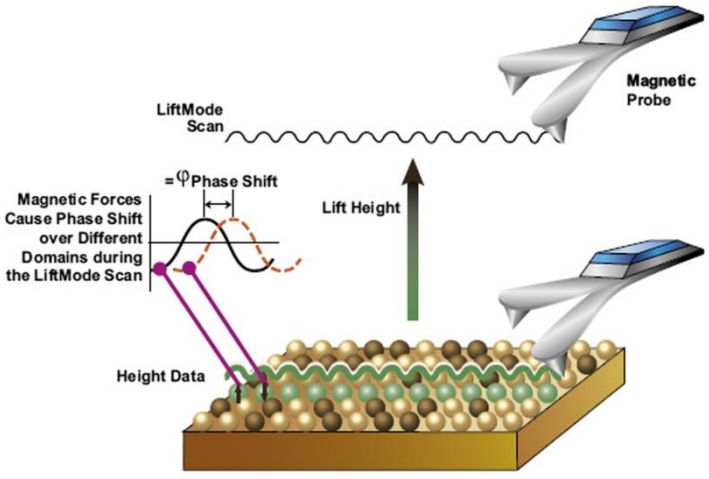

Figure 3-82: Magnetic Force Microscopy (MFM) [147]

For duplex alloys, ferromagnetic ferritic phase can be easily detected and distinguished from the paramagnetic austenite [144]. The lateral resolution for MFM is about 30-50 nm [145]. As the lateral resolution is given by a two-dimensional vector field Ar(x, y, z 0) that is related to the sensitivity of the instrument (settings), to the probe geometry and magnetisation, to the

working distance Zo, and to the spatial variation of the sample microfield H(x,y,z0) real obtainable spatial resolution depends on the user expertise and the tip used [146].

3.7.5 Electron Backscatter Diffraction (EBSD)

EBSD or backscatter Kikuchi diffraction (BKD) is a microstructural-crystallographic technique based on SEM which is used for sub-micron microstructure characterisation. An electron beam is diffracted on the sample surface which is 70° tilted to the incident beam, and forms a characteristic pattern, so called Kikuchi pattern. A detector collects the diffracted electrons and screens the pattern on the monitor. This pattern is characteristic of the crystalline structure and its orientation, which can be used to identify and index crystal systems to characterise grains and grain boundaries, and to analyse strain by misorientation measurements [148].

3.7.6 X-ray Diffraction (XRD)

XRD is a non-destructive measuring technique which renders information about crystal structure, chemical composition, and physical properties such as stress of the material. A crystalline sample is irradiated with a parallel beam of monochromatic x-rays (the atomic lattice of the sample behaves as a 3-dimensional diffraction grating) where the x-ray beam diffracts to specific angles and generates diffraction patterns. The diffracted x-rays in polycrystalline materials are in the shape of a cone as shown Figure 3-83.

The diffraction pattern includes the position (angle) and intensities of the diffracted beam. Inter-planar atomic spacings (d-spacings) are calculated from the position of the angles. The positions (d) of diffracted peaks contain information about the lattice parameter and atomic arrangements. Changes in stress in the microstructure cause changes in d and an angular shift of the diffraction peak.

Using two detectors for stress measurements enables more rapid data acquisition since both sides of the diffraction cone are simultaneously captured. This allows quasi in-situ stress determination. The principle is illustrated schematically in Figure 3-83.

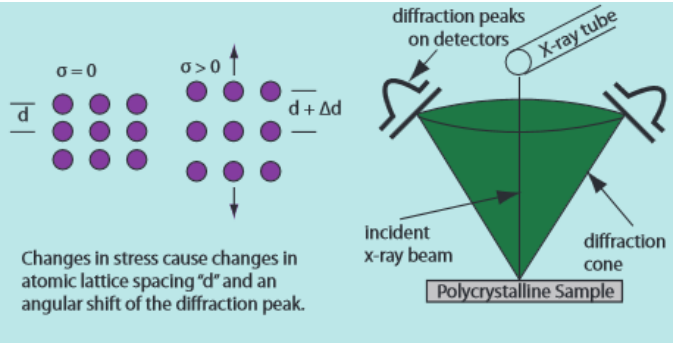

Figure 3-83: Principle of X-ray diffraction residual stress measurement with two detectors [149]

The x-ray diffraction measurement system *i*XRD from Proto was used. The system was capable of determining the stress in each individual phase separately by the use of two different x-ray generating tubes. The stress in austenite was measured using characteristic x-rays generated by a Mn-source, and the stress in ferrite was measured using Cr-source. The experimental setup is pictured in Figure 3-84(a).

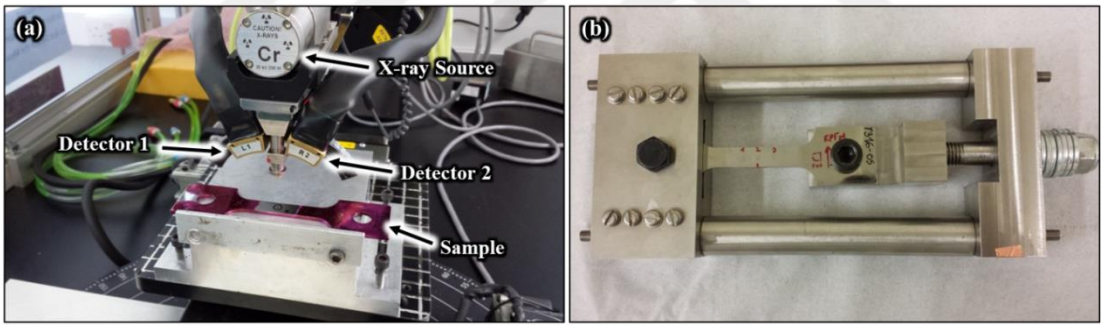

Figure 3-84: (a) XRD stress measurement setup, (b) self-designed tensile rig

The tensile samples were attached on the back with a strain gauge and the strain simultaneously recorded with a strain gauge control unit with 1 µ-strain precision. The tensile samples were loaded with a self-designed rig and measured for stress Figure 3-84(b).

3.8 Mechanical Testing Methods

3.8.1 Hardness Measurement

Hardness is the mechanical resistance of a material to an indentation by another, harder material and is often measured by indentation techniques. A hardness tester (indenter) is pushed on the sample surface and leaves an indentation. The size of the indentation is a quantitative measure for the hardness of the specimen, and depending on the size of the indenter used (macro, micro, nano, or pico) hardness can be obtained.

There are a few hardness measuring methods of which the most common is the 'Vickers' method. The Vickers method uses a diamond indenter in the form of a pyramid with a square base and an angle of 136° between opposite faces (Figure 3-85(a)). A 3-dimensional view of a Vickers micro hardness indent is shown in Figure 3-85(b).

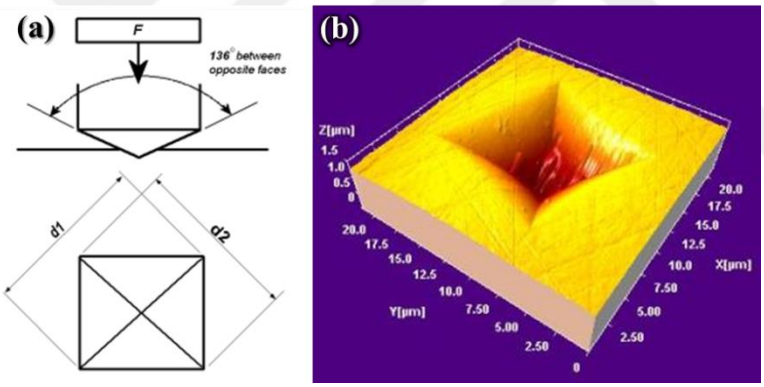

Figure 3-85: (a) Vickers hardness technique [150], (b) 3D view of a Vickers hardness indentation [151]

3.8.2 Tensile Testing

Tensile testing is performed to measure the resistance of a material to static or slowly applied force [152]. A tensile sample is subjected to a uniaxial tension until its failure. The strain rates are usually in the order of 10^{-4} to 10^{-2} s^{-1}.

Flat and round bar tension specimens are typically chosen depending on the shape and dimensions of the real material [115, 152, 153]. A typical flat bar tensile specimen is shown in Figure 3-86.

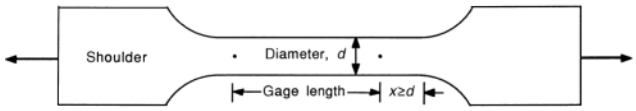

Figure 3-86: Typical tensile specimen [153]

The test provides mechanical properties of the sample tested including yield and tensile strength, elongation (at yield or break), modulus of elasticity (Young's modulus), Poisson's ratio, toughness, and strain-hardening characteristics. In general, a stress-strain curve is obtained from a tensile testing (Figure 3-87).

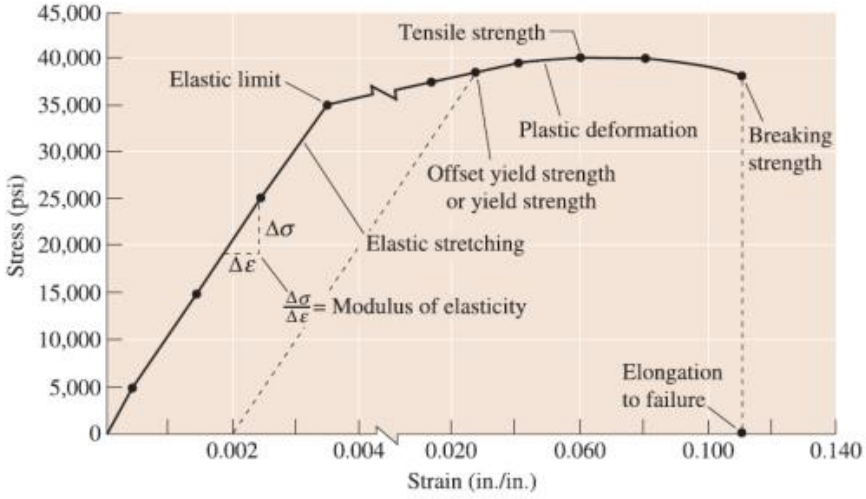

Figure 3-87: Stress-strain curve [152]

4 References

[1] Nuclear Decommissioning Authority. Geological Disposal, Steps Towards Implementation - Executive Summary. Didcot, Oxfordshire: Nuclear Decommissioning Authority, 2010.

[2] T.W. Hicks, T.D. Baldwin, P.J. Hooker, P.J. Richardson, N.A. Chapman, I.G. McKinley, F.B. Neall. Concepts for the Geological Disposal of Intermediate-level Radioactive Waste. Oakham, Rutland, UK: Galson Sciences Ltd., 2008.

[3] I.G. Crossland, S.P. Vines. Why a cementitous repository. Didcot, Oxfordshire: United Kingdom Nirex Limited, 2001. p.1-28.

[4] C. Padovani, O. Albores-Silva, A. Charles. Corrosion control of stainless steels in indoor atmospheres – laboratory measurements under $MgCl_2$ deposits at constant relative humidity (Part 1), Corrosion (2014).

[5] C. Padovani, R. Winsley, N. Smart, P. Fennell, C. Harris, K. Christie. Corrosion control of stainless steels in indoor atmospheres – practical experience (Part 2), Corrosion (2014).

[6] Micromasch. DPER14 Probe. Tallinn, Estonia: Micromasch. p.DPER14 Probe.

[7] N.R. Smart. Literature Review of Atmospheric Stress Corrosion Cracking of Stainless Steels - Report to Nirex. Abingdon, Oxfordshire, UK: Serco Assurance, 2007.

[8] 12.2: The Arrangement of Atoms in Crystalline Solids. vol. 2015. Internet: UC Davis ChemWiki, 2015.

[9] European Space Agency. vol. 2013: European Space Agency (ESA), 2013. p.Elementrary cells for ferrite and austenite.

[10] J. Elmer, D. Olson, D. Matlock. Thermal expansion characteristics of stainless steel weld metal, Welding J. 61 (1982) 293.

[11] M. Pohl, O. Storz, T. Glogowski. Effect of intermetallic precipitations on the properties of duplex stainless steel, Materials Characterization 58 (2007) 65-71.

[12] J. Charles. Duplex stainless steels-a review after DSS'07 held in Grado, Steel Research International 79 (2008) 455-465.

[13] J. Charles, J. Mithieux, P. Santacreu, L. Peguet. The Ferritic Stainless Steel Family: The Appropriate Answer to Nickel Volatility? 6th European Stainless Steel Conference Science and Market Helsinki. Helsinki, 2008.

[14] ETH Zurich. Kapitel 6 - Plastisches Verhalten der Metalle. vol. 2013. Internet, 2013.

[15] W. Bergmann. Werkstofftechnik, Carl Hanser Verlag, Munich, 2005.

[16] B.S. Mitchell. An Introduction to Materials Engineering and Science for Chemical and Materials Engineers, John Wiley & Sons, Canada, 2004.

[17] M. Ferry. Alloys: Iron. in: Editors-in-Chief: Franco B, Gerald LL, Peter W, (Eds.). Encyclopedia of Condensed Matter Physics. Elsevier, Oxford, 2005. pp. 46-53.

[18] CustomPartNet. Sheet Metal Forming. vol. 2015. Internet: CustomPartNet, 2009. p.Neutral Axis.

[19] Wikipedia. Deformation (engineering). vol. 2015. Internet: Wikipedia, 2015. p.Typical stress vs. strain diagram indicating the various stages of deformation.

[20] H.-J. Bargel, G. Schulze, H. Hilbrans, K.-H. Hübner, O. Krüger. Werkstoffkunde. 9th Edition ed., Springer-Verlag, Heidelberg, Germany, 2005.

[21] H.-J. Eckstein. Korrosionsbeständige Stähle, Deutscher Verlag für Grundstoffindustrie GmbH, Leipzig, Germany, 1990.

[22] P. Marcus, F. Mansfeld. Analytical Methods in Corrosion Science and Engineering, Taylor & Francis Group, Boca Raton, FL, USA, 2006.

[23] P.A. Schweitzer. Fundamentals of Metallic Corrosion - Atmospheric and Media - Corrosion of Metals. Second ed., CRC Press, Taylor & Francis Group, 2007.

[24] Azom.com. Stainless Steel - Grade 316L - Properties, Fabrication and Applications. vol. 2012: Azom.com,, 2011.

[25] B. McFarlane. Stainless Steel Plate. vol. 2015. Internet: Brown McFarlane, 2015.

[26] M. McGuire. Stainless Steels for Design Engineers, ASM International, Ohio, USA, 2008.

[27] F. Wischnowski. Einfluss mikrostruktureller Gefügeveränderungen auf die Korrosionsresistenz von nichtrostenden ferritisch-austenitischen Duplex-Stählen. vol. PhD Thesis. Bochum, Germany: Technical University of Bochum, 1995. p.264.

[28] W.D. Callister, D.G. Rethwisch. Fundamentals of materials science and engineering: an integrated approach, John Wiley & Sons, 2012.

[29] Lula et al. Duplex Stainless Steels, American Society for Metals, Mars, Pennsylvania, 1983.

[30] K.H. Lo, C.H. Shek, J.K.L. Lai. Recent developments in stainless steels, Materials Science and Engineering: R: Reports 65 (2009) 39-104.

[31] C.-J. Huang, D.J. Browne, S. McFadden. A phase-field simulation of austenite to ferrite transformation kinetics in low carbon steels, Acta Materialia 54 (2006) 11-21.

[32] X. Li, A.P. Miodownik, N. Saunders. Modelling of materials properties in duplex stainless steels, Materials Science and Technology 18 (2002) 861-868.

[33] Practical Guidelines for the Fabrication of Duplex Stainless Steel. 2nd ed., International Molybdenum Association (IMOA), London, 2009.

[34] A. Iversen, B. Leffler. Aqueous Corrosion of Stainless Steels. In: Cottis RA, Graham MJ, Lindsay R, Lyon SB, Richardson JA, Scantlebury JD, Stott FH, (Eds.). Shreir's Corrosion, vol. 3: Elsevier, 2010.

[35] I. Calliari, M. Pellizzari, M. Zanellato, E. Ramous. The phase stability in Cr–Ni and Cr–Mn duplex stainless steels, Journal of Materials Science 46 (2011) 6916-6924.

[36] Azom.com. Stainless Steel - Grade 2205. vol. 2012. Staffs: Azom.com,, 2011.

[37] Masteel UK Limited. UNS S32750 SuperDuplex Stainless Steel. vol. 2012. Birmingham, 2009.

[38] T. Børvik, H. Lange, L.A. Marken, M. Langseth, O.S. Hopperstad, M. Aursand, G. Rørvik. Pipe fittings in duplex stainless steel with deviation in quality caused by sigma phase precipitation, Materials Science and Engineering: A 527 (2010) 6945-6955.

[39] J. Charles, S. Bernhardsson. Duplex Stainless Steels '91 - Volume 1. In: Charles J, Bernhardsson S, (Eds.). Duplex Stainless Steels '91, vol. 1. Beaune, Bourgogne, France: Les editions de physique, 1991.

[40] O.K. Chopra, H.M. Chung. Aging degradation of cast stainless steels: Effects on mechanical properties. In: Materials and Components Technology Division ANL, (Ed.), 1987. p.Medium: ED; Size: Pages: 34.

[41] H.M. Chung, O.K. Chopra. Microstructures of cast-duplex stainless steel after long-term aging, 1985.

[42] H.M. Chung, O.K. Chopra. Kinetics and mechanism of thermal aging embrittlement of duplex stainless steels, 1987.

[43] F. Iacoviello, F. Casari, S. Gialanella. Effect of "475 °C embrittlement" on duplex stainless steels localized corrosion resistance, Corrosion Science 47 (2005) 909-922.

[44] O.H. Ibrahim, I.S. Ibrahim, T.A.F. Khalifa. Effect of Aging on the Toughness of Austenitic and Duplex Stainless Steel Weldments, Journal of Materials Science & Technology 26 (2010) 810-816.

[45] K.H. Lo, C.T. Kwok, W.K. Chan, D. Zeng. Corrosion resistance of duplex stainless steel subjected to long-term annealing in the spinodal decomposition temperature range, Corrosion Science 55 (2012) 267-271.

[46] M.K. Miller, I.M. Anderson, J. Bentley, K.F. Russell. Phase separation in the Fe-Cr-Ni system, Applied Surface Science 94–95 (1996) 391-397.

[47] J.-O. Nilsson, G. Chai. The physical metallurgy of duplex stainless steels. International Conference & Expo Duplex 2007. Grado, Italy: Assoziazone Italiana Di Metallurgia (AIM), 2007.

[48] T. Nys, P.M. Gielen. Spinodal decomposition in the Fe−Cr system, Metallurgical Transactions 2 (1971) 1423-1428.

[49] H. Oettel, H. Schumann. Metallografie - Mit einer Einführung in die Keramografie. 15., revised and enlarged ed., Wiley-VCH, Weinheim, Germany, 2011.

[50] C. Örnek, A.H. Ahmed, D.L. Engelberg. Effect of Microstructure on Atmospheric-Induced Corrosion of Heat-treated Grade 2205 and 2507 Duplex Stainless Steels. Eurocorr 2012. Istanbul, Turkey: Dechema, 2012. p.1-10.

[51] A.F. Padilha, D.M. Escriba, E. Materna-Morris, R.L. Plaut. Chi-phase precipitation in a duplex stainless steel, Materials Characterization 60 (2009) 1214-1219.

[52] T.A. Palmer, J.W. Elmer, S.S. Babu. Observations of Ferrite/Austenite Transformations in the Heat Affected Zone of 2205 Duplex Stainless Steel Spot Welds Using Time Resolved X-Ray Diffraction. Materials Science and Engineering A. Livermore, CA, USA: Lawrence Livermore National Laboratory, Oak Ridge National Laboratory, 2003.

[53] S.S.M. Tavares, M.R. da Silva, J.M. Pardal, H.F.G. Abreu, A.M. Gomes. Microstructural changes produced by plastic deformation in the UNS S31803 duplex stainless steel, Journal of Materials Processing Technology 180 (2006) 318-322.

[54] S.S.M. Tavares, A. Loureiro, J.M. Pardal, T.R. Montenegro, V.C.d. Costa. Influence of heat treatments at 475 and 400 °C on the pitting corrosion resistance and sensitization of UNS S32750 and UNS S32760 superduplex stainless steels, Materials and Corrosion 63 (2012) 522-526.

[55] S.S.M. Tavares, R.F.d. Noronha, M.R.d. Silva, J.M. Neto, S. Pairis. 475°C Embrittlement in a duplex stainless steel UNS S31803, Materials Research 4 (2001) 237-240.

[56] S. Topolska, J. Łabanowski. Effect of microstructure on impact toughness of duplex and superduplex stainless steels, Journal of Achievments in Materials and Manufacturing Engineering 36 (2009).

[57] K.W. Wong, C.H. Shek, W. Zhang, J.K.L. Lai. σ phase dissolution in duplex stainless steel at elevated temperature studied by thermal analysis, Materials Letters 62 (2008) 3991-3994.

[58] J.-O. Nilsson, P. Liu. Aging at 400–600°C of submerged arc welds of 22Cr–3Mo–8Ni duplex stainless steel and its effect on toughness and microstructure, Materials Science and Technology 7 (1991) 853-862.

[59] A. Redjaïmia, J.P. Morniroli, P. Donnadieu, G. Metauer. Microstructural and analytical study of heavily faulted Frank-Kasper R-phase precipitates in the ferrite of a duplex stainless steel, Journal of Materials Science 37 (2002) 4079-4091.

[60] A. Redjaïmia, T. Otarola, A. Mateo. Orientation Relationships between the δ-ferrite Matrix in a Duplex Stainless Steel and its Decomposition Products: the Austenite and the χ and R Frank-Kasper Phases. in: Richter S, Schwedt A, (Eds.). EMC 2008 14th European Microscopy Congress 1–5 September 2008, Aachen, Germany. Springer Berlin Heidelberg, 2008. pp. 479-480.

[61] R.A. Cottis, L.L. Shreir. Shreir's corrosion, Elsevier, Amsterdam; London, 2010.

[62] Z. Ahmad. Principles of Corrosion Engineering and Corrosion Control, Butterworth-Heinemann, Elsevier, Burlington, England, 2006.

[63] R.-H. Jung, H. Tsuchiya, S. Fujimoto. XPS characterization of passive films formed on Type 304 stainless steel in humid atmosphere, Corrosion Science 58 (2012) 62-68.

[64] C. Leygraf, T.E. Graedel. Atmospheric Corrosion, John Wiley & Sons, Canada, 2000.

[65] M.G. Fontana. Corrosion Engineering, McGraw-Hill International Editions, Singapore, 1987.

[66] T.E. Graedel, R.P. Frankenthal. Corrosion Mechanisms for Iron and Low Alloy Steels Exposed to the Atmosphere, Journal of The Electrochemical Society 137 (1990) 2385-2394.

[67] R.F.A. Pettersson, J. Flyg. Electrochemical evaluation of pitting and crevice corrosion resistance of stainless steels in NaCl and NaBr. Stockholm, Sweden: Outokumpu, 2004.

[68] T. Prosek, A. Iversen, C. Taxen, D. Thierry. Low-Temperature Stress Corrosion Cracking of Stainless Steels in the Atmosphere in the Presence of Chloride Deposits, Corrosion Science 65 (2009) 13.

[69] J. Ritter. The Application of Duplex Stainless Steels in Different Media. Surface and Materials Engineering, Corrosion Laboratory, vol. Bachelors. Aalen, Germany: Aalen University of Applied Sciences, 2013.

[70] S. Aoki, K. Ito, H. Yakuwa, M. Miyasaka, J.i. Sakai. Potential Dependence of Preferential Dissolution Behavior of a Duplex Stainless Steel in Simulated Solution inside Crevice, Zairyo-to-Kankyo 60 (2011) 363-367.

[71] S. Aoki, H. Yakuwa, K. Mitsuhashi, J.i. Sakai. Dissolution Behavior of α and γ Phases of a Duplex Stainless Steel in a Simulated Crevice Solution, ECS Transactions 25 (2010) 17-22.

[72] J.-S. Lee, K. Fushimi, T. Nakanishi, Y. Hasegawa, Y.-S. Park. Corrosion behaviour of ferrite and austenite phases on super duplex stainless steel in a modified green-death solution, Corrosion Science 89 (2014) 111-117.

[73] D.J.W. Oldfield. Nickel effect: Lower rate of corrosion in stainless, Emerald Group Publishing Limited 37 (1990) 9-11.

[74] Y.C. Lu, M.B. Ives, C.R. Clayton. Synergism of alloying elements and pitting corrosion resistance of stainless steels, Corrosion Science 35 (1993) 89-96.

[75] C. Örnek, D.L. Engelberg. SKPFM Measured Volta Potential Correlated with Strain Localisation in Microstructure of Cold-rolled Grade 2205 Duplex Stainless Steel, Corrosion Science (2015).

[76] C. Örnek, D.L. Engelberg. Effect of Cold Deformation Mode on Stress Corrosion Cracking Susceptibility of 2205 Duplex Stainless Steel, Corrosion Science (2015).

[77] C. Örnek, D.L. Engelberg. Environment-Assisted Stress Corrosion Cracking of Grade 2205 Duplex Stainless Steel Under Low-temperature Atmospheric Exposure, Corosion Science (2015).

[78] M. Tullmin, P.R. Roberge. Atmospheric Corrosion. in: Revie RW, (Ed.). Uhlig's Corrosion Handbook. John Wiley & Sons, 2000.

[79] A.W. Revie, H.H. Uhlig. Corrosion and Corrosion Control - An Introduction to Corrosion Science and Engineering. Fourth ed., John Wiley & Sons, USA, 2008.

[80] R.W. Revie. Uhlig's Corrosion Handbook. 3rd ed., John Wiley & Sons, Electrochemical Society, Hohoke, New Jersey, Canada, 2011.

[81] Nuclear Decommissioning Authority. Optimising the number and location of interim Intermediate Level Waste (ILW) storage facilities on Magnox Limited and EDF Energy sites in England and Wales - Credible Options - Main Paper. Nuclear Decommissioning Authority, 2013.

[82] G.O. Lloyd. Atmospheric Corrosion. Teddington, Middlesex: National Physical Laboratory,, 2010.

[83] A. Nishikata, Y. Ichihara, Y. Hayashi, T. Tsuru. Influence of Electrolyte Layer Thickness and pH on the Initial Stage of the Atmospheric Corrosion of Iron, Journal of The Electrochemical Society 144 (1997) 1244-1252.

[84] G. Schikorr. Über den Mechanismus des atmosphärischen Rostens des Eisens, Materials and Corrosion 14 (1963) 69-80.

[85] T. Tsuru, K.-I. Tamiya, A. Nishikata. Formation and growth of micro-droplets during the initial stage of atmospheric corrosion, Electrochimica Acta 49 (2004) 2709-2715.

[86] Y. Tsutsumi, A. Nishikata, T. Tsuru. Initial Stage of Pitting Corrosion of Type 304 Stainless Steel under Thin Electrolyte Layers Containing Chloride Ions, Journal of The Electrochemical Society 152 (2005) B358-B363.

[87] U.R. Evans, C.A.J. Taylor. Mechanism of atmospheric rusting, Corrosion Science 12 (1972) 227-246.

[88] Y. Tsutsumi, A. Nishikata, T. Tsuru. Pitting corrosion mechanism of Type 304 stainless steel under a droplet of chloride solutions, Corrosion Science 49 (2007) 1394-1407.

[89] P. Ernst, R.C. Newman. Explanation of the effect of high chloride concentration on the critical pitting temperature of stainless steel, Corrosion Science 49 (2007) 3705-3715.

[90] D.E. Williams, R.C. Newman, Q. Song, R.G. Kelly. Passivity breakdown and pitting corrosion of binary alloys, Nature 350 (1991) 216-219.

[91] S. Li, L.H. Hihara. Atmospheric-Corrosion Electrochemistry of NaCl Droplets on Carbon Steel, Journal of The Electrochemical Society 159 (2012) C461-C468.

[92] J. Zhang, J. Wang, Y. Wang. Electrochemical investigations of micro-droplets formed on metals during the deliquescence of salt particles in atmosphere, Electrochemistry Communications 7 (2005) 443-448.

[93] A.K. Neufeld, I.S. Cole, A.M. Bond, S.A. Furman. The initiation mechanism of corrosion of zinc by sodium chloride particle deposition, Corrosion Science 44 (2002) 555-572.

[94] M. Ebert, M. Inerle-Hof, S. Weinbruch. Environmental scanning electron microscopy as a new technique to determine the hygroscopic behaviour of individual aerosol particles, Atmospheric Environment 36 (2002) 5909-5916.

[95] R.S. Lillard, D.G. Kolman, M.A. Hill, M.B. Prime, D.K. Veirs, L.A. Worl, P. Zapp. Assessment of Corrosion-Based Failure in Stainless Steel Containers Used for the Long-Term Storage of Plutonium-Based Salts, Corrosion 65 (2009) 175-186.

[96] L.M. Russell, Y. Ming. Deliquescence of small particles, The Journal of Chemical Physics 116 (2002) 311-321.

[97] F. King. Corrosion Resistance of Austenitic and Duplex Stainless Steels in Environments Related to UK Geological Disposal. 2009.

[98] N. Mi, M. Ghahari, T. Rayment, A.J. Davenport. Use of inkjet printing to deposit magnesium chloride salt patterns for investigation of atmospheric corrosion of 304 stainless steel, Corrosion Science 53 (2011) 3114-3121.

[99] A. Cook, N. Stevens, J. Duff, A. Mishelia, T. Leung, S. Lyon, J. Marrow, W. Ganther, I. Cole. Atmospheric-Induced Stress Corrosion Cracking of Austenitic Stainless Steels under Limited Chloride Supply. 18th International Corrosion Congress 2011. Perth, Australia, 2011.

[100] A.J. Davenport, N. Mi, M. Ghahari, T. Rayment. Use of inkjet printing to deposit magnesium chloride salt patterns for investigation of atmospheric corrosion of 304 stainless steel, Corrosion Science 53 (2011) 3114-3121.

[101] L. Greenspan. Humidity Fixed Points of Binary Saturated Aqueous Solutions, Journal of Research of the National Bureau of Standards - A. Physics and Chemsitry 81A (1977).

[102] A. Cook, J. Marrow, N. Stevens, J. Duff, A. Mishelia, T.S. Leung, S. Lyon, W. Ganther, I. Cole. Atmospheric-induced stress corrosion cracking of austenitic stainless steels under limited chloride supply. 18th International Corrosion Conference, vol. 2. Perth, Australia, 2011. p.1438-1449

[103] N.R. Smart, C.P. Jackson, C.R. Tice. Record of Nirex Workshop on Atmospheric Pitting Corrosion of Stainless Steel. In: Assurance S, (Ed.). Abingdon, Oxfordshire, 2007.

[104] N.R. Smart, A.M. Pritchard, A. Turnbull. Review of Environmental Conditions for Storage of ILW Radioactive Waste Containers. Abingdon, Oxfordshire, 2010. p.1-65.

[105] N.R. Smart, J.W. Stairmand, D.R. Tice. Literature Review of Atmospheric Stress Corrosion Cracking of Stainless Steels. Abingdon, Oxfordshire, England: Serco Assurance Ltd., 2007.

[106] T. Prosek, A. Iversen, C. Taxen. Low Temperature Stress Corrosion Cracking of Stainless Steels in the Atmosphere in Presence of Chloride Deposits. NACE, vol. Paper No. 08484: NACE International, 2008. p.17.

[107] T. Prosek, A. Le Gac, D. Thierry, S. Le Manchet, C. Lojewski, A. Fanica, E. Johansson, C. Canderyd, F. Dupoiron, T. Snauwaert, F. Maas, B. Droesbeke. Low-Temperature Stress Corrosion Cracking of Austenitic and Duplex Stainless Steels Under Chloride Deposits, Corrosion Science 70 (2014) 1052-1063.

[108] N.D. Fairweather, N. Platts, D.R. Tice. Stress-Corrosion Crack Initiation Of Type 304 Stainless Steel In Atmospheric Environments Containing Chloride: Influence Of Surface Condition, Relative Humidity, Temperature And Thermal Sensitization. NACE International Corrosion 2008. New Orleans, Louisiana (US): NACE International, 2008.

[109] T. Prosek, A.L. Gac, D. Thierry, S.L. Manchet, A. Fanica, C. Lojewski, E. Johansson, C. Canderyd, F. Maas, F. Dupoiron, T. Snauwaert. Duplex stainless steel in storage tanks (DUPLEXTANK). Brussels: Directorate-General for Research and Innovation, Directorate G — Industrial Technologies, Unit G.5 — Research Fund for Coal and Steel, 2013. p.1-135.

[110] N. Arnold, P. Gümpel, T. Heitz, P. Pscheidl. Chloridinduzierte Korrosion von Nichtrostenden Stählen in Schwimmhallen-Atmosphären Teil 1: Elektrolyt Magnesium-Chlorid (30%), Materials and Corrosion 48 (1997) 679-686.

[111] N. Arnold, P. Gümpel, T.W. Heitz. Chloridinduzierte Korrosion von nichtrostenden Stählen in Schwimmhallen-Atmosphären Teil 2: Einfluß von Hypochloriten, Materials and Corrosion 49 (1998) 482-488.

[112] N. Arnold, P. Gümpel, T.W. Heitz. Chloridinduzierte Korrosion von nichtrostenden Stählen in Schwimmhallen-Atmosphären Teil 3: Einfluß einer realen Schwimmhallen-Atmosphäre, Materials and Corrosion 50 (1999) 140-145.

[113] J.-i. Tani, M. Mayuzumi, N. Hara. Stress corrosion cracking of stainless-steel canister for concrete cask storage of spent fuel, Journal of Nuclear Materials 379 (2008) 42-47.

[114] International Molybdenum Association. Practical Guidelines for the Fabrication of Duplex Stainless Steels. London: International Molybdenum Association (IMOA), 2009.

[115] B. Heine. Werkstoffprüfung - Ermittlung von Werkstoffeigenschaften Carl Hanser Verlag GmbH & Co. KG, Munich, Germany, 2011.

[116] U. Volz. 3D Oberflächenmesstechnik. Bruker, 2012.

[117] G. Binnig, C.F. Quate, C. Gerber. Atomic Force Microscope, Physical Review Letters 56 (1986) 930-933.

[118] M. Nonnenmacher, M.P. O'Boyle, H.K. Wickramasinghe. Kelvin probe force microscopy, Applied Physics Letters 58 (1991) 2921-2923.

[119] T. Glatzel, S. Sadewasser, M.C. Lux-Steiner. Amplitude or frequency modulation-detection in Kelvin probe force microscopy, Applied Surface Science 210 (2003) 84-89.

[120] S. Sadewasser, T. Glatzel. Kelvin Probe Force Microscopy Measuring and Compensating Microscopy, Springer, Heidelberg, 2012.

[121] T. Ouisse, F. Martins, M. Stark, S. Huant, J. Chevrier. Signal amplitude and sensitivity of the Kelvin probe force microscopy, Applied Physics Letters 88 (2006) 043102.

[122] T. Glatzel, M.C. Lux-Steiner, E. Strassburg, A. Boag, Y. Rosenwaks. Principles of Kelvin Probe Force Microscopy. in: Kalinin S, Gruverman A, (Eds.). Scanning Probe Microscopy. Springer New York, 2007. pp. 113-131.

[123] V. Guillaumin, P. Schmutz, G.S. Frankel. Characterization of Corrosion Interfaces by the Scanning Kelvin Probe Force Microscopy Technique, Journal of The Electrochemical Society 148 (2001) B163-B173.

[124] A.B. Cook, Z. Barrett, S.B. Lyon, H.N. McMurray, J. Walton, G. Williams. Calibration of the scanning Kelvin probe force microscope under controlled environmental conditions, Electrochimica Acta 66 (2012) 100-105.

[125] D.B. Blücher, J.-E. Svensson, L.-G. Johansson, M. Rohwerder, M. Stratmann. Scanning Kelvin Probe Force Microscopy: A Useful Tool for Studying Atmospheric Corrosion of MgAl Alloys In Situ, Journal of The Electrochemical Society 151 (2004) B621-B626.

[126] N. Sathirachinda, R. Pettersson, J. Pan. Depletion effects at phase boundaries in 2205 duplex stainless steel characterized with SKPFM and TEM/EDS, Corrosion Science 51 (2009) 1850-1860.

[127] W.J. Moore, D.O. Hummel, G. Trafara, K. Holland-Moritz. Physikalische Chemie. Physikalische Chemie. Walter de Gruyter, New York, 1986. pp. 1236.

[128] J.O.M. Bockris, A.K.N. Reddy, M. Gamboa-Aldeco. Modern Electrochemistry 2A. Fundamentals of Electrodics, vol. 2A. New York: Kluwer Academic Publishers, 2002. p.1-817.

[129] H. Kaesche. Corrosion of metals : physicochemical principles and current problems, Springer, Berlin [u.a.], 2003.

[130] V.S. Bagotsky. Fundamentals of Electrochemistry. The Electrochemical Society Series. Hoboken, New Jersey: Wiley-Interscience, 2006.

[131] Moore, W. J. Physikalische Chemie. 4. Auflage ed., Walter de Gruyter, 1986.

[132] A. Nazarov, D. Thierry. Application of Volta potential mapping to determine metal surface defects, Electrochimica Acta 52 (2007) 7689-7696.

[133] C. Örnek, D.L. Engelberg, S.B. Lyon, T.L. Ladwein. Effect of "475°C Embrittlement" on the Corrosion Behaviour of Grade 2205 Duplex Stainless Steel Investigated Using Local Probing Techniques. Eurocorr 2013. Estoril, Portugal: European Corrosion Congress, 2013.

[134] S. Aoki, K. Ito, H. Yakuwa, M. Miyasaka, J. Sakai, rsquo, ichi. Potential Dependence of Preferential Dissolution Behavior of a Duplex Stainless Steel in Simulated Solution inside Crevice, Zairyo-to-Kankyo 60 (2011) 363-367.

[135] J.-S. Lee, K. Fushimi, T. Nakanishi, Y. Hasegawa, Y.-S. Park. Corrosion behaviour of ferrite and austenite phases on super duplex stainless steel in a modified green-death solution, Corrosion Science (2014).

[136] G.S. Frankel, V. Guillaumin, P. Schmutz. Characterization of Corrosion Interfaces by the Scanning Kelvin Probe Force Microscopy Technique, Journal of The Electrochemical Society 148 (2001) B163-B173.

[137] M. Rohwerder, F. Turcu. High-resolution Kelvin probe microscopy in corrosion science: Scanning Kelvin probe force microscopy (SKPFM) versus classical scanning Kelvin probe (SKP), Electrochimica Acta 53 (2007) 290-299.

[138] P. Eaton, P. West. Atomic Force Microscopy. Oxford, UK: Oxford University Press, 2010.

[139] S.V. Kalinin, A. Gruverman. Scanning Probe Microscopy of Functional Materials. In: Kalinin SV, Gruverman A, (Eds.). Nanoscale Imaging and Spectroscopy. New York: Springer, 2010.

[140] J. Koryta, J. Dvorak, L. Kavan. Principles of Electrochemistry. Second Edition ed., John Wiley & Sons Ltd., Chichester, West Sussex, England, 1993.

[141] H.-J. Butt, K. Graf, M. Kappl. Physics and Chemistry of Interfaces, WILEY-VCH GmbH & Co. KGaA, Darmstadt, Germany, 2003.

[142] Bruker Corporation. LiftMode. In: p28-LiftMode-main, (Ed.), vol. 506 x 371 x 24 BPP: Bruker Corporation, 2013.

[143] Bruker Corporation. Surface Potential Microscopy. In: p31-Surface-Potential-Microscopy-SPoM-main, (Ed.), vol. 414 x 392 x 24 BPP: Bruker Corporation, 2013.

[144] K.R. Gadelrab, G. Li, M. Chiesa, T. Souier. Local characterization of austenite and ferrite phases in duplex stainless steel using MFM and nanoindentation, Journal of Materials Research 27 (2012) 1573-1579.

[145] A. Moser, M. Xiao, P. Kappenberger, K. Takano, W. Weresin, Y. Ikeda, H. Do, H.J. Hug. High-resolution magnetic force microscopy study of high-density transitions in perpendicular recording media, Journal of Magnetism and Magnetic Materials 287 (2005) 298-302.

[146] U. Hartmann, T. Göddenhenrich, C. Heiden. Magnetic force microscopy: Current status and future trends, Journal of Magnetism and Magnetic Materials 101 (1991) 263-270.

[147] Bruker Corporation. Magnetic Force Microscopy. In: p29-Magnetic-Force-Microscopy-MFM-main, (Ed.), vol. 528 x 357 x 24 BPP: Bruker Corporation, 2013.

[148] EBSD. vol. 2012: Oxford Instruments, 2011.

[149] Proto Manufacturing. X-ray Diffraction Residual Stress Measurement - An Introduction. Website: Proto Manufacturing, 2011.

[150] Gordon England. Vickers hardness testing technique. In: Vickers, (Ed.): Gordon England,, 2013.

[151] Image Metrology A/S. 3D hardness indent. In: hardness2, (Ed.). Hørsholm, Denmark: Image Metrology A/S, 2013.

[152] D.R. Askeland, P.P. Fulay. Essentials of Materials Science and Engineering, Cengage Lerarning, Toronto, Canada, 2009.

[153] J.R. Davis, J.R. Davis & Associates. Tensile Testing, ASM International, Ohio, USA, 2004.

5 Overview of Publications and Presentations

Results obtained in the framework of this PhD thesis addressing the performance of grade 2205 duplex stainless steel can be summarised in three key research directions:

(I) ***Influence of Stress and Strain on Corrosion Susceptibility:*** resulted in three journal papers and two associated conference presentations

(II) ***Environment-Assisted Cracking (EAC):*** resulted in two journal papers and one under preparation in future works section

(III) ***Effect of Heat-treatment on Corrosion and EAC Performance***: resulted in four journal papers, one magazine article, and one conference paper with presentation.

An overview of all published papers is given below, with Figure 5-1 providing a schematic overview of all manuscripts, publications and conference papers.

5.1 Influence of Stress and Strain on Corrosion Susceptibility

(a) ***SKPFM Measured Volta Potential Correlated with Strain Localisation in Microstructure to Understand Corrosion Susceptibility of Cold-rolled Grade 2205 Duplex Stainless Steel****, Corrosion Science, article in press (2015). DOI: 10.1016/j.corsci.2015.06.035*

(a-1) Presentation & Paper at European Corrosion Congress 2014, Pisa, Italy

Title: Kelvin Probe Force Microscopy and Atmospheric Corrosion of Cold-rolled Grade 2205 Duplex Stainless Steel. EuroCorr14 Proceedings Paper No. 7213

(a-2) Presentation & Paper at EBSD Conference 2014, London

Title: Combined EBSD and KPFM Investigation of Cold Deformed Duplex Stainless Steels for Corrosion Performance Optimisation

(b) ***A Comparison of the Effect of Deformation Mode on Microstructure PerformStress Corrosion Cracking Susceptibility of Grade 2205 Duplex Stainless Steel under Low-Temperature Atmospheric Exposure***.

(b-1) Presentation at European Corrosion Congress 2015, Graz, Austria

Title: On the Effect of Local Strain and Stress on Environment Assisted Cracking Susceptibility of Grade 2205 Duplex Stainless Steel

(b-2) **Presentation at 8th Stainless Steel Conference 2015, Graz, Austria**
Title: Effect of Cold Deformation Mode on Environment Assisted Cracking of 2205 Duplex Stainless Steel

(c) ***An Experimental Investigation into Strain Partitioning of Duplex Stainless Steel Using Digital Image Correlation, X-Ray Diffraction, and Scanning Kelvin Probe Force Microscopy****, Journal of Strain Analysis for Engineering Design (2015). Under review.*

5.2 Environment-Assisted Cracking (EAC) Propensity

(a) ***Probing Propensity of Grade 2205 Duplex Stainless Steel Towards Atmospheric Chloride-induced Stress Corrosion Cracking****, Corrosion Engineering, Science, and Technology, 49, 535-539 (2014). DOI: 10.1179/1743278214Y.0000000205*

(b) Low-Temperature Environmentally Assisted Cracking of Grade 2205 Duplex Stainless Steel Beneath a $MgCl_2$:$FeCl_3$ Salt Droplet*, NACE Corrosion (2015).* http://dx.doi.org/10.5006/1888

(c) Current/Future Work (for publication in Corrosion Science): ***Quasi In-situ Time-dependent Characterisation of Atmospheric-Induced Stress Corrosion Cracking of Duplex Stainless Steel***.

5.3 Effect of Heat Treatment on Corrosion and EAC Performance

a. **<u>475°C Embrittlement</u>**

i. Effect of 475°C Embrittlement on Microstructure Development and Mechanical Properties of Grade 2205 Duplex Stainless Steel.

ii. Effect of "475°C Embrittlement" on the Corrosion Behaviour of Grade 2205 Duplex Stainless Steel Investigated Using Local Probing Techniques*, Corrosion Management Magazine, 115, 9-11 (2013)*

iii. A Mechanistic Model to Describe the Corrosion Behaviour of 475°C Embrittled Duplex Stainless Steel Microstructure – A Comprehensive Study via Scanning Kelvin Probe Force Microscope, Corrosion Science.

iv. Effect of 475°C Embrittlement on Atmospheric Chloride-Induced Stress Corrosion Cracking Behaviour of Grade 2205 Duplex Stainless Steel.

b. <u>750°C Sigma Phase Embrittlement</u>

i. Correlative EBSD and SKPFM Characterisation of Microstructure Development to Assist Determination of Corrosion Propensity in Grade 2205 Duplex Stainless Steel. *Journal of Materials Science (2015),* February 2016, Volume 51, Issue 4, pp 1931-1948.

(i-1) Presentation & Paper at European Corrosion Congress 2012, Turkey

Title: Effect of Microstructure on Atmospheric-induced Corrosion of Heat-treated Grade 2205 and 2507 Duplex Stainless Steels

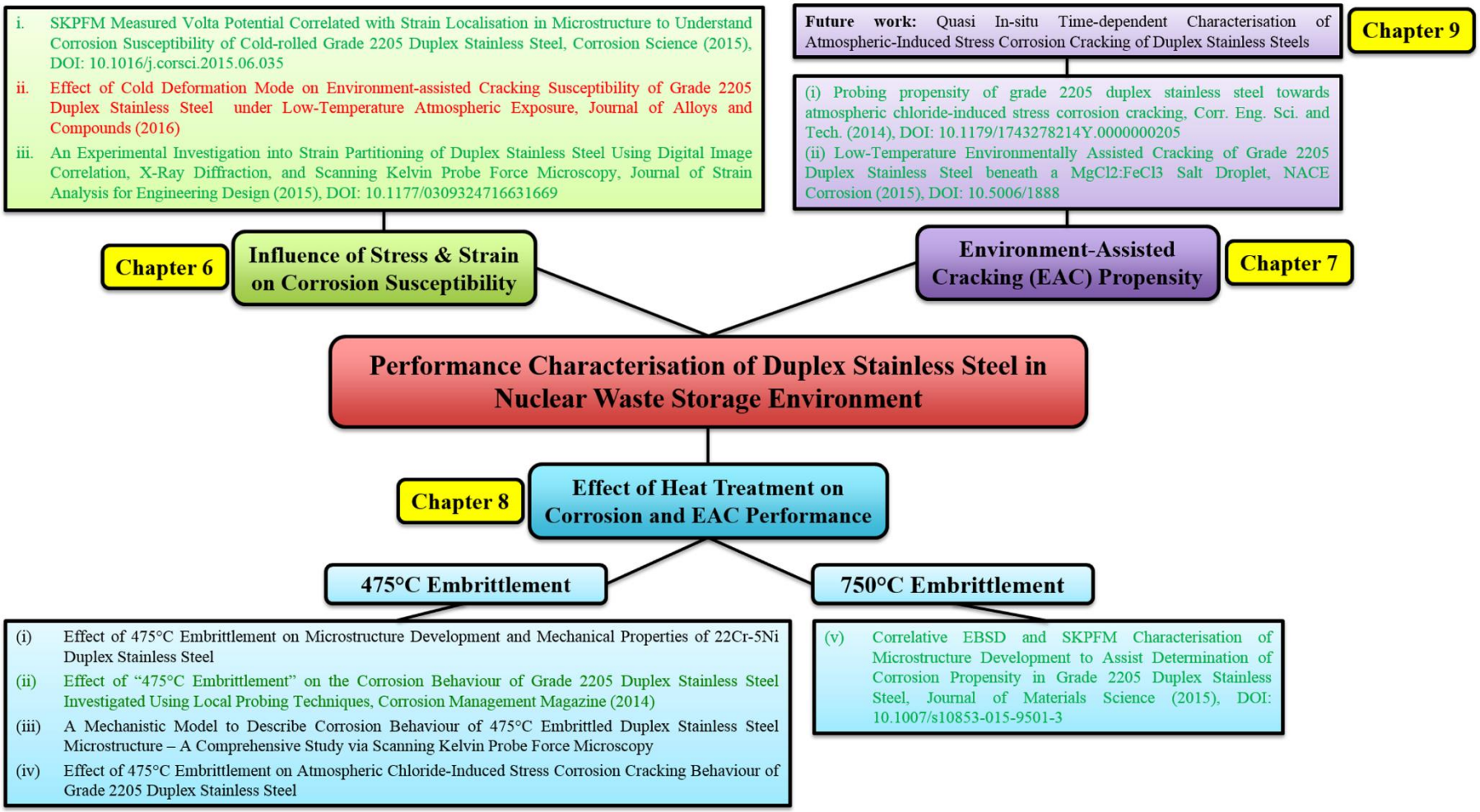

Figure 5-1: Overview of publications arising from this PhD thesis (green = published, red = under review, black = in preparation/future work)

6 Influence of Strain and Stress on Corrosion Susceptibility

6.1 General Introduction

The microstructure has major influence on corrosion and stress corrosion cracking behaviour, especially, in duplex stainless steels due to their inherent multi-phase structure. The phase fraction and overall distribution, grain geometries and morphology, and processing-dependent non-equiaxed structure determine stress and strain partitioning of the phases in the microstructure. Due to compositional and crystallographic differences of ferrite and austenite, galvanic interactions, both on macro and micro scale can always be expected, which can influence the prevailing corrosion mechanism. Mechanistic understanding of stress corrosion cracking processes is possible when the microstructural response to strain and stress and corrosion is known.

Localised corrosion has been believed for decades to occur in a stochastic nature with random and unforeseeable initiation sites for pitting corrosion. However, in duplex stainless steels galvanic interaction between microstructural constituents is, usually, the driving force for corrosion. Ferrite and austenite form net anodic and net cathodic sites, or vice versa, whereupon less pitting corrosion but selective dissolution of one phase becomes more likely the prevailing corrosion mechanism.

Furthermore, the formation of heterogeneous deformation sites within the duplex microstructure due to the effect of strain partitioning is inevitable during mechanical processing of the material. Regions with discrete enhanced plasticity can concentrate in one phase more than the other, whereupon location-selective pitting corrosion susceptibility can be assumed. The nature of deformation i.e. whether tensile, bending, or rolling will contribute to a different extent on the development of heterogeneous deformation structures in duplex stainless steels which can be expected to influence the corrosion and stress corrosion cracking performance. In order to understand all these phenomena a well-planned systematic experimental approach is vital.

In the first paper of this chapter (chapter 6.2), the microstructure will be characterised using the EBSD technique allowing in-depth structural analysis of microstructural constituents. It will be shown that the development of discrete regions with enhanced

plasticity can be screened and semi-quantitatively characterised. Cross-correlation of SKPFM measured Volta potential assessments can help to understand the prevalent corrosion mechanism and possibly be used in prediction models to characterise localised corrosion events. In the second paper (chapter 6.3), the effect of various deformation modes will be discussed in light of microstructural development and response to corrosion properties.

6.2 SKPFM Measured Volta Potential Correlated with Strain Localisation in Microstructure to Understand Corrosion Susceptibility of Cold-rolled Grade 2205 Duplex Stainless Steel

C. Örnek & D. L. Engelberg

Materials and Performance Centre & Corrosion and Protection Centre,
School of Materials, The University of Manchester, Sackville Street, Manchester, M13 9PL, United Kingdom

6.2.1 Abstract

Scanning Kelvin Probe Force Microscopy (SKPFM) of annealed and cold-rolled grade 2205 duplex stainless steel has been correlated with microstructure analysis using Electron Back-Scattered Diffraction (EBSD). In annealed microstructure Volta potential differences indicated micro-galvanic coupling between ferrite and austenite reasoning selective dissolution of ferrite. The introduction of cold work reduced the difference between both phases, but the development of local extremes in Volta potential was observed. Microstructure analysis revealed the presence of larger misorientation concentrations at these sites, which can explain the changes in observed corrosion behaviour, from selective dissolution in the annealed condition to localised corrosion attack after cold-rolling.

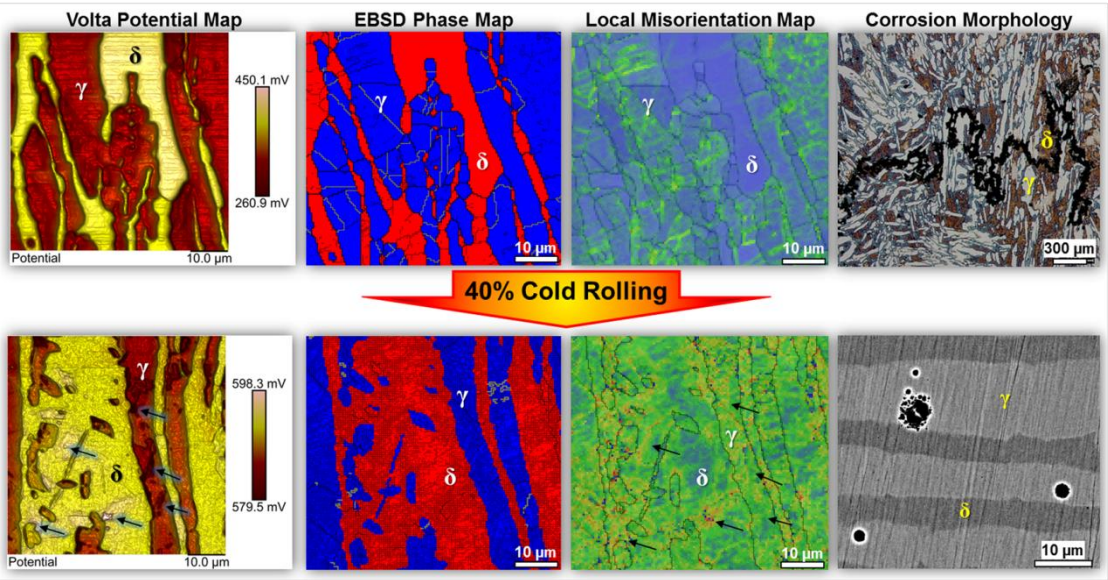

Keywords: *Duplex stainless steel; SKPFM; Cold rolling; Local misorientation; EBSD; Atmospheric Corrosion*

6.2.2 Introduction

Duplex stainless steels (DSS) are frequently used for engineering applications, with complex shapes of components obtained via cold-rolling or shaping of plate and sheet material. Plastic deformation in polycrystalline material is generally heterogeneous, and leads to the development of misorientation variations and gradients in the microstructure, typically associated with strain localisation [1]. In duplex stainless steels, strain localisation is complex due to the mismatch of mechanical properties between body-centred-cubic ferrite (δ - bcc) and face-centred-cubic austenite (γ - fcc), which manifests itself during plastic deformation. Load sharing between both crystallographic phases is observed leading to heterogeneous deformation within the microstructure, with micro-yielding near grain boundaries in the ferrite, augmented by plastic deformation and dislocation pile-ups in the austenite [2, 3]. Pitting corrosion [4, 5] and crack nucleation [6] is often triggered at such sites, but cracks have also been observed to nucleate at slip bands due to the presence of local differences in elastic anisotropy [7].

The magnitude of misorientation within grains increases with the introduction of plastic strain, which is often used as a quantitative measure to describe the degree of microstructure deformation [1]. However, the introduction of plastic strain can also result in sub-structure formation associated with the re-arrangement of dislocations. Free dislocations generated during plastic deformation can readily re-arrange themselves, leading to the development of Low-Angle Grain Boundaries (LAGB) [1, 8, 9]. Plastic deformation results in an increase of the dislocation density which also affects local surface work function and hence the electrochemical potential [10]. The Electron Work Function (EWF) reflects the electron activity [10, 11] and is the minimum energy required to remove electrons from inside a metal to a position far away from the surface on the atomic scale, but still close to the metal to be influenced by ambient electric fields [10-17]. It is not a material property but characteristic of the surface and is sensitive to pre-existing deformation, surface oxide layers, roughness, temperature, and adsorbents [15, 17, 18]. The EWF has been reported to decay with the induction of plastic deformation up to about

40% plastic strain after saturation is reached which was observed to be independent from the type of the material and was enhanced by the rate of deformation [10]. An increase of plastic strain and strain rate decreased the EWF hence the change in EWF could be attributed to the dislocation density in the microstructure. Furthermore, it was demonstrated that at grain boundaries the EWF decreased, in contrast to the grain interior of nanostructure materials, indicating that at such sites the electron activity is high with the result that the surface became more electrochemically reactive [11]. Such an increase in electrochemical reactivity affects local and overall corrosion performance of the material [11].

The related Volta potential (Ψ) is the potential difference between a position infinitely far away from the surface and a position just outside the surface, and is the measureable quantity characterising electrochemical behaviour of a metal [12, 17]. The scanning Kelvin probe force microscopy (SKPFM) technique allows detection of local EWF (if the EWF of the tip is known), or Volta potential differences ($\Delta\Psi$) between an atomic force microscopy tip (usually Pt coated) and the metal surface [14, 15, 19]. The lateral resolution of SKPFM can be as high as 10's of nm in ambient air, with a sensitivity up to 10-20 meV [19]. Volta potential is a characteristic property of a metal surface and can be used to understand electrochemical processes [16]. It is sensitive to any kind of surface defects, chemical variations, and residual stress [13, 17]. Volta potential differences in microstructure have been used to predict corrosion behaviour [10, 15, 18, 20-22]. Regions with larger ($\Delta\Psi$) indicate increased surface reactivity [11, 15, 18], and even a correlation between Volta potential differences measured in nominally dry air and their free corrosion potential (E_{corr}) pre-determined under immersed conditions has been reported [18].

Furthermore, a relationship between E_{corr} measured under thin electrolyte and the Volta potential difference was demonstrated [23]. Linear correlation of Volta potential measured via the Kelvin probe technique measured in air with the free corrosion behaviour (E_{corr}) upon immersed specimens [24], and this relationship was demonstrated to hold true for potentials measured via SKPFM [23]. However, SKPFM Volta potential differences in air may not always correlate with corrosion potentials measured in aqueous solution, and interpretation of SKPFM data regarding corrosion phenomena need to be treated with caution [15]. This shortfall can be minimised by conducting SKPFM measurements in

humid air (>60% relative humidity), where several mono-layers of water are present on the metal surface, mimicking "solution-like" behaviour [25].

The purpose of the work reported in this study was to investigate the effect of plastic deformation on local microstructure Volta potential differences (ΔΨ) and compare these results with atmospheric corrosion observations. The idea is that through the introduction of plastic deformation steep gradients of ΔΨ on confined regions can be formed in the microstructure which may correlate with local strain heterogeneities and act as susceptible sites for localised corrosion and also for stress corrosion cracking. A duplex microstructure was chosen to maximise the effect of plastic strain on microstructure behaviour. Grade 2205 duplex stainless steel is considered by the UK's nuclear industry as a candidate container material for storage of intermediate-level radioactive waste (ILW) which undergoes various deformations [26]. Localised corrosion and, in particular, environment-assisted cracking has been considered as the main material degradation concern that may limit the integrity of ILW containers, which mechanistic understanding is required to support container lifetime predictions.

6.2.3 Experimental

A solution-annealed (mill annealed) grade 2205 DSS plate with a composition (in wt.-%) of 22.4Cr, 5.8Ni, 3.2Mo, 1.5Mn, 0.4Si, 0.016C, 0.18N, and Fe (bal.) was used in this study. The chemical composition of ferrite and austenite was determined by energy dispersive X-ray (EDX) technique interfaced to a scanning electron microscopy (SEM) as 25.0Cr, 4.3Ni, 4.3Mo, 1.7Mn, 0.5Si, and Fe (normalised) for ferrite, and 22.1Cr, 6.9Ni, 2.6Mo, 1.9Mn, 0.4Si, and Fe (normalised) for austenite, all in wt.-%. Cold rolling of the plate was performed with a thickness reduction of 40%, and rectangular coupon specimens (8 x 8 x 8 mm^3) were cut from both the as-received and cold-rolled material. The surface of these coupons was prepared by grinding to 4000-grit, followed by mirror-finish polishing using 3, 1, ¼, and 0.1µm diamond paste, and finalised with an OP-S polishing treatment.

Electron Back-Scattered Diffraction (EBSD) was used for material characterisation, by extracting grain size, crystallographic phase fraction, and local misorientation (LMO), with the latter indicative of the distribution of plastic strain in the microstructure. A FEI Quanta 650 scanning electron microscope (SEM) interfaced with a Nordlys EBSD detector from

Oxford Instruments with Aztec V2.2 software was used for data acquisition. A step size of 0.15 µm over an area of 856 x 746 µm² with an accelerating voltage of 20 kV was used for data acquisition. Data post processing was carried out with HKL Channel 5 software. High-Angle Grain Boundaries (HAGB's) were defined with misorientation ≥15° and Low Angle Grain Boundaries (LAGB's) between >1° and <15°. The grain size was determined by the mean linear intercept method as the mean of vertical and horizontal directions (twins disregarded). LMO maps were generated by using a 3x3 binning and a 5° threshold for the sub-grain angle threshold. This analysis gives the average LMO for a misorientation below the pre-determined sub-grain angle threshold, and this method was used to locate regions with higher concentrations of misorientation in the microstructure. The latter is typically associated with local micro-deformation in the form of plastic strain, due to the presence of dislocations [1].

All SKPFM measurements were performed prior to EBSD analysis of the same area to allow correlation of the results. A MultiMode 8 atomic force microscope from Veeco Instruments (AFM) with Nanoscope V8.15 acquisition programme from Bruker was used. OSCM-PT probe was employed for Volta potential (ΔΨ) measurements. The interleave lift height was 50 nm. The SKPFM scan size was 50 x 50 µm² for the mill-annealed and 55 x 55 µm² for the 40% cold-rolled sample. The tip was biased in order to zero the contact potential difference; therefore, positive potential differences measured indicate larger electronic activity of the microstructure. The reliability of the probe used was assessed by measuring the Volta potential difference of high quality HOPG (Highly Oriented Pyrolytic Graphite) which is the highest-quality synthetic form of graphite and commonly used to calibrate AFM probes [27]. Maximum potential differences of 1-2 mV were measured indicating good quality of the tip and maximum sensitivity of the system. The potential difference measured prior to and after the test was identical supporting the stability of the tip.

SKPFM tests were carried out in ambient air at a temperature of 30°C with 38 ± 1% Relative Humidity (RH) or in a controlled environment of 33 ± 1°C and 86 ± 1% RH. These humidity values were chosen to obtain information about the effect of water multi-layer coverage on Volta-potential differences, invoking "solution-like" behaviour [25]. The humidity was controlled in a sealed AFM chamber. Air was bubbled through a 5 litre flask containing 5 M NaCl solution, heated by a water bath to 60°C, creating a humid gas

atmosphere which was directed to the chamber (a Perspex enclosure) housing the entire AFM setup. According to *Leygraf et al.* [25], at least six to ten monolayers of water with chloride species should form at 86% RH supporting a correlation of Volta potential measurements with local electrochemical activity. Temperature and relative humidity (RH) were recorded during the measurement with an EL-USB-2-LCD temperature and humidity data logger.

SKPFM data analysis was performed with the software NanoScope Analysis 1.5. Topography maps were flattened using 1st order flattening. Data acquisition was carried out with 512 x 512 pixel resolution, with all values reported relative to the work function of the AFM tip (Pt-tip). Potentials measured with higher and lower values with respect to the AFM tip indicate a net anodic and net cathodic activity, respectively. Large Volta potential differences measured with respect to Pt mean lower absolute Volta potentials of the measured region/feature in the microstructure and, hence, higher corrosion activity. Volta potential maps of cold-rolled specimen measured in 86% RH environment were flattened and inverted in order to enhance potential contrast of local potential "hot-spots". Higher and lower potential values indicate net cathodic and net anodic activity, respectively, in this case only.

Atmospheric corrosion tests were performed on 4000-grit surface finished coupons. Tests were performed by exposing samples to 80°C and 27% RH for 212 hrs. Water droplets containing $MgCl_2$ were applied onto the surface, yielding chloride deposition densities ranging from 145 µg/cm² to 1450 µg/cm². An Eppendorf micropipette was used to dispense the liquid with the volume of the droplet 0.5 µl producing an overall droplet radius of 1.7 mm (the effect of secondary spreading of the droplet was not considered). This exposure regime is close to the deliquescence point of $MgCl_2$, resulting in a concentrated, very aggressive $MgCl_2$ solution. Post exposure, the corrosion morphology was analysed with a Keyence VHX-200 optical microscope and the FEI Quanta 650 SEM. To identify whether the ferrite or the austenite phase had corroded, the mill-annealed sample was additionally etched in aqueous 40 wt.-% KOH solution, using 5 V for 5 seconds. This electrolytic etch stains the ferrite [28]. The cold-rolled specimen was analysed in the SEM in the backscattered electron imaging mode, to distinguish between ferrite and austenite.

6.2.4 Results and Discussion

To demonstrate the effect of cold-rolling on microstructure development, EBSD phase maps of all three process orientations (ND, RD, and TD) of the annealed and 40% cold-rolled microstructures are shown in Figure 6-1. Cold-rolling induced changes in grain shape and grain morphology, particularly in the austenite. The average grain size of ferrite as a sum of all process directions decreased from 7.3 ± 0.3 µm in the annealed condition to 5.1 ± 1.9 µm after 40% deformation, whilst the austenite grain size decreased from 7.1 ± 0.9 µm to 4.2 ± 1.3 µm. The average aspect ratio (vertical to horizontal mean length) in all process directions decreased from 1.8 to 1.2 in ferrite, and from 1.6 to 1.1 in austenite. This decrease in grain size can possibly be attributed to severely deformed and broken-up grains after cold deformation.

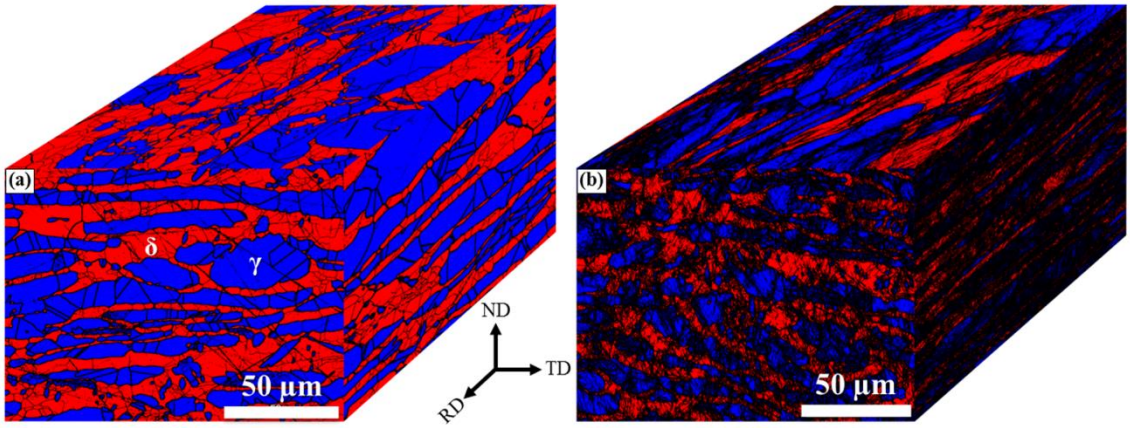

Figure 6-1: EBSD phase maps of (a) annealed microstructure and (b) after 40% cold-rolling, with austenite shown in blue and ferrite in red. The thick black lines are HAGB's and thin lines LAGB's.

Other phases such as sigma (σ) or chi (χ) phase were not present in the microstructure. The austenite to ferrite phase ratio as an average of all three processing orientations was 44:56 and 47:53 for the solution annealed and 40% cold-rolled condition, respectively. The small increase in ferrite content with cold rolling is within typical microstructure variations observed in duplex stainless steel. There are also reports about the formation of deformation-induced bcc-martensite in duplex stainless steels, which would be co-indexed as ferrite since the Kikuchi patterns of martensite overlap with the Kikuchi patterns of ferrite in EBSD analysis. The martensite is typically needle-shaped and forms within the austenitic phase [29]. However, EBSD analysis of the 40% cold-rolled sample in Figure 1 did not show any needle-shaped features.

Topography and Volta potential maps in air (38% RH) of the annealed sample with corresponding EBSD phase and LMO maps of the same region are shown in Figure 6-2. The topography and Volta potential maps showed good correlation with the EBSD phase map, facilitating observation of both crystallographic phases to the corresponding ΔΨ values. Austenite and ferrite had distinctively different potential values, with ferrite showing higher potential values than austenite, meaning expected higher electrochemical activity. Mean ΔΨ values of 408 ± 16 mV and 320 ± 11 mV were measured for ferrite and austenite, respectively. The mean potential difference between both phases is about 70-90 mV, with steep potential gradients across interphases. Similar potential differences of 50-60 mV between ferrite and austenite, with ferrite indicating the less noble phase (anode) and austenite the nobler phase (cathode) has been reported by *Sathirachinda et al.* who investigated solution-annealed and sensitised microstructure and correlated local elemental depletion with local ΔΨ assessments [30]. The probe used was SCM-PIT with Pt-Ir coating and slightly different to that used in this study (OSCM-Pt probe with Pt coating). Small differences in chemical compositions and heat treatment history may also have contributed to different potentials measured. However, similar interphase potential gradients to our study were measured.

The potential variation within each phase is small (Figure 6-2b), and no obvious potential hot-spots (individual sites with high local ΔΨ at confined regions) are detected. This indicates existence of a driving force for galvanic interaction between both phases, with expected onset of electrochemical activity at interphase boundaries and dissolution towards the ferrite. Differences in ΔΨ generally indicate a driving force for galvanic interaction, whereas local potential hot-spots or regions with steep potential changes (gradients) indicate susceptible sites for localised corrosion [31]. Selective corrosion attack in duplex stainless steel has frequently been observed on ferrite to occur in mild chloride-bearing environments, with nucleation at or in the vicinity of ferrite-austenite interphase boundaries, whilst austenite showed less corrosion and stress corrosion cracking susceptibility [32-41]. The corrosion potential (E_{corr}) of ferrite in chloride media is lower than that of austenite despite its lower chromium and molybdenum content. Preferred nitrogen and nickel partitioning in the austenite renders enhanced passivation behaviour and, hence, electrochemical nobility in chloride environments [38, 39, 42, 43].

These data are in close agreement with the studies conducted by *Sathirachinda et al.* who also observed smooth potential distribution in the solution-annealed microstructure which seemed to have disrupted after sensitisation treatments showing local Volta potential extremes associated with enhanced susceptibility to localised corrosion which was confirmed by corrosion immersion tests using aggressive acidic chloride electrolyte [30]. The ferrite phase was seen to corrode primarily while the austenite seemed to remain unaffected which clearly demonstrated the galvanic interaction between ferrite and austenite where ferrite formed the net anode and austenite the net cathode [30].

The LMO map (Figure 6-2d) indicates strain localisation mainly concentrated within ferrite and at small grain clusters with both ferritic and austenitic grains. The mean LMO has a maximum value of 2°, confirming the presence of only small local strain variations. LMO was similar in both phases, meaning that selective attack cannot be associated with LMO values.

The topography and corresponding Volta potential maps for the 40% cold-rolled condition in air (38% RH) are shown in Figure 6-3. The mean potential of the entire region showed an overall $\Delta\Psi$ rise of 170-190 mV with respect to the annealed microstructure condition. This large potential shift is expected to also result in a more corrosion susceptible microstructure (less noble).

The driving force for a corrosion attack seemed to have increased after cold rolling possibly due to a strain-induced alteration in the electron band structure of the passive oxide layer caused by an enhancement of defects such as dislocation density (and other defects), where the amount of LAGB's and HAGB's increased. Lower work functions can result from defect-induced alteration in the electron band structure of passive oxide layers due to shifts in the Fermi level position caused by a change in the electron band gap of the oxide [44]. It has been shown in literature that the passivating layer is typically weakened by the introduction of large amounts of cold deformation, so that the corrosion current density and passive current density significantly increases upon immersion in chloride containing media [45]. It is likely that dislocation multiplication in the microstructure induced by cold deformation can affect the passivating characteristics of both crystallographic phases, which in turn resulted in an increase of the mean $\Delta\Psi$ in the duplex microstructure. Since the Volta potential depends strongly on the electronic structure of the

surface oxide layer of the metal (and other adsorbents) and due to the fact that substantially larger ΔΨ was measured, the reduction of the practical nobility of the cold-rolled microstructure must be related to defect-caused degradation of the surface oxide layer which seemed show to local heterogeneities across the surface [44].

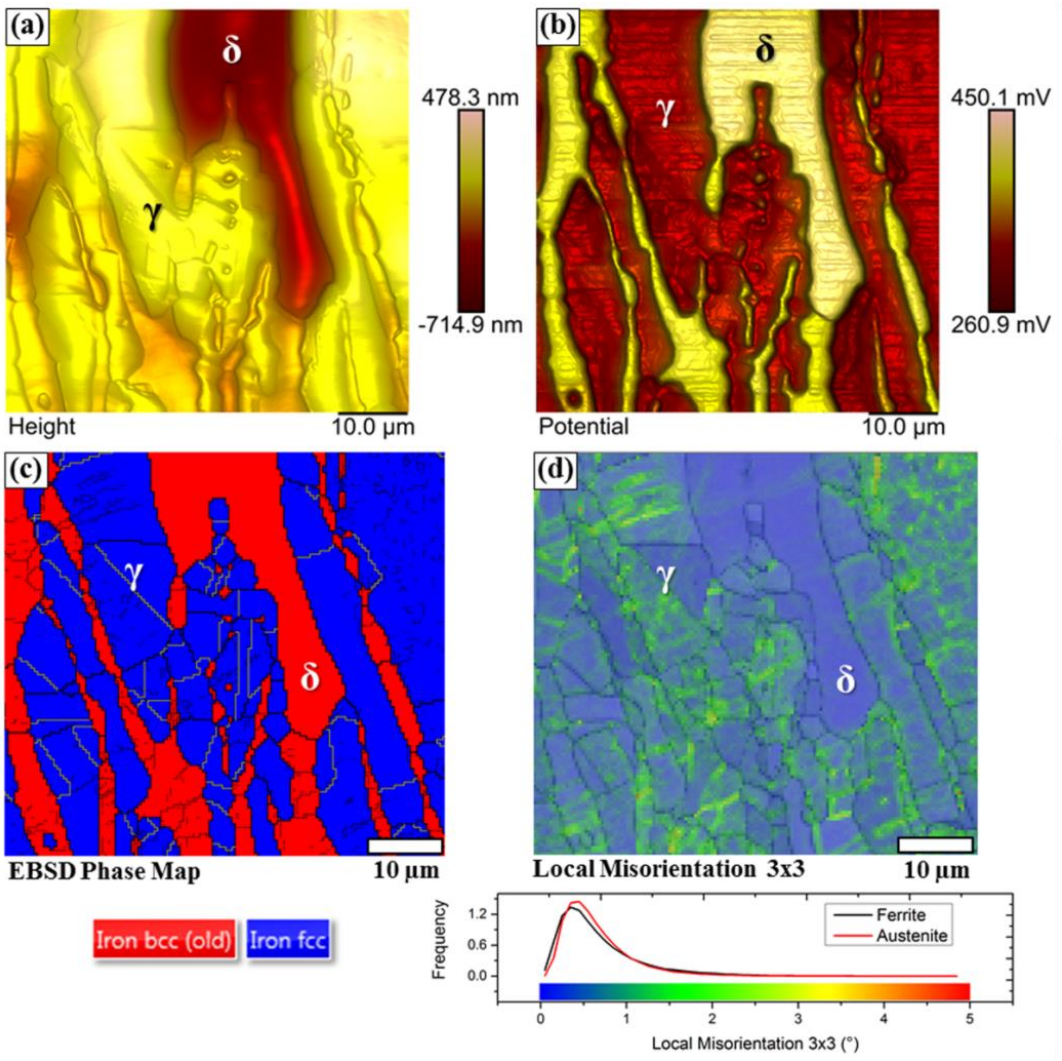

Figure 6-2: SKPFM on annealed sample showing (a) surface topography and (b) Volta potential maps at 38% RH, with (c) the corresponding EBSD phase map, and (d) local misorientation map (LMO) indicating the distribution of plastic strain. Thick black lines are HAGB's, thin black lines LAGB's, and yellow lines are twin boundaries (CSL Σ3).

In addition, the ΔΨ difference measured between ferrite and austenite decreased to only about 5-10 mV difference, with ferrite assuming Volta potential values of 593 ± 5 mV, whilst austenite showed 589 ± 5 mV. Hence, the driving force for micro-galvanic interaction between both phases is expected to have decreased significantly by cold deformation. However, local (ΔΨ) potential hot-spots within both phases have become

visible which were not present prior to cold work, indicating preferential sites of localised electrochemical activity (arrows in Figure 6-3b). There were numerous local hot-spots, indicating enhanced selective net anodic activity in the ferrite with typical (ΔΨ) values of 598 ± 2 mV. This indicates a higher local electronic activity at these confined regions.

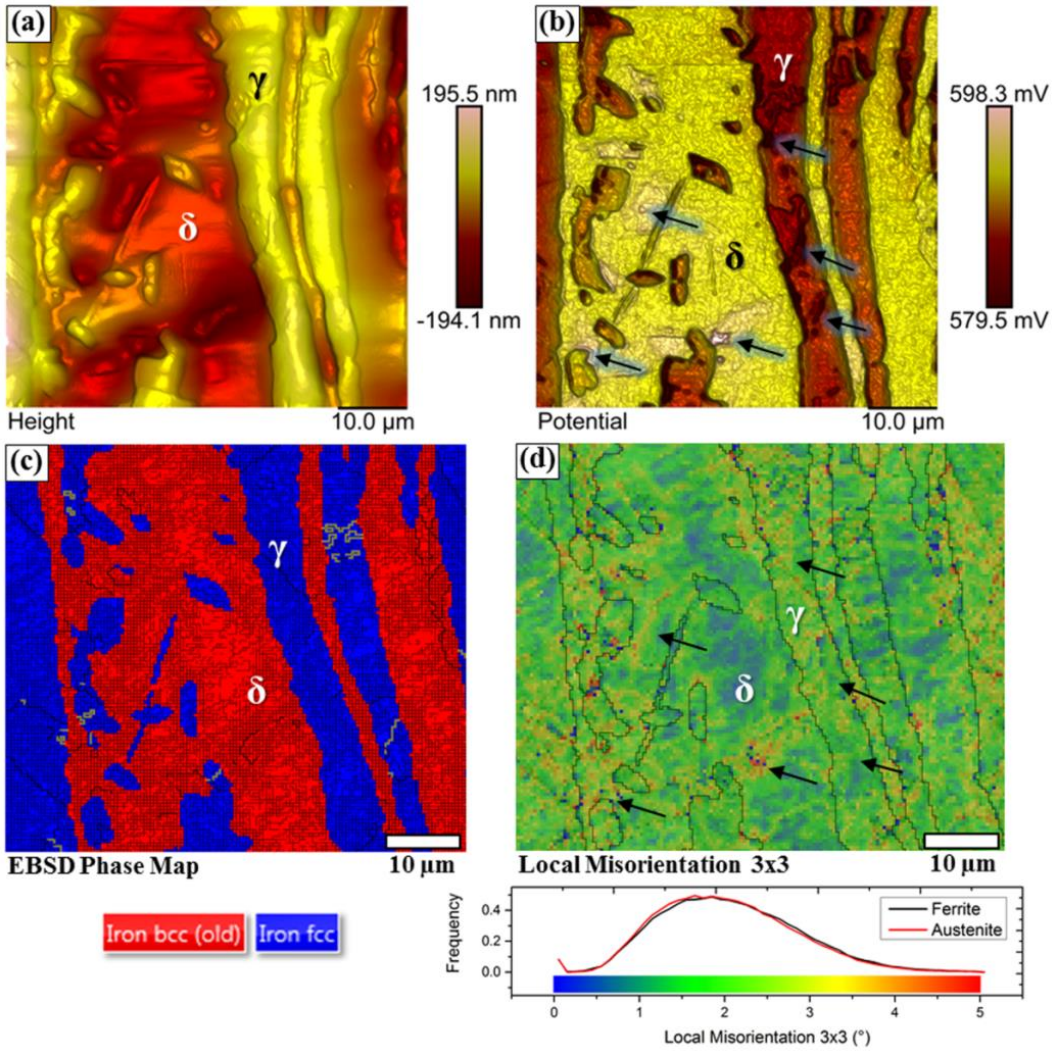

Figure 6-3: SKPFM of 40% cold-rolled duplex stainless steel with (a) topography map, (b) Volta potential map at 38% RH, and (c) corresponding EBSD phase map, and (d) LMO map indicating local strain (black lines show phase boundaries). Thick black lines are HAGB's, thin black lines LAGB's, and yellow lines are twin boundaries (CSL Σ3); with the arrows in (b&d) show local potential hot-spots.

In addition, hot-spots with lower ΔΨ were formed in austenite with values of 580 ± 3 mV. Such sites would indicate lower electronic activity i.e. enhanced selective net cathodic behaviour but potential gradients surrounding hot-spot zones can trigger local galvanic activity, hence enhance the surface reactivity at these confined regions and so facilitate

preferential electrochemical attack. Large potential gradients at these confined regions, measured over short distances are expected to trigger localised attack in contrast to regions with smaller potential gradients.

In general, large ΔΨ gradients can affect the galvanic interaction between individual phases. After cold deformation, the overall potential gradient at the interphases decreased, which indicates a reduction of galvanic interaction between ferrite and austenite. Such sites would still be expected to behave preferentially active, but a selective attack on ferrite only, as observed in the annealed condition, would not be expected. Furthermore, the region over which potential changes occurred in the cold-rolled condition became larger, and sites of local potential gradients (hot-spots) were observed in both phases meaning that both ferrite and austenite would be expected to be electrochemically active, but ferrite obviously more due to the nobler potential. The variation of ΔΨ within each crystallographic phase is most likely associated with the presence of dislocation-related strain fields adjacent to interphases, due to the inherent crystallographic mismatch between ferrite and austenite. The EBSD phase map (Figure 6-3c) shows LAGB's concentrated in both ferrite and austenite, with highly deformed regions consisting of accumulated LAGB's particularly visible at the interphase (Figure 6-3d). The observed SKPFM hot-spots in Figure 6-3b seemed to be associated with some of the misorientation hot-spots observed in Figure 6-3d. Also, the mean LMO shows a broader distribution with a maximum value of nearly 5°, indicating the presence of large local strain variations in the microstructure. It should be noted that during plastic deformation local chemical variations and surface roughness can be altered, which would also contribute to the measured ΔΨ.

Further SKPFM analysis was performed in humid air (86% RH) to assess whether the observed local (ΔΨ) differences at low RH were also present. The surface topography map with corresponding Volta potential maps at 38% RH and 86% RH of the 40% cold-rolled specimen are shown in Figure 6-4. Both Volta potential maps were flattened using 1st flattening order and mathematically inverted to obtain an enhanced contrast of local potential hot-spots. The latter produces a better contrast but reverses the potential ranking order (i.e. austenite has higher potential difference). Several local ΔΨ hot-pots were observed in both the ferrite and austenite, indicating local corrosion-activity. These local potential variations with discrete potential extremes causing potential contrasts indicate micro-galvanic coupling within both phases and at interphase boundaries. Some larger,

trench-like regions in austenite are also present, indicating similar (ΔΨ) differences. These regions are currently subject to further investigations.

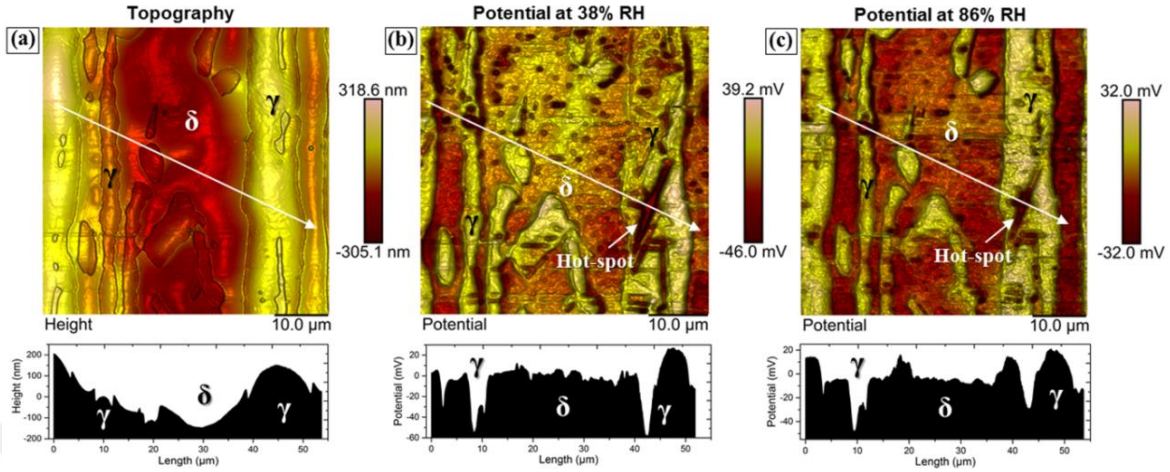

Figure 6-4: SKPFM of 40% cold-rolled 2205 duplex stainless steel with (a) topography map, (b) mathematically inverted Volta potential map at 38% RH, and (c) Volta potential map at 86% RH. The inversion of the Volta potential map clearly shows local potential hot-spots. Local potential hot-spots remained in humid environment indicating corrosion-active sites. Potential maps were flattened using 1st order flattening therefore the values are relative only.

In dry air, the passivating layer of stainless steels consists of a thin film oxide/oxyhydroxide layer, usually 1-3 nm [25, 46, 47]. In humid air above 60% RH, at least ten monolayers of water will be adsorbed resulting in thicker passivating layers which decreases the Volta potential difference [25, 48]. It has been reported that this potential drop is in the order of 50-100 mV [48]. However, the measurement in Figure 6-4 gives a potential drop of 200 mV in 86% RH compared to 38% RH. Water molecules could have adsorbed onto the Pt probe which may have resulted in a minor change in the Volta potential of the Pt probe.

The corrosion behaviour of the mill-annealed and 40% cold-rolled microstructures after exposure for 212 hrs to 86% RH atmospheric environment is shown in Figure 6-5. The ferrite selectively corrodes in this environment [32-35], supported by observations in Figure 6-5(a+b). The corrosion attack showed a filiform-like appearance, percolating through the microstructure. Corrosion initiated on interphase boundaries and propagated preferentially over ferrite regions indicating net anodic behaviour while austenite was the net cathode. Slight attack on some austenite parts, however, has been observed indicating less favoured corrosion attack occurring from the ferrite towards the austenite phase. After

cold rolling almost no selective corrosion of the ferrite was observed, but localised corrosion attack occurred at discrete sites primarily located in the austenite (Figure 6-5c+d). Local initiation sites of pitting corrosion in austenite were primarily located in the grain interior, possibly related to regions containing local plastic strains. Alternatively, some of these discrete sites may also be associated with strain-induced martensite, which has been reported for duplex stainless steels [49, 50].

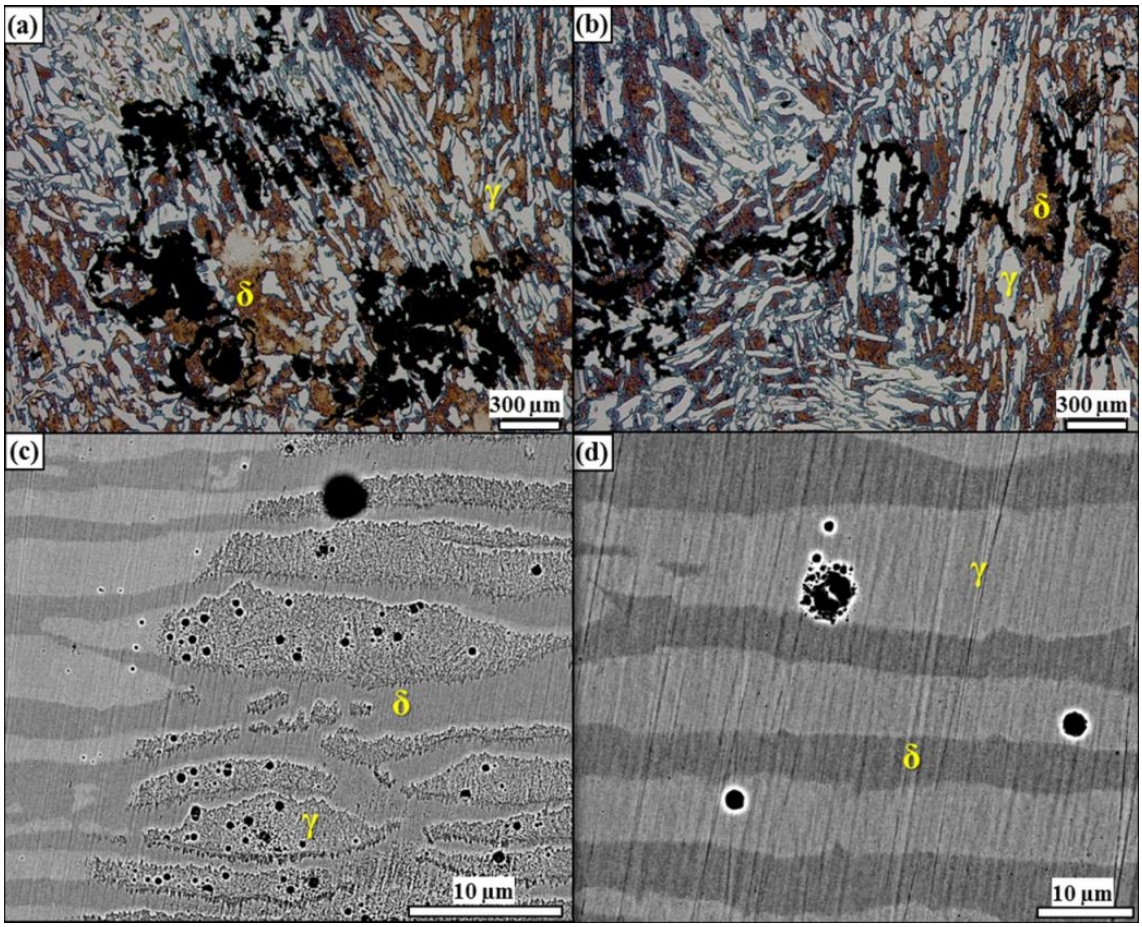

Figure 6-5: Corrosion morphology after exposure to atmospheric corrosion with (a) optical micrograph of mill-annealed microstructure showing selective corrosion on ferritic regions (stained) with 145 µg/cm² DD and (b) with 290 µg/cm² DD of chloride ($MgCl_2$), and (c+d) SEM images of the 40% cold-rolled microstructure showing numerous pits formed primarily in austenite after exposure to 1450 µg/cm² DD of chloride ($MgCl_2$).

These observations are in line with data shown in Figure 6-3 and Figure 6-4, supporting the notion that local microstructure can affect macroscopic corrosion behaviour. The work also highlights how the degradation mechanisms of a material can change as a function of microstructure strain condition. The change from selective corrosion to localised attack

could be a potential concern for components with thin wall thickness, and local susceptible sites that follow from cold working may also facilitate stress corrosion crack initiation.

6.2.5 Conclusions

1) Volta potential differences of the solution-annealed microstructure measured over austenite and ferrite differed by 70-90 mV, with ferrite indicating a net anodic potential. The latter is expected to facilitate micro-galvanic coupling between ferrite and austenite, resulting in selective dissolution of the ferrite with atmospheric exposure to $MgCl_2$ containing solutions.
2) The introduction of 40% cold-roll reduction significantly reduced the Volta potential difference between ferrite and austenite, but in parallel increased the mean Volta potential difference of the entire microstructure.
3) Volta potential differences maps of the cold-rolled microstructure showed local potential hot-spots (highly active sites at confined regions) with exposure to both 38% and 86% RH environment, indicating corrosion-active sites
4) After 40% cold rolling, localised pitting corrosion in austenite and only little attack on ferrite was observed, supporting changes to the overall corrosion response of the duplex stainless steel microstructure

6.2.6 Acknowledgement

The authors acknowledge Radioactive Waste Management (RWM) (NPO004411A-EPS02) and EPSRC (EP/I036397/1) for financial support. The authors are grateful for the kind provision of Grade 2205 Duplex Stainless Steel plate by Rolled Alloys. The authors also appreciate the valuable comments provided by Dr Robert Winsley, Radioactive Waste Management Ltd. and Dr Anthony Cook, The University of Manchester.

6.2.7 References

[1] C. Fukuoka, K. Morishima, H. Yoshizawa, K. Mino. Misorientation development in grains of tensile strained and crept 2.25%Cr–1%Mo steel, Scripta Materialia 46 (2002) 61-66.

[2] J. Johansson, M. Odén. Load sharing between austenite and ferrite in a duplex stainless steel during cyclic loading, Metall and Mat Trans A 31 (2000) 1557-1570.

[3] J.-O. Nilsson, G. Chai. The physical metallurgy of duplex stainless steels. International Conference & Expo DUPLEX 2007. Grado, Italy: ASSOCIAZIONE ITALIANA DI METALLURGIA - AIM, 2007.

[4] G.S. Frankel. Pitting Corrosion of Metals: A Review of the Critical Factors, Journal of The Electrochemical Society 145 (1998) 2186-2198.

[5] W. Ozgowicz, A. Kurc-Lisiecka, A. Grajcar. Corrosion Behaviour of Cold-Deformed Austenitic Alloys. in: Aliofkhazraei M, (Ed.). Resistance to Corrosion and Passivity of 316L Stainless Steel Directionally Solidified Samples, Developments in Corrosion Protection. InTech, 2014.

[6] T. Prosek, A. Le Gac, D. Thierry, S. Le Manchet, C. Lojewski, A. Fanica, E. Johansson, C. Canderyd, F. Dupoiron, T. Snauwaert, F. Maas, B. Droesbeke. Low-Temperature Stress Corrosion Cracking of Austenitic and Duplex Stainless Steels Under Chloride Deposits, Corrosion Science 70 (2014) 1052-1063.

[7] U. Krupp, A. Giertler, M. Söker, H. Fu, B. Dönges, H.J. Christ, K. Istomin, A. Hüsecken, U. Pietsch, C.P. Fritzen, W. Ludwig. Significance and Mechanism of the Crack Initiation Process during Very High Cycle Fatigue of Duplex Stainless Steel, Procedia Engineering 74 (2014) 143-146.

[8] J.D. Kordatos, G. Fourlaris, G. Papadimitriou. The effect of cooling rate on the mechanical and corrosion properties of SAF 2205 (UNS 31803) duplex stainless steel welds, Scripta Materialia 44 (2001) 401-408.

[9] K. Mino, C. Fukuoka, H. Yoshizawa. Evolution of intragranular misorientation during plastic deformation, Nippon Kinzoku Gakkaishi/Journal of the Japan Institute of Metals 64 (2000) 50-55.

[10] W. Li, M. Cai, Y. Wang, S. Yu. Influences of tensile strain and strain rate on the electron work function of metals and alloys, Scripta Materialia 54 (2006) 921-924.

[11] D.Y. Li. Electron work function at grain boundary and the corrosion behavior of nanocrystalline metallic materials, MRS Online Proceedings Library 887 (2005) null-null.

[12] Moore, W. J. Physikalische Chemie. 4. Auflage ed., Walter de Gruyter, 1986.

[13] A. Nazarov, D. Thierry. Application of Volta potential mapping to determine metal surface defects, Electrochimica Acta 52 (2007) 7689-7696.

[14] M. Nonnenmacher, M.P. O'Boyle, H.K. Wickramasinghe. Kelvin probe force microscopy, Applied Physics Letters 58 (1991) 2921-2923.

[15] M. Rohwerder, F. Turcu. High-resolution Kelvin probe microscopy in corrosion science: Scanning Kelvin probe force microscopy (SKPFM) versus classical scanning Kelvin probe (SKP), Electrochimica Acta 53 (2007) 290-299.

[16] V.S. Bagotsky. Fundamentals of Electrochemistry. The Electrochemical Society Series. Hoboken, New Jersey: Wiley-Interscience, 2006.

[17] J.O.M. Bockris, A.K.N. Reddy, M. Gamboa-Aldeco. Modern Electrochemistry 2A. Fundamentals of Electrodics, vol. 2A. New York: Kluwer Academic Publishers, 2002. p.1-817.

[18] G.S. Frankel, V. Guillaumin, P. Schmutz. Characterization of Corrosion Interfaces by the Scanning Kelvin Probe Force Microscopy Technique, Journal of The Electrochemical Society 148 (2001) B163-B173.

[19] S. Sadewasser, T. Glatzel. Kelvin Probe Force Microscopy Measuring and Compensating Microscopy, Springer, Heidelberg, 2012.

[20] W. Li, D.Y. Li. Effect of surface geometrical configurations induced by microcracks on the electron work function, Acta Materialia 53 (2005) 3871-3878.

[21] W. Li, D.Y. Li. Variations of work function and corrosion behaviors of deformed copper surfaces, Applied Surface Science 240 (2005) 388-395.

[22] W. Li, D.Y. Li. Influence of surface morphology on corrosion and electronic behavior, Acta Materialia 54 (2006) 445-452.

[23] A.B. Cook, Z. Barrett, S.B. Lyon, H.N. McMurray, J. Walton, G. Williams. Calibration of the scanning Kelvin probe force microscope under controlled environmental conditions, Electrochimica Acta 66 (2012) 100-105.

[24] S. Yee, R.A. Oriani, M. Stratmann. Application of a Kelvin Microprobe to the Corrosion of Metals in Humid Atmospheres, Journal of The Electrochemical Society 138 (1991) 55-61.

[25] C. Leygraf, T.E. Graedel. Atmospheric Corrosion, John Wiley & Sons, Canada, 2000.

[26] T.W. Hicks, T.D. Baldwin, P.J. Hooker, P.J. Richardson, N.A. Chapman, I.G. McKinley, F.B. Neall. Concepts for the Geological Disposal of Intermediate-level Radioactive Waste. Oakham, Rutland, UK: Galson Sciences Ltd., 2008.

[27] R.V. Lapshin. Automatic lateral calibration of tunneling microscope scanners, Review of Scientific Instruments 69 (1998) 3268-3276.

[28] ASTM International. ASTM A 923 - Standard Test Methods for Detecting Detrimental Intermetallic Phase in Duplex Austenitic/Ferritic Stainless Steels. West Conshohocken, PA: ASTM International, 2003.

[29] J.Y. Choi, J.H. Ji, S.W. Hwang, K.-T. Park. Strain induced martensitic transformation of Fe–20Cr–5Mn–0.2Ni duplex stainless steel during cold rolling: Effects of nitrogen addition, Materials Science and Engineering: A 528 (2011) 6012-6019.

[30] N. Sathirachinda, R. Pettersson, J. Pan. Depletion effects at phase boundaries in 2205 duplex stainless steel characterized with SKPFM and TEM/EDS, Corrosion Science 51 (2009) 1850-1860.

[31] M. Femenia, J. Pan, C. Leygraf. Characterization of Ferrite-Austenite Boundary Region of Duplex Stainless Steels by SAES, Journal of The Electrochemical Society 151 (2004) B581-B585.

[32] C. Örnek, A.H. Ahmed, D.L. Engelberg. Effect of Microstructure on Atmospheric-Induced Corrosion of Heat-treated Grade 2205 and 2507 Duplex Stainless Steels. Eurocorr 2012. Istanbul, Turkey: Dechema, 2012. p.1-10.

[33] C. Örnek, D.L. Engelberg. Effect of “475°C Embrittlement” on the Corrosion Behaviour of Grade 2205 Duplex Stainless Steel Investigated Using Local Probing

Techniques. Corrosion Management. Northampton, UK: The Institute of Corrosion, 2013. p.9-11.

[34] C. Örnek, D.L. Engelberg. Kelvin Probe Force Microscopy and Atmospheric Corrosion of Cold-rolled Grade 2205 Duplex Stainless Steel. Eurocorr 2014. Pisa, Italy: European Federation of Corrosion, 2014. p.1-10.

[35] D.L. Engelberg, C. Örnek. Probing propensity of grade 2205 duplex stainless steel towards atmospheric chloride-induced stress corrosion cracking, Corrosion Engineering, Science and Technology 49 (2014) 535-539.

[36] A.M. do Nascimento, M.C.F. Ierardi, A.Y. Kina, S.S.M. Tavares. Pitting corrosion resistance of cast duplex stainless steels in 3.5%NaCl solution, Materials Characterization 59 (2008) 1736-1740.

[37] M. Femenia, J. Pan, C. Leygraf, P. Luukkonen. In situ study of selective dissolution of duplex stainless steel 2205 by electrochemical scanning tunnelling microscopy, Corrosion Science 43 (2001) 1939-1951.

[38] S. Aoki, K. Ito, H. Yakuwa, M. Miyasaka, J.i. Sakai. Potential Dependence of Preferential Dissolution Behavior of a Duplex Stainless Steel in Simulated Solution inside Crevice, Zairyo-to-Kankyo 60 (2011) 363-367.

[39] S. Aoki, H. Yakuwa, K. Mitsuhashi, J.i. Sakai. Dissolution Behavior of α and γ Phases of a Duplex Stainless Steel in a Simulated Crevice Solution, ECS Transactions 25 (2010) 17-22.

[40] R.A. Cottis, R.C. Newman. Stress Corrosion Cracking Resistance of Duplex Stainless Steels. Health and Safety Executive, 1993. p.58.

[41] B. Cottis, M. Graham, R. Lindsay, S. Lyon, T. Richardson, D. Scantlebury, H. Stott. Shreir's Corrosion - Volume 2. In: Cottis B, Graham M, Lindsay R, Lyon S, Richardson T, Scantlebury D, Stott H, (Eds.), vol. 1. Manchester: Elsevier B.V.,, 2010.

[42] C.-M. Tseng, W.-T. Tsai, H.-Y. Liou. Effect of nitrogen content on the environmentally-assisted cracking susceptibility of duplex stainless steels, Metall and Mat Trans A 34 (2003) 95-103.

[43] J.-S. Lee, K. Fushimi, T. Nakanishi, Y. Hasegawa, Y.-S. Park. Corrosion behaviour of ferrite and austenite phases on super duplex stainless steel in a modified green-death solution, Corrosion Science 89 (2014) 111-117.

[44] R. Hausbrand, M. Stratmann, M. Rohwerder. The Physical Meaning of Electrode Potentials at Metal Surfaces and Polymer/Metal Interfaces: Consequences for Delamination, Journal of The Electrochemical Society 155 (2008) C369-C379.

[45] A.S. Hamada, L.P. Karjalainen, M.C. Somani. Electrochemical corrosion behaviour of a novel submicron-grained austenitic stainless steel in an acidic NaCl solution, Materials Science and Engineering: A 431 (2006) 211-217.

[46] T.E. Graedel, R.P. Frankenthal. Corrosion Mechanisms for Iron and Low Alloy Steels Exposed to the Atmosphere, Journal of The Electrochemical Society 137 (1990) 2385-2394.

[47] S.D. Cramer, B.S. Covino. ASM Handbook, Volume 13A: Corrosion: Fundamentals, Testing, and Protection. vol. 13: ASM International, 2003.

[48] P. Marcus, F. Mansfeld. Analytical Methods in Corrosion Science and Engineering, Taylor & Francis Group, Boca Raton, FL, USA, 2006.

[49] L.W. Tsay, M.C. Young, C.S. Shin, S.L.I. Chan. Hydrogen-enhanced cracking of 2205 duplex stainless steel, Fatigue & Fracture of Engineering Materials & Structures 30 (2007) 1228-1236.

[50] Y. Guo, J. Hu, J. Li, L. Jiang, T. Liu, Y. Wu. Effect of Annealing Temperature on the Mechanical and Corrosion Behavior of a Newly Developed Novel Lean Duplex Stainless Steel, Materials 7 (2014) 6604-6619.

6.3 A Comparison of the Effect Deformation Mode on Stress Corrosion Cracking Susceptibility of Grade 2205 Duplex Stainless Steel under Low-Temperature Atmospheric Exposure

C. Örnek & D.L. Engelberg

Materials and Performance Centre & Corrosion and Protection Centre,
School of Materials, The University of Manchester, Sackville Street, Manchester, M13 9PL, United Kingdom

6.3.1 Abstract

The effect of bending, rolling, and tensile deformation on strain and stress development in microstructure of grade 2205 duplex stainless steel was investigated and compared to its susceptibility to atmospheric-induced stress corrosion cracking (AISCC) using chloride-bearing droplets under atmospheric exposure at 50°C and 80°C. X-ray diffraction (XRD) stress measurements revealed the highest stress development in microstructure with bending deformation, which was in line with electron backscatter diffraction (EBSD) analyses showing intense strain localisation, whereas tensile deformation resulted in larger strain and stress development than in cold-rolled microstructure. Enhanced susceptibility to atmospheric corrosion and AISCC was observed after bending deformation, with tensile-strained and cold-rolled microstructures being less susceptible to AISCC.

Keywords: *Duplex stainless steel; Cold deformation; Atmospheric corrosion; Stress corrosion cracking; EBSD; XRD*

6.3.2 Introduction

Duplex stainless steel (DSS) has been increasingly implemented as a structural material in a wide range of application such as nuclear, petrochemical, medical, and automotive. Over the last decade, an increasing use of DSS's was recorded and a growing demand has been forecast [1]. These steels are lean in alloying elements in comparison to their austenitic counterparts, and provide good mechanical properties with excellent resistance to corrosion and stress corrosion cracking (SCC) [2]. The introduction of cold work is routine

practice in industry, and it is now accepted that the degree of deformation significantly changes microstructure, mechanical, as well as corrosion properties.

For manufacturing DSS components into complex shapes and designs, rolling, shaping, and drawing is typically performed, which ultimately results in microstructure deformation with strain and stress partitioning in the duplex microstructure. The latter is based on the mismatch of mechanical deformation behaviour between ferrite and austenite, which in turn can affect microstructure corrosion and SCC susceptibility [3]. The knowledge about microstructure and processing history has crucial importance in understanding and predicting corrosion and SCC phenomena. The duplex microstructure is complex; it consists, usually, of a balanced ratio of ferrite (δ) and austenite (γ) in comparable fractions [4]. There is often residual strain present in the microstructure due to different thermal expansion coefficients of ferrite and austenite which causes heterogeneous strain fields during rapid cooling processes [5, 6]. Furthermore, the grains of forged duplex alloys are non-equiaxed and elongated in rolling or milling direction leading to a texture-like banded structure with discontinuous island-like austenite grains embedded in a continuous ferrite matrix [7]. The population of microstructural features, including the distribution of existing phases, grain boundaries with their characters, geometries, and morphologies, and stress and strain states are important to know to assess the performance of the material.

Grade 2205 DSS is currently implemented as a storage container material of intermediate-level radioactive waste (ILW) to house UK's waste form over 100's of years [8, 9]. Aerosol coastal chloride-bearing particulates can deposit on the container surface during storage and become wet within a wider range of relative humidity (RH) forming highly aggressive thin-film electrolytes and leading to localised corrosion. This phenomenon has become known as atmospheric corrosion [10-14]. $MgCl_2$ is one of the most detrimental salts which can form up to 12 M chloride electrolyte at its deliquescence relative humidity (DRH) at room temperature and, therefore atmospheric corrosion may be a potential challenge for the integrity of ILW containers. In the presence of residual stress, a transition to a phenomenon known as atmospheric-induced stress corrosion cracking may further endanger the durability of ILW containers [10-14]. The internal surface of the container can reach temperatures up to 50°C. The containers are subject to cold deformation and welding during fabrication which may affect the microstructure of the steel [15-17].

In this work the effect of cold work has been investigated under conditions relevant to the storage of ILW. Rolling, bending, and tensile deformation was applied on plate and sheet grade 2205 DSS, and the microstructure development was characterised by EBSD, with XRD being implemented to measure the stress evolution in ferrite and austenite as a function of the level of cold work. The microstructure after cold deformation was exposed to droplets of $MgCl_2$ in a temperature- and humidity-controlled environment, and the susceptibility to atmospheric corrosion and AISCC was investigated. The implications of these observations are discussed in light of microstructure optimisation for application in demanding environment.

6.3.3 Experimental

Sheet and plate grade 2205 DSS, supplied by *Rolled Alloys UK*, with a composition given in The materials were solution-annealed by the manufacturer (*Outokumpu, Sweden*) at 1050°C for 1 hour and denoted as 'as-received'. The thickness of the plate and sheet materials was 10 mm and 2 mm, respectively. Tensile, bending, and rolling deformation was introduced and the effect of microstructure development and susceptibility to AISCC was investigated.

Table 6-1, was used in this work. The materials were solution-annealed by the manufacturer (*Outokumpu, Sweden*) at 1050°C for 1 hour and denoted as 'as-received'. The thickness of the plate and sheet materials was 10 mm and 2 mm, respectively. Tensile, bending, and rolling deformation was introduced and the effect of microstructure development and susceptibility to AISCC was investigated.

Table 6-1: Chemical compositions (in wt.-%) of grade 2205 duplex stainless steel used in this study

Grade	C	Si	Mn	P	S	Cr	Ni	Mo	N	Nb	Cu	Co	Fe
Plate	0.016	0.40	1.50	0.021	0.001	22.40	5.80	3.20	0.180	-	-	-	bal.
Sheet	0.015	0.42	1.41	0.020	0.001	22.44	5.75	3.32	0.155	0.006	0.21	0.12	bal.

*Measured via SEM-EDX

Cold rolling with a thickness reduction of 20% and 40% was carried out on bars cut from the plate material with dimension of 10 mm (width) x 10 mm (thickness) x 80 mm (length). The latter was along the rolling direction (RD) of the microstructure. Coupons in

sizes of 10 mm by 10 mm were prepared from as-received and cold-rolled plate materials and used for metallographic assessment and corrosion testing.

U-bending deformation was performed on the sheet metal. Flat strap specimens with dimensions of 70 mm (length) x 20 mm (width) x 2mm (thickness) were prepared by cutting along the RD. An engineering draft is of the specimen in shown in Figure 6-6(b). A hole was drilled in both ends of each flat specimen with a radius of 5.2 mm in order to fixate the specimen after bending. Bending deformation was carried out with a self-designed clevis-pin bending setup, as shown in Figure 6-6(a), giving the sheet metal a U-shape. The bending was performed on an *Instron 5569* testing machine under compression mode with a load cell of 50 kN and a loading rate of 10 mm/min. The radius of the pin used was 10 mm. After the bending process, the sample was fixated on both ends (non-deformed parts) using an M5 bolt and an M5 nut to keep it under elastic strain. A photograph of the U-bend specimen is shown in Figure 6-6(d).

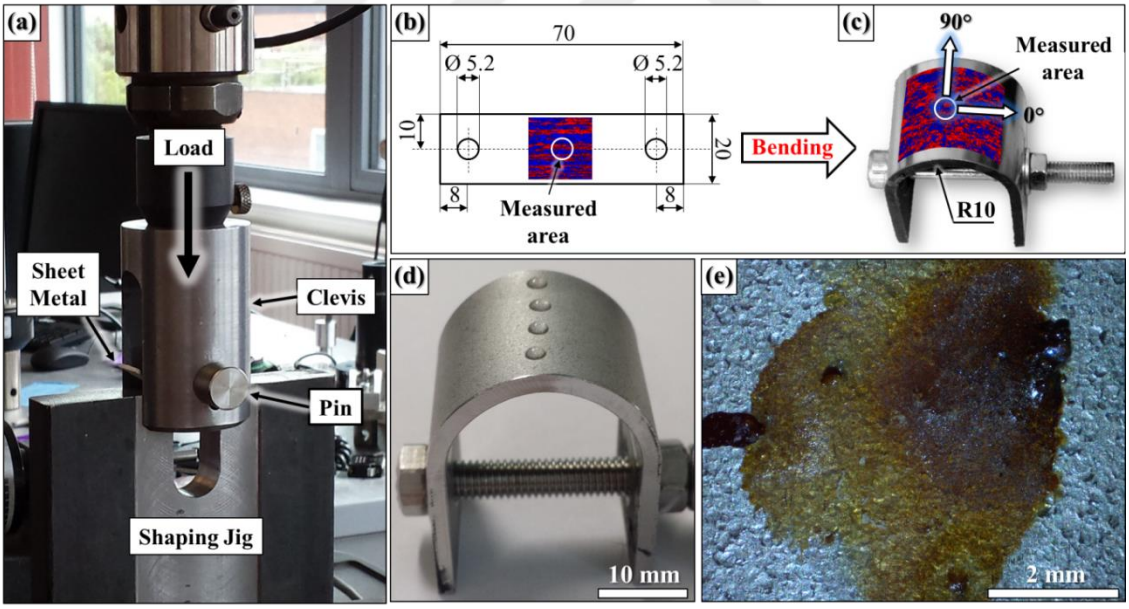

Figure 6-6: (a) Showing U-bending deformation setup, (b) engineering draft of the sheet metal used, (c) XRD measurement specification, (d) U-bend specimen with deposited salt-laden water droplets, (e) stereographic image of one of the water droplets after exposure to atmospheric corrosion

Tensile straining was performed on a flat tensile specimen with a gauge length of 50 mm machined from the sheet material along the RD. The specimen was mechanically ground to 1200-grit emery paper and electro-polished using a 20 vol.-% perchloric acid and 80 vol.-% methanol electrolyte with 20 Volts for 60 seconds at -35°C.

6.3.3.1 Microstructure Characterisation

The microstructure of both plate and sheet materials were analysed by Electron Back-Scattered Diffraction (EBSD) for grain boundary characterisation, grain size, and local misorientation. Rectangular coupon specimens were cut from 20% and 40% cold-rolled material in dimensions of 10 mm x 10 mm. The surface of these coupons, the tensile specimen, and the flat sheet specimens (to be used for U-bending) was prepared by grinding to 4000-grit, followed by mirror-finish polishing using 3, 1, ¼, and 0.1µm diamond paste, and finalised with an OP-S polishing (contains 40 nm silica colloid particles) treatment for one hour. The U-bend specimen was analysed before and after bending under fixated condition (i.e. under elastic strain), and the tensile specimen was analysed after tensile strain.

EBSD was used for material characterisation by extracting grain size, grain boundary information, crystallographic phase fraction, and local misorientation (LMO), with the latter indicative of the distribution of plastic strain. An FEI Quanta 650 scanning electron microscope (SEM) interfaced with a Nordlys EBSD detector from Oxford Instruments with AZtec V2.2 software was used for data acquisition. A step size of 0.15 to 0.74 µm over a sufficiently large area covering 1000's of grains with an accelerating voltage of 20 kV was used. Data post processing was carried out with HKL Channel 5 software. High-Angle Grain Boundaries (HAGB's) were defined with misorientation ≥15° and Low Angle Grain Boundaries (LAGB's) between >1° and <15°. The grain size was determined by the mean linear intercept method as the mean of the vertical and horizontal directions. LMO maps were generated by using a 3x3 binning and a 5° threshold for the sub-grain angle threshold. This analysis gives the average LMO for a misorientation below the pre-determined sub-grain angle threshold, and this method was used to locate regions with higher concentrations of misorientation in the microstructure. The latter is typically associated with local micro-deformation in the form of plastic strain, due to the presence of dislocations [10].

6.3.3.2 Atmospheric Corrosion Tests

Atmospheric corrosion tests were performed to study the effect of deformation mode on corrosion and stress corrosion cracking behaviour. To study the effect of rolling deformation, as-received, 20%, and 40% cold-rolled specimens were used with 4000-grit

surface finish. The U-bend specimen was not mechanically polished and kept in its as-finished condition. The tensile specimen was used in electro-polished condition as previously described.

Tests were performed by depositing water droplets containing $MgCl_2$ and a mixture of $FeCl_3$+$MgCl_2$ (0.68:1 mol ratio of $FeCl_3$:$MgCl_2$) onto the surface of each specimen used, yielding surface chloride coverage (initial deposition density) ranging from 145 µg/cm² to 1450 µg/cm², and exposing to 50°C and 30% relative humidity (RH) and 80°C and 27% RH from 9 to 455 days. Further detailed test conditions can be taken from Table 6-2. An Eppendorf micropipette was used to dispense the liquid with 0.5 µl droplet volume producing an overall droplet radius of 1.7 mm (the effect of secondary spreading of the droplet was not considered therefore all data referred to as initial deposition densities). This exposure regime is close to the deliquescence point of $MgCl_2$, resulting in a concentrated, very aggressive $MgCl_2$ solution in the range of 10-12 M of chloride [11-13].

Table 6-2: Atmospheric corrosion test conditions

Deformation used	Material	Condition	Surface condition	ε_{true} [%]	Electrolyte used	Surface Cl^- coverage [µg/cm²]	RH [%]	T [°C]	Time [d]
Rolling	Plate	As-received (AR)	4000-grit	-	$MgCl_2$	286	30	50	200
		AR + 10% cold-rolled		-9.5	$MgCl_2$	286	27	80	14
		AR + 20% cold-rolled		-18.2	$MgCl_2$	286	27	80	7
		AR + 40% cold-rolled		-33.6	$MgCl_2$	1450	27	80	9
Rolling + Tensile		AR + 20% cold-rolled		-18.2 and +6.3	$MgCl_2$	25	30	50	362
						286	30	50	362
Bending	Sheet	AR + bent into U-shape	0.25 µm + OP-S finish	8.7	$MgCl_2$	286	30	50	455
						571	30	50	455
Tensile		As-received	electro-polished	2	$MgCl_2$	145	30	50	220
					$FeCl_3$+ $MgCl_2$	290	30	50	220
				0.2	$MgCl_2$	1450	30	50	368

After exposure, the specimens were rinsed with deionised water and the corrosion products were removed by immersion in hot 10 wt.-% citric acid solution. The corrosion morphology was analysed with an FEI Quanta 650 SEM. Ferrite and austenite was distinguished by their channelling contrast difference and morphological appearance giving ferrite a darker appearance.

6.3.3.3 XRD Stress Measurements

X-ray diffraction (XRD) stress measurements were performed on OP-S finished and electro-polished specimens in order to exclude surface deformation effects associated with mechanical grinding and polishing. XRD measurements were carried out on a Proto iXRD Combo testing machine (Proto Manufacturing Inc., Michigan, USA), equipped with a two detector system. Cr and Mn x-ray sources were used to measure the strain in ferrite and austenite, respectively. Further measurement setup parameters are listed in Table 6-3. The stress measurement setup is shown schematically in Figure 6-7. Prior to the test, the x-ray diffractometer was calibrated to determine the zero stress position of the peak of the diffracted x-rays using a stress-free standard sample, provided by the manufacturer. This was repeated for a stressed specimen using a stressed standard sample to determine the stress peak position. Multiple exposure technique with 11 angles was used for inter-planar d-spacing measurements. Two x-ray measurement orientations, i.e. 0° and 90° Phi angles, in RD and orthogonal to RD process orientations of each specimen were chosen, which were in alignment with the microstructure orientation. Each measured orientation corresponds to the stress direction as specified in the inserts in Figure 6-6(c). The measurement position was in the centre of each specimen. Pre- and post-bent specimens were measured exactly on the same position.

Table 6-3: X-ray diffraction measurement conditions

X-ray type	**Cr-Kα**	**Mn-Kα**
Source voltage, current	20 kV, 4 mA	20 kV, 4 mA
Aperture size	2 mm	2 mm
Bragg angle, 2θ	156.4	152.8
Diffraction plane	(2 1 1)	(3 1 1)
Wavelength	2.291 Å	2.1034 Å
Max. measurement angle, β	27°	27°
Number of β angles	11	11
β angles	27	27
β oscillation angle	3°	3°
Phi angles	0 and 90°	0 and 90°
Exposure time	2 sec	2 sec
Number of exposure profiles	10	10
Number of exposures gain	30	30
X-ray elastic constant $S_1^{(hkl)}$	1.28 x 10^{-6} MPa	1.2 x 10^{-6} MPa
X-ray elastic constant $½S_2^{(hkl)}$	5.92 x 10^{-6} MPa	7.18 x 10^{-6} MPa
Peak fit	Gaussian	Gaussian

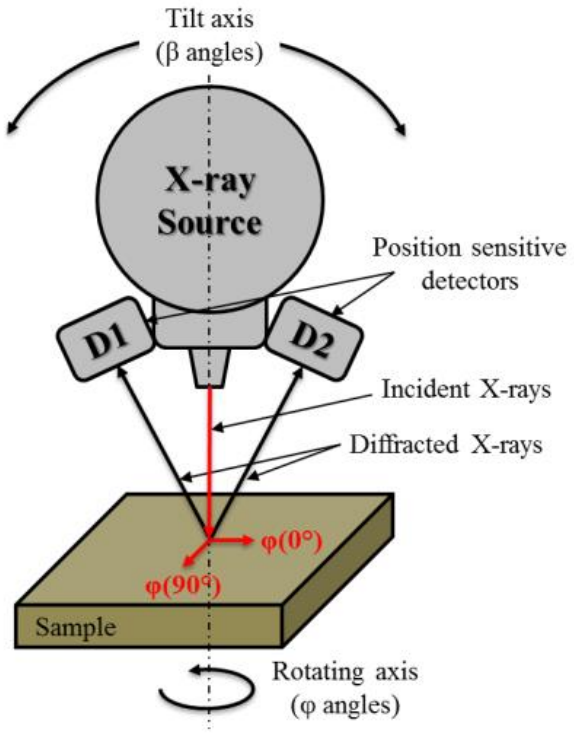

Figure 6-7: XRD stress measurement setup (schematic illustration)

6.3.4 Results and Discussion

6.3.4.1 Microstructure Characterisation

6.3.4.1.1 Microstructure Development after Cold Rolling

The microstructure in rolling direction (RD) of 2205 duplex stainless steel in its as-received condition consisted of 43% ferrite (δ) and 57% austenite (γ), with ferrite/ferrite-, austenite/austenite-, and austenite/ferrite-grain boundaries, as can be seen in the EBSD phase map in Figure 6-8(a). The austenite had discrete and discontinuous shape with isle-like morphology and was embedded in the ferrite matrix forming a continuous network across the entire microstructure. The average grain size was 6.9 ± 8.3 µm for ferrite and 5.7 ± 6.1 µm for austenite with an aspect ratio of 0.39 and 0.65, respectively indicating elongated grains towards the RD, with ferrite to a higher extent than austenite. Large fraction of coincidence sites lattice (CSL) Σ3 (twins) boundaries were detected in austenite with 44.18% beside all other CSL boundaries indicating low energy, and hence, smooth austenite grain structure. The low angle grain boundary (LAGB) fraction of austenite was 0.6% only clearly indicating highly smooth structure in contrast to that of ferrite, which

showed a large fraction of 21.3% indicating strain accumulation in the ferrite structure. Further results are listed in Table 6-4.

Narrow regions of intense strain denoted as ‘strain localisation’ were observed primarily located in ferrite grains and on interphase boundaries as shown in the local misorientation (LMO) map in Figure 6-8 (f). No apparent strain localisation was observed in sub-grain boundaries within austenite grains clearly showing a more smooth structure in austenite than in ferrite. Ferrite and austenite have different thermal expansion coefficients therefore thermal-induced strain is often present in the microstructure during rapid cooling processes leading to non-uniform strain and stress distribution across the microstructure. Peak LMO values for ferrite and austenite were determined to be at 0.05° with a frequency value of 9.03 for ferrite and 8.94 for austenite portending little strain in the overall microstructure. The aspect ratio of ferrite and austenite were 0.39 and 0.65, respectively indicating largely elongated grains in RD with ferrite substantially larger than austenite.

The microstructure development after 20% cold rolling is shown in the EBSD phase map in Figure 6-8(b). An increase of the number and intensity of heterogeneous plastic strain spots were seen. Apparently, new LAGB’s and HAGB’s were formed heterogeneously in ferrite and austenite regions. Clusters of LAGB’s generated high LMO concentrations in narrow zones as shown in the corresponding LMO map shown in Figure 6-8(g). The degree of peak LMO increased from 0.05° to 0.35° for both phases. Ferrite had more heterogeneous strain spots than austenite for LMO values up to 3.65° but austenite showed more discrete strain sites in some higher LMO degrees (>3.65°) indicating larger strain development in austenite than ferrite. Strain localisation is the precursor of local material failure due to plastic instability, which can also become prime susceptible locations to corrosion and stress corrosion cracking [14].

The average grain sizes of ferrite and austenite decreased from 7.9 to 6.6 µm and 5.7 to 4.6 µm, respectively, well-possibly due to the compressive nature of rolling deformation and grain boundary multiplication associated. The maximum grain size of ferrite and austenite also decreased after 20% cold rolling from 30.3 and 40 µm to 25.4 and 17.1 µm, respectively. The grains were squeezed against each other perpendicular to the RD so that the austenite spacing and ferrite spacing significantly shrunk.

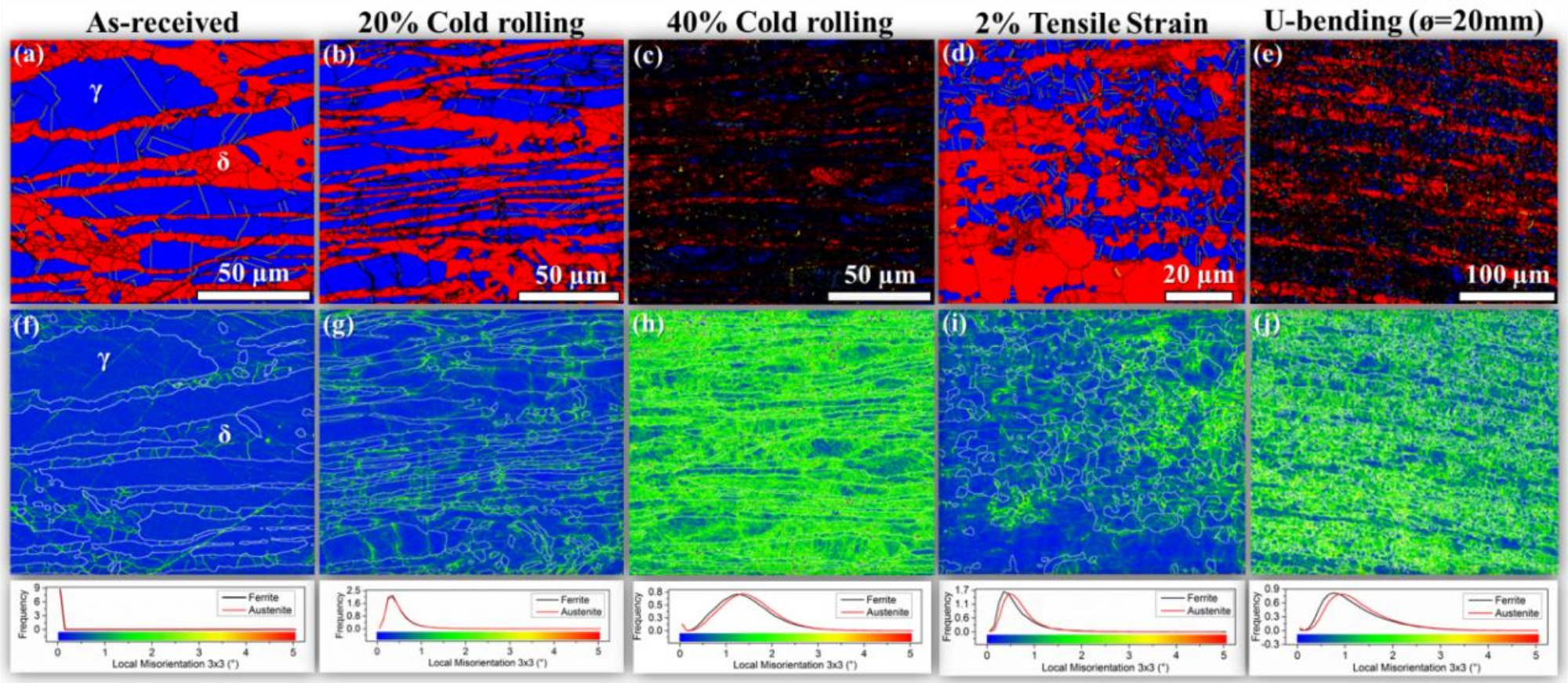

Figure 6-8: EBSD mapping results showing the effect of deformation on microstructure development and strain partitioning: (a-e) showing phase maps of deformed microstructure with ferrite (red) and austenite (blue) and with HAGB's and LAGB's (black lines) and CSL Σ3 boundaries (yellow lines), (f-j) showing the corresponding local misorientation map of the deformed microstructure with phase boundaries (in white)

Regions with narrow austenite and ferrite spacing showed more intense strain localisation than regions with larger ferrite and austenite grains as can be seen in Figure 6-8(g). Such sites would be expected to suffer preferentially from localised corrosion and/or selective dissolution depending on the aggressivity of the corrosive.

The number of CSL Σ3 of austenite significantly decreased after 20% cold rolling clearly indicating energy uptake of low energy boundaries. The fraction of LAGB to HAGB was doubled in ferrite while in austenite this became 7-times larger, showing that austenite was significantly more deformed than ferrite. However, the austenite structure can perform more stress relaxation during plastic deformation wherefore heterogeneous strain 'hot-spots' were primarily seen in austenite. The ratio of all LAGB's to all HAGB's increased substantially from 2.0 to 8.7 evidencing rolling-induced sub-grain boundary multiplication.

Further increase of the amount and intensity of heterogeneous strain hot-spots were observed occurring after 40% cold rolling associated with the development of a severe deformation network in the microstructure which can be seen Figure 6-8(c) with the corresponding LMO map given in Figure 6-8(h). Strain localisation intensified on austenite grains indicating most plastic deformation accommodated by the austenite. The number of CSL Σ3 boundaries in austenite further decreased to 1.13% by a factor of 10 with respect to the 20% cold-rolled microstructure. The CSL Σ3 boundaries were highly interrupted indicating large deformation-induced grain boundary energy uptake. Seemingly, there is a non-linear relationship between the change of CSL Σ3 boundary fraction and the amount of cold rolling. It decreased by a factor of 4 after 20% cold rolling and decreased further by a factor of 10 after 40% cold rolling. It seemed that the relaxation capability was highly diminished after 40% cold rolling.

The ratio of the fraction of LAGB's to the fraction of HAGB's ($\frac{f_{LAGB}}{f_{HAGB}}$) significantly increased to 34.9 in austenite and 43.6 in ferrite, indicating a linear relationship between $\frac{f_{LAGB}}{f_{HAGB}}$ of both phases and the amount of cold rolling, with austenite showing ~3.8x steeper gradient than ferrite. The $\frac{f_{LAGB}}{f_{HAGB}}$ of ferrite was doubled after 20% cold rolling and further doubled after 40% cold rolling, while $\frac{f_{LAGB}}{f_{HAGB}}$ of austenite increased by a factor of 7.3 and 7.9 after 20% and 40% cold rolling, respectively. This indicated that the formation of

LAGB's in austenite increased by a factor of 7.5x and in ferrite by a factor of 2x. Thus, LAGB formation in austenite was ~3.8x faster than in ferrite.

The ratio of all LAGB's to HAGB's ($\frac{f_{LAGB(\delta)}+f_{LAGB(\gamma)}}{f_{HAGB(\delta)}+f_{LAGB(\gamma)}}$) also increased substantially to 50.1 after 40% cold rolling yielding 20-25% larger change than after 20% cold rolling. Also shown here, there relationship between total number of newly generated LAGB's and amount of cold work was non-linear. The grain size of both microstructure constituents further decreased after 40% cold rolling. Ferrite decreased to 4.9 µm and austenite to 4.1 µm. This shrinkage was also manifested by the maximum grain size which decreased to 12.8 µm and 12.9 µm for ferrite and austenite, respectively.

Table 6-4: EBSD quantitative grain geometry and boundary analysis results

Deformation used	State	ε_{eng} [%]	ε_{true} [%]	Phase	Phase fraction [%]	Grain size [µm]	Std. dev. [µm]	Max. grain size [µm]	Aspect ratio (X_V/X_H)	CSL Σ3 [%]	$\frac{f_{LAGB}}{f_{HAGB}}$	$\frac{f_{LAGB(\delta)}+f_{LAGB(\gamma)}}{f_{HAGB(\delta)}+f_{LAGB(\gamma)}}$
Rolling in RD	before	0	0	**δ**	43	7.9	8.3	30.3	0.39	0.04	21.3	2.0
				γ	57	5.7	6.1	40.0	0.65	44.18	0.6	
				Total	100	6.3	6.9	32.0	0.55	44.22	-	
	20%	-20	-18.2	**δ**	47	6.6	7.7	25.4	0.36	0.00	43.6	8.7
				γ	53	4.6	4.6	17.1	0.52	11.50	4.4	
				Total	100	5.3	6.0	25.4	0.45	11.50	-	
	40%	-40	-33.6	**δ**	45	4.9	6.6	12.8	0.45	0.01	87.2	50.1
				γ	55	4.1	4.5	12.9	0.55	1.13	34.9	
				Total	100	4.4	5.4	12.9	0.52	1.14	-	
Bending in RD	before	0	0	**δ**	46	4.2	5.1	24.3	0.84	0.22	12.8	2.2
				γ	54	2.2	1.9	16.5	0.93	23.10	1.7	
				Total	100	2.7	3.4	24.3	0.91	23.32	-	
	after	9.1	8.7	**δ**	47	5.1	5.3	25.2	0.80	0.17	3.8	6.5
				γ	53	2.5	2.0	19.6	0.92	9.67	16.0	
				Total	100	3.4	3.7	25.2	0.89	9.84	-	
Tensile straining in RD	In-Strain	2	2.0	**δ**	47	4.2	4.7	27.4	0.82	0.20	10.0	3.4
				γ	53	1.9	1.4	8.3	0.97	22.70	1.8	
				Total	100	2.7	3.2	27.4	0.91	22.90	-	

ε_{eng}: engineering strain, ε_{true}: true strain, f: fraction, LAGB: low angle grain boundaries, HAGB: high angle grain boundaries

6.3.4.1.2 Microstructure Development after Tensile Deformation

The microstructure of the as-received sheet material consisted of substantially smaller grains size than that of the plate material. The grain size of ferrite and austenite was 4.2 µm and 2.2 µm, respectively. The maximum grain size measured in ferrite and austenite was 24.3 µm and 16.5 µm, respectively clearly indicating finer grain structure of the sheet material. Moreover, the high aspect ratios of ferrite (0.84) and austenite (0.93) were still a sign of elongated grain structures in RD which is significantly different to the plate material. Seemingly, varying mechanical and electrochemical properties with material processing orientation can be expected. Austenite had almost half amount of CSL Σ3 boundaries (23.1%) in comparison to that in the plate microstructure, and ferrite seemed to show 5-times more twin boundaries in the sheet material. The $\frac{f_{LAGB}}{f_{HAGB}}$ of ferrite and austenite was 12.8 and 1.7, respectively portending less deformation history of ferrite and less relaxation occurred in austenite in comparison to their counterparts in the plate material. Further EBSD grain geometry and grain boundary measurement results are shown in Table 6-4. Despite the difference in grain geometry and morphology, the as-received sheet duplex steel showed a highly smooth microstructure apparent by the LMO analysis which was very similar to that of the as-received plate material.

After 2% elastic-plastic strain, no significant changes regarding to the grain geometry and morphology as well as to the grain boundaries were observed. However, the $\frac{f_{LAGB(\delta)}+f_{LAGB(\gamma)}}{f_{HAGB(\delta)}+f_{LAGB(\gamma)}}$ increased slightly from 2.2 to 3.4 indicating the formation of new LAGB's in the microstructure. The aspect ratio of ferrite and austenite slightly increased due to elastic-plastic stretching along the tensile axis. In certain regions in the microstructure higher concentrated sub-grain boundaries were seen situating in some ferrite and austenite grains as shown in Figure 6-8(d). The corresponding LMO map is given in Figure 6-8(i) showing heterogeneous LMO developments evolving in the same regions with high concentrations of LAGB's suggesting that such sites may become enhanced susceptible to localised corrosion and/or stress corrosion cracking. Plastic deformation of 2% caused a substantial shift of the peak LMO values from 0.05° to 0.35° for ferrite and 0.45° for austenite. Seemingly, strain localisation development was more pronounced in the austenite than in ferrite suggesting that microstructure changes in the austenite is more affected by tensile straining than rolling and bending deformation.

Tensile strain seemed to create large microscopic strain localisation primarily affecting the austenite phase possibly due to its easier yielding and plastic deformation capability than ferrite.

6.3.4.1.3 Microstructure Development after U-bending

The microstructure of the sheet material after bending into a U-shape is shown in Figure 6-8(e). Severe deformation occurred noticeable from the large fraction of LAGB's. The grain size of ferrite and austenite increased by 0.9 µm and 0.3 µm, respectively indicating preferential grain elongation along the bending axis, which is parallel to the RD of the microstructure. The decreased aspect ratio (vertical/horizontal) also confirmed the formation of elongated grains, primarily of the ferrite phase. Seemingly, despite the larger deformation occurred in austenite, the grain geometry and morphology of ferrite changed to a larger extent than that of austenite possibly due to its lower elastic and plastic compliance.

The fraction of CSL Σ3 boundaries also decreased after U-bending with ferrite showing a decrease from 0.22 to 0.17% and the austenite from 23.1 to 9.67% indicating a deformation-induced energy uptake in both phases by bending deformation. The grain structure of ferrite and austenite showed a highly disrupting appearance. Large grain boundary multiplication occurred during deformation particularly in austenite grains.

Unlike in the cold-rolled microstructures, $\frac{f_{LAGB}}{f_{HAGB}}$ of ferrite decreased remarkably from 12.8 to 3.8, while $\frac{f_{LAGB}}{f_{HAGB}}$ of austenite largely increased from 1.7 to 16 after the bending process. The decrease in ferrite was a sign of a remarkably increasing fraction of HAGB's, while the increase in austenite was evidence of an increasing fraction of LAGB's, both prefiguring lesser heterogeneous strain fields in ferrite but more strain localisation occurring in austenite. The latter could be noticed by large heterogeneous LMO developments as shown in the LMO map given in Figure 6-8(j). Large strain evolution in the microstructure was apparent by the presence of large fraction of high LMO values in both phases. The peak LMO value of ferrite was at 0.75° and that of austenite lied at 1.05° indicating larger strain development in austenite than ferrite. Bending along RD seemed to show unbalanced strain partitioning between austenite and ferrite which became more apparent after cold rolling.

In summary, it can be concluded that bending deformation had the largest effect on microstructure development and strain evolution associated with cold deformation, followed by tensile plastic deformation. Microstructure modification was significantly more pronounced after bending deformation than 20% rolling, despite the almost twice amount of plastic deformation. Consequently, rolling deformation can be regarded as less critical in contrast to other deformation modes, this well-probably due to its compressive nature. Bending is fully tensile in nature, and torsion moments may also be involved leading to high strain and altered microstructure than other deformation modes with similar equivalent amount of plastic deformation.

6.3.4.2 Stress Evolution with Cold Deformation

XRD stress measurement results of all cold-deformed materials were plotted in a column graph as given in Figure 6-9(a+b). Ferrite and austenite in the plate material were compressive in their as-received conditions. This is evident of ferrite in 0° measuring direction which is parallel with the cylinder roller axis where compressive forces were acting on.

The stress in austenite became highly tensile after 20% cold rolling despite the compressive strain (ε_{true} = -18.2%) with 394 ± 20 MPa in 0° (in RD) and 248 ± 10 MPa in 90° (perpendicular to RD), whilst stress in ferrite became also slightly tensile in 0°, but was still compressive in 90°. Stress distribution in duplex stainless steel is always heterogeneous due to its two-phase microstructure, the different crystal structure of ferrite and austenite, and varying grain geometry and morphology [5, 6]. The amount of compressive stress decreased after 20% cold rolling despite the compressive strain acting perpendicular to the RD. The stress distribution in normal direction (ND) and transverse direction (TD) also changed after cold rolling; a more comprehensive perspective on the effect of rolling deformation will be published elsewhere. The tensile strain acting in RD, however, could compensate and even overwhelm the compressive strain in the microstructure.

Significantly higher tensile stress evolution was observed happening in the austenite phase after 40% cold rolling. Increased tensile stresses in 0° with 693 ± 38 MPa and in 90° with 371 ± 18 MPa were measured. Seemingly, rolling deformation is associated with severe tensile stress evolution in the austenite, especially in the RD plane in 2205 duplex stainless

steel. Ferrite, however, became compressive in 0° and did not seem to remarkably change in 90° after 40% cold rolling. The stress development of ferrite was erratic while in austenite a clear correlation of stress evolution with rolling deformation could be noticed, namely tensile stress evolution was seen increasing with the level of cold rolling. This is due to the different stress evolution response depending on the microstructure processing orientation, i.e. the stress acting on the ND and TD planes were significantly different to the stress determined in the RD plane. Therefore, stress measurement in one plane of a microstructure processing direction only may not reflect the entire stress distribution in the whole duplex microstructure due to its anisotropic nature.

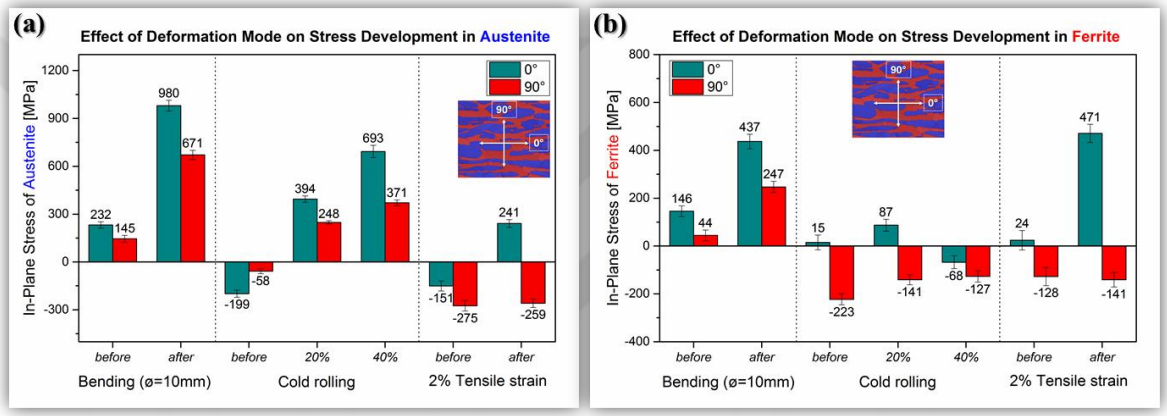

Figure 6-9: X-ray diffraction stress measurement results showing the effect of deformation on the stress evolution of (a) austenite and (b) ferrite

After bending deformation into U-shape both ferrite and austenite were highly strained along RD, hence, the evolution of high tensile stresses in both 0° and 90° measurement directions occurred. Austenite showed high tensile stress values with 980 ± 33 MPa in 0° and 671 ± 28 MPa in 90°, and ferrite showed lower tensile stresses with 437 ± 31 MPa in 0° and 247 ± 24 MPa in 90°. Austenite had effectively twice more tensile stress in 0° and 2.7-times larger stress in 90° than ferrite. This is in agreement with EBSD local misorientation results showing large strain localisation in austenite and, with a lesser extent, in ferrite. Apparently, a correlation of strain localisation, as earlier shown in Figure 6-8(e+j), with stress development exists. Thus, it can be argued that the stress evolution after bending deformation is more pronounced than after rolling plasticity.

Bending deformation is highly polylithic creating a diversified and complex poly-axial stress distribution across the entire microstructure causing a larger deformation effect than

rolling. It is quite evident that rolling and bending have substantially different influences on microstructure development and strain and stress evolution after cold deformation. Bending deformation, however, had clearly the most severe effect on strain and stress development.

Tensile straining of 2% elastic-plastic deformation only revealed already high stress evolution in the microstructure, with ferrite showing high values than austenite along the RD (0°). No apparent stress change was measured in 90° indicating predominating monolithic stress nature acting in the microstructure. The stress in 90° remained compressive in both ferrite and austenite phases. The stress in ferrite was twice larger than the stress in austenite, which is the opposite in contrast to the stress evolution after bending and rolling deformation. This contradiction remained unclear. Seemingly, tensile deformation leads to different stress development of austenite and ferrite, with the latter showing high tensile stresses. Larger tensile stresses can, apparently, be developed in the ferrite than in austenite in purely-tensile deformation. Such information certainly has practical relevance and can be of utmost importance to understand and predict corrosion and environment-assisted cracking.

6.3.4.3 Atmospheric Corrosion Morphology

The corrosion morphology of as-received microstructure after 200 days exposure to 286 µg/cm² chloride at 30% RH and 50°C is shown in Figure 6-10(a). Selective dissolution of the ferrite phase was the prime corrosion mechanism, which is usual for duplex stainless steels occurring in chloride-bearing corrosive environments [15-21]. Despite the lower Cr and Mo but higher Ni and N content of austenite, the corrosion potential of ferrite is lower than that of austenite in chloride-containing medium [22-26].

6.3.4.3.1 Effect of Rolling Deformation

The introduction of 10% cold rolling caused a change in the prime corrosion mechanism from net selective dissolution of ferrite to a more-likely net pitting corrosion in ferrite and austenite as shown in Figure 6-10(b-d). The effect of cold rolling on the corrosion susceptibility of 2205 duplex stainless steel has been earlier discussed [15]. In short, rolling deformation renders enhanced corrosion propensity due to local strain development in the microstructure affecting the corrosion mechanisms. The selective corrosion of ferrite

becomes compromised with localised corrosion susceptibility of the austenite with increasing amount of cold rolling due to the development of highly-active local deformation sites (hot-spots), which is also reflected in Volta potential differences measured between a Pt-probe and the surface [15, 17]. These Volta potential "hot-spots", obtained by Scanning Kelvin Probe Force Microscopy, seemed to be primarily associated with regions containing higher plastic strain [15, 17].

Pit growth seemed to propagate by selective dissolution of ferrite regions within the pit with significantly lower dissolution rates occurring on austenite, as shown in Figure 6-10(c). Nevertheless, net selective dissolution of ferrite in certain regions seemed to be the prevailing corrosion mechanism together with pronounced pitting corrosion in austenite, as shown in Figure 6-10(d). It can be assumed that those regions, which suffered from pitting corrosion, contained heterogeneous strain hot-spots, as earlier discussed, and became preferentially anodic by time. Seemingly, strain localisation can change local corrosion potential and, hence, enhance galvanic interacting forces between ferrite and austenite and create large corrosion potential differences within the same phase causing preferential attack on susceptible sites. In earlier work, the effect of 40% rolling deformation on the Volta potential difference of the microstructure was discussed in more detail [15]. Local Volta potential hot-spots at confined regions were evolved primarily in the austenite phase associated with strain localisation facilitating localised pitting corrosion on these sites [15]. It remained unclear if the material suffered from stress corrosion cracking since crack-like features on adjacent sites of a corrosion pit were seen, which can be seen in Figure 6-10(b). This feature seemed to be in parallel alignment with the RD where the tensile stress acted on. Further studies are required to elucidate this observation.

Rolling deformation deteriorated the overall corrosion performance with increasing amount of cold work, becoming apparent upon corrosion exposure of 20% cold-rolled microstructure to 286 µg/cm² at 30% RH and 80°C after 1 week. Usually, the onset of first corrosion events in 2205 duplex stainless steel takes more than 10 days under these exposure conditions, and it was as sign of overall loss of corrosion resistance to see localised corrosion within one week of exposure. Selective dissolution of ferrite on confined regions resembling a pit-like attack was also observed being the prevailing corrosion mechanism of 20% cold-rolled microstructure, as shown in Figure 6-10(e).

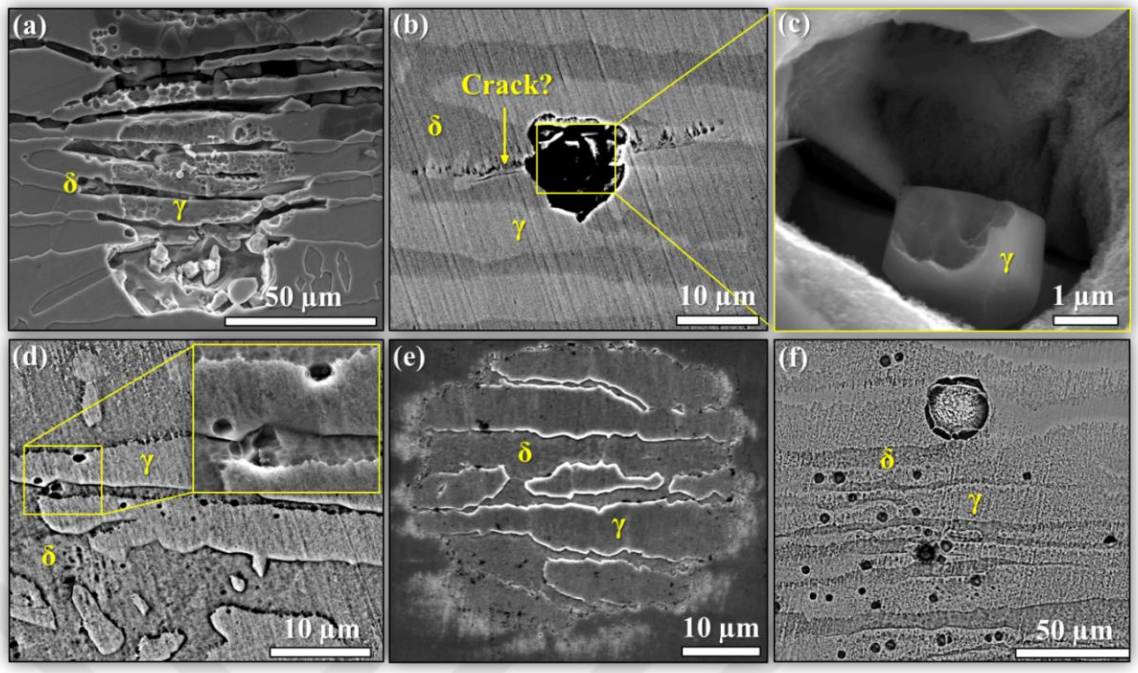

Figure 6-10: SEM images of the plate microstructure showing the effect of rolling deformation with effective compressive strain on corrosion morphologies after exposure to thin-film chloride-bearing electrolytes: (a) showing net selective dissolution of ferrite on as-received microstructure after 200 days exposure to 286 µg/cm² chloride at 30% RH and 50°C, (b-d) showing preferential pitting corrosion in ferrite and, to a larger extent, in austenite and also net selective dissolution of ferrite in 10% cold-rolled microstructure (ε_{true} = -9.5%) after 2 weeks exposure to 286 µg/cm² chloride at 27% RH and 80°C, (e) showing selective dissolution of ferrite in 20% cold-rolled (ε_{true} = -18.2%) microstructure after 1 week exposure to 286 µg/cm² chloride at 27% RH and 80°C, and (f) showing preferential pitting corrosion on austenite in 40% cold-rolled microstructure (ε_{true} = -33.6%) after 9 days exposure to 1450 µg/cm² chloride at 27% RH and 80°C

Pitting corrosion was also observed similar to that seen in the 10% cold-rolled specimen. Seemingly, selective dissolution of ferrite is the prime corrosion mechanism in the first instance at the beginning of corrosion which gets overwhelmed by pitting corrosion on discrete regions, primarily situating in austenite sites after longer exposure time. This became more pronouncedly apparent on the microstructure which was undergone to 40% rolling deformation. Substantial amount of pitting corrosion sites, almost entirely locating in the austenite phase, was observed after 9 days exposure to 1450 µg/cm² chloride at 27% RH and 80°C. Such sites were earlier characterised to be associated with LMO hot-spots and discrete cathodic local Volta potential hot-spots triggering preferential corrosion initiation [15].

6.3.4.3.2 Effect of Bending Deformation

Bending deformation with 8.7% true strain (ε_{true}) of the as-received non-polished sample caused pitting corrosion after 455 days exposure to 286 µg/cm² chloride at 30% RH and 50°C, as shown in Figure 6-11(a). The oxide scale on the surface was dissolved primarily for the first instance during the corrosion process, and then pitting corrosion was initiated. Superficial fine-scale micro-cracks were observed to have formed on the oxide scales, as shown in Figure 6-11(a). Environment-assisted cracking was apparently promoted to nucleate on the oxide scale. The pit was obviously the net anode; therefore, regions adjacent to the pit must have been cathodic suspecting cathodic hydrogen evolution which may have led to hydrogen-assisted cracking or hydrogen embrittlement of the oxide scale. The non-polished specimen seemed to have shown higher atmospheric corrosion and environment-assisted cracking propensity in comparison to the polished sample.

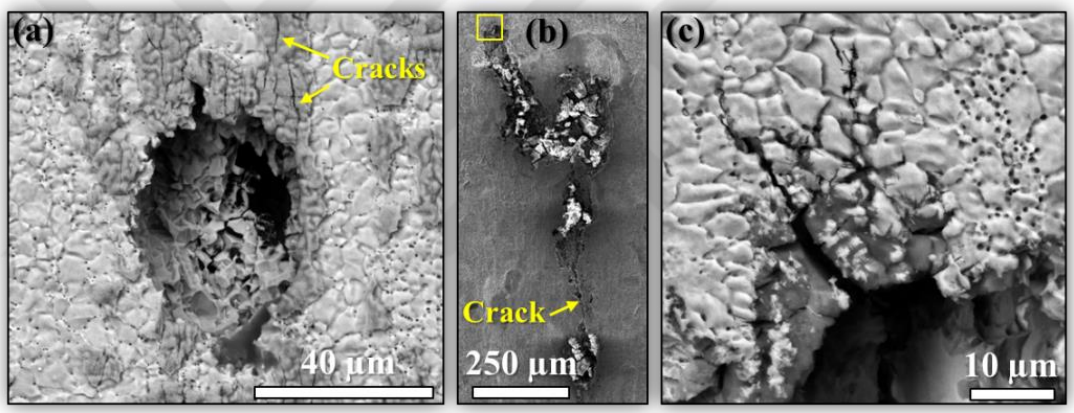

Figure 6-11: SEM images of the as-received sheet material showing the effect of bending deformation with 9.1% effective engineering strain (ε_{true} = 8.7%) on corrosion morphologies after exposure to thin-film chloride-bearing electrolytes: (a) showing severe pitting corrosion with numerous superficial micro-cracks formed on as-received non-mechanically surface ground and polished possibly limited on the oxide scale only after 455 days exposure to 286 µg/cm² chloride at 30% RH and 50°C, (b+c) showing severe stress corrosion crack formation in the same material as (a) after 455 days exposure to 571 µg/cm² chloride at 30% RH and 50°C, with (c) being a magnified view of the highlighted region in (b) showing multiple pitting corrosion and stress corrosion initiation sites. Note that the stress axis is perpendicular to the images.

Exposure with 571 µg/cm² chloride led to severe environment-assisted cracking occurrence and larger corrosion area than the previous deposit as shown in Figure 6-11(b). The crack length was measured to be more than 1 mm showing in parallel alignment towards the stress axis which is perpendicular to the image. Short-branched cracks were observed in the highlighted region in Figure 6-11(b) as shown in a magnified view in Figure 6-11(c) probably located in austenite regions. In addition, in certain regions numerous small-scale

corrosion pits were observed as can be seen in Figure 6-11(c) probably indicating enhanced susceptibility to localised corrosion of the oxide scale. The grain boundaries could be easily noticed and these pits seemed to preferentially nucleate on grain boundaries. One reason could be that during rapid anodic dissolution of the oxide scale, some grain boundaries could have been dissolved without affecting the grain interiors.

6.3.4.3.3 Effect of Tensile Deformation

The effect of elastic-plastic tensile strain was studied on the as-received sheet sample with 2% effective true strain. No significant corrosion events were observed after 220 days exposure with 145 µg/cm² chloride at 30% RH and 50°C, except from a few micrometre-scale corrosion pits, as shown in Figure 6-12(a). Exposure with 290 µg/cm² chloride ($FeCl_3$+$MgCl_2$) contaminated with Fe^{3+} cations to 30% RH and 50°C caused, however, severe overall corrosion with two deep corrosion grooves given in Figure 6-12(b). There was no selective dissolution of any phase, nor could the corrosion morphology be linked to certain microstructure sites which indicate that the oxidation power of the thin-film electrolyte was quite high. Ferric ions must have shifted the oxidation potential of the electrolyte to higher values so that the corrosion potential of the metal decreased to a larger extent and probably decreased the transpassive corrosion potential to a point where the metal could actively dissolve.

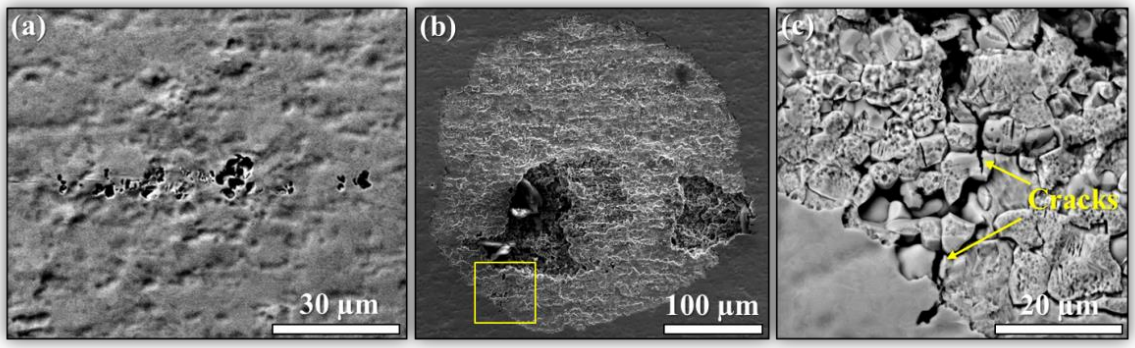

Figure 6-12: SEM images of the as-received sheet materials showing the effect of purely tensile deformation with 2% effective elastic-plastic strain (ε_{true} = 2.0%) on corrosion morphologies after exposure to thin-film chloride-bearing electrolytes: (a) a few micron-scale localised corrosion events occurring after 220 days exposure to 145 µg/cm² chloride at 30% RH and 50°C, (b+c) localised corrosion and general-type dissolution attack after 220 days exposure to 290 µg/cm² chloride ($FeCl_3$+$MgCl_2$) at 30% RH and 50°C, with (c) multiple micro-crack sites possibly in austenite grains. Stress axis is oriented perpendicular to the images.

The central part of the corroded area was net anodic with respect to the peripheries; therefore, nucleation of environment-assisted cracking was not possible in net anodic sites. In contrast, at peripheral areas, as indicated by the highlighted region in Figure 6-12(b), stress corrosion cracking with several crack incubates well-potentially located in the austenite phase was observed, as can be seen in Figure 6-12(c). Ferric ions are strong oxidisers and may have, therefore, altered entirely the corrosion morphology. Severe corrosion attack occurred under even low surface chloride deposits and low temperature which may not been observed in the absence of ferric ions.

Multiple closely-spaced micrometre-scale corrosion pits were observed occurring in a highly-dense cluster-like array forming all together a larger shallow corrosion pit, as shown in Figure 6-13(a). In other regions, selective dissolution of ferrite occurred, while numerous corrosion pits with some chloride and/or hydrogen-assisted stress corrosion cracks were observed in austenite, as shown in Figure 6-13(b+c). Obviously, 0.2% elastic strain was enough to invoke stress corrosion cracking. Elastic strain seemed to affect the corrosion performance of austenite more than that of ferrite since net selective dissolution of ferrite and partial dissolution and preferential pitting corrosion of austenite were observed occurring simultaneously.

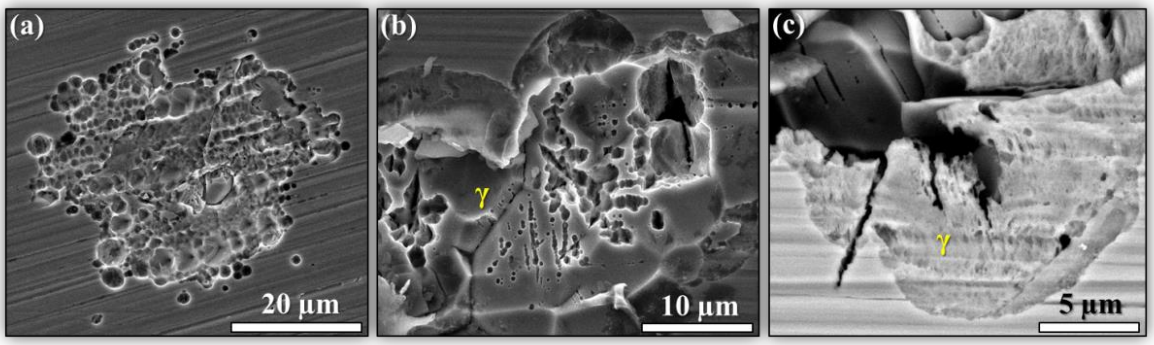

Figure 6-13: SEM images of the as-received sheet material showing the effect of effective elastic tensile strain (0.2%) on corrosion morphologies after exposure to thin-film chloride-bearing electrolytes: (a) showing multiple close-spaced pitting corrosion events occurring with (b-c) showing selective dissolution of ferrite with preferential pitting corrosion occurring on slip planes of austenite with some small-scale micro-cracks formed in austenite under electrolyte deposits containing 1450 µg/cm² chloride exposed to 30% RH environment at 50°C for 368 days. Stress axis is oriented to the horizontal of the images.

6.3.4.3.4 Effect of Rolling and Tensile Deformation

More pronounced corrosion and stress corrosion cracking events were observed occurring on the 20% cold-rolled microstructure, loaded with 6.3% elastic-plastic tensile strain, after 362 days of exposure to 30% RH environment at 50°C, with salt droplets containing a chloride deposition density of 286 µg/cm². Net selective dissolution of ferritic sites, with partially dissolved austenite regions, was seen forming the prime corrosion mechanism together with localised pitting corrosion events happening mainly on slip planes on the austenite, which can be seen in Figure 6-14(a+b). Furthermore, chloride stress corrosion micro-cracks with typical branching character were observed occurring in the austenite as shown in Figure 6-14(a-c). Numerous closely-spaced corrosion pits with sub-micron sizes were seen to have developed separately side-by-side in austenite grains acting as crack incubates, as shown in Figure 6-14(b). Some crack incubates could grow to form micro-cracks. Obviously, under these low-deposition and low-temperature conditions chloride stress corrosion cracking was possible.

Significantly lesser corrosion attack was observed occurring underneath the water droplet with 25 µg/cm² chloride exposed to 30% RH at 50°C for 362 days. No clear selective dissolution was observed occurring in either phase. Both phases corroded simultaneously with, however, somewhat larger corrosion rate on the ferrite than the austenite, which can be seen in Figure 6-14(d). A large number of deformation structures were seen emerging from both ferrite and austenite regions indicating severe plastic deformation. The prime electrolytic dissolution mechanism of austenite seemed to be localised pitting corrosion, as shown in the image insert, which is a magnified view of the highlighted region in Figure 6-14(d). Pronounced attack occurred on the interphase boundaries in contrast to other regions. Multiple closely-spaced localised corrosion pits were observed in austenite grains, which mostly could induce short micro-cracks, as can be seen in Figure 6-14(e). The mechanism of these cracks remained unclear. The crack morphology portends at chloride-induced stress corrosion cracking but, usually, this does not occur in such a dense array. Therefore, more likely hydrogen-assisted stress corrosion cracking or both acted together was the reason for the crack occurrence.

In some regions, selective-like corrosion attack with an odd morphology was observed on austenite, which can be seen in Figure 6-14(f), possibly along highly strained regions. It is unclear why adjacent, highly deformed ferrite regions remained unaffected. In general, the

austenite phase was much more prone to environment-assisted cracking than ferrite, and the cracks in austenite mostly initiated and propagated individually on slip planes from localised corrosion pits, which can be seen in the SEM images in Figure 6-14(g+h). When cracks encountered certain sub-grain boundaries their crack pathway could be re-directed along the sub-grain boundary interface.

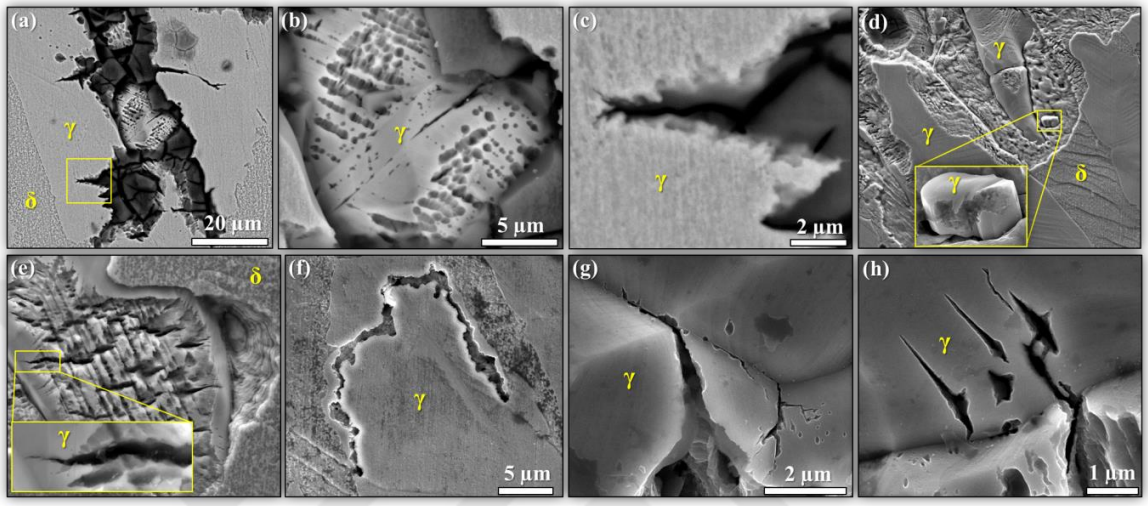

Figure 6-14: SEM images of the as-received sheet material showing the effect of 20% rolling deformation together with 6.3% effective elastic-plastic tensile strain (ε_{true}) on corrosion morphologies after exposure to thin-film chloride-bearing electrolytes: (a-c) showing selective dissolution of ferrite with preferential stress corrosion cracking and pitting corrosion occurring in austenite after 362 days exposure to 286 µg/cm² chloride at 30% RH and 50°C, (d) showing simultaneous dissolution of ferrite and austenite with (e) showing preferential pitting corrosion and EAC in austenite and with (f) showing selective localised attack occurring in austenite after 362 days exposure to 25 µg/cm² chloride at 30% RH and 50°C, (g+h) showing stress corrosion crack incubates forming on slip planes and sub-grain boundaries in austenite after 362 days exposure to 286 µg/cm² chloride at 30% RH and 50°C. Stress axis is oriented to the horizontal to the images.

6.3.5 Conclusions

The effect of rolling, bending, elastic-plastic, and elastic deformation on microstructure development and environment-assisted cracking propensity of 2205 duplex stainless steel under low-temperature atmospheric chloride deposits ($MgCl_2$) was investigated. Following conclusions can be drawn:

1) EBSD local misorientation mapping confirmed the presence of multiple heterogeneous strain hot-spots in the microstructure after introduction of any type of cold work (rolling, bending, tensile), with bending deformation showing the highest degree of strain, followed by rolling and tensile deformation.

2) High magnitude of strain localisation in the austenite phase was observed in highly deformed microstructure, which increased with the degree of deformation independent from the deformation mode.
3) XRD stress measurements revealed substantial tensile stress development with increasing level of cold deformation, with austenite showing higher tensile stresses than ferrite after bending and rolling deformation, while ferrite shows higher stresses than austenite in tensile-deformed microstructure.
4) Selective dissolution of ferrite was the prevailing corrosion mechanism in as-received microstructure which seemed to be compromised by localised corrosion caused by cold working, with bending deformation showing the most severe effect followed by tensile-strained and rolled microstructures, with austenite providing more sites for pitting corrosion than ferrite with the increasing degree of cold work.
5) Bending deformation promoted environment-assisted cracking, with tensile deformation having slightly lower influence, while 20-40% cold rolling seemed to be less sufficient to promote cracking.
6) The austenite phase became selectively prone to stress corrosion cracking with increasing magnitude of cold work, especially after bending and tensile deformation, while rolling deformation enhanced the pitting corrosion propensity only and seemed to be insufficient to nucleate environment-assisted cracks in the austenite.
7) The ferrite phase was less prone to environment-assisted cracking than the austenite and seemed to increasingly corrode with the magnitude of cold work introduced, especially promoted after bending deformation, with a lesser degree after tensile and rolling deformation.

6.3.6 Acknowledgement

The authors acknowledge Radioactive Waste Management (RWM) (NPO004411A-EPS02) and EPSRC (EP/I036397/1) for financial support. The authors are grateful for the kind provision of Grade 2205 Duplex Stainless Steel plate by Rolled Alloys. Mr Gary Harrison, University of Manchester is thanked for his support during XRD stress measurements.

6.3.7 References

[1] J. Chater. The European market for duplex stainless steels: rapid growth expected. Stainless Steel World. Zutphen, The Netherlands: KCI Publishing B.V., 2010. p.1-4.

[2] E. Settoon. Comparative study of corrosion and environmental cracking properties of 316L and lean duplex alloys. Stainless Steel World. Zutphen, The Netherlands: KCI Publishing B.V., 2011.

[3] J.-O. Nilsson, G. Chai. The physical metallurgy of duplex stainless steels. International Conference & Expo Duplex 2007. Grado, Italy: Associazone Italiana Di Metallurgia - AIM, 2007.

[4] F. Wischnowski. Einfluss mikrostruktureller Gefügeveränderungen auf die Korrosionsresistenz von nichtrostenden ferritisch-austenitischen Duplex-Stählen. vol. PhD Thesis. Bochum, Germany: Technical University of Bochum, 1995. p.264.

[5] J. Johansson, M. Odén, X.H. Zeng. Evolution of the residual stress state in a duplex stainless steel during loading, Acta Materialia 47 (1999) 2669-2684.

[6] J. Johansson, M. Odén. Load sharing between austenite and ferrite in a duplex stainless steel during cyclic loading, Metall and Mat Trans A 31 (2000) 1557-1570.

[7] R.N. Gunn. Duplex Stainless Steel - Microstructure, Properties, and Applications. 2nd ed., Abington Publishing, Cambridge, England, 2003.

[8] F. King. Corrosion Resistance of Austenitic and Duplex Stainless Steels in Environments Related to UK Geological Disposal. 2009.

[9] Nuclear Decommissioning Authority. Geological Disposal, Steps Towards Implementation - Executive Summary. Didcot, Oxfordshire: Nuclear Decommissioning Authority, 2010.

[10] C. Fukuoka, K. Morishima, H. Yoshizawa, K. Mino. Misorientation development in grains of tensile strained and crept 2.25%Cr–1%Mo steel, Scripta Materialia 46 (2002) 61-66.

[11] Y. Tsutsumi, A. Nishikata, T. Tsuru. Initial Stage of Pitting Corrosion of Type 304 Stainless Steel under Thin Electrolyte Layers Containing Chloride Ions, Journal of The Electrochemical Society 152 (2005) B358-B363.

[12] Y. Tsutsumi, A. Nishikata, T. Tsuru. Pitting corrosion mechanism of Type 304 stainless steel under a droplet of chloride solutions, Corrosion Science 49 (2007) 1394-1407.

[13] T. Prosek, A. Le Gac, D. Thierry, S. Le Manchet, C. Lojewski, A. Fanica, E. Johansson, C. Canderyd, F. Dupoiron, T. Snauwaert, F. Maas, B. Droesbeke. Low-Temperature Stress Corrosion Cracking of Austenitic and Duplex Stainless Steels Under Chloride Deposits, Corrosion Science 70 (2014) 1052-1063.

[14] A.B. Cook, J. Duff, N. Stevens, S. Lyon, A. Sherry, J. Marrow. Preliminary Evaluation of Digital Image Correlation for In-situ Observation of Low Temperature Atmospheric-Induced Chloride Stress Corrosion Cracking in Austenitic Stainless Steels, ECS Transactions 25 (2010) 119-132.

[15] C. Örnek, D.L. Engelberg. SKPFM Measured Volta Potential Correlated with Strain Localisation in Microstructure of Cold-rolled Grade 2205 Duplex Stainless Steel, Corrosion Science (2015).

[16] C. Örnek, J. Walton, T.L. Ladwein, S.B. Lyon, D.L. Engelberg. A Corrosion Model for 475°C Embrittlement in Duplex Stainless Steel – a Comprehensive Study via Scanning Kelvin Probe Force Microscopy, (2015).

[17] C. Örnek, D.L. Engelberg. Kelvin Probe Force Microscopy and Atmospheric Corrosion of Cold-rolled Grade 2205 Duplex Stainless Steel. Eurocorr 2014. Pisa, Italy: European Federation of Corrosion, 2014. p.1-10.

[18] C. Örnek, A.H. Ahmed, D.L. Engelberg. Effect of Microstructure on Atmospheric-Induced Corrosion of Heat-treated Grade 2205 and 2507 Duplex Stainless Steels. Eurocorr 2012. Istanbul, Turkey: Dechema, 2012. p.1-10.

[19] A.M. do Nascimento, M.C.F. Ierardi, A.Y. Kina, S.S.M. Tavares. Pitting corrosion resistance of cast duplex stainless steels in 3.5%NaCl solution, Materials Characterization 59 (2008) 1736-1740.

[20] S.S.M. Tavares, V.G. Silva, J.M. Pardal, J.S. Corte. Investigation of stress corrosion cracks in a UNS S32750 superduplex stainless steel, Engineering Failure Analysis (2013).

[21] S.S.M. Tavares, A. Loureiro, J.M. Pardal, T.R. Montenegro, V.C.d. Costa. Influence of heat treatments at 475 and 400 °C on the pitting corrosion resistance and sensitization of UNS S32750 and UNS S32760 superduplex stainless steels, Materials and Corrosion 63 (2012) 522-526.

[22] P.J. Uggowitzer, L. Weber. Partitioning of chromium and molybdenum in super duplex stainless steels with respect to nitrogen and nickel content, Materials Science and Engineering: A 242 (1998) 222-229.

[23] H.-J. Eckstein. Korrosionsbeständige Stähle, Deutscher Verlag für Grundstoffindustrie GmbH, Leipzig, Germany, 1990.

[24] S. Aoki, K. Ito, H. Yakuwa, M. Miyasaka, J.i. Sakai. Potential Dependence of Preferential Dissolution Behavior of a Duplex Stainless Steel in Simulated Solution inside Crevice, Zairyo-to-Kankyo 60 (2011) 363-367.

[25] S. Aoki, H. Yakuwa, K. Mitsuhashi, J.i. Sakai. Dissolution Behavior of α and γ Phases of a Duplex Stainless Steel in a Simulated Crevice Solution, ECS Transactions 25 (2010) 17-22.

[26] J.-S. Lee, K. Fushimi, T. Nakanishi, Y. Hasegawa, Y.-S. Park. Corrosion behaviour of ferrite and austenite phases on super duplex stainless steel in a modified green-death solution, Corrosion Science 89 (2014) 111-117.

6.4 An Experimental Investigation into Strain and Stress Partitioning of Duplex Stainless Steel Using Digital Image Correlation, X-Ray Diffraction, and Scanning Kelvin Probe Force Microscopy

C. Örnek & D.L. Engelberg

Corrosion and Protection Centre, School of Materials,
The University of Manchester, Sackville Street, Manchester, M13 9PL, United Kingdom

6.4.1 Abstract

The evolution of microstructure strain partitioning during quasi in-situ tensile loading of grade 2205 duplex stainless steel has been investigated. Digital Image Correlation (DIC) revealed the development of discrete tensile strain initially in austenite and at interphase boundaries, and further extending into the ferrite with increasing load. Higher-resolution DIC observations indicated strain hardening of austenite, followed by deformation of the ferrite. DIC analysis of a 20% cold-rolled microstructure revealed tensile strain development at interphases, with discrete tensile and compressive strain pockets observed within the austenite. X-ray diffraction (XRD) measurements indicated the presence of tensile stresses primarily developing in the ferrite, with full width at half maximum (FWHM) values indicating plastic strain accumulation primarily in the austenite. The effect of tensile loading of Volta potential differences, obtained via Scanning Kelvin Probe Force Microscopy (SKPFM), highlighted the development of discrete anodic and cathodic sites with the introduction of strain. A Volta potential roughness parameter (Ψ_{Ra}) is introduced describing Volta potential changes as a function of strain. This observation supports the concept of an enhanced propensity of local electrochemical activity with increasing applied strain in duplex stainless steel.

Keywords: *Duplex stainless steel; Digital image correlation (DIC); Strain partitioning; X-ray diffraction (XRD); Scanning Kelvin Probe Force Microscopy (SKPFM)*

6.4.2 Introduction

Duplex stainless steels are nowadays used for application in demanding environments due to their excellent mechanical and electrochemical properties [1]. A balanced ratio of ferrite (δ) and austenite (γ) is typically present in duplex microstructures [2], with the grain morphology elongated in rolling direction, leading to banded structures of discrete austenite grains embedded in a ferritic matrix [3]. The body-centred-cubic (bcc) ferrite has different mechanical properties compared to the face-centred-cubic (fcc) austenite [4], and consequently there is a mismatch during deformation in the microstructure, leading to strain and stress partitioning [5]. Residual strain is typically present in duplex microstructures due to different thermal expansion coefficients of both phases, resulting in the formation of heterogeneous strain fields in the microstructure [6, 7].

Grade 2205 duplex stainless steel is currently proposed as material option for intermediate-level radioactive waste (ILW) storage containers in the UK [8, 9]. It is therefore important to assess its microstructure with respect to the development of local strain and stress fields, primarily to understand how stress and strain affect corrosion and crack nucleation propensity. Knowledge about the evolution of critical strain components and their relation to corrosion sites in the microstructure will allow optimisation of material performance [10-12].

The aim of the work reported in this paper was to obtain information about the effect of strain partitioning and its relation to local changes of Volta potentials in grade 2205 duplex stainless steel. Microstructure observations during quasi in-situ tensile loading obtained via DIC are compared to stress and strain development measured by XRD, and the development of Volta potential changes in microstructure obtained via SKFPM. The implications of these observations are discussed in light of microstructure optimisation for application of duplex stainless steel in demanding environments.

6.4.3 Experimental

A solution-annealed (1100°C, water quench) grade 2205 duplex stainless steel plate with 10 mm thickness and a chemical composition of 22.4% Cr, 5.8%Ni, 3.2%Mo, 1.5%Mn, 0.4%Si, 0.18%N, 0.016%C, 0.021%P, 0.001%S, and Fe (bal.) was used in this study. Micro-tensile specimens with 50 mm length, 1 mm thickness, 25 mm gauge length, and 3

mm gauge width were machined from as-received and 20% cold-rolled plate material. The surface of all micro-tensile specimens were ground to 4000-grit using SiC sandpapers followed by a 3 and 1 µm polishing finish using diamond paste. Electrolytic etching was performed to reveal the microstructure in 40% KOH at 5 Volts for 10 seconds, resulting in a stained ferrite.

DIC was performed on a set of images taken during straining of micro-tensile specimens of as-received and 20% cold-rolled samples using a micro-tensile testing machine from Kammrath & Weiss (Germany). Straining was performed in discrete displacement increments of 5 to 10 µm using an elongation rate of 0.3 µm/s. Force-displacement values were recorded from the crosshead/actuator of the tester. Macroscopic strain was calculated from the applied displacement over the total gauge length, and stress was determined from the applied force as a function of the initial cross-section area of the micro-tensile specimen.

The as-received specimen was strained to 0.8% macroscopic strain with images of the microstructure recorded using a Keyence VHX-200 optical microscope at 400x magnification. This corresponded to an imaged region of 800 x 600 µm². The image resolution was 1600 x 1200 pixels, resulting in a pixel size of 0.5 µm. The average grain size of ferrite and austenite was 7 ± 1 µm and 6.5 ± 1 µm, as reported in earlier work [13]. The tensile specimen was further strained to 1.4% macroscopic strain (+0.6% strain) and images of the microstructure obtained using the Keyence VHX-200 optical microscope at 1000x magnification, resulting in an imaged microstructure area of 320 x 240 µm² and a pixel size of 0.2 µm. The specimen was then unloaded, the whole setup transferred to an FEI Quanta 650 scanning electron microscope (SEM), and the sample reloaded to 6% total macroscopic strain, with images recorded in secondary electron (SE) mode at 500x magnification. This corresponded to a horizontal field of view of 600 µm, and the image resolution in the SEM was 2048 x 1768 pixels, giving a pixel size of 0.3 µm. The 20% cold-rolled specimen was strained to 4% macroscopic strain and the microstructure imaged using a Keyence VHX-200 optical microscope at 200x and 600x magnification. This corresponded to an imaged microstructure area of 1600 x 1200 µm² and 533 x 400 µm², respectively, resulting in a pixel size of 1 µm and 0.3 µm, respectively. The image resolution was 1600 x 1200 pixels. Table 6-5 gives a summary of all straining experiments performed with key parameters.

DIC of each sample was carried out after introducing a small amount of pre-strain (0.02-0.04%) to observe the initial microstructure response. Images were then obtained at the end of each applied strain increment, and DIC of optical and SEM images of successive increments was carried out. DIC analysis was also carried out for images acquired at the end of each test and correlated with the first image of the unstrained condition.

Table 6-5: Overview of strain measurements and pixel resolution for DIC analysis

Material	Step	Strain	Observation	Magnification	Area	Pixel resolution	Final Interrogation Window Size
As-received	1	0 to 0.8%	Optical microscope	400x	800 x 600 µm²	0.5 µm	32 x 32 pixels
	2	0.8 to 1.4%*	Optical microscope	1000x	320 x 240 µm²	0.2 µm	32 x 32 pixels
	3	0 to 6%	SEM	500x	597 x 515 µm²	0.3 µm	96 x 96 pixels
20% cold-rolled	1	0 to 4%	Optical microscope	200x	1600 x 1200 µm²	2 µm	16 x 16 pixels
				600x	533 x 400 µm²	0.3 µm	24 x 24 pixels

*specimen was unloaded after 1.4% macroscopic strain

LaVision DaVis (V8.2.2) was used for DIC analysis with all images converted into 8-bit greyscale. Shift and rotation correction was applied to correct for rigid body translations, and a 2D deformation time-series using integral correlation with sum of differential vector fields was performed. A geometric mask was applied, and multiple pass iterations (decreasing) with 512 x 512 pixels or 256 x 256 pixels interrogation window size, 25% window overlap, 3 passing sequence, followed by a smaller window size (between 96 x 96 and 16 x 16 pixels) with 50% window overlap and 2 passing sequence was applied for displacement vector calculations. A correlation coefficient of 0.3 was used. The maximum normal strain and maximum shear strain was obtained for each test.

To determine the noise of the system (strain uncertainty), two images of a non-deformed sample were taken and a small amount of in-plane rigid body translation applied. DIC was applied to these images and the maximum strain uncertainty determined, with this analysis performed for each microstructure and magnification used in this study. The strain uncertainties were obtained for different interrogation window sizes, as summarised in Figure 6-15. Strain uncertainties were predominantly localised in the austenite due to fewer features formed by KOH etching. Therefore, strain uncertainties in the ferrite were in general at least one order of magnitude smaller than those reported in Figure 6-15.

XRD surface residual stress measurements were performed on a flat tensile specimen with a gauge length of 40 mm, a width of 10 mm, and 2 mm thickness. The specimen was at

first mechanically ground to 1200-grit using SiC sandpapers, followed by electropolishing using a 20 vol.-% perchloric acid and 80 vol.-% methanol electrolyte at 20 Volts, a temperature of -35°C, for 60 seconds. XRD measurements were carried out on a Proto iXRD Combo testing machine (Proto Manufacturing Inc., Michigan, USA), equipped with a two detector system. Cr and Mn x-ray sources were used to measure the strain in ferrite and austenite, respectively. The tensile sample was loaded to pre-set displacements with the strain measured in one phase, followed by changing the x-ray tube and measurement of strain in the other phase. The strain in the ferrite and austenite was measured under loading condition, after the application of three discrete displacement steps at 0.05%, 0.1%, and 0.19% macroscopic strain, followed by a measurement after unloading the sample. The measurement position was in the centre of the gauge section of the specimen.

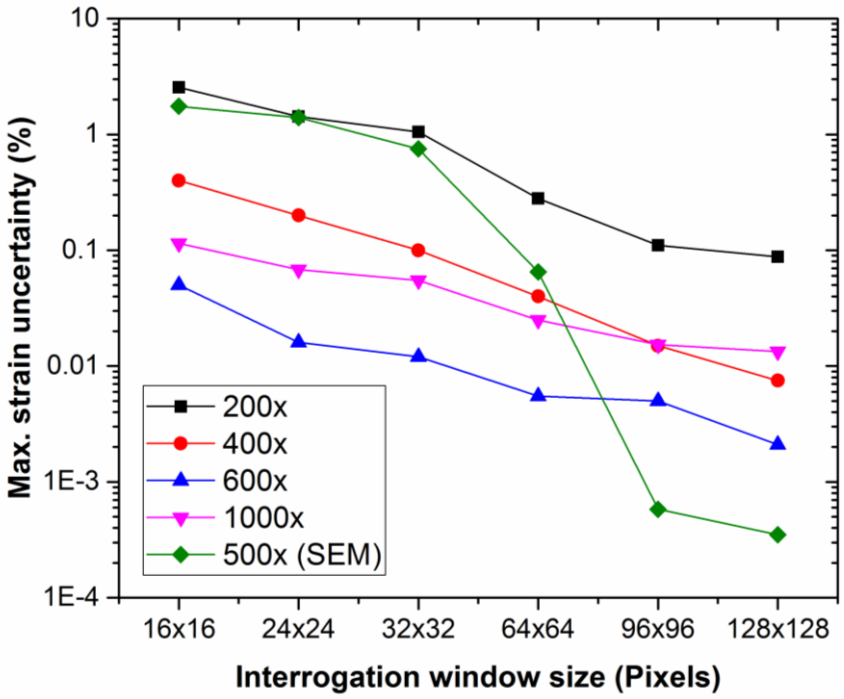

Figure 6-15: Maximum strain uncertainties of DIC-processed images for each image dataset

All XRD measurement parameters are listed in Table 6-6. Figure 6-16 describes schematically the experimental setup, with the image insert in Figure 6-25 showing the tensile rig used and corresponding sample coordinate system. Prior to the test, the x-ray diffractometer was calibrated using a stress-free standard (powder material provided by the manufacturer) and a stressed standard (ferritic and austenitic steel samples provided by the

manufacturer) to accurately determine stress-peak positions. The multiple exposure technique with 11 measurement angles was used for inter-planar d-spacing measurements. Two stress tensors at 0° and 90° phi angles were obtained; with phi 0° being parallel to the loading axis of the sample (each measured orientation corresponds to the stress direction as specified in the image insert in Figure 6-16). The measurement position was in the centre of the specimen. Stress and full-width at half maximum (FWHM) values of the peak intensities were obtained from the Proto iXRD Combo software for each measurement and plotted versus macroscopic strain.

Table 6-6: Parameters used for x-ray diffraction measurements

X-ray type	**Cr-Kα**	**Mn-Kα**
Source voltage, current	20 kV, 4 mA	20 kV, 4 mA
Aperture size	2 mm	2 mm
Bragg angle, 2θ	156.4	152.8
Diffraction plane	(2 1 1)	(3 1 1)
Wavelength	2.291 Å	2.1034 Å
Max. measurement angle, β	27°	27°
Number of β angles	11	11
β angles	27	27
β oscillation angle	3°	3°
Phi angles	0 and 90°	0 and 90°
Exposure time	2 sec	2 sec
Number of exposure profiles	10	10
Number of exposures gain	30	30
X-ray elastic constant $S_1^{(hkl)}$	1.28 x 10^{-6} MPa	1.2 x 10^{-6} MPa
X-ray elastic constant ½$S_2^{(hkl)}$	5.92 x 10^{-6} MPa	7.18 x 10^{-6} MPa
Peak fit	Gaussian	Gaussian

SKPFM measurements were performed using a Dimension 3100 Atomic Force Microscope (AFM) from Digital Instruments (USA). The theoretical background and a description of SKPFM measured Volta potentials is described elsewhere [12, 14-16]. In summary, SKPFM is typically operated in a two-pass mode, with the first pass determining the surface topography, followed by a second pass carried out at a pre-determined height (typically 50-100 nm) to measure Volta potential differences. The measured Volta potential difference between the tip used and the surface reflects the electronic activity of the metal surface at this analysis point. OSCM-PT (Pt-coated Si) probes were used for Volta potential (ΔΨ) measurements, with a lift height of 50 nm. The SKPFM scan size was 80 µm x 80 µm. Data analysis was performed with the software NanoScope Analysis

version 1.5. Topography and potential maps were flattened using 1st order flattening in order to enhance contrast, but quantitative data analysis was performed on raw data without flattening. SKPFM data acquisition was carried out with 512 x 512 pixel resolution, with all values reported relative to the work function of the AFM-tip (Pt-tip). Potentials measured with higher and lower values with respect to the tip indicate net anodic and net cathodic activity, respectively. The Volta potential distribution was expressed as a Volta potential roughness (Ψ_{Ra}) parameter to describe Volta potential variations as a function of the ferrite and austenite phase. The roughness parameter was determined from Volta potential maps by using NanoScope Analysis 1.5 software (Bruker, USA), with Ra of the Volta potential line profile in each phase extracted and quantified. Ra describes the arithmetic average of the absolute values of roughness profile ordinates [17]. Here, Ra was determined by extracting the mean of Volta potential variations in each profile measured over each crystallographic phase. One region in the centre of the sample was mapped for Volta potential differences, with 0%, 0.23%, and ≈10% total macroscopic strain, with the latter being a different region than the others. The sample was measured in the unloaded condition and was therefore removed from the tensile tester for each SKPFM measurement.

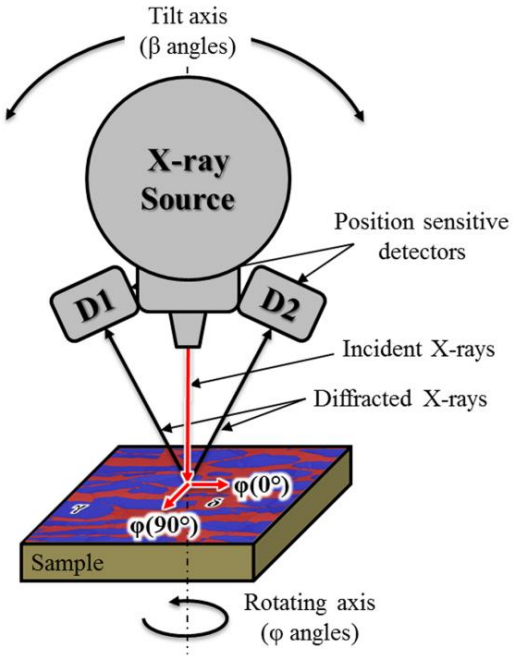

Figure 6-16: Schematic illustration of x-ray diffraction measurement setup

6.4.4 Results and Discussion

The as-received microstructure had a ratio of 43 ± 1% ferrite (δ) and 57 ± 1% austenite (γ) determined via image analysis of optical micrographs. The austenite was discrete with an island-like morphology, surrounded by the ferrite matrix. Typical microstructures of the as-received and 20% cold-rolled material condition are shown in Figure 6-17.

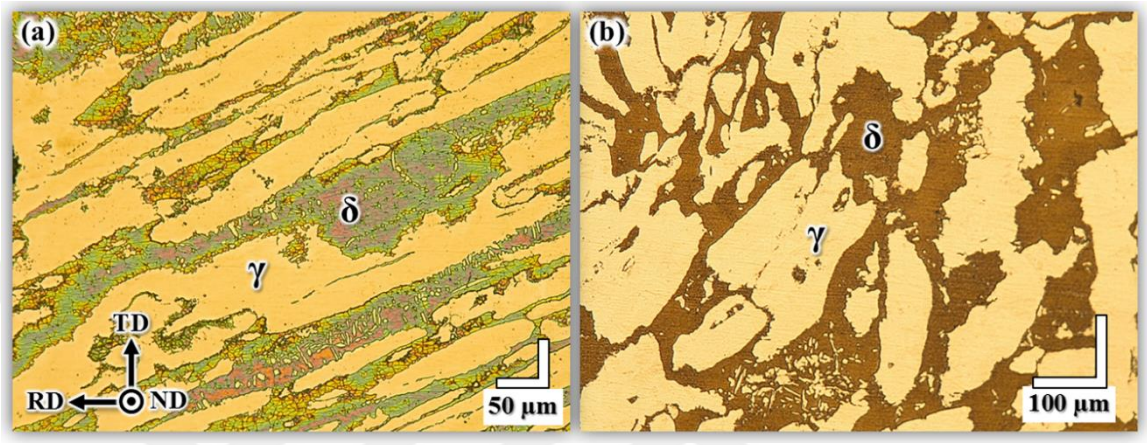

Figure 6-17: Optical micrograph of (a) as-received and (b) 20% cold-rolled duplex stainless steel microstructure. Arrows indicate microstructure processing orientation towards transverse direction (TD), rolling direction (RD), and normal direction (ND).

The stress-strain curves of the as-received and 20% cold-rolled micro-tensile specimens are shown in Figure 6-18. The yield strength ($Rp_{0.2}$), ultimate tensile strength (UTS), and strain to failure (ε_f) was 470 MPa, 690 MPa, 27% for the as-received and 800 MPa, 870 MPA, 5% for the 20% cold-rolled sample.

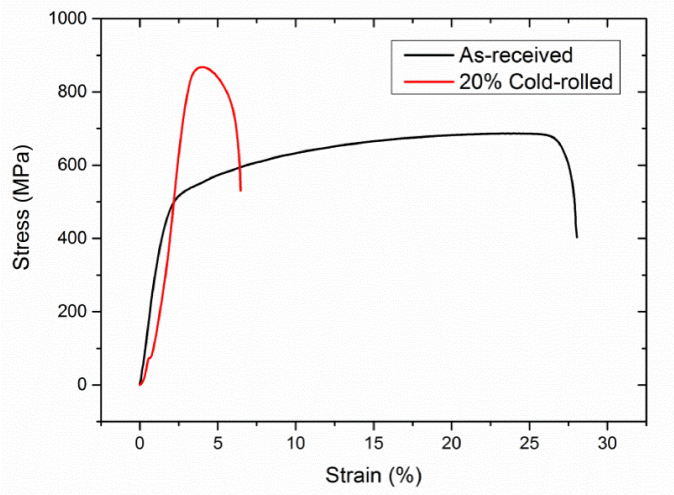

Figure 6-18: Stress-strain behaviour of as-received and 20% cold-rolled 2205 duplex stainless steel

6.4.4.1 DIC of As-received Microstructure

The results of the as-received microstructure after tensile straining to 0.04% and 0.8% macroscopic strain are shown in Figure 6-19. Small strain heterogeneities can already be seen after the application of 0.04% strain, primarily located in austenite regions. After further straining to 0.8%, most normal strain was still localised in austenite grains, but with more pronounced strain fields at some interphase boundaries.

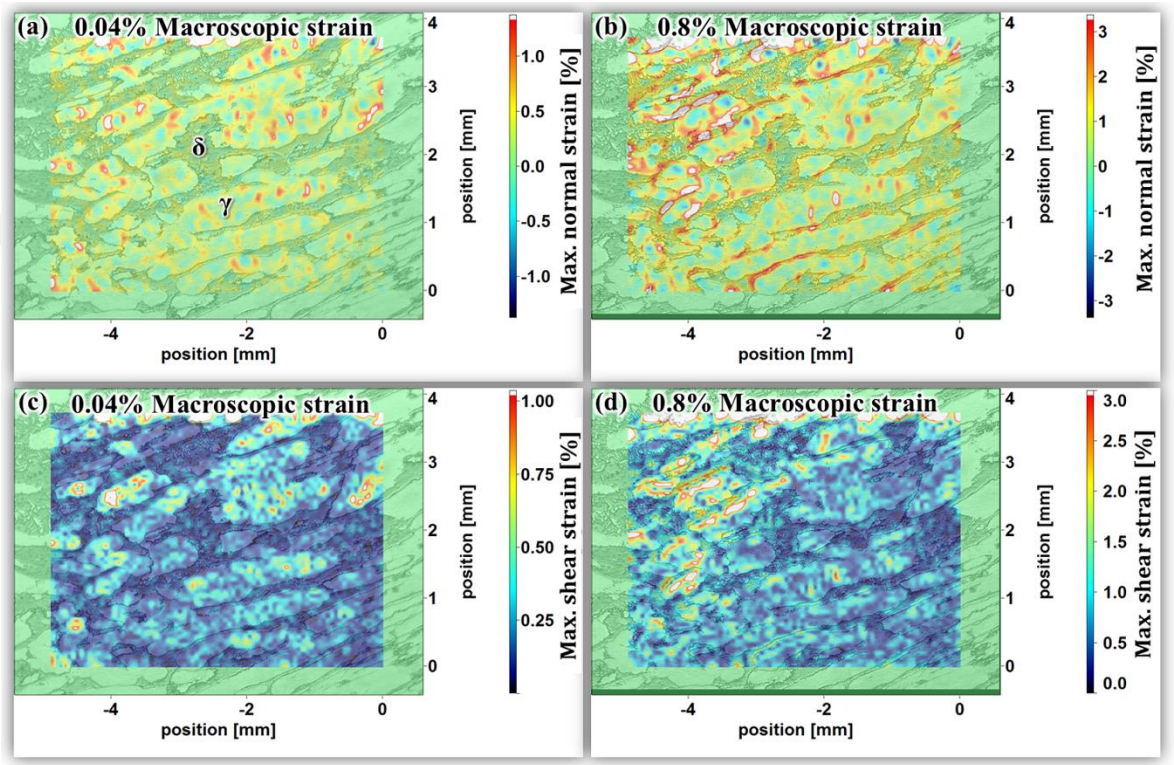

Figure 6-19: DIC analysis of the as-received microstructure with 0.04% and 0.8% macroscopic tensile strain with (a,b) showing maximum normal strain evolution with strain localisation in austenite and interphase regions, and (c,d) showing maximum shear strain evolution concentrating primarily in austenite. Loading was applied to the horizontal axis of the images. Optical micrographs (400x magnification) of etched microstructure with KOH in normal direction. Interrogation window size: 32 x 32 pixels.

Figure 6-19(a,b) indicates that the strain distribution in the ferrite was far more homogeneous, whilst in the austenite and, to a lesser extent in certain regions, at interphase boundaries distinctive heterogeneous strain fields developed with increasing strain magnitude. *El Bartali* [18] also reported heterogeneous strain fields at interphase boundaries, with the latter related to different crystallographic orientations of grains making up these interphases. There is often a strong Kurdjumov-Sachs orientation relationship existing in duplex stainless steels between the ferrite and austenite, in the form

of $[110](1\text{-}11)_{\gamma}$ // $[111](1\text{-}10)_{\delta}$. This infers that slip transfer across interphases is facilitated if this orientation criterion is satisfied, leading to enhanced dislocation mobility [19]. However, intense heterogeneous strain fields can lead to micro-crack formation at sites where this orientation relationship does not exist, which can result in slip bands arresting at interphase boundaries [18].

Large crystallographic misorientations between neighbouring grains and the resulting slip system differences between both phases therefore limit dislocation motion. Strain localisation, in certain cases at least, can be indicative of stress localisation, and vice versa, hence intense heterogeneous strain fields can result in preferential corrosion as well as potential crack nucleation sites. In earlier work it was shown that numerous heterogeneous strain fields at discrete regions, determined by local misorientation measurement using electron backscatter diffraction (EBSD), were found in cold-rolled grade 2205 duplex stainless steel microstructure, and such sites showed electrochemical activity with exposure to a chloride-containing atmospheric environment [12].

Some regions under compression or tension observed after 0.04% strain in Figure 6-19(a) were able to balance their strain fields after increasing the strain to 0.8%. Since tensile straining was incrementally performed, i.e. after each straining step a time elapse was necessary to record an image of the microstructure, the material had time to creep, which may have affected the location of the small magnitude of normal strain locations in Figure 6-19(a).

Figure 6-19(c,d) show that shear strain was localised in austenite regions, significantly only suggesting that shear deformation at interphase boundaries was less favoured than within the austenite grains. Austenite possesses 12 closely-packed slip systems and allows easy dislocation mobility in almost all crystallographic directions while the ferrite possesses less closely-packed slip systems, which typically possess higher critically resolved shear stresses for their activation [4]. Furthermore, the Peierls stress in the ferrite is typically higher than that in the austenite, rendering the austenite more ductility than ferrite. Therefore, plastic deformation of ferrite occurs usually after the first austenite grains have deformed, until the austenite is work-hardened.

The application of an additional +0.012% and +0.6% deformation in Figure 6-20, after changing to a higher magnification (1000x) to reach a maximum total applied strain of

1.4% showed that the strain evolution became saturated or decelerated at interphase boundaries, whilst strain hardening of austenite continued, with in parallel the ferrite starting to accommodate larger strains. Strain hardening occurred preferentially in certain austenite grains indicating favoured grain orientation towards the loading direction. Both normal and shear strain indicated slip activity in the austenite, whereas only little strain activity was seen in the ferrite. This indicates that ferrite had a higher stiffness than austenite.

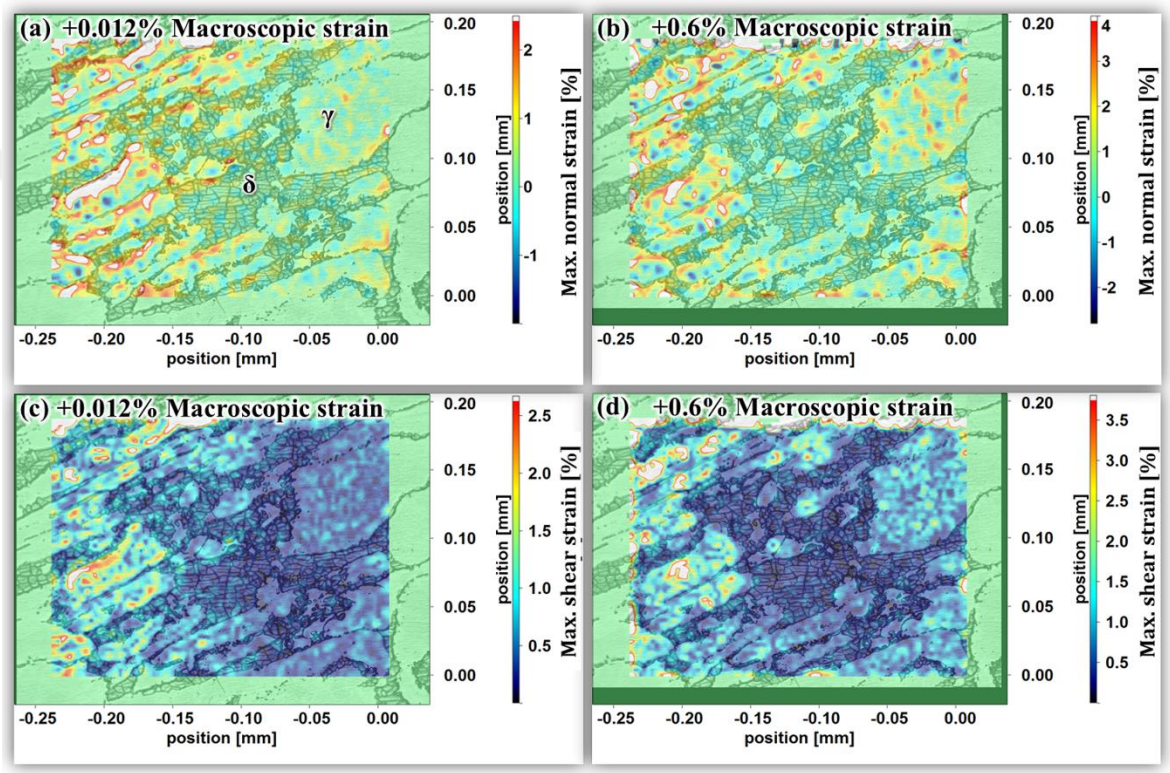

Figure 6-20: Higher resolution DIC analysis of the as-received microstructure with application of an additional 0.012% and 0.6% macroscopic tensile strain (in total 1.4% strain) with (a,b) showing maximum normal strain evolution and (c,d) showing maximum shear strain evolution. Loading was applied to the horizontal axis of the images. Optical micrographs recorded with 1000x magnification. Interrogation window size: 32 x 32 pixels.

Figure 6-21 shows the duplex microstructure after unloading and reloading the sample for SEM analysis to 0.024% and 6% macroscopic strain, showing intense heterogeneous strain fields with high strain gradients primarily in austenite grains and at a few ferrite-austenite interphase boundaries. The presence of discrete regions with tensile strain was typically accompanied by neighbouring regions with compressive strain fields. The extent of these compressive strain fields was larger than previously observed in Figure 6-20 due to the larger strain applied. Furthermore, the contrast of tensile and compressive regions was

apparent, and the spacing between them was small, resulting in high strain gradients. This infers that un- and reloading caused further strain development with local strain re-distribution.

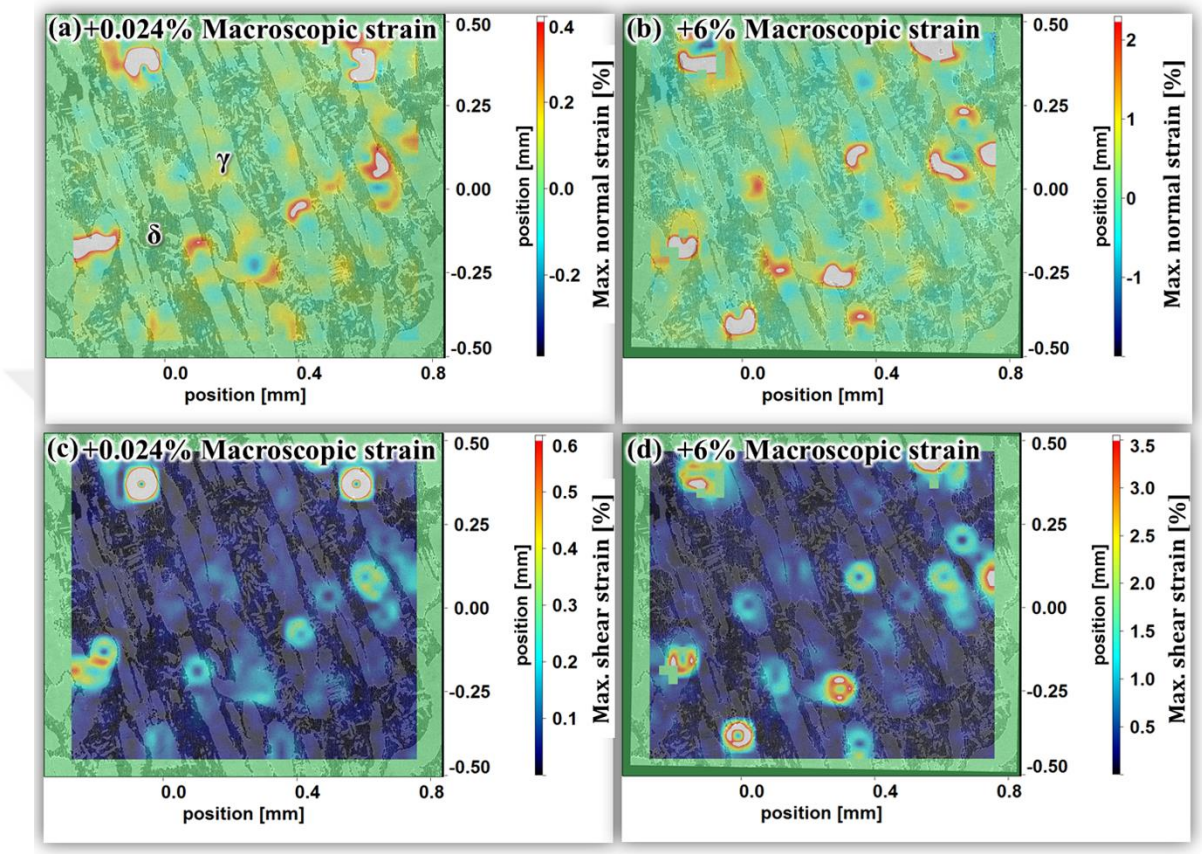

Figure 6-21: DIC analysis of the as-received microstructure with 0.024% and 6% macroscopic tensile strain highlighting with (a,b) showing maximum normal strain and (c,d) showing maximum shear strain. Loading was applied to the vertical axis of the images. Images were taken with an SEM at 500x magnification. Interrogation window size: 96 x 96 pixels.

In Figure 6-21(c,d) is shown that shear strain mainly developed in the austenite, with the maximum shear strain in certain regions larger than the maximum normal strain, suggesting that work hardening had occurred due to shear deformation in the austenite. The presence of regions with compressive strain in austenite is most-likely related to grains with less favoured orientation with respect to the loading direction. Adjacent grains with favoured orientation have possibly deformed, so that less-favoured grains laying in-between deformed sites were compressed leading to the introduction of negative strains. Even after the introduction of 6% macroscopic strain no distinct heterogeneous strain evolution in the ferrite was observed.

6.4.4.2 DIC of 20% Cold-rolled Microstructure

DIC results of the 20% cold-rolled microstructure after introduction of 0.012% and 4% macroscopic strain are shown in Figure 6-22. Heterogeneous strain concentrations appeared primarily in austenite and at interphase boundaries, both compressive and tensile in nature (Figure 6-22(a,b)). Compressive strain seemed to be related to the austenite, with ferrite showing no clear change up to 4% macroscopic strain. Discrete regions containing shear deformation were present in the austenite and at interphase boundaries at 0.012% macroscopic strain, and the ferrite seemed to accommodate more strain. Cold rolling clearly work-hardened the microstructure, and up to 5-times larger strain development in austenite was observed than in ferrite.

The strain heterogeneity was significantly increased in the cold-rolled microstructure compared to the as-received condition, and regions with high concentrations of strain were observed in the vicinity of sites with less localised strain or regions with compressive strain fields.

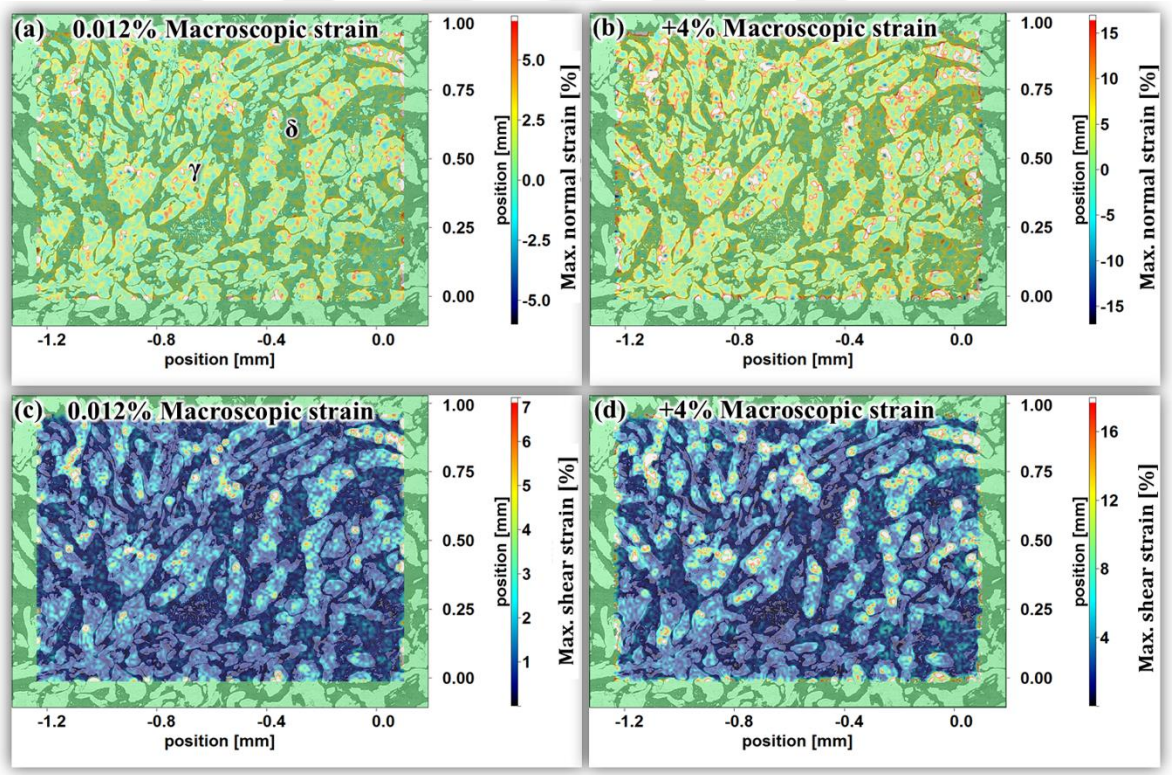

Figure 6-22: DIC analysis of 20% cold-rolled microstructure after 0.012% and 4% total macroscopic strain with (a,b) maximum normal strain evolution and (c,d) maximum shear strain evolution. Mechanical loading direction was to the horizontal axis of the images. Optical micrographs recorded with 200x magnification. Interrogation window size: 16 x 16 pixels.

Higher resolution DIC analysis shown in Figure 6-23 confirmed that large strain gradients exist within both phases. The strain distribution across the austenite was distinctively larger indicating more deformation occurred compared to the ferrite. The austenite in the cold-rolled microstructure was significantly strain-hardened and seemed to have accommodated additional strain by plastic deformation of the ferrite. Large heterogeneous strain fields also developed in ferrite and at interphase boundaries indicating a slip activity shift from highly strained austenite grains to neighbouring ferritic regions (Figure 6-23(c,d)).

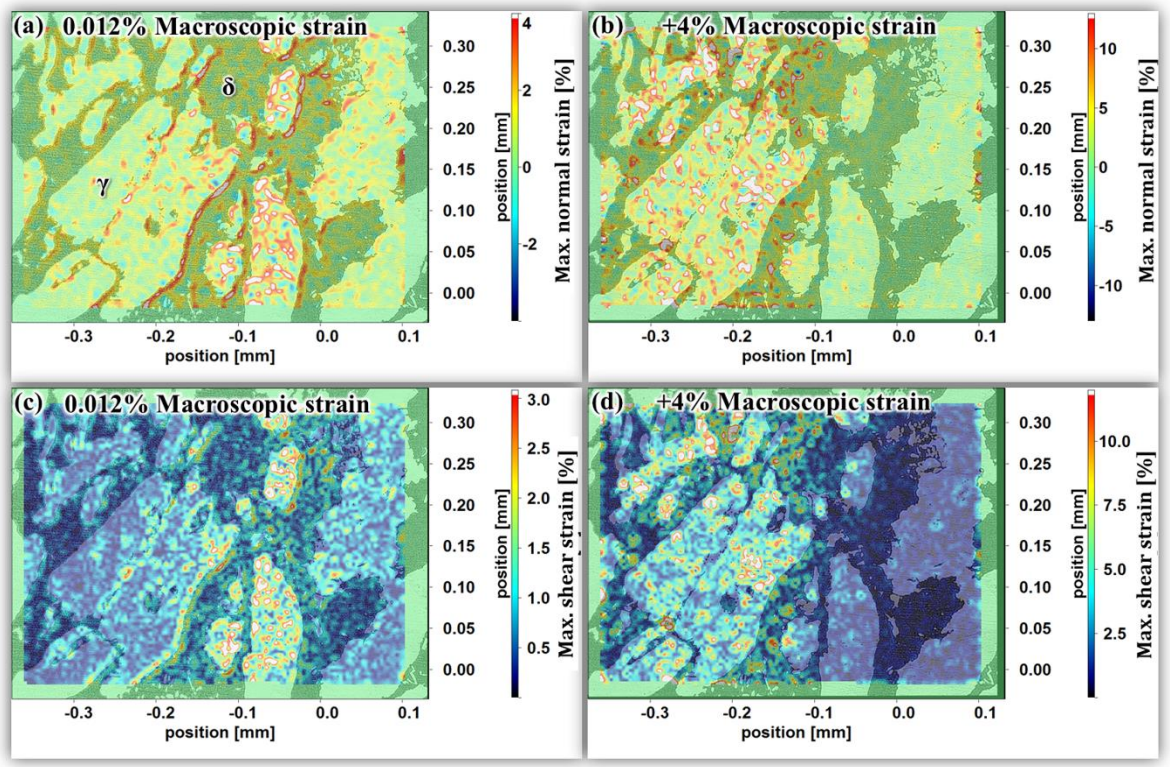

Figure 6-23: DIC analysis of 20% cold-rolled microstructure after 0.012% and 4% total macroscopic strain with (a,b) maximum normal strain evolution and (c,d) maximum shear strain evolution. Mechanical loading direction was to the horizontal axis of the images. Optical micrographs recorded with 600x magnification. Interrogation window size: 24 x 24 pixels.

6.4.4.3 Summary of DIC observations

Strain hardening is primarily concentrated in the austenite phase in as-received microstructure due to much easier slip activity than in ferrite and lower stiffness. Most elastic and plastic strain is accommodated at certain regions in the austenite during mechanical loading as can be seen in Figure 6-24(a), showing the maximum strain intensities from DIC-processed images versus applied strain. Slip activity in ferrite is

significantly lower than in austenite, and strain fields at the interphase boundaries are higher than in ferrite. However, strain fields developing in ferrite and at interphase regions quickly reach saturation enabling further strain hardening of the austenite phase.

In the 20% cold-rolled microstructure austenite was still accommodating most strain, with higher maximum normal strain intensities due to increasing strain concentrations and associated gradients as can be seen in Figure 6-24(b). The presence of discrete strain fields indicated accumulation of local deformation at confined regions. The ferrite and interphase regions showed accommodation of strain, which probably promoted slip activity in ferrite in the cold-rolled microstructure.

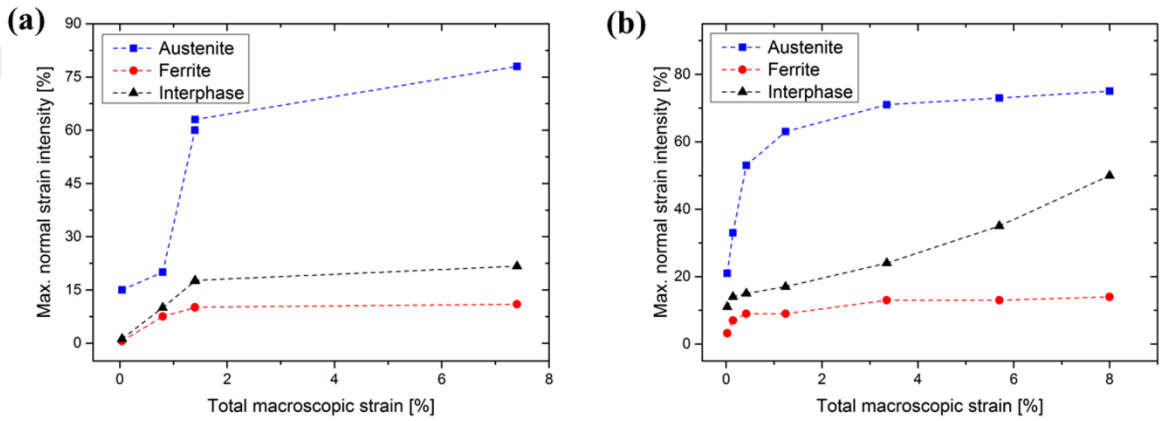

Figure 6-24: Maximum strain intensities of normal strain component measured in DIC mapped areas of (a) as-received and (b) 20% cold-rolled microstructures

6.4.4.4 X-ray Diffraction Surface Stress Determination

The quasi in-situ XRD stress measurement results are summarised in Figure 6-25. Both ferrite and austenite contained compressive stresses in the as-received condition. Loading to 531 µ% strain (0.05%) indicated an increase of 150-170 MPa in both ferrite and austenite. The overall stress in ferrite became tensile, and the austenite became more balanced along the loading direction (phi = 0°). No clear change of residual stresses in the other direction (phi = 90°) was seen. Further loading to 1009 µ% (0.1%) strain showed stress development in both the ferrite (additional ~220 MPa) and in austenite (additional ~120 MPa).

Application of a final loading cycle to 1931 µ% (0.2%) strain increased the stress in both the ferrite and austenite by approximately 120 MPa. The increase of stress in ferrite and austenite along phi 0° seemed to be proportional in both phases with increasing applied

load. With further increase of applied macroscopic strain, it is likely that the stress development in ferrite saturated earlier, ultimately resulting in the development of higher stresses in the austenite than in ferrite. Therefore, strain localisation in microstructure does not necessarily lead to stress evolution at sites containing high strain in duplex stainless steel.

Unloading the sample revealed the presence of a residual stress in the ferrite (phi = 0°) of 226 MPa, with the austenite showing a reduction of the previously measured stress to a value close to 0 MPa.

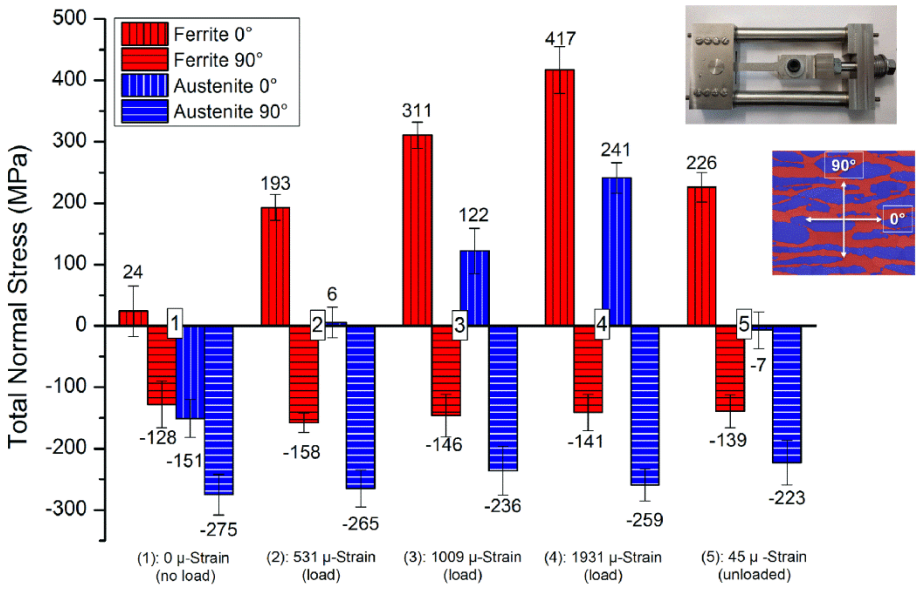

Figure 6-25: Quasi in-situ XRD stress measurement of austenite and ferrite in the as-received duplex stainless steel microstructure

The FWHM values of ferrite and austenite as a function of macroscopic strain are compared in Figure 6-26. The FWHM of the austenite phase showed an overall increase compared to the ferrite, indicating the accommodation of more plastic strain in austenite with larger macroscopic deformations. The FWHM value is sensitive to the variation in microstructure and stress-strain accumulation in the material. Typically, an increase in stacking faults and structural disorders widens the XRD peaks, and the presence of tensile stress causes an increase in the FWHM, with relaxation processes typically decreasing its magnitude [20, 21]. After unloading the FWHM of ferrite remained the same as last

straining step, whereas the FWHM increased in the austenite indicating accommodation of plastic strain in the austenite.

The FWHM values of ferrite and austenite as a function of bulk strain are compared in Figure 6-26. The FWHM of the austenite phase showed an overall larger increase compared to the ferrite, indicating the accommodation of more plastic strain in austenite with larger bulk deformations. After unloading the FWHM of ferrite remained the same as last straining step, whereas the FWHM increased in the austenite indicating relaxation and further increase of plastic strain in the austenite.

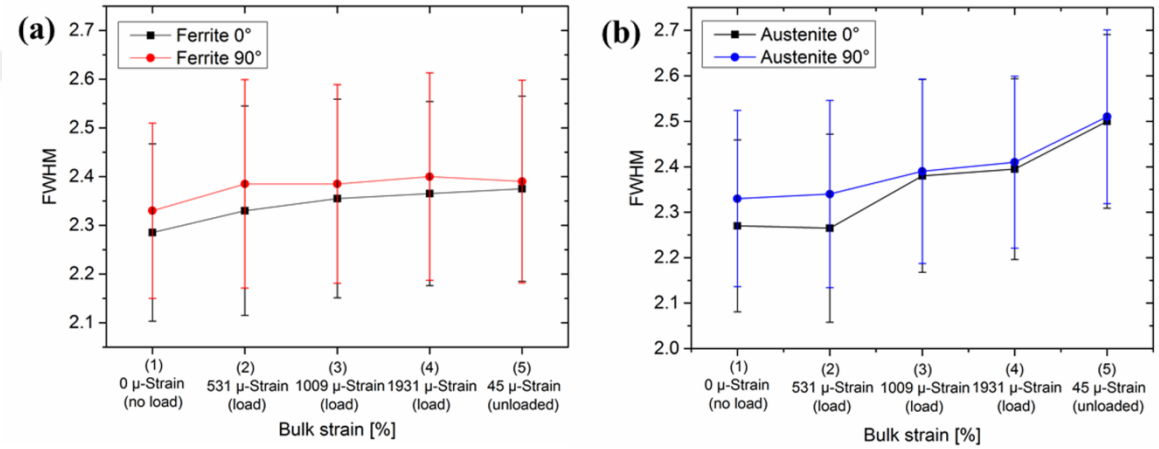

Figure 6-26: XRD FWHM values of (a) ferrite and (b) austenite of as-received microstructure as a function of total macroscopic strain

6.4.4.5 SKPFM Volta Potential Measurements

Surface topography and SKPFM Volta potential maps of the as-received, 0.23% and ~10% tensile strained microstructure are shown in Figure 6-27. The Volta potential distribution within the as-received microstructure was smooth in each crystallographic phase, with only long-ranged potential gradients. The austenite phase showed a Volta potential roughness (Ψ_{Ra}) of 2.7 mV with a maximum potential variation of 21 mV across the entire phase, compared to a Volta potential roughness of ferrite of 3.6 mV with a maximum potential variation of 30 mV. A total Volta potential difference of 30 ± 15 mV was measured between ferrite and austenite, with the austenite having lower potential differences than ferrite indicating superior electrochemical properties. Volta potential correlation of ferrite and austenite regions with local electrochemical activity was earlier reported for 2205

duplex stainless steel [12]. Usually, the ferrite is preferentially attacked in chloride-containing environment, whilst the austenite is more corrosion resistant [11, 12, 22-25].

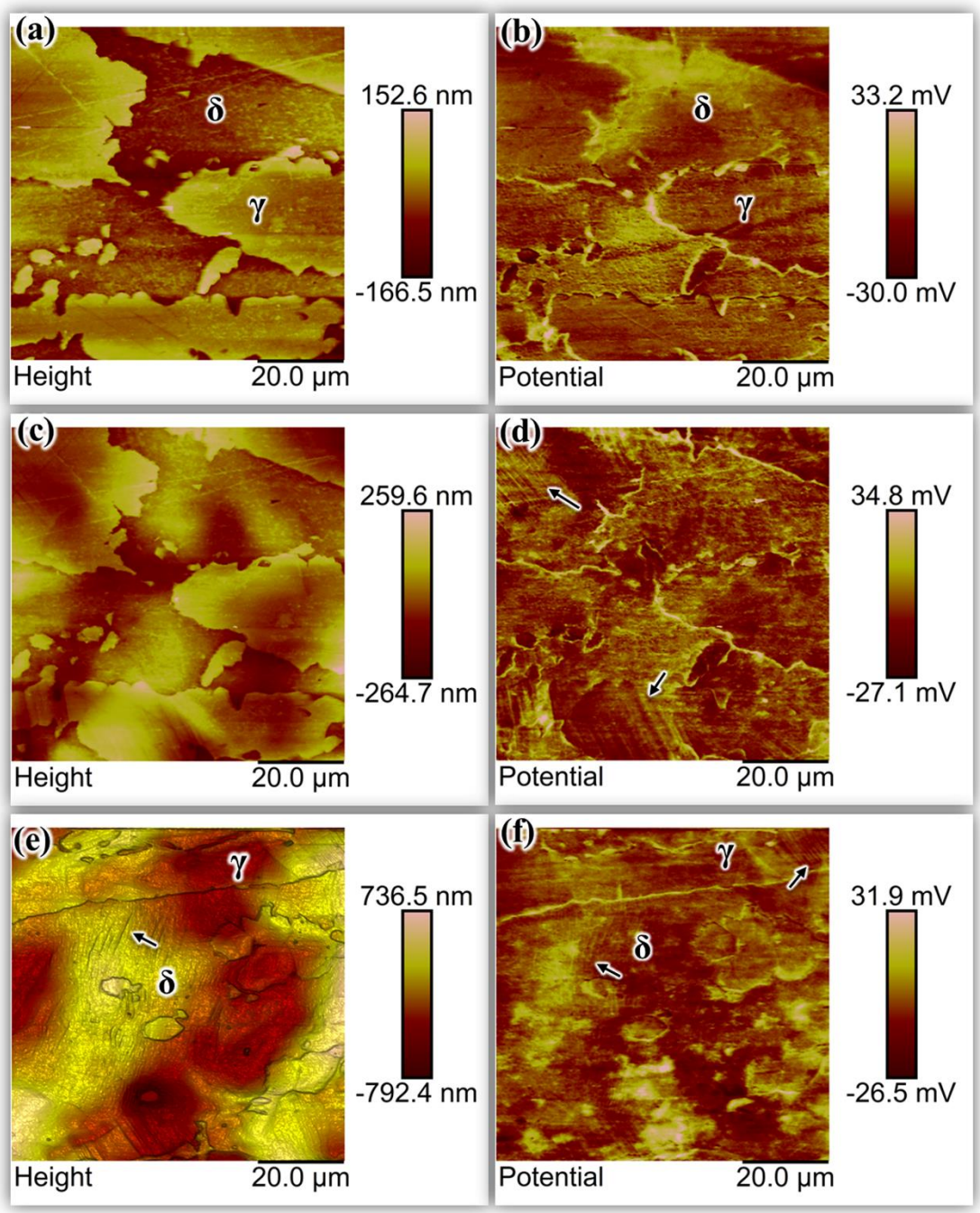

Figure 6-27: SKPFM Volta potential analysis after tensile straining with (a) the topography of as-received microstructure with (d) the corresponding Volta potential differences map, (b,e) after 0.23% strain, and (c,f) after ~10% plastic strain. Note that all potential maps were flattened to enhance potential contrast differences. Loading direction was oriented to the horizontal of the images.

Volta potential differences between ferrite and austenite increased to 40 ± 30 mV after the application of 0.23% strain (in Figure 6-27(b)), with large scatter across the entire microstructure. The Volta potential roughness of ferrite and austenite increased to 4.1 mV and 5.4 mV, respectively, with potential variations of 32 mV for the ferrite and 33 mV for the austenite phase. This supports previous observations of changes occurring in the austenite and in the ferrite after tensile straining, with reports of the development of discrete cathodic and anodic Volta potential sites at confined regions (hot-spots). The first slip bands were observed in the austenite, with Volta potential differences measured over slip bands having larger anodic character, in contrast to regions without slip band deformation. It is well known that the passive layer can be disrupted during plastic deformation processes, which typically generates bare metal surface. Such sites can play a vital role in the initiation of corrosion processes.

Further plastic deformation to ≈10% total macroscopic strain enhanced the deformation activity in the bulk material, with more slip bands emerging primarily in the austenite, but also in the ferrite as shown in Figure 6-27(c). The Volta potential differences between ferrite and austenite decreased to 20 ± 15 mV. Austenite was on average slightly more cathodic than the ferrite by only 5 mV, indicating that plastic deformation decreased the Volta potential differences within the duplex microstructure. This would mean that a lower galvanic interactivity between ferrite and austenite is expected. Similar observation was reported after 40% cold rolling of 2205 duplex stainless steel [12]. Anodic and cathodic Volta potential fields at confined regions (hot-spots) with discrete geometries became more apparent indicating a possible driving force for local galvanic activity. Similar observation was also observed on copper, with an increase of dislocation density due to plastic deformation was found to decrease the electron work function of copper, indicating enhanced electrochemical activity [26].

The Volta potential roughness parameter (Ψ_{Ra}) increased to 5.8 mV for the austenite and 6.3 mV for the ferrite, with a maximum potential variation in each phase further of 35 and 43 mV for austenite and ferrite, respectively. This indicates heterogeneous Volta potential sites in each phase, promoting local galvanic activity. The Volta potential roughness and maximum Volta potential variation of ferrite and austenite as a function of tensile strain is summarised in Figure 6-28. Here the effect of applied strain on changes in Volta potential differences of ferrite and austenite becomes clearer, indicating initially small changes in

the ferrite, accompanied by larger potential changes in the austenite. This is in line with DIC observations of strain localisation at interfaces and austenite, followed by the ferrite taking up more strain. The latter seems to affect the Volta potential differences as well, as summarised in Figure 6-28.

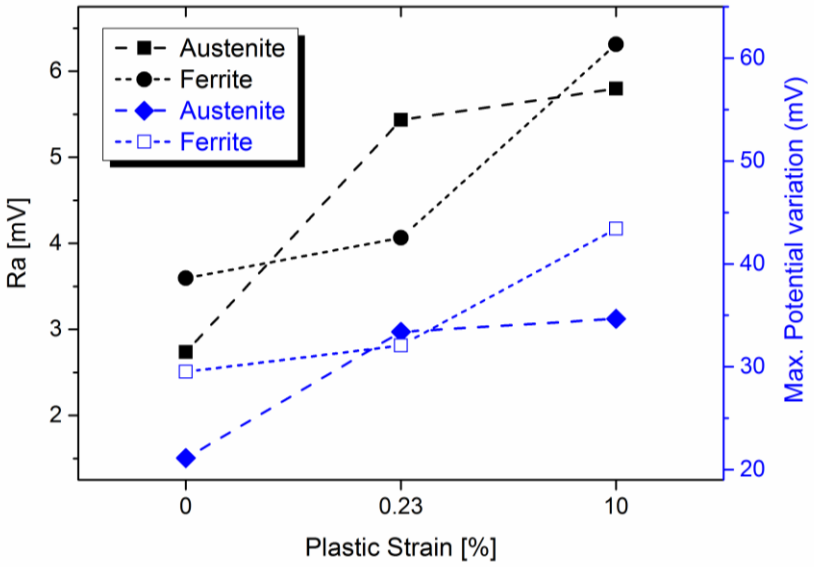

Figure 6-28: SKPFM analysis of Volta potential roughness (Ra) values with maximum potential variation

6.4.5 Conclusions

Strain partitioning with Volta potential development in 2205 duplex stainless steel has been analysed and can be summarised:

1) Digital image correlation analysis of quasi in-situ strained micro-tensile specimens showed local strain development primarily in the austenite. Discrete heterogeneous strain fields within austenite grains indicated higher work hardening behaviour and stiffness of austenite than ferrite.
2) Work hardening of the austenite enabled the ferrite to accommodate more plastic strains which led to the evolution of heterogeneous strain fields within ferrite regions.
3) X-ray diffraction stress measurements showed that strain localisation does not necessarily indicate stress localisation; ferrite showed almost double the stress than austenite during quasi in-situ straining to 0.2% macroscopic strain.

4) SKPFM Volta potential measurements showed reduced Volta potential differences between ferrite and austenite with the introduction of macroscopic deformation.
5) The introduction of tensile strain increased the Volta potential roughness (Ψ_{Ra}) and the maximum potential variation across ferrite and austenite phases, leading to the development of discrete cathodic and anodic Volta potential sites.

6.4.6 Acknowledgement

The authors acknowledge Radioactive Waste Management (RWM) (NPO004411A-EPS02) and EPSRC (EP/I036397/1) for financial support. The authors are grateful for the kind provision of Grade 2205 Duplex Stainless Steel plate by Rolled Alloys. Mr Gary Harrison, University of Manchester is thanked for his support during XRD stress measurements.

6.4.7 References

[1] E. Settoon. Comparative study of corrosion and environmental cracking properties of 316L and lean duplex alloys. Stainless Steel World. Zutphen, The Netherlands: KCI Publishing B.V., 2011.

[2] F. Wischnowski. Einfluss mikrostruktureller Gefügeveränderungen auf die Korrosionsresistenz von nichtrostenden ferritisch-austenitischen Duplex-Stählen. vol. PhD Thesis. Bochum, Germany: Technical University of Bochum, 1995. p.264.

[3] R.N. Gunn. Duplex Stainless Steel - Microstructure, Properties, and Applications. 2nd ed., Abington Publishing, Cambridge, England, 2003.

[4] H.-J. Bargel, G. Schulze, H. Hilbrans, K.-H. Hübner, O. Krüger. Werkstoffkunde. 9th Edition ed., Springer-Verlag, Heidelberg, Germany, 2005.

[5] J.-O. Nilsson, G. Chai. The physical metallurgy of duplex stainless steels. International Conference & Expo Duplex 2007. Grado, Italy: Associazone Italiana di Metallurgia (AIM), 2007.

[6] J. Johansson, M. Odén, X.H. Zeng. Evolution of the residual stress state in a duplex stainless steel during loading, Acta Materialia 47 (1999) 2669-2684.

[7] J. Johansson, M. Odén. Load sharing between austenite and ferrite in a duplex stainless steel during cyclic loading, Metall and Mat Trans A 31 (2000) 1557-1570.

[8] F. King. Corrosion Resistance of Austenitic and Duplex Stainless Steels in Environments Related to UK Geological Disposal. 2009.

[9] Nuclear Decommissioning Authority. Geological Disposal, Steps Towards Implementation - Executive Summary. Didcot, Oxfordshire: Nuclear Decommissioning Authority, 2010.

[10] A.B. Cook, S.B. Lyon, N.P.C. Stevens, M. Gunther, G. McFiggans, R.C. Newman, D.L. Engelberg. Assessing the risk of under-deposit chloride-induced stress corrosion cracking in austenitic stainless steel nuclear waste containers, Corrosion Engineering, Science and Technology 49 (2014) 529-534.

[11] D.L. Engelberg, C. Örnek. Probing propensity of grade 2205 duplex stainless steel towards atmospheric chloride-induced stress corrosion cracking, Corrosion Engineering, Science and Technology 49 (2014) 535-539.

[12] C. Örnek, D.L. Engelberg. SKPFM measured Volta potential correlated with strain localisation in microstructure to understand corrosion susceptibility of cold-rolled grade 2205 duplex stainless steel, Corrosion Science 99 (2015) 164-171.

[13] C. Örnek, D.L. Engelberg. Correlative EBSD and SKPFM characterisation of microstructure development to assist determination of corrosion propensity in grade 2205 duplex stainless steel, Journal of Materials Science (2015) 1-18.

[14] T. Pan. Corrosion behavior of a duplex stainless steel under cyclic loading: a scanning Kelvin probe force microscopy (SKPFM) based microscopic study, J Appl Electrochem 42 (2012) 1049-1056.

[15] M. Rohwerder, F. Turcu. High-resolution Kelvin probe microscopy in corrosion science: Scanning Kelvin probe force microscopy (SKPFM) versus classical scanning Kelvin probe (SKP), Electrochimica Acta 53 (2007) 290-299.

[16] P. Schmutz, G.S. Frankel. Characterization of AA2024-T3 by Scanning Kelvin Probe Force Microscopy, Journal of The Electrochemical Society 145 (1998) 2285-2295.

[17] I.O.f.S. (ISO). ISO 4287:1997 - Geometrical product specifications (GPS)–Surface texture: Profile method–Terms, definitions and surface texture parameters. Switzerland: International Organization for Standardization (ISO), 1997.

[18] A. El Bartali, V. Aubin, S. Degallaix. Fatigue damage analysis in a duplex stainless steel by digital image correlation technique, Fatigue & Fracture of Engineering Materials & Structures 31 (2008) 137-151.

[19] B. Verhaeghe, F. Louchet, B. Doisneau-Cottignies, Y. Bréchet, J.-P. Massoud. Micromechanisms of deformation of an austenoferritic duplex stainless steel, Philosophical Magazine A 76 (1997) 1079-1091.

[20] S. Rai, B.K. Choudhary, T. Jayakumar, K.B.S. Rao, B. Raj. Characterization of low cycle fatigue damage in 9Cr–1Mo ferritic steel using X-ray diffraction technique, International Journal of Pressure Vessels and Piping 76 (1999) 275-281.

[21] J.-M. Kim, H.-T. Chung. Electrochemical characteristics of orthorhombic LiMnO2 with different degrees of stacking faults, Journal of Power Sources 115 (2003) 125-130.

[22] S. Aoki, H. Yakuwa, K. Mitsuhashi, J.i. Sakai. Dissolution Behavior of α and γ Phases of a Duplex Stainless Steel in a Simulated Crevice Solution, ECS Transactions 25 (2010) 17-22.

[23] S. Aoki, K. Ito, H. Yakuwa, M. Miyasaka, J.i. Sakai. Potential Dependence of Preferential Dissolution Behavior of a Duplex Stainless Steel in Simulated Solution inside Crevice, Zairyo-to-Kankyo 60 (2011) 363-367.

[24] J.-S. Lee, K. Fushimi, T. Nakanishi, Y. Hasegawa, Y.-S. Park. Corrosion behaviour of ferrite and austenite phases on super duplex stainless steel in a modified green-death solution, Corrosion Science (2014).

[25] C. Örnek, D.L. Engelberg, S.B. Lyon, T.L. Ladwein. Effect of "475°C Embrittlement" on the Corrosion Behaviour of Grade 2205 Duplex Stainless Steel Investigated Using Local Probing Techniques. Eurocorr 2013. Estoril, Portugal: European Corrosion Congress, 2013.

[26] W. Li, D.Y. Li. Variations of work function and corrosion behaviors of deformed copper surfaces, Applied Surface Science 240 (2005) 388-395.

7 Environment-assisted Cracking (EAC) Propensity

7.1 General Introduction

Grade 2205 duplex stainless steel may be rendered susceptible to stress corrosion cracking or hydrogen embrittlement in environments above 50°C. Most research on environment-assisted cracking of 2205 duplex stainless steel was carried out on elevated temperatures with harsh exposure conditions which, often, have little or even no practical relevance for ILW storage applications in the UK. Corrosion and cracking events have been reported to occur at and below 50°C for 2205 duplex stainless steel but the corrosive conditions were extremely high which may be questioned for their practical relevance. Therefore, questions have arisen about the cracking susceptibility and crack velocities of 2205 duplex stainless steel in application-relevant environments that is contaminated surfaces with 10's to a few 1000's of deposition densities of chloride, typically containing Mg^{2+} as cation which is the most critical salt constituent in sea water evaporates.

The long-term behaviour of 2205 duplex stainless steel under atmospheric corrosion exposure conditions is unknown. Most tests reported were limited to exposure times less than 1 year, and post-mortem examinations to validate whether stress corrosion cracking occurred was often performed by optical microscopy analysis only which has spatial resolution limit, typically not better than 1 µm. No stress corrosion cracking was observed under magnesium chloride deposits containing less than a few 1000's of chloride deposition densities which led to the conclusion that 2205 duplex stainless steel is safe from stress corrosion cracking. However, crack incubation times of duplex stainless steels are by far longer than their austenitic counterparts and short testing times (< 6 months) may not reflect long-term stress corrosion cracking resistance of duplex stainless steels. In addition, small cracks may have already initiated but could not be detected in optical microscopy analysis wherefore electron microscopy imaging may be required.

Over many decades, cracking events occurring in chloride-bearing media have been described as chloride-induced stress corrosion cracking, and hydrogen embrittlement has been, usually, observed under cathodically charged conditions, or in media containing extensive hydrogen, such as H_2S, only. It has often been believed that the presence of one type of cracking excludes the other and both do not occur simultaneously.

Furthermore, ferritic stainless steels have been often regarded as immune against stress corrosion cracking in chloride-bearing environments which led to the conclusion that the ferrite phase in duplex stainless steel may not be rendered susceptible to stress corrosion cracking, in particular under atmospheric chloride deposits.

In this chapter, it will be shown that 2205 duplex stainless steel can be rendered susceptible to stress corrosion cracking under non-severe atmospheric corrosion conditions containing chloride species and that the pH plays vital role in stress corrosion cracking, as such it decreases crack incubation time and increases crack growth rates. Chloride-induced stress corrosion cracking will occur in the austenite phase only in neutral or little acidic conditions while at very low pH conditions hydrogen embrittlement or hydrogen-assisted stress corrosion cracking of ferrite and, to some extent, in austenite as well can be additionally prevalent. Short cracks will be discussed in light of their impact on the structural integrity of ILW container material.

7.2 Probing Propensity of Grade 2205 Duplex Stainless Steel towards Atmospheric Chloride-induced Stress Corrosion Cracking

D. L. Engelberg & C. Örnek

Materials and Performance Centre & Corrosion and Protection Centre,
School of Materials, The University of Manchester, Sackville Street, Manchester, M13 9PL, United Kingdom

7.2.1 Abstract

The propensity of grade 2205 duplex stainless steel towards atmospheric chloride-induced stress corrosion cracking at 50°C has been investigated. Electron backscatter diffraction has been used to characterise crystallographic phases present in an as-received and at 750°C heat-treated microstructure. Screening tests in chloride-containing aqueous environments were employed to investigate the corrosion behaviours, indicating significantly increased corrosion rates when exposed to HCl or $FeCl_3$–containing solutions. Stress corrosion cracking testing with atmospheric exposures for 1 year showed selective dissolution of the ferrite, with localised corrosion accompanied by stress corrosion micro-cracks in the austenite. This work demonstrates that grade 2205 duplex stainless steel microstructure may be rendered susceptible to stress corrosion cracking under atmospheric exposure conditions at 50°C.

Keywords: *Duplex Stainless Steel, Microstructure, Electron Backscatter Diffraction (EBSD), Stress Corrosion Cracking, Localized Corrosion, Selective Corrosion.*

7.2.2 Introduction

The UK's Intermediate Level radioactive Waste (ILW) is stored in Type 316L and 304L austenitic stainless steels containers and drums, which have so far shown excellent resistance in service to Atmospheric Chloride-Induced Stress Corrosion Cracking (AISCC) [1, 2]. The disposal scenario for ILW considers above ground interim storage for several decades, followed by an extended storage period in a Geological Disposal Facility (GDF) before the facility vaults are backfilled and sealed. However, since no GDF is yet available and the time-scale for implementing the latter is becoming more-and-more uncertain, an extended

period of interim storage is currently anticipated. It is therefore key to underpin existing knowledge of the behaviour of stainless steels under extended storage periods, in particular whether anticipated environmental conditions lie within the safe operating envelope to ensure the long-term integrity of ILW packages.

It has been demonstrated that AISCC can occur in types 304 and 316 austenitic stainless steels in laboratory exposures at temperatures far below 60°C, by using controlled salt deposits (e.g. $MgCl_2$, $CaCl_2$, artificial seawater) in a range of relative humidities (RH) [3-6]. Though, it has been recognised that conditions employed for AISCC laboratory testing frequently rely on far too aggressive, non-representative environmental conditions [4, 6, 7]. In parallel to have more corrosion and SCC resistant material options available it is important to test these materials for their propensity towards AISCC, such as high-alloyed austenitic stainless steels (e.g. grade 904 [3]) or duplex stainless steels (e.g. grades 2205 & 2304 [3]). Most duplex stainless steel grades are considered as having superior SCC resistance to their austenitic counterparts, making this material attractive as a potential replacement option for more durable ILW storage containers [3, 8, 9].

The work reported in this paper is part of a larger research project to explore the propensity of grade 2205 duplex stainless steel microstructure towards AISCC. Long-term material behaviour with exposure periods of 1 year under chloride-containing atmospheric exposures is reported in this paper.

7.2.3 Experimental Methods

The material used in this study was an as-received, mill-annealed grade 2205 duplex stainless steel (UNS32205) plate with a composition of (wt.) 22.4% Cr, 5.8% Ni, 3.2% Mo, 1.5%Mn, 0.4% Si, 0.016%C, 0.18%N and Fe% (bal.). Rectangular specimens were cut from the as-received plate and the microstructure metallographically characterised. A second set of samples was heat treated in air at 750°C for 300 minutes followed by a water quench to simulate the effect of second phase precipitation on microstructure behaviour. Metallographic assessments of microstructure were performed on 0.06 µm colloidal-silica (OP-S) fine polished sample surfaces. Electron Backscatter Diffraction (EBSD) was carried out to identify and quantify crystallographic phases using a FEI Quanta 650 scanning electron microscope interfaced with a HKL Nordlys EBSD detector and Aztec Version 2.2

data acquisition software. Data post processing was undertaken with Oxford Instruments Channel 5 software and the in-house software programme Vmap. The high angle grain boundary threshold was set to misorientations >15°.

Corrosion screening tests were conducted by exposing small coupon samples (10 x 10 x 10 mm^3) to aqueous chloride-containing solutions. Immersion tests were conducted to obtain information about the corrosion propensity of both microstructures. Coupon samples were exposed in glass beakers for 49 days at 50°C to (i) 1 molar hydrochloric acid (HCl), (ii) 0.5 and (iii) 1 molar $MgCl_2$, and (iv) 0.167 molar $FeCl_3$. The corrosion behaviour of all coupon samples was determined by weight loss and examination of the post-exposure coupon surfaces using scanning electron microscopy imaging.

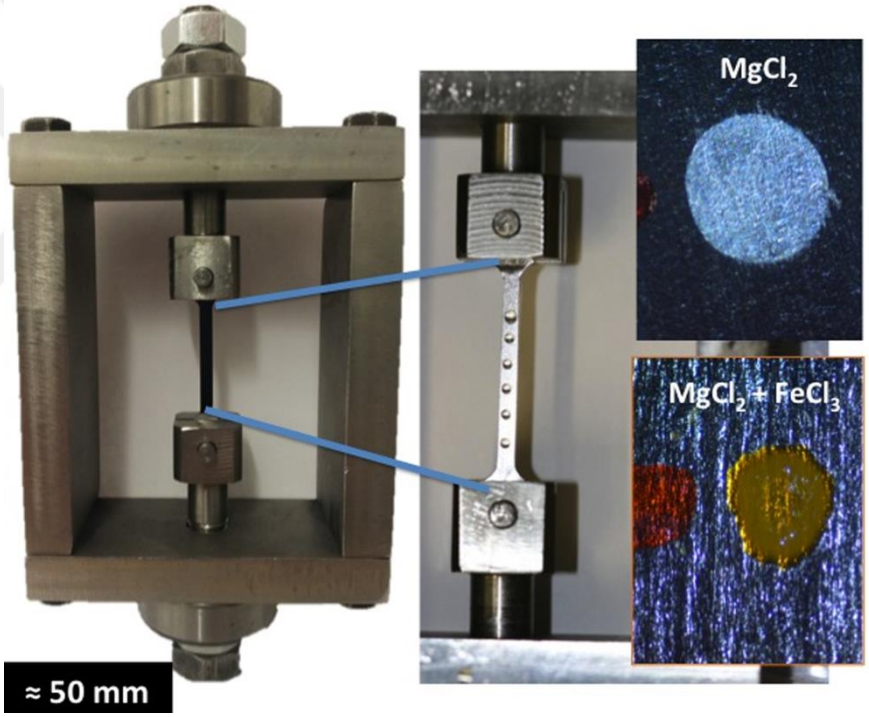

Figure 7-1: Home-made direct tension AISCC test rig with miniature tensile sample and 6 deposited salt droplets (shown in the inset image). The appearance of a typical droplet of $MgCl_2$ (top) and $MgCl_2$ with $FeCl_3$ (bottom) is shown on the right.

AISCC tests were carried out by depositing droplets of various concentrations of aqueous $MgCl_2$, $FeCl_3$, or mixtures of $MgCl_2$: $FeCl_3$ solutions onto the surfaces of micro-tensile samples, and exposing the sample to controlled environmental conditions at 50°C and 30% RH in a Binder KBF 240 climate chamber. Droplets with chloride deposition densities from

0.2 to a maximum of 2000 µg/cm^2 with droplet volumes between 0.5 and 2.5 µl were investigated. A number of microstructures tests were set-up containing as-received, 10% to 40% cold rolled, and at 750°C for 5 hours heat-treated samples. Some of the exposed sample surfaces were stained in a 20 wt.-% KOH solution to provide contrast for imaging analysis and correlation, and to identify which crystallographic phase corroded first. Different levels of strain were applied to these samples via the direct tension set-up shown in Figure 7-1. During the 12 months exposure period all samples were removed from the climatic chamber at regular intervals and the surface imaged with a stereomicroscope. (Note: fluctuations in RH with values of up to 60% were observed during the last two weeks of exposure and all long-term tests were therefore terminated after 12 months only). After AISCC exposure all samples were rinsed in hot water, the extent of corrosion/cracks imaged in a microscope, and the sample then thoroughly cleaned in 10 wt.-% citric acid at 80°C to remove salt deposits and corrosion products. This paper reports the first preliminary results of these AISCC exposures with a more comprehensive investigation under way.

7.2.4 Results & Discussion

The as-received and 750°C heat-treated microstructures are shown in Figure 7-2. Analysis of the as-received microstructure indicates that only austenite (γ) and ferrite (δ/α) were present with a ratio of 57 : 43 %. Image analysis of KOH etched samples gave a similar ratio, and confirmed that the as-received microstructure was free of second phase precipitates (or beyond the detection limit). The microstructure can be described as large austenitic islands embedded in a ferritic matrix, where ferrite has a continuous structure (Figure 7-2 a). A mean grain size of 7-8 µm in both the ferrite and the austenite phase was obtained, with however maximum grain dimensions measured of up to 35-45 µm.

The 750°C heat-treated microstructure is shown in Figure 7-2(b), containing 47% austenite, 36% ferrite, 14-15% sigma (σ), and ca. 2% chi (χ)-phase. High-resolution EBSD analysis also indicated the presence of ca. 0.5% Cr_2N in the microstructure. According to phase transformation kinetics in the 750°C temperature regime, part of the ferrite transforms via the eutectoid reaction: $\delta/\alpha \rightarrow \sigma + \chi + Cr_2N$ (e.g. [10-12]). Secondary austenite (γ_2) may also form at this heat treatment temperature, which could however not be differentiated by EBSD from the pre-existing austenite in the microstructure. $M_{23}C_6$ type chromium carbides are also

expected to have formed during the annealing process in similar fraction to Cr_2N [11]. Interestingly, the overall fraction of austenite was expected be the same or even larger than in the as-received microstructure, but was found to be ca. 10% lower. The reason for this is not clear, but may be related to the small sampling volume for EBSD analysis.

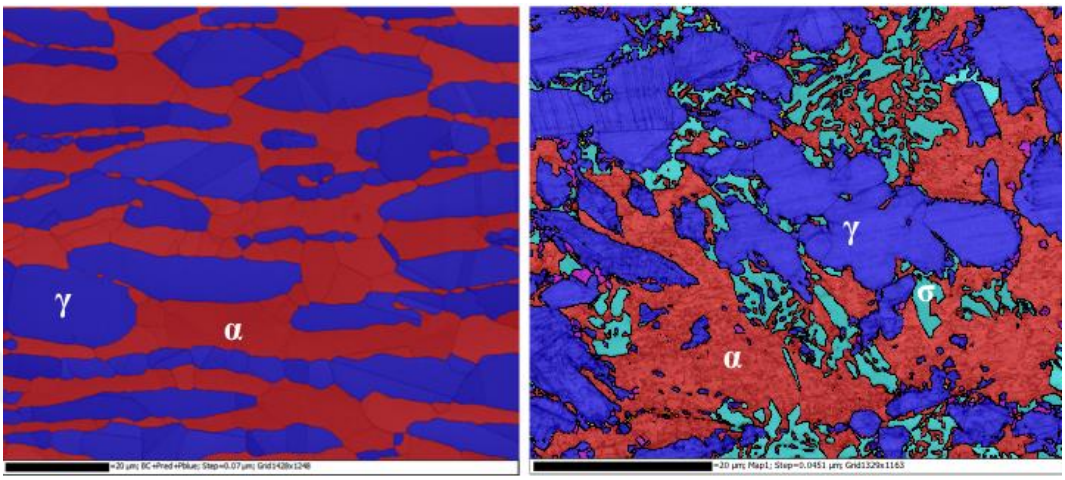

Figure 7-2: EBSD phase maps of the (a) as-received and (b) 750°C heat-treated microstructures, with ferrite (α) in red, austenite (γ) in blue, sigma phase (σ) in turquoise, chi phase (χ) in lilac, and Cr_2N in yellow, with superimposed interface and grain boundaries in light-grey.

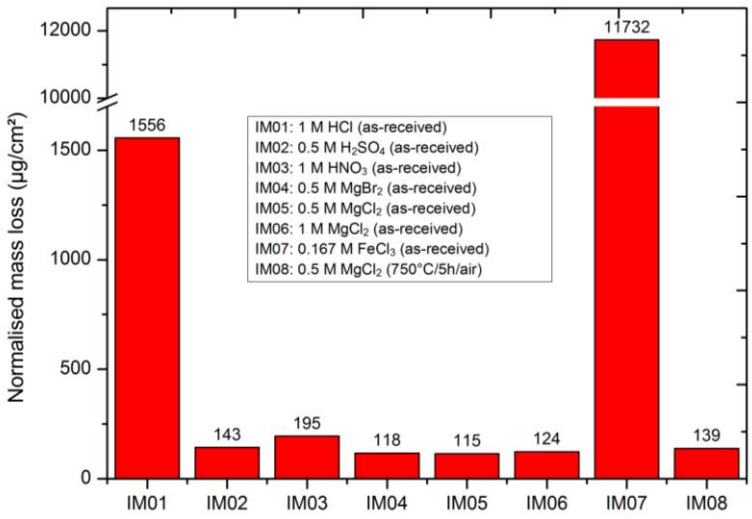

Figure 7-3: Weight loss results of as-received (IM01, 05, 06, 07) and 750°C heat-treated (IM08) samples after immersion in different aqueous environment for 49 day at 50°C.

7.2.4.1 Corrosion Screening in Aqueous Environment

The weight loss of samples immersed in various aqueous environments is summarised in Figure 7-3. Samples exposed to 0.5 and 1 M $MgCl_2$ solutions (IM05, 06) indicated similar weight loss with corrosion rates of 1-2 μm/yr, if a density of 7.8g/cm^3 is assumed. Figure 7-4(a) shows images of the as-received microstructures after exposure to 0.5 M $MgCl_2$ showing that pitting corrosion and lacy cover formation had occurred. Pit nucleation seemed to be associated with the austenitic phase, with however growth occurring along both phases. Interestingly, exposure of the at 750°C heat-treated microstructure to 0.5 M $MgCl_2$ gave similar weight loss results to the as-received material (IM08), indicating that only localised corrosion had occurred in this sample. This was confirmed by inspecting the surface of this sample in the microscope.

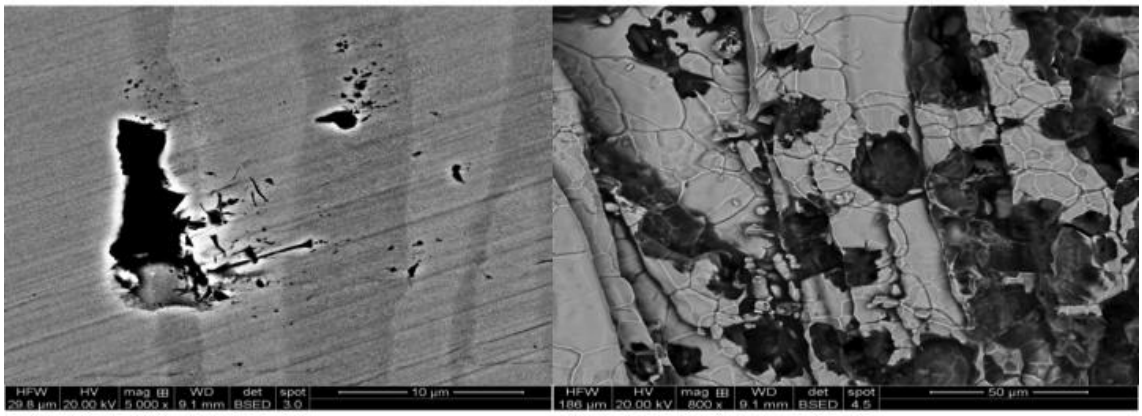

Figure 7-4: Images of the surface of the as-received microstructure after 49 days of immersion in (a) 0.5 M $MgCl_2$ (IM05) and (b) in 0.167 M $FeCl_3$ (IM07).

In contrast exposure of the as-received microstructure to 1 M HCl and 0.167 M $FeCl_3$ resulted in corrosion rates respectively 10 and 100 times larger. The application of HCl was chosen to provide information about the effect of pH on localised corrosion in chloride-bearing environment. The reduced nickel content of duplex stainless steel compared to their austenitic counterparts is deleterious when exposed to reducing conditions, such as HCl-containing solutions [13]. The effect of $FeCl_3$ on the significantly increased corrosion rate can most likely be related to the higher oxidising potential and therefore pitting corrosion promoting nature of this environment compared to $MgCl_2$ (e.g. ASTM G48). Figure 7-4(b) shows the surface of the as-received sample after exposure to $FeCl_3$ containing solution, indicating severe pitting corrosion accompanied by widespread selective corrosion of the ferrite. These tests were carried out at 50°C, which is far above typical threshold pitting

temperatures reported for $FeCl_3$ solution exposure, e.g. for 6% $FeCl_3$ 15–30°C [13]. It is also not clear whether selective dissolution or micro-galvanic coupling between the ferrite and austenite is responsible for the selective corrosion attack. Interestingly, similar behaviour of a selective corrosion pathway, by dissolving the ferrite whilst the austenite remains mostly unaffected was observed during $MgCl_2$ induced-atmospheric corrosion tests of duplex grade 2205 and 2507 stainless steels [14].

7.2.4.2 Atmospheric-induced Stress Corrosion Cracking Testing at 50°C

The surface of an as-received micro-tensile sample with a droplet containing 0.5 µl mixed $MgCl_2$:$FeCl_3$ and a chloride deposition density of 390 µg/cm^2 is shown in Figure 7-5. The sample was tensile strained before exposure to 3% and regular observations indicated corrosion occurring after less than 63 days, which was apparent by corrosion products present within the salt droplet. After 1 year of exposure and termination of the test small stress corrosion cracks were observed (Figure 7-5(b)). These micro-cracks seemed predominantly be associated with local corrosion sites in the austenite, and the presence of almost parallel cracks also indicated the possible involvement of slip planes in the local nucleation processes. Chloride-induced SCC is typically driven by a tri-axial stress state in the presence of a tensile principal stress, whereas the presence of compressive principal stress may retard cracks [15, 16]. The observed cracks in Figure 7-5 (b) are small in length, but nevertheless may grow over time. The observed crack length in austenite varied between 100's nm to 15 µm.

Chloride-induced SCC of duplex stainless steel has been reported in a range of environments, often associated with boiling $CaCl_2$ or $MgCl_2$ solution at temperatures in excess of 100°C [9]. SCC was also shown to occur in grades 2205 and 2507 below the yield stress at temperatures of 70°C and 80°C using a seawater drop evaporation test methods [17]. AISCC on U-bend samples of grade 2205 was observed under large 30% $MgCl_2$ droplets at 40°C and 35% RH [6] Interestingly, The conditions applied here in our paper to produce AISCC were far more benign, with exposure to only 50°C; though with the addition of $FeCl_3$. The full set of exposed samples is currently assessed and will be reported in another publication.

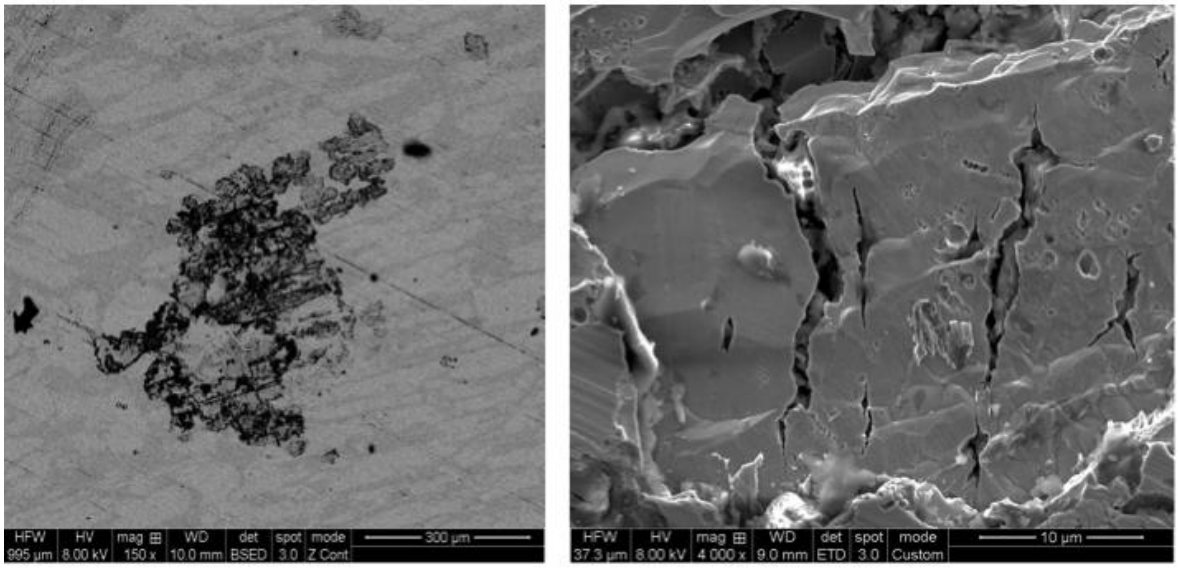

Figure 7-5: SEM images of (a) local attack on the as-received sample after 1 year of exposure at 50°C, and (b) higher resolution image of local corrosion sites with micro stress corrosion cracks in the austenite. The sample was strained to 3%, and a 0.5 µl droplet of 390 µg/cm² $MgCl_2$ with $FeCl_3$.

7.2.5 Conclusions

1) Two different grade 2205 microstructure were investigated, with the as-received microstructure only containing austenite and ferrite, whereas the 750°C heat-treated microstructure also had sigma, chi, and chromium nitride second phases.
2) Immersion corrosion tests in 0.167 M ferric chloride indicated weight loss after 49 days exposure at 50°C, followed by 1 M hydrochloric acid. This showed the effect of ferric ions as corrosion promoters. The effect of magnesium chloride and magnesium bromide on the weight loss was similar and apparently of weaker aggressivity than ferric chloride and hydrochloric acid. Slightly more corrosion was observed on 0.5 M sulphuric acid and 1 M nitric acid exposed samples in comparison to the salt solutions. This clearly showed the effect of chloride. After heat treatment at 750°C/5h, grade 2205 suffers from corrosion resistance loss in comparison to its as-received (precipitate-free) condition.
3) AISCC tests showed selective corrosion of the ferrite, whereas the austenite showed pits and micro cracks after one year exposure at 50°C, with maximum crack lengths observed in the austenite up to 15 µm.

7.2.6 Acknowledgements

The authors acknowledge EPSRC (EP/I036397/1) and NDA (NPO004411A-EPS02) for financial support. DLE acknowledges valuable discussions with Dr Cristiano Padovani (NDA) and Dr Alison Davenport (University of Birmingham). We are grateful for the kind provision of Grade 2205 Duplex Stainless Steel plate by Rolled Alloys.

7.2.7 References

[1] (NDA), N.D.A., *Geological Disposal - Package Evoluiton Status*. 2010.

[2] Fennel, P.A.H., Smart, N.R.; Winsley, R.J.; Reddy, B.; Rance, A.P.; Padovani, C., *Characterisation of Environmental Conditions in an ILW Store*. 2012, AMEC (D.005265/001).

[3] Prosek, T., Iversen, A., Taxén, C., Thierry. D.: , *Low-Temperature Stress Corrosion Cracking of Stainless Steels in the Atmosphere in the Presence of Chloride Deposits.* Corrosion, 2009. **65**(2): p. 105-117.

[4] Cook, A.B.; Lyon, S.B.; Stevens, N. P. C.; Gunther, M.; Newman, R.C.; Engelberg, D.L., *Assessing the Risk of Under-Deposit Chloride-Induced Stress Corrosion Cracking in Austenitic Stainless Steel Intermediate Level Nuclear Waste Containers.* Corrosion, Engineering, Science and Technology, 2014. **49**(6): p. 529-534.

[5] Albores-Silva, O.E.C., E.A.; Padovani, C., *Effect of chloride deposition on the stress corrosion behaviour of 316L stainless steel used for intermediate level radioactive waste containers.* Corrosion Engineering, Science and Technology, 2011. **46**(2): p. 124-128.

[6] Arnold, N.G., P.; Heitz, T.; Pscheidl, P., *Chloride induced corrosion on stainless steels at indoor swimming pools atmospheres - Part 1 : electrolyte magnesium-chloride (30 YO).* Materials and Corrosion, 1997. **48**: p. 679-686.

[7] Cook, A.B.G., B.; Lyon, S.B.; R.C. Newman, R.C.; Engelberg, D.L., *Towards a more Realistic Experimental Protocol for the Study of Atmospheric Chloride-Induced Stress Corrosion Cracking in Intermediate Level Radioactive Waste Container Materials*, in MRS *Scientific Basis for Nuclear Waste Management XXXVII*. 2014, MRS: Barcelona.

[8] King, F., *Corrosion Resistance of Austenitic and Duplex Stainless Steels in Environments Related to UK Geological Disposal*. 2009, Quintessa Report: QRS-1384C-R1: Report to the NDA.

[9] Kangas, P. and J.M. Nicholls, *Chloride-induced Stress Corrosion Cracking of Duplex Stainless Steels - Models, Test Methods and Experience.* Materials and Corrosion, 1995. **46**: p. 354-365.

[10] Michalska, J. and M. Sozanska, *Qualitative and Quantitative Analysis of Sigma and Chi Phases in 2205 Duplex Stainless Steel.* Material Characterization, 2006. **56**: p. 355-362.

[11] Calliari, I.B., K.; Dabalà, M.; Ramous, E., *Measuring secondary phases in duplex stainless steels.* JOM Journal of the Minerals, Metals and Materials Society, 2009. **61**(1): p. 80-83.

[12] Nilsson, J.-O.; Kangas, P.; Wilson, A.; Karlsson, T., *Mechanical properties, microstructural stability and kinetics of σ-phase formation in 29Cr-6Ni-2Mo-0.38N superduplex stainless steel.* Metallurgical and Materials Transactions A, 2000. **31**(1): p. 35-45.

[13] *Practical Guidelines for the Fabrication of Duplex Stainless Steels*. 2009, International Molybdenum Association: London, UK.

[14] Örnek, C.; Ahmed, A.H.; Engelberg, D.L., *Effect of Microstructure on Atmospheric-Induced Corrosion of Heat-treated Grade 2205 and 2507 Duplex Stainless Steels*, in *EuroCorr2012*. 2012: Istanbul, Turkey. p. Paper 1355.

[15] Trethewey, K.R., *Some Observations on the Current Status in the Understanding of Stress-Corrosion Cracking of Stainless Steels.* Materials and Design, 2008. **29**(2): p. 501-507.

[16] Trethewey, K.R.; Wenman, M.; Chard-Tuckey, P.; Roebuck, B., *Correlation of Meso- and Micro-scale Hardness Measurements with the Pitting of Plastically-deformed Type 304L Stainless Steel.* Corrosion Science, 2008. **50**(4): p. 1132-1141.

[17] Hinds, G. and A. Turnbull, *Threshold Temperature for Stress Corrosion Cracking of Duplex Stainless Steel Under Evaporative Seawater Conditions.* Corrosion 2008. **64**(2): p. 101-106.

7.3 Low-Temperature Environmentally Assisted Cracking of Grade 2205 Duplex Stainless Steel Beneath a $MgCl_2$:$FeCl_3$ Salt Droplet

Cem Örnek[1,2], Xiangli Zhong[3], and Dirk L. Engelberg[1,2]

[1]Corrosion and Protection Centre, School of Materials, The University of Manchester, Sackville Street Campus, Manchester, M13 9PL, United Kingdom

[2]Materials Performance Centre, School of Materials, The University of Manchester, Sackville Street Campus, Manchester, M13 9PL, United Kingdom

[3]Electron Microscopy Centre, The University of Manchester, Sackville Street Campus, Manchester, M13 9PL, United Kingdom

7.3.1 Abstract

The corrosion and environment-assisted cracking susceptibility of grade 2205 duplex stainless steel beneath a $FeCl_3$:$MgCl_2$ containing salt deposit has been investigated. Long-term exposure to atmospheric environment at 50°C and 30% relative humidity resulted in different forms of corrosion and the formation of cracks depending on the location under the salt-laden droplet. Selective dissolution with closely-spaced micro-cracks of the ferrite suggested hydrogen embrittlement towards the center of the droplet, with chloride-induced stress corrosion cracking and selective dissolution of the austenite observed towards the rim of the deposit. Cracks in the ferrite had cleavage-like appearances, typically forming within existing cracks, whereas the austenite had branched cracks, initiating from crevices and pits. These observations are discussed in light of expected electrochemical potential variations beneath the droplet.

Key words: *Duplex stainless steel; Atmospheric Corrosion; Hydrogen Embrittlement; Stress Corrosion Cracking; Selective Corrosion*

7.3.2 Introduction

Duplex stainless steels (DSS) possess superior mechanical and electrochemical properties compared to their austenitic and ferritic counterparts. A balanced phase ratio of ferrite to austenite provides synergistic microstructure effects, where one crystallographic phase protects and supports the other phase [1-6]. How and in which way the microstructure provides resistance is a combination of material condition and environmental exposure

characteristics [1, 3]. For example, selective corrosion of ferrite was observed in grade 2205 DSS under chloride-containing salt-laden deposits at 50-70°C and 30-50% relative humidity (RH) [7-12]. Corrosion of ferrite occurred despite the higher chromium and molybdenum contents compared to the austenite, and this behavior was also observed under immersed conditions [13-17], supported by similar findings with far less attack on the austenite [13, 14, 18]. However, when duplex stainless steels are exposed to sulphurous media the austenite phase has been reported to corrode preferentially [19, 20]. Typically, at high anodic over-potentials the austenite tends to be primarily attacked [16-18, 21, 22]; hence the prevailing redox potential of the environment determines the selective corrosion morphology of duplex stainless steels [16, 17, 22].

The austenite phase also becomes more susceptible to localized corrosion with increasing cold deformation due to the development of highly-active local deformation sites (hot-spots), which is also reflected in Volta potential differences measured between a Pt-probe and the surface [23, 24]. These Volta potential "hot-spots", obtained by Scanning Kelvin Probe Force Microscopy (SKPFM), are primarily associated with regions containing plastic strain [23, 24]. Therefore, the corrosion susceptibility of individual phases in duplex stainless steels should be considered in light of alloy composition, solution chemistry, local electrochemical potential, as well as microstructure processing condition.

Initiation and growth of localized corrosion can occur in atmospheric environment, and, hence transition to atmospheric-induced stress corrosion cracking (AISCC) is frequently facilitated [25-27]. Key environmental parameter controlling AISCC are mainly the RH and temperature, with the amount of salt (often stated as salt/chloride deposition density), the deposit size and distribution, salt composition, and the time of wetness considered to play an important role [26-34]. Organic species have also been reported to promote corrosion and stress corrosion cracking (SCC) in stainless steels [31, 32]. Chloride-containing salt deposits can form concentrated thin-film electrolyte layers at the salt-metal interface with exposure to deliquescence relative humidity conditions [28, 30-32, 35-37]. The chloride concentration of such thin-film electrolytes can be up to 12 M at the deliquescence point of the salt, if for example $MgCl_2$ is used. The concentration can reach 15 M at 50°C, or become even higher in the presence of other chloride salts, such as $FeCl_3$ [11, 35, 36, 38, 39]. The RH, the temperature, and the type of salt cation determine the chloride concentration of the electrolyte layer and, hence the corrosion activity [28, 31, 32, 37].

Although SCC has widely been studied in stainless steels, the effect of microstructure mechanics on the failure behavior has often been not considered at all. Most research has been carried out at temperature above 100°C, or by using fairly aggressive environments. Research on AISCC of duplex stainless steels was typically conducted by exposing the material to excessive concentrations of chloride, resulting in exposure conditions less relevant to real service application [11, 12, 40-42]. Materials subjected to environmental conditions in the lower temperature regime (≤ 50°C), for example, to simulate storage conditions for intermediate-level radioactive waste (ILW) containers may become susceptible to localized corrosion during long-term storage [43-47]. The container surfaces are typically exposed to atmospheres with changing RH's, in which the chloride contamination of the surface accumulates over time [44-47]. Knowledge of material behavior in chloride containing atmospheres has therefore vital importance to guarantee long-term structural integrity of DSS waste storage containers.

The work reported in this paper investigates the relationship between DSS microstructure and local exposure conditions beneath a salt-laden droplet at 50°C. Key aim was to determine local microstructure propensity towards environment-assisted cracking, with the idea to develop an experimental methodology for identifying sites that act as AISCC initiation precursors. The results reported describe the initiation of environment-assisted cracking in as-received grade 2205 DSS using $FeCl_3$:$MgCl_2$ salt-laden deposits.

7.3.3 Experimental Methods

7.3.3.1 Microstructure Analysis

The material used in this study was as-received grade 2205 duplex stainless steel plate (UNS32205) with a composition of (wt.) 22.4% Cr, 5.8% Ni, 3.2% Mo, 1.5%Mn, 0.4% Si, 0.016%C, 0.18%N, and Fe% (bal.), supplied by Rolled Alloys UK. The material was in a mill-annealed treatment condition (1050°C for 1 hour). Rectangular specimens of the normal, transverse, and rolling directions (ND-TD-RD) were prepared and metallographic assessment carried out on 0.06 μm colloidal-silica (OP-S) polished surfaces. These specimens were used for microstructure assessments using electron backscatter diffraction (EBSD) technique.

EBSD analysis was undertaken to quantify crystallographic phases and grain morphology using an FEI Quanta 650 scanning electron microscope (SEM) interfaced with an HKL Nordlys EBSD detector and AZtec Version 2.2 acquisition software. Microstructure characterization was performed with an accelerating voltage of 20 kV over an area of 2000 x 1750 µm² using 770 nm step size for phase analysis, and a second scan over an area of 1110 x 971 µm² using 135 nm step size for grain boundary and microstructure strain analysis. 2x2 binning was used for the pixel readout of the CCD camera.

EBSD data post processing was undertaken with Oxford Instruments HKL Channel 5 software. The high angle grain boundary (HAGB) threshold was set to a misorientation of 15° and low angle grain boundaries (LAGB) were characterized as misorientations between >1° and <15°. Grain size analysis was carried out with a mean linear intercept method using 50 lines in vertical and horizontal directions in Channel 5. Local misorientation maps were created with a filter size of 5x5 and a maximum sub-grain threshold angle of 5°. This routine provides local misorientation distributions to identify regions with remaining plastic deformation (in the form of intergranular misorientation gradients). The latter routine determines the average misorientation between a pixel and its surrounding pixels, and assigns this value to that pixel. Misorientations above a certain threshold are discarded to exclude interference of sub-grain and grain boundaries.

Energy-dispersive X-ray spectroscopy (EDX) analysis was carried out to identify crystallographic phases when EBSD assessment was not possible using an INCA Penta FETx3 EDX system from Oxford Instruments interfaced with a Zeiss Ultra V55 SEM. An accelerating voltage of 20 kV was used in high current mode to achieve a good x-ray signal. INCA Suite version 5.05 (2014) was used for post-processing analysis. Ferrite and austenite were measured for Fe, Cr, Ni, Mo, Mn, and Si content in weight percent (wt.-%). Between 5 and 10 different regions were measured over ferrite and austenite regions to obtain a representative mean elemental composition of both phases.

7.3.3.2 Atmospheric-induced Stress Corrosion Cracking Testing

One micro-tensile specimen of 50 mm length, with a gauge section of 25 mm, 1 mm thickness, and 3 mm width were manufactured with the length of the specimen along the normal direction (ND) of the as-received plate. The specimen surface was ground to 1200-grit finish, degreased in acetone and ethanol, followed by a thorough rinse in distilled water.

This surface finish was used for corrosion studies. A self-designed direct tension rig was used to strain the micro-tensile specimen in tension to 0.3% strain with the extension manually determined using a digital caliper (for more information about the rig see reference [48]).

A water droplet with a mixture of $FeCl_3$:$MgCl_2$ (0.68 : 1 mol ratio) was applied onto the tensile specimen's surface. The volume of the droplet was 0.5 µl and an Eppendorf micropipette was used to dispense the liquid. This volume produced an initial chloride deposition density of 290 µg/cm² within a contact area of 2.45 mm². The deposited droplet then shrunk to a smaller and elliptical shape with an area of ca. 1 mm²; yielding a nominal maximum chloride deposition density of 950 µg/cm² if the entire deposited salt would be assumed to be present in the droplet (Figure 7-7(a)). However, traces of the salt deposits are expected to have contaminated the initially dispensed area. The effect of secondary spreading of the droplet was not considered.

The direct tension rig with the strained micro-tensile sample was placed in the in a Binder KBF climate humidity cabinet and exposed to 50°C and 30% RH for 368 days; fluctuations in RH with values of up to 60% were observed during the last 2 weeks of exposure and the test was therefore terminated. During the time of exposure, the tension rig was periodically removed from the humidity chamber and the droplet imaged with a Zeiss Stemi 2000-C stereo-microscope interfaced with an AxioCam ERc5s camera. After terminating the test, the sample was thoroughly rinsed in distilled water to dissolve salt and corrosion products, followed by an additional cleaning cycle in an aqueous 10 wt.-% citric acid solution at 80°C for 2 hours to remove remaining corrosion products. The corrosion morphologies of the specimen were investigated using light optical microscopy and SEM.

7.3.4 Results

7.3.4.1 Microstructure

The microstructure of grade 2205 DSS is shown in Figure 7-6(a), with the ferrite (δ) forming the matrix phase. The austenite (γ) has elongated discrete grains, intersected by straight twin boundaries (yellow), and is embedded in the ferritic matrix [6, 49].

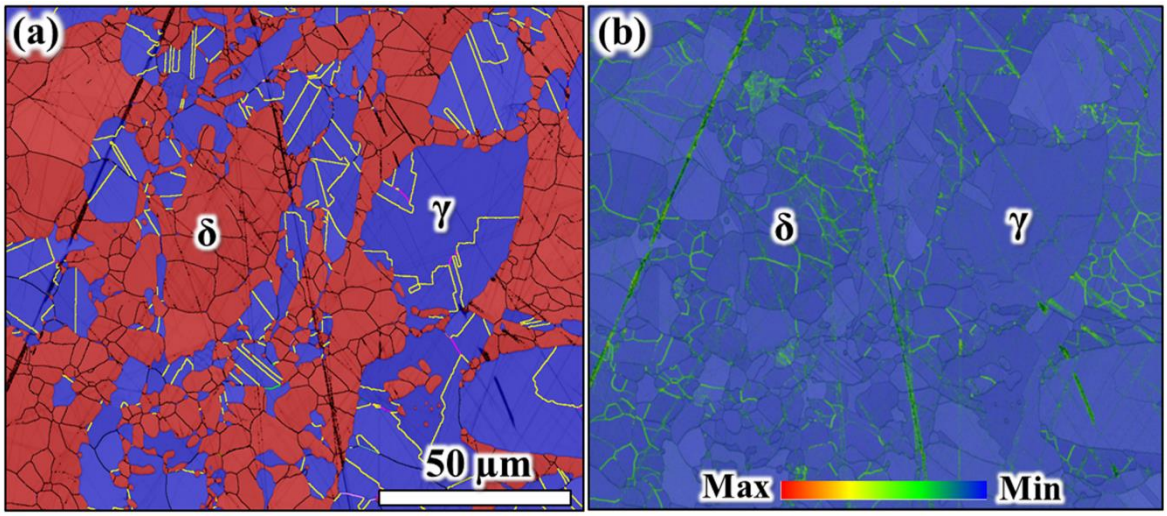

Figure 7-6: (a) EBSD phase map in normal direction (ND) with austenite (blue), ferrite (red), low and high angle grain boundaries (black), and twin boundaries (yellow), (b) EBSD local misorientation map (5x5) showing strain localization at LAGBs in the ferrite, and small austenitic grain clusters. The color bar indicates the level of strain (red = max; blue = min.).

Both ferrite and austenite grains have equiaxed morphology displaying ferrite/ferrite, ferrite/austenite, and austenite/austenite grain boundaries. In the as-received condition, the austenite is largely strain-free whilst the ferrite shows discrete regions with small local strain pockets, typically adjacent to ferrite/ferrite grain boundary regions, highlighted in the local misorientation map in Figure 7-6(b). Despite the large strain mismatch in DSS [5, 50, 51], no distinctive strain localization was observed adjacent to interphase boundaries in the as-received condition. However, plastic deformation of the material in the form of tensile straining is expected to result in shear band formation primarily in the austenite, promoted by the low stacking fault energy [52]. The average grain size was 6.8 ± 0.4 µm for austenite and 7.6 ± 0.5 µm for ferrite, with a phase ratio of 58% to 42% respectively; though the mean phase fraction of EBSD maps taken in all three process orientations (ND-TD-RD) was slightly lower at 57% austenite and 43% ferrite. The nominal chemical composition (wt.-%) of both phases was determined by EDX, with the austenite having a composition of Fe 65.4±0.25 – Cr 21.9±0.17 – Ni 7.1±0.17 – Mo 2.6±0.17, and the ferrite of Fe 62.9±0.25 – Cr25.7±0.18 – Ni3.8±0.15 – Mo4.8±0.19. The ferrite was rich in Cr and Mo, whereas the austenite was enriched in Ni.

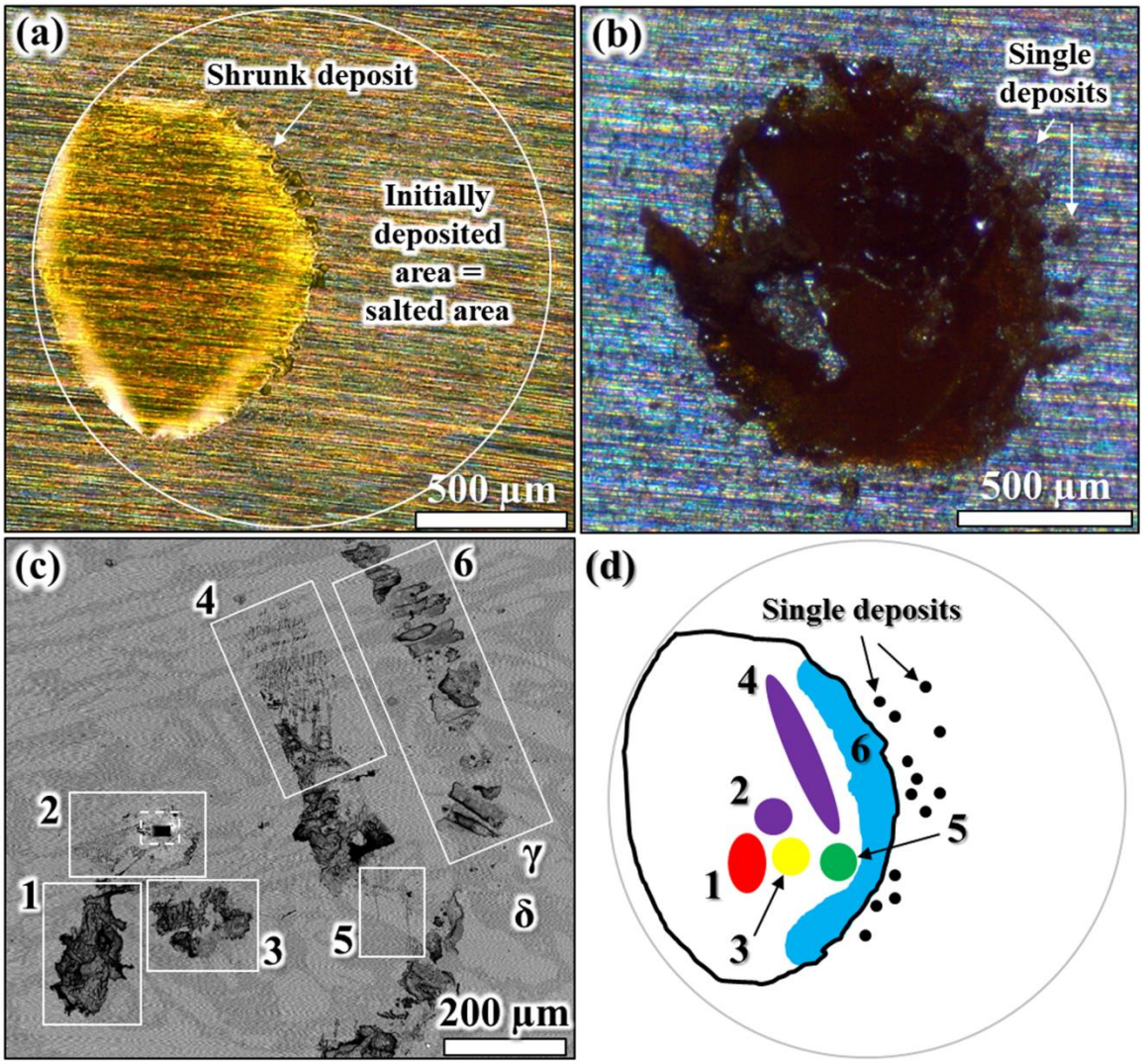

Figure 7-7: (a) Optical image of the initial area (circle) of the deposit, which shrunk to a smaller size, (b) optical image of the deposit after 1 year of exposure to 50°C and 30% RH, (c) BSE-SEM image showing the corrosion morphology under the salt-laden deposit after cleaning, (d) schematic illustration of the different corrosion-affected regions observed in (c).

7.3.4.2 Atmospheric-induced Stress Corrosion Cracking

The area of the micro-tensile specimen covered by the salt-laden droplet is shown in Figure 7-7(a). The color of the deposit became dark brown after one year of exposure to 50°C and 30% RH, resulting in formation of Fe-oxidation products (Figure 7-7(b)). The areas of the corrosion attack beneath the deposit after cleaning in citric acid are shown in Figure 7-7(c). The microstructure is readily visible in the form of a relief pattern of both phases, with austenite appearing brighter and ferrite forming the darker matrix phase. A distinctive pattern of corrosion attack can be seen across the deposited area. Most corrosion was observed

slightly offset to the center and at the periphery/rim of the dried droplet, displaying a variety of corrosion morphologies.

The entire area under the droplet was divided into six regions, labelled with numbers 1-6 in Figure 7-7(c,d). Assessment of the different regions revealed corrosion of both phases at the anodic center, selective dissolution and hydrogen embrittlement (HE) or hydrogen-related cracking of the ferrite between the center and the rim, with dissolution, pitting/crevice corrosion, and chloride-induced stress corrosion cracking of the austenite at the periphery of the droplet. Most severe corrosion attack occurred at the center of the salt-laden electrolyte, which was seen to show most metal dissolution and deepest attack, with dissolution of ferrite and austenite. The extent of corrosion attack diminished gradually towards the droplet rim.

Region 1 is close to the center of the deposit showing dissolution of both ferrite and austenite. The strongest attack occurred in this region in the form of local material loss, illustrated by the SEM image in Figure 7-8. Corrosion seemed to have progressed in relation to slip lines or crystallographic grain orientation. The pH of $MgCl_2$ deposit close to their deliquescence point has been reported to lie about 2 [30], and it is a known that ferric ions further decrease the pH by hydrolysis of water. Therefore the pH of the thin-film electrolyte is estimated to have dropped to pH 1 or below beneath the $MgCl_2$:$FeCl_3$ salt droplet [30, 74, 75]. Due to a low pH in the droplet both hydrogen evolution and oxygen reduction could have enhanced the anodic activity, with hydrogen evolution possibly being the prime cathodic reaction.

Adjacent to the droplet center, numerous closely-spaced micro-cracks in the ferrite were found with little evidence of local corrosion precursors, denoted as region 2 in Figure 7-7(c). The observed cracks were arrayed all parallel to each other, having sub-micrometer to micrometer sizes. These cracks generally arrested at ferrite-austenite interphase boundaries (Figure 7-9) with their appearance suggesting a HE-related nucleation mechanism.

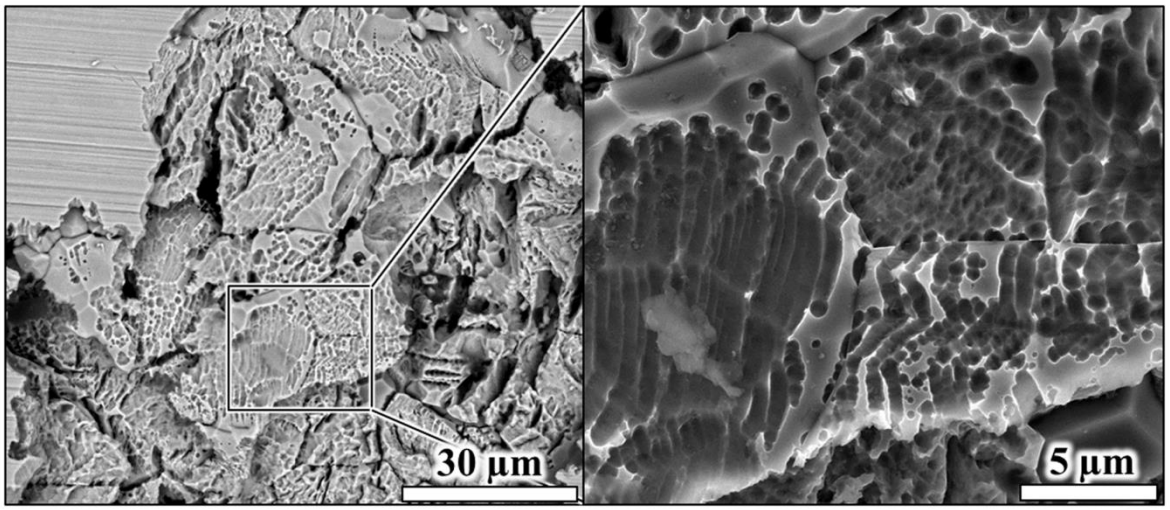

Figure 7-8: SEM images showing general corrosion of ferrite and austenite in region 1.

The occurrence of HE in duplex stainless steel is not limited to the ferrite. Austenite can also be prone to hydrogen-induced or hydrogen-assisted cracking when certain conditions prevail. Apparently, to some extent, HE-related effects, similar to those observed in the ferrite, were also present in the austenite, shown in the highlighted region in Figure 7-9(a) (dashed lines). These transgranular micro-cracks were observed in the austenite in close proximity to selectively corroded ferrite grains as shown in Figure 7-9(a) and Figure 7-10(a-c). The adjacent ferrite dissolved selectively, providing neighboring regions with a need for cathodic currents. Here, cracks most-likely nucleated at the interphase boundary and propagated towards the austenite grain interior. However, nucleation sites within the austenite grain were also observed as can be seen in Figure 7-10(c). All micro-cracks in the austenite nucleated from local corrosion sites or dissolved interphase regions only. Furthermore, micro-deformation bands were apparent in austenite grains, shown by the arrow in Figure 7-10(a), indicating strain from tensile loading. These may have also played a crucial role in the crack nucleation process.

A dissolved region of ferrite adjacent to several micro-cracks on top of an exposed austenite grain was further sectioned by Focused Ion Beam (FIB) milling. The milling was carried out in 50 nm slice steps along the horizontal axis to observe possible sub-surface interactions of HE-related cracks, with the FIB region shown by the rectangle in Figure 7-11. The dissolution process of the ferrite most likely stopped after encountering the austenite grain, although there is also one micro-crack visible in the austenite. The FIB analysis in Figure 7-12 shows that the cracks in the ferrite (most likely related to HE) and along interfaces are

inter-connected below the surface. The cracks are transgranular, but become intergranular when encountering an austenite grain with further propagation along interphases. Some crack nuclei with sharp tips and penetration depth of up to 5 µm were also observed in the austenite (see Figure 7-12). The crack penetration in general was superficial (<10 µm), but certainly deeper than the shallow deformation layer of the near-surface region.

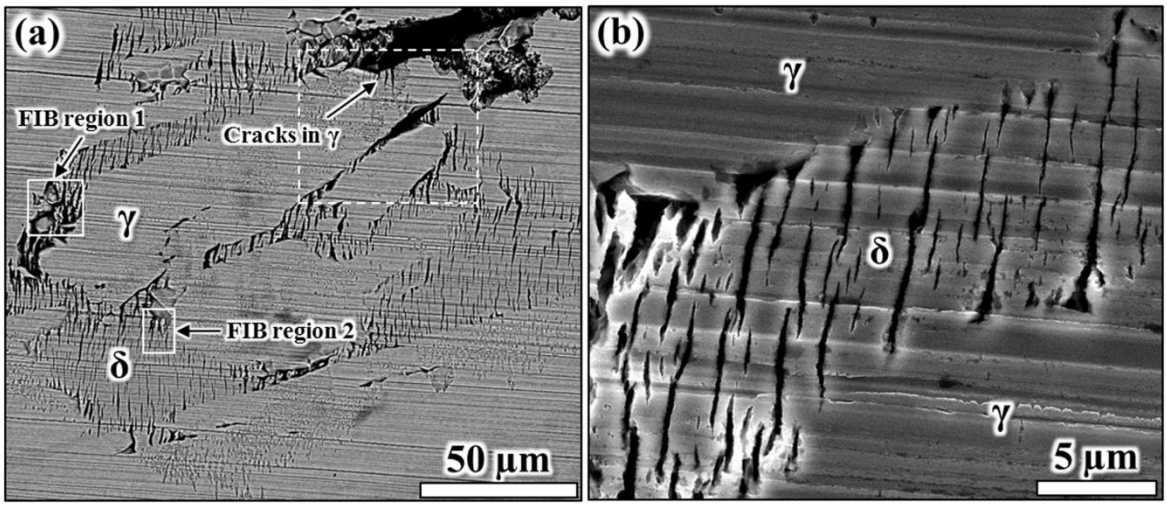

Figure 7-9: SEM-images of region 2 with parallel, close-spaced micro-cracks formed in ferrite with only little evidence of pitting corrosion precursors. Stress axis is horizontal to the images. The regions for FIB analysis are also shown. (b) Higher magnification image of a ferritic region with cracks.

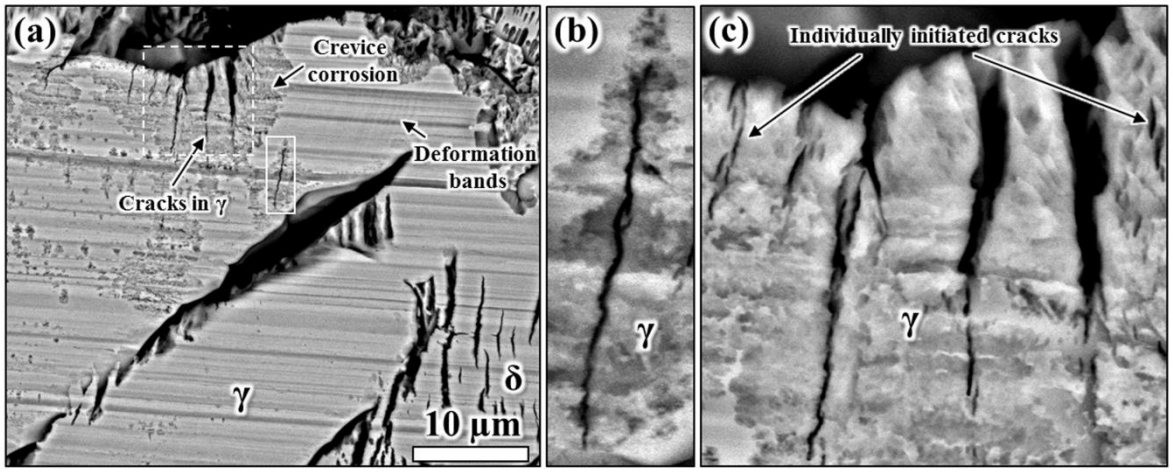

Figure 7-10: (Region 2) High magnification SEM images of the dashed region in Figure 7-9(a) highlighting (a) close-spaced, transgranular micro-cracks in austenite, (b) intra-granular crack in austenite, and (c) multiple cracks in austenite. Note (b) and (c) are magnified views of the highlighted regions in (a).

Further FIB milling (see Figure 7-13) was carried out on a heavily cracked ferrite region (15 nm slice thickness). The cracks were clearly superficial with a maximum penetration depth of about 2 µm and did not penetrate the neighboring austenite grain. In contrast to the cracks

observed in FIB region 1, the grain orientation of the austenite grain did not favor crack nucleation which leads to the assumption that crack propagation from ferrite to austenite is possible for certain grain orientation conditions only.

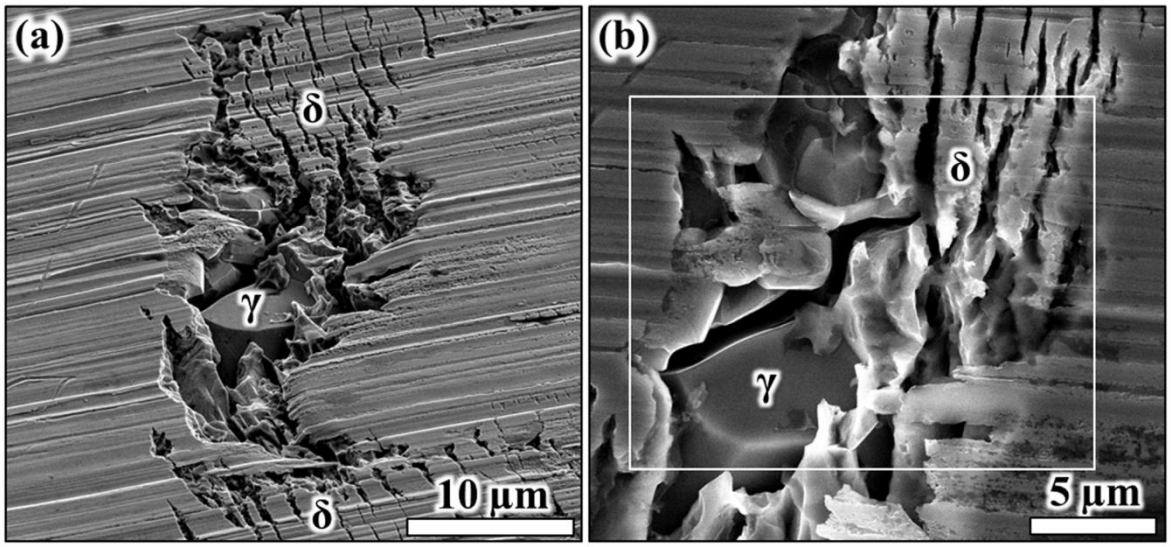

Figure 7-11: (Region 2) (a) Region with micro-cracks in both ferrite and austenite and, (b) FIB region 1 shown in Figure 7-9(a).

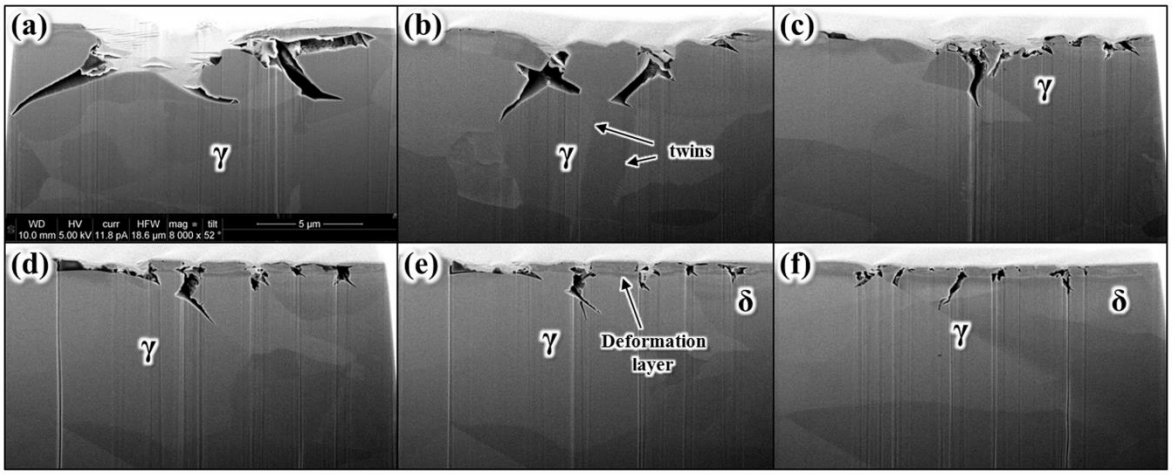

Figure 7-12: (a-f) FIB section slice-and-view of various slice positions of the highlighted region (region 2) in Figure 7-11(b) with austenite and ferrite grains outlined. A shallow deformation layer from surface preparation is also visible (with twin grain boundaries indicative of austenite grains).

A high-resolution assessment of region 2 (Figure 7-7) also revealed a number of micro-cracks in the ferrite that were associated with local corrosion sites, as shown in Figure 7-14(a). These sites in Figure 7-14(a) were not at interphase boundaries; with all observed cracks parallel to each other. The origin of these local corrosion sites is not known and could also be an artefact of the aggressive droplet environment, which may dissolve impurities or

secondary phases (nitrides, inclusions) in the wake of nucleated cracks. Localized corrosion sites could be also linked to local deformation associated with strain localization or strain-induced martensite [24]. It is commonly known that corrosion pits can favor cracking processes, and possibly these corrosion sites favored cracking in the ferrite.

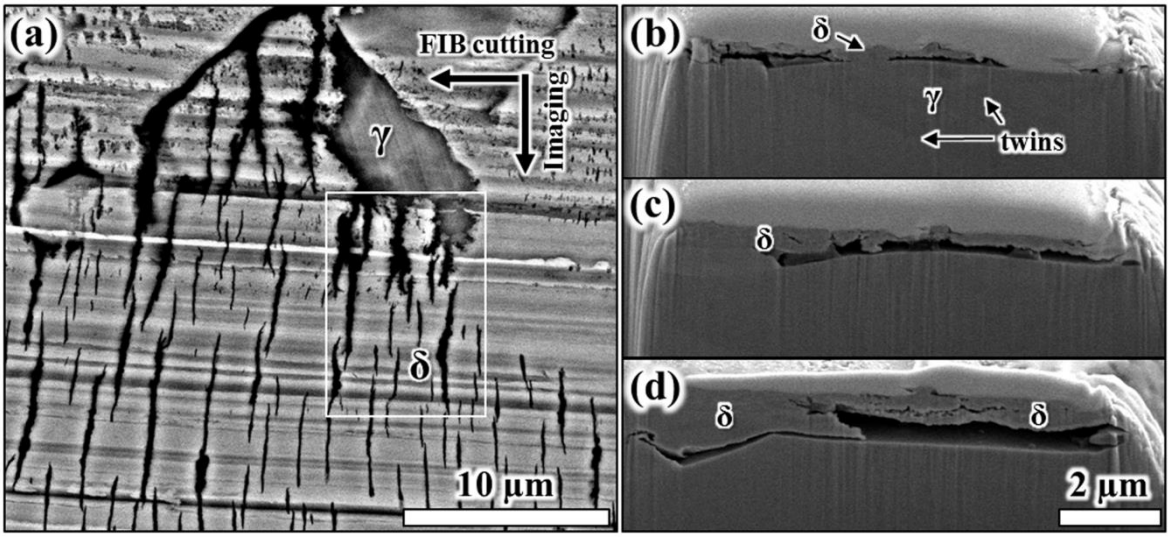

Figure 7-13: (a) FIB-milled ferrite region (FIB region 2 in Figure 7-9(a)), (b-d) SEM images of the FIB-milled region with different slice-view positions. Some cracks penetrated through the ferrite and were linked along the interface without penetration into the austenite.

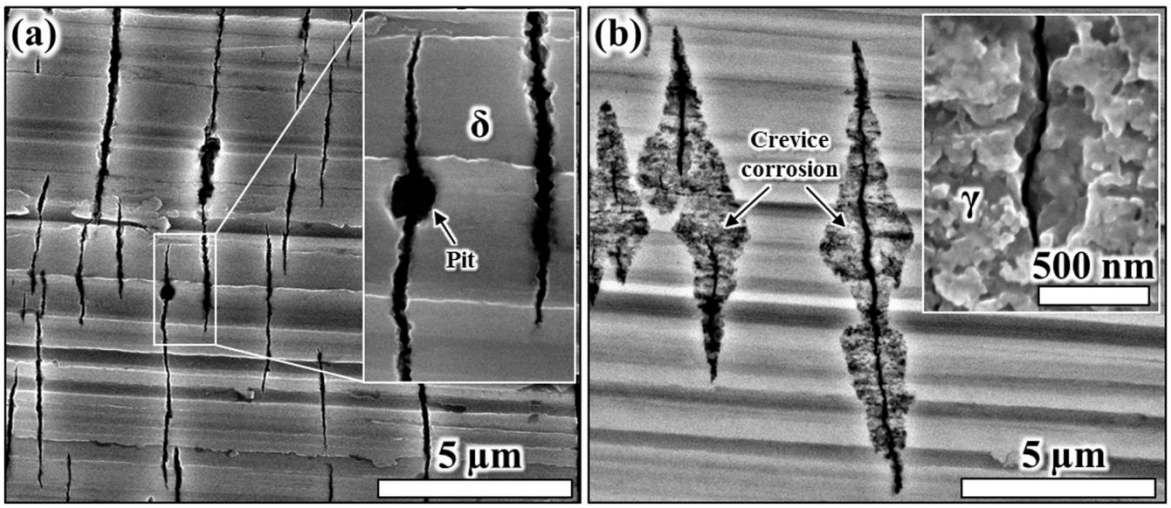

Figure 7-14: (Region 2) SEM images showing environment-assisted cracking morphology of (a) ferrite and (b) austenite. The inset images give higher magnification views of regions of interest. The stress axis is oriented to the horizontal of the images.

Similar micro-cracks to those shown in Figure 7-10 are also shown in Figure 7-14(b). These cracks were found in the austenite with crack morphology showing parallel or step-wise morphology across slip planes. Moreover, the surface area close to these cracks showed

dissolution-like corrosion attack adjacent to crack openings, indicating that an aggressive environment was present. It is not clear how these corrosion sites are linked to the observed cracks, and whether these sites are a result of the cracks or the cause. One possible explanation is the formation of crevices along corroded slip lines, which then developed into cracks with the aggressive crevice solution being exerted in due course.

Figure 7-15(a,b) shows selective dissolution of the ferrite, which occurred in region 3. This site is parallel to region 2, and the net anodic dissolution tendency may have been reduced by an increased cathodic activity as reported earlier. This is then expected to result in anodic dissolution of the weaker, more susceptible ferrite phase, in contrast to dissolution of both phases in the center (region 1).

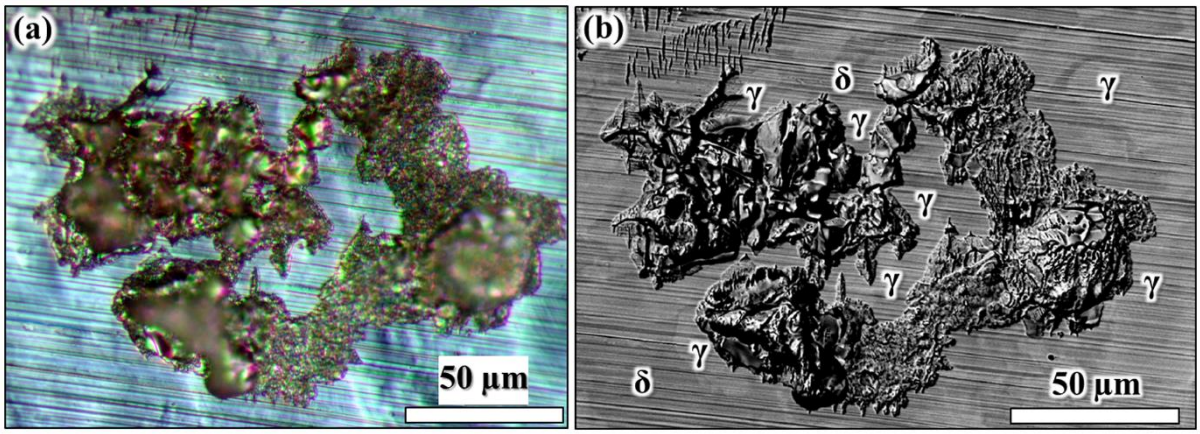

Figure 7-15: (a) Optical micrograph showing region 3 in higher magnification with (b) SEM image showing selective dissolution of ferrite with some partially corroded austenite grains.

In region 4 cracks were seen in the ferrite and austenite. In the ferrite, cracks were observed to nucleate within existing cracks highlighted in Figure 7-16(a,b) with wide crack openings and no evidence of corrosion precursors. Transgranular micro-cracks in austenite were observed shown in Figure 7-17(a,b), with local attack along slip-planes acting as precursors for parallel crack nucleation sites. The cracks in austenite, however, contained kinks and branches, which is more indicative of chloride-induced SCC. It seems that local potential differences existed in this region with cathodic sites suggesting HE occurred in ferrite, and most likely more anodic sites resulting in SCC of the austenite.

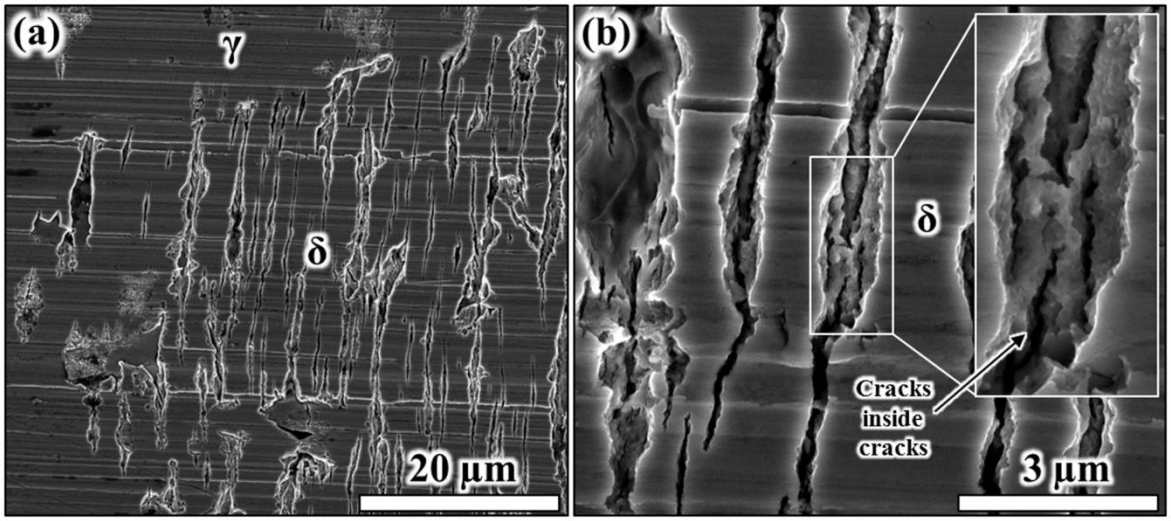

Figure 7-16: SEM images of region 4 showing (a) parallel cracks in the ferrite and (b) cracks formed within existing cracks.

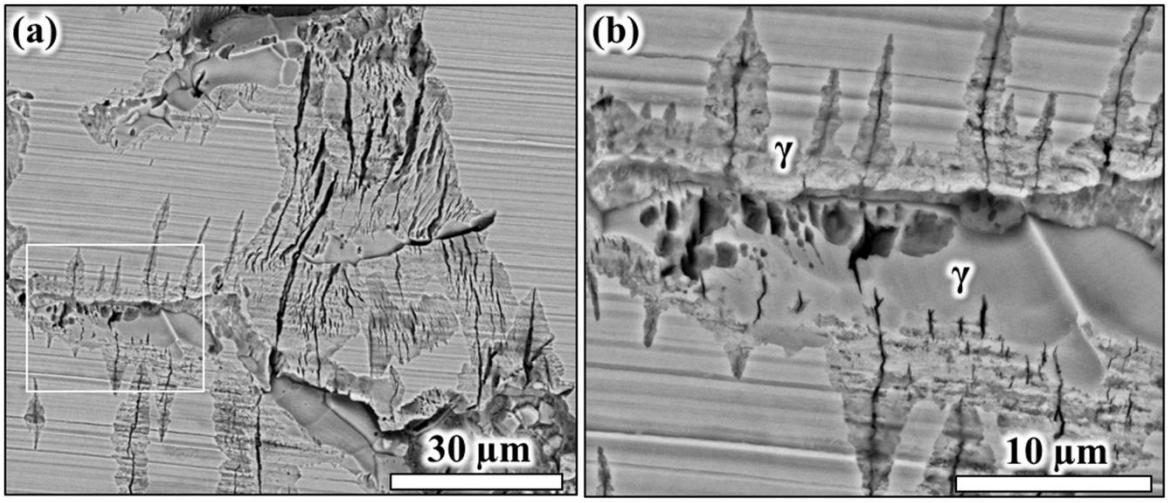

Figure 7-17: SEM images of micro-cracks in region 4 with (a) cracks in austenite and ferrite and (b) selective dissolution of the interphase boundary and adjacent grains, with localized corrosion at slip lines. Stress axis is to the horizontal of the images.

Closer to the periphery of the deposit (region 5) a number of transgranular cracks in both austenite and ferrite were observed seen in Figure 7-18(a). EBSD mapping over the corroded region adjacent to theses cracks proved that both ends are ferritic, with a large (>25 µm length) austenite area right in the middle (insert in Figure 7-18(a)). Slip bands emanating from an austenite grain are apparent by the contrast difference in the backscatter imaging mode indicating plastic deformation. Strain localization can trigger SCC [33], and slip bands in general promote crack nucleation as well as propagation [30, 76, 84]. The cracks in austenite seemed to be finer and superficial (Figure 7-18(c)). The latter SEM image is a

magnified view of the region with dashed red lines in Figure 7-18(a). In earlier work it was shown how plastic deformation led to favored sites for localized corrosion [23, 24]. Localized corrosion of ferrite and interphase boundaries was observed shown in Figure 7-18(b,c), indicating that adjacent sites at the interphase boundary formed the net anode, with cracks nucleating and propagating into grain interiors. In this case, possibly due to advantageous crystallographic orientations between ferrite and austenite, the crack could propagate through the austenite.

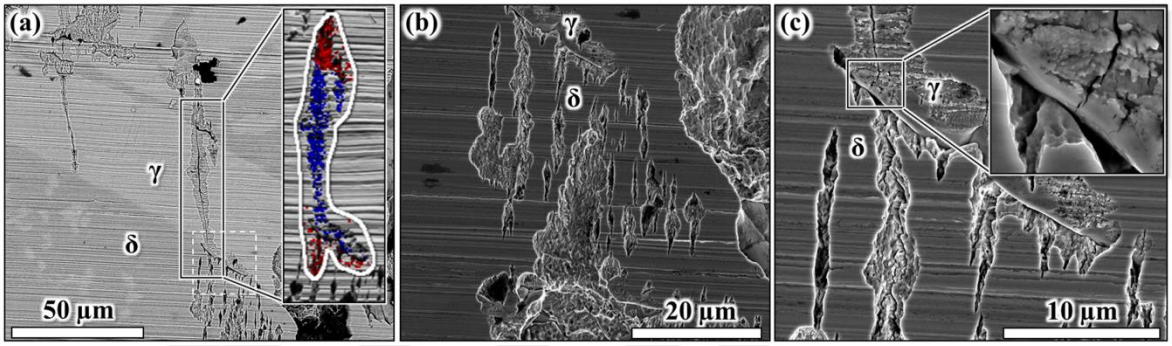

Figure 7-18: (a) SEM image with transgranular crack in austenite linked with cracks in ferrite, with the insert in (a) showing the EBSD phase map of the region (blue austenite, red ferrite), (b) SEM image with cracks and localized corrosion in ferrite, (c) SEM images with superficial cracks in austenite and ferrite. Stress axis is to the horizontal of the images.

At the peripheral area of the droplet in region 6 selective and localized dissolution of the austenite was observed, which was in contrast to selective attack of ferrite in the droplet interior. Typical examples of localized corrosion with lacy-cover-like pitting attack are shown in Figure 7-19(a,b). Pits with lacy covers have been described by *Ernst et al.,* who discussed the pit formation mechanism in detail for austenitic stainless steels under immersed conditions [87]. The presence of lacy cover pits under atmospheric thin-film droplets in duplex stainless steels has not been reported so far. Lacy cover pitting occurred only on regions where austenite was attacked and dissolved preferentially. Analysis of the corrosion morphology along the periphery of the droplet confirmed selective dissolution of some austenitic regions, with also minor attack on the ferrite, shown in Figure 7-20(a,b). EBSD phase analysis confirmed that the ferritic phase remained after dissolution of austenite, as shown in Figure 7-20(b). As demonstrated by *Aoki et al.* and *Lee et al.* ferrite and austenite assume different corrosion potentials in chloride environment and selective dissolution of a phase depends on the applied potential or potential of the electrolyte [16, 17, 22].

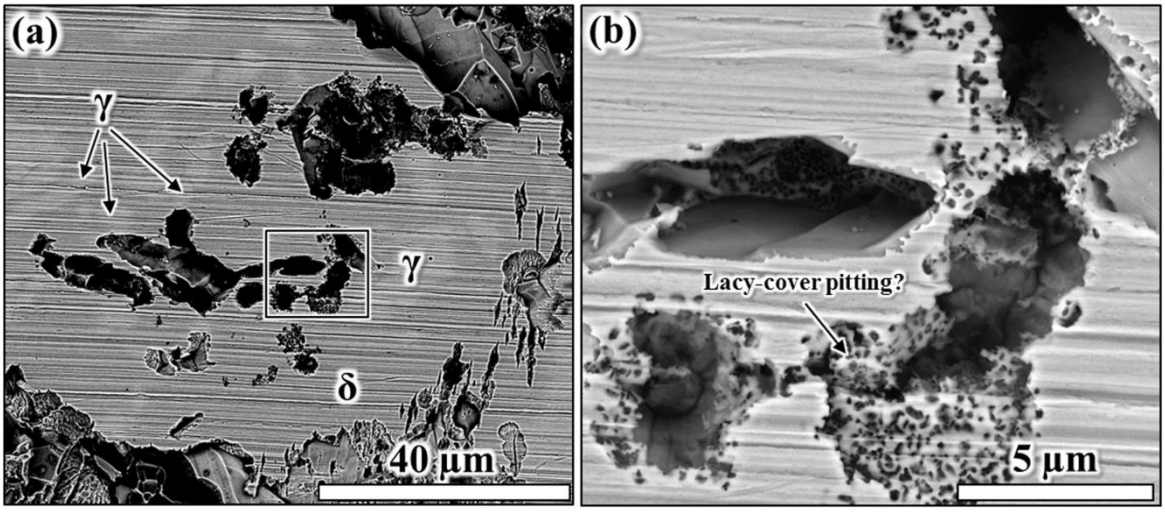

Figure 7-19: (a) SEM image showing selective dissolution of austenite with (b) lacy cover-like corrosion or de-alloying occurring in ferrite and austenite.

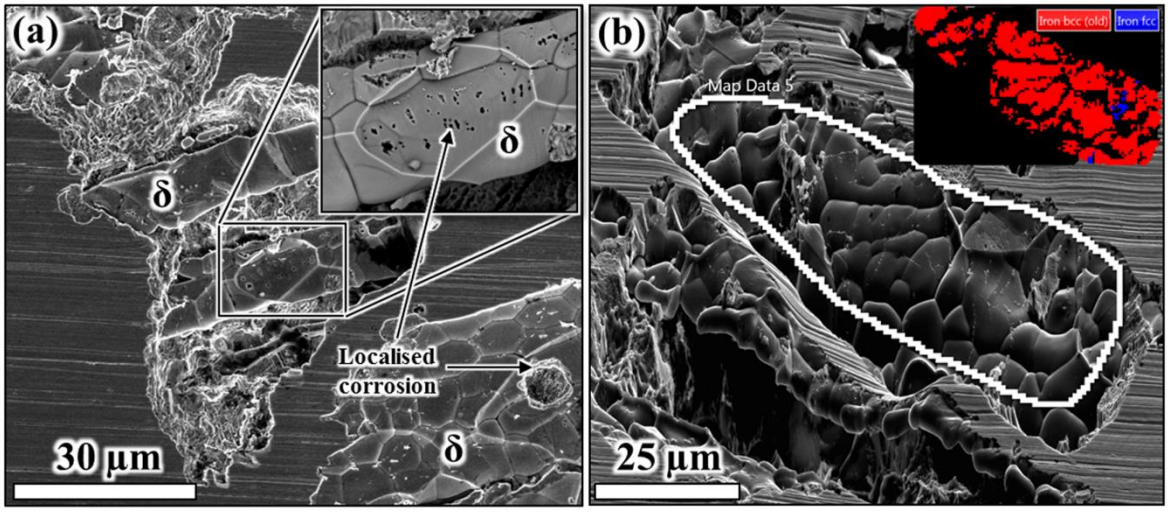

Figure 7-20: SEM images of the **c**orrosion morphology in region 6 with (a) selective dissolution of austenite with localized corrosion on ferrite (slip planes), and (b) superimposed EBSD map confirming the ferritic nature of this site.

7.3.5 Discussion

The different corrosion morphologies observed are evidence of non-homogeneous local corrosion potential distribution. Most severe attack occurred close to the center indicating the highest active corrosion potentials. Regions with dissolved grains are indicative of net anodic activity, and multiple discrete anodic sites with varying corrosion morphologies were observed, pointing towards the presence of local anodes and cathodes. The location of the net anode was expected in the center of the salt-laden area, according to the atmospheric corrosion model introduced by Evans, who described the formation of local anodes and

cathodes on mild steel [53-56]. In the Evans study, the anode was found in the center of the droplet due to limited oxygen supply, with the rim of the droplet forming the cathode due to oxygen replenishment, and a brownish colored ring in the form of Fe corrosion products forming in between cathodic and anodic areas. The formation of oxygen concentration cells between the actively dissolving central area (anode) and the peripheral droplet region (cathode) formed an active-passive coupling system [53-57].

The occurrence of corrosion on passive stainless steel surfaces under a droplet deposit, however, consists typically of one or more local anodically confined sites (e.g. pits/crevices), with cathodic regions distributed around these sites over the area covered by the deposit [24, 57-60]. As shown in Figure 7-7(c), the anodic areas were not entirely at the center of the droplet, which is in line with previous observations [7, 23, 24, 48, 58]. Stainless steels are spontaneously passive and show local pit initiation and propagation, different to that observed in mild steels [57]. Oxygen reduction under atmospheric conditions on stainless steel is usually activation-controlled, requiring the local chemistry to initiate anodic sites [57, 61, 62]. These are typically related to microstructure inhomogeneities (e.g. MnS inclusions, or $Cr_{23}C_6$ at triple junctions/boundaries) rather than diffusion distances in thin film electrolytes. The Evans model has apparently constraints to explain the atmospheric corrosion mechanism for stainless steels.

To make it more complicated, in DSS electrochemical coupling typically exist between the ferrite and austenite phase. On homogeneous materials, the two electrochemical half reactions, the cathodic reaction (e.g. hydrogen evolution, oxygen reduction) and anodic metal dissolution, are conjugate and occur simultaneously over the entire surface. On duplex stainless steel, however, spatially separated multiple corrosion cells are acting with varying net anodic and net cathodic effects, due to galvanic differences and respective coupling effects between both phases [63]. Passivity influences corrosion behavior of stainless steels, and in duplex stainless steel, ferrite and austenite also have different passive behavior due to distinctively different chemical compositions [16, 17, 22, 64, 65]. Ferrite is usually the more active phase in mild chloride media due to lower nitrogen and nickel contents, resulting in 50-100 mV lower corrosion potentials than that of austenite [10-12, 16, 17, 64-66]. There is a Galvani potential difference of 30-80 mV reported between ferrite and austenite [16, 17, 63, 65, 66], which is also in line with reported Volta potential differences [7, 23, 24, 66-70], seemingly sufficient to lead to selective dissolution of the ferrite [10-12, 14, 16, 17, 23, 24,

66, 71, 72]. However, dependent on the environment potential, the corrosion behavior of ferrite and austenite may reverse in the presence of inhibiting ions or other active species forming (more oxidizing electrochemical environment) leading to selective attack occurring on austenite while ferrite is galvanically protected [16, 17, 22, 64-66]. Cold deformation may also change the acting corrosion mechanism from selective dissolution of the ferrite to a more localized corrosion pattern, acting preferentially on the austenite [24]. Another example is short-term ageing at 475°C of DSS, which can lead to increased electrochemical nobility of the ferrite, resulting in reversed corrosion morphologies in the form of selective attack of the austenite [8, 14, 73].

When the DSS surface is passive, the cathodic and anodic reactions only proceed at very slow rates. In contrast, on de-passivated DSS surfaces both anodic and cathodic processes can be operating simultaneously, often at varying rates on ferrite and austenite, depending upon the corrosion potential of each phase. This can theoretically lead to active metal dissolution and passivity-related corrosion, such as pitting and crevice corrosion, stress corrosion cracking, and hydrogen-related cracking phenomena, with the latter possible if increased local hydrogen concentrations are liberated [63]. The occurrence of environment-assisted cracking is therefore a matter of the local microstructure, superimposed by stress or strain conditions, and available environment chemistry. This explains why with exposure to $MgCl_2$-$FeCl_3$ containing droplet deposits, a range of distinctive corrosion and crack morphologies were observed.

Region 1 (Central Region) – General Microstructure Dissolution

The diffusion and surface availability of dissolved oxygen is higher near the edge of the droplet than at the center. Therefore, in a perfect circular droplet the anode is formed right in the droplet center and the cathode at the periphery of the droplet [54]. However, this may not be the case, such as shown here, where the deposit shape assumes a non-circular shape, which ultimately results in changes to the spatial location of the anode. Furthermore, concentration gradients within the liquid layer due to thickness variation, with inherently different oxygen supply can lead to a net anode offset to the geometrical center of the deposit.

Furthermore, the oxidation potential under the droplet in region 1 probably shifted towards more anodic values, resulting in anodic dissolution of both austenite and ferrite towards the center. In the center region, larger anodic currents must have therefore been prevalent which

resulted in general dissolution of the microstructure. The high anodic current density possibly controlled the corrosion process, with the local corrosion potential also affected by the oxidizing effect of ferric ions, which are known to act as strong oxidizing catalysts [30, 76, 77]. The dissolution rate in the center (region 1) therefore most likely exceeded a critical rate for environment-assisted crack nucleation in both the ferrite and austenite.

The kinetics for hydrogen evolution processes are faster than oxygen reduction in low pH environment, due to the hydrogen evolution reaction exhibiting distinctly lower over-potentials than the oxygen reduction reaction, hence hydrogen evolution processes may have become the prevailing cathodic reaction. With oxygen present both cathodic reaction could act simultaneously. The oxygen supply is usually diffusion controlled in thin electrolyte layers, with oxygen reduction reactions then adding a larger cathodic activity to the droplet rim.

Both cathodic reactions; hydrogen evolution and oxygen reduction must have acted simultaneously but to a varying extent depending on the location under the droplet due to varying droplet thicknesses and varying local electrochemistry. If it is assumed that hydrogen reduction was the prime cathodic reaction at some sites, fast general dissolution and environment-assisted cracking in the form of hydrogen embrittlement (HE) or hydrogen-related cracking may occur. The latter, though, is more likely in the ferrite than in the austenite. However, at the rim where cathodic reactions are prevalent, possibly oxygen reduction may have balanced the reduction rate of hydrogen, resulting in different selective corrosion phenomena (regions 4-6) than observed closer to the center (regions 1-3).

On and near to the droplet periphery oxygen supply is abundant, therefore, cathodic oxygen reduction reactions either in the form of the consumption of hydronium ions or water molecules should have increased the pH leading to local potential ennoblement, while a pH drop towards the center of the droplet due the consumption of oxygen and enhanced hydrolysis reactions leading to reduction of local potential nobility. This in turn must have led to a long-distance galvanic coupling between the peripheral areas (net cathodic) and central regions (net anodic) under the droplet due to a (significant) pH gradient development across the droplet-metal surface interface, which have led to a general dissolution of both ferrite and austenite grains (region 1) despite their different corrosion potentials. However, the corrosion morphology did not manifest itself as a usual hemispherical corrosion pit,

which would have indicated homogeneous dissolution. Instead corrosion facets with some localized corrosion appearances were observed indicating possible local repassivation, which was most likely associated with the micro-galvanic interaction between ferrite and austenite and also between high- and low-strained regions (strain localization effects). The droplet chemistry most-likely changed over time, such as metal ion enrichment and local rise of pH, facilitating local repassivation, in particular on such sites were the critical chloride concentration and local dissolution potential to maintain active dissolution decreased.

Region 2 – Selective Dissolution and Hydrogen-related Cracking

The low pH and hydrogen evolution reactions can cause uptake of atomic hydrogen as a solute in the metal lattice, with a higher affinity of ferrite to hydrogen and higher solubility. Hydrogen-dislocation interaction, such as pinning of edge dislocations, can then result in multiple crack initiation sites without the need for additional applied mechanical loads [63, 78]. HE can occur by superposition of anodic dissolution and cathodic reactions, and do not require net cathodic potentials [63]. A small concentration of dissolved hydrogen is sufficient to embrittle microstructure, without the need for severe electrolytic corrosion reactions [63]. Atmospheric corrosion can therefore lead to hydrogen-embrittlement-related cracks in the presence of ferric ions. Low pH-controlled cathodic hydrogen reactions adjacent to the anodic regions (region 1), in conjunction with water hydrolysis reactions similar to $M(H_2O)_n{}^{m+} + H_2O \leftrightarrows M(H_2O)_{n-1}(OH)^{(m-1)+} + H_3O^+ \dashrightarrow [\dots] + H_{ad}$ may have liberated hydrogen which affected the ferrite and led to cracking. Within the concepts of fracture mechanisms, this is often referred to environment-assisted cracking (EAC), in the special variant of hydrogen-induced stress corrosion cracking (HISCC) or hydrogen embrittlement [63].

Fielder et al. investigated stress corrosion cracking (SCC) behavior of grade 2205 DSS in low pH chloride-bearing media and also observed cracks initiating without any evidence of pit or crevice precursors [25]. They referred to SCC, but in light of low pH environments, HE or hydrogen-assisted SCC is also a likely mechanism for cracking of the ferrite [78, 79]. HE, in contrast to chloride-induced SCC, does not necessitate any corrosion precursors, and can initiate directly at bare surfaces [79]. In addition, it is known that cracking can be promoted by the presence of hydrogen in two ways: firstly, by the reduction of the passive layer existing on the metal surface and, secondly by hydrogen-vacancy interactions [80]. In the first aspect, hydrogen supports surface mobility by the removal of high melting point

products from the surface. With respect to the second point, it is believed that hydrogen increases the self-diffusion of the metal atoms, and high concentrations of hydrogen accumulating at stressed regions can therefore lead to cracks [80]. Hence, the cracks in the ferrite phase in Figure 7-9 are most likely related to HE-related phenomena.

The appearance of chloride-induced SCC is typically branched, but linked to one major crack [63, 81-83]. In contrast, the crack morphology of HE typically involves multiple initiation sites, either intergranular or by the presence of straight parallel lines. Most of the cracks shown in Figure 7-9(a) were relatively small with typical lengths of 10's of nm to a maximum of 20 µm, without ramifications, cross-links, or pit nucleation sites. Effects of the applied tensile load on local de-cohesion and micro-crack development are apparent. In the literature, crack formation in the ferrite in chloride-containing media is generally referred to as HE [30, 79, 84, 85]. It should be noted that micro-crack formation in the ferrite was not observed with $MgCl_2$ exposure alone (without $FeCl_3$) using similar exposure conditions, reported in earlier investigations [7, 24, 48]. The ferric ions most-likely played a significant role in crack formation in ferrite, such as intensifying water hydrolysis reactions and shifting the redox potentials (at least locally) to higher potentials. In such environment the oxidizing strength is stronger and can lead to more severe corrosion attack.

The work of *Zucchi et al.* [85] describes a cathodically polarized grade 2205 DSS in artificial sea water (pH = 6.5), with and without the addition of S^{2-} species, observing transgranular cracks in the ferrite with similar morphology as the cracks shown in Figure 7-9(a,b). The severity of these cracks aggravated with adding S^{2-} species or increased applied cathodic potentials. Subsequent analysis showed that these cracks initiated in the ferrite and were arrested by the austenite. SEM observations showed that the nature of the cracks was transgranular brittle cleavage, characteristic of HE [85].

Ferritic stainless steels have in general superior SCC resistance to austenitic steels in chloride media [1-3, 86], though are susceptible to HE. The corrosion potential is usually lower than their crack nucleation potential which is related to the deformation mode of the body-centered-cubic (bcc) lattice structure as well as poor re-passivation characteristics compared to the austenite [86]. The synergistic effect of the duplex microstructure in terms of EAC is apparent in Figure 7-9, with cracks forming in one phase, which are then shielded and even stopped by encountering the other phase, enhancing the overall material performance.

Region 3 – Selective Dissolution of Ferrite

Stainless steels exhibit in acidic aerated chloride solutions with strong oxidizing power noble corrosion potentials with typically no active-passive transition [84]. Corrosion of one phase in duplex stainless steel is possible only when the oxidizing power of the electrolyte decreases the separation of the local corrosion potential and local pitting potential [16, 17, 22, 30]. Spontaneous attack occurring on the ferrite (Figure 10) with significantly less dissolution happening on the austenite is indicative of a local corrosion potential ennoblement due to the evolution of an aggressive local. The dissolution of ferrite or austenite depends on the local electrode potential, with ferrite being 50-100 mV more active than austenite [10-12, 16, 17, 64-66]. The dissolution of ferrite indicates that the local electrode potential exceeded the corrosion potential of ferrite leading to a selective attack.

Region 4 and 5 – Hydrogen Embrittlement (HE) and Stress Corrosion Cracking (SCC)

HE of stainless steels is typically reported to be the responsible failure mechanism in hydrogenous electrolytes such as hydrogen sulfide or sulfuric acid or under cathodically protection [88, 89]. HE in non-sulphurous chloride media is less common, but still likely. Hydrogen absorption is very fast, and cracking occurring in corrosive systems in abundance of hydrogen is chiefly due to HE [88, 89]. The decrease of pH usually facilitates HE, and the range of concentrations of hydrogen at which HE takes place is wide in strong acidic media such as HCl [88]. It can be assumed that HCl formed under the atmospheric $FeCl_3$:$MgCl_2$ electrolyte and the pH could have been at 1-2 or even lower which could have enhanced the uptake of hydrogen on primarily ferrite regions leading to HE or hydrogen-related cracking of ferrite. HE is typically associated with electrochemical cathodic processes in which atomic hydrogen is liberated on the cathode [88, 89].

If both regions 1 and 2 are considered as net anodic, region 2, 4, and 5 are net cathodic in contrast to, and hydrogen produced in these regions most-likely penetrated into ferrite, since the penetration in the lattice of ferrite is easier than into the lattice of austenite despite of higher solubility of hydrogen in the austenite than in the ferrite. Furthermore, corrosion activities in ferrite regions are typically occurring with higher rates than in austenite due to lower corrosion potential of ferrite than that of austenite in most chloride electrolytes [16, 17, 22, 64, 66, 90]. HE is intensified in media that accelerated corrosion, and there is a linear relationship reported to exist between hydrogen absorption and the rate of corrosion with hydrogen depolarization [88].

Furthermore, high carbon contents in stainless steel have been reported to decrease the propensity of hydrogen uptake [88]. Hence, the carbon content of ferrite is typically 5- to 10-times lower than that of austenite, which renders the austenite higher resistance against HE. Chromium has also been reported to increase susceptibility to HE of steels, while nickel increases the resistance against HE [88]. Ferrite is enriched in chromium and austenite is enriched in nickel, therefore, ferrite is a priori more prone to HE than austenite. Little amount of hydrogen is typically sufficient to cause HE, and under static tensile load HE is facilitated. Moderate plastic deformation increases the susceptibility of penetration of hydrogen into the lattice, and it is known that hydrogen tends to accumulate more on stressed zones [88, 89]. Despite larger deformation occurring in the austenite, ferrite is more stressed due to its body-centered-cubic lattice structure, and hence, more susceptible to hydrogen uptake [50, 51]. So, in consideration of the crack morphology of the ferrite in regions 2, 4, and 5, HE or hydrogen-related cracking was most-likely the mechanism responsible for cracking in the ferrite and also in some austenite grains situating in closest vicinity of embrittled ferrite regions.

In contrast, the crack morphology of the austenite at the droplet periphery (region 5, see Figure 7-18) and at the subsurface in region 2 and 4 (see Figure 7-12) suggests SCC as the most-likely the responsible cracking mechanism of austenite. At the droplet periphery, the electrochemical potential was nobler than the droplet center, and cracking was favored in austenite in region 5 suggesting that the cracking potential was around the active-passive transition, while the ferrite remained passive due to one order of magnitude lower corrosion current densities than that of ferrite at this potential [16, 17, 22, 90]. The surface crack morphologies in ferrite and austenite in region 2 and region 4 showed severe embrittlement, suggesting, therefore, HE as the prime cracking mechanism. The subsurface showed, however, single cracks propagating through the austenite phase only.

Region 6 – Localized and Selective Corrosion of Austenite

Short-distance galvanic interactions between ferrite and austenite regions must have developed due to different corrosion potentials of ferrite and austenite, with the austenite being the net anode at the periphery and the ferrite forming the net anode in the vicinity of the droplet center. The reason for a selective attack of the austenite may be associated with the local pH increase at the droplet periphery, which must have shifted the local redox potential to nobler potentials accelerating the dissolution of austenite larger than that of

ferrite leading to selective corrosion of the austenite. In consideration of the mixed potential theory, ferric ions must have shifted the local corrosion potential on regions at the droplet rim to more noble values and, hence, led to an increase of the local corrosion rate, leading to a selective attack of the austenite.

Assuming a higher oxygen electrolyte concentration at the rim, it can be assumed that more oxidizing conditions existed. However, the ferrite was also not immune and some small local corrosion sites in the ferrite were observed, shown in Figure 7-20(a). These sites may also be related to either slip bands or regions of strain localization or the presence of impurities in ferrite, showing preferential corrosion and acting as active corrosion sites, as demonstrated in earlier work [23, 24].

The observations also demonstrate that the corrosion behavior of duplex stainless steel cannot be simply described by empirical pitting indices alone (e.g. PREN – Pitting Resistance Equivalent Number), based on their chemical composition only. More work is needed to fully understand all observations, and the prospect to apply $MgCl_2$-$FeCl_3$ droplets for investigating different failure mechanisms is promising.

7.3.6 Conclusions

1) Atmospheric environmentally assisted cracking on as received grade 2205 has been observed under salt-laden deposit containing a mixture of $FeCl_3$:$MgCl_2$ with exposure to 50°C and 30% RH for 368 days.
2) The area under the droplet was divided into different regions, revealing corrosion of both phases at the anodic center, selective dissolution and hydrogen embrittlement of the ferrite between the center and the rim, with dissolution, pitting/crevice corrosion and chloride-induced stress corrosion cracking of the austenite at the periphery of the droplet.
3) Cracks in ferrite and austenite were between 10's of nm to 10's of μm long, with most cracks arrested or diverted by encountering the other phase.
4) The observation of different failure morphologies as a function of location within the droplet indicated local variations of electrochemical potentials.

7.3.7 Acknowledgement

The authors acknowledge financial support from EPSRC (EP/I036397/1) and the Nuclear Decommissioning Authority (NPO004411A-EPS02). The authors are also grateful for the provision of duplex stainless steel by Rolled Alloys and Böhler Austria GmbH. The authors are thankful to Dr Christiano Padovani and Dr Robert Winsley, Radioactive Waste Management Ltd. for valuable discussions. The authors appreciate the support of John Lindsay (University of Manchester) for FIB microscopy.

7.3.8 References

[1] J. Charles, S. Bernhardsson. Duplex Stainless Steels '91 - Volume 1. In: Duplex Stainless Steels '91. Beaune, Bourgogne, France: Les editions de physique, 1991.

[2] J. Charles, S. Bernhardsson. Duplex Stainless Steels '91 - Volume 2. In: Duplex Stainless Steels '91. Beaune, Bourgogne, France: Les editions de physique, 1991.

[3] Lula et al. Duplex Stainless Steels, American Society for Metals, Mars, Pennsylvania, 1983.

[4] J.-O. Nilsson. Super duplex stainless steels, Materials Science and Technology 8 (1992) 685-700.

[5] J.-O. Nilsson, G. Chai. The physical metallurgy of duplex stainless steels. International Conference & Expo Duplex 2007. Grado, Italy: Associazione di Italiana di Metallurgia, 2007.

[6] F. Wischnowski. Einfluss mikrostruktureller Gefügeveränderungen auf die Korrosionsresistenz von nichtrostenden ferritisch-austenitischen Duplex-Stählen. PhD thesis. Bochum, Germany: Technical University of Bochum, 1995. p.264.

[7] C. Örnek et al. Effect of Microstructure on Atmospheric-Induced Corrosion of Heat-treated Grade 2205 and 2507 Duplex Stainless Steels. Eurocorr 2012. Istanbul, Turkey: Dechema, 2012.

[8] C. Örnek, D.L. Engelberg. Effect of “475°C Embrittlement” on the Corrosion Behaviour of Grade 2205 Duplex Stainless Steel Investigated Using Local Probing Techniques. Corrosion Management. Northampton, UK: The Institute of Corrosion, 2013. p.9-11.

[9] T. Prosek. Material classification for climbing anchors - Phase 2: Development of an anchor classification and related test procedure for the evaluation of stress corrosion cracking (SCC) and corrosion resistances of climbing anchors. Brest (France): Institut de la Corrosion (French Corrosion Institute), 2014. p.1-27. Report no. IC 88588.

[10] T. Prosek et al. Low Temperature Stress Corrosion Cracking of Stainless Steels in the Atmosphere in Presence of Chloride Deposits. NACE, vol. Paper No. 08484: NACE International, 2008. p.17.

[11] T. Prosek et al. Low-Temperature Stress Corrosion Cracking of Stainless Steels in the Atmosphere in the Presence of Chloride Deposits, Corrosion 65 (2009) 105-117.

[12] T. Prosek et al. Low-Temperature Stress Corrosion Cracking of Austenitic and Duplex Stainless Steels Under Chloride Deposits, Corrosion 70 (2014) 1052-1063.

[13] A.M. do Nascimento et al. Pitting corrosion resistance of cast duplex stainless steels in 3.5%NaCl solution, Materials Characterization 59 (2008) 1736-1740.

[14] S.S.M. Tavares et al. Influence of heat treatments at 475 and 400 °C on the pitting corrosion resistance and sensitization of UNS S32750 and UNS S32760 superduplex stainless steels, Materials and Corrosion 63 (2012) 522-526.

[15] M. Femenia et al. In situ study of selective dissolution of duplex stainless steel 2205 by electrochemical scanning tunnelling microscopy, Corrosion Science 43 (2001) 1939-1951.

[16] S. Aoki et al. Potential Dependence of Preferential Dissolution Behavior of a Duplex Stainless Steel in Simulated Solution inside Crevice, Zairyo-to-Kankyo 60 (2011) 363-367.

[17] S. Aoki et al. Dissolution Behavior of α and γ Phases of a Duplex Stainless Steel in a Simulated Crevice Solution, ECS Transactions 25 (2010) 17-22.

[18] A. Bautista et al. Selective corrosion of duplex stainless steel bars in acid, Materials and Corrosion 66 (2013) 347-356.

[19] J. Ritter. The Application of Duplex Stainless Steels in Different Media. Surface and Materials Engineering, Corrosion Laboratory, Bachelor thesis. Aalen, Germany: Aalen University of Applied Sciences, 2013.

[20] F. Ruel et al. The transition between Sulfide Stress Cracking and Stress Corrosion Cracking of the 2304 DSS as a function of T and pH in H2S environment. Eurocorr 2014. Pisa, Italy: Dechema Germany, 2014.

[21] R.F.A. Pettersson, J. Flyg. Electrochemical evaluation of pitting and crevice corrosion resistance of stainless steels in NaCl and NaBr. Acom magazine 3-2014. Stockholm, Sweden, Outokumpu, 2004. p.2-9.

[22] J.-S. Lee et al. Corrosion behaviour of ferrite and austenite phases on super duplex stainless steel in a modified green-death solution, Corrosion Science 89 (2014) 111-117.

[23] C. Örnek, D.L. Engelberg. Kelvin Probe Force Microscopy and Atmospheric Corrosion of Cold-rolled Grade 2205 Duplex Stainless Steel. Eurocorr 2014. Pisa, Italy: European Federation of Corrosion, 2014.

[24] C. Örnek, D.L. Engelberg. SKPFM measured Volta potential correlated with strain localisation in microstructure to understand corrosion susceptibility of cold-rolled grade 2205 duplex stainless steel, Corrosion Science 99 (2015) 164-171.

[25] J.W. Fielder et al. Properties and in-service performance - The stress corrosion cracking behaviour of stainless steel at temperatures below 50°C - Final report. Report No. EUR 18001 EN. Luxembourg: British Steel plc, 1998.

[26] A.B. Cook et al. Assessing the risk of under-deposit chloride-induced stress corrosion cracking in austenitic stainless steel nuclear waste containers, Corrosion Engineering, Science and Technology 49 (2014) 529-534.

[27] A.B. Cook et al. Towards a more Realistic Experimental Protocol for the Study of Atmospheric Chloride-Induced Stress Corrosion Cracking in Intermediate Level Radioactive Waste Container Materials, MRS Online Proceedings Library 1665 (2014) 225-230.

[28] A. Cook et al. Atmospheric-induced stress corrosion cracking of austenitic stainless steels under limited chloride supply. 18th International Corrosion Conference, vol. 2. Perth, Australia, 2011. p.1438-1449

[29] S.B. Lyon et al. Atmospheric corrosion of nuclear waste containers. Diamond ’10 Conference Decommissioning, Immobilisation and Management of Nuclear Waste for Disposal. Manchester, UK, 2010.

[30] B. Cottis et al. Shreir's Corrosion - Volume 2. Elsevier B.V., Manchester, 2010.

[31] C. Leygraf, T.E. Graedel. Atmospheric Corrosion, John Wiley & Sons, Canada, 2000.

[32] P.A. Schweitzer. Fundamentals of Metallic Corrosion - Atmospheric and Media - Corrosion of Metals. Second ed., CRC Press, Taylor & Francis Group, 2007.

[33] A.B. Cook et al. Preliminary Evaluation of Digital Image Correlation for In-situ Observation of Low Temperature Atmospheric-Induced Chloride Stress Corrosion Cracking in Austenitic Stainless Steels, ECS Transactions 25 (2010) 119-132.

[34] F. King. Corrosion Resistance of Austenitic and Duplex Stainless Steels in Environments Related to UK Geological Disposal. 2009. Report no. QRS-1384C-R1.

[35] Y. Tsutsumi et al. Initial Stage of Pitting Corrosion of Type 304 Stainless Steel under Thin Electrolyte Layers Containing Chloride Ions, Journal of The Electrochemical Society 152 (2005) B358-B363.

[36] Y. Tsutsumi et al. Pitting corrosion mechanism of Type 304 stainless steel under a droplet of chloride solutions, Corrosion Science 49 (2007) 1394-1407.

[37] F. Mansfeld. Atmospheric corrosion rates, time-of-wetness and relative humidity, Materials and Corrosion 30 (1979) 38-42.

[38] A. Nishikata et al. Influence of Electrolyte Layer Thickness and pH on the Initial Stage of the Atmospheric Corrosion of Iron, Journal of The Electrochemical Society 144 (1997) 1244-1252.

[39] T. Tsuru et al. Formation and growth of micro-droplets during the initial stage of atmospheric corrosion, Electrochimica Acta 49 (2004) 2709-2715.

[40] N. Arnold et al. Chloridinduzierte Korrosion von Nichtrostenden Stählen in Schwimmhallen-Atmosphären Teil 1: Elektrolyt Magnesium-Chlorid (30%), Materials and Corrosion 48 (1997) 679-686.

[41] N. Arnold et al. Chloridinduzierte Korrosion von nichtrostenden Stählen in Schwimmhallen-Atmosphären Teil 2: Einfluß von Hypochloriten, Materials and Corrosion 49 (1998) 482-488.

[42] N. Arnold et al. Chloridinduzierte Korrosion von nichtrostenden Stählen in Schwimmhallen-Atmosphären Teil 3: Einfluß einer realen Schwimmhallen-Atmosphäre, Materials and Corrosion 50 (1999) 140-145.

[43] C. Padovani et al. Corrosion control of stainless steels in indoor atmospheres – practical experience (Part 2), Corrosion 71 (2014) 646-666.

[44] N.R. Smart. Literature Review of Atmospheric Stress Corrosion Cracking of Stainless Steels - Report to Nirex. Abingdon, Oxfordshire, UK. Serco Assurance, 2007. Report reference SA/EIG/14921/C011 Issue 1.

[45] N.R. Smart et al. Record of Nirex Workshop on Atmospheric Pitting Corrosion of Stainless Steel. Serco Assurance. Abingdon, Oxfordshire, 2007. Report reference SA/EIG/40921/C006 Issue 01.

[46] N.R. Smart et al. Review of Environmental Conditions for Storage of ILW Radioactive Waste Containers. Abingdon, Oxfordshire, 2010. p.1-65. Report reference SERCO/TASE/E.2028/P3443 Issue 04.

[47] N.R. Smart et al. Waste container durability: monitoring of a stainless steel 4 metre box over 12 years, Mineralogical Magazine 76 (2012) 2891-2899.

[48] D.L. Engelberg, C. Örnek. Probing propensity of grade 2205 duplex stainless steel towards atmospheric chloride-induced stress corrosion cracking, Corrosion Engineering, Science and Technology 49 (2014) 535-539.

[49] H. Oettel, H. Schumann. Metallografie - Mit einer Einführung in die Keramografie. 15., revised and enlarged ed., Wiley-VCH, Weinheim, Germany, 2011.

[50] J. Johansson, M. Odén. Load sharing between austenite and ferrite in a duplex stainless steel during cyclic loading, Metall and Mat Trans A 31 (2000) 1557-1570.

[51] J. Johansson et al. Evolution of the residual stress state in a duplex stainless steel during loading, Acta Materialia 47 (1999) 2669-2684.

[52] W. Ozgowicz et al. Corrosion Behaviour of Cold-Deformed Austenitic Alloys. in: Aliofkhazraei M, (Ed.). Resistance to Corrosion and Passivity of 316L Stainless Steel

Directionally Solidified Samples, Developments in Corrosion Protection. InTech, 2014.

[53] U.R. Evans. The Ferroxyl Indicator in Corrosion Research, with Special Reference to the Controversy Regarding the Cause of Pitting, The Metal Industry 11 (1926) 1-2.

[54] U.R. Evans, C.A.J. Taylor. Mechanism of atmospheric rusting, Corrosion Science 12 (1972) 227-246.

[55] C. Chen et al. Scanning Kelvin probe analysis of the potential distribution under small drops of electrolyte. Materials science forum, vol. 289: Trans Tech Publ, 1998. p.181-192.

[56] C. Chen, F. Mansfeld. Potential distribution in the Evans drop experiment, Corrosion science 39 (1997) 409-413.

[57] G. Frankel et al. Localised corrosion: general discussion, Faraday Discussions 180 (2015) 381-414.

[58] A.J. Davenport et al. Use of inkjet printing to deposit magnesium chloride salt patterns for investigation of atmospheric corrosion of 304 stainless steel, Corrosion Science 53 (2011) 3114-3121.

[59] S.M. Ghahari et al. In situ synchrotron X-ray micro-tomography study of pitting corrosion in stainless steel, Corrosion Science 53 (2011) 2684-2687.

[60] L. Guo et al. Synchrotron tomography study of atmospheric pitting corrosion of stainless steel during wet-dry cycles. 224th ECS Meeting: The Electrochemical Society, 2013.

[61] R.C. Newman. 2001 W.R. Whitney Award Lecture: Understanding the Corrosion of Stainless Steel, Corrosion 57 (2001) 1030-1041.

[62] D.E. Williams et al. Passivity breakdown and pitting corrosion of binary alloys, Nature 350 (1991) 216-219.

[63] H. Birnbaum et al. Environment induced cracking of metals, Nace 10 (1990) 55-109.

[64] Y.H. Yau, M.A. Streicher. Galvanic Corrosion of Duplex FeCr-10%Ni Alloys in Reducing Acids, Corrosion 43 (1987) 366-373.

[65] B. Deng et al. Critical pitting and repassivation temperatures for duplex stainless steel in chloride solutions, Electrochimica Acta 53 (2008) 5220-5225.

[66] W.-T. Tsai, J.-R. Chen. Galvanic corrosion between the constituent phases in duplex stainless steel, Corrosion Science 49 (2007) 3659-3668.

[67] N. Sathirachinda et al. Depletion effects at phase boundaries in 2205 duplex stainless steel characterized with SKPFM and TEM/EDS, Corrosion Science 51 (2009) 1850-1860.

[68] N. Sathirachinda et al. Characterization of Phases in Duplex Stainless Steel by Magnetic Force Microscopy/Scanning Kelvin Probe Force Microscopy, Electrochemical and Solid-State Letters 11 (2008) C41-C45.

[69] N. Sathirachinda et al. Scanning Kelvin probe force microscopy study of chromium nitrides in 2507 super duplex stainless steel – Implications and limitations, Electrochimica Acta 56 (2011) 1792-1798.

[70] N. Sathirachinda et al. Study of nobility of chromium nitrides in isothermally aged duplex stainless steels by using SKPFM and SEM/EDS, Corrosion Science 52 (2010) 179-186.

[71] R. Pettersson et al. Corrosion Performance of Welds in Duplex, Superduplex and Lean Duplex Stainless Steels. Corrosion 2013, conference paper no. 2657, NACE International, 2013.

[72] S.S.M. Tavares et al. Investigation of stress corrosion cracks in a UNS S32750 superduplex stainless steel, Engineering Failure Analysis (2013).

[73] C. Örnek. Thermal Heat Treatments of Duplex and Super Duplex Stainless Steels in the 400 to 550°C Range and Their Influence on the Corrosion Properties. Bachelor thesis. Aalen, Germany: Aalen University of Applied Sciences, 2011.

[74] G.S. Frankel. Pitting Corrosion of Metals: A Review of the Critical Factors, Journal of The Electrochemical Society 145 (1998) 2186-2198.

[75] T.E. Graedel, R.P. Frankenthal. Corrosion Mechanisms for Iron and Low Alloy Steels Exposed to the Atmosphere, Journal of The Electrochemical Society 137 (1990) 2385-2394.

[76] P.L. Andresen et al. Corrosion Mechanisms in Theory and Practice. Marcel Dekker, New York, 2002.

[77] A. Cox, S.B. Lyon. An electrochemical study of the atmospheric corrosion of mild steel – III. The effect of sulphur dioxide, Corrosion Science 36 (1994) 1193-1199.

[78] S.P. Lynch. 2 - Hydrogen embrittlement (HE) phenomena and mechanisms. in: Raja VS, Shoji T, (Eds.). Stress Corrosion Cracking. Woodhead Publishing, 2011. pp. 90-130.

[79] S. Lynch. Hydrogen embrittlement phenomena and mechanisms, Corrosion Reviews 30 (2012) 105-123.

[80] J. Galvele. A stress corrosion cracking mechanism based on surface mobility, Corrosion Science 27 (1987) 1-33.

[81] S.A. Shipilov et al.. Environment-induced cracking of materials, Elsevier, Vol. 1&2. Amsterdam, 2008.

[82] S.P. Lynch. 1 - Mechanistic and fractographic aspects of stress-corrosion cracking (SCC). in: Raja VS, Shoji T, (Eds.). Stress Corrosion Cracking. Woodhead Publishing, 2011. pp. 3-89.

[83] V. Raja, T. Shoji. Stress corrosion cracking: theory and practice, Elsevier, 2011.

[84] A.J. Sedriks. Corrosion of Stainless Steels. 2nd edition, John Wiley & Sons, Canada, 1996.

[85] F. Zucchi et al. Hydrogen embrittlement of duplex stainless steel under cathodic protection in acidic artificial sea water in the presence of sulphide ions, Corrosion Science 48 (2006) 522-530.

[86] J. Charles et al. The Ferritic Stainless Steel Family: The Appropriate Answer to Nickel Volatility? 6th European Stainless Steel Conference Science and Market, Helsinki, 2008.

[87] P. Ernst et al. The mechanism of lacy cover formation in pitting, Corrosion Science 39 (1997) 1133-1136.

[88] G.V. Karpenko, I.I. Vasilenko. Stress Corrosion Cracking of Steels. 2nd Edition. Freund Publishing, distributed Trans Tech Publication, Aedermannsdorf, Switzerland, 1979, p. 1-185.

[89] P. Gangloff et al. Environment-Induced Cracking of Metals. NACE, Houston, Texas, USA, 1988, p. 1-624.

[90] E. Symniotis. Galvanic Effects on the Active Dissolution of Duplex Stainless Steels, Corrosion 46 (1990) 2-12.

8 Effect of Heat Treatment on Corrosion and EAC Performance

8.1 General Introduction

The fabrication of ILW storage containers includes mechanical shaping and welding which, usually, deteriorates corrosion and stress corrosion cracking performance. The as-received material obtained from the manufacturer may not be free from precipitates and welding can lead to a variety of precipitation and also change the grain structure. The formation of precipitates is usually accompanied by elemental depletion zones around adjacent regions leading to enhanced localised corrosion susceptibility and often embrittlement.

In stainless steels, there are two main precipitation temperature existence areas which can cause severe embrittlement and loss of corrosion performance. *475°C embrittlement* occurs in the temperature window between 250-550°C. The ferrite phase is primarily unstable in this temperature regime and suffers from a variety of microstructure decomposition due to an existing miscibility gap in the Fe-Cr and Fe-Ni binaries and the driving force for chemical decomposition of alloying elements in high-alloyed stainless steels. *750°C embrittlement or σ-phase embrittlement* occurs in the temperature window between 600-1000°C which usually leads to more severe loss of mechanical and electrochemical properties than caused by 475°C embrittlement.

The focus of the majority of all research performed so far have been on microstructure development and mechanical property changes associated with ageing treatments in the 475°C temperature window. The response of the 475°C embrittlement phenomenon to corrosion properties was less studied, and no data exist about the effect of the 475°C embrittlement on atmospheric-induced stress corrosion cracking behaviour of 2205 duplex stainless steel.

The absolute majority of all works reported ascribed the detrimental effects on mechanical and electrochemical properties on the decomposition of the ferrite phase only, and reasoned or neglected possible phase reactions occurring in the austenite phase. Furthermore, there has been no work or report published so far doing comprehensive and detailed analysis of microstructural development as such that all microstructure decomposition and phase

transformation products were not characterised at a glance. The stages of decomposition and phase reactions at different ageing conditions have not been fully characterised.

Moreover, the reason of the change of the corrosion performance of duplex stainless steels associated with 475°C embrittlement has not been extensively studied, and there has been no corrosion models made available explaining the increase for the critical pitting corrosion resistance of short-term aged microstructure and the decrease of the overall corrosion performance after long-term ageing.

In contrast, the sigma-phase embrittlement has been extensively studied in the literature, but a comprehensive microstructure analysis of 2205 duplex stainless steel has been scarcely reported. Mostly, sigma, chi, secondary austenite, carbides, and nitrides have been separately studied by transmission electron microscopy, and a comprehensive study incorporating an overall assessment of all precipitates together and linking their effect with each other to express local and overall corrosion and stress corrosion cracking behaviour were not seen.

A mechanistic understanding of the materials corrosion performance requires the knowledge about the type, chemical composition, structure, geometry, morphology, and location of secondary phases formed in the microstructure during the heat exposure. The corrosion and stress corrosion cracking susceptibility of duplex stainless steels can be highly altered by microstructural variation associated with the formation of secondary phases.

In this chapter, the 475°C and 750°C embrittlement phenomena will be revised and their effects on microstructure development will be thoroughly discussed in light of local and overall mechanical and corrosion property changes. Decompositional and phase reaction products will be introduced and their locations in the microstructure with structural, geometrical, and morphological information given. The environment-assisted cracking performance for ILW storage-relevant conditions will be thoroughly discussed and the benefits or consequences of both embrittlement phenomena explained.

8.2 Effect of 475°C Embrittlement on Microstructure Development and Mechanical Properties of 22Cr-5Ni Duplex Stainless Steel

C. Örnek*[1,2,3], J.J.H. Lim[1], M. G. Burke[1], T. Hashimoto[2], & D. L. Engelberg[1,2,3]

[1]Materials and Performance Centre,
School of Materials, The University of Manchester,
Sackville Street, Manchester, M13 9PL, United Kingdom

[2]Corrosion and Protection Centre,
School of Materials, The University of Manchester,
Sackville Street, Manchester, M13 9PL, United Kingdom

[3]Research Centre for Radwaste & Decommissioning
School of Materials, The University of Manchester,
Sackville Street, Manchester, M13 9PL, United Kingdom

8.2.1 Abstract

A 22Cr-5Ni duplex stainless steel has been aged for up to 255 hours at 475°C and the microstructure development correlated to changes in local and bulk mechanical properties. Tensile testing of aged microstructures confirmed the occurrence of 475°C embrittlement, manifested in a reduction in ductility with longer ageing times. The embrittlement was accompanied by an increase in bulk hardness, with micro- and nano-hardness measurements showing the same trend, resulting in peak hardness after 255 hours of ageing. XRD residual stress analyses revealed an initial increase of compressive stresses in the ferrite, followed by an overall reduction of stresses in both austenite and ferrite. EBSD augmented by XRD phase analysis confirmed on overall increase of austenite fraction due to phase reactions occurring mainly in the ferrite. After 255 hours of ageing, most of the ferrite was decomposed by spinodal decomposition consisting of Cr-enriched α'' and Fe-rich α', with discrete R-phase precipitates. R-phase preferentially nucleated on sub-grain boundaries with sizes between 50-400 nm.

Keywords: *475°C Embrittlement; Duplex Stainless Steel; Spinodal decomposition; X-Ray Diffraction (XRD) Stress Measurement; Electron Back-Scatter Diffraction (EBSD); Transmission Electron Microscopy (TEM)*

8.2.2 Introduction

Duplex stainless steels (DSS) are highly corrosion and stress corrosion cracking resistant materials with remarkable mechanical properties. The microstructure consists of ferrite (δ) and austenite (γ), usually in a balanced ratio, and is tailored to provide excellent electrochemical behavior with good mechanical strength, ductility, and fracture toughness. DSS's have been successfully used in many critical applications including petrochemical, off-shore, marine, and nuclear [1-3]. The mechanical strength and toughness of DSS's derive from their high-alloyed chemical composition and small grain size, typically in the order of 5-10 µm. Mechanical properties and the stress corrosion cracking (SCC) behavior is influenced by the ferrite to austenite ratio [4]. Strength and creep resistance are usually governed by the ferrite, whereas ductility and toughness are controlled by the austenite [5]. The best overall performance with respect to SCC resistance is reported for ratios with equal volume fractions of ferrite and austenite [5, 6].

Service temperatures between 250-550°C can limit DSS application due to loss of toughness and ductility arising from microstructure embrittlement [5, 7-10]. The highest rate of embrittlement in 22Cr-5Ni DSS has been reported to occur at 475°C; therefore this phenomenon is denoted as '475°C embrittlement' or low temperature embrittlement in the literature [5, 9, 10]. Microstructure embrittlement in this temperature range causes degradation of mechanical properties associated with microstructure decomposition reactions on sub-micro-meter to nano-meter scale. The 475°C embrittlement is usually attributed to phase reactions occurring in the ferrite phase, with the volume fraction of ferrite believed to be a major factor determining component life-time [9-11].

Embrittlement is usually ascribed to spinodal decomposition of the ferrite, namely the formation of Cr-enriched α''-phase and Fe-rich α'-phase, or the formation of Cr-enriched α''-precipitates embedded in a Fe-rich α'-matrix after long-term ageing [9, 12-16]. However, additional phases can also form in the ferrite and coexist with the spinodal decomposition products, such as G-phase, carbides, nitrides, secondary austenite, χ-, π-, τ-, I-, S-, J-, Z-, R- and Laves-phases [7, 9-12, 17-27], which also can have significant impact on mechanical properties. Decomposition and phase reactions in austenite similar to that of ferrite may also occur due to an existing miscibility gap in the Fe-Ni equilibrium phase diagram [28-32]. Therefore, the phenomenon of '475°C embrittlement' in duplex stainless steels may be

associated with a variety of phase transformations occurring in ferrite and in austenite as well. However, ferrite is substantially more prone to phase transformation than austenite due to larger Cr and Mo contents and higher diffusion rates of alloying elements, resulting in faster reaction kinetics in the ferrite [10, 33, 34]. Therefore, major interest of characterisation of 475°C embrittlement has mainly focused on phase transformation occurring in the ferrite phase.

Ferrite, with its high Cr content, can undergo phase separation and precipitation reactions due to the existence of a miscibility gap in the Fe-Cr binary equilibrium system. Ferrite is not stable within the miscibility gap and decomposes into two phases, Fe-rich body-centered-cubic (BCC) α' and Cr-rich BCC α''. Other secondary phases can coexist resulting in further precipitation within the ferrite. Unfortunately, no common denotation for this phenomenon exists in the literature. Some authors stated the reaction as $\delta \rightarrow \alpha + \alpha'$, while others stated as $\alpha/\delta \rightarrow \alpha' + \alpha''$, or $\alpha \rightarrow \alpha_1 + \alpha_2$. In both cases, α' can be confused with martensite. It is useful, therefore, to state and mention clearly the structure and composition, such as Fe-rich α', to avoid misinterpretations. It is further useful to denote the reaction mechanism, such as Cr-rich $\alpha''_{spinodal}$ or $\alpha''_{precipitate}$.

The phase separation of ferrite into Fe-rich (Cr-poor) α' and Cr-rich (Fe-poor) α'' domains can occur either through spinodal decomposition or by classic nucleation and growth outside of the spinodal regime but still within the miscibility gap as schematically shown in Figure1(a). Spinodally-decomposed microstructure consists of domains of Fe-enriched $\alpha'_{spinodal}$ and Cr-enriched $\alpha''_{spinodal}$, with interconnected and intertwined structure. Their appearance is usually a mottled structure with a noticeable contrast variation in electron microscopy. The Fe-rich $\alpha'_{spinodal}$ forms the matrix where Cr-rich $\alpha''_{spinodal}$ domains are embedded [16, 35-40].

Based on nucleation and growth, discrete Cr-rich α'' particles, either in the form of needle [11, 17] or globular precipitates [41], can be formed, whereas the Fe-enriched BCC α' forms the matrix [16, 19, 42]. The microstructure appearance of phase separation by nucleation and growth and by spinodal decomposition is different. The latter forms a three-dimensionally interconnected structure producing uniform, fine-scale, two-phase mixture which can be described mathematically [43, 44], while the precipitates are embedded in the ferritic matrix [16, 35-40]. However, both mechanisms can operate at the same time [45, 46] and coexist

with other precipitates [9, 19, 45], possibly enhancing the effect of embrittlement. Both phase separation mechanisms; classical nucleation and growth and spinodal decomposition are illustrated schematically in Figure 8-1. At the final stage of the chemical reactions within the miscibility gap, both $\alpha'_{spinodal}$ and $\alpha'_{precipitate}$ and $\alpha''_{spinodal}$ and $\alpha''_{spinodal}$ have equivalent chemical compositions, but different structural morphologies. Thus each mechanism leads to different physical and electrochemical properties of the bulk metal.

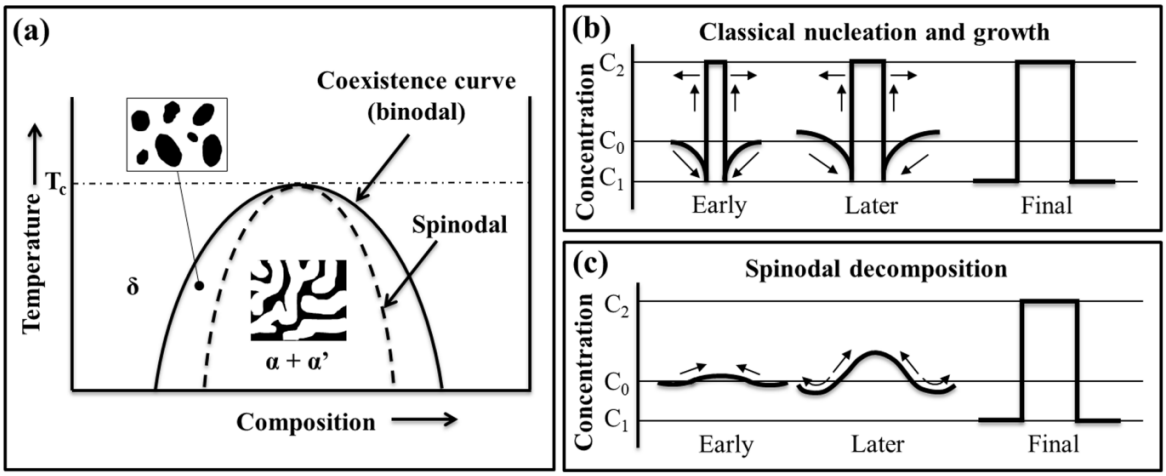

Figure 8-1: (a) Schematic illustration of the miscibility gap in binaries*;* (b) schematic illustration of phase separation mechanisms, reproduced with the kind permission of John Wiley & Sons from the reference [37]

Amongst the large variety of phases identified that have formed in the low temperature embrittlement window, the intermetallic R- and G-phases are also thought to be responsible for the 475°C embrittlement phenomena. G-phase (molybdenum silicide) precipitates have been reported to be of globular morphology with sizes between 20-50 nm according to *Mateo et al*. [20], 2-7 nm according to *Hamaoka et al.* [47], 8-11 nm according to *Danoix et al.* [42], and <50 nm according to *Shiao et al.* [22], having a face-centered-cubic (FCC) structure with Fm3m space group and (1.09 nm, 1.12 nm, 1.14 nm) lattice parameters [48].

Frank-Kasper-R-phase precipitates belong to the tetrahedrally close-packed phases with rhombohedral unit cell (reverse hexagonal lattice). Their lattice parameters are reported to be a = 0.901 nm and α = 74.5°. They usually assume a disc-shaped or lenticular morphology with sizes between 50-400 nm and are enriched in Mo and Si [9, 12, 13, 19, 21, 24, 49, 50]. The precipitation of τ-phase occurs by a diffusional process and exhibits a needle-like appearance with *Fmmm* space group and lattice parameters with a = 0.4054 nm, b = 0.3436 nm, and c = 0.2867 nm.

Secondary austenite formation in ferrite has been reported to occur in diffusion-less manner via a double-shear nucleation process [12, 50] which can assume Widmannstätten morphology [22]. *Shiao et al.* distinguished three different mechanisms of secondary austenite formation (γ_2), also called 'new austenite' (γ_{new}), which can have different morphological appearance with possibly different chemical composition [22]. One is formed on ferrite/ferrite grain boundaries via nucleation and growth by the consumption of ferrite producing a band-like shape along ferritic grain boundaries. Another is formed on the interface between ferrite and austenite grain boundaries by a direct reversion of ferrite to austenite due to elemental redistribution with, usually, Ni depletion around the newly formed austenite and a precipitation-free zone. In the ferrite grain-interior, a further form of secondary austenite can be formed having Widmannstätten structure [22] which is well-known in ferritic steels for causing severe embrittlement [51].

The work reported in this paper aims to provide an in-depth understanding of microstructure development with correlation to changes in mechanical properties as a function to 475°C heat treatment. The mechanical behavior and residual stress evolution were compared to microstructure changes on micro- and nano-scale.

8.2.3 Experimental

A mill-annealed (as-received) grade 22Cr-5Ni duplex stainless steel plate with a composition (in wt.-%) of 22.4Cr, 5.8Ni, 3.2Mo, 1.5Mn, 0.4Si, 0.016C, 0.18N and Fe (bal.) was used for all microstructure investigations in this study. Rectangular coupon specimens were cut from as-received plate and heat treated at 475 ± 5°C for 5, 20, 50, and 255 hours followed by a water-quench. The furnace temperature was controlled at 475 ± 5°C using a K-type thermocouple. The surface of the specimens was prepared by grinding to 4000-grit, followed by fine polishing using 3, 1, ¼, and 0.1 µm diamond paste, finalized with an OP-S active oxide polishing suspension treatment containing 40 nm colloidal silica particles (pH 9-10). Microstructure characterization, local strain and stress data, and micro- and nano-hardness values were obtained from these surfaces.

8.2.3.1 Tensile Testing

Tensile tests were performed to obtain mechanical properties of flat tensile specimens, with parameters determined as 0.2% offset yield stress, $R_{p0.2}$, and ultimate yield stress, R_m. Tensile tests were performed on an *Instron 5569* tensile testing machine with an extensometer from MTS. The strain rate was 2 mm/min. Tensile specimens with 50 mm gauge length, 10 mm gauge width, and a total length of 80 mm were machined from 2 mm thick grade 2205 DSS sheet. The composition of the mill-annealed sheet material was 22.44Cr, 5.75Ni, 3.32Mo, 1.41Mn, 0.42Si, 0.015C, 0.155N, 0.006Nb, 0.21Cu, 0.12Co, and Fe (bal.).

8.2.3.2 Hardness Testing

Macro-hardness testing was augmented by micro- and nano-hardness measurements to obtain information about the behavior of individual microstructure constituents with 475°C embrittlement treatment. Macro-hardness measurements were carried out on a Vickers macro-hardness device *(Georg Reicherter Briviskop 187.5)* with a load of 30 kg (HV30). For each sample, ten hardness indentations were made, and the arithmetical mean with standard deviation calculated. All samples had 600-grit SiC paper ground surface.

Micro-hardness measurements were conducted with the *Struers Duramin* micro-hardness tester *(Ballerup, Denmark)* with a Vickers indenter and a test load of 0.098 N (HV0.01). A total of 50 hardness measurements were obtained from each specimen: 25 measurements in the austenite and 25 measurements in the ferrite phases. The arithmetic mean of all micro-hardness results was calculated for all specimens.

Nano-indentation measurements were performed on all specimens using the *Nano Indenter XP* from *MTS Nano Instruments*. A *Berkovich* indenter with three-sided pyramidal shape and 65.03° angle between the load axis of the tip was used to keep the projected area-to-depth ratio constant. 10 x 10 indentations with a penetration depth of 200 nm and 10 nm distance between the indentations were made in a serpentine array on each specimen. From each indenting local nano-hardness values at maximum load were obtained. The tested area was analyzed by the *FEI Quanta 650* scanning electron microscope (SEM) and electron backscatter diffraction (EBSD) to ascribe each indent to either ferrite or austenite.

Indentations which penetrated into the interphase regions were not considered, resulting in 30-40 valid indentations for each microstructure crystallographic phase.

8.2.3.3 X-ray Diffraction Stress Analysis

A *Proto iXRD Combo* X-ray Diffractometer *(Proto Manufacturing Inc., Michigan, USA)* was used to measure surface residual stress profiles, with typically ± 20 MPa error band for all data [52, 53]. The testing machine is equipped with a two detector system, and a schematic illustration of the measurement setup is given in Figure 8-2. Cr and Mn x-ray tubes were used to measure the strain in ferrite and austenite, respectively, with a penetration depth of approximately 10-15 µm (99% absorption by work piece at Ψ = 0°) [53-55]. Sin-2Ψ measurements were performed at eleven Ψ tilt angles (β angles on the *Proto iXRD*) with a 3° oscillation between at each *β* angle, with all further setup parameters listed in Table 8-1.

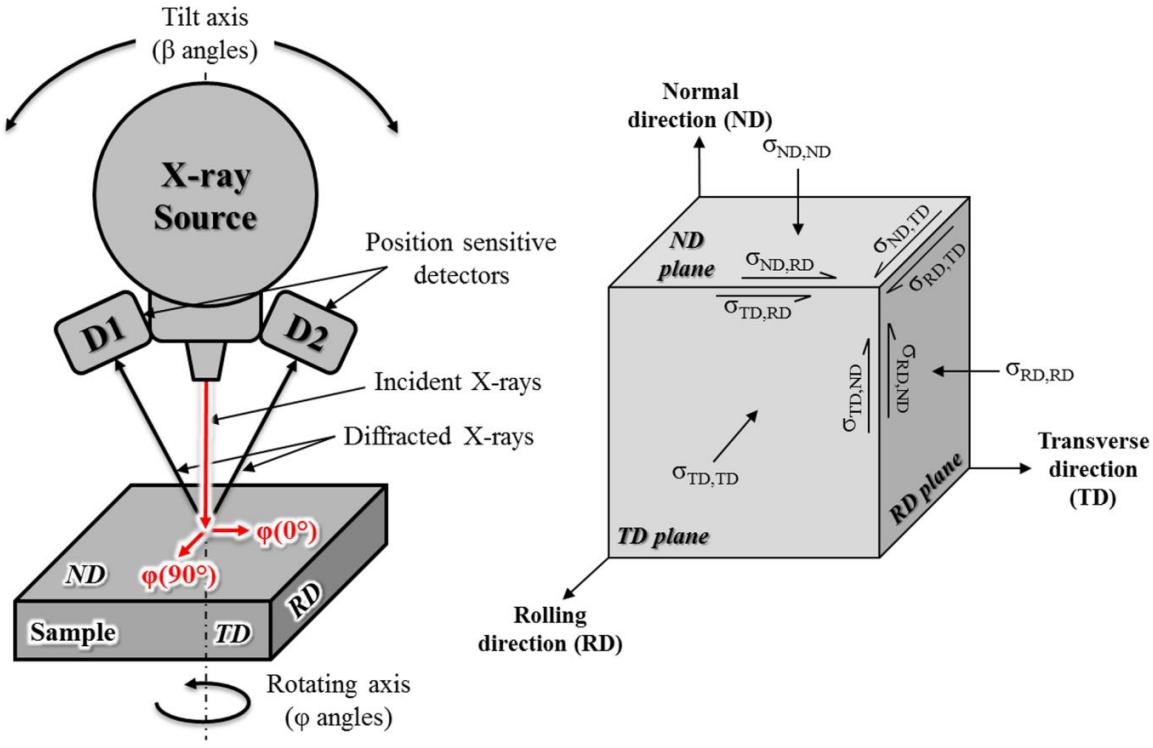

Figure 8-2: (left) Schematic illustration of XRD stress measurement setup with (right) definition of the process orientations with corresponding stress directions

Prior to the tests, the x-ray diffractometer was calibrated to determine the zero stress position. Stress-free and pre-stressed standard samples were used for calibration. The multiple exposure technique was used and the inter-planar d-spacing of the respective planes

measured. Two x-ray measurement orientations, i.e. 0° and 90° φ (Phi) angles, in all process orientations of each specimen were chosen, which was in alignment with the microstructure orientation. Each measured orientation corresponds to the stress direction as specified in Figure 8-2.

Table 8-1: X-ray measurement conditions using Proto iXRD machine

X-ray type	**Cr-Kα**	**Mn-Kα**
Source voltage, current	20 kV, 4 mA	20 kV, 4 mA
Aperture size	2 mm	2 mm
Bragg angle, 2θ	156.4	152.8
Diffraction plane	(2 1 1)	(3 1 1)
Wavelength	2.291 Å	2.1034 Å
Max. measurement angle, β	±27°	±27°
Number of β angles	11	11
β angles (Ψ)	27, 22.29, 17.24, 11.8, 4.48, **0**, -4.48, -11.8, -17.24, -22.29, -27	
β oscillation angle	3°	3°
Phi angles	0 and 90°	0 and 90°
Exposure time	2 sec	2 sec
Number of exposure profiles	10	10
Number of exposures gain	30	30
X-ray elastic constant $S_1^{(hkl)}$	1.28 x 10^{-6} MPa	1.2 x 10^{-6} MPa
X-ray elastic constant ½$S_2^{(hkl)}$	5.92 x 10^{-6} MPa	7.18 x 10^{-6} MPa
Peak fit	Gaussian	Gaussian

8.2.3.4 Scanning Electron Microscopy

SEM analyses were performed to characterize microstructure morphology and location of crystallographic phases. An *FEI Quanta 650* and *FEI Magellan* high-resolution SEM was used for analyzing electro-polished thin foils and surface-polished coupon specimens. Sample preparation of the thin foils is given below. Surface polishing of the coupon specimens comprised grinding to 4000-grit using SiC sandpapers, followed by 3, 1, ¼, and 0.1 µm polishing using diamond paste, which was finalized by an end-polishing using OP-S for 60 minutes.

EBSD was employed to characterize the microstructure, including the assessment of grain size, austenite and ferrite phase fraction, and local misorientation (LMO), with the latter indicative of the distribution of residual strain. An *FEI Quanta 650* SEM interfaced with a

Nordlys EBSD detector from *Oxford Instruments* with *AZtec V2.2* software was used for data acquisition. The experimental parameters for EBSD analysis included a step size of 150 nm over an area of 856 x 746 µm² with an accelerating voltage of 20 kV and a 2x2 binning of the CCD readout. High resolution imaging and EBSD analysis was also performed in an *FEI Magellan*, interfaced with a *Nordlys* EBSD detector from Oxford Instruments. The experimental parameters for these analyses included an accelerating voltage of 15 kV with 2x2 binning and a step size of 10-20 nm of an area covering fine ferrite grain-interiors (<5 µm). Data post-processing was performed using HKL *Channel 5* software. High-Angle Grain Boundaries (HAGB's) were defined with misorientation ≥15° and LAGB's between >1° and <15°. The grain size was determined by the mean linear intercept method as the mean of the vertical and horizontal directions (twins disregarded).

8.2.3.5 Transmission Electron Microscopy

Thin foil specimens were prepared from mill-annealed and aged specimens by electro-polishing 80-100 µm thick 3.0 mm diameter disc samples in the *Tenupol-5* twin jet polisher (*Struers, Denmark*) with a *Jubalo* closed-cycle refrigeration system. The samples were electro-polished at 20 kV in an electrolyte of a mixture of 20% perchloric acid and 80% methanol at a temperature of -40°C. All specimens were subsequently examined in an *FEI Tecnai F20 200 kV* analytical transmission electron microscope (TEM) equipped with an *Oxford Instruments Xmax80TLE SDD* energy-dispersive x-ray detector (EDX) operated with an *AZtec* analysis system, and an *FEI Talos* Field Emission Gun analytical TEM equipped with *Super X (4 SDDs)*.

Phase fraction analysis was carried out on the as-received and all aged specimens using XRD and EBSD analysis. EBSD phase fraction analyses were performed on large area covering at least 2000 grains. XRD analyses were performed on the *Bruker D8 Discover*. The scan range was 40.0-130.0° 2θ with a step size of 0.02° 2θ. Co-Kα_1 x-ray source with 35kV accelerating voltage and 40 mA current was used. From the obtained XRD profiles the required lattice parameters for ferrite and austenite were selected from the ICDD PDF cards 04-007-9753 (ferrite) and 04-002-3692 (austenite), which were then read into *Topas V4.2.0.2*. For data refinement the lattice size, scale, peak fitting type, atomic coordinates, temperature factors, preferred orientation etc. were adjusted to achieve best fit. The Rietveld weight percent (RWP) value was kept as low as possible. XRD results of the as-received and

for the 255 hours aged specimen are shown in Figure 8-3 for representation. The fitted curve for each peak position analysis is shown in red. The subtracted curve (in grey) gives the best possible fit. Remaining spikes formed the experimental error (noise); therefore all results are to the best of ±2% precision.

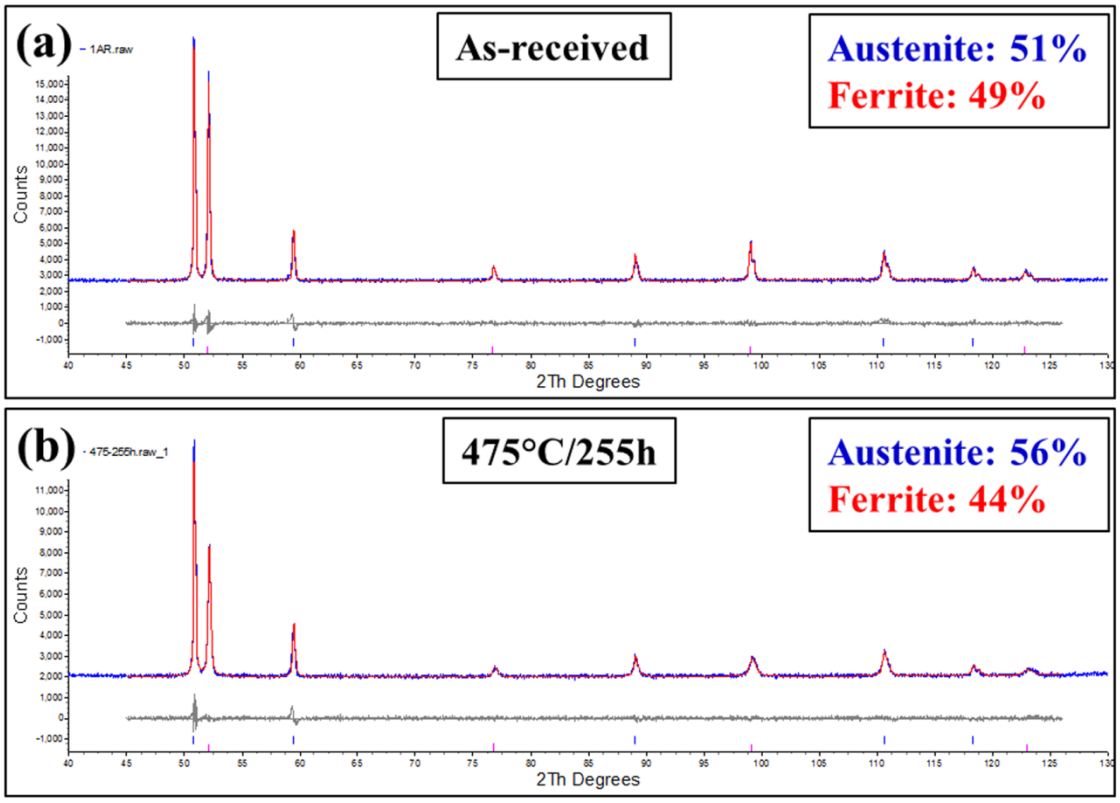

Figure 8-3: XRD peak fitting of (a) as-received and (b) 255 hours aged samples with superimposed fit (red line) and the difference (subtracted) in grey.

8.2.4 Results and Discussion

8.2.4.1 Tensile Testing

All tensile test results for the as-received, 20, 50, and 255 hours aged specimens are shown in Figure 8-4. The elongation to failure (A) was halved after 20 hours ageing from 50 ± 5 % to 28 ± 6 %, showing clear signs of embrittlement. The largest embrittlement was observed in the 255 hours aged specimen with only 12 ± 4 % of elongation. The yield stress, $R_{p0.2}$, increased with the increase in ageing to 735 ± 35 MPa after 255 hours of ageing. The maximum yield strength rose from 830 ± 20 MPa to 1030 ± 20 MPa after 255 hours of ageing. Precipitates and spinodal decomposition can impede dislocation movement, and

hence, the onset of plasticity. This leads to an increase in yield strength which is associated with a decrease in toughness. Ageing at 475°C caused obviously microstructure strengthening at the expense of increasing embrittlement.

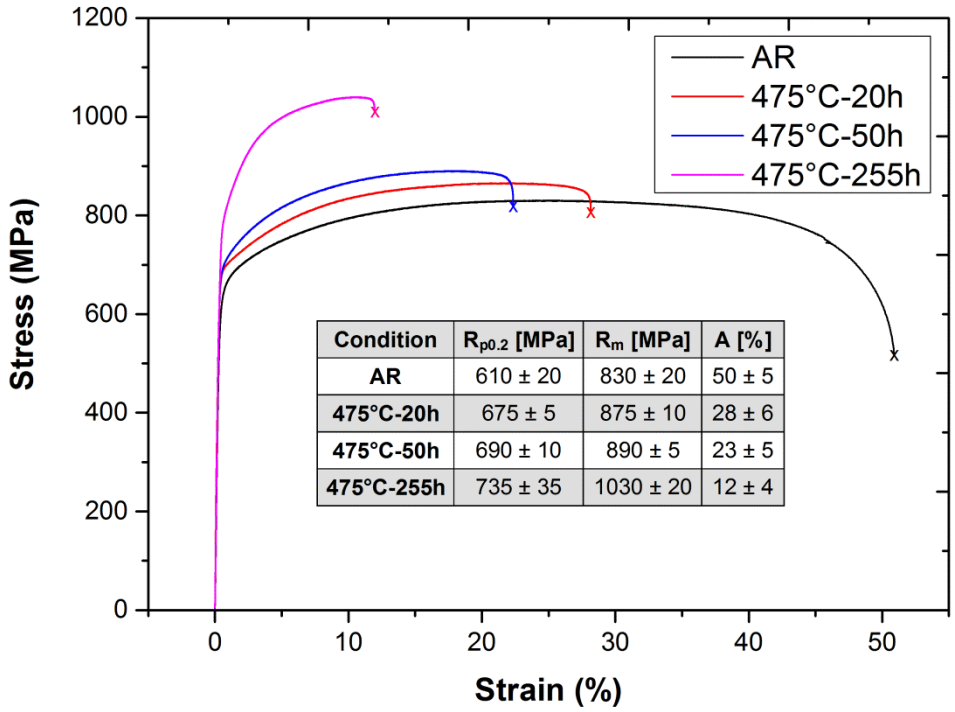

Condition	$R_{p0.2}$ [MPa]	R_m [MPa]	A [%]
AR	610 ± 20	830 ± 20	50 ± 5
475°C-20h	675 ± 5	875 ± 10	28 ± 6
475°C-50h	690 ± 10	890 ± 5	23 ± 5
475°C-255h	735 ± 35	1030 ± 20	12 ± 4

Figure 8-4: Stress-strain behaviour as a function of ageing time at 475°C (AR: as received, R_m: ultimate tensile strength, A: elongation to failure, $Rp_{0.2}$: yield strength)

8.2.4.2 Macro-, Micro-, and Nano-Hardness Development

The micro- and macro-hardness test results are summarized in Figure 8-5. A slight increase with ageing up to 50 hours was observed, with a significant rise in macro-hardness in the specimen aged for 255 hours, clearly indicating the effect of the 475°C embrittlement heat treatment. The micro-hardness of the ferrite followed a similar trend, except of the 20 hours aged specimen, with maximum hardness observed after 255 hours. Phase transformation reactions occurred mainly in ferrite, which resulted obviously in a hardness increase. The hardness of austenite remained constant between a minimum of 263 and a maximum of 290 HV0.01. This indicates that no significant microstructure change occurred which could have influenced the hardness values in austenite.

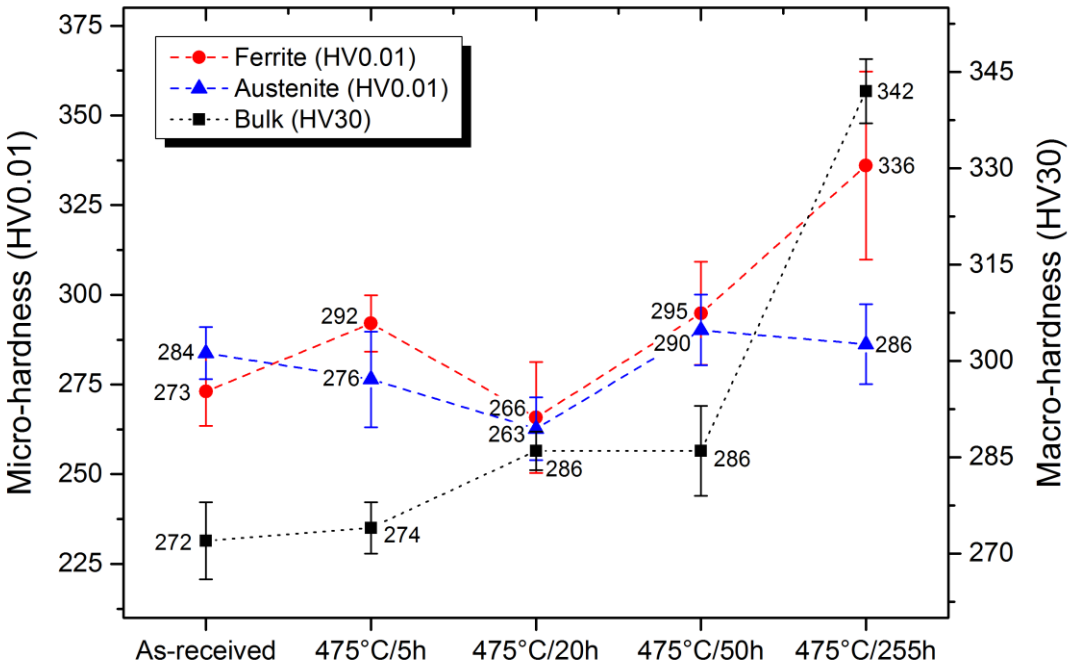

Figure 8-5: Macro-hardness (bulk) and micro-hardness development with 475°C exposure for up to 255 hours

The nano-hardness and Young's modulus data of 0.25 µm diamond paste polished samples are shown in Figure 8-6(a-b). There is a significant nano-hardness increase for both ferrite and austenite with ageing times up to 255 hours, with a dip in hardness observed after 50 hours ageing. TEM analysis (see below) revealed only spinodal decomposition products with increased dislocation density in the 5 and 20 hours ageing specimens. No precipitates were observed in the specimens aged up to 20 hours, and the increase in hardness of ferrite must therefore be due to spinodal decomposition. In the microstructure of the 50 hours ageing specimen R-phase precipitates were observed in the ferrite, which most likely affected the overall hardness of ferrite, causing a decrease of nano-hardness. The highest hardness and largest data variability was measured in the ferrite after 255 hours of ageing, possibly due to the increased number of R-phase precipitates in conjunction with the spinodal decomposition products. The austenite showed a similar trend until 50 hours ageing, with no significant change with 255 hours of ageing. Overall, the austenite seemed to possess a higher hardness than the ferrite up to 50 hours of ageing, which is related to surface deformation caused by the polishing treatment. All samples were therefore re-assessed after fine polishing to 0.1 µm diamond paste followed by an OP-S finish.

For comparison, nano-hardness and Young's modulus data for the OP-S finished specimens are shown in Figure 8-6(a-b). The austenite phase now has a lower hardness than the ferrite, supporting surface deformation effects in the 0.25 µm diamond paste polished samples. The austenite seemed to be more prone to surface hardening compared to the ferrite. However, overall similar trends are present in Figure 8-6(a-b) and Figure 8-6(c-d), with the latter showing nano-hardness values on average 0.5-0.8 GPa lower.

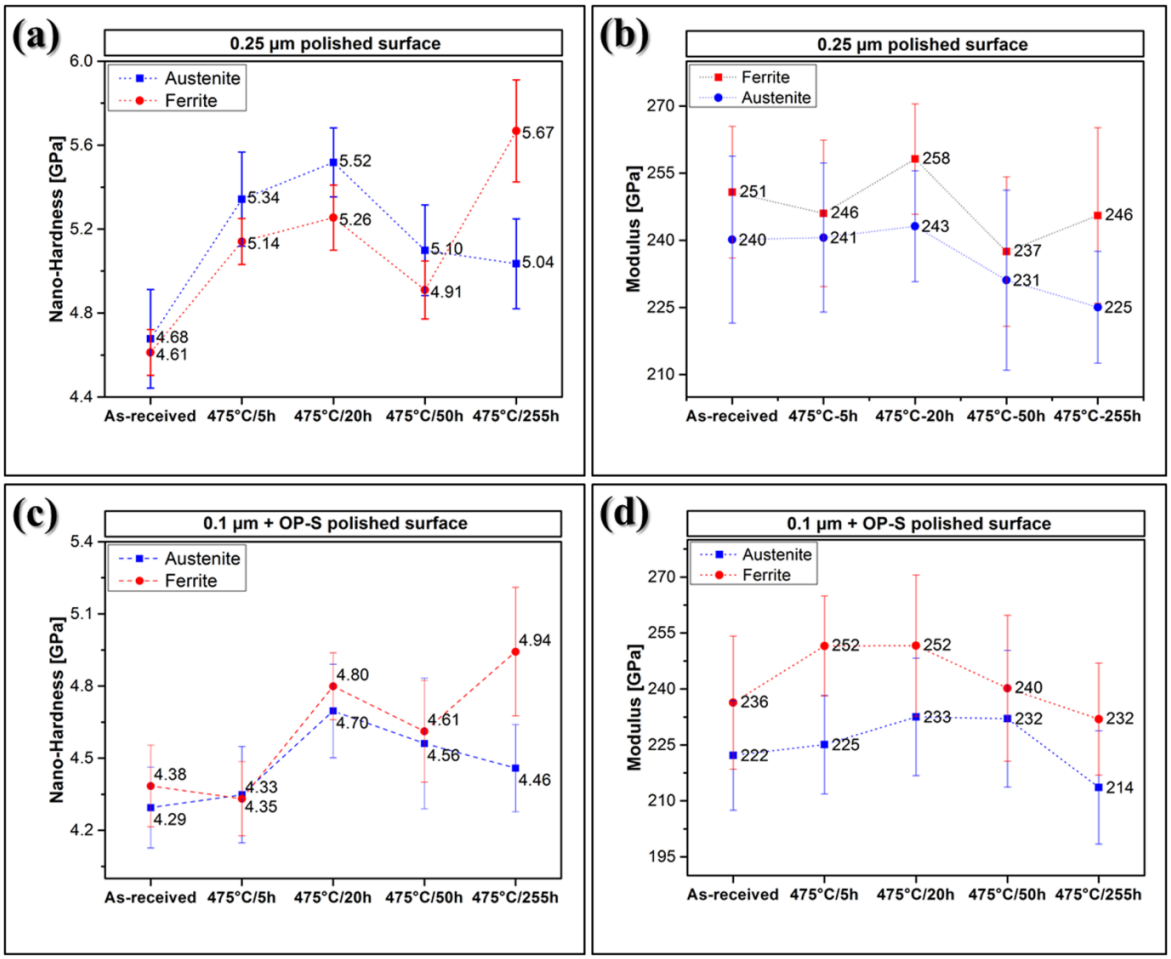

Figure 8-6: Nano-hardness and Young's modulus samples aged for up to 255 hours specimens: (a) nano-hardness with (b) Young's modulus data of 0.25 µm surface polished microstructure, and (c) nano-hardness with (b) modulus data of OP-S surface finished microstructure

Also there is a hardness drop after 50 hours of ageing in the austenite, but the reason for this observation is not clear. *Chung et al.* [30] and *Garner et al.* [56] reported that "spinodal-like" decomposition reactions are possible in the austenite, which would explain the increase in hardness. *Horvarth et al.* [32] in contrast observed a similar rise hardness of the austenite and related this to the formation of spherical Cr_2N particles, Orowan loops, and a large

density of newly formed dislocations. However, further work is needed to elucidate why the hardness increased in the austenite. No decomposition phenomena were observed in the austenite in our study.

8.2.4.3 X-ray Diffraction Stress Development

XRD stress measurements for austenite and ferrite in all process orientations of the microstructure (Figure 8-2 in ND-TD-RD) are shown in Figure 8-7(a-b). The stress in austenite in the as-received condition was compressive in RD and TD, with ND showing minor tensile stresses. The stress distribution in as-received ferrite was different, mainly compressive in ND and TD, with some tensile stresses in RD. Overall, the entire microstructure seemed to possess more compressive surface stress components.

After 5 hours ageing at 475°C, the tensile nature of ND in the austenite changed into compressive stresses, while all other orientations remained unaffected. The stress distribution in ferrite behaved in a similar way, with only TD developing tensile surface residual stresses.

After 20 hours ageing, large compressive stresses were developed in the ND plane in both austenite and ferrite. The compressive stresses in RD and TD planes in austenite further increased with a likewise stress development in ferrite. It seemed that the entire microstructure became more compressively stressed, which might be related to the spinodal decomposition reaction in the ferrite. Spinodal decomposition may have caused negative stress fields due to local chemical strain misfit arising from elemental concentration fluctuations, leading to slight expansion of the entire lattice. Expansion of the ferritic matrix lattice may have also affected austenite grains leading to a compressive stress development in austenite.

After 50 hours ageing, both phases indicated changes in the residual stress profiles, with austenite showing balanced stresses in RD and ND process directions, but not in the TD plane. The compressive stresses in ferrite also shrank significantly. However, other reactions in the austenite must have occurred simultaneously since the initial compressive nature from the mill-annealing process was lost, possibly caused by decomposition products and/or dislocation reactions. All residual stresses in the ferrite and austenite were significantly reduced and balanced after 255 hours of ageing. The nucleation of R-phase precipitates (see

below) seemed to have the largest effect on the stress development in the microstructure, since large variations occurred between 20 and 50 hours and 50 and 255 hours of ageing time.

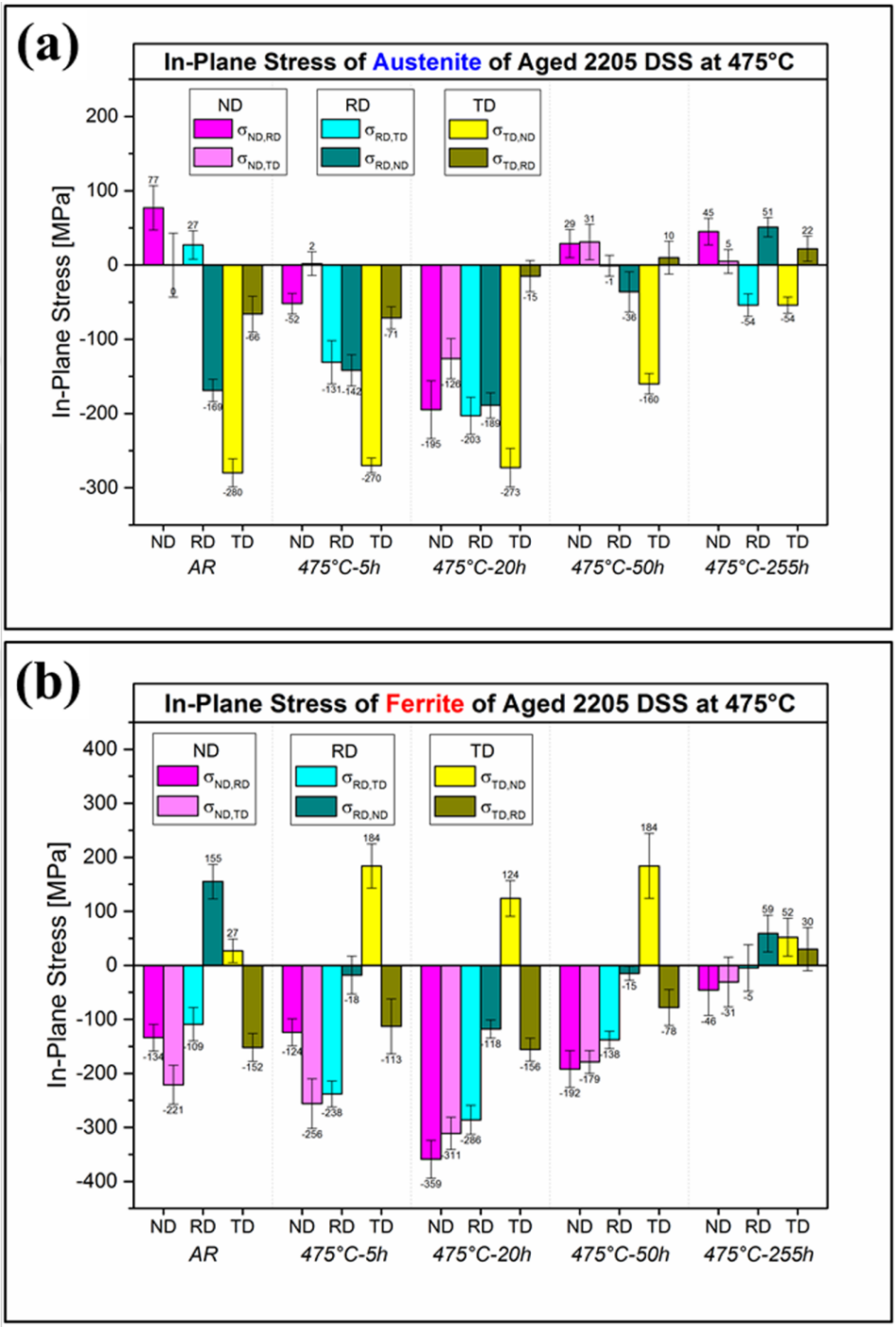

Figure 8-7: XRD stress measurements of all process orientations as a function of ageing time at 475°C with (a) in-plane residual stress data for austenite and (b) residual stress data for ferrite.

8.2.4.4 XRD & EBSD Phase Fraction Analysis

The phase fraction of ferrite and austenite in all aged specimens were analysed by XRD and EBSD and compared with the as-received condition. The results are summarized in Figure 8-8. The austenite to ferrite ratio, measured through XRD, increased from 52:48 ± 2% to 59:41 ± 2% after 255 hours of ageing, while EBSD results showed a similar increase from initially 54:46 ± 1% to 57:43 ± 1%. Thus, secondary austenite must have formed or primary austenite must have grown on the expense of ferrite during ageing. The formation of secondary austenite in 20.9Cr-9.9Ni duplex stainless steel [22] and 308 austenitic stainless steel [45] has been reported and associated with decreasing volume fractions of ferrite during ageing in the 475°C temperature window. The growth of primary austenite by the formation of new austenite was analysed by *Shiao et al.* [22], reporting the consumption of secondary austenite by the growth of primary austenite grains [22]. Furthermore, *Takizawa and co-workers* [57] investigated the effect of ferrite content on stress corrosion susceptibility on a 23Cr-1Mo-1.5Mn duplex stainless steel and observed a decrease of the ferrite content by 5-10% after ageing at 475°C for 690 hours.

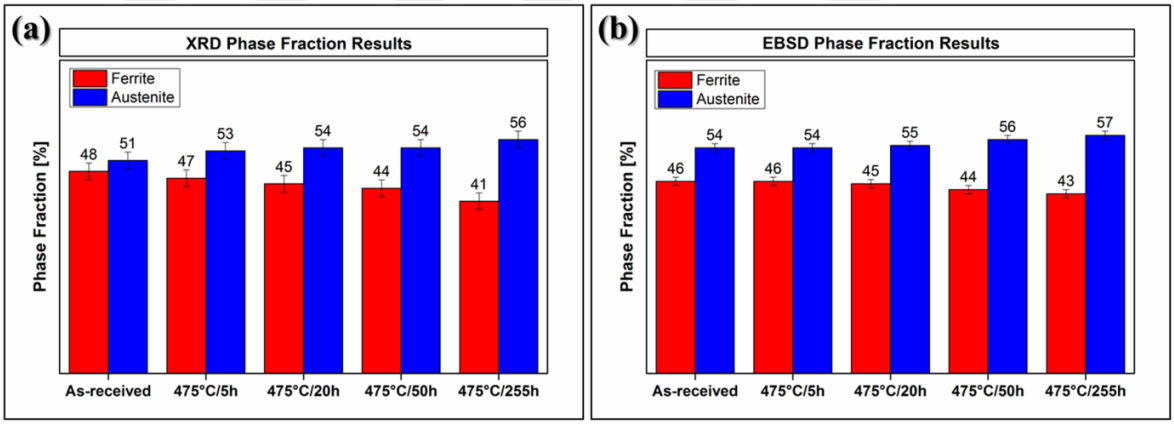

Figure 8-8: (a) XRD and (b) EBSD phase fraction analysis as a function of ageing time at 475°C

8.2.4.5 Microstructure Characterization (SEM & TEM)

The microstructure of the as-received specimen in all process orientations is shown in the EBSD phase maps in Figure 8-9. Ferrite (δ-BCC) and austenite (γ-FCC) phases with typical ferrite/ferrite-, ferrite/austenite-, and austenite/austenite-grain and interphase boundaries can be seen forming the duplex microstructure. The phase ratio of austenite to ferrite (as-received) were 58:42, 54:46, and 56:44 in ND, TD, and RD process orientations, respectively, giving the reported average ratio of 46:54 (Figure 8-8). The as-received

microstructure had a process direction related appearance, with non-equiaxed austenite and ferrite grains, particularly in RD and TD. The grain size of ferrite was 7.6, 7.0, and 7.3 µm in ND, TD, and RD, respectively, whilst the grain size of austenite was 6.8, 6.4, and 8.2 µm, respectively. The average aspect ratio (vertical to horizontal mean length) of all process directions were 1.1, 1.9, and 2.5 for ferrite, and 1.2, 1.6, and 1.9 for austenite in ND, TD, and RD. The largest aspect ratio and smallest grain size, particularly of austenite, clearly showed large deformation history during the manufacturing processes.

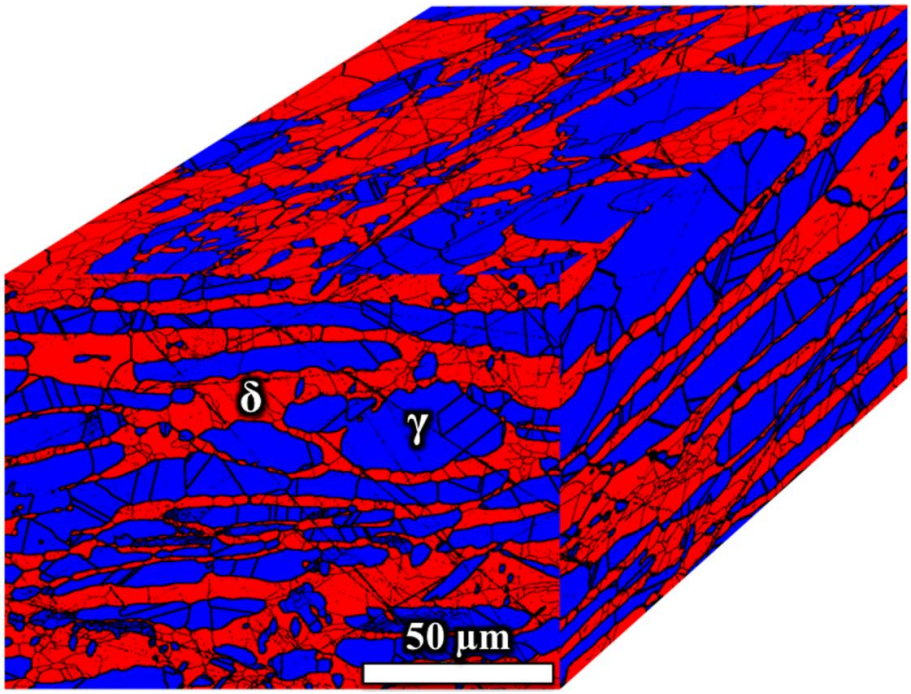

Figure 8-9: EBSD phase map showing the as-received microstructure in all process orientations. HAGB's are shown in thick black lines, whilst LAGB's are those with thin black lines.

A large number of grain boundaries were present in both phases. The low-angle grain boundary (LAGB) to high-angle grain boundary (HAGB) ratio was determined to be 45:55, indicating the presence of deformation in the microstructure. However, the absolute fraction of LAGB's in the as-received material may be an artefact of the LAGB threshold, since LAGB thresholds for stainless steels in the literature are typically reported between 1.6 and 2, rather than the threshold of 1 used in this study [58, 59]. More detailed microstructural information of the austenite and ferrite were obtained through TEM analysis (Figure 8-10). The austenite grains were characterized by the presence of stacking faults and some dislocations, consistent with a recrystallized structure. The ferrite contained dislocations and loops, consistent with a deformed and/or recovered microstructure. This indicates the

presence of residual strain from the thermo-mechanical process history of the as-received material. No crystallographic phases other than the austenite and ferrite were detected in the as-received material.

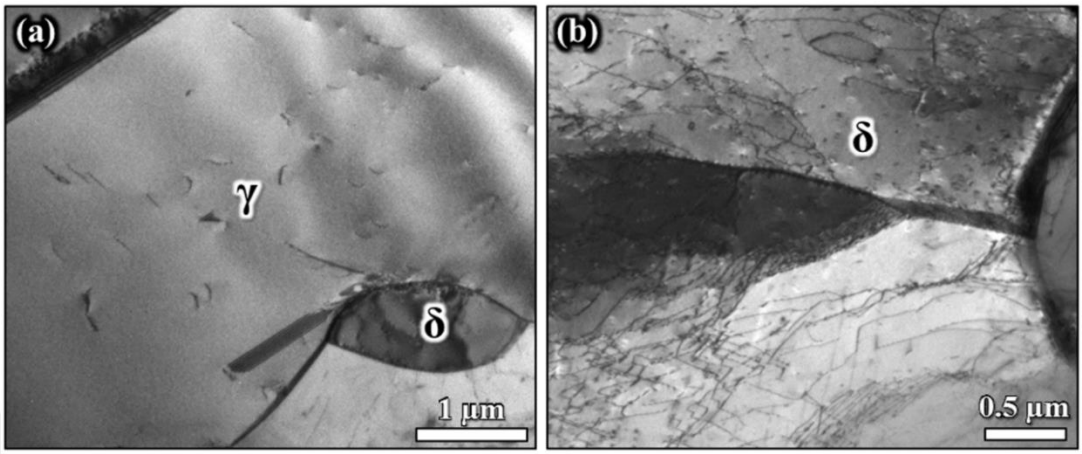

Figure 8-10: As-received microstructure using TEM bright field imaging showing (a) a smooth structure and stacking faults in austenite and (b) a pile of dislocations and loops in ferrite.

The sample aged for 5 hours had a mottled contrast in the ferrite, possibly associated with spinodal decomposition products, as shown in the HAADF image in Figure 8-11. The mottled contrast is related to compositional differences between Fe-rich α' and Cr-enriched α''. No other phases were observed.

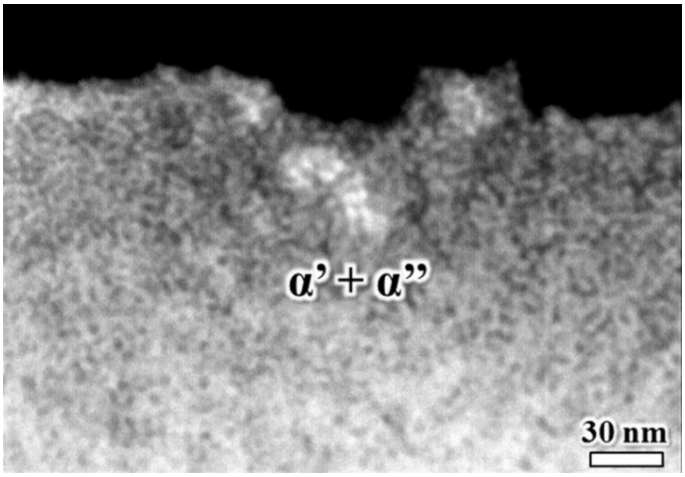

Figure 8-11: TEM image of the microstructure aged at 475°C for 5 hours showing a mottled contrast in ferrite associated with spinodal decomposition consisting of Fe-rich α' and Cr-enriched α'' (HAADF image)

The microstructure of the specimen aged for 20 hours was characterized by the presence of dislocation structures consisting of numerous dislocation loops in the ferrite with dislocation

forests formed on ferritic sub-grain boundaries, all indicating high dislocation activity. These can be seen in the bright field TEM images in Figure 8-12(a-b). These loops were still present after the ageing process. Small discrete realms of strain contrast, possibly associated with precipitation incubates, were observed in the ferrite which can be seen in Figure 8-12(b). The mottled contrast in the ferrite associated with spinodal decomposition products became more apparent in comparison to the specimen aged for 5 hours. This is possibly an indication of enhancement of the amplitude of spinodal decomposition (i.e. distance of Cr-enriched α'' and Fe-rich α' regions) in ferrite, which can be seen in Figure 8-12(c). In austenite, numerous stacking faults and a deformation structure was observed shown in Figure 8-12(d).

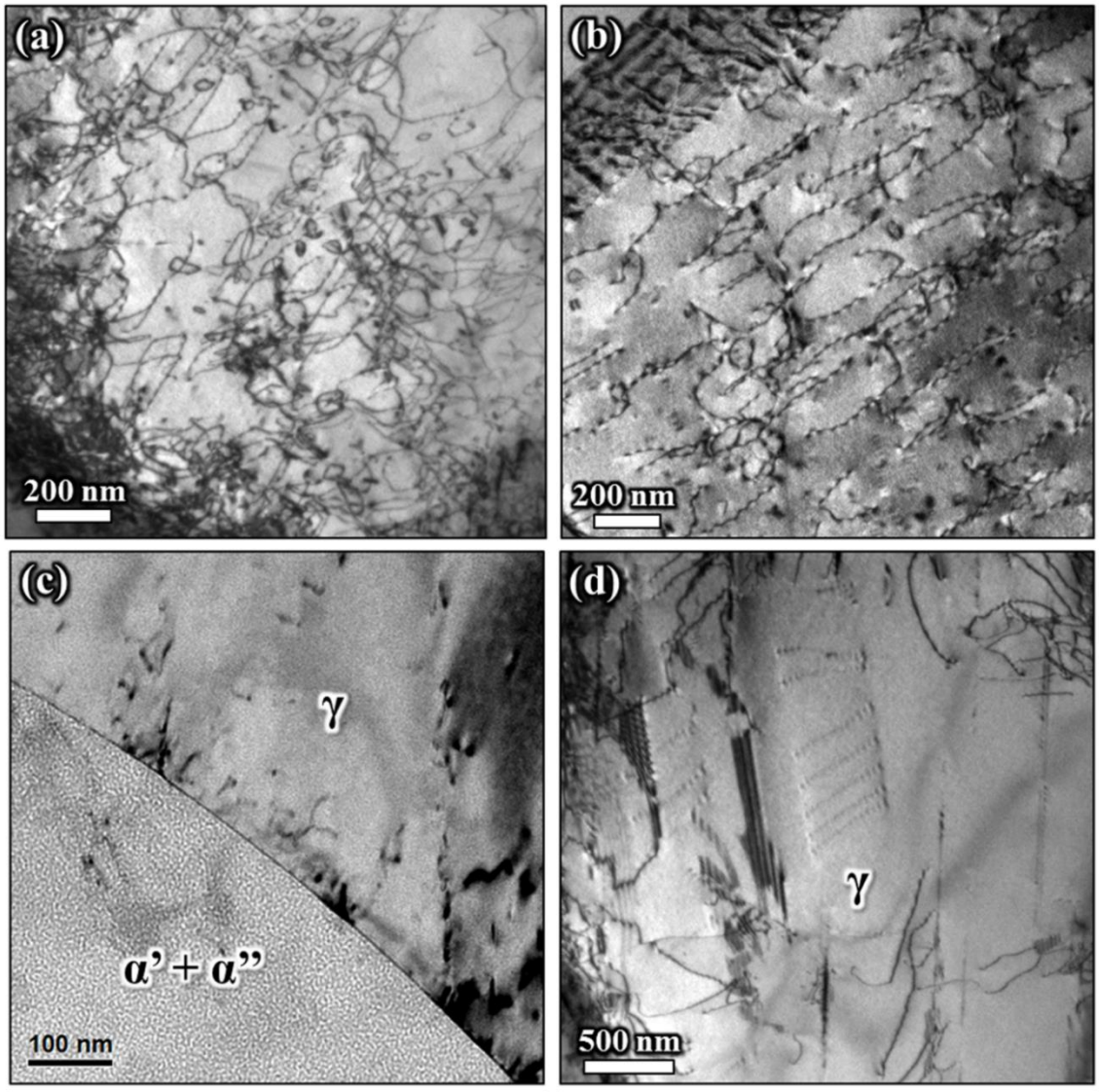

Figure 8-12: TEM bright field analysis of the microstructure aged at 475°C for 20 hours showing (a-b) a pile of dislocations and loops in the ferrite with (c) showing the mottled contrast in ferrite associated with spinodal decomposition, and (d) stacking faults and a deformation structure in austenite

The microstructure of ferrite also revealed bright speckles after 50 hours of ageing, clearly indicating other precipitates which can be seen in the SEM images shown in Figure 8-13(a-c). The majority of all precipitates was located in the ferrite or on interphase boundaries and exhibited a disc or lenticular morphology. SEM-EDX analysis of these precipitates indicated enrichments in Mo with Si, Cr, and Ni. The chemical composition and morphology of these precipitates suggested that they are consistent with R-phase.

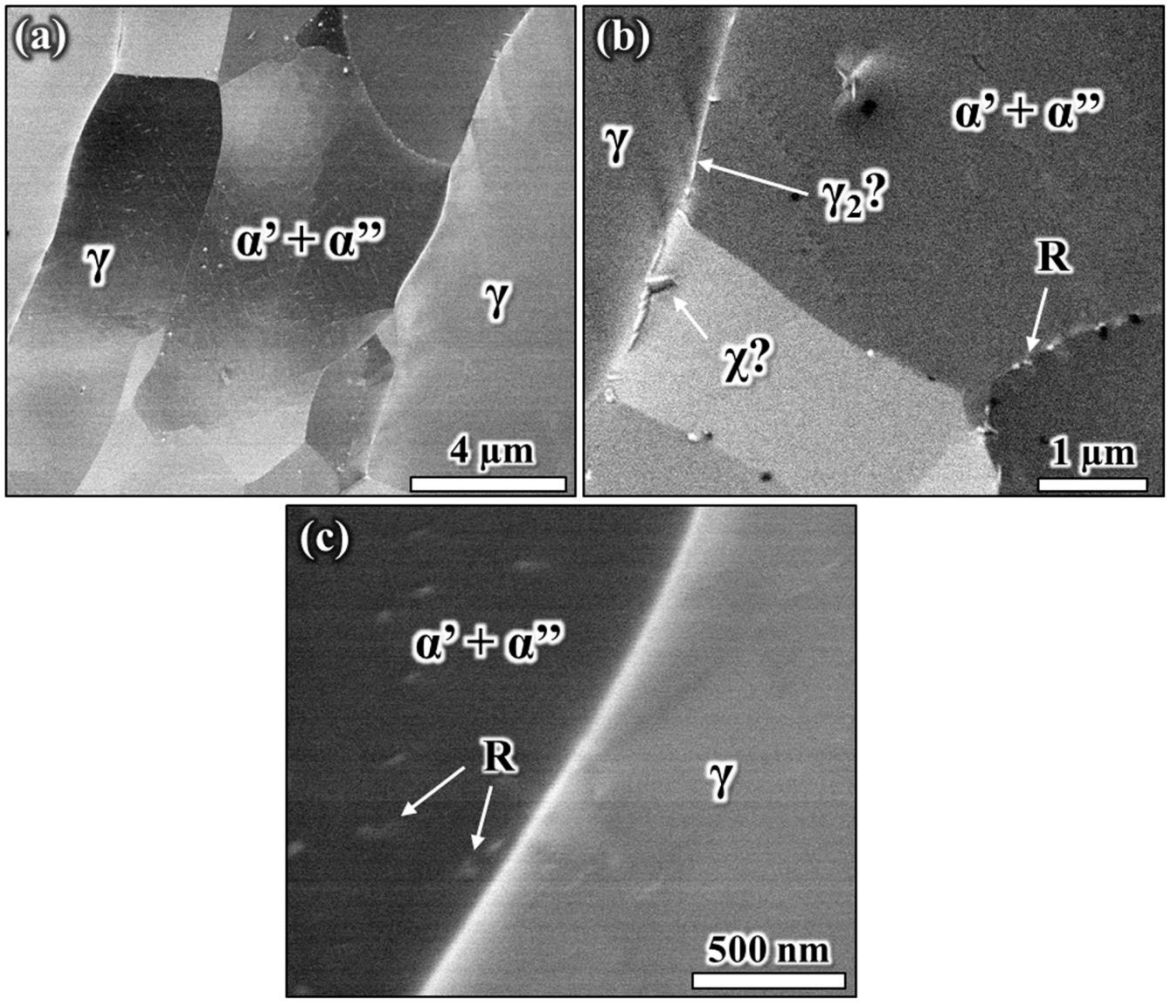

Figure 8-13: SEM analysis of the microstructure aged at 475°C for 50 hours showing (a) showing decomposed ferrite and austenite in low magnification (SE image), (b) R-phase and further unidentified precipitates formed in ferrite and on interphase boundaries, and (c) R-phase precipitates in the decomposed ferrite in high magnification (SE image)

In addition, two other precipitates formed along some ferrite-austenite interphase boundaries, visible as features with brighter contrast than the matrix. One is continuous, and the other has discrete trapezoid shape, which can also be seen in Figure 8-13(b). The discrete particles are enriched in Cr and Mo. The appearance, location, and its chemical compositions

suggest these discrete precipitates are intermetallic χ-phase precipitates, by reference to *Nilsson et al.* who could detect χ-phase intermetallic in a 22Cr-3Mo-8Ni duplex stainless steel aged at 400°C for 100 hours. *Redjaimia et al.* [25] reported χ-phase in Fe-22Cr-5Ni-3Mo-0.03C duplex stainless steel after heat treatments at 550°C with similar appearance of the particle shown in Figure 8-13(b).

Intermetallic phases such as χ and σ are eutectoidically transformed by decomposition of ferrite. Usually, there are binary even ternary products formed, so secondary austenite and carbides could co-exist in the microstructure. Therefore, the continuous precipitates on the interphase, at least some of them, could be carbides, possibly type $M_{23}C_6$ but also M_7C. *Virtek et al.* found $M_{23}C_6$ precipitates with a chemical composition of 72Cr-21Fe-4Ni-3Mn formed at the ferrite-austenite interface on 20.3Cr-9.6Ni-0.05C stainless steel after ageing at 475°C. Carbides can be formed at lower temperatures [10], so their presence cannot be excluded. However, these continuous precipitates could also be secondary austenite, since the latter is also formed at ferrite/ferrite and austenite/ferrite grain boundaries and at dislocations in the ferrite grain-interior.

Furthermore, particles with a faint bright contrast were observed in austenite, shown in the SEM images in Figure 8-13(a+c). These might be indicative for phase transformation products in the austenite. Decomposition phenomena in austenite, in theory, can occur in a similar way like in ferrite since there is a miscibility gap with a spinodal regime reported in the Fe-Ni binary phase diagram [28]. *Horvarth et al.* [32] reported numerous spherical Cr_2N particles formed in 22.9Cr-5.7Ni and 25.6Cr-4Ni duplex stainless steels after short-time ageing treatments. This suggests that fine-scaled nitrides might have formed in the austenite.

Redjaimia et al. [12] estimated an incubation time of 85 hours for Fe-22Cr-5Ni-3Mo-0.03C duplex stainless steel aged at 600°C. *Nilsson et al.* [19] observed R-phase precipitates formed in 22Cr-3Mo-8Ni duplex stainless steel aged at 550°C after 10 hours and aged at 600°C for 3.3 hours, which were already visible in low magnification SEM images. They concluded an incubation time for R-phase at 500°C beyond 24 hours. However, this statement is not clear since in their SEM images for samples aged at 550°C for 24h clear bright speckles are indicative to precipitates in the ferrite [19]. An incubation for R-phase precipitation can therefore be assumed to lie at 475°C between >20 hours and ≤50 hours ageing.

Significant microstructural changes were evident after ageing at 475°C for 255 hours. The microstructure containing decomposed ferrite and austenite is shown in Figure 8-14(a). A large number of decomposition products with at least three different types of precipitates, noticeable from the different morphologies, were formed in ferrite with one having disc- or lenticular shape in sizes between 200-400 nm. This supports the presence of R-phase precipitates, which can be seen in Figure 8-14(b), nucleated on inter- and intra-granular sites in ferrite grain interiors and at ferrite grain boundaries. This observation is in agreement with *Nilsson et al.* [19], *Redjaimia et al. [12, 50]*, and *Karlsson et al.* [21] who observed R-phase precipitates at 550°C, 600°C and 675°C, respectively. Mo- and Si-depleted zones at and adjacent to R-precipitates were also detected. No phase transformation products could be observed in the austenite, except for a few bright spots with faint contrast similar to the regions observed after 50 hours of ageing.

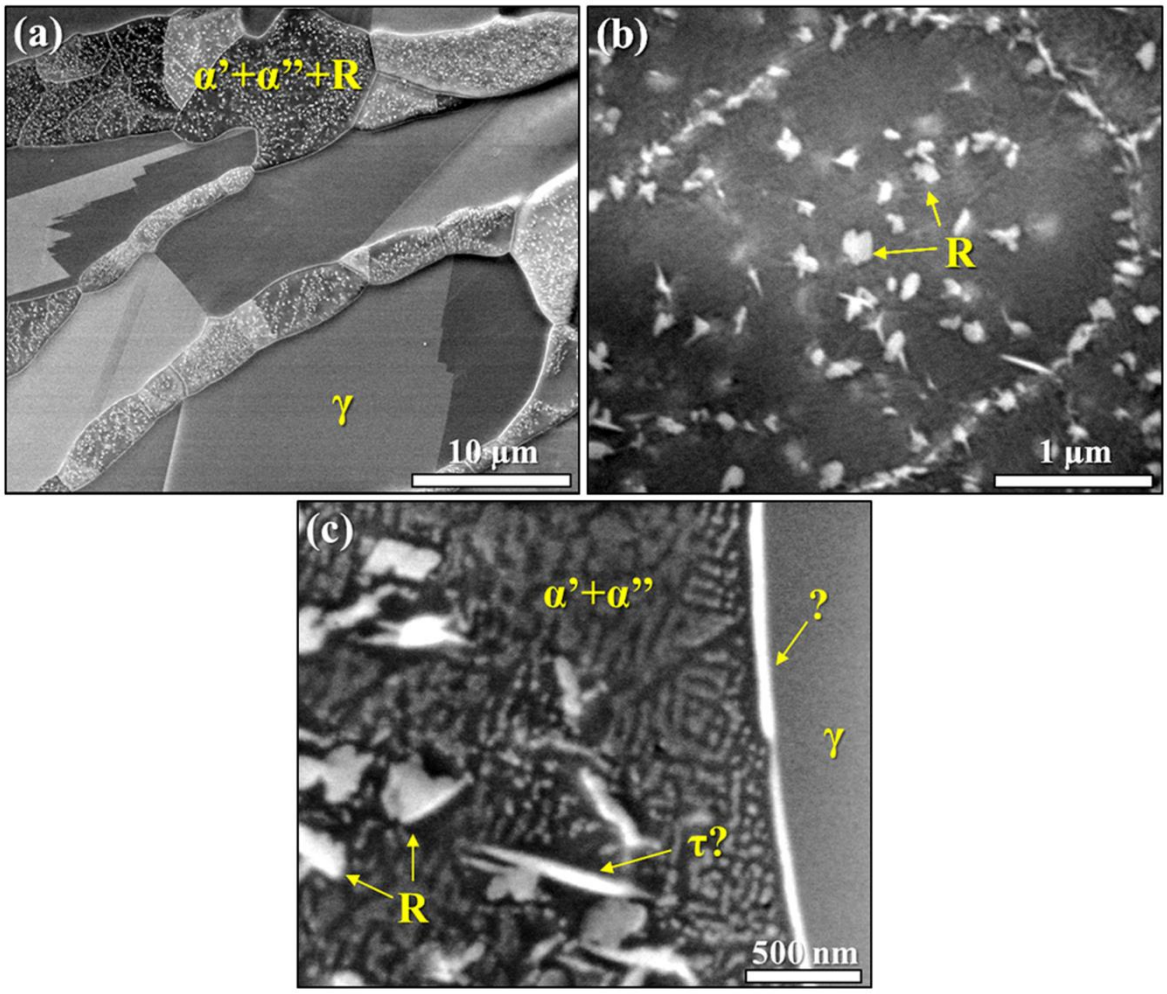

Figure 8-14: Microstructure development after ageing at 475°C for 255 hours showing (a) an overview of the microstructure (SEM-BSD image) with (b) decomposition products (R, α', and α'') formed in ferrite (SEM-SE image), and (c) showing an image with higher magnification (SEM-TLD image).

The finely-dispersed, periodically modulated structure (mottled contrast) associated with spinodal decomposition in ferrite became more apparent in SEM analyses, shown in Figure 8-14(c). This mottled structure is the intertwined, three-dimensionally interconnected Cr-rich α'' and Fe-rich α'-phase, which was confirmed by TEM diffraction analysis. The bright appearing features are Cr-Mo-enriched α''. They have higher topographical height than the Fe-enriched α'-matrix, indicating a thicker passivating layer, because of lower dissolution kinetics which is due to a high Cr content.

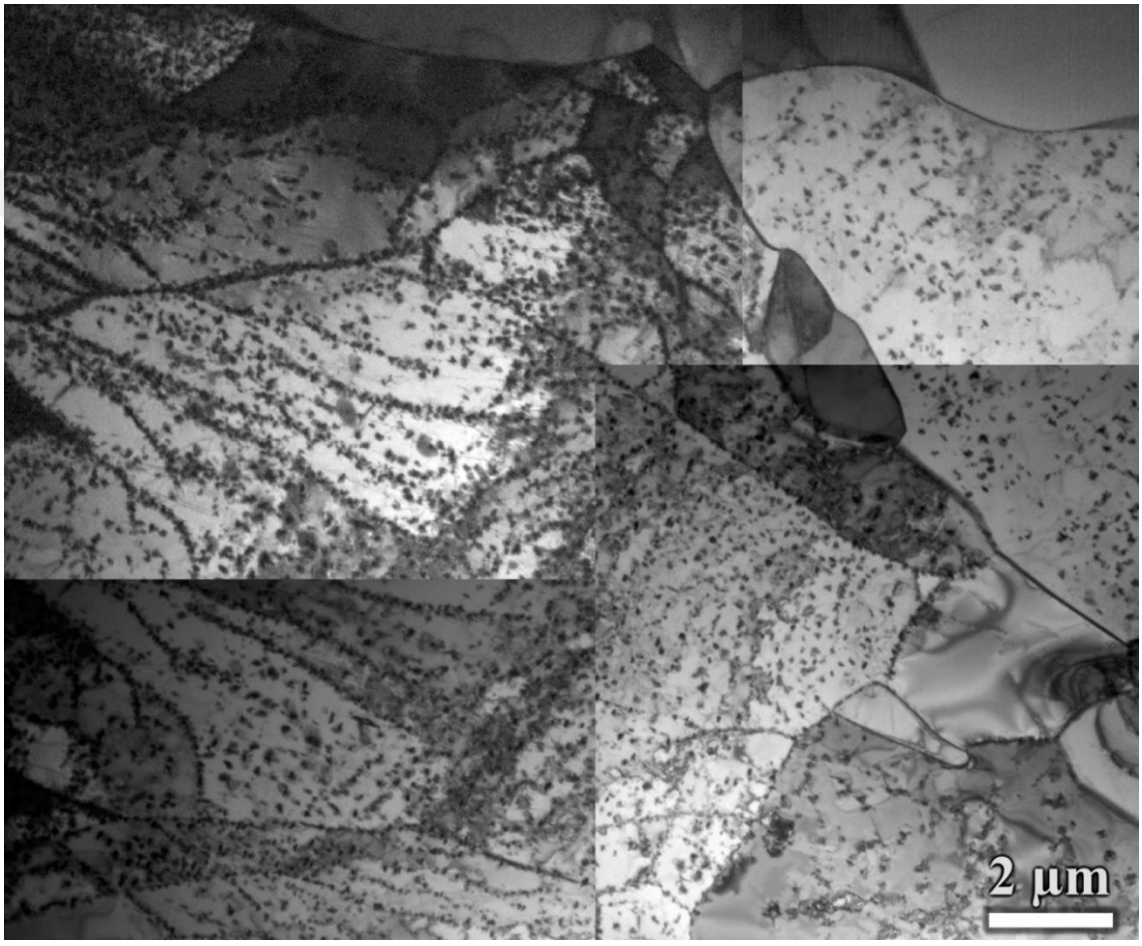

Figure 8-15: TEM bright field montage of the microstructure aged at 475°C for 255 hours over a large ferrite area containing precipitates

The spinodal arm width of α'' was determined to be 15-30 nm, and the ferrite seemed to have decomposed entirely. Scanning Kelvin Probe Force Microscopy analysis over spinodally decomposed ferrite showed a 60-70 mV Volta potential difference between α' and α'' indicating large galvanic interaction [60]. Further needle-like precipitates, possibly τ-phase, were seen in the SEM image in Figure 8-14(c). The number of R-phase precipitates

formed the majority of all precipitates. An overview of the entire precipitation network is shown in the montage TEM bright field image in Figure 8-15. Certain ferrite regions were enriched in R-precipitates, with HAGB and LAGB's seemed to be preferential nucleation sites. R-phase precipitates arrayed along slip planes and LAGB's can be seen in Figure 8-16. Apparently, the formation of R was non-homogeneous and discrete precipitation occurred in certain ferrite regions.

Higher magnification TEM images of a region containing R-phase precipitates revealed stronger diffraction contrast than the surrounding ferrite matrix, as shown in the BF- and DF-TEM images in Figure 8-17. R-precipitates seemed to be heavily faulted and had lenticular morphologies, in good agreement with previous studies [12, 19, 21, 50].

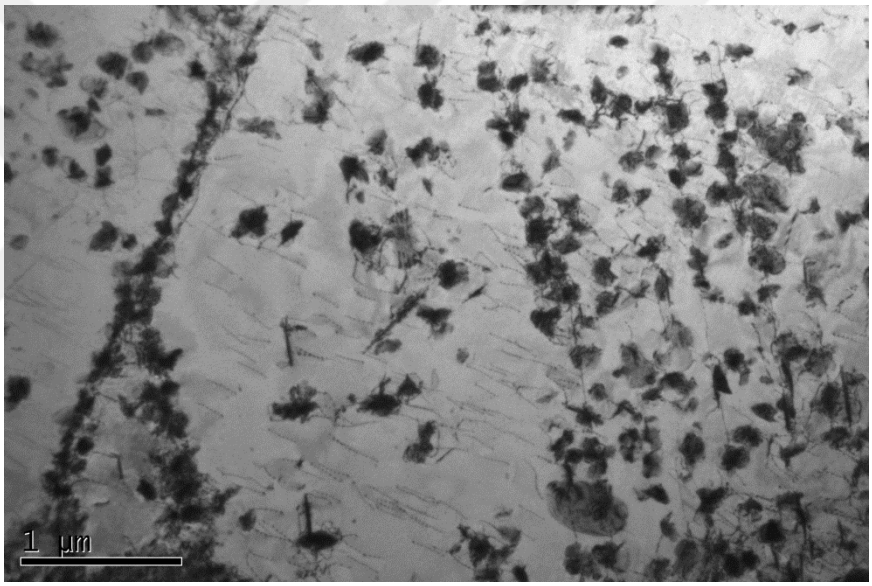

Figure 8-16: TEM bright field image of the microstructure aged at 475°C for 255 hours with R-phase precipitates in the ferrite

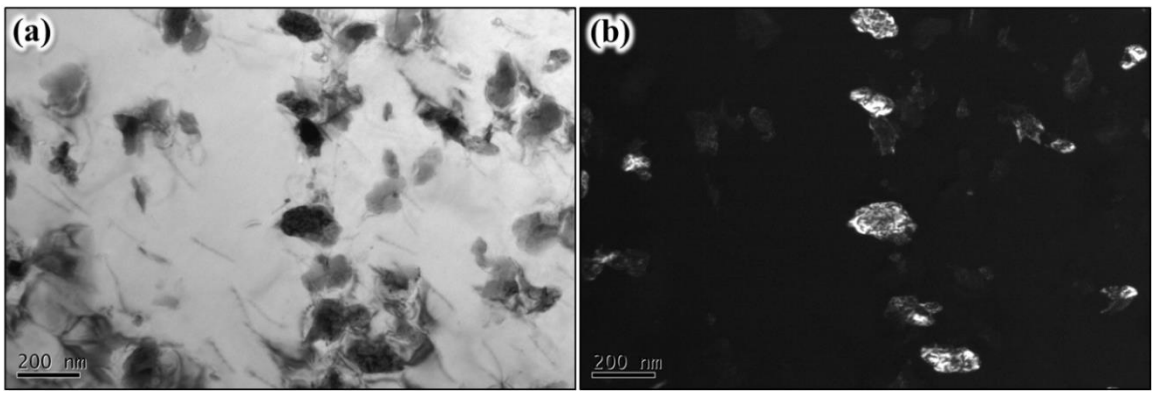

Figure 8-17: TEM analysis of the microstructure aged at 475°C for 255 hours showing R-precipitates at higher resolution with (a) bright-field image, (b) the corresponding dark field image.

8.2.4.6 Local Misorientation Mapping

Local misorientation (LMO) map and the corresponding phase map of the as-received microstructure are shown in Figure 8-18. The as-received microstructure showed smooth LMO variation across the entire microstructure, in spite of the presence of numerous general and special grain boundaries. A few LMO hot-spots were detected mainly on ferrite LAGB's and HAGB's and on small austenite grain clusters deriving from the process history of the material. The degree of LMO of the entire microstructure was low, with austenite showing slightly higher degree of misorientation than ferrite. Ferrite and austenite have different thermal expansion coefficients and deformation behavior. During quenching austenite can distort easier than ferrite which may lead to localized strain development in austenite, particularly in small grain clustered regions. Ferrite cannot bear large thermal stresses during quenching, hence, small in-grain distortions can cause localized strain development on LAGB's and HAGB's.

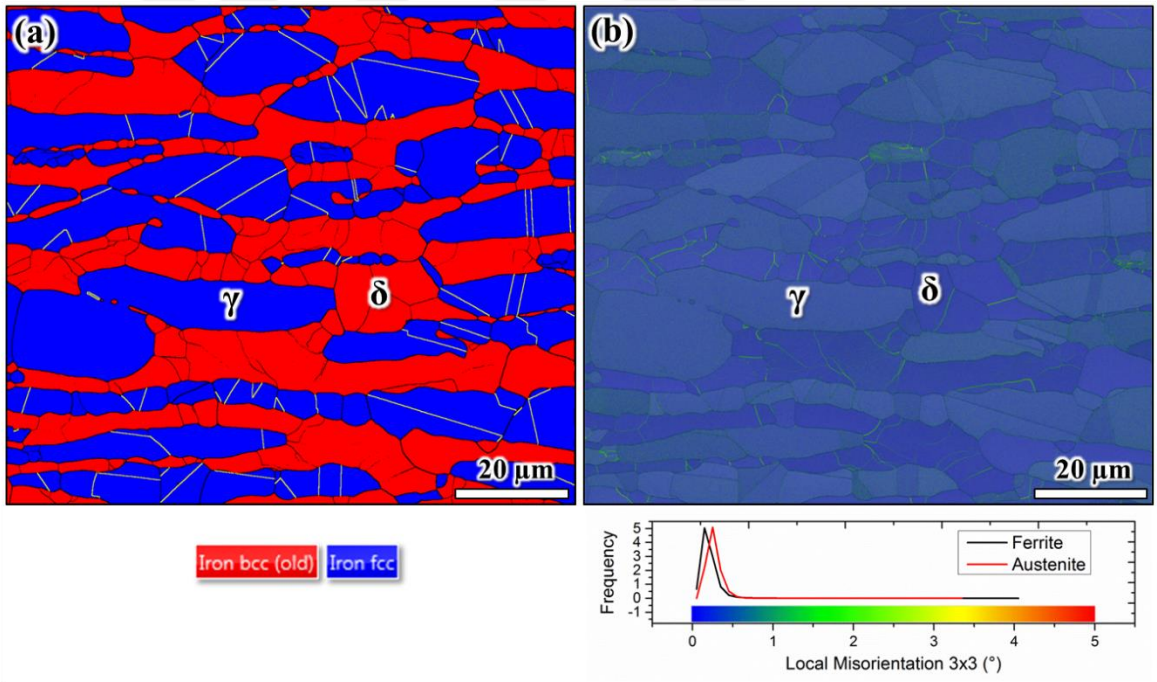

Figure 8-18: (a) EBSD phase map of as-received microstructure with (b) corresponding LMO map. Thick black lines are HAGB's, thin black lines are LAGB's, and yellow lines are twin boundaries (CSL Σ3). A few weak LMO hot-spots can be seen mainly located on ferritic grain boundaries and on fine austenite grain cluster regions.

Ageing at 475°C for 255 hours caused an increase of the number of LMO hot-spots in ferrite, while in austenite a weaker trend was seen. The LMO map and corresponding EBSD phase

map for the aged microstructure are shown Figure 8-19. The degree of LMO shifted towards higher values indicating an increase in localized strain. The phase transformation products formed in austenite seemed to have promoted the formation of discrete heterogeneous LMO hot-spots on ferrite boundaries.

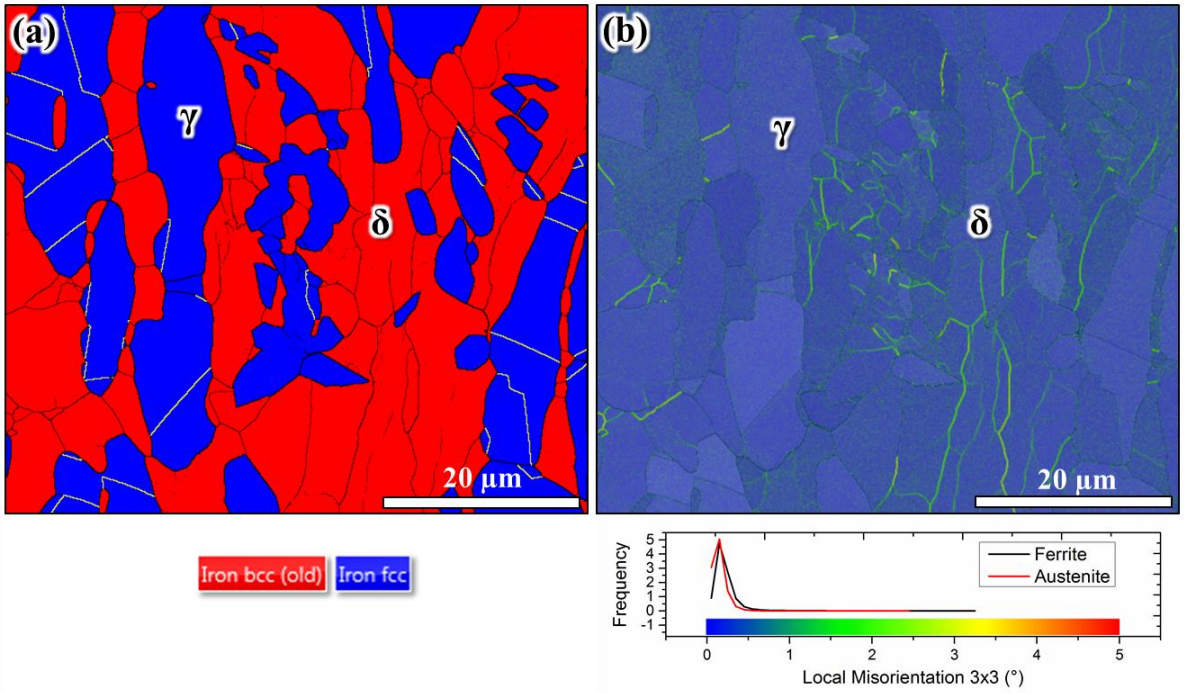

Figure 8-19: (a) EBSD phase map of the microstructure aged at 475°C for 255 hours with (b) corresponding LMO map. Thick black lines are HAGB's, thin black lines are LAGB's, and yellow lines are twin boundaries (CSL Σ3). There are numerous LMO hot-spots visible primarily in the ferrite.

8.2.5 Conclusions

Ageing treatments of 22Cr-5Ni duplex stainless steel at 475°C for 5, 20, 50, and 255 hours resulted in microstructure changes mainly in the ferrite phase, which directly affected the mechanical properties.

1) Macro-, micro-, and nano-indentation measurements showed hardness changes after 255 hours of ageing only, with the ferrite responsible for the increase in hardness.
2) Higher yield strengths were observed which was associated with a loss of elongation to failure with increasing degree of 475°C embrittlement.
3) XRD stress measurements revealed a reduction of compressive stresses in both ferrite and austenite as a function of 475°C embrittlement treatment, reaching a balanced microstructure after 255 hours of ageing.

4) Spinodal decomposition, consisting of Fe-rich α' and Cr-rich α'', were observed in ferrite with increasing amplitude as a function of ageing time.
5) R-phase precipitates with disc or lenticular shape could be detected after 50 hours ageing, which grew further from ~50 nm to 200-400 nm after 255 hours of ageing.

8.2.6 Acknowledgement

The authors acknowledge EPSRC (EP/I036397/1) and NDA (NPO004411A-EPS02) for financial support. The authors are grateful for the kind provision of Grade 22Cr-5Ni Duplex Stainless Steel plate by Rolled Alloys. Further thanks to Gary Harrison, School of Materials, for his support during XRD measurements.

8.2.7 References

[1] J. Charles. Duplex Stainless Steels, A Review after DSS '07 held in Grado. Aperam.

[2] J. Charles, S. Bernhardsson. Duplex Stainless Steels '91 - Volume 1. In: Charles J, Bernhardsson S, (Eds.). Duplex Stainless Steels '91, vol. 1. Beaune, Bourgogne, France: Les editions de physique, 1991.

[3] J. Charles, S. Bernhardsson. Duplex Stainless Steels '91 - Volume 2. In: Charles J, Bernhardsson S, (Eds.). Duplex Stainless Steels '91, vol. 1. Beaune, Bourgogne, France: Les editions de physique, 1991.

[4] S. Li, Y. Wang, X. Wang. Effects of ferrite content on the mechanical properties of thermal aged duplex stainless steels, Materials Science and Engineering: A 625 (2015) 186-193.

[5] Lula et al. Duplex Stainless Steels, American Society for Metals, Mars, Pennsylvania, 1983.

[6] R. Pettersson, E. Johansson. Stress corrosion resistance of duplex grades. In: Charles J, (Ed.). Duplex World 2010. Beaunne, France: Duplex Stainless Steel World, 2010.

[7] F. Wischnowski. Einfluss mikrostruktureller Gefügeveränderungen auf die Korrosionsresistenz von nichtrostenden ferritisch-austenitischen Duplex-Stählen. vol. PhD Thesis. Bochum, Germany: Technical University of Bochum, 1995. p.264.

[8] O.K. Chopra, H.M. Chung. Aging degradation of cast stainless steels: Effects on mechanical properties. In: Materials and Components Technology Division ANL, (Ed.), 1987. p.Medium: ED; Size: Pages: 34.

[9] K.H. Lo, C.H. Shek, J.K.L. Lai. Recent developments in stainless steels, Materials Science and Engineering: R: Reports 65 (2009) 39-104.

[10] H.-J. Eckstein. Korrosionsbeständige Stähle, Deutscher Verlag für Grundstoffindustrie GmbH, Leipzig, Germany, 1990.

[11] J.K. Sahu, U. Krupp, R.N. Ghosh, H.J. Christ. Effect of 475°C embrittlement on the mechanical properties of duplex stainless steel, Materials Science and Engineering: A 508 (2009) 1-14.

[12] A. Redjaïmia, J.P. Morniroli, P. Donnadieu, G. Metauer. Microstructural and analytical study of heavily faulted Frank-Kasper R-phase precipitates in the ferrite of a duplex stainless steel, Journal of Materials Science 37 (2002) 4079-4091.

[13] T.H. Hwang, J.H. Kim, K.H. Kim, W.J. Moon, C.Y. Kang. Effect of R-phase on impact toughness of 25Cr-7Ni-4Mo super duplex stainless steel, Met. Mater. Int. 20 (2014) 13-17.

[14] H.M. Chung, O.K. Chopra. Characterization of Duplex Stainless Steels by TEM, SANS, and APFIM Techniques. in: Altergott W, Henneke E, (Eds.). Characterization of Advanced Materials. Springer US, 1990. pp. 123-147.

[15] M. Nyström, B. Karlsson. Fatigue of duplex stainless steel influence of discontinuous, spinodally decomposed ferrite, Materials Science and Engineering: A 215 (1996) 26-38.

[16] K.L. Weng, H.R. Chen, J.R. Yang. The low-temperature aging embrittlement in a 2205 duplex stainless steel, Materials Science and Engineering: A 379 (2004) 119-132.

[17] J.K. Sahu. Effect of 475°C Embrittlement on the Fatigue Behaviour of a Duplex Stainless Steel. Maschinenbau, vol. PhD. Siegen: University of Siegen, 2008. p.1-131.

[18] J.O. Nilsson. Super duplex stainless steels, Materials Science and Technology 8 (1992) 685-700.

[19] J.-O. Nilsson, P. Liu. Aging at 400–600°C of submerged arc welds of 22Cr–3Mo–8Ni duplex stainless steel and its effect on toughness and microstructure, Materials Science and Technology 7 (1991) 853-862.

[20] A. Mateo, L. Llanes, M. Anglada, A. Redjaimia, G. Metauer. Characterization of the intermetallic G-phase in an AISI 329 duplex stainless steel, Journal of Materials Science 32 (1997) 4533-4540.

[21] L. Karlsson, L. Ryen, S. Pak. Precipitation of Intermetallic Phases in 22% Cr Duplex Stainless Weld Metals. The kinetics of intermetallic phase formation in the temperature range 675°-1000°C (1247°-1832°F) and effects on mechanical properties and corrosion resistance, American Welding Society (1995).

[22] J.J. Shiao, C.H. Tsai, J.H. Huang, J.J. Kai. Phase transformations in ferrite phase of a duplex stainless steel aged at 500°C, Scripta Metallurgica et Materialia 29 (1993) 1451-1456.

[23] A. Redjaïmia, G. Metauer. Diffusion controlled precipitation of austenitic bi-crystals possessing twin related orientation in the ferrite of a duplex stainless steel, Journal of Materials Science 36 (2001) 1717-1725.

[24] K. Yamamoto, Y. Kimura, Y. Mishima. Precipitation of the Icosahedral Quasicrystalline Phase, R-phase and Laves Phase in Ferritic Alloys, MATERIALS TRANSACTIONS Vol. 45 (2004) 357-360.

[25] A. Redjaïmia, A. Proult, P. Donnadieu, J.P. Morniroli. Morphology, crystallography and defects of the intermetallic χ-phase precipitated in a duplex (δ + γ) stainless steel, Journal of Materials Science 39 (2004) 2371-2386.

[26] S.-H. Byun, N. Kang, T.-H. Lee, S.-K. Ahn, H. Lee, W.-S. Chang, K.-M. Cho. Kinetics of Cr/Mo-rich precipitates formation for 25Cr-6.9Ni-3.8Mo-0.3N super duplex stainless steel, Met. Mater. Int. 18 (2012) 201-207.

[27] A. Redjaimia, P. Ruterana, G. Metauer, M. Gantois. Identification and characterization of a novel intermetallic compound in a Fe-22 wt % Cr-5 wt % Ni-3 wt % Mo-0.03 wt % C duplex stainless steel, Philosophical Magazine A 67 (1993) 1277-1286.

[28] C.R. Brooks, S.B. Fitch. Transmission electron microscopy observations of the lamellar structure in the Arispe iron meteorite, Materials Characterization 45 (2000) 365-377.

[29] H.M. Chung. Spinodal decomposition of austenite in long-term-aged duplex stainless steel. 1989. p.Medium: X; Size: Pages: 25.

[30] H.M. Chung. Aging and life prediction of cast duplex stainless steel components, International Journal of Pressure Vessels and Piping 50 (1992) 179-213.

[31] O.K. Chopra, H.M. Chung, T.F. Kassner, W.J. Shack. Environmentally assisted cracking of LWR materials, 1995.

[32] W. Horvath, W. Prantl, H. Stroißnigg, E.A. Werner. Microhardness and microstructure of austenite and ferrite in nitrogen alloyed duplex steels between 20 and 500°C, Materials Science and Engineering: A 256 (1998) 227-236.

[33] M. Ferry. Alloys: Iron. in: Editors-in-Chief: Franco B, Gerald LL, Peter W, (Eds.). Encyclopedia of Condensed Matter Physics. Elsevier, Oxford, 2005. pp. 46-53.

[34] L.C.D. Fielding, E.J. Song, D.K. Han, H.K.D.H. Bhadeshia, D.-W. Suh. Hydrogen diffusion and the percolation of austenite in nanostructured bainitic steel, 2014.

[35] S.M. Allen. Spinodal Decomposition. in: Editors-in-Chief: KHJB, Robert WC, Merton CF, Bernard I, Edward JK, Subhash M, Patrick V, (Eds.). Encyclopedia of Materials: Science and Technology (Second Edition). Elsevier, Oxford, 2001. pp. 8761-8764.

[36] J.W. Cahn, J.E. Hilliard. Spinodal decomposition: A reprise, Acta Metallurgica 19 (1971) 151-161.

[37] M. Tomozawa. Compositional Changes as Evidence for Spinodal Decomposition in Glass, Journal of the American Ceramic Society 61 (1978) 444-447.

[38] G. Wahlberg, G. Dunlop, L., An Atom Probe Study OF 475°C Embrittlement of Duplex Stainless Steels, J. Phys. Colloques 49 (1988) C6-289-C286-292.

[39] K. Yaldram, K. Binder. Spinodal decomposition of a two-dimensional model alloy with mobile vacancies, Acta Metallurgica et Materialia 39 (1991) 707-717.

[40] J. Zhou, J. Odqvist, M. Thuvander, P. Hedström. Quantitative Evaluation of Spinodal Decomposition in Fe-Cr by Atom Probe Tomography and Radial Distribution Function Analysis, Microscopy and Microanalysis 19 (2013) 665-675.

[41] F. Iacoviello, F. Casari, S. Gialanella. Effect of "475 °C embrittlement" on duplex stainless steels localized corrosion resistance, Corrosion Science 47 (2005) 909-922.

[42] F. Danoix, P. Auger, S. Chambreland, D. Blavette. A 3D study of G-phase precipitation in spinodally decomposed α-ferrite by tomographic atom-probe analysis, Microsc. Microanal. Microstruct. 5 (1994) 121-132.

[43] V. Sofonea, K.R. Mecke. Morphological characterization of spinodal decomposition kinetics, Eur. Phys. J. B 8 (1999) 99-112.

[44] T. Godfrey, J., M. Hetherington, G., J. Sassen, M., G. Smith, D.W. The Characterization of Spinodal Structures in Duplex CF3 Steels, J. Phys. Colloques 49 (1988) C6-421-C426-426.

[45] J.M. Vitek, S.A. David, D.J. Alexander, J.R. Keiser, R.K. Nanstad. Low temperature aging behavior of type 308 stainless steel weld metal, Acta Metallurgica et Materialia 39 (1991) 503-516.

[46] J.K.L. Lai, K.H. Lo, C.H. Shek. Stainless Steels: An Introduction and Their Recent Developments, Bentham eBooks, Dubai, United Arab Emirates, 2012.

[47] T. Hamaoka, A. Nomoto, K. Nishida, K. Dohi, N. Soneda. Effects of aging temperature on G-phase precipitation and ferrite-phase decomposition in duplex stainless steel, Philosophical Magazine 92 (2012) 4354-4375.

[48] I. Shuro, H.H. Kuo, T. Sasaki, K. Hono, Y. Todaka, M. Umemoto. G-phase precipitation in austenitic stainless steel deformed by high pressure torsion, Materials Science and Engineering: A 552 (2012) 194-198.

[49] J. Cui, I.-S. Park, C.-Y. Kang, K. Miyahara. Degradation of Impact Toughness due to Formation of R Phase in High Nitrogen 25Cr-7Ni-Mo Duplex Stainless Steels, ISIJ International 41 (2001) 192-195.

[50] A. Redjaïmia, T. Otarola, A. Mateo. Orientation Relationships between the δ-ferrite Matrix in a Duplex Stainless Steel and its Decomposition Products: the Austenite and the χ and R Frank-Kasper Phases. In: Richter S, Schwedt A, (Eds.). EMC 2008 14th European Microscopy Congress 1–5 September 2008, Aachen, Germany. Springer Berlin Heidelberg, 2008. pp. 479-480.

[51] H.-J. Bargel, G. Schulze, H. Hilbrans, K.-H. Hübner, O. Krüger. Werkstoffkunde. 9th Edition ed., Springer-Verlag, Heidelberg, Germany, 2005.

[52] Q. Luo, A.H. Jones. High-precision determination of residual stress of polycrystalline coatings using optimised XRD-sin2ψ technique, Surface and Coatings Technology 205 (2010) 1403-1408.

[53] M.E. Fitzpatrick, A.T. Fry, H.F. A. Determination of residual stresses by X-ray diffraction, National Physical Laboratory, Teddington, Middlesex, United Kingdom, 2005.

[54] W.T. Becker, R.J. Shipley. ASM Handbook, Volume 11 - Failure Analysis and Prevention. ASM International. p.2909.

[55] A.S.M.Y. Munsi, A.J. Waddell, C.A. Walker. A Method for Determining X-ray Elastic Constants for the Measurement of Residual Stress, Strain 39 (2003) 3-10.

[56] F.A. Garner, H.R. Brager, R.A. Dodd, T. Lauritzen. Ion-induced spinodal-like decomposition of Fe-Ni-Cr invar alloys, Nuclear Instruments and Methods in Physics Research Section B: Beam Interactions with Materials and Atoms 16 (1986) 244-250.

[57] K. Takizawa, Y. Shimizu, E. Yoneda, I. Tamura. Effects of Cold Work, Heat Treatment and Volume Fraction of Ferrite on Stress Corrosion Cracking Behavior of Duplex Stainless Steel, Tetsu-to-Hagane 67 (1981) 353-361.

[58] D.L. Engelberg, R.C. Newman, T.J. Marrow. Effect of thermomechanical process history on grain boundary control in an austenitic stainless steel, Scripta Materialia 59 (2008) 554-557.

[59] D.L. Engelberg, T.J. Marrow, R.C. Newman, L. Babouta. Grain boundary engineering for crack bridging: A new model for intergranular stress corrosion crack (IGSCC) propagation. in: Rebak SA, Shipilov RH, Jones JM, Oliver B, (Eds.). Environment-Induced Cracking of Materials, vol. 1. Elsevier, Amsterdam, 2008. pp. 69-79.

[60] C. Örnek, J. Walton, T.L. Ladwein, S.B. Lyon, D.L. Engelberg. A Corrosion Model for 475°C Embrittlement in Duplex Stainless Steel – a Comprehensive Study via Scanning Kelvin Probe Force Microscopy, Electrochimica Acta (2015). Submitted.

8.3 Effect of "475°C Embrittlement" on the Corrosion Behaviour of Grade 2205 Duplex Stainless Steel Investigated Using Local Probing Techniques

C. Örnek[1], D.L. Engelberg[1], S.B. Lyon[1], T.L. Ladwein[2]

[1]*Corrosion and Protection Centre, University of Manchester, Sackville Street, M13 9PL, UK*
[2]*Aalen University of Applied Sciences, Beethovenstraße 1, 73430 Aalen, Germany*

8.3.1 Abstract

The work reported in this paper correlates microstructure development after low temperature embrittlement heat treatments with pitting corrosion susceptibility in grade 2205 duplex stainless steel. Heat-treatments at 475°C for up to 255 hours were carried out and microstructures characterised using scanning electron microscopy (SEM) and micro-hardness testing. Local electrochemical measurements using an electrochemical micro-cell were carried out and the critical pitting temperature (CPT) determined. Short-duration heat treatments for up to 10 hours showed an increase in CPT, attributed to an improved electrochemical character of the ferrite. Long-term heat treatments (>50 hours) indicated a decrease in CPT due to the precipitation of other precipitates and the formation of elemental depletion zones.

Key words: *475°C embrittlement; duplex stainless steel; critical pitting temperature; electrochemical micro-cell; micro-hardness*

8.3.2 Introduction

Duplex stainless steels (DSS) are prone to phase transformations when exposed to temperatures in excess of 250°C [1]. Microstructure changes are typically accompanied by embrittlement and the loss of corrosion resistance, affecting the endurance and performance of these alloys. 475°C embrittlement is related to the formation of Cr-enriched α''-phase and Cr-depleted α'-phase, though other secondary precipitates such as G- and R-phase can also form [1-4]. Extensive work exists in the literature about the effect of ageing treatment on mechanical properties [5-8], however, the effect of low temperature embrittlement heat

treatments and spinodal decomposition on corrosion properties of duplex stainless steels is not clear. In this paper microstructure development and hardness of 475°C embrittlement were compared to critical pitting temperatures in chloride-containing environment, determined using an electrochemical micro-cell technique.

8.3.3 Experimental

Solution annealed grade 2205 duplex stainless steel plate material was used for all tests with the chemical composition given in Table 8-2. Coupon samples with dimensions of ca. 15mm x 10mm x 10mm were heat treated at 475°C ± 5°C for 5, 10, 20, 50, and 255 hours, followed by a water quench.

Table 8-2: Chemical compositions of material used

Grade	C	Si	Mn	P	S	Cr	Ni	Mo	N	Fe
2205	0.016	0.40	1.50	0.021	0.001	22.4	5.80	3.20	0.180	bal.

Macro-hardness tests were carried out with a Vickers indent (HV30), using the mean of 10 indentations. Micro-hardness measurements were performed on stress-free surfaces with a Struers micro-hardness tester (HV0.01). Ferrite and austenite micro-hardness values were measured and the mean of 20 - 25 indentations is reported. All micro-hardness indentation diameters were smaller than 9.1 μm, placed in the centre of a crystallographic phase region, with each indentation encompassing less than 75% of the area of each phase region. The results should, however, only be considered as a trend of the change in hardness for each phase, since an effect of the indentation size with respect to the finite phase region size cannot be excluded. A SEM was used to measure the dimensions of the indents, and errors are calculated as the standard deviation with respect to the mean.

The CPT of all coupon samples was probed with an electrochemical microcell as shown in Figure 8-20. The tip of the electrochemical microcell was a polymer tube (PE) with an area of 0.125 cm². The working electrode was placed onto a Peltier element for temperature control with a temperature control accuracy of ±0.1°C. The CPT was determined in 5°C temperature intervals, starting from room temperature (RT) up to the temperature where stable pitting was observed. A Gamry Reference 600 potentiostat with an Ag/AgCl reference

electrode and a Pt counter electrode were used for all measurements. The electrolyte was a 3 wt.-% NaCl solution. The Open Circuit potential (OCP) was measured for 3 minutes, followed by a potentiodynamic scan from -300mV to +1500mV vs. OCP using a scan rate of 1 mV/s. The CPT was defined as the temperature where the current density showed a steep increase of at least two orders of magnitude with respect to the measured passive current density (before reaching the trans-passive region). All tests were repeated three times to confirm repeatability.

8.3.4 Results

Macro- and micro-hardness measurements are summarised in Figure 8-22. The increase in macro-hardness with aging times indicates changes in the microstructure; given the heat treatment conditions this can be attributed to the occurrence of 475°C embrittlement. A significant increase after 255 hours of ageing was observed. A similar trend was observed in the micro-hardness measurements. Aging of up to 50 hours at 475°C seems not to cause significant hardness changes, but an increase in the micro-hardness of the ferrite after 255 hours is noticeable. The austenite did not show an increase in hardness.

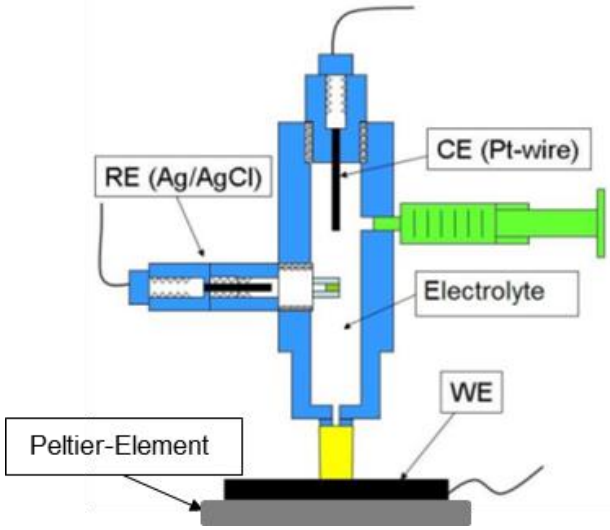

Figure 8-20: Local probing electrochemical microcell (WE = working electrode, CE = counter electrode, RE = reference electrode) [9]

The CPT of all heat-treated samples is shown in Figure 8-21. The as received grade 2205 microstructure had a CPT of 40°C. A CPT increase from 40°C to 50°C with 5 and 10 hours

aging was observed, with a slight drop after 20 and 50 hours aging to 45°C. The 255 hours heat-treated condition could only be tested in fully immersed conditions, and a CPT of 30±3°C was determined.

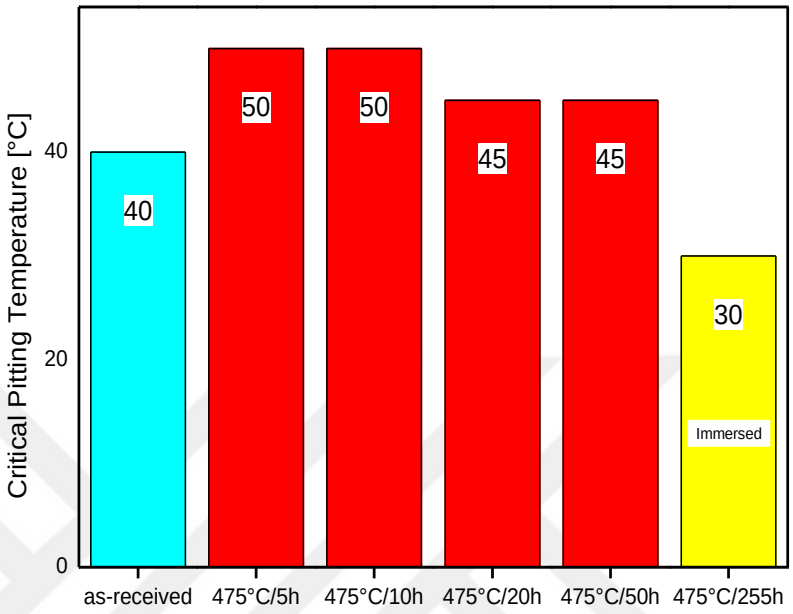

Figure 8-21: Critical pitting temperatures for grade 2205 aged at 475°C

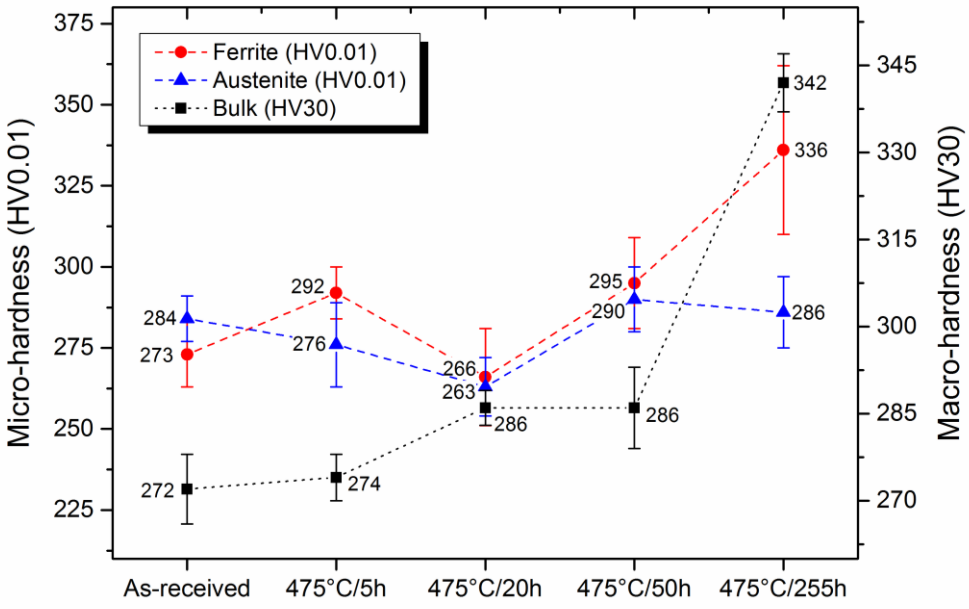

Figure 8-22: Macro-hardness of bulk material and micro-hardness of austenite and ferrite; dashed lines in both diagrams indicate possible trend

Micrographs of the surface attack after CPT testing of the as-received material is shown in Figure 8-24a-b, and the 5 hours aged sample in Figure 8-24c-d. In the as-received microstructure the austenite seemed to protrude in all micrographs, indicating a proportionally higher dissolution rate of the ferrite. After 5 hours of aging the opposite trend was observed, indicating a higher dissolution rate of the austenite.

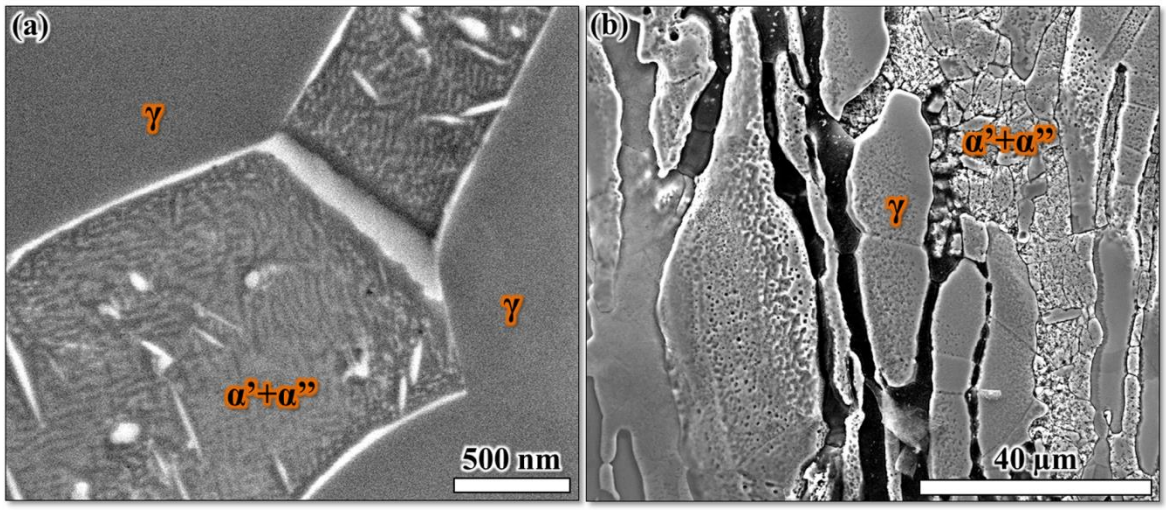

Figure 8-23: Microstructure of 475°C/255h: (a) spinodal decomposition in the ferritic region, (b) main attack occurred on the ferritic regions with slight pitting-like attack on the austenite

The EBSD map in Figure 8-24d confirms the protruding microstructural features in Figure 8-24c as ferrite. The dissolution behaviour of both phases seemed to be balanced after 20 hours ageing. After longer ageing times of 50 hours and 255 hours, larger attack on the ferrite is again observed, with the corresponing image of the 255 hours aged sample shown in Figure 8-23b. However, the austenite showed small pits which might be due to de-alloying effects [10]. In the microstructure after 255 hours aging, the presence of a spinodal decomposition could even be observed at high resolution in the SEM, shown in Figure 8-23a.

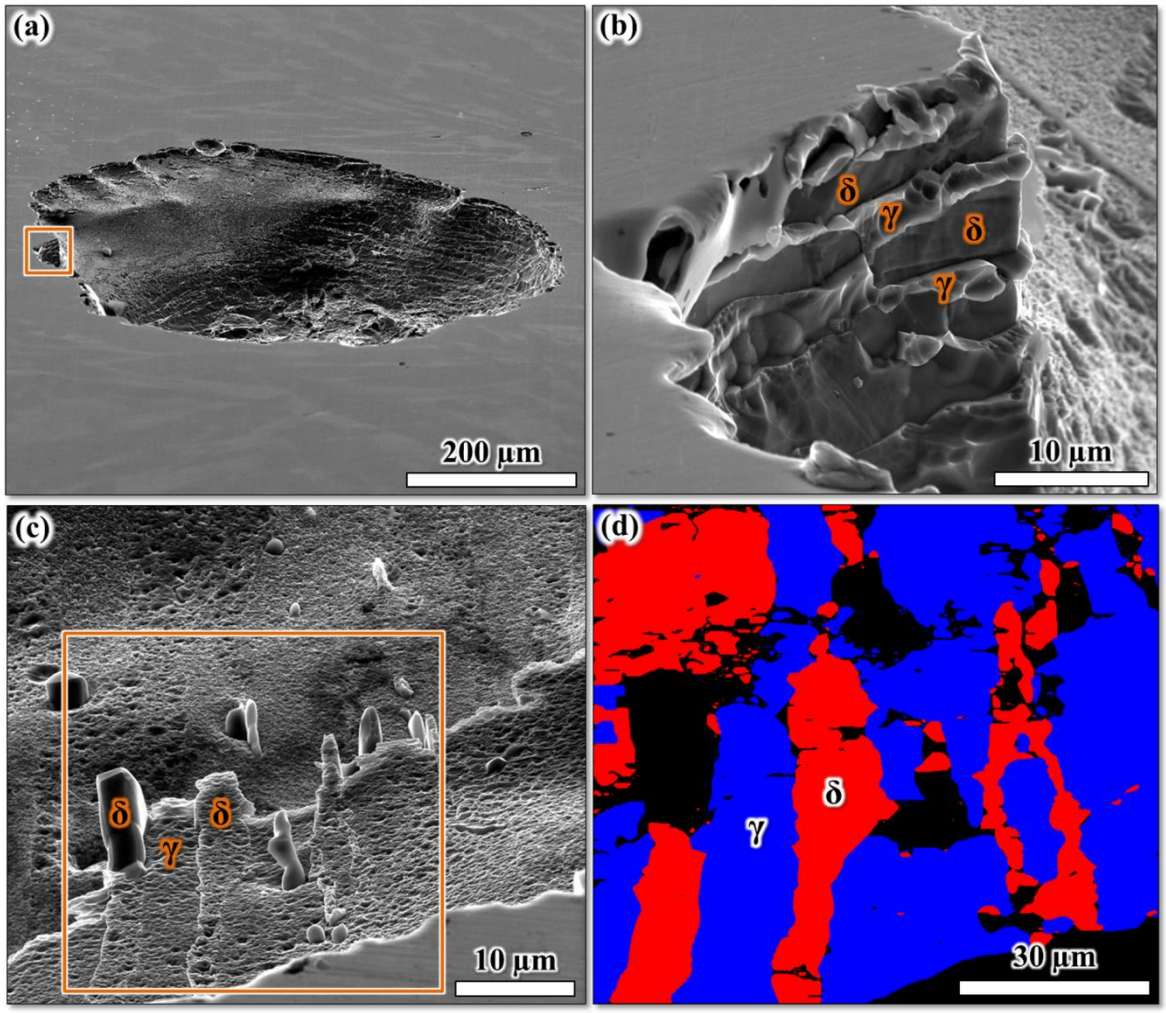

Figure 8-24: (a-b) SEM image of the pitting of the as-received condition, (c) 475°C/5h and (d) EBSD map of the region shown in (c), with blue representing the austenite, red the ferrite, and black non-indexed points

8.3.5 Discussion

The hardness increase indicates the occurrence of 475°C embrittlement with ageing in excess of 50 hours, well-possibly attributed to phase transformation reactions in the ferrite (Figure 8-23a). After 5 hours aging the corrosion behaviour of the ferrite seems to be enhanced as the micrograph in Figure 8-24 points to a lesser corrosion attack on ferritic sites, in parallel to an increase in the CPT (Figure 8-21).

Tavares et al. observed comparable results in which the CPT of super duplex grade 2507 increased by 15°C from 72°C to 87°C in 1 M NaCl for samples aged for 8 hours, and the CPT then decreased after 12 hours aging to 63°C [11]. It is believed that spinodal decomposition in the early aging conditions let to an improvement of the corrosion properties due to a better passivation behaviour, and precipitated secondary phases deteriorated the

electrochemical properties. Seemingly, this effect reversed after 20 hours of aging, as the CPT decreased. SEM (and TEM investigations, not reported here) on the 5 and 20 hours aged specimens showed a spinodally-decomposed microstructure in the ferrite, and after 50 and 255 hours aging other types of precipitates were also observed (Figure 8-23), with the spinodal microstructure consisting of Cr-enriched α''-phase and Cr-poor α'-phase visible as fractal background contrast in the ferrite in Figure 8-23a. However, once more precipitates were formed with longer ageing treatments the corrosion behaviour decreased rapidly.

TEM and SEM analysis could clearly show at least three different precipitates in the ferrite and at the ferrite/austenite interphase, ranging in sizes between about 40 to 250 nm. EDX measurements confirmed that some were enriched in Cr and Mo, with elemental depletions adjacent to their locations, which is believed to be the reason for the observed decrease in CPT. The size and number of those precipitates increased after 255 hours of aging, possibly causing micro-galvanic effects within the ferrite. The latter may also be augmented by elemental depletion adjacent to these precipitates, inducing an increased corrosion susceptibility of the ferrite.

8.3.6 Conclusions

1) Macro-hardness measurements (HV30) indicated microstructure embrittlement after 255 hours aging at 475°C. Micro-hardness measurements (HV0.01) showed an increase in hardness of the ferrite, with no significant change in the austenite.
2) An increase in CPT for short-term aging treatments up to 10 hours at 475°C was observed, followed by a drop after 255 hours aging.
3) The dissolution characteristics indicate that the ferrite is associated with the change in corrosion resistance for both short- and long-term aging treatments.
4) Spinodal decomposition is believed to enhance the corrosion properties for aging times up to 10 hours, with other precipitates affecting the corrosion resistance due to the formation of elemental depletion zones.

8.3.7 Acknowledgment

The authors are grateful for the provision of grade 2205 plate material by Rolled Alloys.

8.3.8 References

[1] H.M. Chung, International Journal of Pressure Vessels and Piping, 50 (1992) 179-213.

[2] H.M. Chung, T.R. Leax, Materials Science and Technology, 6 (1990) 249-262.

[3] L. Karlsson, L. Ryen, S. Pak, American Welding Society, (1995).

[4] K. Yamamoto, Y. Kimura, Y. Mishima, MATERIALS TRANSACTIONS, Vol. 45 (2004) 357-360.

[5] C.-J. Park, H.-S. Kwon, M.M. Lohrengel, Materials Science and Engineering: A, 372 (2004) 180-185.

[6] F. Danoix, P. Auger, D. Blavette, Microscopy and Microanalysis, 10 (2004) 349-354.

[7] W. Horvath, W. Prantl, H. Stroißnigg, E.A. Werner, Materials Science and Engineering: A, 256 (1998) 227-236.

[8] A. Hendry, Z.F. Mazur, K.H. Jack, Metal Science, 13 (1979) 482-486.

[9] M. Sorg, in: A.U.o.A. Sciences (Ed.) NACE Poster session 2012, Aalen University of Applied Sciences, 2012.

[10] H. Leinonen, P. Pohjanne, T. Saukkonen, T. Schildt, in: NACE, One Petro, 2011.

[11] S.S.M. Tavares, A. Loureiro, J.M. Pardal, T.R. Montenegro, V.C.d. Costa, Materials and Corrosion, 63 (2012) 522-526.

8.4 A Mechanistic Model to Describe the Corrosion Behaviour of 475°C Embrittled Duplex Stainless Steel Microstructure - A Comprehensive Study via Scanning Kelvin Probe Force Microscopy

C. Örnek[1,2,3], J. Walton[1], T. L. Ladwein[4], S. B. Lyon[1,2], D. L. Engelberg[1,2,3]

[1]Corrosion and Protection Centre,
School of Materials, The University of Manchester,
Sackville Street, Manchester, M13 9PL, United Kingdom

[2]Materials and Performance Centre,
School of Materials, The University of Manchester,
Sackville Street, Manchester, M13 9PL, United Kingdom

[3]Research Centre for Radwaste & Decommissioning
School of Materials, The University of Manchester,
Sackville Street, Manchester, M13 9PL, United Kingdom

[4]Aalen University of Applied Sciences,
Beethovenstraße 1, 73430 Aalen, Germany

8.4.1 Abstract

A mechanistic model to describe the corrosion behaviour of 475°C embrittlement in duplex stainless steel microstructure has been developed. Scanning Kelvin Probe force Microscopy (SKPFM) measured Volta potentials have been correlated to microstructure development as a function of ageing treatment at 475°C. The corrosion behaviour of microstructures was assessed using electrochemical polarisation tests, with Magnetic Force Microscopy (MFM) analysis applied to inform about microstructure changes in the ferritic matrix. Spinodal decomposition of the ferrite was found to initially increase the corrosion resistance of the microstructure, but the nucleation and growth of precipitates, such as R-phase and other second phases (e.g. χ and Cr_2N), caused a significant reduction of the corrosion resistance with longer ageing exposures. Element depletion zones adjacent to R-phase and intergranular precipitates were found with SKPFM. The corrosion behaviour of the microstructures is described as a function of amplitude and spatial distribution of SKPFM-informed Volta potential measurements.

Keywords: *475°C Embrittlement; Duplex Stainless Steel; Scanning Kelvin Probe Force Microscopy (SKPFM); Magnetic Force Microscopy (MFM); Critical Pitting Temperature (CPT)*

8.4.2 Introduction

Duplex Stainless Steels (DSS) have been used for structural and functional applications in a broad range of industry sectors [1]. Their two-phase microstructure typically consists of a balanced fraction of ferrite (δ) and austenite (γ) resulting in beneficial properties, such as high strength and toughness, with outstanding corrosion and stress corrosion cracking resistance. However, when exposed to higher temperature regimes DSS suffer from microstructure changes due to phase transformations arising from the strong interactions of alloying elements [2-4]. These microstructure changes can be accompanied by the occurrence of embrittlement and loss in corrosion resistance, which restricts their use for high performance applications.

High temperature phase transformations, which usually occur between 600°C and 950°C, are typically accompanied by significant reductions in corrosion resistance, mainly attributed to the formation of element depletions adjacent to σ-FeCr (sigma) phase precipitates [5-7]. Ferrite can undergo eutectoid transformations into several phases, including σ-phase with secondary austenite (γ_2), χ-phase, carbides (mainly $M_{23}C_6$), nitrides (CrN and Cr_2N), or carbonitrides [1, 5, 7-9]. Chromium nitrides can cause significant changes in microstructure performance [10, 11] and hardness [12], despite their small volume fractions and sizes (usually below 2 µm) [12, 13].

Exposure to lower temperatures between 250°C to 550°C, often referred to "475°C embrittlement", also results in variations of mechanical and electrochemical properties [14-28]. This has been attributed to phase separation mechanisms due to the existing miscibility gap in the Fe-Cr equilibrium phase diagram [7, 29, 30]. Phase separation occurs in the ferrite of the duplex steel resulting in a finely-dispersed modulated microstructures with Cr-enriched (Fe-depleted) body-centred-cubic α''-phase and Cr-depleted (Fe-enriched) body-centred cubic α'-phase [5, 21, 29, 31-33]. The final spinodal structure assumes a finely-dispersed, periodically modulated microstructure consisting of intertwined and interconnected Cr-rich α''- and Cr-poor α'-regions [21, 23, 29, 31, 34-38]. Within the

miscibility gap, and dependent on the chemical composition of the alloy, the phase separation mechanism is either based on nucleation and growth or spinodal decomposition [5, 22, 23, 34, 39, 40].

In addition to low temperature phase separation reactions forming α'/α'' [3, 21, 25-27, 30, 33, 35, 37, 41-46], other transformation products can also be nucleated at temperatures above 250°C. These include, for example, G-phase [5, 47-52], R-phase [5, 51, 53, 54], secondary austenite, γ_2 [5, 7], σ-phase, Laves phases [53, 55, 56], chromium carbides [5, 7], and nitrides [4, 5, 7, 12]. More complicated precipitates such π-phase, τ-phase, and ε-Cu-phase can also coexist within the spinodal decomposition regime [5, 7, 57]. It has been reported that these crystallographic phases form mainly in ferritic regions [3, 4, 6, 12, 14-16, 18-27, 29-34, 36, 37, 39, 41-43, 45, 47, 50, 58-69], though some researchers observed phase transformation in austenite as well [12, 25, 70, 71].

Brooks et al. [72] reported spinodal decomposition in austenite of a 6.7 wt.-% Ni containing iron meteorite due to an existing miscibility gap in the Fe-Ni binary phase diagram. *Chung et al.* and *Garner et al.* reported spinodal decomposition in the austenite [25, 26, 70]. *Horvarth et al.* [12] observed spherical Cr_2N precipitates in austenite in grade 22Cr-5Ni DSS, smaller than 200 nm, after ageing at 500°C. Thus, secondary phases can be formed in the austenite. More detailed information about microstructure development during ageing at 475°C is discussed in earlier work [73].

The effect of ageing in the low temperature 475°C embrittlement regime on corrosion properties of duplex stainless steels has been studied by many research groups [16, 18, 19, 61-64, 74], and all found that long-term ageing affects microstructure corrosion resistance. However, no model exists which describes microstructure corrosion behaviour of the effect of 475°C embrittlement. The aim of this paper is to characterise and correlate microstructure development of 475°C heat-treated samples with their Volta potentials differences. A mechanistic model for the corrosion performance of 475°C embrittlement has been developed to explain the change of corrosion behaviour with ageing treatment.

Background of Scanning Kelvin Probe Force Microscopy (SKPFM)

SKPFM measures the local electron work function, which is related to the Volta potential, of a microstructure. The driving force for corrosion is the difference between the chemical potential in a metal, the chemical potential (Fermi level) of the electrolyte/solution, and the

electrostatic potential difference or Galvani potential difference between the anode and the cathode. The chemical differences and Galvani potential differences between the metal and the electrolyte determine the possibility and the extent of metal dissolution.

Metals form due to their large affinity to oxygen an oxide layer onto the surface, which is an unequal adsorption of charges with opposite sign on the two sides of the interface leading to a potential drop across the surface. This potential drop is called dipole or surface potential (χ) and is the energy needed to bring an electron from the metal surface (Galvani potential regime) to a point beyond the surface where short-range atomic interactions are not prevailing, usually a distance of about 10 nm from the surface. Moreover, species with hydroxyl bonding with an additional possible net preferential orientation usually adhere leading to an increased surface potential regime and, hence, a larger potential drop across the surface. However, long-range atomic interaction still exist at this point, and further energy is required to move the electron further from the surface away. This energy required to bring an electron from a distance just above the surface to a longer range distance is the Volta potential (ψ). Volta and surface potentials form the inner potential ϕ, also called as Galvani potential, and describe the full electrostatic energy needed to bring a test charge from infinity into the metal bulk material. Volta potential describe therefore the energy needed to bring a charge (electron) from infinity to just above the surface where it does not feel its image charge, usually a distance of 10 nm to the surface [75-77].

If two dissimilar metals are connected due to their different work functions a contact potential is formed at the contact area. The contact potential difference (CPD) is equivalent to the Volta potential difference across the two different metal surfaces, as schematically shown in Figure 8-25. The Volta potential (ψ) can strongly be affected by the surface potential of the metal and is a function of temperature, pressure, and humidity. The potential values might also change over time due to surface reactions.

Regions of decreased ψ can help to assess and possibly predict locations with higher risk of corrosion [78]. *Nazarov et al.* [78] did work on the effect of surface defects and residual stress on Kelvin probe measured potential to assess the likelihood pitting corrosion and stress corrosion cracking. They could show that regions with high stress localisation, which show in general lower corrosion potentials, also had lower SKP measured potentials. There is

obviously a relationship between surface defects and local electrochemical potentials, which affects material dissolution characteristics.

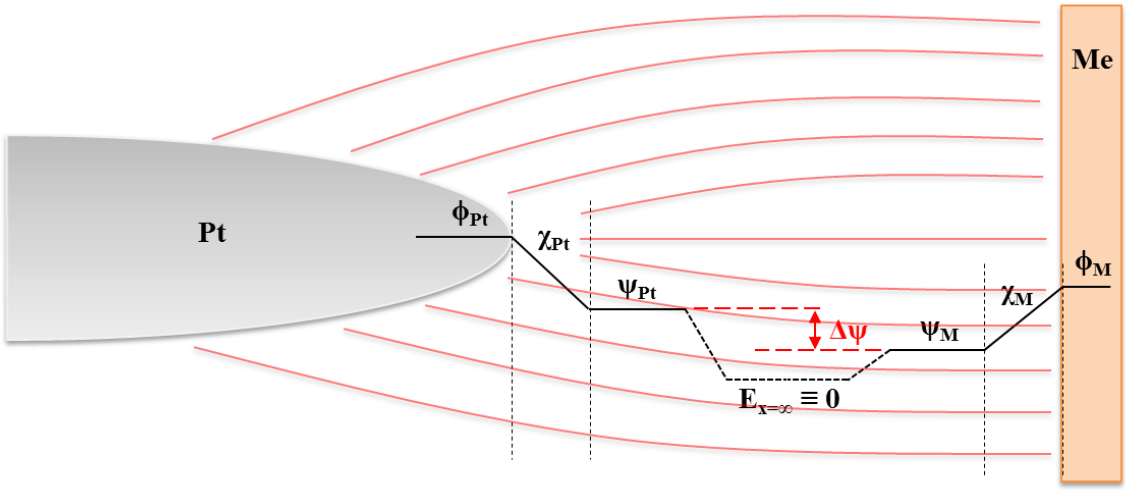

Figure 8-25: Schematic illustration of Galvani (ϕ), Surface (χ), and Volta (ψ) potentials and the Volta potential difference measured ($\Delta\psi$) via SKPFM. Note that platinum (Pt) is the reference probe.

However, the Kelvin probe can be used to assess local corrosion phenomena if immersion-like conditions could be created. This can be achieved by controlling the relative humidity (RH) of the environment during the measurement. Usually, in dry air, the surface of a metal consists of a chemically bonded monolayer of hydroxyls [79]. No water layer is attached below 30% RH. Monolayers of water molecules can adhere on the metal surface if the RH is increased, and beyond 60% RH, more than three adhering water monolayers are formed on the surface. According to *Leygraf et al*. [79], in aqueous films thicker than three layers bulk solution-like conditions can be assumed. SKPFM measurements in humid air ≥ 60% RH could therefore be used to correlate measured local Volta potential differences ($\Delta\psi$) with local electrochemical properties of the metal. Hence, the local practical nobility of a material and the role of microstructural constituents/features in electrochemical processes can be assessed.

In SKPFM, a sharp tip (often Pt-coated n-Si) is rastered over the flat surface. In the first path the topography is scanned in tapping or intermittent contact mode. Then the probe is lifted up to a user-defined height (often 50-100 nm) and rescanned in the second path (also called lift mode) by following the recorded topographic profile by switching off the Piezo-vibrator (no mechanical oscillating force) and nulling the existing electrostatic force between the

metal surface to be investigated and the Pt-probe. This existing electrostatic force corresponds to the work function difference ($\Delta\Phi$), Volta potential difference ($\Delta\psi$), and any additional surface charge effects [80-86]. One-path techniques such as the PeakForce Tapping mode can also be used to determine topographic details with much better topographical and potential spatial resolution [87]. The spatial resolution of the potential measured is smaller than 30 nm with approximately ± 1 mV precision [88]. However, as described elsewhere [85], many artefacts can lead to misinterpretations, so it is strongly advised to act with caution.

8.4.3 Experimental

The material used was grade 22Cr-5Ni duplex stainless steel plate and sheet from Outokumpu Stainless AB. Both materials were solution-annealed by the manufacturer at 1100°C for one hour and quenched in water, denoted as-received in this study. The chemical compositions are summarised in Table 8-3. SEM analysis of the ferrite and austenite phase using Energy Dispersive X-ray (EDX) analysis was carried out to inform about element partitioning in the 22Cr-5Ni plate material. The mean of >10 individual measurements is shown in Table 8-3.

Table 8-3: Chemical compositions (in wt.-%) of both 2205 duplex stainless steels used. (*The chemical composition from SEM/EDX analysis in ferrite and austenite of the plate material is also shown).

Grade	C	Si	Mn	P	S	Cr	Ni	Mo	N	Nb	Cu	Co	Fe
Plate	0.016	0.40	1.50	0.021	0.001	22.40	5.80	3.20	0.180	-	-	-	bal.
Ferrite*	n.a.	0.5	1.7	n.a.	n.a.	25.0	4.3	4.3	n.a.	-	-	-	bal.
Austenite*	n.a.	0.4	1.9	n.a.	n.a.	22.1	6.9	2.4	n.a.	-	-	-	bal.
Sheet	0.015	0.42	1.41	0.020	0.001	22.44	5.75	3.32	0.155	0.006	0.21	0.12	bal.

Coupon specimens were cut from the plate with dimensions of 15 mm x 10 mm x 10 mm (L x W x T). From the sheet small samples with dimensions of 10 mm x 10 mm x 2 mm (L x W x T) were cut. Specimens were then heat-treated in a Carbolite chamber furnace under argon gas shielding at 475±5°C for 5, 10, 20, 50, and 255 hours and subsequently water quenched. The plate material was used for SKPFM measurements, with both sheet and plate used for electrochemical pitting corrosion tests.

Microstructure characterisation of the plate was carried out by electron back-scatter diffraction (EBSD) using an *FEI Quanta 650* and an *FEI Magellan* scanning electron microscope (SEM). EBSD analysis was performed on transmission electron microscopy (TEM) foils. These were prepared by first grinding samples to 70-100 µm thickness, followed by punching out 3 mm diameter discs, which were then electro-polished in a 80 vol.-% perchloric acid : 20 vol.-% methanol electrolyte at 20 V and -35°C using a *Struers Tenupol-5 Twin Jet Electro Polisher*. The scan area was 768 x 672 µm with a step size of 390 nm and 4x4 binning. Oxford Instrument *AZtec* acquisition and *Channel5 HKL* analysis software were used, with 15° chosen as critical misorientation angle for grain boundary detection.

Local electrochemical analysis was performed to determine the critical pitting temperature (CPT) and critical pitting potential (CPP) of both duplex stainless steel materials. The sheet was assessed in 0.25M $MgCl_2$ solution and acidified 0.25M $MgCl_2$ + 1M HCl environments by immersing the sample in a conventional 3-electrode cell using a saturated calomel reference (SCE) electrode. The plate material was assessed in 0.5M NaCl solution using a miniature electrochemical cell (shown in [89]). The tip of the electrochemical cell was a polymer tube (polypropylene), with an area of 12.57 mm^2. A platinum counter electrode and Ag/AgCl reference electrode was used for these studies, but the potentials converted to SCE. Samples (working electrode) were connected to a Gamry Reference 600 potentiostat, and prior to all tests specimens were abraded to 1200-grit SiC finish. The samples were polarised with a scan rate of 1 mV/s after determining the open-circuit potential (OCP) for 3 minutes. The scan range was -300 mV vs. OCP up to +1300 mV vs. Ag/AgCl.

For increasing the temperature during CPT testing, samples were placed onto a Peltier element, achieving temperature control of ±1°C. The critical pitting temperature (CPT) response was determined in 5±1°C steps, beginning at room temperature (RT) until pits were observed. The CPT of the metal's ageing condition was defined by a steep and stable increase of the current density below 1000 mV vs. Ag/AgCl. Once pitting was observed the test was repeated two times, and the corroded surface was imaged with an optical light microscope after each test. The CPT test was deemed as successful when the corrosion pits were located far enough from the polymer tube in order to exclude crevice corrosion occurrence, otherwise the test was repeated. All pitting corrosion tested samples were also analysed in the SEM.

For SKPFM characterisation, specimens were mounted in an epoxy resin and ground to 4000-grit with SiC paper, followed by diamond suspension polishing to a 0.1 µm finish. A final oxide particle solution (OP-S) end polishing treatment containing 60 nm silicide abrasive particles with a few drops of concentrated sulphuric acid and nitric acid (in a bottle of 100 ml of OP-S solution) was used for sample fine polishing. The acid was added to enhance the surface etching response, to obtain stress-free surfaces. The samples were carefully cleaned using ethanol, acetone, and hot water. For the high-resolution SKPFM imaging electro-polished TEM specimens were used in order to map the spinodally-decomposed microstructure. Electro-polishing was performed on 3 mm diameter and 100 µm thick discs in 80 vol.-% perchloric to 20 vol.-% methanol electrolyte at 20 V and -35°C using a *Struers Tenupol-5 Twin Jet Electro Polisher*.

SKPFM and Magnetic Force Microscopy (MFM) measurements were carried on a *Dimension 3100* with a *Nanoscope 3a controller* from *Digital Instruments* and *MultiMode 8* with *Nanoscope 5 controller* from *Veeco*. Pt-coated AFM probes *OSCM-PT* from *Bruker* were used to map the surface topography and the corresponding Volta potential. The scan size of AFM mapping was between 500 nm x 500 nm and 80 µm x 80 µm, dependent on the microstructural features to be characterised. The scan rate was adjusted to the tip velocity and ranged between 10-30 µm/s, which corresponds to 0.2-0.5 Hz. The images contained 512 x 512 pixels. All SKPFM maps were processed using *Nanoscope V1.5* software (*Bruker*). Topography/height maps were flattened with 1st flattening order. Volta potential differences maps were not flattened.

Volta potential mapping was performed under room climatic conditions at a temperature of approximately 25°C and 30% RH. The 5 hours aged sample was also investigated in 71% RH, allowing assumptions about the corresponding electrochemical behaviour under open-circuit conditions. The humidity was controlled by evaporating a 5 M NaCl solution from a heated flask in a water bath at 60°C, which was in an enclosure which sealed the entire AFM setup. According to *Leygraf et al.* more than 3 monolayers of water should have formed on the metal surface under this environmental condition, enabling bulk-solution-like behaviour to be probed [79].

In this paper higher SKPFM measured potentials (= larger potential difference) in the potential maps correspond to anodic sites due to a larger absolute work function difference

between the tip of the bias-controlled AFM probe (Pt) and the microstructure feature of the grounded sample. According to this definition, cathodic sites have lower Volta potential differences than anodic parts. To remove an electron from the cathode to where the electron does not feel its image charge is more difficult than in the case of the anode [81].

8.4.4 Results

The typical duplex microstructure of as-received grade 22Cr-5Ni plate is shown with the EBSD phase map in Figure 8-26. The phase ratio of austenite to ferrite was 53±1% to 47±1%, with average grain sizes of respectively 7.3±0.3 µm and 7.1±0.9 µm. The aspect ratio (vertical to horizontal mean length) was determined as the mean of all three process directions as 1.8 in ferrite and 1.6 in austenite, respectively. Austenite had a high fraction of low energy twin boundaries, shown by presence of straight yellow boundaries in Figure 8-26. The microstructure is typical for a solution-annealed stainless steel, and a similar microstructure is also present in the sheet material.

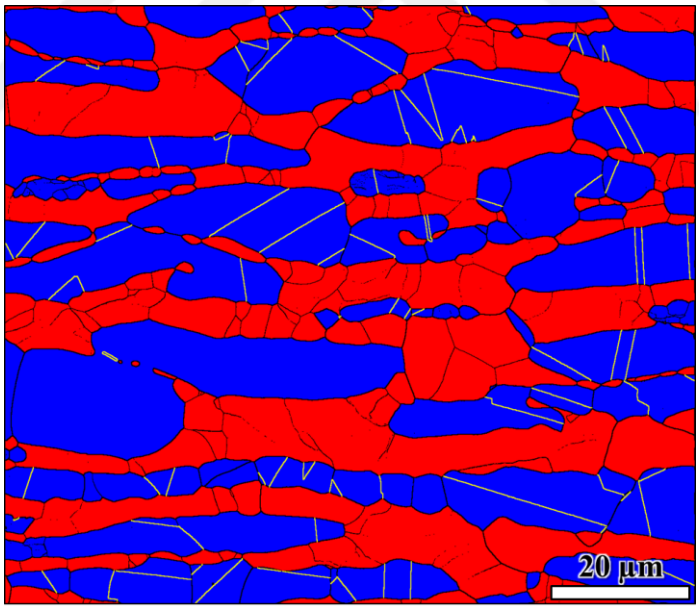

Figure 8-26: EBSD phase map of the as-received condition with ferrite (in red) and austenite (in blue). Black lines show grain boundaries and yellow line twin boundaries.

The microstructure and local phase composition of the ferrite changed with ageing time at 475°C. Spinodal decomposition was observed after a few hours exposure to elevated temperature in the form of a mottled interconnected structure, making up the background pattern in Figure 8-27. An in-depth description of microstructure development and

associated mechanical behaviour of the plate material used in this study is presented elsewhere [74]. In summary, an increasing amplitude of spinodal decomposition products of Fe-rich (α') and Cr-rich (α'') were observed in the ferrite as a function of longer ageing times. Features with brighter contrast in Figure 8-27(a) were identified as Mo-Cr enriched R-phase precipitates. R-phase was already detected after 50 hours ageing in the form of disc or lenticular-shaped precipitates, which grew in size from ~50 nm to 200-400 nm after 255 hours of ageing exposure. A range of other precipitates were also noted, including a lath-like phase situated within ferrite grains, believed to be τ-phase (Figure 8-27(a)). A range of other intergranular precipitates denoted as γ_2, χ, and carbides in Figure 8-27 were also present, and these are here in this paper all referred to as precipitates (P).

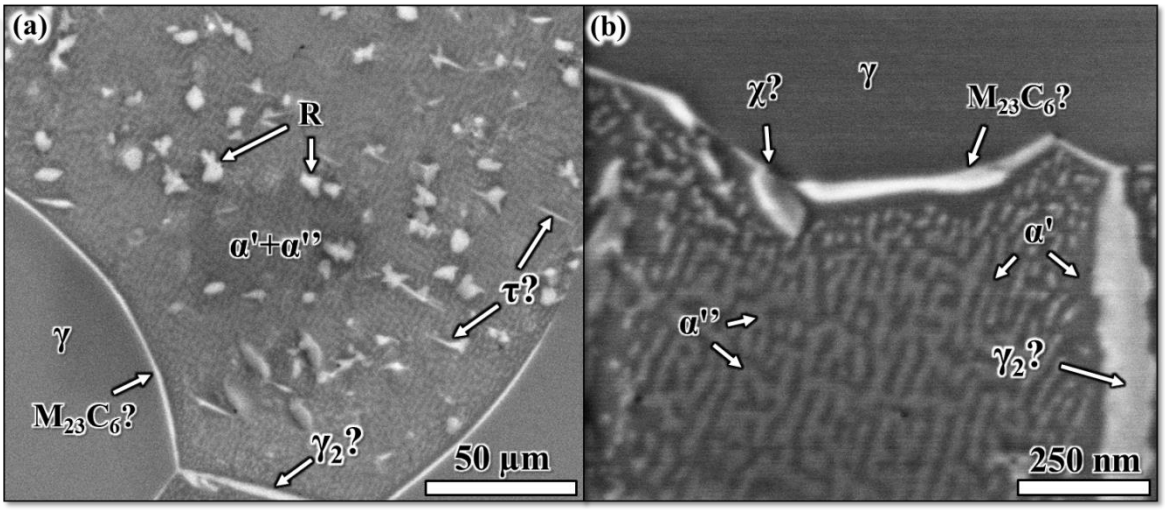

Figure 8-27: Microstructure morphology of 22Cr-5Ni duplex stainless steel aged for 255 hours; (a) Mo-Si-Cr-Ni-enriched R-phase precipitates (bright) located in the ferrite with further other secondary phases present in the ferrite (τ?) or grain boundaries (γ_2, χ, carbides?); (b) Spinodally decomposed (mottled structure) Fe-rich α' (dark) and Cr-rich α'' (bright) can be seen.

8.4.4.1 Pitting Corrosion Behaviour

The pitting potential measured in 0.25M $MgCl_2$ and 0.5M NaCl versus ageing time is shown in Figure 8-28. In both electrolytes the as-received specimen did not show pitting corrosion at room temperature (RT), and localised breakdown of the passive film was first seen at 40°C, which was defined as its critical pitting temperature (CPT). In contrast, the sample aged for 255 hours suffered from localised corrosion at RT in $MgCl_2$ and 30°C in NaCl. Short ageing treatments with 5 and 10 hours exposure increased the pitting corrosion resistance. The most resistant material condition was the 10 hours aged sample, with a trend of decreasing pitting temperature with longer and shorter ageing times. All samples suffered

from pitting attack after potentio-dynamic polarisation at 50°C, except the 10 hours aged specimen. Both materials and test set-ups showed similar trends of the CPT with a maximum of 5°C difference (one temperature increment).

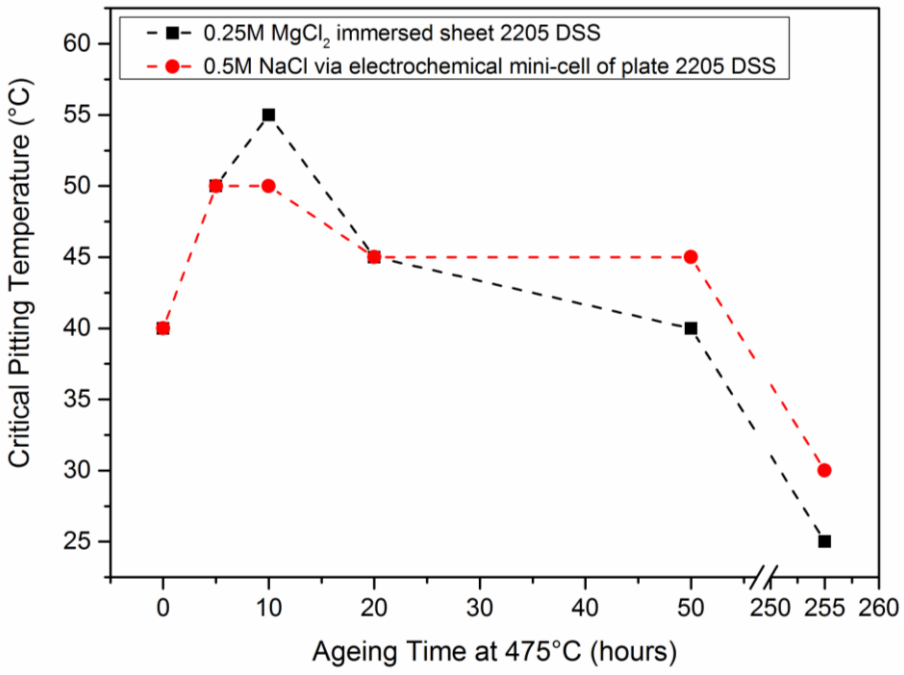

Figure 8-28: Critical pitting temperature evaluation of 22Cr-5Ni duplex stainless steel sheet and plate as a function of test environment ($MgCl_2$, NaCl) and 475°C ageing time.

Figure 8-29 shows the measured potential when a sudden current increase was observed, indicative either of localised film breakdown or entering trans-passive region. The 0.25M $MgCl_2$ + 1M HCl was chosen to investigate whether pitting corrosion can be induced at RT on these duplex stainless steel microstructures. In this environment pitting corrosion was observed on the as-received specimen at RT at 950 mV vs. SCE, clearly before the onset of transpassivity. The specimens aged for 5, 10, and 20 hours did not show pitting corrosion at RT indicating higher CPT values. The specimen aged for 50 hours suffered from pitting at 615 mV, with the 255 hours aged specimen indicating local film breakdown at 250 mV vs. SCE. The 255 hours aged microstructure also suffered from pitting in 0.25M $MgCl_2$ electrolyte at RT (Figure 8-28, Figure 8-29) indicating a very high susceptibility of this microstructure.

The CPP in 0.25M $MgCl_2$ at 50°C showed an increase with ageing time up to 10 hours ageing, with an abruptly decrease with longer ageing exposures indicative of enhanced

pitting corrosion susceptibility of heavily embrittled specimens. Figure 8-29 shows pitting corrosion occurring on the as-received specimen at 540 mV while the pitting initiation potentials for the aged specimens for 5, 20, 50, and 255 hours were 575 mV, 705 mV, 555 mV, and 270 mV, respectively.

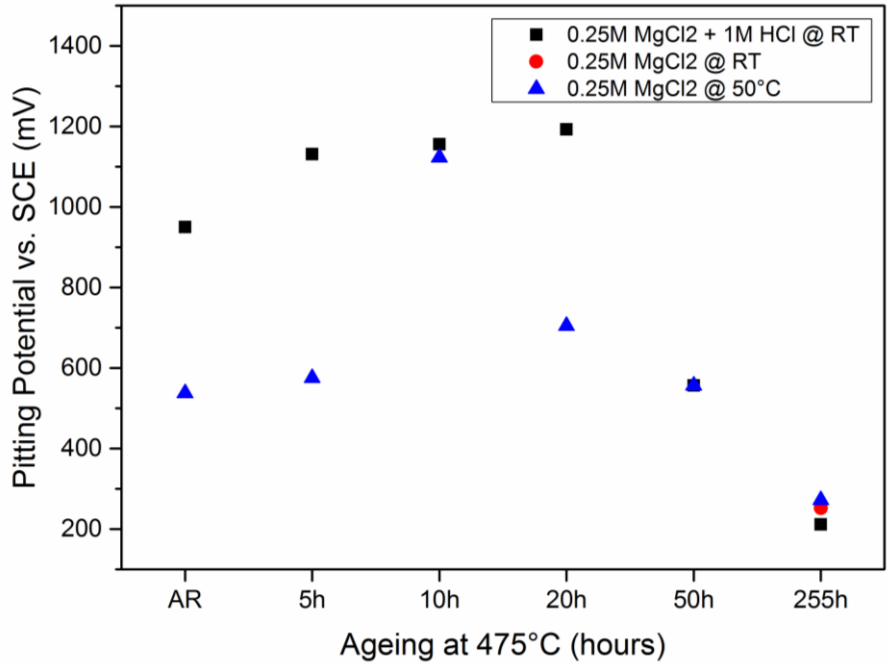

Figure 8-29: Pitting potential of 22Cr-5Ni duplex stainless steel sheet measured in different media.

In order to further assess the passivation behaviour of the as-received specimen and specimens aged for 5 and 50 hours in 0.5M NaCl, samples were potentio-dynamically polarised under immersed conditions at a temperature far above the CPT for each condition at 60°C, shown in Figure 8-30. The as-received specimen showed pitting corrosion around 500 mV with a passivity range of about 400 mV. The specimen aged for 5 hours suffered from pitting corrosion at about 650 mV with a passivity range of about 600 mV, whereas the specimen aged for 50 hours pitted at about 250 mV with a narrow passive range of only about 200 mV. This clearly demonstrated the increased pitting corrosion resistance microstructure with short (5-10 hours) exposures to the 475°C embrittlement regime.

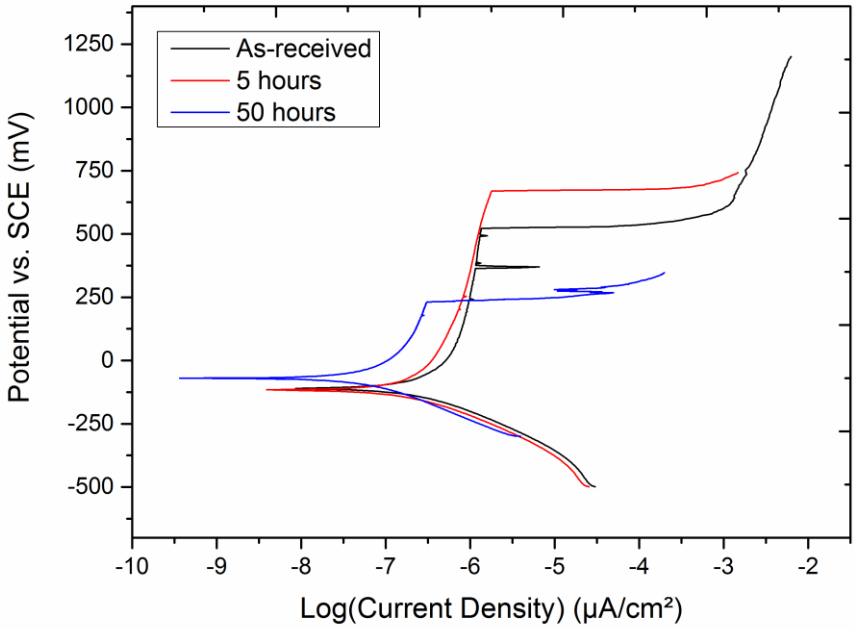

Figure 8-30: Potentio-dynamic polarisation behaviour of as-received 2205 duplex stainless steel plate and aged specimens at 475°C for 5 and 50 hours in 0.5M NaCl electrolyte at 60°C

8.4.4.2 SKPFM and MFM Measurements

8.4.4.2.1 As-received Microstructure

The topography of a measured area of 80 x 80 µm² with corresponding Volta potential difference and magnetic frequency maps of the as-received specimen are shown in Figure 8-31. The topography in Figure 8-31(a) shows a maximum height difference of about 80 µm between ferrite and austenite regions. Topographically higher sites were determined to be ferritic by the magnetic frequency measurement shown in Figure 8-31(c) since the ferrite is ferromagnetic (low magnetic frequency response) and austenite paramagnetic (high magnetic frequency response) [90-92]. Austenite also shows lower Volta potential differences than ferrite, indicating an expected net cathodic behaviour of the austenite phase and a net anodic behaviour of ferrite. It should be noted the reason for topographical lower coordinates of austenite is due to a preferential dissolution of austenite due to sulphuric and nitric acids in the fine polishing treatment. Nitric acid can support the passivation of stainless steels, and the higher chromium content in ferrite is a possible reason for this observation. The pH of the polishing solution is estimated to be around 0, so under strong oxidising conditions the dissolution of austenite can be larger than that of ferrite [93, 94]. The potential

of the solution is shifted towards higher oxidation potentials so that austenite is favouringly dissolved.

The potential variation within both ferrite and austenite regions were quite homogeneous and smooth. A potential variation of 10-20 mV was measured within each phase, with the ferrite showing a potential of 574 mV in average, with a maximum potential of 584 mV and a minimum potential of 564 mV. In contrast, the average potential of austenite was 530 mV, with maximum and minimum potentials of 540 mV and 520 mV, respectively. There is a net potential difference of about 40-50 mV between ferrite and austenite, indicating a driving force for micro-galvanic coupling, with ferrite being less noble than the austenite under the measurement conditions used.

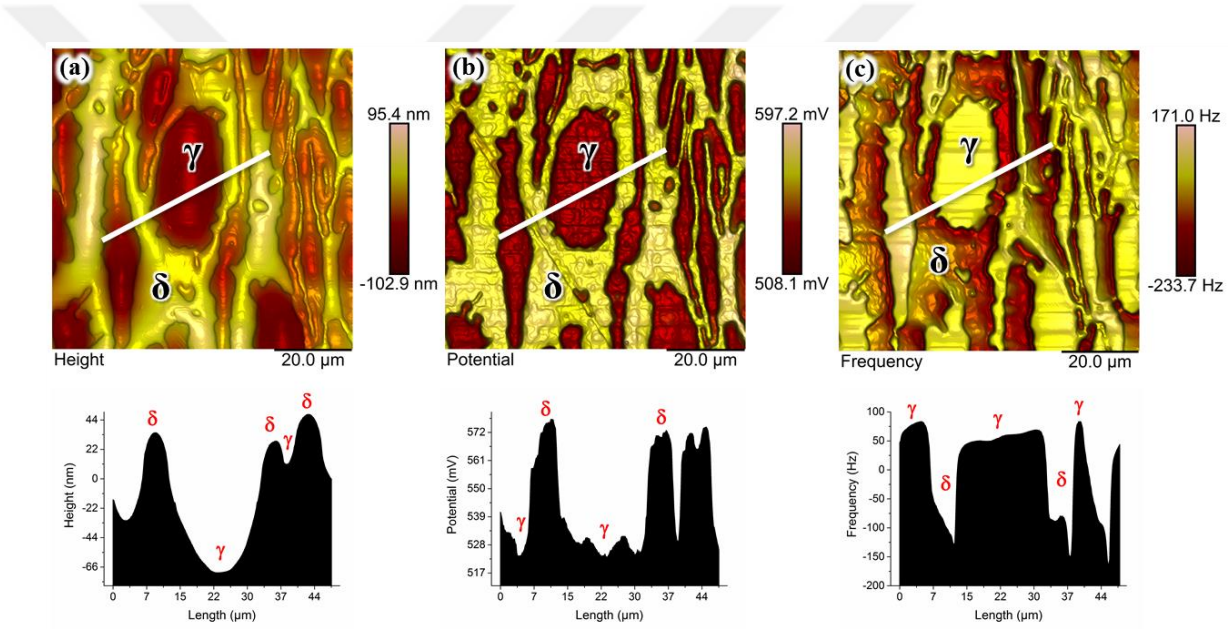

Figure 8-31: SKPFM/MFM on as-received 22Cr-5Ni duplex stainless steel with (a) showing the topography of an area of 80 x 80 µm², (b) the corresponding Volta potential differences map, and (c) the corresponding magnetic frequency map of the same measured region

8.4.4.2.2 475°C / 5 hours Ageing

The topography map of the specimen aged for 5 hours measured over an area of 40 x 40 µm² with the corresponding Volta potential and magnetic phase maps are shown in Figure 8-32. The magnetic phase map in Figure 8-32(c) revealed the duplex microstructure and facilitated allocation of mapped potential and topographic features to the different phases. The ferrite and austenite had both similar Volta potentials, indicating no discrete differences between cathodic and anodic sites. Some regions of ferrite and austenite had higher Volta potential

differences than others, and the average of Volta potential differences measured over ferrite/austenite was 261 mV, with a measured maximum of 312 mV and 210 mV minimum potential. The entire microstructure showed an enhancement of nobility after ageing treatment with respect to the as-received state.

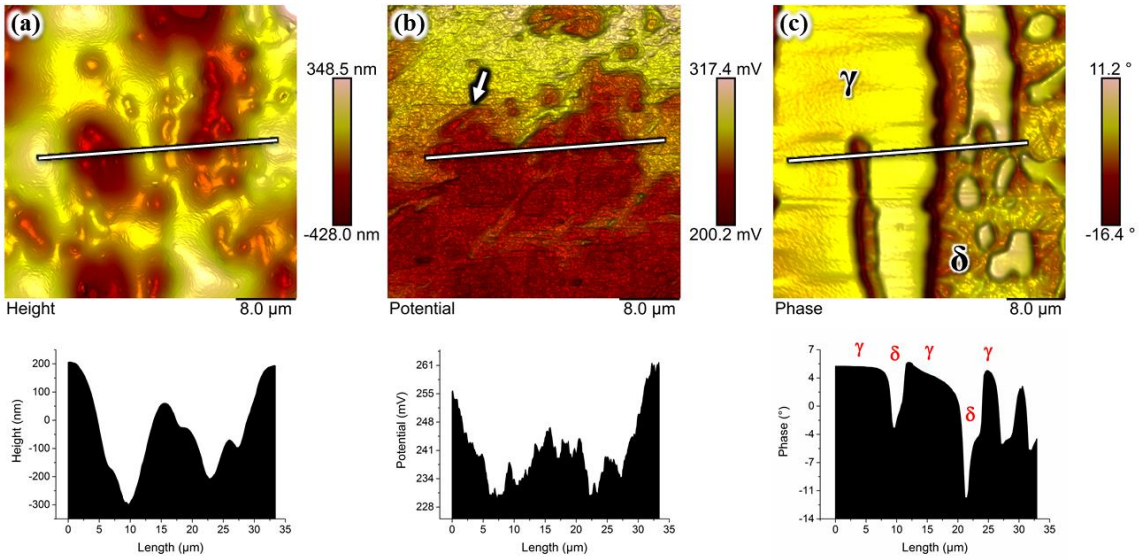

Figure 8-32: SKPFM/MFM on 22Cr-5Ni duplex stainless steel aged at 475°C for 5 hours with (a) showing the topography of an area of 40 x40 µm², (b) showing the corresponding Volta potential differences map, and (c) the corresponding magnetic phase map of the same measured region

Furthermore, SKPFM measurements were repeated under a controlled RH of 71% to inform about the Volta potential response in bulk solution-like environment for comparison to local electrochemical properties. The Volta potential difference measured in 71% RH environment is shown in Figure 8-33. The average Volta potential measured was 263 mV, and seemed to be not affected by the adhering monolayers of water. It should be noted that it took about one hour to stabilise the RH of 71% during the introduction of water vapour humidity, and measurements were carried out when no change of humidity was seen.

The Volta potential variation within the entire measurement area, however, significantly dropped from 51 mV (in dry air) to 20 mV in 71% RH environment. Highest (max.) and lowest (min.) potential values measured were 282 mV and 243 mV, respectively. This clearly demonstrated that ferrite and austenite assumed similar nobility with no clear difference between anodic and cathodic sites.

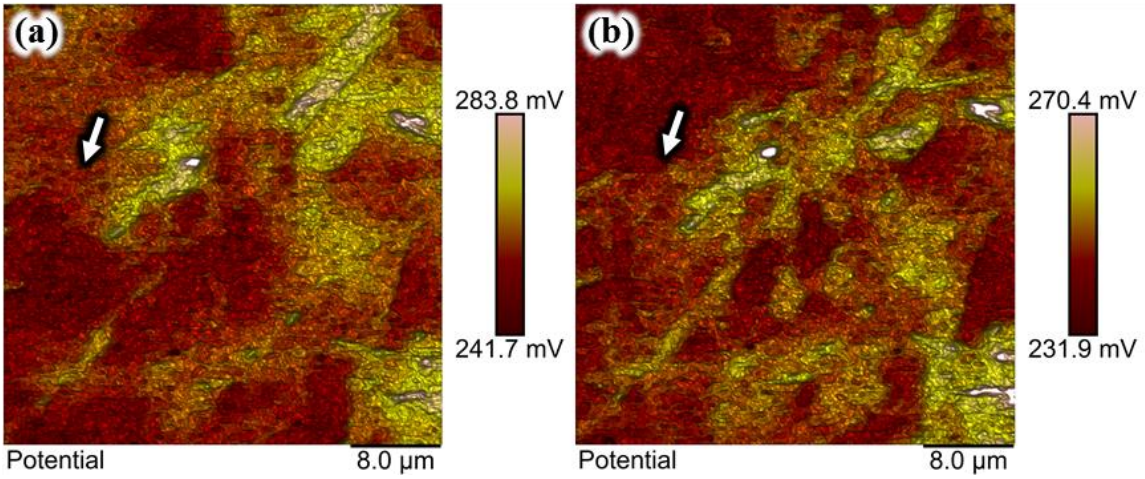

Figure 8-33: SKPFM on 22Cr-5Ni duplex stainless steel aged at 475°C for 5 hours with (a) showing the Volta potential differences map at 71% rel. humidity and (b) at 71% rel. humidity after 1 hour. The white arrows in (a) and (b), and in Figure 8-32(b) show the same position.

8.4.4.2.3 475°C / 20 hours Ageing

The topography of the specimen aged for 20 hours measured over an area of 80 x 80 µm² showed elevated austenitic regions which conveniently facilitated a microstructure surface morphology contrast, as shown in Figure 8-34(a). The height variation within the austenite was larger than that of ferrite. Some austenite grain boundaries are also visible in the topography map, indicating chemical attack during polishing due to grains with different grain orientation. In some regions the height of ferrite and austenite were similar. The magnetic frequency map of the same region, shown in Figure 8-34(c), clearly revealed the microstructure. The corresponding Volta potential difference map, which can be seen in Figure 8-34(b), shows that a significant potential difference between ferrite and austenite is apparent again, indicating micro-galvanic coupling. The average Volta potential difference measured over austenite was 361 mV, highest and lowest peak potentials of 380 mV and 342 mV, respectively. The average potential measured over ferrite was 439 mV with peak potentials of 463 mV and 415 mV, giving a difference of ca. 80 mV.

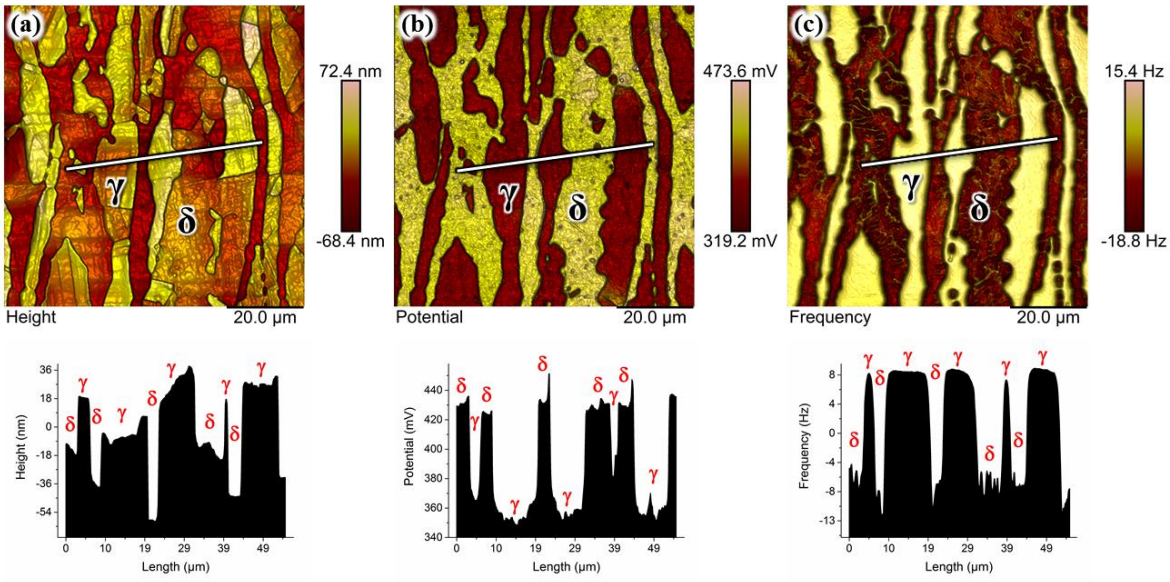

Figure 8-34: SKPFM/MFM of 22Cr-5Ni duplex stainless steel aged at 475°C for 20 hours with (a) showing the topography of an area 80 x 80 µm², (b) the corresponding Volta potential differences map, and (c) the corresponding magnetic frequency map.

8.4.4.2.4 475°C / 50 hours Ageing

After 50 hours ageing at 475°C ferrite was the elevated topographical phase again similar to the as-received condition (Figure 8-35(a)). The reason for the topographical change with ageing is not clear, and the magnetic frequency map shown in Figure 8-35(c) confirmed the phase allocation of ferrite. A reduction of magnetic properties of the ferrite was noticed in comparison to the as-received condition, possibly due to spinodal decomposition and other phase reaction occurring. This is indicative of phase transformation products, and may well be related to the presence of R, χ, γ_2, or τ phase. Regions of ferrite which adapted similar magnetic frequencies as the austenite are pointed out by the arrows in the magnetic frequency map in Figure 8-35(c). Moreover, the magnetic frequency variation within the ferrite became more apparent, i.e. the magnetic domains became noticeable.

The Volta potential differences map in Figure 8-35(b), showed a potential difference of only 17 mV between ferrite and austenite. The Volta potential difference measured over ferrite was 510±3 mV; whist that measured over austenite was 493±8 mV. This inferred micro-galvanic coupling between both phases, but to a far smaller extent than in the as-received and for 20 hours aged microstructures. Only small Volta potential variations of each phase were present, with a few potential hot-spots, pointed out by the black arrows in Figure 8-35(b). The latter indicates electrochemically active sites with increased micro-galvanic

coupling between these hot-spots and adjacent microstructure sites. Such sites are most likely related to R-phase precipitates.

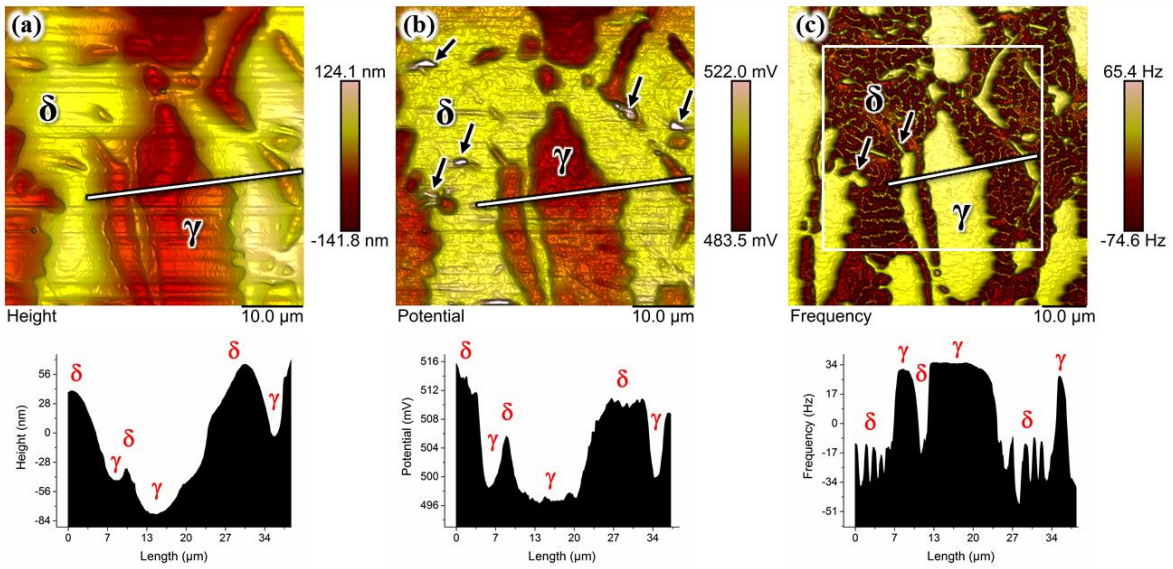

Figure 8-35: SKPFM/MFM on 22Cr-5Ni duplex stainless steel aged at 475°C for 50 hours with (a) showing the topography of an area 50 x 50 µm², (b) the corresponding Volta potential differences map, and (c) the corresponding magnetic frequency map (mapping area 65 x 65 µm²).

8.4.4.2.5 475°C / 255 hours Ageing

The Volta potential differences map of the spinodally decomposed microstructure after 255 hours ageing is shown in Figure 8-36(a) with the corresponding magnetic frequency map in Figure 8-36(b). A significant Volta potential differences increase was observed over the entire microstructure. An average Volta potential difference of 1090±70 mV was measured over the ferrite (precipitates excluded) with large variation, whilst 1125±175 mV was measured over the austenite. Both spinodally-decomposed ferrite (α'+α'') and austenite showed large Volta potential differences, indicating an increased electrochemical activity of both phases. The austenite even showed smeared potential zones adjacent to phase boundaries indicating element depletion zones.

Precipitates, indicated as "P" in Figure 8-36(a), showed highest potentials of up to 1725 mV, with an average of 1400±325 mV. On adjacent sites, lower Volta potential differences of ca. 800 mV were observed, which spanned over a width of 100-300 nm, indicating the presence of element depletion zones in the vicinity of these intergranular precipitates. Protruding features from the ferrite (not at interphase boundaries) were assigned to Mo-Si-Ni-Cr-enriched R-phase precipitates [73]. A region containing R-phase and other precipitates (P)

was re-scanned at higher resolution, shown in Figure 8-37. At phase boundaries primarily carbides, secondary austenite and/or χ phase are believed to have been present [74]. The majority of all larger precipitates were R phase (P_2,), which had significantly lower Volta potential differences than the other precipitates. The width of their depletion zones was in the order of 50-100 nm. Carbides or secondary austenite have most likely formed a network along most interphase boundaries, as pointed out by P1 and P3 in Figure 8-37(a). They had the lowest Volta potential differences in contrast to all other secondary phases.

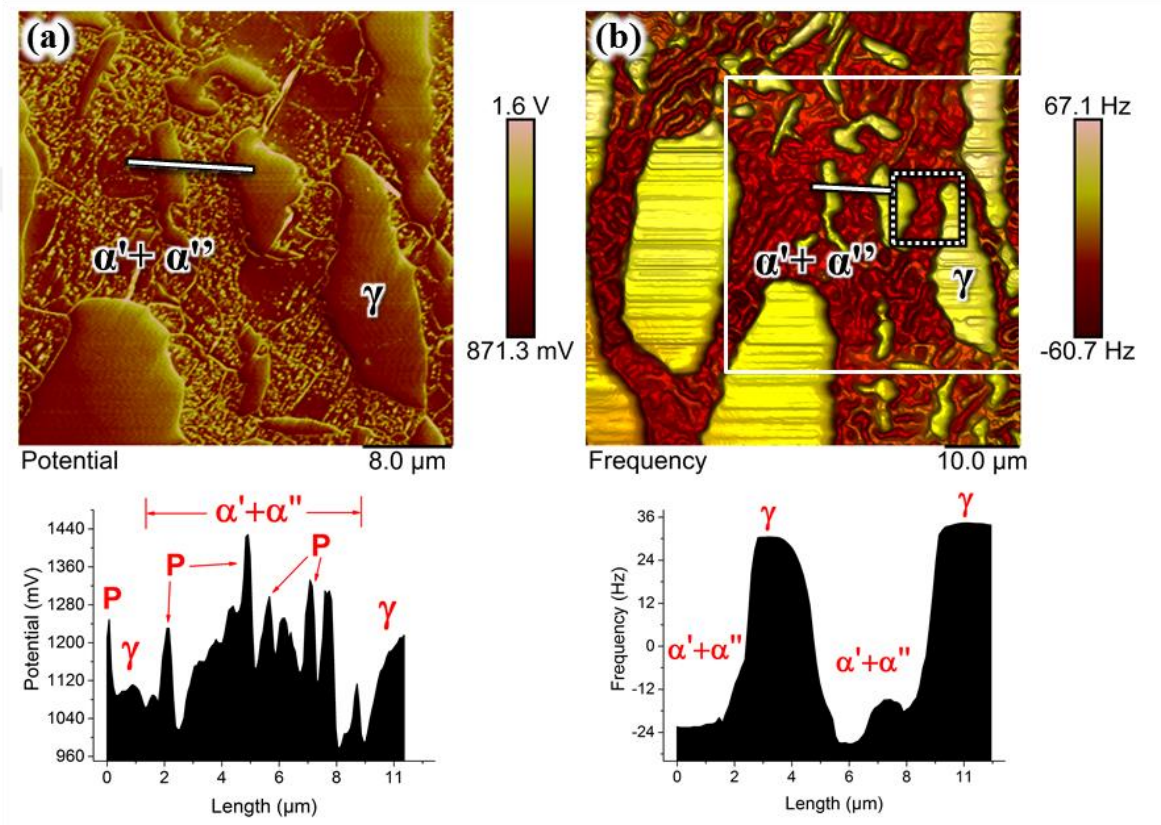

Figure 8-36: SKPFM/MFM on 22Cr-5Ni duplex stainless steel aged at 475°C for 255 hours with (a) showing Volta potential differences map and (b) the corresponding magnetic frequency map over a measured area of 40 x 40 µm². Note that ferrite (δ) was decomposed into α'+α'', R-phase, and other precipitates (P).

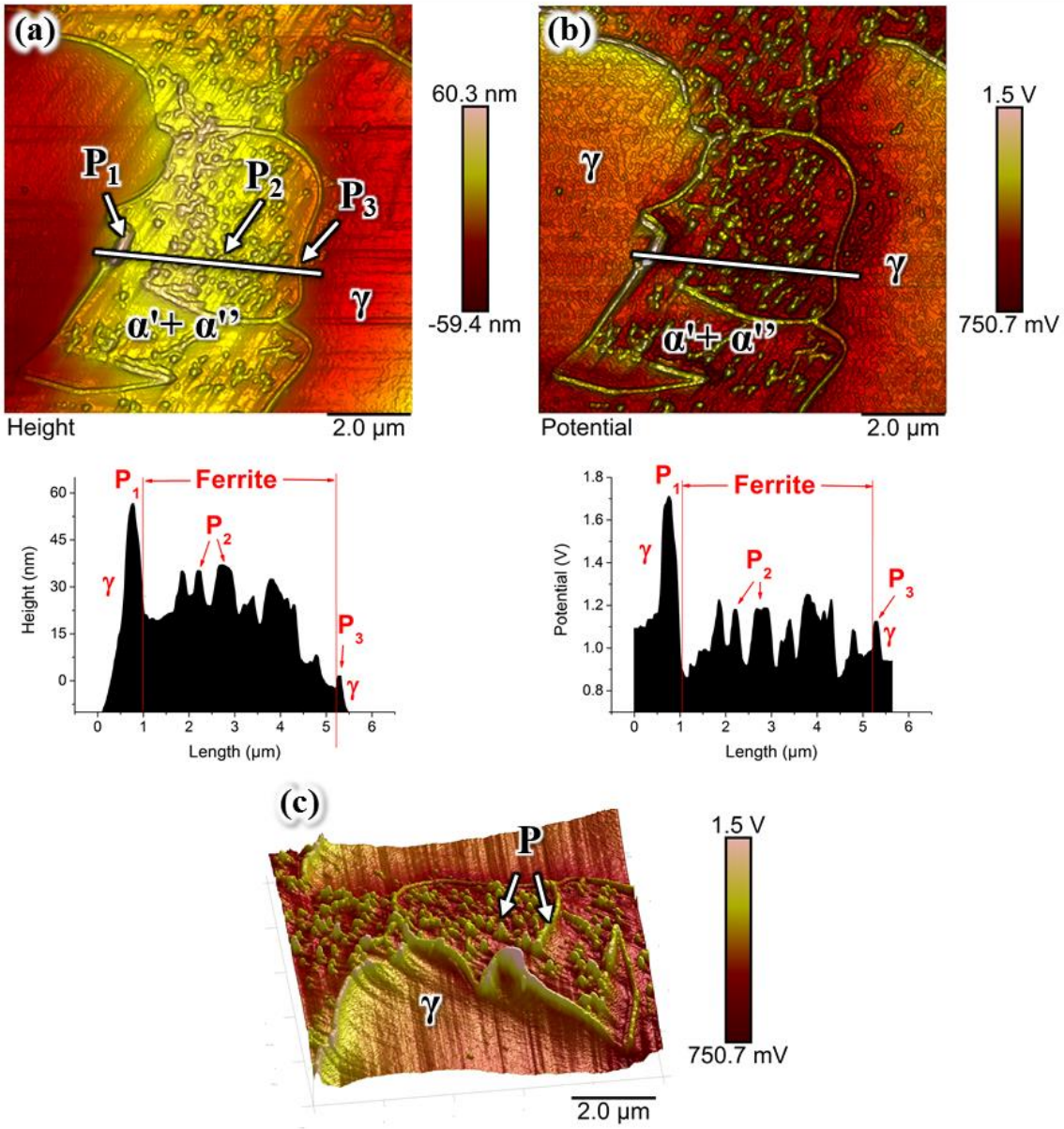

Figure 8-37: SKPFM/MFM on 22Cr-5Ni duplex stainless steel aged at 475°C for 255 hours with (a) showing the topography of a 10 x 10 μm² area, (b) the corresponding Volta potential differences map, and (c) a 3D topography view overlaid with potential (100° rotated anti clockwise) showing that all anodic features (precipitates) protrude from the surface. Precipitates located in the ferrite are primarily R-phase (P_2), while those situated on phase boundaries (P_1 & P_3) could be γ_2, χ, and carbides. Note the "smeared" potential zone in austenite indicating elemental depletion, hence enhanced local electronic activity.

In order to obtain topography and local Volta potential information about the spinodally-decomposed phases, α' and α'', a high-resolution PeakForce Tapping mode AFM assessment in lift mode was carried out. In PeakForce Tapping mode, the topography can be scanned at a far higher resolution for which the potential contrast between microstructural features is highly enhanced due to better trace-retrace curve fitting [87].

Figure 8-38(a) shows the topography of the measured region containing spinodal decomposition products and other precipitates. The spinodal "arms", which are defined as the thickness or diameter of the spinodal products, were determined to be 15-30 nm wide, which lies in the same order of magnitude as our previous work [73]. It should be noted that the potential map was flattened due to measurement-related artefacts, so the values are quantitative in accordance with the previously shown results only. High potential regions are assumed to be the Cr-enriched α'', and regions with lower Volta potential differences forming the Cr-depleted (Fe-rich) α'-matrix. There is a Volta potential difference of up to 60-70 mV between α' and α'' indicating nano-galvanic interactivity.

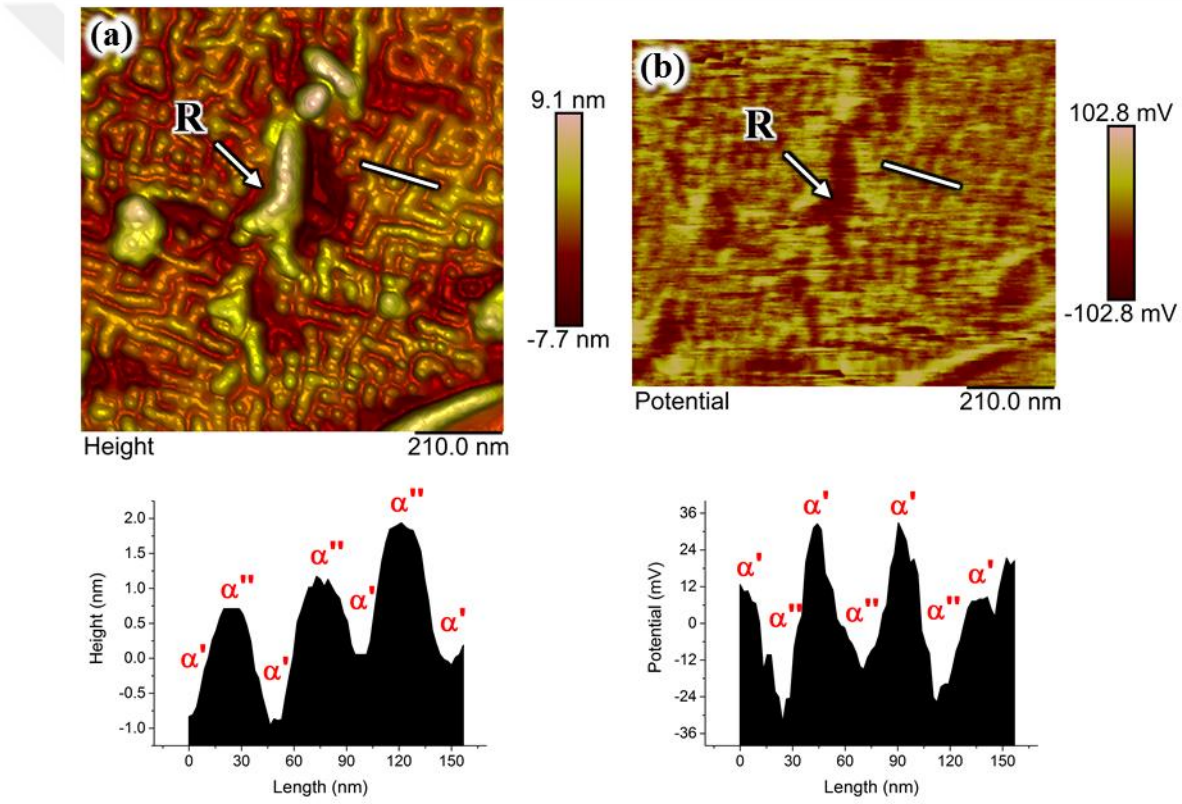

Figure 8-38: SKPFM/MFM on spinodally decomposed ferrite of 22Cr-5Ni duplex stainless steel aged at 475°C for 255 hours with (a) showing the topography of a 1 x 1 µm² measurement area and (b) the corresponding Volta potential difference map. Note that the potential map had to be flattened by a first order due to measurement artefacts but no smoothing was performed. Cr-rich α'' protrude from the surface and are cathodic with respect to Fe-rich α' (potential difference is up to 70 mV).

8.4.5 Discussion

8.4.5.1 Pitting Corrosion Behaviour

The pitting corrosion tests showed a clear enhancement of the corrosion resistance after short-term ageing at 475°C for up to 10 hours. Similar pitting behaviour with ageing time in the 475°C temperature window has also been reported by *Tavares et al.* [61] who observed a CPT increase of up to 16°C after ageing for 8 and 10 hours. They observed preferential pitting in the ferrite of the as-received microstructure, with both ferrite and austenite showing localised corrosion after 8 hours of aging. Figure 8-28 and Figure 8-29 clearly show a significant increase in corrosion resistance, followed by a steep decay with ageing treatments in excess of 10 hours. This is in line with observations of the formation of a number of precipitates in the microstructure as well as changes in the spinodal decomposed microstructure [73]. A major difference observed was the arm distance (or amplitude) of the spinodally decomposed Cr-rich α''- and Cr-poor α'-regions, which increased from 2-3 nm after 5 hours of exposure, to 15-30 nm after 255 hours ageing [73]. The development of Cr-rich α'' with small arm widths reported for shorter ageing treatments was most likely the reason for the observed rise in CPT, whilst the precipitates observed after 50 and 255 hours exposures caused a steep fall of corrosion resistance. The reason for this observation is discussed in the SKPFM section below.

8.4.5.2 SKPFM and MFM Measurements

8.4.5.2.1 As-received Microstructure

The as received microstructure showed distinctive Volta potential differences between the ferrite and the austenite. Generally, micro-galvanic coupling in the microstructure can lead to selective corrosion of one of the phases. The measured potential difference of approx. 60 mV could be the reason for the preferential corrosion behaviour. In earlier work the selective corrosion of ferrite in chloride environments was reported [17, 89, 90, 95, 96]. Dissolution of austenite can also occur, but only with a further increase of the electrochemical potential towards the anodic direction [61, 93, 94, 97, 98].

The homogeneous distribution of measured Volta potential differences of maximum 20 mV measured over the austenite and ferrite indicated no local potential hot-spots. Only interphase regions were found to show larger potential variations with steep potential

gradients, indicating that these regions could act as possible nucleation sites for corrosion. The large potential gradients at interphase boundaries were present over narrow distances of 1-2 µm only, possibly due to a dense concentration of stored energy indicating a higher density of dislocations, which are present at grain boundaries or strained regions [99]. Moreover, the phase mismatch between austenite and ferrite can lead to additional strain localisation at interphase boundaries. The interphase in DSS is typically more susceptible when exposed to harsh environments. Earlier work has shown that preferential attack often occurs on those sites during atmospheric corrosion of duplex 22Cr-5Ni and super duplex 25Cr-7Ni stainless steels [17, 90, 95].

Local stress fields and chemical variations affect local corrosion properties of individual phases in the microstructure, which can be detected by SKPFM [78, 99]. Different chemical compositions of ferrite and austenite are inherently present in DSS microstructure (Table 8-3), which ultimately leads to different characteristics of the passive surface film. The latter is manifested by different SKPFM measured Volta potential differences between ferrite and austenite, as earlier shown. Austenite contains higher Ni content, which on one side reduces pit growth rates, but may not (or even negatively) affect pit nucleation characteristics [100].

8.4.5.2.2 475°C / 5 hours Ageing

The drop of measured Volta potential differences over the entire microstructure after 5 hours ageing is a consequence of phase transformations occurring. The measured local Volta potential differences over ferrite dropped from 574±9 mV to 261±43 mV, and those measur ed over austenite decreased from 529±10 mV to 261±43 mV. This drop of about 300 mV in average for the entire microstructure means that the overall microstructure became nobler. The increase in nobility after 5 hours of ageing was also confirmed by SKPFM measurements in high humidity environments where a bulk-solution like electrolyte can be assumed. Both, ferrite and austenite had similar potential values, indicating similar electrochemical behaviour. These observations were also supported by similar topographic appearance after sample preparation (Figure 8-32).

Microstructure analysis of the 475°C heat-treated microstructures was reported in [74], comprising of high-resolution SEM and TEM analyses. The latter showed spinodal decomposition with a spinodal arm width of 2-3 nm after short ageing treatments, leading to an increase of corrosion resistance [17, 89, 101]. The Cr-enriched spinodal product (α'') has

much stronger passivation characteristics, leading to slower dissolution kinetics compared to the as-received condition. Since no other secondary phases were formed (R-phase or P), spinodal decomposition was the reason for the increase in corrosion properties.

8.4.5.2.3 475°C / 20 hours Ageing

After 20 hours ageing, the observed microstructure had changed with ferrite easily distinguished from austenite. A micro-galvanic cell was established again between ferrite and austenite with approximately 60±10 mV Volta potential differences. Volta potential differences measured in average over the entire microstructure showed an increase which means that the electrochemical nobility decreased. This suggests that the peak of maximum nobility enhancement lies at or around 5 hours of ageing. The spinodal decomposition products present after 20 hours seemed to degrade the measured Volta potential when compared to the 5 hours ageing treatment. TEM investigations reported a growth of the spinodally-decomposed network resulting in 5-8 nm arm distances between Cr-rich α''-zones which was in good agreement with the work of *Weng et al.* who observed spinodal decomposition in 22Cr-5Ni DSS with 3-4 nm and 4-5 nm spinodal arm diameters after 8 and 16 hours ageing at 475°C, respectively [31, 73]. The latter investigations also showed that no other secondary phases were present in the microstructure, ruling effects of R-phase or intergranular P phases.

The variation of Volta potentials measured over ferrite and austenite decreased to approximately 25 mV, with a few steep potential gradients located primarily at interphase boundaries (Figure 8-34). A few ferrite and austenite grain sub-grain facets indicated slight differences in electrochemical nobility of grains with different crystallographic orientations. However, the variation of the measured potential over each phase was larger than that measured in the as-received microstructure, indicating larger tendency for micro-galvanic coupling activity. In addition, local potential hot-spots located at interphase boundaries indicated preferentially active nucleation sites.

8.4.5.2.4 475°C / 50 hours Ageing

The Volta potential differences measured over ferrite and austenite after 50 hours ageing increased compared to the specimen aged for 20 hours. The ferrite and austenite had about 170 mV and 160 mV less noble potentials, respectively. The potential gradient within each

phase and on interphase boundaries also increased, indicating the development of heterogeneous potential regions in the ferrite, austenite, and at interphase boundaries (Figure 8-35). However, the average potential measured over the entire microstructure was still lower than that measured over the as-received microstructure. Furthermore, a depletion zone in the vicinity of the δ-γ interface was observed (Figure 8-35b), indicating that the microstructure on the ferritic side adjacent to the interphase boundaries changed more than those in austenite, probably due to secondary phase precipitation.

TEM and SEM investigations confirmed plate-like secondary phase particles precipitated within the ferrite with sizes varying between 20-65 nm [73]. Diffraction analysis of these precipitates showed a close match to diffraction patterns of R-phase precipitates [53, 54, 56], and it is reported that R-phase can coexist with α' and α'' below 600°C [51, 53, 54, 56]. Chemical analysis by TEM-EDX showed that the R-phase is enriched in Mo, Cr, Si, and Ni. Accordingly, an elemental depletion layer of these elements is expected within the ferrite. The presence of a range of other intergranular precipitates was also reported after 50 hours of ageing [73], and it seems that these intergranular precipitates also consumed electrochemically noble elements, such as Cr, Mo, and Ni, since the observed interphase Volta potential difference was also reduced ((Figure 8-35(b).

8.4.5.2.5 475°C / 255 hours Ageing

The microstructure response here was dominated by the presence of secondary phases in the microstructure, and the largest microstructure transformation was observed after 255 hours ageing at 475°C [73]. The spinodal decomposition products in the ferrite, α' and α'', grew further resulting in a spinodal arm width of 15-30 nm, which was easily recognised via SEM analysis as shown in Figure 8-27. The R-phase precipitates also grew to sizes of 200-400 nm. Volta potential differences measured over these precipitates were larger than those measured over other microstructural constituents, due to their increased Cr, Mo, Ni, and Si contents. However, a large variation of measured Volta potential differences was observed, probably related to different chemistry and/or structure of the precipitates. The Volta potential adjacent to the precipitates had 60-220 nm depletion widths, with typical variations of 200-350 mV. Depletion in Cr and Mo often leads to preferential corrosion attack at such sites, which would explain the reduced pitting corrosion behaviour reported in Figure 8-28.

8.4.5.2.6 Summary of SKPFM Results

All Volta potential differences determined by SKPFM are summarised in Table 8-4 and Figure 8-39. The scatter of the measured data together with interphase potential gradients, the interphase potential width, and information about R-phase precipitates are also shown. The interphase Volta potential width was measured perpendicular to interphase boundaries, with the interphase gradient determined over length increments of 1 μm across interphase boundaries.

The Volta potential differences measured over ferrite and austenite significantly changed with each ageing condition. This is most likely related to spinodal decomposition of the ferrite, which leads to an increase in nobility of the ferrite. The corrosion resistance is negatively affected by the precipitates of R-phase (and other phases), resulting in elemental depletion zones around them. This is reflected by small changes in the Volta potential between the ferrite and austenite for up to 50 hours of ageing, followed by a steep rise with 255 hours exposure (Figure 8-39).

The interphase Volta potential gradient decreased to only about 7 mV/μm with 50 hrs ageing treatments, whereas the interphase Volta potential width increased to 2.75 ± 0.75 μm (Table 8-4). Elemental redistribution may have occurred on both phases due to diffusion and phase transformation reactions, since a similar width was also observed after 255 hours ageing exposure. The overall microstructure corrosion characteristics have severely degraded with longer exposure to the 475°C embrittlement temperature regime.

Table 8-4: SKPFM measured potentials of microstructure components in 22Cr-5Ni duplex stainless steel

Sample	Ferrite	Austenite	R-Phase	δ-γ Interphase Gradient	δ-γ Interphase Potential Width	Depletion Zone at R-Phase	
	mV	mV	mV	mV/μm	μm	mV	nm
AR	574 ± 9	529 ± 10	-	25 ± 1	0.5 ± 0.2	-	-
5 h	261 ± 43	261 ± 43	-	close to 0	close to 0	-	-
20 h	438 ± 23	356 ± 21	-	100 ± 2	0.8 ± 0.4	-	-
50 h	509 ± 10	495 ± 29	-	6.8 ± 4.4	2.75 ± 0.75	-	-
255 h	1260 ± 160	1220 ± 120	1300 ± 130	306 ± 194	2.25 ± 0.75	200-350	60-220

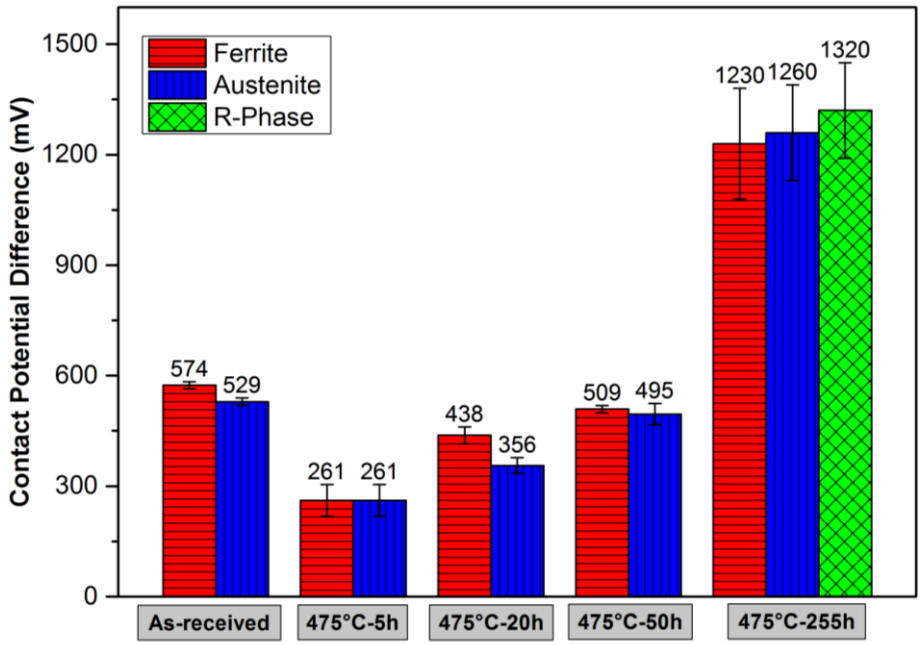

Figure 8-39: Summary of SKPFM measured Volta potential differences measured over ferrite, austenite and R-phase precipitates.

8.4.5.3 Mechanistic Model to Describe Corrosion Behaviour

The passivity of stainless steels relies on the Cr(III)-oxides/hydroxides in the passive layer. The Cr_2O_3 has the ability to anchor water molecules and hydroxyl ions to prevent chloride ions from migrating through the passive layer [102]. Therefore, the spinodally decomposed region containing Cr-enriched α'' in the ferrite should show enhanced passivating behaviour.

A schematic diagram in Figure 8-40 shows the observed SKPFM-informed corrosion resistance, which is a simplified version of the data shown in Figure 8-39. The spinodal decomposition occurring in ferrite in the early ageing conditions let to an improvement of the corrosion properties due to enhanced passivation, with the precipitation of secondary phases deteriorated these electrochemical properties with longer exposure. The corrosion resistance increased with short-term ageing in the 475°C temperature window due to the enhanced corrosion resistance of ferrite. Both ferrite and austenite reaches similar corrosion resistance after around 5 to 10 hours of ageing, which then decreases due to secondary phase precipitation at interphases and within the ferrite leading to element depletion phenomena.

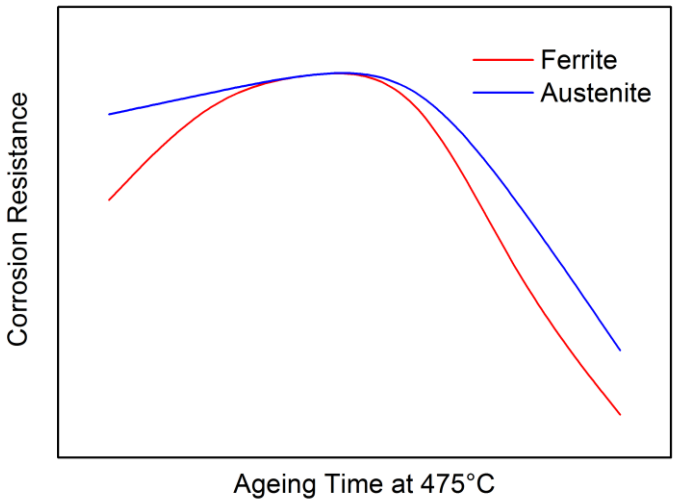

Figure 8-40: Schematic illustration of the assumed behaviour of the corrosion resistance of ferrite and austenite in duplex stainless steel over time, aged in the 475°C temperature regime.

Since spinodal decomposition causes an increase of the concentration of Cr (and possibly Mo as well) in α'' dominated regions, the spatial distribution of this phase may determine the overall passivation behaviour. In fact, the passive layer of stainless steels for ferrite and austenite is reported to be around 2-5 nm thick [28, 102, 103]. If a passive layer thickness of 5 nm is considered, the 2-3 nm wide α''-zones of the 5 hours annealed sample could in fact form a stronger oxide layer, compared to the Cr-depleted α'-zones. The Cr-O:Fe-O ratio is also expected to be higher in α''-phase, also leading to a beneficial electrochemical effect. This would provide an enhanced Cr-Mo effect in the ferritic phase, with enhanced passivation behaviour. This mechanistic model of changes in corrosion resistance of the ferrite due to spinodal decomposition is schematically illustrated in Figure 8-41.

The ferrite in as-received microstructure of grade 22Cr-5Ni DSS contains more Cr and Mo (Table 8-3), but these chemical compounds are homogeneously distributed without short-range atomic order. This is indicated by the blue line (t=0) in Figure 8-41. Short-time heat treatments at 475°C, corresponding to t=1, cause small Cr content fluctuations across the ferrite leading to spinodal decomposition which can be described by wave functions [104]. Each half wave length can be regarded as the spinodal arm width, with the upper amplitude describes the Cr-enriched α''-phase and the lower amplitude the Cr-depleted α'-phase. The bulk ferrite would therefore behave like a material with higher Cr content, having thicker

and stronger passivation layer characteristics (t=2 in Figure 8-41). This effect will obviously lead to enhanced corrosion performance.

Increasing the spinodal arm width, with in parallel precipitation of other phases then affects the passivation characteristics of the material. The gap between two α'' regions increases and probably exceeded the critical point where the passivation layer becomes not sufficient any more. Local Cr-depletion zones (possibly Mo as well) are then formed at and adjacent to α'' zones and R-phase precipitates, causing a loss of effective passive layer resistance, as schematically shown in Figure 8-42. This is similar to the classical sensitisation phenomenon reported with exposure to higher temperature regimes.

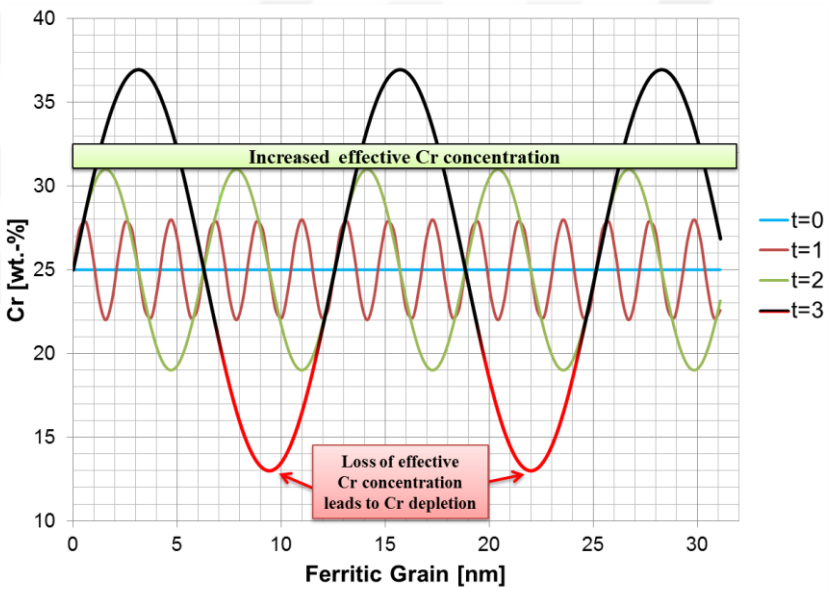

Figure 8-41: Mechanistic model describing for corrosion resistance improvement by spinodal decomposition: (t=0): Cr distribution in as-received condition; (t=1-3): after annealing in the 475°C embrittlement temperature regime, with t=3 > t=2 > t=1 indicating descending exposure times.

The measured Volta potential difference over austenite was already nobler than the Volta potential difference measured over ferrite, supporting the overall enhanced corrosion resistance of the duplex microstructure. The net Volta potential differences measured over the austenite also decreased together with the ferrite, indicating that microstructure changes may have occurred in the austenite as well. SEM and TEM investigations showed no sign for secondary phase transformation products [73]. However, the presence of short-range clustered atoms, or change in element composition due to diffusion cannot be excluded which could have affected the corrosion behaviour of austenite, as described by Chung et al.

[25]. *Horvarth et al.* [12] reported Cr_2N plate-like precipitates formed with exposure to 500°C, which could have enhanced the electrochemical nobility of the austenite in a similar way.

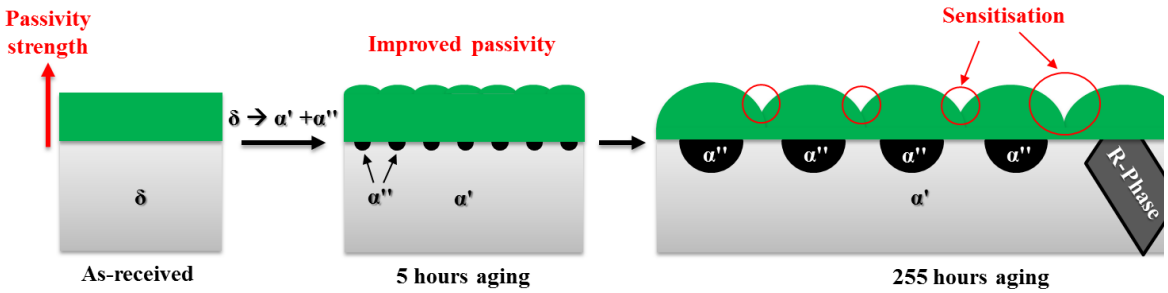

Figure 8-42: Mechanistic model for the mechanism of passivation layer change during heat treatment at 475°C.

8.4.6 Conclusions

1) The microstructure of 22%Cr-5%Ni duplex stainless steel transformed as a function of 475°C embrittlement heat treatment, in the form of spinodal decomposition of the ferrite, formation of R-phase, and a number of intergranular phases.
2) The CPT increased to a peak after 5 to 10 hours of ageing exposure, followed by a drop of corrosion resistance with longer 475°C heat treatment times. Volta potential differences measured over ferrite and austenite correlated with the observed CPT measurements.
3) The spinodal decomposed microstructure had Volta potential differences between Cr-rich α'' and Fe-rich α'phase of up to 60 mV, indicating local galvanic coupling.
4) The α'' had a higher practical nobility than α' phase, and spinodal decomposition were the reason for corrosion property improvement, with other precipitates causing microstructure degradation. SKPFM measured element deletion zones were measured around R-phase precipitates and interface regions.
5) A mechanistic model to link measured SKPFM potentials in microstructure to the overall corrosion resistance of 475°C embrittled microstructures has been introduced.

8.4.7 Acknowledgement

The authors acknowledge Radioactive Waste Management (RWM) (NPO004411A-EPS02) and EPSRC (EP/I036397/1) for financial support. The authors are grateful for the kind provision of Grade 2205 Duplex Stainless Steel plate by Rolled Alloys. The authors also appreciate the valuable comments provided Dr Anthony Cook, The University of Manchester.

8.4.8 References

[1] J. Charles, S. Bernhardsson. Duplex Stainless Steels '91 - Volume 1. In: Charles J, Bernhardsson S, (Eds.). Duplex Stainless Steels '91, vol. 1. Beaune, Bourgogne, France: Les editions de physique, 1991.

[2] A.F. Padilha, D.M. Escriba, E. Materna-Morris, R.L. Plaut. Chi-phase precipitation in a duplex stainless steel, Materials Characterization 60 (2009) 1214-1219.

[3] M. Hättestrand, P. Larsson, G. Chai, J.-O. Nilsson, J. Odqvist. Study of decomposition of ferrite in a duplex stainless steel cold worked and aged at 450–500°C, Materials Science and Engineering: A 499 (2009) 489-492.

[4] J.-O. Nilsson, G. Chai. The physical metallurgy of duplex stainless steels. International Conference & Expo DUPLEX 2007. Grado, Italy: ASSOCIAZIONE ITALIANA DI METALLURGIA - AIM, 2007.

[5] J.O. Nilsson. Super duplex stainless steels, Materials Science and Technology 8 (1992) 685-700.

[6] K.H. Lo, C.H. Shek, J.K.L. Lai. Recent developments in stainless steels, Materials Science and Engineering: R: Reports 65 (2009) 39-104.

[7] H.-J. Eckstein. Korrosionsbeständige Stähle, Deutscher Verlag für Grundstoffindustrie GmbH, Leipzig, Germany, 1990.

[8] Lula et al. Duplex Stainless Steels, American Society for Metals, Mars, Pennsylvania, 1983.

[9] J. Charles, S. Bernhardsson. Duplex Stainless Steels '91 - Volume 2. In: Charles J, Bernhardsson S, (Eds.). Duplex Stainless Steels '91, vol. 1. Beaune, Bourgogne, France: Les editions de physique, 1991.

[10] N. Sathirachinda, R. Pettersson, S. Wessman, U. Kivisäkk, J. Pan. Scanning Kelvin probe force microscopy study of chromium nitrides in 2507 super duplex stainless steel—Implications and limitations, Electrochimica Acta 56 (2011) 1792-1798.

[11] N. Sathirachinda, R. Pettersson, S. Wessman, J. Pan. Study of nobility of chromium nitrides in isothermally aged duplex stainless steels by using SKPFM and SEM/EDS, Corrosion Science 52 (2010) 179-186.

[12] W. Horvath, W. Prantl, H. Stroißnigg, E.A. Werner. Microhardness and microstructure of austenite and ferrite in nitrogen alloyed duplex steels between 20 and 500°C, Materials Science and Engineering: A 256 (1998) 227-236.

[13] S.-H. Byun, N. Kang, T.-H. Lee, S.-K. Ahn, H. Lee, W.-S. Chang, K.-M. Cho. Kinetics of Cr/Mo-rich precipitates formation for 25Cr-6.9Ni-3.8Mo-0.3N super duplex stainless steel, Met. Mater. Int. 18 (2012) 201-207.

[14] O.K. Chopra, H.M. Chung. Long-term embrittlement of cast duplex stainless steels in LWR systems: semiannual report. In: Chung HM, Engineering USNRCOoNRRDo, (Eds.). Washington, D.C. :: Division of Engineering, Office of Nuclear Regulatory Research, U.S. Nuclear Regulatory Commission, 1989.

[15] J.L. González-Carrasco, M.L. Escudero, F.J. Martín, M.C. García-Alonso, J. Chao. Influence of the 475°C hardening of MA 956 on its corrosion behaviour at room temperature, Corrosion Science 43 (2001) 1081-1094.

[16] F. Iacoviello, F. Casari, S. Gialanella. Effect of "475 °C embrittlement" on duplex stainless steels localized corrosion resistance, Corrosion Science 47 (2005) 909-922.

[17] C. Örnek, D.L. Engelberg, S.B. Lyon, T.L. Ladwein. Effect of "475°C Embrittlement" on the Corrosion Behaviour of Grade 2205 Duplex Stainless Steel Investigated Using Local Probing Techniques. Eurocorr 2013. Estoril, Portugal: European Corrosion Congress, 2013.

[18] C.-J. Park, H.-S. Kwon, M.M. Lohrengel. Micro-electrochemical polarization study on 25% Cr duplex stainless steel, Materials Science and Engineering: A 372 (2004) 180-185.

[19] J.S. Park, Y.K. Yoon. Evaluation of thermal aging embrittlement of duplex stainless steels by electrochemical method, Scripta Metallurgica et Materialia 32 (1995) 1163-1168.

[20] A. Plumtree, R. Gullberg. Embrittlement of a continuously cooled Fe-25 Cr alloy, Metallurgical Transactions A 7 (1976) 1451-1458.

[21] J.K. Sahu, U. Krupp, R.N. Ghosh, H.J. Christ. Effect of 475°C embrittlement on the mechanical properties of duplex stainless steel, Materials Science and Engineering: A 508 (2009) 1-14.

[22] J.W. Cahn. Hardening by spinodal decomposition, Acta Metallurgica 11 (1963) 1275-1282.

[23] J.W. Cahn, J.E. Hilliard. Spinodal decomposition: A reprise, Acta Metallurgica 19 (1971) 151-161.

[24] K. Chandra, R. Singhal, V. Kain, V.S. Raja. Low temperature embrittlement of duplex stainless steel: Correlation between mechanical and electrochemical behavior, Materials Science and Engineering: A 527 (2010) 3904-3912.

[25] H.M. Chung. Spinodal decomposition of austenite in long-term-aged duplex stainless steel. 1989. p.Medium: X; Size: Pages: 25.

[26] H.M. Chung. Aging and life prediction of cast duplex stainless steel components, International Journal of Pressure Vessels and Piping 50 (1992) 179-213.

[27] F. Danoix, P. Auger, D. Blavette. Hardening of Aged Duplex Stainless Steels by Spinodal Decomposition, Microscopy and Microanalysis 10 (2004) 349-354.

[28] C. Eckstein, H.J. Spies, J. Albrecht. Untersuchungen zum Einfluss des Stickstoffs auf das Lochkorrosionsverhalten hochlegierter austenitischer Cr-Ni-Mo-Stähle (Teil II), Materials and Corrosion 55 (2004) 861-864.

[29] M.K. Miller, I.M. Anderson, J. Bentley, K.F. Russell. Phase separation in the Fe-Cr-Ni system, Applied Surface Science 94–95 (1996) 391-397.

[30] T. Nys, P.M. Gielen. Spinodal decomposition in the Fe−Cr system, Metallurgical Transactions 2 (1971) 1423-1428.

[31] K.L. Weng, H.R. Chen, J.R. Yang. The low-temperature aging embrittlement in a 2205 duplex stainless steel, Materials Science and Engineering: A 379 (2004) 119-132.

[32] Y. Saito. Computer Simulation of Spinodal Decomposition in Duplex Stainless Steels, Materials Science Forum 706 - 709 (2012) 1509-1514.

[33] C.H. Shek, Y.Z. Shao, K.W. Wong, J.K.L. Lai. Spatial fractal characteristic of spinodal decomposition in Fe-Cr-Ni duplex stainless steel, Scripta Materialia 37 (1997) 529-533.

[34] S.M. Allen. Spinodal Decomposition. in: Editors-in-Chief: KHJB, Robert WC, Merton CF, Bernard I, Edward JK, Subhash M, Patrick V, (Eds.). Encyclopedia of Materials: Science and Technology (Second Edition). Elsevier, Oxford, 2001. pp. 8761-8764.

[35] M. Hillert, M. Cohen, B.L. Averbach. Formation of modulated structures in copper-nickel-iron alloys, Acta Metallurgica 9 (1961) 536-546.

[36] S.Y. Hu, L.Q. Chen. Spinodal decomposition in a film with periodically distributed interfacial dislocations, Acta Materialia 52 (2004) 3069-3074.

[37] H.D. Solomon, L.M. Levinson. Mössbauer effect study of '475°C embrittlement' of duplex and ferritic stainless steels, Acta Metallurgica 26 (1978) 429-442.

[38] M. Nyström, B. Karlsson. Fatigue of duplex stainless steel influence of discontinuous, spinodally decomposed ferrite, Materials Science and Engineering: A 215 (1996) 26-38.

[39] Y.-S. Li, S.-X. Li, T.-Y. Zhang. Effect of dislocations on spinodal decomposition in Fe–Cr alloys, Journal of Nuclear Materials 395 (2009) 120-130.

[40] J.E. Morral, J.W. Cahn. Spinodal decomposition in ternary systems, Acta Metallurgica 19 (1971) 1037-1045.

[41] F. Danoix, P. Auger, A. Bostel, D. Blavette. Atom probe characterization of isotropic spinodal decompositions: spatial convolutions and related bias, Surface Science 246 (1991) 260-265.

[42] A. Hendry, Z.F. Mazur, K.H. Jack. Influence of nitrogen on 475°C embrittlement of high-chromium ferritic steels, Metal Science 13 (1979) 482-486.

[43] J.J. Shiao, C.H. Tsai, J.H. Huang, J.J. Kai. Phase transformations in ferrite phase of a duplex stainless steel aged at 500°C, Scripta Metallurgica et Materialia 29 (1993) 1451-1456.

[44] O.K. Chopra, H.M. Chung. Aging degradation of cast stainless steels: Effects on mechanical properties. In: Materials and Components Technology Division ANL, (Ed.), 1987. p.Medium: ED; Size: Pages: 34.

[45] F. Danoix, P. Auger. Atom Probe Studies of the Fe–Cr System and Stainless Steels Aged at Intermediate Temperature: A Review, Materials Characterization 44 (2000) 177-201.

[46] F. Findik. Improvements in spinodal alloys from past to present, Materials & Design 42 (2012) 131-146.

[47] I. Shuro, H.H. Kuo, T. Sasaki, K. Hono, Y. Todaka, M. Umemoto. G-phase precipitation in austenitic stainless steel deformed by high pressure torsion, Materials Science and Engineering: A 552 (2012) 194-198.

[48] Y.X. Chen, R. Yu, D.X. Li. Orientation relationships and interfaces between NiAl and G-phase Ni16Hf6Si7, Materials Letters 49 (2001) 25-28.

[49] F. Danoix, P. Auger, S. Chambreland, D. Blavette. A 3D study of G-phase precipitation in spinodally decomposed α-ferrite by tomographic atom-probe analysis, Microsc. Microanal. Microstruct. 5 (1994) 121-132.

[50] T. Hamaoka, A. Nomoto, K. Nishida, K. Dohi, N. Soneda. Effects of aging temperature on G-phase precipitation and ferrite-phase decomposition in duplex stainless steel, Philosophical Magazine 92 (2012) 4354-4375.

[51] L. Karlsson, L. Ryen, S. Pak. Precipitation of Intermetallic Phases in 22% Cr Duplex Stainless Weld Metals. The kinetics of intermetallic phase formation in the temperature range 675°-1000°C (1247°-1832°F) and effects on mechanical properties and corrosion resistance, American Welding Society (1995).

[52] A. Mateo, L. Llanes, M. Anglada, A. Redjaimia, G. Metauer. Characterization of the intermetallic G-phase in an AISI 329 duplex stainless steel, Journal of Materials Science 32 (1997) 4533-4540.

[53] K. Yamamoto, Y. Kimura, Y. Mishima. Precipitation of the Icosahedral Quasicrystalline Phase, R-phase and Laves Phase in Ferritic Alloys, MATERIALS TRANSACTIONS Vol. 45 (2004) 357-360.

[54] J. Cui, I.-S. Park, C.-Y. Kang, K. Miyahara. Degradation of Impact Toughness due to Formation of R Phase in High Nitrogen 25Cr-7Ni-Mo Duplex Stainless Steels, ISIJ International 41 (2001) 192-195.

[55] T.F. de Andrade, A.M. Kliauga, R.L. Plaut, A.F. Padilha. Precipitation of Laves phase in a 28%Cr–4%Ni–2%Mo–Nb superferritic stainless steel, Materials Characterization 59 (2008) 503-507.

[56] J.-O. Nilsson, P. Liu. Aging at 400–600°C of submerged arc welds of 22Cr–3Mo–8Ni duplex stainless steel and its effect on toughness and microstructure, Materials Science and Technology 7 (1991) 853-862.

[57] G.L. Zhixia ZHANG, Zhou XU. Precipitation of Epsilon Copper in Ferrite Antibacterial Stainless Steel, J. Mater. Sci. Technol. 24 (2008) 775-780.

[58] Y.S. Yi, T. Shoji. Detection and evaluation of material degradation of thermally aged duplex stainless steels: electrochemical polarization test and AFM surface analysis, Journal of Nuclear Materials 231 (1996) 20-28.

[59] Z.-X. Wang, F. Xue, W.-H. Guo, H.-J. Shi, G.-D. Zhang, G. Shu. Investigation of thermal aging damage mechanism of the Cast Duplex Stainless Steel, Nuclear Engineering and Design 240 (2010) 2538-2543.

[60] S.S.M. Tavares, R.F.d. Noronha, M.R.d. Silva, J.M. Neto, S. Pairis. 475°C Embrittlement in a duplex stainless steel UNS S31803, Materials Research 4 (2001) 237-240.

[61] S.S.M. Tavares, A. Loureiro, J.M. Pardal, T.R. Montenegro, V.C.d. Costa. Influence of heat treatments at 475 and 400 °C on the pitting corrosion resistance and sensitization of UNS S32750 and UNS S32760 superduplex stainless steels, Materials and Corrosion 63 (2012) 522-526.

[62] C.-J. Park, H.-S. Kwon. Effects of aging at 475 °C on corrosion properties of tungsten-containing duplex stainless steels, Corrosion Science 44 (2002) 2817-2830.

[63] J.E. May, C.A.C.d. Souza, P.A.d.P. Nascente, P. Soares, C.M. Lepienski, S.E. Kuri. Effect of thermal aging conditions on the corrosion properties and hardness of a duplex stainless steel, Materials Research 13 (2010) 431-436.

[64] K.H. Lo, C.T. Kwok, W.K. Chan, D. Zeng. Corrosion resistance of duplex stainless steel subjected to long-term annealing in the spinodal decomposition temperature range, Corrosion Science 55 (2012) 267-271.

[65] J.S. Langer, M. Bar-on, H.D. Miller. New computational method in the theory of spinodal decomposition, Physical Review A 11 (1975) 1417-1429.

[66] W.K. Choo, J.H. Kim, J.C. Yoon. Microstructural change in austenitic Fe-30.0wt%Mn-7.8wt%Al-1.3wt%C initiated by spinodal decomposition and its influence on mechanical properties, Acta Materialia 45 (1997) 4877-4885.

[67] K. Chandra, V. Kain, V.S. Raja, R. Tewari, G.K. Dey. Low temperature thermal ageing embrittlement of austenitic stainless steel welds and its electrochemical assessment, Corrosion Science 54 (2012) 278-290.

[68] J.E. Brown, G.D.W. Smith. Atom probe studies of spinodal processes in duplex stainless steels and single- and dual-phase Fe-Cr-Ni alloys, Surface Science 246 (1991) 285-291.

[69] A. Bhattacharya, D. Yang, P.M. Singh. STRESS CORROSION CRACKING OF HEAT TREATED 2205 DUPLEX STAINLESS STEEL IN CAUSTIC SOLUTIONS. NACE Corrosion 2009. Atlanta, GA: NACE International, 2009.

[70] F.A. Garner, H.R. Brager, R.A. Dodd, T. Lauritzen. Ion-induced spinodal-like decomposition of Fe-Ni-Cr invar alloys, Nuclear Instruments and Methods in Physics Research Section B: Beam Interactions with Materials and Atoms 16 (1986) 244-250.

[71] C.W. Yang, D.B. Williams, J.I. Goldstein. A revision of the Fe-Ni phase diagram at low temperatures (<400 °C), Journal of Phase Equilibria 17 (1996) 522-531.

[72] C.R. Brooks, S.B. Fitch. Transmission electron microscopy observations of the lamellar structure in the Arispe iron meteorite, Materials Characterization 45 (2000) 365-377.

[73] C. Örnek, J.H. Lim, M.G. Burke, T. Hashimoto, D.L. Engelberg. Effect of 475°C Embrittlement on Microstructure Development and Mechanical Properties of Grade 2205 Duplex Stainless Steel, Metall and Mat Trans A (2015). Submitted.

[74] Y.Q. Wang, B. Yang, J. Han, F. Dong, Y.L. Wang. Localized Corrosion of Thermally Aged Cast Duplex Stainless Steel for Primary Coolant Pipes of Nuclear Power Plant, Procedia Engineering 36 (2012) 88-95.

[75] J.O.M. Bockris, A.K.N. Reddy, M. Gamboa-Aldeco. Modern Electrochemistry 2A. Fundamentals of Electrodics, vol. 2A. New York: Kluwer Academic Publishers, 2002. p.1-817.

[76] V.S. Bagotsky. Fundamentals of Electrochemistry. The Electrochemical Society Series. Hoboken, New Jersey: Wiley-Interscience, 2006.

[77] Moore, W. J. Physikalische Chemie. 4. Auflage ed., Walter de Gruyter, 1986.

[78] A. Nazarov, D. Thierry. Application of Volta potential mapping to determine metal surface defects, Electrochimica Acta 52 (2007) 7689-7696.

[79] C. Leygraf, T.E. Graedel. Atmospheric Corrosion, John Wiley & Sons, Canada, 2000.

[80] P.L. Andresen, B. Baroux, J.W. Braithwaite, C.R. Clayton, P. Combrade, J.H.W.d. Wit, F.P. Fehlner, G. Ferrari, F.P. Ford, G.S. Frankel, M.J. Graham, G. Grundmeier, M. Keddam, D. Landolt, C. Leygraf, B. MacDougall, T. Magnin, P. Marcus, R.C. Newman, I. Olefjord, J. Oudar, E. Protopopoff, M. Rohwerder, W. Sand, H.-H.

Srehblow, M. Stratmann, D. Thierry, D.H.v.d. Weijde. Corrosion Mechanisms in Theory and Practice. In: Marcus P, (Ed.). New York: Marcel Dekker, 2002. p.726.

[81] G.S. Frankel, V. Guillaumin, P. Schmutz. Characterization of Corrosion Interfaces by the Scanning Kelvin Probe Force Microscopy Technique, Journal of The Electrochemical Society 148 (2001) B163-B173.

[82] S.V. Kalinin, A. Gruverman. Scanning Probe Microscopy of Functional Materials. In: Kalinin SV, Gruverman A, (Eds.). Nanoscale Imaging and Spectroscopy. New York: Springer, 2010.

[83] P. Marcus, F. Mansfeld. Analytical Methods in Corrosion Science and Engineering, Taylor & Francis Group, Boca Raton, FL, USA, 2006.

[84] M. Nonnenmacher, M.P. O'Boyle, H.K. Wickramasinghe. Kelvin probe force microscopy, Applied Physics Letters 58 (1991) 2921-2923.

[85] M. Rohwerder, F. Turcu. High-resolution Kelvin probe microscopy in corrosion science: Scanning Kelvin probe force microscopy (SKPFM) versus classical scanning Kelvin probe (SKP), Electrochimica Acta 53 (2007) 290-299.

[86] S. Sadewasser, T. Glatzel. Kelvin Probe Force Microscopy Measuring and Compensating Microscopy, Springer, Heidelberg, 2012.

[87] S.B. Kaemmer. Introduction to Bruker's ScanAsyst and PeakForce Tapping AFM Technology. Official Bruker Website: Bruker Corporation, 2011.

[88] T. Glatzel, M.C. Lux-Steiner, E. Strassburg, A. Boag, Y. Rosenwaks. Principles of Kelvin Probe Force Microscopy. in: Kalinin S, Gruverman A, (Eds.). Scanning Probe Microscopy. Springer New York, 2007. pp. 113-131.

[89] C. Örnek, D.L. Engelberg. Effect of "475°C Embrittlement" on the Corrosion Behaviour of Grade 2205 Duplex Stainless Steel Investigated Using Local Probing Techniques. Corrosion Management. Northampton, UK: The Institute of Corrosion, 2013. p.9-11.

[90] C. Örnek, A.H. Ahmed, D.L. Engelberg. Effect of Microstructure on Atmospheric-Induced Corrosion of Heat-treated Grade 2205 and 2507 Duplex Stainless Steels. Eurocorr 2012. Istanbul, Turkey: Dechema, 2012. p.1-10.

[91] N. Sathirachinda, R. Gubner, J. Pan, U. Kivisäkk. Characterization of Phases in Duplex Stainless Steel by Magnetic Force Microscopy/Scanning Kelvin Probe Force Microscopy, Electrochemical and Solid-State Letters 11 (2008) C41-C45.

[92] M. Song. Atmospheric-Induced Corrosion of Cold Worked Grade 2205 Duplex Stainless Steel. School of Materials, Corrosion and Protection Centre, vol. Master of Science. Manchester: University of Manchester, 2013. p.101.

[93] S. Aoki, K. Ito, H. Yakuwa, M. Miyasaka, J.i. Sakai. Potential Dependence of Preferential Dissolution Behavior of a Duplex Stainless Steel in Simulated Solution inside Crevice, Zairyo-to-Kankyo 60 (2011) 363-367.

[94] S. Aoki, H. Yakuwa, K. Mitsuhashi, J.i. Sakai. Dissolution Behavior of α and γ Phases of a Duplex Stainless Steel in a Simulated Crevice Solution, ECS Transactions 25 (2010) 17-22.

[95] C. Örnek, D.L. Engelberg. Kelvin Probe Force Microscopy and Atmospheric Corrosion of Cold-rolled Grade 2205 Duplex Stainless Steel. Eurocorr 2014. Pisa, Italy: European Federation of Corrosion, 2014. p.1-10.

[96] D.L. Engelberg, C. Örnek. Probing propensity of grade 2205 duplex stainless steel towards atmospheric chloride-induced stress corrosion cracking, Corrosion Engineering, Science and Technology 49 (2014) 535-539.

[97] J.-S. Lee, K. Fushimi, T. Nakanishi, Y. Hasegawa, Y.-S. Park. Corrosion behaviour of ferrite and austenite phases on super duplex stainless steel in a modified green-death solution, Corrosion Science (2014).

[98] A.M. do Nascimento, M.C.F. Ierardi, A.Y. Kina, S.S.M. Tavares. Pitting corrosion resistance of cast duplex stainless steels in 3.5%NaCl solution, Materials Characterization 59 (2008) 1736-1740.

[99] W. Li, M. Cai, Y. Wang, S. Yu. Influences of tensile strain and strain rate on the electron work function of metals and alloys, Scripta Materialia 54 (2006) 921-924.

[100] D.J.W. Oldfield. Nickel effect: Lower rate of corrosion in stainless, Emerald Group Publishing Limited 37 (1990) 9-11.

[101] C. Örnek. Thermal Heat Treatments of Duplex and Super Duplex Stainless Steels in the 400 to 550°C Range and Their Influence on the Corrosion Properties. vol. BSc. Aalen: Aalen University of Applied Sciences, 2011. p.136.

[102] A. Kocijan, C. Donik, M. Jenko. The Corrosion Behaviour of Duplex Stainless Steel in Chloride Solutions Studied by XPS, Materials and Technology 43 (2009) 195-199.

[103] J.H. Qiu. Passivity and its breakdown on stainless steels and alloys, Surface and Interface Analysis 33 (2002) 830-833.

[104] C. Pareige, S. Novy, S. Saillet, P. Pareige. Study of phase transformation and mechanical properties evolution of duplex stainless steels after long term thermal ageing (>20 years), Journal of Nuclear Materials 411 (2011) 90-96.

8.5 Effect of 475°C Embrittlement on Atmospheric Chloride-Induced Stress Corrosion Cracking Behaviour of Grade 2205 Duplex Stainless Steel

C. Örnek*[1,2], S. A. M. Idris[2,3], P. Reccagni[2], and D. L. Engelberg[1,2]

[1]Materials and Performance Centre,
School of Materials, The University of Manchester,
Sackville Street, Manchester, M13 9PL, United Kingdom

[2]Corrosion and Protection Centre,
School of Materials, The University of Manchester,
Sackville Street, Manchester, M13 9PL, United Kingdom

[3]Brunei Shell Petroleum Sendirian Berhad
Jalan Utara, Panaga, Seria KB2933
Negara Brunei Darussalam

8.5.1 Abstract

The effect of ageing treatment at 475°C and bending deformation of 2205 duplex stainless steel on atmospheric chloride-induced stress corrosion cracking propensity has been investigated. EBSD analyses showed more severe heterogeneous plastic strain development in the microstructure after bending in transverse direction than in rolling direction, with the austenite phase accommodating most deformation in rolling direction, while the ferrite seemed to be more strained after bending in transverse direction. XRD stress measurements revealed highest tensile stresses in austenite which increased slightly as a function of short-term ageing, while the tensile stress in ferrite increased substantially with the degree of 475°C embrittlement. Stress corrosion cracking propensity under atmospheric chloride exposure pronouncedly increased by 475°C embrittlement. Austenite was most susceptible to cracking in short-term aged microstructures (up to 50 hours), while the ferrite became most brittle after long-term ageing (255 hours).

Keywords: *Duplex stainless steel (DSS); 475°C embrittlement; Atmospheric Stress Corrosion Cracking; Electron backscatter diffraction (EBSD) local misorientation; X-ray diffraction (XRD) residual stress; Cold bending*

8.5.2 Introduction

Duplex stainless steels (DSS) have been widely used as stress corrosion cracking resistant materials in the marine, off-shore, petrochemical, and nuclear industries, providing superior mechanical properties to many equivalent austenitic stainless steels [1, 2]. There is a strongly believed synergistic microstructural interaction existing between ferrite and austenite, responsible for the unique mechanical and electrochemical properties [3, 4]. However, service temperatures in excess of 250°C or welding can result in embrittlement and loss of corrosion performance [5-7]. In the 250-550°C temperature window, low temperature embrittlement, also known as '475°C embrittlement' can cause severe loss in toughness and ductility due to phase transformation reactions occurring in the microstructure [5, 7, 8].

Phase reactions in ferrite have been deemed responsible for embrittlement [7, 9, 10] although similar phase reactions in austenite also have been reported [8, 11, 12]. The microstructure is unstable in that temperature window, and the ferrite phase is majorly decomposed by phase separation and precipitation reactions. Spinodal decomposition of ferrite (δ) into Cr-enriched α'' and Fe-rich (Cr-depleted) α' spinodal structures and/or nucleation and growth of α''-particles embedded in a α-matrix, usually, occurs spontaneously at the outset with ageing and is often followed by the formation of precipitates, such as χ and Frank-Kasper R-phase, and Mo-Si G-phase [5, 7, 9-11, 13-15].

The phase separation products (α' + α''), in general, do not exceed dimensions larger than 100 nm while precipitates, such as G- or R-phase, can grow to sizes larger than 500 nm [6, 9, 10, 13-15]. Spinodally-decomposed ferrite with R-phase and other precipitates have previously been reported occurring in 2205 (25% Cr, 5% Ni) duplex stainless steel at 475°C ageing temperature [16]. Ferrite was deemed responsible for the increase of local and overall hardness by ageing at 475°C which probably also caused substantial loss of toughness [16].

There has been extensive research done on microstructural characterisation and mechanical property changes of 475°C embrittlement [6, 7, 10, 17-19]. It is common that embrittlement gradually increases with ageing time, possibly reaching saturation after long exposure times. Corrosion properties and associated stress corrosion cracking performance, however, have been sparsely studied, and mechanistic understanding of stress corrosion cracking propensity of duplex stainless steels requires still detailed investigations. So far, most research on stress corrosion cracking was carried out in extremely aggressive environments [20-30] and often

with temperatures in excess of 100°C [22, 28, 29, 31, 32]. Low temperature stress corrosion cracking performance (<100°C) in particular for atmospheric conditions has pivotal importance for many engineering applications.

In this work grade 2205 DSS was used to investigate correlative/synergistic effects of 475°C embrittlement and cold bending on microstructure strain and stress development as a function of ageing time. Atmospheric chloride stress corrosion cracking propensity at low temperature (75°C) was also investigated using magnesium chloride surface deposits as a function of ageing time and bending process orientation. The data reported are linked to the framework of comprehensive characterisation works in this topic [16, 33-35].

8.5.3 Experimental

Solution mill-annealed (as-received) sheet 2205 duplex stainless steel (*OutoKumpu*) with 2 mm thickness was used in this study. The nominal chemical composition (in wt.-%) was 22.44Cr, 5.75Ni, 3.32Mo, 1.41Mn, 0.42Si, 0.015C, 0.155N, 0.006Nb, 0.21Cu, 0.12Co, and Fe (bal.). The sheet was cut along the rolling direction (RD) and transverse direction (TD) to produce strips with dimensions of 70 mm x 20 mm x 2 mm (L x W x T). Two holes with 5.2 mm diameter were drilled on both sides of the strips. A sketch of the strips and how these were further shaped into U-bend samples and measured by electron backscatter diffraction (EBSD) is schematically shown in Figure 8-43(b+c).

The strip materials were exposed to heat treatments at 475 ± 5°C for 5, 10, 20, 50, and 255 hours ageing time followed by water quench. The surface of all specimens was prepared by grinding up to 4000-grit using SiC sand papers.

Strip metals with RD and TD directional microstructure were subjected to bending tests to produce U-bends. The test was done on an *Instron 5569* testing machine under compression mode with a load cell of 50 kN and a loading rate of 10 mm/min. The bending setup can be seen in Figure 8-43(a). After plastic deformation, the U-bend specimens were tightened using stainless steel bolts and nuts to keep the elastic deformation constantly applied.

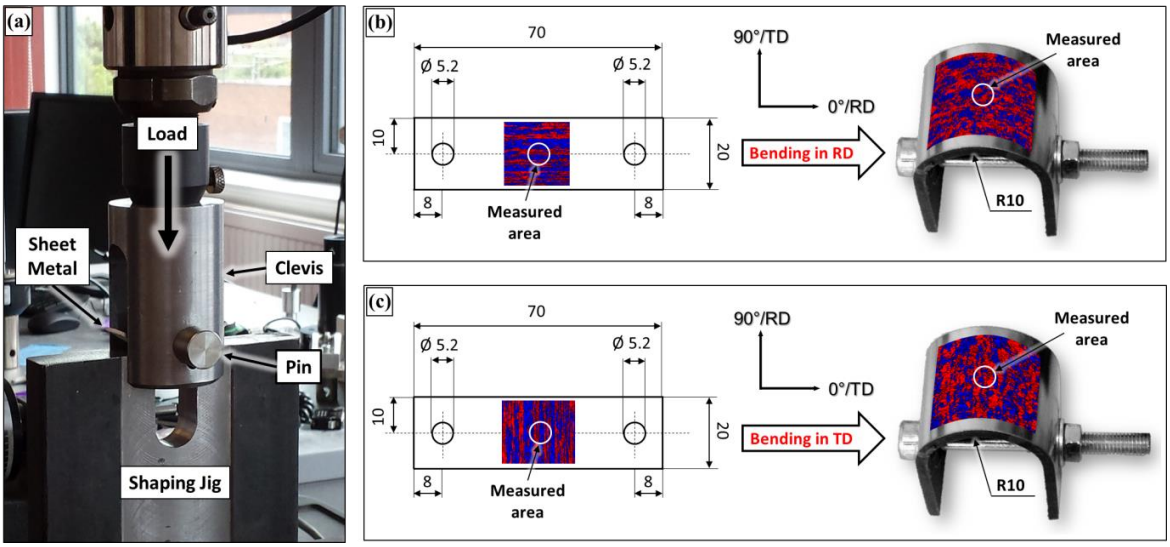

Figure 8-43: (a) U-bend shaping jig with (b) sheet metal dimensions and bending processing orientation in rolling direction (RD) and (c) in transverse direction (TD). The circle in each specimen indicates the position of XRD stress measurements before and after bending. The angles indicate the measurement direction in 0° and 90°.

8.5.3.1 Microstructure Analysis

Microstructural characterisation was carried out on mirror-finish polished as-received strip materials using 3, 1, and ¼, µm diamond paste, with finalised OP-S polishing treatment containing silica colloids with 8-14 nm sizes for one hour. As-received strip with TD direction was further characterised after bending process.

Electron backscatter diffraction (EBSD) analysis was performed over a scan area of 711 x 622 µm² of the pre-bent and 728 x 728 µm² of the post-bent as-received TD strip using an *FEI Quanta 650* scanning electron microscope (SEM) interfaced with a *Nordlys* EBSD detector and *Aztec V2.2* software for data acquisition from *Oxford Instruments*. 20 kV accelerating voltage with 527 nm and 773 nm step size was used for pre-bent and post-bent microstructural analyses, both scanned on the same area.

Data post processing including grain size analysis was carried out using *HKL Channel 5* software. High-Angle Grain Boundaries (HAGB's) were defined with misorientation ≥15° and Low Angle Grain Boundaries (LAGB's) between >1° and <15°. The grain size was determined by the mean linear intercept method as the mean of the vertical and horizontal directions. 50 intercept lines were used for grain boundary detection. The aspect ratio of the average grain size of ferrite and austenite was determined for as-received and each bent microstructure. The aspect ratio (V/H) was defined as the quotient of the average grain sizes

obtained from vertical linear interception (V) and those obtained from horizontal linear interception (H) with V and H facing towards RD and TD, respectively (Figure 8-47). The fraction of coincidence site lattice (CSL) Σ3 (twins) in austenite and ferrite was obtained and correlated with the U-bend process. Phase fractions of ferrite and austenite of pre-bent and post-bent samples were extracted.

Local misorientation (LMO) maps were generated by using a 3x3 binning and a 5° threshold for the sub-grain angle threshold. This analysis gives the average LMO for a misorientation below the pre-determined sub-grain angle threshold, and this method was used to locate regions with higher concentrations of misorientation in the microstructure. The latter is typically associated with local micro-deformation in the form of plastic strain, due to the presence of dislocations [36].

8.5.3.2 Hardness Tests

Macro-hardness measurements were carried out on a *Georg Reicherter Briviskop 1875* Vickers macro-hardness machine on all plate samples. Measurements were done on pre-bent and post-bent U-bend samples. For pre-bent samples, ten hardness indentations were produced with five indentations made on each end of the samples, as seen in Figure 8-44(a). Three indentations were made on the apex of the U-bend samples after bending of the same measured strip, as seen in Figure 8-44(b). The corresponding hardness was then calculated from the statistical mean of the hardness measurements.

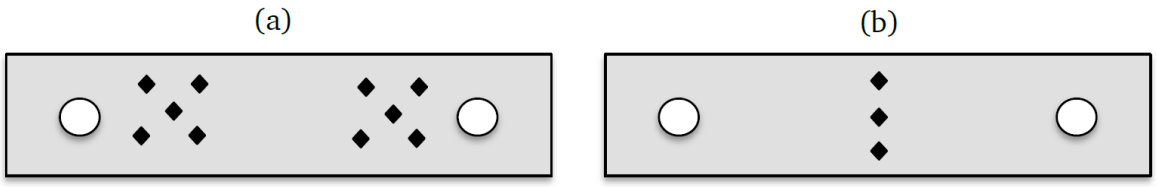

Figure 8-44: Schematic representation of hardness indentation locations of pre-bent (a) and post-bent U-bend samples

8.5.3.3 XRD Stress Measurements

X-ray diffraction (XRD) stress measurements were carried out on the *Proto iXRD Combo* testing machine (*Proto Manufacturing Inc., Michigan, USA*), equipped with a two detector system. Cr and Mn x-ray sources were used to measure the strain in ferrite and austenite, respectively. Further measurement setup parameters are listed in Table 8-5.

Table 8-5: X-ray measurement conditions

X-ray type	Cr-Kα	Mn-Kα
Source voltage, current	20 kV, 4 mA	20 kV, 4 mA
Aperture size	2 mm	2 mm
Bragg angle, 2θ	156.4	152.8
Diffraction plane	(2 1 1)	(3 1 1)
Wavelength	2.291 Å	2.1034 Å
Max. measurement angle, β	±27°	±27°
Number of β angles	11	11
β angles (Ψ)	27, 22.29, 17.24, 11.8, 4.48, **0**, -4.48, -11.8, -17.24, -22.29, -27	
β oscillation angle	3°	3°
Phi angles	0 and 90°	0 and 90°
Exposure time	2 sec	2 sec
Number of exposure profiles	10	10
Number of exposures gain	30	30
X-ray elastic constant $S_1^{(hkl)}$	1.28 x 10^{-6} MPa	1.2 x 10^{-6} MPa
X-ray elastic constant $½S_2^{(hkl)}$	5.92 x 10^{-6} MPa	7.18 x 10^{-6} MPa
Peak fit	Gaussian	Gaussian

Prior to the test, the x-ray diffractometer was calibrated to determine the zero stress position of the peak of the diffracted x-rays. Stress-free and stressed standard samples, provided by the manufacturer, were used for calibration. Multiple exposure technique with 11 angles was used for inter-planar d-spacing measurements. Two x-ray measurement orientations, i.e. 0° and 90° Phi angles, in RD and TD process orientations of each specimen were chosen, which were in alignment with the microstructure orientation. Each measured orientation corresponds to the stress direction as specified in Figure 8-43(b+c). The measurement position was in the centre of each specimen. Pre- and post-bent specimens were measured exactly on the same position.

8.5.3.4 Atmospheric-induced Stress Corrosion Cracking Tests

Atmospheric stress corrosion cracking (ASCC) tests were performed by exposing samples to thin film electrolytes at 75 ± 3°C and 28-50% relative humidity (RH) for 35 days. For this, in total three water droplets containing $MgCl_2$ were applied onto the surface of all U-bend samples, yielding an initial $MgCl_2$ deposition density of 20 µg/cm² (drop 1), 332 µg/cm² (drop 2), and 3835 µg/cm² (drop 3) for each deposited droplet. Drop 1, 2, and 3

correspond to a chloride deposition density of 15 µg/cm², 247 µg/cm², and 2856 µg/cm², respectively.

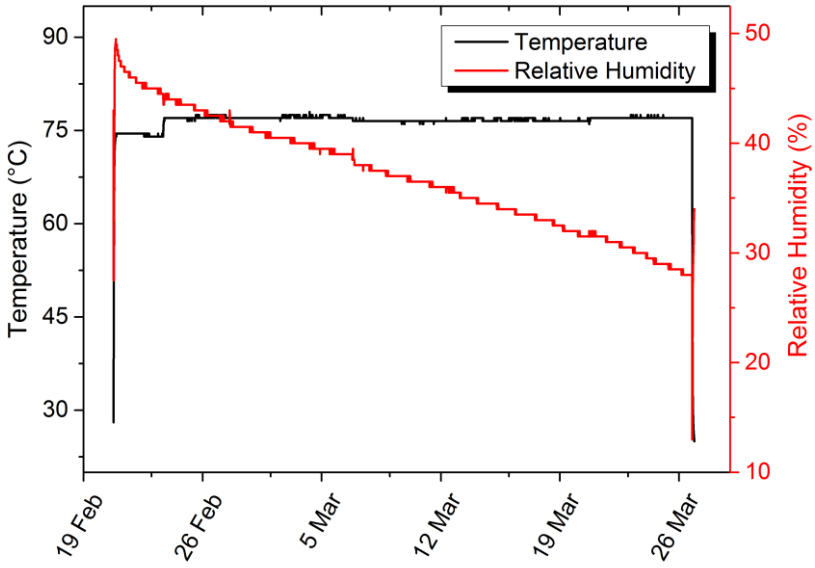

Figure 8-45: Temperature and relative humidity reading during exposure (5 min/reading point)

An Eppendorf micropipette was used to dispense the liquid with the volume of the droplet of 0.5, 1.5, and 2.5 µl producing an overall droplet radius of 1.8, 2.3, and 2.8 mm, respectively for droplet 1, 2, and 3 (the effect of secondary spreading of the droplet during the test was not considered, therefore the exposed chloride concentrations need to be regarded as 'initial' chloride densities). The samples were placed in a Perspex box. The humidity was controlled by a saturated solution of $MgCl_2$ which was produced in 100 ml glassware and placed in the Perspex box together with the specimens. The box was sealed with a special temperature-resistant sealant and placed into a furnace set to 80°C. With this exposure regime the deliquescence point of $MgCl_2$, resulting in a concentrated very aggressive $MgCl_2$ solution was intended to be set. The temperature and relative humidity over the entire testing time was recorded with an EL-USB-2+ standalone data logger. The results are given in Figure 8-45.

At the end of the test, each deposited area of all exposed samples was imaged with a Zeiss stereo microscope. All samples were then cleaned in 70°C citric acid solution for 2 hours to remove all corrosion products without having any attack on the metal substrate. A

photograph of a U-bend specimen deposited with salt-laden droplets and a stereo-graphic image of a deposit after 35 days exposure time showing atmospheric corrosion is shown in Figure 8-46 for representation.

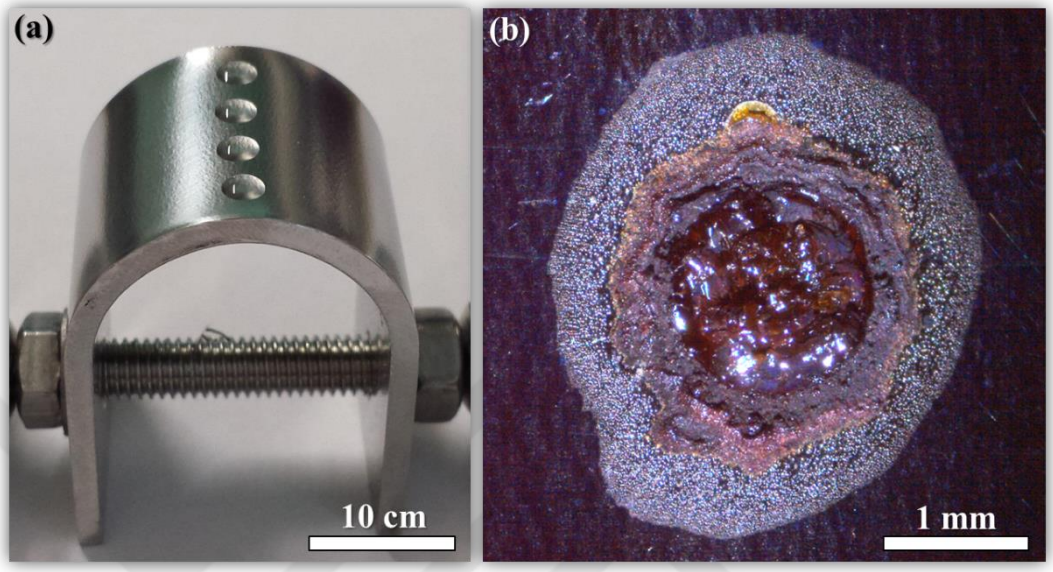

Figure 8-46: (a) Photograph of a U-bend specimen deposited with salt-laden droplets containing $MgCl_2$; (b) Stereo-microscopic image of one of the deposits after atmospheric corrosion test

The corrosion morphology was analysed with the *FEI Quanta 650* and *Zeiss Ultra V55* SEM. The corrosion area and volume of each deposit was measured with the *Keyence VK-X200 3D* laser scanning confocal microscope using 20x and 50x lenses in stitching mode. Corrosion area calculations were further performed on SEM micrographs by converting the image into a binary and determining the area of corrosion. Corrosion area and volume were plotted versus ageing time at 475°C.

Stress corrosion cracking was assessed without disassembling the samples. The extent of stress corrosion cracking was determined as the crack length per nominal corrosion area and plotted against ageing time with consideration for the longest crack only. The longest crack was measured on high resolution SEM images by means of *ImageJ* image processing program.

8.5.4 Results

8.5.4.1 Microstructure Development

The microstructure of sheet 2205 DSS consisted of phase fractions of 54% austenite and 46% ferrite in its as-received condition (pre-bent). The average grain size of ferrite (δ) and austenite (γ) was 4.2 ± 5.1 µm and 2.2 ± 1.9 µm, respectively. Austenite grains, arrayed in a broad band-like structure and embedded in the ferrite matrix, were observed in the normal direction (ND) as shown in the EBSD phase map in Figure 8-47(a). The microstructure showed evidence of production history effects, noticeable from the elongated grains towards RD with ferrite/ferrite, ferrite/austenite, and austenite/austenite grain boundaries. No secondary phases were detected. The fraction of coincidence site lattice (CSL) Σ3 in austenite was determined as 23.10%, and 0.22% in ferrite. The aspect ratio (vertical divided by the horizontal intercept grain size length) of ferrite and austenite was determined as 0.84 and 0.93, respectively, meaning that the grains of both phases were slightly elongated towards the RD. Numerous LAGB's were detected in the microstructure, in contrast to HAGB's. The fraction of LAGB's (f_{LAGB}) to HAGB's (f_{HAGB}) of ferrite and austenite was 63.26% to 36.74% and 92.77% to 7.23%, respectively. The fraction of all LAGB's to all HAGB's of the entire microstructure was 2.15 indicating proportionally more than twice larger amount of LAGB's than HAGB's in the microstructure. More quantitative data and an overview of all EBSD results can be taken from Table 8-6.

After U-bending in TD, the phase fraction of austenite to ferrite changed to 48:52 showing a clear decrease of the austenite content. The microstructure was heavily deformed with largely elongated ferrite and austenite grains towards the bending direction, as shown in Figure 8-47(b). The band-like austenite structure seemed to have been disrupted after the bending process. The average grain size of ferrite and austenite increased to 5.1 ± 5.0 µm and 3.7 ± 2.8 µm, respectively, which indicates large grain stretching by elastic and plastic deformation. The fraction of CSL Σ3 in austenite decreased to 7.11% and in ferrite to 0.14% indicating distortion of twin boundaries and a grain boundary energy uptake. The aspect ratio of ferrite and austenite severely increased to 1.61 and 1.71, respectively, meaning that austenite and ferrite grains were highly deformed in bending direction (TD), with the latter indicating proportionally higher deformation. The f_{LAGB} to f_{HAGB} ratio of ferrite and austenite changed from 12.84 to 7.72 and from 1.72 to 4.04, respectively, meaning that more pre-

existing LAGB's transformed into HAGB's than new LAGB's were formed in ferrite, while in austenite the number of newly formed LAGB's have almost tripled. The fraction of all LAGB's to all HAGB's highly increased to 5.39 indicating severe plastic deformation occurring after bending in TD.

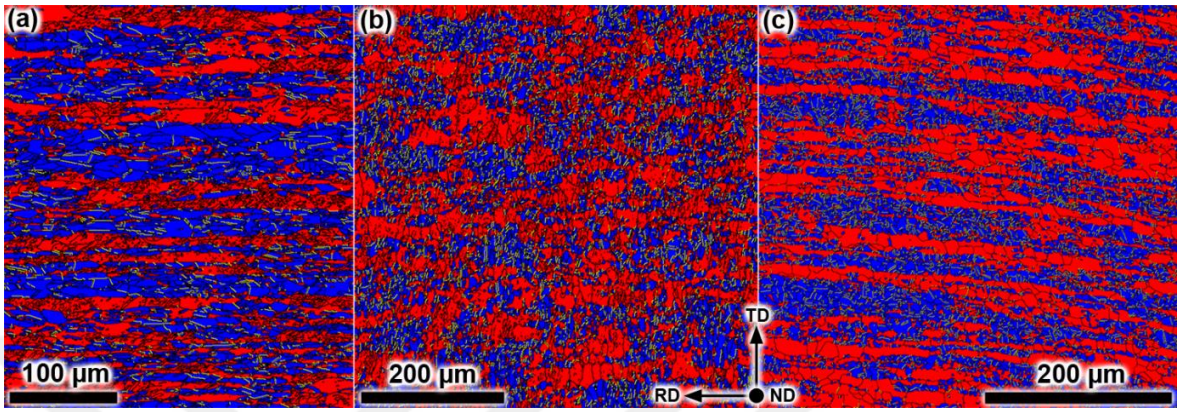

Figure 8-47: EBSD phase maps show the microstructure of 2205 DSS (a) before and after bending in (b) TD and in (c) RD. Black lines are phase boundaries and HAGB's, and yellow lines are CSL Σ3 twin boundaries.

After bending in RD, the phase fraction of austenite to ferrite changed to 47:53, also showing a clear decrease of the austenite content in the microstructure. Large deformation can be noticed along the bending direction, as shown in Figure 8-47(c). The band-like austenite structure showed more pronouncedly elongated appearance, in contrast to the other maps. The average grain size of ferrite and austenite increased to 5.1 ± 5.3 µm and 2.5 ± 2.0 µm, meaning that the grain size of austenite did not seem to have substantially changed. The fraction of CSL Σ3 in austenite and ferrite decreased to 9.67% and 0.17%, respectively, indicating also distortion of twin boundaries and grain boundary energy uptake, but proportionally to a lower extent than after bending in TD. The aspect ratio of ferrite and austenite decreased only slightly to 0.80 and 0.92, respectively, indicating no significant change in grain morphology of both ferrite and austenite grains. The f_{LAGB} to f_{HAGB} ratio of ferrite decreased to 3.83 indicating less generation of new LAGB's than the transformation of LAGB's into HAGB's. The f_{LAGB} to f_{HAGB} ratio of austenite, in contrast, significantly increased to 15.99 which is almost 9.5-times larger than that of the pre-bent microstructure, indicating substantial amount of newly generated LAGB's which was significantly higher than those transformed into HAGB's. The fraction of all LAGB's to all HAGB's highly increased to 6.52 clearly demonstrating large change in grain boundary structure in the microstructure after bending in RD.

Local misorientation analysis of the post-bent microstructures of both bent specimens showed severe deformation occurred in both austenite and ferrite in contrast to the as-received state. Local misorientation maps are given in Figure 8-48(a-c). The degree of local misorientation largely shifted over a wide range to high values up to 5° indicating large strain formation across the entire microstructure after cold-deformation. The as-received microstructure was very smooth with formation of some local misorientation hot-spots which are indicative to somewhat higher strain localisation, but still negligible in comparison to the bent microstructures.

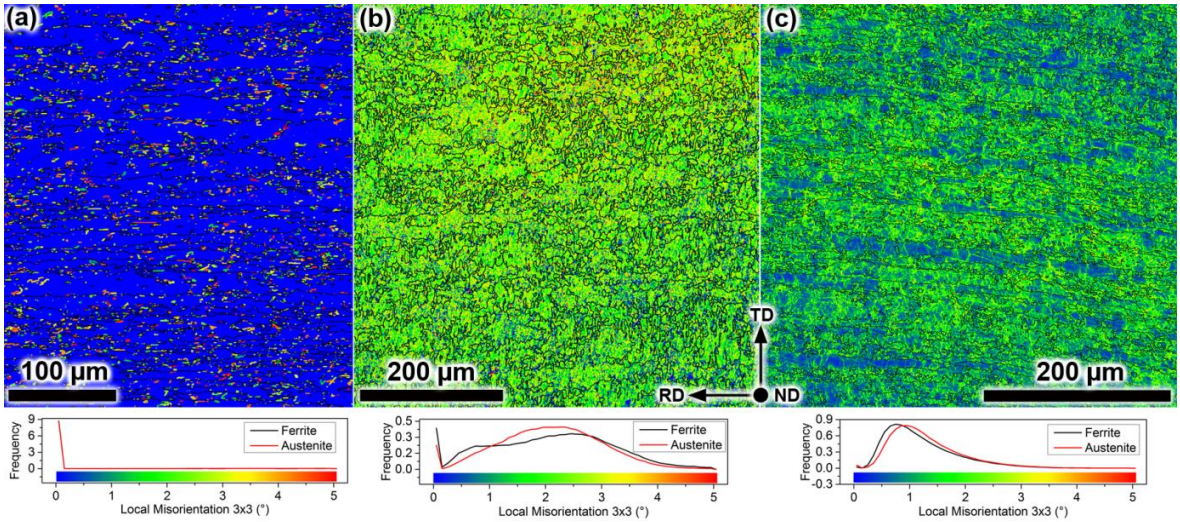

Figure 8-48: EBSD local misorientation maps show local misorientation (indicative to strain) with 3x3 kernel averaging of 2205 DSS (a) before and after bending in (b) TD and in (c) RD. Black lines are phase boundaries. Note that the misorientation profiles of ferrite and austenite in (a) overlaps with each other.

Almost twice larger degree of local misorientation of the microstructure bent in TD than that in RD was observed indicating more severe effect on microstructural change with respect to strain when bending in TD. Austenite seemed to suffer more from deformation causing a somewhat larger degree of local misorientation in comparison to ferrite. This was observed in both bending directions. In the microstructure bent in RD, localisation/accumulation of local misorientation in austenite, indicative to plastic strain, was observed, possibly suggesting that austenite is affected more than ferrite after bending in RD, and ferrite was affected more than austenite after bending in TD.

Table 8-6: Quantitative EBSD grain geometry and morphology data

Sample	Phase	Fraction [%]	G_S [µm]	σ [µm]	Aspect ratio (X_V/X_H)	CSL Σ3 [%]	f_{LAGB} [%]	f_{HAGB} [%]	f_{LAGB} / f_{HAGB}	$All_{LAGB(\delta+\gamma)}$ / $All_{HAGB(\delta+\gamma)}$
As-received	δ	46	4.2	5.1	0.84	0.22	92.77	7.23	12.84	-
	γ	54	2.2	1.9	0.93	23.10	63.26	36.74	1.72	-
	Total	100	2.8	3.4	0.91	23.32	-	-	-	2.15
Bent in RD	δ	53	5.1	5.3	0.80	0.17	94.11	5.89	3.83	-
	γ	47	2.5	2.0	0.92	9.67	79.29	20.71	15.99	-
	Total	100	3.4	3.7	0.89	9.84	-	-	-	6.52
Bent in TD	δ	52	5.1	5.0	1.61	0.14	88.54	11.46	7.72	-
	γ	48	3.7	2.8	1.71	7.10	80.15	19.85	4.04	-
	Total	100	4.3	2.9	1.67	7.24	-	-	-	5.39

G_S: Average grain size; σ: standard deviation; f: fraction

8.5.4.2 Hardness Behaviour

Hardness measurement results of all pre-bent and bent samples, plotted versus ageing time at 475°C, are shown in Figure 8-49.

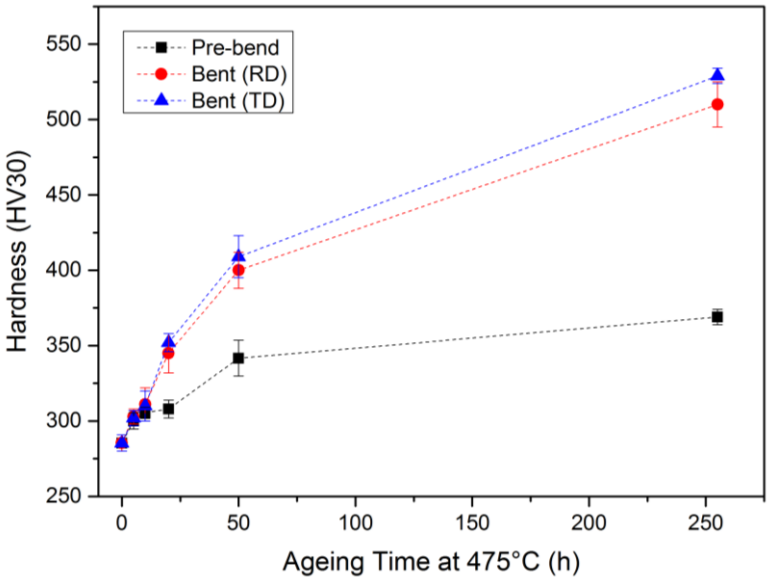

Figure 8-49: Hardness behaviour of pre-bent and bent 2205 DSS as a function of ageing time at 475°C

The hardness increased from 285 ± 5 HV30 to 369 ± 5 HV30 after 255 hours ageing, indicating 475°C embrittlement. The same trend but with higher hardness values was observed for bent specimens in both bending directions. The hardness assumed after bending in RD and TD 510 ± 15 HV30 and 529 ± 5 HV30, respectively. The hardness of the pre-bent

(as-received) and all bent specimens up to 10 hours ageing time did not differ, possibly indicating a negligible degree of embrittlement for short-term ageing at 475°C.

8.5.4.3 XRD stress measurements

8.5.4.3.1 Pre-bent Microstructure

In-plane stress values of ferrite and austenite for each ageing condition prior to and after bending in RD and TD were plotted as a function of ageing time at 475°C as can be seen in Figure 8-50(a-d). Both bending working of as-received specimens led to tensile stress development of austenite occurring in both measurement directions (0° & 90°) to a larger extent than in ferrite.

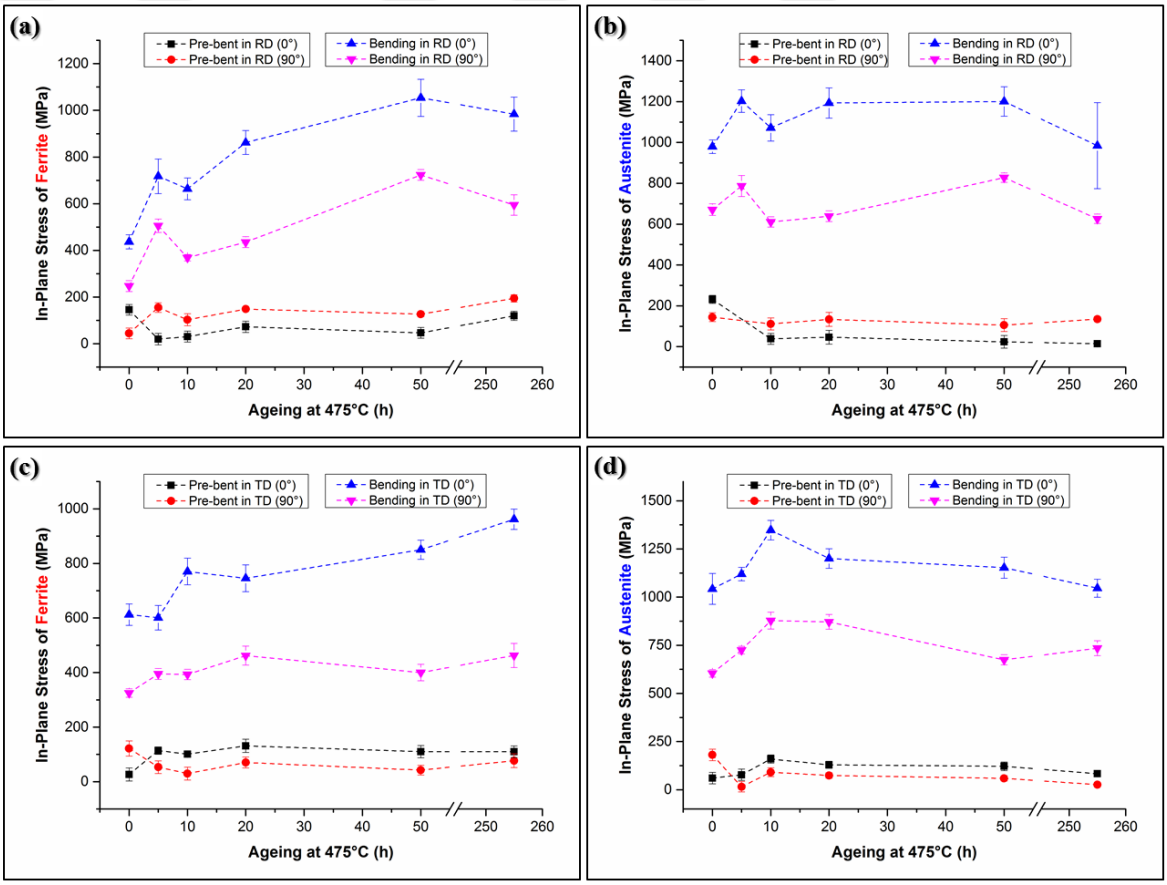

Figure 8-50: In-plane stress development in ferrite and austenite of 2205 DSS as a function of ageing at 475°C: (a-b) before and after bending in RD; (c-d) before and after bending in TD.

The in-plane stress of austenite of the pre-bent specimen (Figure 8-50(a)) decreased with ageing time from 232 ± 20 MPa in 0° (i.e. in RD) to 15 ± 10 MPa after ageing at 475°C for

255 hours, while in 90° (i.e. in TD) no significant stress changes were noticed. The in-plane stress of ferrite, however, increased from 44 ± 23 MPa to 194 ± 15 MPa in 90° (in TD) after 255 hours ageing, while no significant changes in stress in 0° (in RD) could be seen.

The in-plane stress of austenite and ferrite of the TD-pre-bent specimen (i.e. designated to be bent in TD), shown in Figure 8-50(c+d), showed almost similar values to those of the RD-pre-bent specimen. The measurement orientation 0° in RD corresponds to 90° in TD and vice versa, but the obtained data showed small variation possibly due to sample preparation artefacts. Austenite seemed to be the phase with the highest stress in the as-received microstructure. The in-plane stress state in ferrite grew with ageing time and adopted similar stress values to those of the austenite after long-term ageing.

8.5.4.3.2 Post-bent Microstructure

After U-bending, the in-plane stress of the entire microstructure raised significantly up to higher tensile stresses. The in-plane stress of austenite in 0° (in RD) and 90° (in TD) of the specimen after bending in RD was 980 ± 33 MPa and 671 ± 29 MPa, respectively. The austenite in the 5 hours-aged microstructure was higher than the austenite in the as-received condition, and showed tensile stresses of 1203 ± 55 MPa (0°) and 787 ± 51 MPa (90°). No significant change of the stress of austenite was seen to develop as a function of ageing time, neither in 0° nor in 90° measurement directions. The stress of ferrite, however, showed a steady increase as a function of ageing. It increased from 437 ± 31 MPa (0°) and 247 ± 24 MPa (90°) to 984 ± 73 MPa (0°) and 595 ± 44 MPa (90°) after 255 hours ageing. The stress of austenite and ferrite seemed to have almost equalised in both measurement directions. Highest stresses were clearly concentrated along the bending direction for both, ferrite and austenite.

The stress of austenite and ferrite after bending in TD showed a similar raise with austenite adopting slightly higher stress values than ferrite. The stress of austenite showed an steady increase from 1042 ± 80 MPa (0°) and 605 ± 20 MPa (90°) to 1348 ± 51 MPa (0°) and 878 ± 44 MPa (90°) as a function of short-term ageing (up to 10 hours, stress peak) and then decreased slightly to 1046 ± 47 MPa and 735 ± 39 MPa as a function of longer ageing (255 hours). The in-plane stress of ferrite rose steadily up from 612 ± 40 (°0) and 325 ± 15 MPa (90°) to 962 ± 37 MPa (0°) and 463 ± 44 MPa (90°) as a function of ageing time. The stress of ferrite and austenite, likewise as the microstructure after bending in RD, seemed to also

balance in 0° after 255 hours ageing. In 90° direction, however, similar observation was not made.

8.5.4.4 Atmospheric-induced Stress Corrosion Cracking Tests

8.5.4.4.1 As-received (bent in RD)

The corrosion morphology under the salt water droplet containing 20 µg/cm² magnesium chloride (drop 1) after exposure is shown in Figure 8-51(a). Numerous nano-metre sized corrosion pits were nucleated preferentially on heavily deformed austenite regions while the ferrite seemed to have remained unaffected. Austenite could be distinguished from ferrite by its bright channelling contrast in the SEM backscattering micrograph and its phase morphology and deformation slip band structures.

Underneath the deposit with 332 µg/cm² of magnesium chloride (drop 2) droplet a few nano-metre sized pits were also seen to have selectively nucleated in the austenite possibly associated with large deformation structures (slip bands) as can be seen in Figure 8-51(b&c). Furthermore, cracks were observed on heavily deformed ferrite regions noticeable from large deformation structures (lips/strips), striking from ferrite regions, having wavy character, indicating severe plastic deformation at and around the crack regions. Micro-cracks of 5-20 µm length were observed in ferrite only, oriented parallel to the stress axis or being ~45° inclined to the stress axis as shown in Figure 8-51(b&c).

Under the droplet containing 3835 µg/cm² magnesium chloride (drop 3) large corrosion attack was observed with longer micro-cracks formed than the previous deposits as can be seen in Figure 8-51(d-f). Selective dissolution of ferrite formed the main corrosion mechanism occurring on the droplet periphery and adjacent sites, while in the droplet centre general dissolution of both ferrite and austenite was observed. Furthermore, some micro-cracks with inter- and transgranular pathway were observed propagating through austenite and ferrite. Most cracks propagated through (austenite?) grain boundaries and stopped after branching in one or more austenite/ferrite grains as can be seen in Figure 8-51(e). These fine-scale cracks could reach in some regions a maximum crack length of 100 µm.

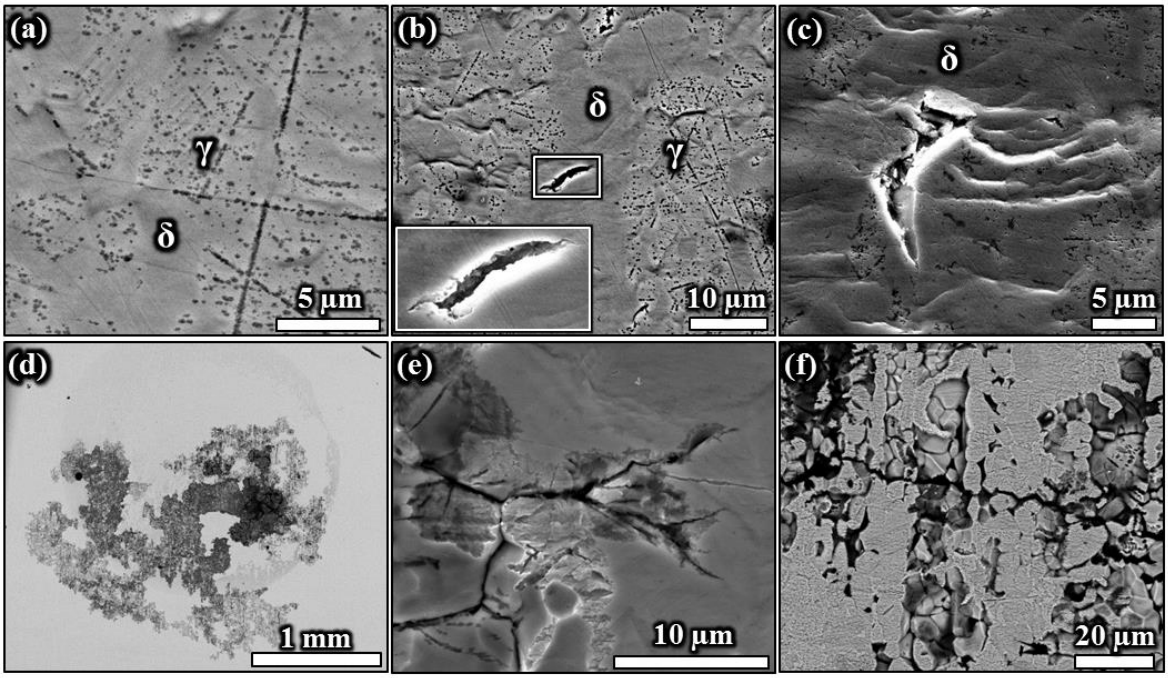

Figure 8-51: Corrosion morphology of as-received 2205 DSS microstructure and bent in RD after the corrosion test: (a) showing preferential nano-pits nucleated in austenite under drop 1 (BSE-SEM image); (b) showing a micro-crack in ferrite with nano-pits preferentially nucleated in austenite under drop 2 (SE-SEM image); (c) showing a micro-crack nucleated in a heavily-deformed ferrite region under drop 2 (SE-SEM image); (d) showing the entire corrosion area under drop 3; (e&f) showing multiply-branched inter- and transgranular stress corrosion cracking under drop 3. Bending axis is oriented to the vertical of the images.

8.5.4.4.2 As-received (bent in TD)

On the U-bend specimen bent in TD and exposed to 20 µg/cm² of magnesium chloride (drop 1) two corrosion pits with 50-60 µm diameters were observed. General dissolution formed the main corrosion mechanism inside the pit with some selective attack occurred on either ferrite or austenite regions as can be seen in Figure 8-52(a). Intergranular corrosion and some micro-cracks were also observed probably on the austenite. These micro-cracks were branched and had a maximum length of 10 µm and seemed to have arrested or were in their incubational stage.

Under the deposit with 332 µg/cm² of magnesium chloride (drop 2) minor selectively attacked ferrite grains with severely fractured austenite grains were observed as shown in Figure 8-52(b).

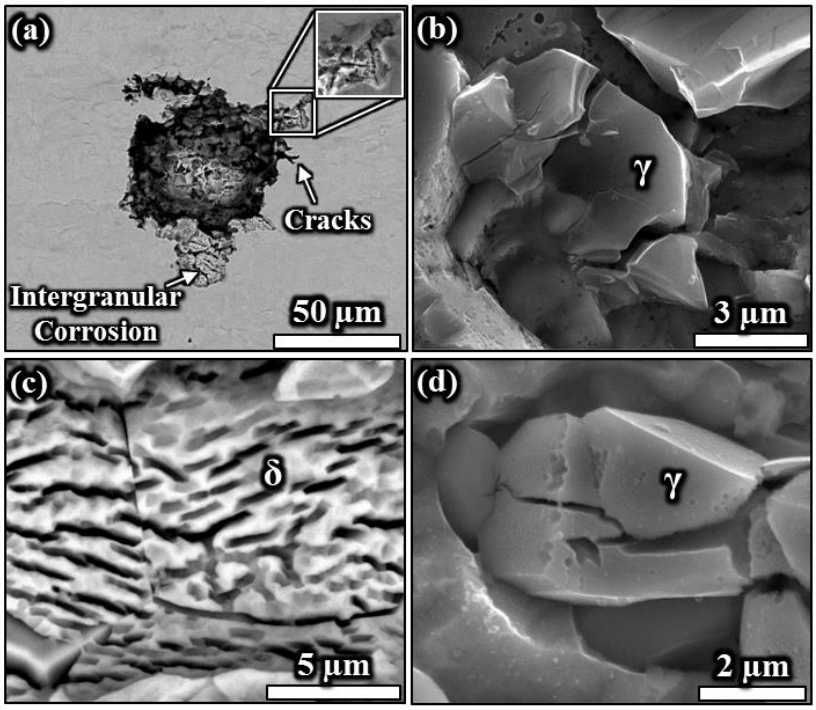

Figure 8-52: Corrosion morphology of as-received 2205 DSS and bent in TD after the corrosion test: (a) showing a corrosion pit with intergranular corrosion and some cracks formed on the pit wall under drop 1 (BSE-SEM image); (b) showing totally fractured austenite grains under drop 2 (SE-SEM image), (c) showing closely-spaced crack-like corrosion morphology in ferrite (BSE-SEM image), and (d) showing a branched transgranular micro-crack in austenite (SE-SEM image), both under drop 3. Bending axis is oriented to the vertical of the images.

Under the salted solution with 3835 µg/cm² magnesium chloride (drop 3) severe corrosion and cracking was observed. General dissolution of both phases was observed to occur with numerous cracks formed in austenite and crack-like corrosion facets in ferrite. The micro-cracks in austenite were indicative to typical chloride stress corrosion cracking showing one major transgranular crack with branching character as can be seen in Figure 8-52(d). The cracks observed were perpendicular oriented to the stress axis. In ferrite, however, multiple closely-spaced crack-like appearances were observed resembling hydrogen-assisted type cracking or hydrogen embrittlement as shown in Figure 8-52(c).

8.5.4.4.3 Ageing at 475°C for 5 hours (bent in RD)

Multiple closely-spaced fine scale cracks were observed occurring primarily in the austenite under droplet 1 on the specimen aged for 5 hours and bent in RD after exposure to 20 µg/cm² magnesium chloride (drop 1) as can be seen in Figure 8-53(a). Austenite seemed to have

suffered more from this type of crack appearance than ferrite. No clear selective dissolution of either phase was observed indicating balanced net anodic and net cathodic corrosion behaviour. A filiform corrosion-like pattern was observed under the deposit with 332 µg/cm² magnesium chloride (drop 2) as shown in Figure 8-53(b). This corrosion morphology did not seem to be associated with microstructure constituents nor processing orientations. Seemingly, there was no clear hint of selective corrosion of ferrite or austenite. Ferrite and austenite could not be distinguished from each other; hence both phases showed similar corrosion behaviour.

After exposure to 3835 µg/cm² magnesium chloride (drop 3) severe general dissolution of ferrite and austenite with chloride-induced stress corrosion cracks forming in austenite were observed as given in Figure 8-53(c). The maximum crack length was measured to be 120 µm.

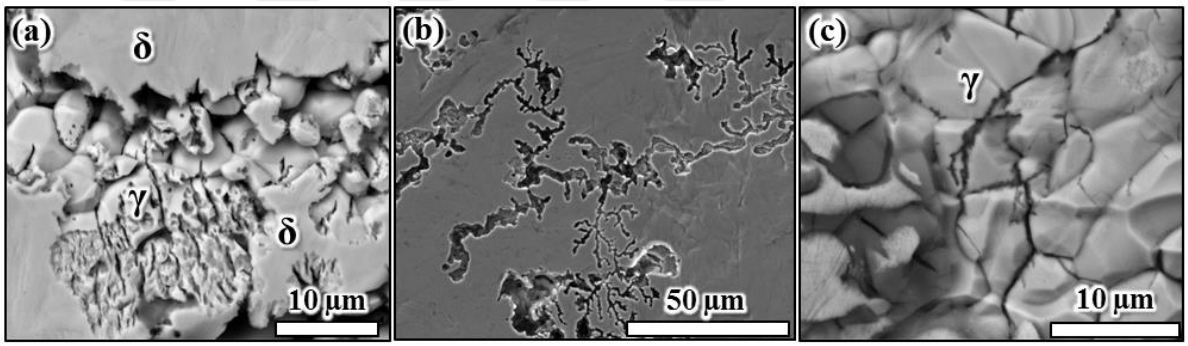

Figure 8-53: Corrosion morphology of 2205 DSS aged at 475°C for 5 hours and bent in RD after the corrosion test: (a) showing closely-spaced and densely-arrayed micro-cracks in austenite with some cracks in ferrite under drop 1 (BSE-SEM image), (b) showing filiform corrosion-like appearance under drop 2 (SE-SEM image), and (c) showing multiply-branched micro-cracks in austenite under drop 3 (BSE-SEM image). Bending axis is oriented to the horizontal of the images.

8.5.4.4.4 Ageing at 475°C for 5 hours (bent in TD)

No corrosion attack was observed under the deposit with 20 µg/cm² magnesium chloride (drop 1) on the specimen aged for 5 hours and bent in TD, clearly showing superior corrosion resistance to the specimen aged for 5 hours and bent in RD. No significant corrosion occurred after exposure to 332 µg/cm² magnesium chloride (drop 2), except from some nano-sized pit nucleated in ferrite and austenite.

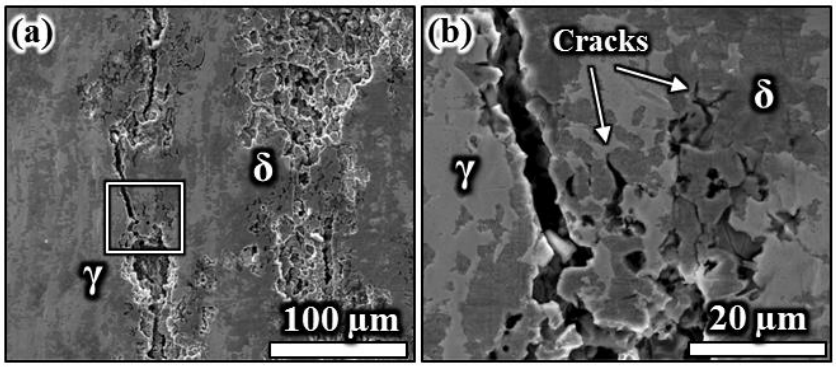

Figure 8-54: Corrosion morphology of 2205 DSS aged at 475°C for 5 hours and bent in TD after the corrosion test: (a&b) showing severe crack formation in ferrite with prime crack propagation through ferrite under drop 3 (both SE-SEM images). Note that (b) is a magnified view of the highlighted region in (a). Bending axis is oriented to the horizontal of the images.

Severe cracks were seen under the deposit containing 3835 µg/cm² magnesium chloride (drop 3) as shown in Figure 8-54(a&b). Seemingly, there was a preferential stress corrosion cracking pathway along the microstructure processing orientation. Cracks seemed to have primarily nucleated in ferrite and propagated transgranular through ferrite grains and/or interphase boundaries. No clear selective dissolution of either phase was observed, indicating balanced net anodic and net cathodic character of both phases. Moreover, there was an obvious relationship of electrochemical attack with the processing orientation of the microstructure. Severe, long and wide cracks were observed with a maximum crack length of 1700 µm, oriented perpendicular to the stress axis. Cracks were found to propagate primarily through the ferrite, obviously two orders of magnitude more severe than the specimen bent in RD. Seemingly, ferrite became more susceptible to stress corrosion cracking than austenite.

8.5.4.4.5 Ageing at 475°C for 10 hours (bent in RD)

Neither corrosion nor cracking was observed on both exposure conditions; 20 and 332 µg/cm² magnesium chloride (drop 1 and 2) on the specimen aged for 10 hours and bent in RD after the corrosion test.

After exposure to 3835 µg/cm² magnesium chloride (drop 3) little net selective corrosion of ferrite seemed to have occurred with preferential dissolution pathway along the RD. Transgranular stress corrosion cracking was selectively formed in austenite as can be seen in Figure 8-55(a). Some cracks seemed to penetrate through ferrite grains as shown in Figure

8-55(b). Furthermore, localised corrosion on slip bands and totally fractured austenite grains were observed as can be seen in Figure 8-55(c), suggesting slip-band dissolution assisted stress corrosion cracking as the prime cracking mechanism of austenite.

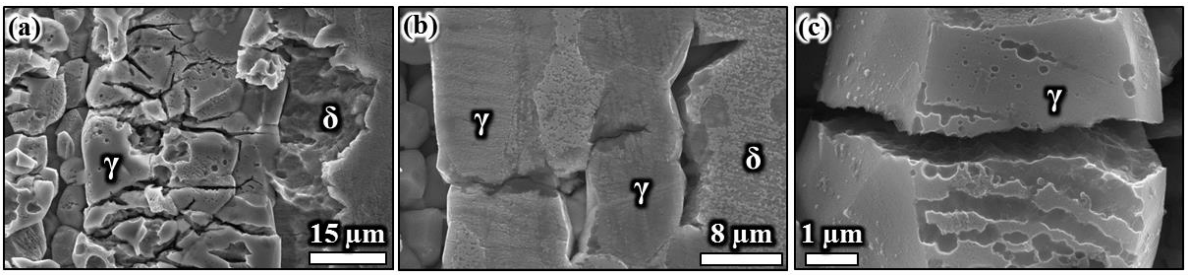

Figure 8-55: Corrosion morphology of 2205 DSS aged at 475°C for 10 hours and bent in RD under the deposit containing 3835 µg/cm² magnesium chloride after the corrosion test: (a) showing multiple micro-crack formation in austenite with selective dissolution of ferrite; (b) showing crack arrest in austenite and ferrite; (c) showing a totally fractured austenite grain (all SE-SEM images). Bending axis oriented to the vertical of the images.

8.5.4.4.6 Ageing at 475°C for 10 hours (bent in TD)

Corrosion and stress corrosion cracking was observed on the specimen aged for 10 hours and bent in TD after exposure to 20 µg/cm² magnesium chloride (drop 1). The depth of attack was quite shallow, possibly a few grains deep only, but large in area. Transgranular micro-cracks were seen in austenite regions with maximum crack length of 30 µm. A filiform corrosion-like morphology was observed under the deposit containing 332 µg/cm² magnesium chloride (drop 2) as shown in Figure 8-56(a).

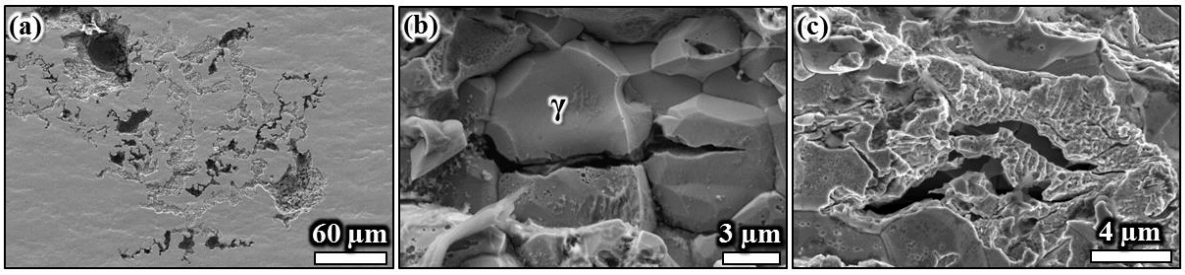

Figure 8-56: Corrosion morphology of 2205 DSS aged at 475°C for 10 hours and bent in TD after the corrosion test: (a) showing filiform-corrosion-like appearance indicating similar corrosion behaviour of ferrite and austenite under drop 2, (b+c) showing severe micro-cracks in austenite under drop 3 (all SE-SEM images). Bending axis is oriented to the vertical of the images.

Under the salt solution with 3835 µg/cm² magnesium chloride (drop 3) severe transgranular stress corrosion cracks were observed in austenite as shown in Figure 8-56(b&c). The maximum crack length was 50 µm, oriented perpendicular to the bending axis.

8.5.4.4.7 Ageing at 475°C for 20 hours (bent in RD)

No significant corrosion except from a few nano-pits nucleated in ferrite with lesser amount occurring in austenite was observed on the specimen aged for 20 hours and bent in RD after exposure to 20 µg/cm² magnesium chloride (drop 1). No sign for any cracking event was observed.

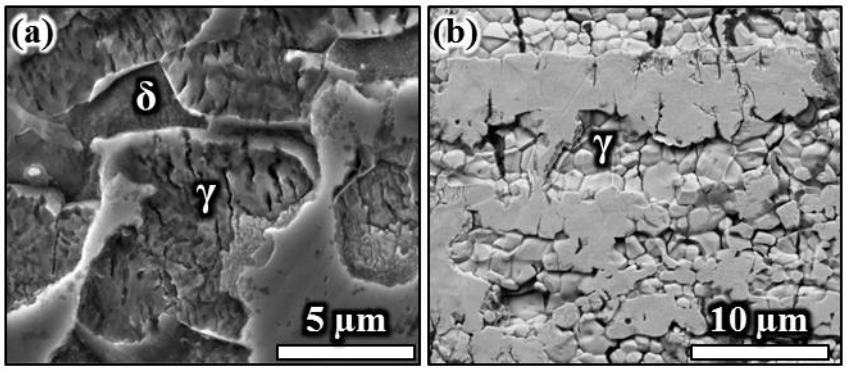

Figure 8-57: Corrosion morphology of DSS aged at 475°C for 20 hours and bent in RD after the corrosion test: (a) showing multiple closely-spaced fine-scale cracks formed in austenite under drop 2 (SE-SEM image); (b) showing micro-cracks in austenite and selective dissolution of ferrite under drop 3 (BSE-SEM image). Bending axis is oriented to the horizontal of the images.

Under the droplet containing 332 µg/cm² magnesium chloride (drop 2) austenite and ferrite seemed to have dissolved to a large extent, with the latter showing net anodic behaviour as can be seen in Figure 8-57(a). Multiple closely-spaced and densely-arranged micro-cracks in austenite were observed possibly indicating hydrogen-assisted stress corrosion cracking. Cracking events in austenite seemed to be accompanied by partial dissolution events.

Large net selective dissolution of ferrite was observed underneath the deposit with 3835 µg/cm² magnesium chloride (drop 3) as shown in Figure 8-57(b). Multiple micro-cracks with large crack width and transgranular crack pathway were observed in austenite with a maximum crack length of 100 µm.

8.5.4.4.8 Ageing at 475°C for 20 hours (bent in TD)

On the specimen aged for 20 hours and bent in TD two pits with maximum sizes of 10 µm were seen to have formed underneath the deposit with 20 µg/cm² magnesium chloride (drop 1), as shown in Figure 8-58(a).

Significant surface attack was observed on the exposed area with 332 µg/cm² magnesium chloride (drop 2). No selective dissolution was observed occurring on either phase possibly indicating similar corrosion behaviour on both ferrite and austenite as can be seen in Figure 8-58(b). A few fins-scale micro-cracks were seen to have nucleated in the austenite while no cracks in ferrite could be seen.

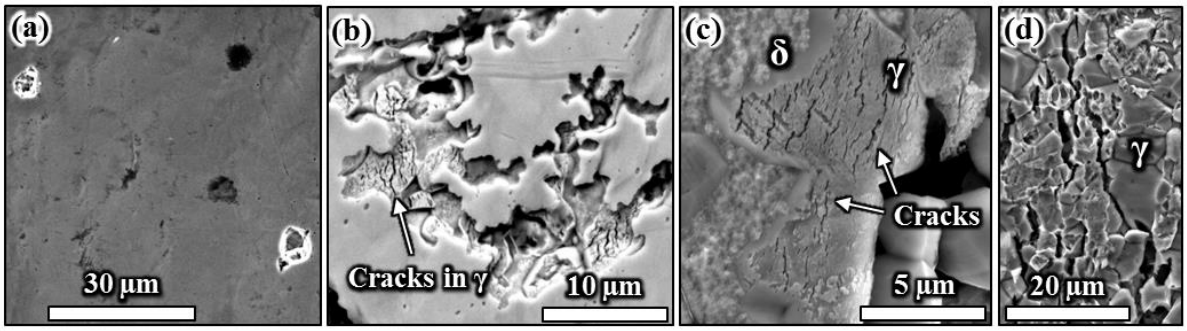

Figure 8-58: Corrosion morphology of 2205 DSS aged at 475°C for 20 hours and bent in TD after the corrosion test: (a) showing two pits formed under drop 1 (SE-SEM image), (b) showing filiform corrosion-like morphology with some micro-cracks nucleated in austenite under drop 2 (BSE-SEM image), (c) showing closely-spaced and densely-arrayed fine-scale cracks in austenite grains under drop 3 (SE-SEM image); (d) showing severe cracks in austenite under drop 3 (SE-SEM image). Bending axis is oriented to the horizontal of the images.

Under the salt droplet with 3835 µg/cm² magnesium chloride (drop 3) numerous fine-scale cracks were seen in austenite while the ferrite seemed to have corroded superficially only, showing a rugged surface next to embrittled austenite grains as shown in Figure 8-58(c). More severe cracks in austenite were seen in other regions as shown in Figure 8-58(d).

8.5.4.4.9 Ageing at 475°C for 50 hours (bent in RD)

Under the deposit having 20 µg/cm² magnesium chloride (drop 1) severe corrosion and cracking in ferrite and austenite was observed on the specimen aged for 50 hours and bent in RD as shown in Figure 8-59(a). Despite of the large number of micro-cracks formed a maximum crack length of 5 µm was measured only.

Longer cracks were seen to have formed primarily in the austenite under the salted area with 332 µg/cm² magnesium chloride (drop 2), as shown in Figure 8-59(b). The cracks formed seemed to be primarily of intergranular nature. The maximum crack length was measured to be 25 µm.

Under the salt solution containing 3835 µg/cm² magnesium chloride (drop 3) severe stress corrosion cracks were observed with multiple transgranular γ-δ-γ crack pathways were observed all over the corroded region as shown in Figure 8-59(c). The maximum crack length measured was 100 µm, oriented perpendicular to the bending axis.

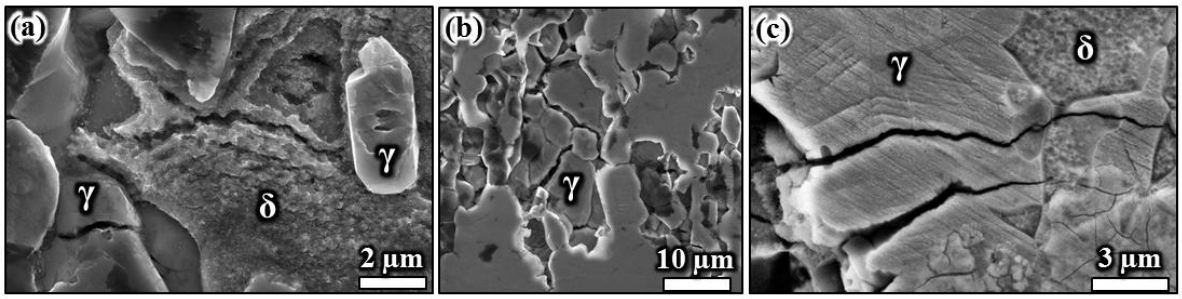

Figure 8-59: Corrosion morphology of 2205 DSS aged at 475°C for 50 hours and bent in RD after the corrosion test: (a) showing cracks formed in ferrite and austenite under drop 1 (SE-SEM image), (b) showing intergranular cracks in austenite under drop 2 (SE-SEM image), and (c) showing transgranular micro-cracks with γ-δ-γ crack path (SE-SEM image). Bending axis is oriented to the vertical of the images.

8.5.4.4.10 Ageing at 475°C for 50 hours (bent in TD)

Selective pitting corrosion occurred on some austenite grains with slip planes acted as preferential nucleation sites, as shown in Figure 8-60(b), on the specimen aged for 50 hours and bent in TD under the deposit with 20 µg/cm² magnesium chloride (drop 1).

General corrosion of ferrite and austenite was observed occurring under the salt solution containing 332 µg/cm² magnesium chloride (drop 2). Numerous crack-like features were seen in the austenite, possibly indicating post-corrosion events happened on cracked regions as can be seen in Figure 8-60(b).

Most severe corrosion events were observed under the deposited area with 3835 µg/cm² magnesium chloride (drop 3). Cracks in ferrite and austenite were observed as shown in Figure 8-60(c). Bright features striking out from the corroded surface of ferrite regions were observed well-possibly indicating R-phase precipitates.

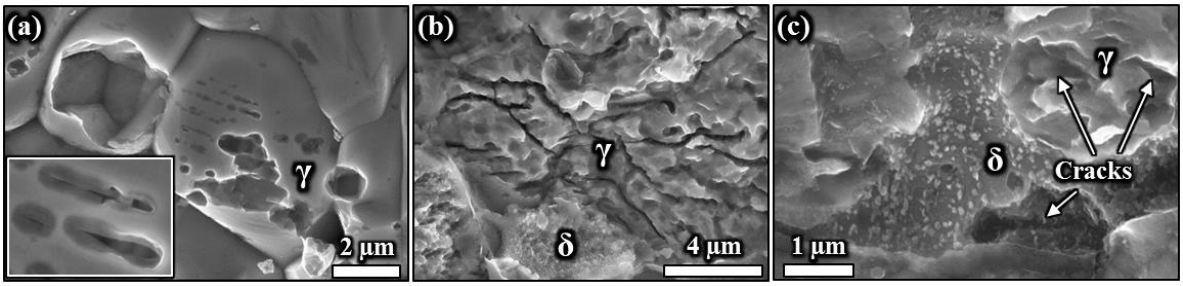

Figure 8-60: Corrosion morphology of 2205 DSS aged at 475°C for 50 hours and bent in TD after the corrosion test: (a) showing localised corrosion on austenite grains under drop 1 (SE-SEM image), (b) showing crack-like features in austenite under drop 2 (SE-SEM image), and (c) showing remaining precipitates in ferrite (bright speckles) and some cracks nucleated in ferrite and austenite under drop 3 (SE-SEM image). Bending axis is oriented to the vertical of the images.

8.5.4.4.11 Ageing at 475°C for 255 hours (bent in RD)

The specimen aged for 255 hours and bent in RD showed the most electrochemical attack in comparison to all previous specimens. The corrosion morphology observed under the salt solution containing 20 µg/cm² magnesium chloride (drop 1) is shown in Figure 8-61(a-d). Crack-like localised corrosion morphologies were observed on austenite grains in the vicinity of partially dissolved ferrite regions, as shown in Figure 8-61(a), indicating net anodic dissolution characteristics of ferrite. Seemingly, corrosion pits nucleated in the austenite which could merge and generated a crack-like appearance. LAGB's and HAGB's acted well-possibly as preferential corrosion nucleation sites in the austenite.

Increased susceptibility to localised corrosion in the austenite was noticed associated with long-term ageing at 475°C. In some areas, partially dissolved austenite grains and severely cracked ferrite regions were observed, as shown in Figure 8-61(b). Apparently, these cracks are clear evidence of inherent embrittlement of ferrite since those cracks were in parallel alignment with the stress direction and the processing orientation of the microstructure (along RD). Seemingly, there is a preferred crack orientation towards the processing orientation. Moreover, in some austenite grains pitting corrosion was observed nucleating underneath fractured ferrite grains as can be seen in Figure 8-61(c), supported by a higher contrast and higher depth information of the BSE-SEM image given in Figure 8-61(d). The maximum crack length measured was 250 µm with parallel orientation relationship with the stress axis.

The extent of corrosion and stress corrosion cracking events were larger under the exposed area with 332 µg/cm² magnesium chloride (drop 2). The maximum crack length measured

was 700 µm orientated perpendicular to the bending axis. The cracks could be noticed already at low magnification which can be seen in Figure 8-61(f). Cracks were preferentially formed in the ferrite. Totally fractured ferrite grains were seen with multiple cracking events and random crack orientations in single ferrite grains indicating severe 475°C embrittlement. Seemingly, the initiation and propagation of stress corrosion cracking occurred in selectively in the ferrite.

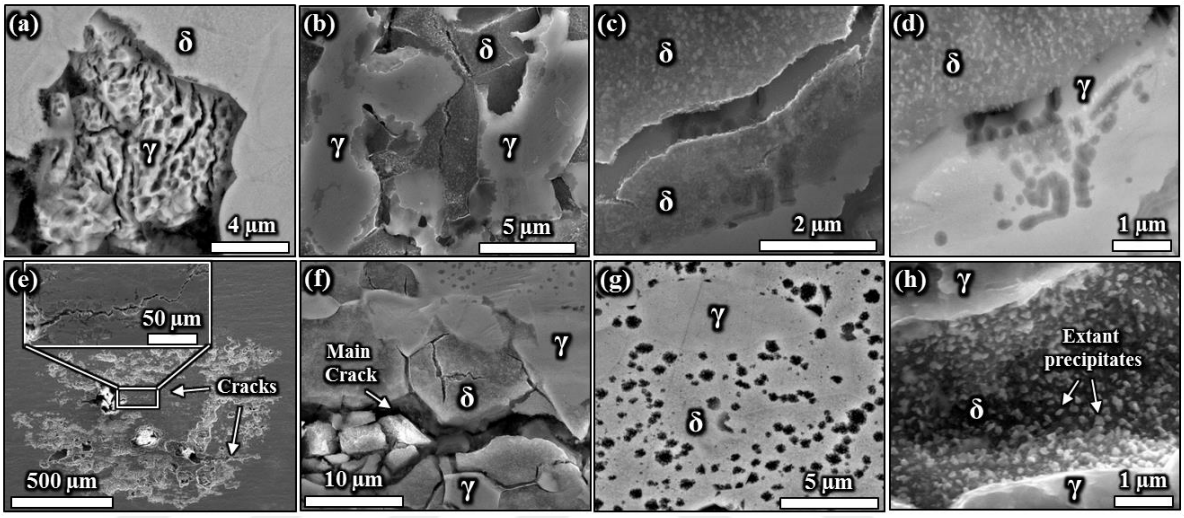

Figure 8-61: Corrosion morphology of 2205 DSS aged at 475°C for 255 hours and bent in RD after the corrosion test: (a) showing crack-like localised corrosion morphology in austenite adjacent to a partially dissolved ferrite grain under drop 1 (BSE-SEM image); (b) showing partially dissolved austenite and severe embrittlement of ferrite under drop 1 (SE-SEM image); (c) showing fractured ferrite grains (SE-SEM image) with (d) showing localised corrosion on austenite underneath a ferrite grain under drop 1(BSE-SEM image); (e) showing severe cracking under drop 2 (SE-SEM image), (f) showing multiple cracks formed in ferrite grains (SE-SEM image), (g) showing numerous corrosion pits nucleated in ferrite (BSE-SEM image); (h) showing extant precipitates at the crack wall under drop 2 (SE-SEM image). Bending axis is oriented to the vertical of the images.

The number and severity of cracks in ferrite were incomparably higher than those formed in austenite apparently indicating severe 475°C embrittlement of ferrite. However, a large loss in the corrosion performance of austenite was also observed visible from numerous partially dissolved austenite grains. Numerous corrosion pits nucleated in the ferrite and interphase boundaries indicating enhanced localised corrosion propensity (Figure 8-61(g)). No clear stress corrosion cracking could be seen in the austenite possibly suggesting that the localised dissolution rate exceeded the crack growth rate. At the bottom of the main crack, extant precipitates (R-phase) were seen striking out from the surface of ferrite regions (bright speckles) as shown in Figure 8-61(h). These precipitates seemed to have net cathodic character with respect to the decomposed ferrite matrix.

Most severe corrosion and cracking was observed under the exposed area with 3835 µg/cm² magnesium chloride (drop 3). Vast general dissolution of both ferrite and austenite on the entire exposed area was seen. Wide and long cracks were seen directing towards the stress direction with a maximum crack length of 1500 µm.

8.5.4.4.12 Ageing at 475°C for 255 hours (bent in TD)

Under the deposit containing 20 µg/cm² magnesium chloride (drop 1) of the specimen aged for 255 hours and bent in TD net selective dissolution of ferrite with severe localised corrosion pitting on austenite was observed, as can be seen in Figure 8-62(a). The selective dissolution pathway seemed to be along the microstructure processing orientation which was in parallel alignment with the stress direction. Selective dissolution of ferrite was observed forming the main metal dissolution mechanism. This observance was significantly different to the corrosion morphology observed on the specimen aged for 255 hours and bent in RD. Multiple closely-spaced and densely arrayed crack-like features were seen in austenite, as shown in Figure 8-62(a).

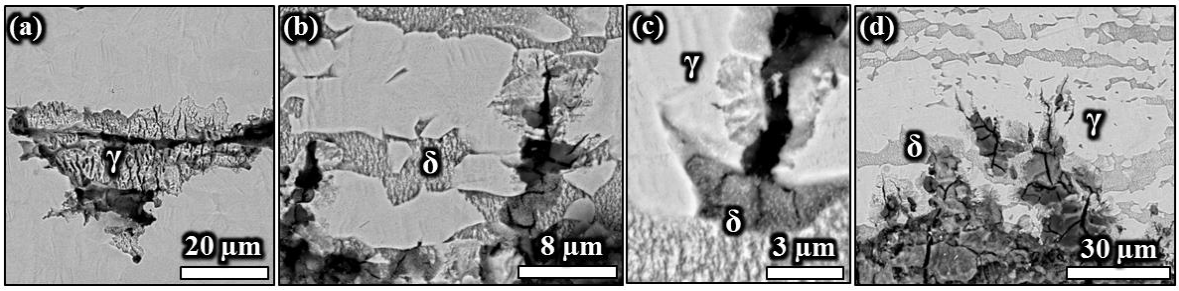

Figure 8-62: Corrosion morphology of 2205 DSS aged at 475°C for 255 hours and bent in TD after exposure test: (a) showing selective dissolution of ferrite and multiple closely-spaced crack-like features in austenite under drop 1 (BSE-SEM image); (b) transgranular cracking through ferrite and austenite under drop 2 (BSE-SEM image); (c&d) showing severe cracking in ferrite and austenite under drop 3 (both BSE-SEM image). Bending axis is oriented to the horizontal of the images.

Numerous transgranular micro-cracks were observed under the exposed salted area with 332 µg/cm² magnesium chloride (drop 2) as shown in Figure 8-62(b). There seemed to be no preferential corrosion direction similar to that observed under drop 1.

Most severe corrosion was observed under the droplet containing 3835 µg/cm² magnesium chloride (drop 3) becoming distinctly clear by general dissolution of both ferrite and austenite all over the exposed area. Severe cracks were seen probably initiating first on ferrite

sites which then propagated through austenite, as shown in Figure 8-62(d). The cracks in ferrite were multiply branched typical for stress corrosion cracking.

8.5.4.5 Quantitative Corrosion and Stress Corrosion Cracking Evaluation

Measured corrosion area and corrosion volume as a function of ageing time and bending direction for each deposit can be seen in Figure 8-63 and Figure 8-64, respectively. The area and volume of corrosion increased with chloride deposition density and with the degree of 475°C embrittlement. This increase was non-linear and seemed to have over-proportionally accentuated in particular for specimen aged for >50 hours. Most corrosion was observed occurring on the specimens aged for 255 hours. Furthermore, the area and volume of corrosion on the specimens bent in TD seemed to manifest larger values than those bent in RD. This became highly apparent under the deposits drop 2 and drop 3. The extent of corrosion under the drop 1 was comparably low on the specimens bent in RD and TD.

The degree of corrosion increased as a function ageing time, showing lowest volume of corrosion on the 10 hours aged specimen bent in TD and 5 hours aged specimen bent in RD. Apparently, best corrosion performance was associated with the volume of corrosion only. The area of corrosion did not perfectly follow this trend. Dividing the volume by the area of corrosion yielded the corrosion depth, and lowest depth of attack was in line with the same trend like the corrosion volume. A parabolic behaviour of metal dissolution as a function of ageing time can be deduced from the trend of the curves. Almost corrosion saturation seemed to occur after 20 hours of ageing (bending in RD) and 10 hours of ageing (bending in TD) under drop 1 & 2 indicating slowed corrosion rate. Corrosion under drop 3, however, did not seem to have saturated even on the microstructure aged for 255 hours. The corrosion volume on the 255 hours aged specimens was up to 5-times larger in comparison to the as-received samples.

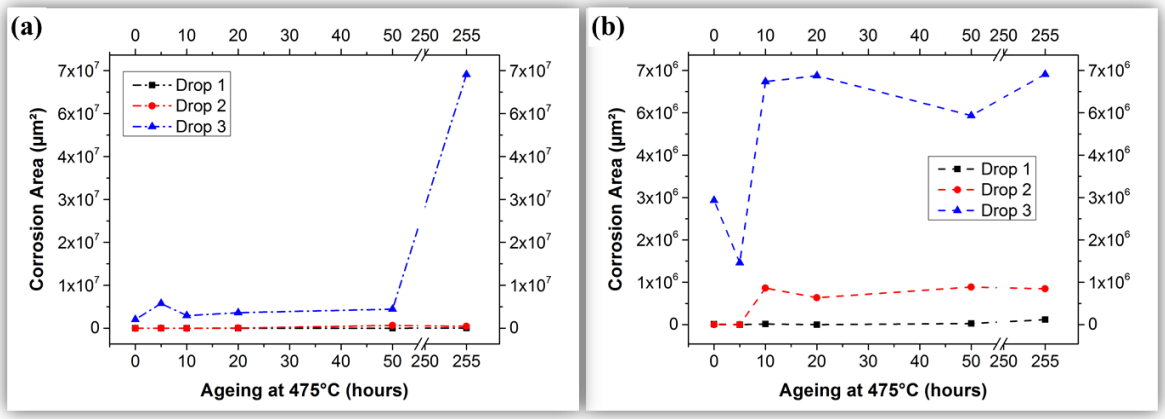

Figure 8-63: Corrosion area as a function of ageing time at 475°C of 2205 DSS bent in (a) RD and (b) in TD

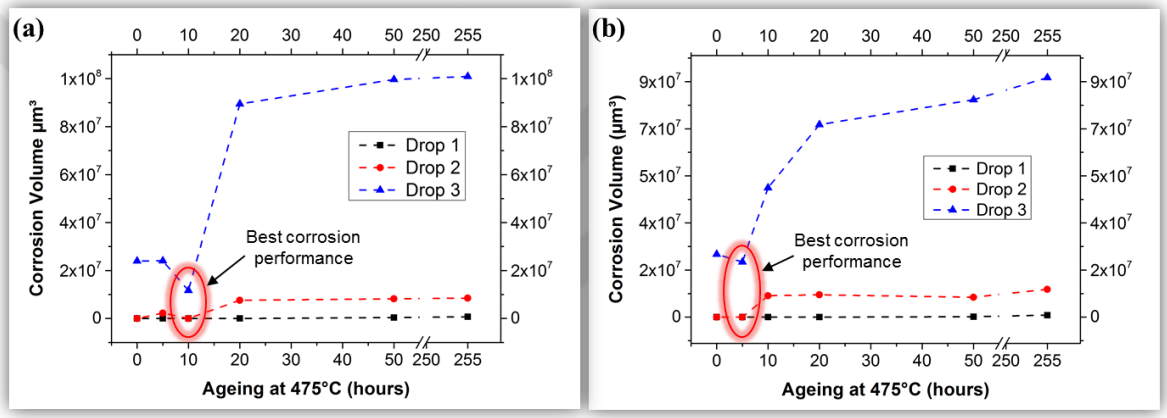

Figure 8-64: Corrosion volume as a function of ageing time at 475°C of 2205 DSS bent in (a) RD and (b) in TD

The longest stress corrosion cracks observed were measured and compared each other as a function of ageing time (Figure 8-65). The trend of the curves for the specimens bent in RD was seen to be in line with the trend of the corrosion volume. However, the cracking behaviour as a function of aged microstructure did neither seem to correlate with the trend of the corrosion volume nor to that of the corrosion area. Lowest crack length was measured on the specimen aged for 10 hours (bent in RD) indicating best stress corrosion cracking performance. Most severe cracking occurred on the 255 hours aged specimen, with increasing maximum crack length in the ascending order of magnitude: drop 1 < drop 2 < drop 3. The maximum crack length measured under drop 1, 2, and 3 were 250, 700, and 1500 µm, respectively.

The U-bend specimens with TD bending orientation showed somewhat different crack length behaviour. Up to 20 hours ageing, all cracks, except of drop 3 of 5 hours ageing, were short cracks with 100 µm maximum length under drop 3. A crack with 1700 µm length was measured under drop 3 for the specimen aged for 5 hours which was longer than the crack observed in drop 3 after 255 hours ageing. Likewise, in drop 2 a longer crack than that under drop 1 and 3 was measured, which seemed to get shorter with further ageing time.

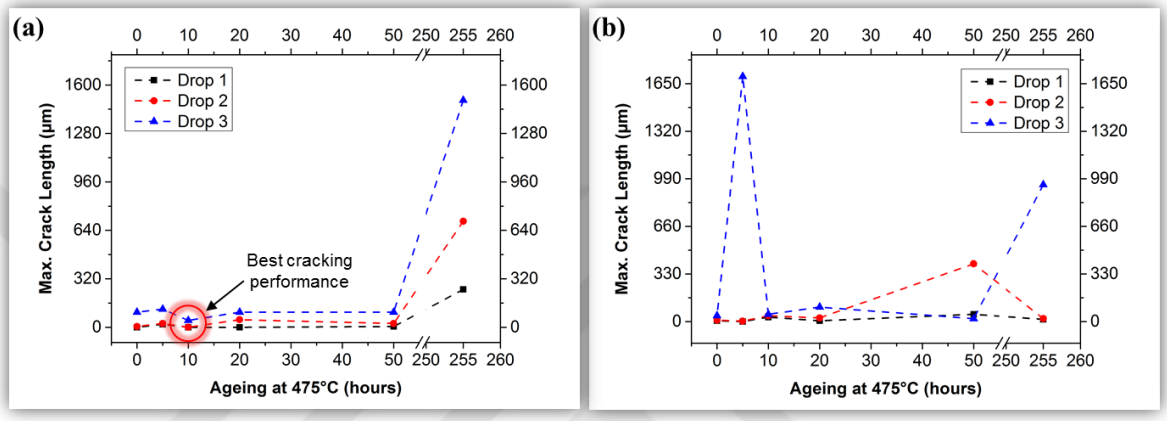

Figure 8-65: Maximum stress corrosion crack length in the dependency of ageing time at 475°C of 2205 DSS bent (a) in RD and (b) in TD

8.5.5 Discussion

8.5.5.1 Microstructure Development

After plastic deformation into U-bend form, the fraction of austenite decreased significantly from 54% to 47% in the microstructure bent in RD and to 48% after bending in TD. A potential reason for this could be due to formation of deformation-induced martensite which might have led to an increased indexing of ferrite. Martensite can be easily mis-indexed as ferrite due to its similar crystallographic structure to ferrite. Deformation-induced martensite in 2205 duplex stainless steels with up to 30% transformed from austenite has been reported to occur after plastic deformation by cold rolling (ε = 3.38) which supports this assumption [37-39].

The bending deformation caused a rise in grain sizes of ferrite and austenite, with the latter being more affected in TD bending direction. The grain structures were apparently more affected after bending in TD than in RD. Bending in TD caused larger grain size alteration

of austenite grains than ferrite grains. The microstructure resembled a sandwich-like appearance consisting of overlaid layers or bands of ferrite and austenite grains, and during deformation of the ferrite consequently the deformation of austenite was additionally forced by the deformation of ferrite grains.

The increase of the LAGB to HAGB ratio is a sign of deformation energy stored as LAGB's in the microstructure. The change of the LAGB to HAGB ratio in austenite was more pronounced after bending in RD than in TD. Austenite can easier deform than ferrite due to its 12 closely-packed slip systems, which ferrite does not have. The LAGB to HAGB ratio substantially decreased after bending deformation in TD and RD, with the latter showing a larger change, which indicated LAGB multiplication associated with plastic deformation. The LAGB to HAGB ratio became larger in austenite than in ferrite after bending in RD than in TD. This was in line with the local misorientation development, showing that austenite contained larger proportions of plastic strain than ferrite after bending in RD, while the opposite was seen in TD bending direction.

Similar results have been recently reported in cold-rolled 2205 DSS in which the amount of high angle and low angle grain boundaries were seen to increase with cold rolling causing an enhancement of micro-deformation and, hence, strain in the microstructure [40]. Severe strain localisation at interphase boundaries and within austenite areas were observed leading to an enhanced general and localised corrosion susceptibility [40]. Severe deformation caused a change of prevalent corrosion mechanisms from a preferential selective dissolution of ferrite in as-received microstructure to a more pronounced pitting corrosion primarily occurring on austenite, as recently reported [40, 41]. This information has crucial importance to mechanistically understand corrosion and environment-assisted cracking behaviour.

8.5.5.2 Hardness Behaviour

Cold deformation usually increases the hardness due to an enhancement of the dislocation density in the microstructure. The hardness did not change after U-bending in RD and TD, although a change was expected. The hardness of the pre-bent specimens increased with ageing time indicating 475°C embrittlement, and it is known that spinodal decomposition can enhance local hardness by impeding dislocation motion in ferrite [42].

Spinodal decomposition and associated precipitation in 2205 DSS was recently reported which significantly increased the hardness [16]. The spinodal decomposition products, α' and α'' must have started to form and grow with ageing until a saturation point was reached. In previous investigations on the same material aged for 255 hours, α' and α'' structures in sizes of ~30 nm were measured including further secondary phases such as R-phase and other type of precipitates [16, 35]. No precipitates were observed on short-term aged microstructures (<50 hours).

Therefore, the increase of hardness for short-term aged specimens (<50 hours) is most likely related to spinodal decomposition. The hardness increased gradually with up to 20 hours of ageing, and increased over proportionally after 50 hours ageing, reaching a maximum hardness after 255 hours of ageing. In previous work, R-phase and further precipitates with sizes 50-400 nm have been reported [16, 35]. The precipitates, apparently, caused additional hardness increase, with probably having larger effect than spinodal decomposition.

Bending deformation in TD led to higher hardness than in RD for all specimens, and the hardness of the 10 hours aged specimens were similar. Spinodal decomposition did not seem to influence the overall hardness budget even after 10 hours ageing but embrittlement would still be expected which will be discussed later. The higher hardness of the specimens bent in TD must be related to the microstructure processing orientation. Spinodal decomposition seemed to effect in a higher hardness increase after bending in TD.

Usually, during hot and cold deformation ferrite and austenite grains in the microstructure develop a band-like structure, resembling a texture-like morphology. As a consequence, the ferrite and austenite interfaces are oriented primarily parallel to the RD whereupon materials properties, such as hardness, become dependent to the processing orientation. Deformation along RD is easier due to less shear deformation occurring across the interphase boundaries since the interface is continuous. Bending in TD causes larger internal friction since the deformation path is not straightforward and must bear discontinuous and disrupted interphase boundaries.

8.5.5.3 XRD Stress Measurements

The in-plane stress of austenite of the pre-bent specimens did not seem to be substantially affected by ageing time, while the stress of ferrite became more tensile after 255 hours of

ageing, which was more pronounced after bending in RD than in TD. Spinodal decomposition and precipitate formation in ferrite is accompanied by volume expansion which seemed to be more pronounced towards RD. Precipitates formed at the interface can hinder dislocation motion forcing the ferrite grains to distort along the RD.

The in-plane stress budget of ferrite and austenite significantly increased after bending in RD and TD with ageing time. The effect of 475°C embrittlement on the stress state of both phases can be clearly noticed. Both phases became tensile in all directions with ageing. Phase reactions occurring in ferrite must have caused severe dislocation multiplication and storage. It would be expected that the microstructure became more susceptible to localised corrosion and stress corrosion cracking due to the tensile stress nature of the microstructure after long-term ageing.

The stress of austenite was higher than the stress of ferrite in the as-received and all conditions aged for up to 50 hours. This might be due to larger plastic strain occurring in austenite than in ferrite, with possible strain-induced martensite formation within the austenite which might have additionally increased the stress budget. Martensite formation is accompanied by physical volume expansion causing strain hardening which is associated with dislocation motion retardation. Both phases adopted similar tensile values after 255 hours of ageing possibly indicating balanced stress states.

8.5.5.4 Atmospheric-Induced Stress Corrosion Cracking Behaviour

8.5.5.4.1 Quantitative Corrosion and SCC Analysis

Aggressive chloride concentration and low pH are, usually, the reason for severe corrosive attack. The temperature and RH play a key role in atmospheric corrosion and associated SCC phenomena. The susceptibility to SCC is highly affected by the relative humidity, having its highest effect at the equilibrium RH for a saturated solution of each chloride type, as shown by Shoji et al. [43]. AISCC affects, usually, the performance of a material to a larger extent than SCC occurring under full immersion conditions because of higher chloride concentration developments around and underneath salt deposits with additional crevice-like effect [44, 45].

In principle, three main assessments were rendered by the exposure tests of 2205 DSS heat-treated at 475°C for short-term (0-20 hours) and long-term (>50 hours) ageing conditions,

and two main assessments were rendered by cold bending into U-bend specimens. One is the effect of ageing treatment, the second is the effect of bending direction of those aged specimens, and the last is the effect of amount of surface chloride coverage per nominal area on corrosion and SCC behaviour.

8.5.5.4.2 Effect of Ageing Treatment

It could be shown that significant microstructural changes such as phase ratio, grain boundary development, and formation of phase reaction products associated with ageing at 475°C influenced the corrosion and SCC propensity. The ageing treatments changed the residual stress budget in the microstructure, and it rendered possible that 475°C embrittlement can be more critical than 750°C embrittlement since σ/χ containing microstructure did not seem to affect the microstructural integrity in caustic environments, in contrast to 475°C embrittlement which produces susceptible microstructure in both caustic and chloride containing media [46].

It was previously reported that short-term (≤10 hours) ageing at 475°C significantly raised the critical pitting temperature which decreased abruptly with further ageing time [33]. *Tavares et al.* reported similar behaviour [47]. A corrosion model explaining a possible reason for the increase of the corrosion resistance has been previously introduced which will be discussed later [35].

In overall, the absolute corrosion volume per nominal area increased with ageing time for all specimens. The specimen bent in RD had its highest corrosion performance after 10 hours ageing under all deposition conditions, while this was after 5 hours ageing after bending in TD. Apparently, the microstructure bending direction significantly changed the corrosion performance of 2205 DSS, i.e. there was a clear difference of 5 hours ageing between bending in RD and TD. However, the corrosion resistance of the material after bending in RD was superior to that after bending in TD for short-term ageing conditions (≤10 hours), but reversed for longer aged conditions (>20 hours).

The SCC resistance correlated well with the corrosion performance of all aged specimens, with bending in RD having its peak cracking resistance after 10 hours ageing, but did not seem to directly correlate with the corrosion volume for specimens bent in TD. The longest crack measured was on the specimen aged for 5 hours and bent in TD despite its peak

corrosion resistance. Seemingly, the material became more prone to corrosion for all specimens bent in TD than those bent in RD, except from the specimen aged for 5 hours. A possible explanation for this phenomenon could be made upon the microstructure development associated with the bending processing direction. Short-term ageing significantly improved the corrosion resistance of the ferrite phase, but the ageing caused 475°C embrittlement which was associated with hardness increase and strain localisation occurring in the hardened phase [16, 35], which may led large strain development during bending, which may have changed the corrosion and SCC propensity. However, the stress measurements did not seem to correlate well with the corrosion and cracking resistance meaning that the measured stress is not a clear function of the degree of metal dissolution and SCC formation, but 475°C embrittlement. Hence, the microstructure seemed to be the reason for this drastic change in corrosion and cracking behaviour, i.e. the phase fraction and LAGB to HAGB ratio etc.

8.5.5.4.3 Effect of Bending Direction

EBSD analyses showed that ferrite was larger affected after bending in TD than in RD, so that the corrosion resistance improvement was compromised with strain and stress development, therefore, affecting the overall corrosion performance. Since austenite was more affected in RD than in TD, ferrite seemed to support the overall corrosion resistance of the microstructure stronger than after bending in TD. It can be said that bending of short-term aged specimens (≤10 hours) in RD causes less decrease of corrosion and SCC performance under chloride deposits than after bending in TD, possibly due to largely affected austenite phase, which may enhanced its susceptibility. However, long-term ageing leads to severe embrittlement of the ferrite phase, and, hence, tensile strain has pronounced effect on corrosion and SCC on the microstructure after bending in RD.

8.5.5.4.4 Effect of the Amount of Surface Chloride Coverage

The corrosion area and volume increased with further ageing time for all deposition conditions due to long-term 475°C embrittlement, which is associated with local sensitisation leading to an overall loss of corrosion resistance and enhanced localised corrosion. The amount of corrosion was more pronounced with increasing deposition densities in the ranking order drop 3 > drop 2 > drop 1. The corrosion extent seemed to be highly influenced by the amount of deposited chloride in a non-linear relationship.

Increasing the chloride deposition density from 15 µg/cm² by a factor of 16.5 (drop 2) increased, except from a few points, the amount of corrosion by more than six orders of magnitude, and with further increase of the amount of chloride by a factor of 11.6 (drop 3) the amount of corrosion seemed to have enlarged by 6 to 7-times only. This clearly demonstrates that there is a strong relationship between the amounts of surface chloride coverage with the extent of corrosion, particularly deposition densities below 250's µg/cm² of chloride having most relevance for practical use. Therefore, in quantitative atmospheric corrosion rate predictions for long-term structural integrity, such as for nuclear waste storage canister materials, extreme precaution must be taken since extrapolation of corrosion data can be virtually not true.

The SCC behaviour showed similar trend to the amount of corrosion, but in a more complex relationship after bending in TD. The number and the order of magnitude of stress corrosion cracks, most usefully expressed as the maximum crack length, observed after bending in RD, increased slightly with ageing up to 50 hours, then steeply increased after 255 hours ageing, which is in accordance with quantitative corrosion data above-mentioned. Lowest susceptibility to cracking was observed after 10 hours of ageing, and most severe cracks were seen on the bent specimens aged for 255 hours. The microstructure, bent in TD, however, showed severe cracking with 1.7 mm length below drop 3 after ageing for 5 hours. Furthermore, the 50 hours specimen showed more severe cracks under drop 2 than the 255 hours specimen. The extent of SCC and the corrosion volume of the microstructure after bending in TD did not seem to correlate with those after bending in RD clearly concluding that the atmospheric corrosion behaviour is more influenced by microstructural properties than other key parameters.

8.5.5.4.5 Analysis of Corrosion and Cracking Morphology

In previous works, the effect of ageing treatment at 475°C on the critical pitting temperature [33] and microstructure development [16] of 2205 duplex stainless steel was discussed, for which a corrosion model was introduced [35]. In short, ageing at 475°C can lead to a fully decomposed ferrite structure forming spinodal decomposition and several precipitates products with no clear phase reactions occurring in austenite. The Volta potential difference, which is associated with electrochemical properties, measured over ferrite and austenite with respect to a Pt-coated tip significantly changed with ageing time. The potentials of ferrite

and austenite decreased with ageing time after 5 hours indicating enhanced electrochemical nobility. The selective corrosion nature of ferrite in as-received (mill-annealed) condition changed after short-time ageing, so that ferrite and austenite assumed almost equal corrosion attack which also indicated electrochemical nobilisation of ferrite caused by spinodal decomposition (α' + α'') leading to enhanced passivation behaviour. This ability of ferrite was lost with further ageing treatment due to precipitates formed and enlarged spinodal decomposition products, and ferrite became severely susceptible to localised and overall corrosion attack, followed by austenite to a lesser extent.

Ferrite and austenite have different corrosion and pitting potentials, therefore a different form and extent of corrosion attack can always be expected. In most 2205 duplex stainless steels, ferrite, usually, dissolves selectively in chloride-bearing media [33, 47-53], which is due to a higher corrosion potential of austenite than ferrite deriving from its higher nickel and nitrogen content [51-53]. Furthermore, ferrite and austenite show inherently different mechanical behaviour during plastic deformation due to their different crystal structure leading to a phase mismatch which is supported by the grain geometry and morphology [3].

In the as-received conditions, ferrite was preferentially attacked by pitting corrosion after bending in RD although austenite was more deformed. The LAGB to HAGB ratio of ferrite was highly increased by almost a factor of 2.5 meaning that numerous LAGB's were formed in ferrite grains and, hence, increased the strain budget causing the formation of local susceptible sites (hot spots). Therefore, austenite suffered from localised corrosion under drop 1 and 2. Localised corrosion of generated strain hot spots can govern the main corrosion mechanism even replace the selective dissolution nature of ferrite after large cold deformation [41]. Austenite was largely deformed in RD, and a larger number of LAGB's were generated than after bending in TD leading to numerous hot spots facilitating localised attack.

In the as-received condition, the microstructure is smooth to a higher order and contains almost no local susceptible sites which may trigger selective corrosion only and/or stress corrosion cracking. However, cold rolling introduces severe plastic deformation so that local susceptible sites (hot-spots) can be formed situating mainly in the austenite phase due to larger deformation capability than ferrite, causing a substantial shift from selective corrosion of ferrite to localised pitting corrosion in austenite [41]. Therefore, pitting corrosion in nano-

metre scale was observed nucleating preferentially in austenite after bending in RD, but not in TD although both phases showed larger stress localisation in the TD microstructure.

There was a corrosion pit with 50-60 μm diameter formed with some selective dissolution and intergranular corrosion of ferrite observed. Ferrite was more strained than austenite after bending in TD, possibly suggesting that ferrite became more susceptible to electrochemical attack. Seemingly, in duplex stainless steels, strain localisation has more severe effect on localised corrosion propensity than stress localisation since austenite was more deformed than ferrite after bending in RD, and ferrite more strained than austenite after bending in TD. This clearly shows the effect of microstructure on the corrosion performance of forged duplex stainless steels having processing-related texture-like microstructure appearance.

Pitting corrosion with no clear selective dissolution of either phase, however, was the prime corrosion event after bending in TD which was due to enhanced susceptibility of both phases well-possibly associated with large amount of formed grain boundaries causing severe strain localisation in ferrite and austenite, as shown earlier. The extent of corrosion decreased with short-term ageing due to electrochemical nobilisation of mainly the ferrite phase associated with spinodal decomposition, as earlier discussed. However, after long-term ageing (>20 hours) a net selective dissolution of ferrite with also large attack on austenite occurred leading to large-scale metal dissolution with further ageing. Short-term ageing enhanced the corrosion performance of 2205 duplex stainless steel, but long-term ageing caused severe loss of the corrosion resistance.

Stress corrosion cracking performance was in good correlation with the overall corrosion performance as a function of ageing time, with all specimens bent in RD. However, the stress corrosion cracking performance of the specimens bent in TD did not seem to correlate well with the corrosion performance as a function of ageing time. The longest crack was observed on the specimen aged for 5 hours. Erratic curve progression of the maximum crack length versus ageing time was noticed for all surface chloride deposits. Seemingly, bending in TD has more critical influence on the corrosion and, more important, stress corrosion cracking behaviour with little calculable predictability of sheet 2205 duplex stainless steel.

The crack morphologies of ferrite and austenite of aged and deformed microstructure were further assessed. Most of the crack morphologies of ferrite suggest chloride-induced stress corrosion cracking but hydrogen-assisted stress corrosion cracking could also be involved,

since on some conditions multiple closely-spaced fine-scale cracks were observed which are indicative to hydrogen-assisted stress corrosion cracking or hydrogen embrittlement [54-56].

Stress corrosion cracking occurred primarily in the austenite phase, which may be considered as the phase primarily responsible for cracking. The cracking propensity generally increased with ageing and reached maximum stress corrosion cracking susceptibility after 255 hours of ageing. There was no cracking of austenite observed on 5 hours aged specimen after bending in TD, in which ferrite was selectively cracked despite the electrochemical nobilisation and peak corrosion performance, possibly suggesting that chloride-induced stress corrosion cracking governed the main cracking mechanism. Ferrite became highly prone to stress corrosion cracking with the degree of 475°C embrittlement, showing most severe cracking after 255 hours of ageing.

Similar explanation could be made on the highly embrittled ferrite after long-term ageing (≥50 hours). Ferrite seemed to be the phase which suffered more from stress corrosion cracking and pitting after bending in RD while austenite cracked after bending in TD, although the opposite was observed for corrosion events, namely preferential pitting corrosion was observed in austenite after bending in RD, while a net selective dissolution of ferrite with general dissolution of ferrite and austenite in other sites was observed after bending in TD. However, in very aggressive corrosive environment (drop 3) both phases suffered highly from corrosion and cracking events.

The crack morphologies in austenite suggest that chloride-induced stress corrosion cracking was potentially the mechanism for cracking of the austenite phase. Despite the quantitatively larger cracking events in the microstructure bent in TD, the maximum crack length was 40 µm only, while a longer crack with 100 µm was measured forming in the microstructure bent in RD. This suggests that bending in RD is more critical than in TD regarding to the corrosion and stress corrosion cracking susceptibility of 2205 duplex stainless steel.

8.5.6 Conclusions

In this study, the effect of ageing at 475°C on microstructure development and the stress corrosion cracking behaviour was assessed, which can be summarised in the following:

1) Large local misorientation development associated with strain was observed after bending in RD and TD, with the latter having 2.5-times greater amplitude
2) The bending process in TD affected the structure of ferrite larger than that of austenite, yielding large strain developments in ferrite, manifested by an abrupt increase of LAGB to HAGB ratio, while after bending in RD the austenite phase was more susceptible to internal structural change manifested also by severe strain development associated with numerous new grain boundary generations
3) Hardness measurements showed clear increasing behaviour with the degree of 475°C embrittlement and with U-bending processing direction, but to a higher extent bending in TD than in RD
4) XRD stress measurements confirmed local stress developments in ferrite and austenite with ageing time and bending processing, with austenite showing larger stress budgets; ferrite showed an increasing trend of stress with ageing time and austenite showed an opposite behaviour
5) The microstructure was rendered highly susceptible to corrosion and stress corrosion cracking as a function of ageing at 475°C and bending direction, and most severe cracks were observed after bending in TD, particularly after long-term ageing (>50 hours)
6) An increase of corrosion performance was observed rendered by short-term ageing for 5 and 10 hours at 475°C for specimens bent in TD and RD, respectively
7) Good correlation was seen to exist between stress corrosion cracking performance with the overall corrosion resistance in the dependency of ageing time on all specimens bent in RD, but this validity was not true for specimens bent in TD
8) Stress corrosion cracking was primarily governed by the austenite phase for all deformed microstructures pre-aged up to 50 hours at 475°C, while ferrite, primarily, fractured after long-term ageing conditions (255 hours)

8.5.7 Acknowledgment

The authors acknowledge Radioactive Waste Management, a wholly owned subsidiary of the Nuclear Decommissioning Authority (NPO004411A-EPS02), and EPSRC (EP/I036397/1) for financial support. The authors are grateful for the kind provision of

Grade 2205 Duplex Stainless Steel plate by Rolled Alloys. Special thanks are addressed to Gary Harrison, School of Materials, for his support during XRD measurements.

8.5.8 References

[1] J. Charles, S. Bernhardsson. Duplex Stainless Steels '91 - Volume 1. In: Charles J, Bernhardsson S, (Eds.). Duplex Stainless Steels '91, vol. 1. Beaune, Bourgogne, France: Les editions de physique, 1991.

[2] J. Charles, S. Bernhardsson. Duplex Stainless Steels '91 - Volume 2. In: Charles J, Bernhardsson S, (Eds.). Duplex Stainless Steels '91, vol. 1. Beaune, Bourgogne, France: Les editions de physique, 1991.

[3] J.-O. Nilsson, G. Chai. The physical metallurgy of duplex stainless steels. International Conference & Expo DUPLEX 2007. Grado, Italy: ASSOCIAZIONE ITALIANA DI METALLURGIA - AIM, 2007.

[4] P. Kangas, J.M. Nicholls. Chloride-induced stress corrosion cracking of Duplex stainless steels. Models, test methods and experience, Materials and Corrosion 46 (1995) 354-365.

[5] H.M. Chung. Aging and life prediction of cast duplex stainless steel components, International Journal of Pressure Vessels and Piping 50 (1992) 179-213.

[6] J.K. Sahu, U. Krupp, R.N. Ghosh, H.J. Christ. Effect of 475°C embrittlement on the mechanical properties of duplex stainless steel, Materials Science and Engineering: A 508 (2009) 1-14.

[7] H.-J. Eckstein. Korrosionsbeständige Stähle, Deutscher Verlag für Grundstoffindustrie GmbH, Leipzig, Germany, 1990.

[8] H.M. Chung. Spinodal decomposition of austenite in long-term-aged duplex stainless steel. 1989. p.Medium: X; Size: Pages: 25.

[9] J.O. Nilsson. Super duplex stainless steels, Materials Science and Technology 8 (1992) 685-700.

[10] J.-O. Nilsson, P. Liu. Aging at 400–600°C of submerged arc welds of 22Cr–3Mo–8Ni duplex stainless steel and its effect on toughness and microstructure, Materials Science and Technology 7 (1991) 853-862.

[11] H.M. Chung, T.R. Leax. Embrittlement of laboratory and reactor aged CF3,CF8, and CF8M duplex stainless steels, Materials Science and Technology 6 (1990) 249-262.

[12] H.M. Chung, O.K. Chopra. Characterization of Duplex Stainless Steels by TEM, SANS, and APFIM Techniques. in: Altergott W, Henneke E, (Eds.). Characterization of Advanced Materials. Springer US, 1990. pp. 123-147.

[13] A. Redjaïmia, T. Otarola, A. Mateo. Orientation Relationships between the δ-ferrite Matrix in a Duplex Stainless Steel and its Decomposition Products: the Austenite

and the χ and R Frank-Kasper Phases. in: Richter S, Schwedt A, (Eds.). EMC 2008 14th European Microscopy Congress 1–5 September 2008, Aachen, Germany. Springer Berlin Heidelberg, 2008. pp. 479-480.

[14] A. Redjaïmia, A. Proult, P. Donnadieu, J.P. Morniroli. Morphology, crystallography and defects of the intermetallic χ-phase precipitated in a duplex (δ + γ) stainless steel, Journal of Materials Science 39 (2004) 2371-2386.

[15] A. Redjaimia, P. Ruterana, G. Metauer, M. Gantois. Identification and characterization of a novel intermetallic compound in a Fe-22 wt % Cr-5 wt % Ni-3 wt % Mo-0.03 wt % C duplex stainless steel, Philosophical Magazine A 67 (1993) 1277-1286.

[16] C. Örnek, J.H. Lim, M.G. Burke, T. Hashimoto, D.L. Engelberg. Effect of 475°C Embrittlement on Microstructure Development and Mechanical Properties of Grade 2205 Duplex Stainless Steel, Metall and Mat Trans A (2015).

[17] J.K. Sahu. Effect of 475°C Embrittlement on the Fatigue Behaviour of a Duplex Stainless Steel. Maschinenbau, vol. PhD. Siegen: University of Siegen, 2008. p.1-131.

[18] J.D. Tucker, M.K. Miller, G.A. Young. Assessment of thermal embrittlement in duplex stainless steels 2003 and 2205 for nuclear power applications, Acta Materialia 87 (2015) 15-24.

[19] K. Chandra, V. Kain, V. Bhutani, V.S. Raja, R. Tewari, G.K. Dey, J.K. Chakravartty. Low temperature thermal aging of austenitic stainless steel welds: Kinetics and effects on mechanical properties, Materials Science and Engineering: A 534 (2012) 163-175.

[20] W.-T. Tsai, S.-L. Chou. Environmentally assisted cracking behavior of duplex stainless steel in concentrated sodium chloride solution, Corrosion Science 42 (2000) 1741-1762.

[21] J.W. Oldfield, B. Todd. Room temperature stress corrosion cracking of stainless steels in indoor swimming pool atmospheres, British Corrosion Journal 26 (1991) 173-182.

[22] C.-M. Tseng, W.-T. Tsai, H.-Y. Liou. Effect of nitrogen content on the environmentally-assisted cracking susceptibility of duplex stainless steels, Metall and Mat Trans A 34 (2003) 95-103.

[23] T. Prosek, A. Le Gac, D. Thierry, S. Le Manchet, C. Lojewski, A. Fanica, E. Johansson, C. Canderyd, F. Dupoiron, T. Snauwaert, F. Maas, B. Droesbeke. Low-Temperature Stress Corrosion Cracking of Austenitic and Duplex Stainless Steels Under Chloride Deposits, Corrosion Science 70 (2014) 1052-1063.

[24] F. Ruel, S. Saedlou, S.L. Manchet, C. Lojewski, K. Wolski. The transition between Sulfide Stress Cracking and Stress Corrosion Cracking of the 2304 DSS as a function of T and pH in H2S environment. Eurocorr 2014. Pisa, Italy: Dechema Germany, 2014.

[25] W.J. Nisbet, G.W. Lorimer, R.C. Newman. A transmission electron microscopy study of stress corrosion cracking in stainless steels, Corrosion Science 35 (1993) 457-469.

[26] N. Arnold, P. Gümpel, T.W. Heitz. Chloridinduzierte Korrosion von nichtrostenden Stählen in Schwimmhallen-Atmosphären Teil 2: Einfluß von Hypochloriten, Materials and Corrosion 49 (1998) 482-488.

[27] N. Arnold, P. Gümpel, T. Heitz, P. Pscheidl. Chloridinduzierte Korrosion von Nichtrostenden Stählen in Schwimmhallen-Atmosphären Teil 1: Elektrolyt Magnesium-Chlorid (30%), Materials and Corrosion 48 (1997) 679-686.

[28] K. Takizawa, Y. Shimizu, E. Yoneda, I. Tamura. Effects of Cold Work, Heat Treatment and Volume Fraction of Ferrite on Stress Corrosion Cracking Behavior of Duplex Stainless Steel, Tetsu-to-Hagane 67 (1981) 353-361.

[29] K. Takizawa, Y. Shimizu, E. Yoneda, H. Shoji, I. Tamura. Effect of Cold Working and Heat Treatment on Stress Corrosion Cracking Behavior of Duplex Stainless Steel, Tetsu-to-Hagane 65 (1979) 617-626.

[30] K. Takizawa, Y. Shimizu, Y. Higuchi, I. Tamura. Effects of Cold Work and 475°C Aging on Corrosion Behavior of Duplex Stainless Steel, Tetsu-to-Hagane 70 (1984) 904-910.

[31] H.-S. Kwon, H.-S. Kim. Investigation of stress corrosion susceptibility of duplex (α + γ) stainless steel in a hot chloride solution, Materials Science and Engineering: A 172 (1993) 159-165.

[32] H. Leinonen, P. Pohjanne, T. Saukkonen, T. Schildt. Effect of Selective Dissolution on Stress Corrosion Cracking Susceptibility of Austenitic and Duplex Stainless Steels in Alkaline Solutions. NACE: One Petro, 2011.

[33] C. Örnek, D.L. Engelberg. Effect of "475°C Embrittlement" on the Corrosion Behaviour of Grade 2205 Duplex Stainless Steel Investigated Using Local Probing Techniques. Corrosion Management. Northampton, UK: The Institute of Corrosion, 2013. p.9-11.

[34] C. Örnek, D.L. Engelberg, S.B. Lyon, T.L. Ladwein. Effect of "475°C Embrittlement" on the Corrosion Behaviour of Grade 2205 Duplex Stainless Steel Investigated Using Local Probing Techniques. Eurocorr 2013. Estoril, Portugal: European Corrosion Congress, 2013.

[35] C. Örnek, J. Walton, T.L. Ladwein, S.B. Lyon, D.L. Engelberg. A Corrosion Model for 475°C Embrittlement in Duplex Stainless Steel – a Comprehensive Study via Scanning Kelvin Probe Force Microscopy, Electrochimica Acta (2015).

[36] K. Mino, C. Fukuoka, H. Yoshizawa. Evolution of intragranular misorientation during plastic deformation, Nippon Kinzoku Gakkaishi/Journal of the Japan Institute of Metals 64 (2000) 50-55.

[37] S.S.M. Tavares, M.R. da Silva, J.M. Pardal, H.F.G. Abreu, A.M. Gomes. Microstructural changes produced by plastic deformation in the UNS S31803 duplex stainless steel, Journal of Materials Processing Technology 180 (2006) 318-322.

[38] S.S.M. Tavares, J.M. Pardal, M.R.d. Silva, C.A.S.d. Oliveira. Martensitic transformation induced by cold deformation of lean duplex stainless steel UNS S32304, Materials Research 17 (2014) 381-385.

[39] Y. Guo, J. Hu, J. Li, L. Jiang, T. Liu, Y. Wu. Effect of Annealing Temperature on the Mechanical and Corrosion Behavior of a Newly Developed Novel Lean Duplex Stainless Steel, Materials 7 (2014) 6604-6619.

[40] C. Örnek, D.L. Engelberg. Kelvin Probe Force Microscopy and Atmospheric Corrosion of Cold-rolled Grade 2205 Duplex Stainless Steel. Eurocorr 2014. Pisa, Italy: European Federation of Corrosion, 2014. p.1-10.

[41] C. Örnek, D.L. Engelberg. SKPFM Measured Volta Potential Correlated with Strain Localisation in Microstructure of Cold-rolled Grade 2205 Duplex Stainless Steel, Corrosion Science (2015).

[42] J.W. Cahn. Hardening by spinodal decomposition, Acta Metallurgica 11 (1963) 1275-1282.

[43] S. Shoji, N. Ohnaka. Effects of Relative Humidity and Kinds of Chlorides on Atmospheric Stress Corrosion Cracking of Stainless Steels at Room Temperature, Corrosion Engineering 38 (1989) 92-97.

[44] M. Tullmin, P.R. Roberge. Atmospheric Corrosion. in: Revie RW, (Ed.). Uhlig's Corrosion Handbook. John Wiley & Sons, 2000.

[45] N.R. Smart. Literature Review of Atmospheric Stress Corrosion Cracking of Stainless Steels - Report to Nirex. Abingdon, Oxfordshire, UK: Serco Assurance, 2007.

[46] A. Bhattacharya, D. Yang, P.M. Singh. Stress Corrosion Cracking of Heat Treated 2205 Duplex Stainless Steel in Caustic Solutions. NACE Corrosion 2009. Atlanta, GA: NACE International, 2009.

[47] S.S.M. Tavares, A. Loureiro, J.M. Pardal, T.R. Montenegro, V.C.d. Costa. Influence of heat treatments at 475 and 400 °C on the pitting corrosion resistance and sensitization of UNS S32750 and UNS S32760 superduplex stainless steels, Materials and Corrosion 63 (2012) 522-526.

[48] R.F.A. Pettersson, J. Flyg. Electrochemical evaluation of pitting and crevice corrosion resistance of stainless steels in NaCl and NaBr. Stockholm, Sweden: Outokumpu, 2004.

[49] C. Örnek, A.H. Ahmed, D.L. Engelberg. Effect of Microstructure on Atmospheric-Induced Corrosion of Heat-treated Grade 2205 and 2507 Duplex Stainless Steels. Eurocorr 2012. Istanbul, Turkey: Dechema, 2012. p.1-10.

[50] D.L. Engelberg, C. Örnek. Probing propensity of grade 2205 duplex stainless steel towards atmospheric chloride-induced stress corrosion cracking, Corrosion Engineering, Science and Technology 49 (2014) 535-539.

[51] S. Aoki, K. Ito, H. Yakuwa, M. Miyasaka, J.i. Sakai. Potential Dependence of Preferential Dissolution Behavior of a Duplex Stainless Steel in Simulated Solution inside Crevice, Zairyo-to-Kankyo 60 (2011) 363-367.

[52] S. Aoki, H. Yakuwa, K. Mitsuhashi, J.i. Sakai. Dissolution Behavior of α and γ Phases of a Duplex Stainless Steel in a Simulated Crevice Solution, ECS Transactions 25 (2010) 17-22.

[53] J.-S. Lee, K. Fushimi, T. Nakanishi, Y. Hasegawa, Y.-S. Park. Corrosion behaviour of ferrite and austenite phases on super duplex stainless steel in a modified green-death solution, Corrosion Science 89 (2014) 111-117.

[54] S.P. Lynch. 2 - Hydrogen embrittlement (HE) phenomena and mechanisms. in: Raja VS, Shoji T, (Eds.). Stress Corrosion Cracking. Woodhead Publishing, 2011. pp. 90-130.

[55] S. Lynch. Hydrogen embrittlement phenomena and mechanisms, Corrosion Reviews 30 (2012) 105-123.

[56] S.P. Lynch. 1 - Mechanistic and fractographic aspects of stress-corrosion cracking (SCC). in: Raja VS, Shoji T, (Eds.). Stress Corrosion Cracking. Woodhead Publishing, 2011. pp. 3-89.

8.6 Correlative EBSD and SKPFM Characterisation of Microstructure Development to Assist Determination of Corrosion Propensity in Grade 2205 Duplex Stainless Steel

C. Örnek & D.L. Engelberg

Materials Performance Centre & Corrosion and Protection Centre,
School of Materials, The University of Manchester,
Sackville Street Campus, Manchester, M13 9PL, United Kingdom

8.6.1 Abstract

Correlative Electron Backscatter Diffraction (EBSD) and Scanning Kelvin Probe Force Microscopy (SKPFM) analysis has been carried out to characterise microstructure development and associated corrosion behaviour of as-received and 750°C heat-treated grade 2205 duplex stainless steel. High-resolution EBSD analysis revealed the presence of σ- and χ-phase, secondary austenite, Cr_2N, and CrN after ageing treatment. SKPFM Volta potential measurements confirmed the formation of discrete reactive sites, indicating local corrosion propensity in the microstructure. Cr_2N, σ-phase, and inter-granular χ-phase had the largest net cathodic activity, followed by CrN and intra-granular χ-phase showing medium electrochemical activity, with ferrite and austenite (including secondary austenite) showing net anodic activity. Corrosion screening confirmed selective corrosion of ferrite in the as-received and 750°C-aged conditions with the corrosion propensity of secondary phases staying in-line with SKPFM observations. Stress corrosion micro-cracks were also observed and are discussed in light of microstructure corrosion propensity.

Keywords: *Duplex stainless steel; Electron Backscatter Diffraction (EBSD); Scanning Kelvin Probe Force Microscopy (SKFPM); Secondary Phases; Stress Corrosion Cracking (SCC); Corrosion Screening*

8.6.2 Introduction

Duplex stainless steels (DSS) offer a synergistic combination of excellent mechanical properties with enhanced corrosion resistance, and these materials are now increasingly used, such as the manufacture of containers for the storage of intermediate-level radioactive

waste (ILW) [1]. Heat treatment, welding, or prolonged exposure to elevated temperatures may lead to undesired phase reactions in these high-alloyed stainless steels [2-5]. For example, the ferrite can decompose into a series of meta-stable and thermodynamically stable phases, whilst the austenite has often been stated to be unaffected [2, 4, 6]. However, phase reactions can also occur in the austenite, increasing the volume fraction of secondary phase products in the microstructure [7-13]. Components made with large wall thicknesses therefore usually contain intermetallic phases due to variations in cooling rates after high temperature treatments, with the core of components typically containing large volume fractions [14, 15].

Phase reactions are more favoured in the ferrite due to the enrichment of Cr and Mo, combined with far higher diffusion rates compared to the austenite [3, 4, 16]. For example, phase reactions in the temperature range between 250-550°C have been known as '475°C embrittlement' [2-5, 17, 18] where in addition to the degradation of mechanical properties a significant reductions in corrosion performance has also been observed [17-21]. Phase reactions occurring in the temperature range between 600-1000°C have become known as 'σ-phase embrittlement' where numerous secondary phases, such as Frank-Kasper phases (σ and χ) and, to some extent, R-phase can be formed [5, 10, 16, 22-35]. These are often accompanied by the precipitation of nitrides (Cr_2N and CrN) and carbides [2, 4, 5, 16, 34, 36, 37].

Determination of the identity and the volume fraction of secondary phases have typically been carried out using image analysis of optical and/or electron microscopic micrographs, often supported by analytical semi-quantitative assessment of the chemical composition by energy dispersive x-ray (EDX) analysis. However, uncertainty and lack of precision of these measurement methods did generally not allow to build-up a comprehensive mechanistic understanding of the behaviour of intermetallic phases during corrosion processes. Investigations to quantitatively describe microstructure development of aged duplex stainless steels at elevated temperatures, especially with respect to the formation of secondary phases, has often been associated with σ- and χ-phase formation based on eutectoid decomposition reaction of the ferrite. The effects of other precipitates such as Cr-nitrides were often not taken into account due to their small volume fractions and geometrical sizes, which makes them difficult to detect [3, 4, 16, 26, 34, 38].

The electron backscatter diffraction (EBSD) technique has developed into a tool for precise mapping of the microstructure for texture, crystallographic phases, and identification of misorientation gradients with information about local plastic strain. Mapping of multiple phases over large areas with high spatial resolution of up to 10's of nm has become possible for quantitative identification of crystallographic information to allow in- and ex-situ observation of microstructure development [39]. EBSD combined with scanning Kelvin probe force microscopy (SKPFM) can provide crystallographic information about the microstructure with local Volta potential information at high spatial resolution (10's of nm's). The latter is a quantitative measure to describe electrochemical reactivity of a metal surface [40-44]. The knowledge about local Volta potential differences allows characterisation of corrosion processes, for example, to understand local micro-galvanic coupling which has importance in bi-phase alloys such as duplex stainless steels [13, 45-50]. Selective dissolution of the ferrite phase in duplex stainless steels, for example, can be explained by the larger Volta potential difference with respect to the Pt reference (lower absolute Volta potential), compared to a smaller measured difference of the austenite [18, 45, 46]. With the introduction of cold work, grade 2205 duplex stainless steel tends to show preferential local corrosion sites associated with localised deformation in the austenite, with these regions related to local Volta potential extremes [45, 51].

The purpose of the work reported in this paper was to link the precipitation of secondary phases after 750°C heat treatment using multi-scale EBSD analysis, to their Volta potential differences using SKPFM. Information from correlative EBSD and SKPFM analyses provide an insight into mechanistic understanding of the atmospheric corrosion and stress corrosion cracking (AISCC) behaviour of grade 2205 duplex stainless steel microstructure.

8.6.3 Experimental

A solution-annealed (as-received) grade 2205 duplex stainless steel plate of 10 mm thickness was used in this work with a composition shown in Table 8-7. EDX spectroscopy measurements of the ferrite and the austenite phases were conducted to inform about alloy partitioning, with the results also provided in Table 8-7. Small miniature tensile samples were manufactured with an overall length of 50 mm, a thickness of 1 mm, with 25 mm gauge length and 3 mm gauge width, as well as coupon samples with dimensions of 10 mm x 10

mm x 10 mm (L x W x T). All samples were aged for 5 hours at 750°C, followed by air-cooling to room temperature. The surface of these samples was mechanically ground to 4000-grit using SiC paper, followed by a 3, 1, ¼, and 0.1 µm diamond paste polishing finish. A final fine-polishing treatment using a modified OP-S suspension (OP-S with a few drops of concentrated HNO_3 and H_2SO_4) was performed for one hour to achieve a smooth, strain free surface finish for EBSD and SKPFM analysis.

Table 8-7: Chemical compositions (wt.-%) of grade 2205 duplex stainless steel used in this study. Semi-quantitative EDX analysis of the ferrite and austenite composition is also provided to inform about element partitioning (n.a. = not analysed)

Grade	C	Si	Mn	P	S	Cr	Ni	Mo	N	Fe
Plate	0.016	0.4	1.5	0.021	0.001	22.4	5.8	3.2	0.18	bal.
Ferrite	n.a.	0.5	1.7	n.a.	n.a.	25	4.3	4.3	n.a.	bal.
Austenite	n.a.	0.4	1.9	n.a.	n.a.	22.1	6.9	2.4	n.a.	bal.

8.6.3.1 Microstructure Analysis

The microstructures of as-received and heat-treated specimens were analysed by EBSD using an FEI Magellan high-resolution Scanning Electron Microscope (SEM). Data acquisition was performed with a Nordlys EBSD detector from Oxford Instruments with AZtec 2.2 software. An accelerating voltage of 10-20 kV was used with low current (spot size) to achieve effective spatial resolutions of 10's of nm [39, 52]. High-resolution EBSD mapping was carried out with step-sizes between 56 nm and 75 nm over an area of 100 µm x 87 µm. For the identification of crystallographic phases parameters listed in Table 8-8 were used. The phase databases were included in AZtec software. Databases from HKL and Inorganic Crystal Structure Database (ICSD) were used for phase acquisition.

Table 8-8: Database with crystallographic geometry parameters for EBSD phase identification

Phase	a	b	c	α	β	γ	Space Group	Database
Ferrite	2.87 Å	2.87 Å	2.87 Å	90°	90°	90°	229	HKL
Austenite	3.66 Å	3.66 Å	3.66 Å	90°	90°	90°	225	HKL
Cr_2N	4.75 Å	4.75 Å	4.43 Å	90°	90°	120°	162	ICSD
CrN	2.97 Å	4.12 Å	2.88 Å	90°	90°	90°	59	ICSD
Sigma	8.80 Å	8.80 Å	4.56 Å	90°	90°	90°	136	HKL
Chi	8.92 Å	8.92 Å	8.92 Å	90°	90°	90°	217	HKL
$Cr_{23}C_6$	10.6 Å	10.6 Å	10.6 Å	90°	90°	90°	62	ICSD

Indexing rates were typically close to 99% and at least six Kikuchi bands were selected for successful phase identification, with the minimum number of detected bands of the corresponding Kikuchi diffraction pattern for each phase given in Figure 8-66. Extra care was taken for indexing secondary phases, such as CrN, Cr_2N, and χ-phase. Data acquisition was first performed using all listed phases. When secondary precipitates were indexed, the data-set was re-assessed by de-selecting individual phases and re-mapping the same area without the corresponding phase. Phase identification proved to be reliable when the previously indexed region of a secondary phase was non-indexed, which confirms and validates the indexing procedure for CrN, Cr_2N, χ, and σ-phase. Indexing of chromium carbides ($Cr_{23}C_6$) for example, revealed to be problematic, since the ferrite or austenite were mis-indexed when the $Cr_{23}C_6$ phase was selected for acquisition. EBSD assessment of $Cr_{23}C_6$ was therefore excluded in our assessment. However, carbide formation in the 750°C temperature range is extremely retarded in modern duplex stainless steel, with nitrides usually formed in far larger quantities leading to a suppression of carbide formation [16, 34].

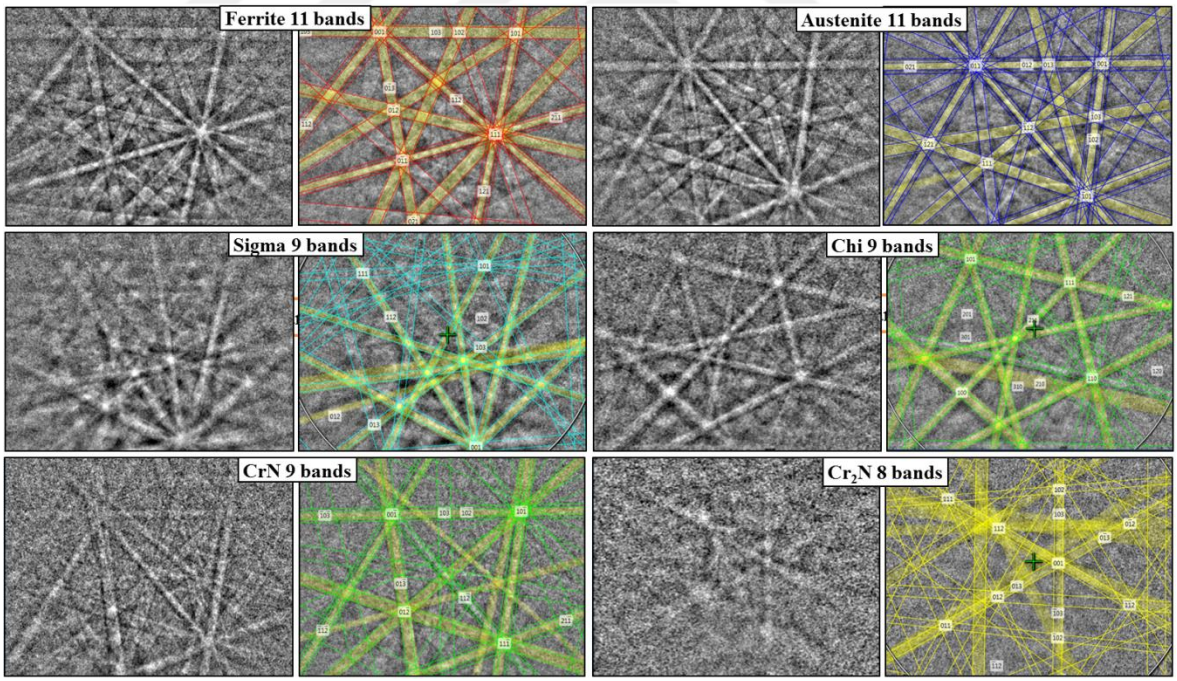

Figure 8-66: Kikuchi diffraction bands of all indexed phases in our study. Each image pair shows unsolved (left) and solved (right) Kikuchi pattern with the minimum number of bands detected for each phase.

All EBSD maps were processed using HKL Channel 5 software and phase fractions and grain sizes were extracted. High angle grain boundaries (HAGB's) were determined with misorientation in excess of 15°, and low angle grain boundaries (LAGB's) were defined with

1-15°. Phase maps were generated with all phases detected, including phase and grain boundaries.

8.6.3.2 Scanning Kelvin Probe Force Microscopy (SKPFM)

SKPFM and Magnetic Force Microscopy (MFM) measurements were carried out with a *Dimension 3100* atomic force microscope (AFM) from *Veeco* interfaced with a *Nanoscope 3a* controller. Pt-coated *OSCM-PT* AFM probes from *Olympus* with 15 nm nominal radius were used to map the surface topography and the corresponding Volta potential difference of the metal with respect to the tip. The scan size of AFM map was between 10-80 µm, depending on the microstructural features to be characterised. The scan rate was adjusted to the tip velocity (10-30 µm/s), which corresponds to a scan rate of 0.2-0.5 Hz. The images contained 512 x 512 pixels yielding effective spatial resolution between 20-156 nm. All maps were processed using *Nanoscope V1.5* software (*Bruker*). Topography/height and potential maps were flattened with 0^{th} flattening order to achieve best contrast within the microstructure; therefore all data are semi-quantitative only.

In this paper, and for the probes used, higher potentials indicate a larger potential difference and correspond to anodic sites due to a larger absolute work function difference between the bias-controlled AFM tip and the microstructure feature of the grounded sample. According to this definition, cathodic sites have therefore lower Volta potentials than their anodic counter-parts [53]. More comprehensive explanation about the meaning of the potential and the Kelvin probe technique can be found elsewhere [43-45, 50, 54, 55].

8.6.3.3 Atmospheric-induced Stress Corrosion Cracking (AISCC) Testing

AISCC susceptibility was investigated on as-received and 750°C heat-treated mini-tensile specimens, which were ground to 4000-grit using SiC sand papers. The heat-treated specimen, however, was afterwards electro-polished in an electrolyte of a mixture of 20% perchloric acid and 80% methanol at 20 V and at a temperature of -40°C. This was done to achieve smooth surface finish for phase identification after the corrosion test.

The as-received and heat-treated mini-tensile specimens were strained to 3% and 1%, respectively in self-designed direct tension rigs [56]. A strain gauge was placed on the backside of each specimen and the sample extension monitored, in-situ, using a LabVIEW programme. Water droplets containing $MgCl_2$ in different concentrations and volumes were

applied onto the surface. The droplets were dispensed with an Eppendorf micropipette. Nominal deposition densities of magnesium chloride and chloride ions were calculated from area measurements as listed in Table 8-9. The deposited droplets changed their shape during exposure due to secondary spreading (see Figure 8-67 for images after exposure); therefore the determined 'initial' deposition densities most likely changed over time.

Table 8-9: Experimental conditions of the AISCC test

Sample	Strain applied	No. of deposit	Volume [ul]	Droplet radius [mm]	Deposited $MgCl_2$ [µg/cm^2]	Deposited chloride [µg/cm^2]
As-received	3%	1	0.5	1.78	1947	1450
Aged at 750°C/5h/air	1%	1	0.5	1.78	20	14.5
		2	0.5	1.78	195	145
		3	0.5	1.78	1947	1450
		4	1.5	2.3	3319	2472
		5	2.5	2.8	3835	2856

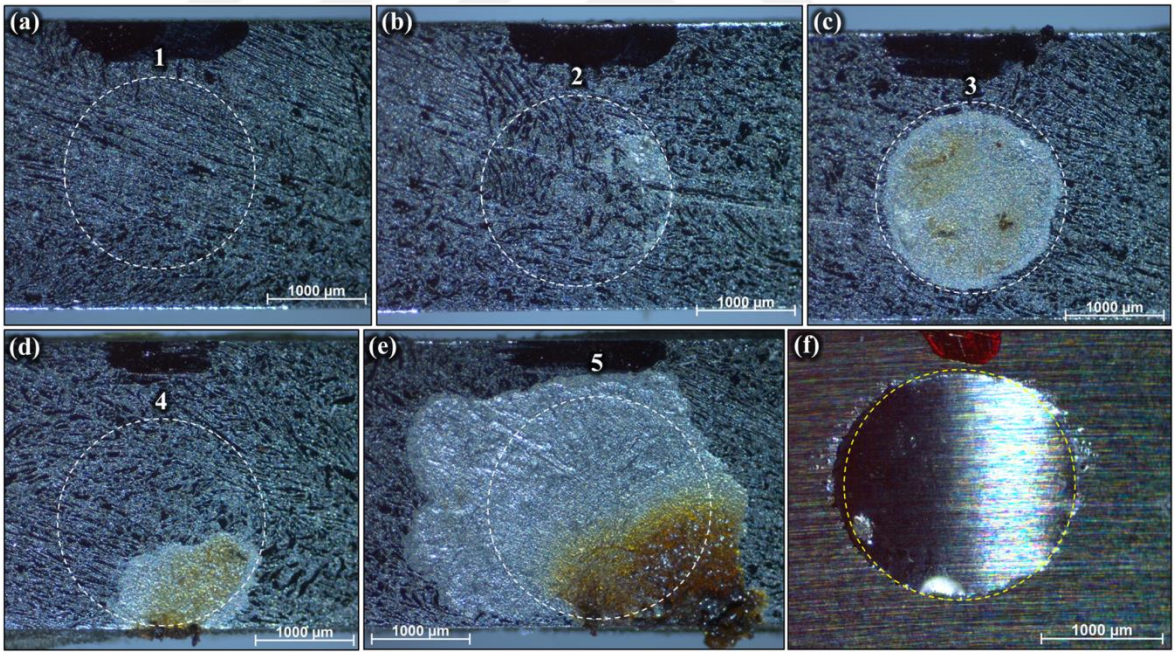

Figure 8-67: Stereo-microscopy images of exposed electrolyte droplets containing magnesium chloride (a-e) of specimen aged at 750°C (droplet 1 to 5) and (f) of as-received sample after exposure to 30% relative humidity at 50°C for 259 days.

The direct tension rigs were placed in a climatically-controlled KBF Binder cabinet for 259 days at 50°C and 30% relative humidity (RH); however, fluctuations in RH up to 60% were observed during the last 2 weeks of exposure associated with equipment problems, therefore,

the test was terminated. During the time of exposure, the direct tension rigs were periodically removed from the humidity chamber to assess whether corrosion had occurred. After terminating the test, the sample was rinsed in distilled water to dissolve salt and corrosion products, followed by an additional cleaning cycle in a 10 wt.-% citric acid solution at 80°C for 2 hours to remove remaining corrosion products.

8.6.4 Results and Discussion

8.6.4.1 EBSD Microstructure Characterisation

The microstructure of the as-received and heat-treated condition is shown as EBSD phase maps in Figure 8-68(a+b). The as-received microstructure consisted of 44±2% ferrite (δ) and 56±2% austenite (γ). The ferrite formed the matrix with the austenite present in the form of island-like, discrete grains or clusters of small grains. The shape of ferrite and austenite grains was elongated due to the hot rolling process during manufacture. The austenite contained large fractions of twin boundaries, shown by the straight lines (yellow) in Figure 8-68(a), with interphase boundaries indicating more concave and convex shapes. The misorientation variation within ferrite and austenite grains was low. The average grain size of ferrite and austenite was 7±1 µm and 6.5±1 µm, respectively.

The specimen aged at 750°C in Figure 8-68(b) contained a large fraction of secondary phases, including σ-, χ-, chromium nitrides (Cr_2N, CrN), and secondary austenite (γ_2) which have formed during the ageing treatment [16, 30]. The normalised phase fraction results is summarised in Table 8-10. High-resolution EBSD maps allowed clear observations of the newly formed microstructure shown in Figure 8-69(a-g). The austenite grain boundaries at the interphase had convoluted morphologies, with newly formed secondary austenite protruding from primary austenite islands as can be seen in Figure 8-69(a).

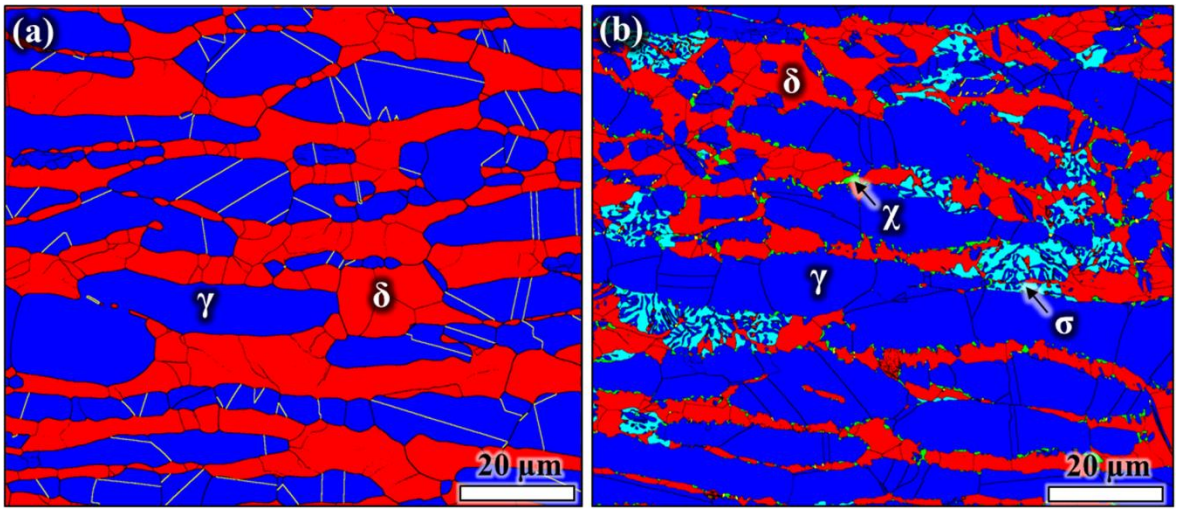

Figure 8-68: EBSD phase maps showing (a) as-received microstructure and (b) microstructure after heat treatment at 750°C for 5 hours. Black lines are phase and high angle grain boundaries. Note that Cr_2N and CrN are not visible at this scale.

The ferrite is thermodynamically unstable and has decomposed [3, 4, 16, 34, 38], with three mechanisms proposed for secondary austenite formation where the eutectoid equilibrium δ → σ + γ_2 is the predominant reaction in the 700-900°C temperature range. The overall fraction of secondary austenite formed was approximately 12%, which was determined by the difference between pre- and post-ageing austenite contents. The eutectoid reaction mainly takes place at δ/γ-interphase boundaries due to increased diffusion rates, leading to segregation of Cr and Mo, resulting in σ-phase formation [4, 12, 16, 26, 30, 32, 34]. The morphology of σ-phase often shows an allotriomorphic appearance due to its preferential growth along phase boundaries and towards ferrite grain interiors [57]. The surrounding regions are then depleted in Cr and Mo, resulting in the formation to secondary austenite [4, 16, 57]. The eutectoid secondary austenite can have a similar appearance to that of σ-phase, as can be seen in Figure 8-68(b) and Figure 8-69(a+b). Secondary austenite in direct contact with primary austenite can also form by growth towards ferrite regions and assume coagulant-like shapes with similar grain orientation as the primary austenite, also shown in Figure 8-69(e).

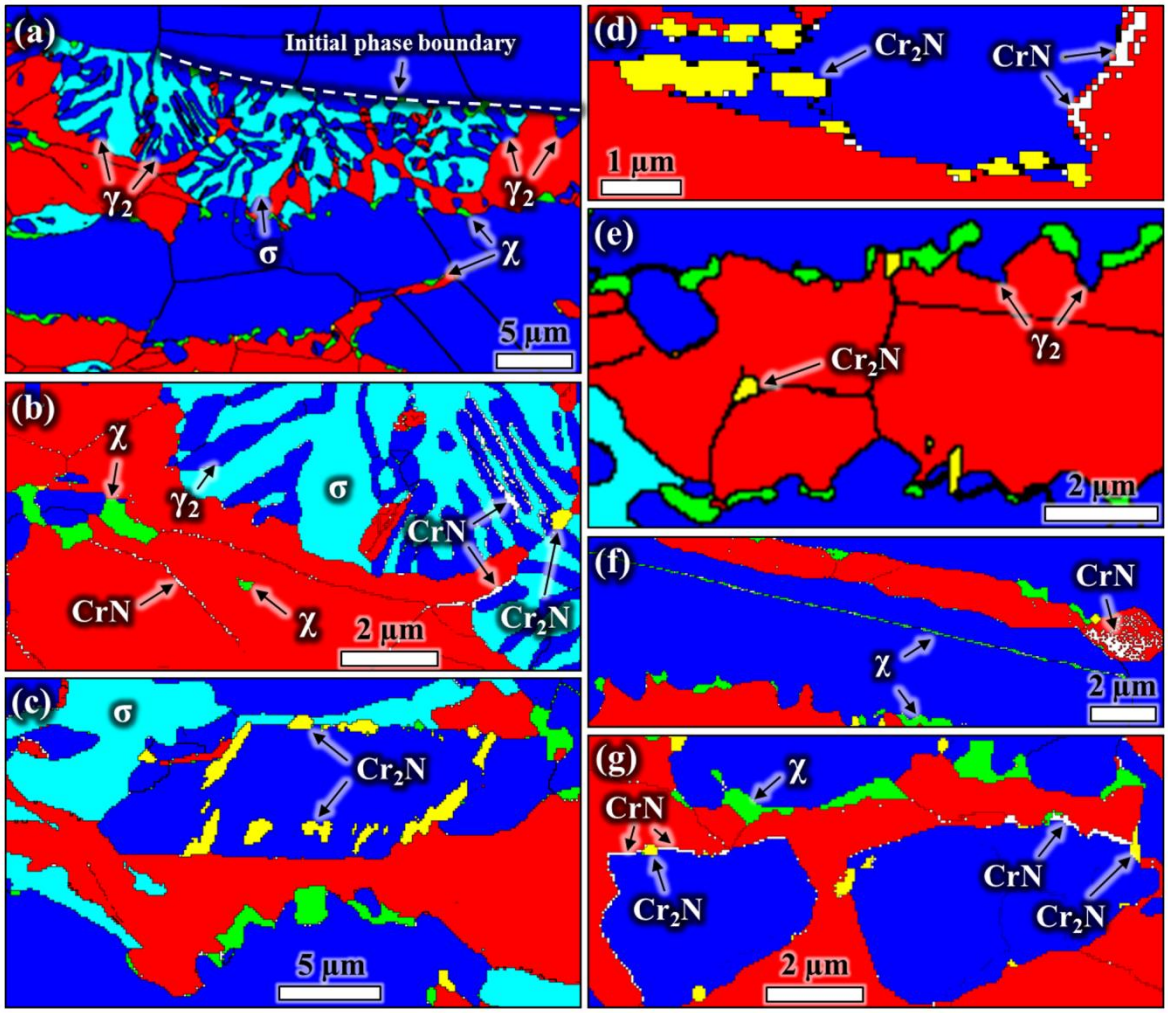

Figure 8-69: High resolution EBSD phase maps of the specimen aged at 750°C for 5 hours showing (a) σ, χ, and γ_2 formation, (b) intra-granular χ phase formation in ferrite with inter-granular CrN formation in ferrite and at σ/γ_2 interphase boundaries, (c+d) Cr_2N formation in austenite and at existing δ/γ phase boundaries, with (d) CrN formation at δ/γ phase boundaries, (e) inter- and intra-granular Cr_2N formation in ferrite, (f) intra-granular CrN formation in δ and χ formation at boundaries and interphases, and (g) CrN, χ, and Cr_2N formation at interphase boundaries.

Table 8-10: Normalised EBSD phase fractions (n/a = not available; *secondary austenite included)

Condition	δ	γ	σ	χ	CrN	Cr_2N
As-received	44	56	n/a	n/a	n/a	n/a
Aged 750°C/5h	26.1	65.5*	5.62	2.08	0.41	0.33

Austenite forming onto primary austenite has also been described as new austenite in the literature [58], but in our case all newly formed austenite induced by ageing is denoted as 'secondary austenite' (γ_2). Both types of secondary austenite have been found to contain reduced Cr contents, particularly if the formation of Cr-rich precipitates is involved, such as σ-phase [30, 59]. The volumetric fraction of secondary austenite is typically twice that of

formed σ-phase, clearly indicating faster reaction kinetics [30]. The corrosion performance of microstructures containing secondary austenite has been reported to cause reduced pitting corrosion resistance [37, 60]. Therefore, the fraction of σ-phase alone is an insufficient parameter for microstructure assessment regarding the corrosion behaviour of duplex stainless steels.

The newly formed secondary austenite had similar grain orientation to the existing austenitic phase, with neither new high-angle or low-angle grain boundaries seen in most newly formed austenite grains. The secondary austenite seemed to have developed through grain growth from primary austenite grains, indicated by the white dashed line in Figure 8-69(a), showing the approximate position of the initial δ/γ phase boundary. Secondary austenite formation was also observed through new austenite formation within ferrite regions associated with eutectoid σ-phase formation in the ferrite producing elongated lamellae-like shapes (allotriomorphic) also shown in Figure 8-69(a+b).

The decomposition of ferrite was accompanied by the formation of σ- and χ-phase. The σ-phase contained no high- and low-angle grain boundaries and showed allotriomorphic morphology. The σ-phase was located between pre-existing primary austenite islands, clearly evidencing that this phase formed by consuming ferrite. Ferrite-austenite phase boundaries and triple junctions of grain boundaries have been reported to act as nucleation sites for σ-phase [16, 22-24, 26-28, 30, 32]. The formation of σ-phase occurred at discrete regions in the microstructure, resulting in clusters of σ-phase and secondary austenite as can be seen in Figure 8-68(b). Furthermore, σ-phase was also found in ferrite grains, highlighted in Figure 8-69(c). The measured fraction of σ-phase was almost 6% (Table 8-10), which is in good agreement with the work of *Michalska et al.* who obtained 6-7% σ-phase in grade 2205 after ageing at 750°C for 5 hours via conventional image analysis [26]. *Elmer et al.* also investigated σ-phase formation in grade 2205, and ageing at 750°C for 10 hours produced 22.7% of σ-phase determined via in-situ synchrotron x-ray diffraction technique [24]. They reported 90% completion of phase reactions after 10 hours ageing, and predicted an overall fraction of 24% of σ-phase by Thermocalc calculations [24]. The size of σ-phase was estimated in Figure 8-69 using horizontal and vertical ferret diameters of 1-7 μm. However, the three-dimensional appearance may result in different ‘structural’ sizes due to the allotriomorphic shape of σ.

A total fraction of 2.1% χ-phase was measured after ageing at 750°C for 5 hours in the microstructure, shown in Figure 8-69. The χ-phase precipitated primarily at δ/γ phase boundaries, with expansion along the circumference of primary austenite grains but growth towards the ferrite. In addition, χ also consumed some austenite as can be seen in Figure 8-69(a-g). However, χ-phase precipitation is not restricted to ferrite or δ/γ phase boundary regions. In austenitic stainless steels, χ, σ, and other secondary phases can also form by consumption of austenite grains [10]. Therefore, similar reactions are also expected to occur in duplex stainless steels. The formation of χ-phase in grade 2205 duplex stainless steel has been reported to occur at temperature approximately 75 Kelvin below that of σ-phase formation, with fastest transformation kinetics at 750°C [16, 30]. Therefore, χ-phase formation has been reported to be more favoured at the initial stages of ageing [16, 22, 26, 27, 30]. *Padilha et al.*, for example, observed qualitatively larger fractions of χ than σ-phase at early ageing stages, with the χ-phase consumed by σ-phase formation after prolonged ageing treatment at 750°C [30]. Several works have reported χ-phase as metastable [22, 30], although computational isothermal sections of Fe-Cr-Ni-Mo-N systems containing 22% Cr and 5% Ni predicted χ as a stable phase, co-existing with σ-phase and Cr_2N [16].

The size of χ-phase was estimated in Figure 8-69 using horizontal and vertical ferret diameters of 0.1-2 μm. Transformation of χ occurred at multiple sites, resulting in a more homogenous formation in the microstructure compared to the clustered σ-phase appearance. The χ-phase precipitates also seemed to pin interphase boundaries, causing bulging of the newly formed secondary austenite, as shown in Figure 8-69(e). Moreover, it was noticed that χ-phase even nucleated within austenite grains, decorating part of a twin boundary, as shown in Figure 8-69(f).

Chromium nitrides, both CrN and Cr_2N, were observed after ageing at 750°C. Both compounds can be seen in Figure 8-69, with the orthorhombic CrN and the hexagonal Cr_2N decorating δ/γ, δ/γ_2, and also σ/γ_2 interphase regions The Cr_2N had more discrete dimensions in the form of larger areas than CrN (Figure 8-69). The morphology of Cr_2N was elongated ellipsoid-shaped. Their sizes varied between 130 nm to 4 μm with high aspect ratios. The CrN had smaller dimensions, typically between 80-620 nm, but CrN was often found in clusters as highlighted in Figure 8-69(f). The total fraction of Cr_2N was 0.33% and the fraction of CrN was 0.41%. There has been work published on Cr_2N and most is in agreement

that Cr_2N is stable and co-exists with χ-phase and σ-phase precipitates [6, 10, 12-16, 27, 28, 34, 36, 48, 61, 62], but far less is known about CrN [11, 36].

The formation of Cr-nitrides is usually associated with increased ferrite contents in duplex stainless steels [11, 36, 61, 62], and large fractions of nitrides have therefore been observed in welds and heat affected zones [11, 34]. The formation of Cr_2N has been reported to either occur during cooling, when ferrite is supersaturated with nitrogen leading to the formation of elongated and discretely-shaped intra-granular precipitates with $\langle 0001\rangle_{Cr_2N} \parallel \langle 011\rangle_{\delta}$ orientation relationship, or during isothermal ageing in the 700-900°C temperature range where inter-granular Cr_2N precipitates are formed on δδ- and δγ-boundaries [16]. In our study, Cr_2N was observed at interphase boundaries, but also within austenite grains indicating that nitride precipitation may be possible in austenite as well as can be clearly seen in Figure 8-69(c+d).

CrN formation occurred within the ferrite, mostly on δ/δ and δ/γ grain boundaries as shown in Figure 8-69(b-g). No CrN was observed in the austenite, but on γ_2/σ phase boundary regions as shown in Figure 8-69(b). An orientation relationship between CrN and ferrite $\langle 110\rangle_{CrN} \parallel \langle 111\rangle_{\delta}$ and $\langle 001\rangle_{CrN} \parallel \langle 1\bar{1}0\rangle_{\delta}$ has been reported [11]. In a grade 2505 duplex stainless steel with 0.14% N both types of Cr-nitrides were observed, when the microstructure was cooled with rapid cooling in the range of 40-150 K/s [11]. The reported CrN precipitates showed a film- or platelet-like appearance, with Cr_2N having a rod-like shape, with the latter forming in larger sizes than CrN precipitates [56].

Both Cr-nitrides are typically enriched in Cr, N, Fe, and Mo, but Cr_2N contains more Cr than CrN, while the opposite holds true for the N content [36, 62]. The extent of elemental depletion zones around these precipitates usually develops as a function of element enrichment within the precipitate and the volumetric size. Since Cr_2N is more enriched in Cr and has a larger size than CrN, it is therefore expected that Cr_2N yields larger Cr depleted regions, resulting in an increased electrochemical activity associated with reduced corrosion resistance [13, 36, 47, 48, 61]. This assumption will be discussed in more detail in light of the SKPFM results.

8.6.4.2 SKPFM Volta Potential Measurements

Maps showing the Volta potential differences measured over regions containing ferrite and austenite in the as-received microstructure with corresponding topography and magnetic frequency maps are shown in Figure 8-70(a-c). Regions showing low Volta potential differences were determined to be non-ferromagnetic and hence austenitic as can be seen in the magnetic frequency map in Figure 8-70(c), indicating net cathodic character. Vice versa, regions of high potential, with net anodic character are ferritic, showing a magnetic frequency response. The Volta potential reflects the electronic activity of a metal, and the larger the potential difference with respect to Pt the lower the actual electronic activity leading to facilitated charge transfer during electrochemical reactions [40, 41]. However, this describes thermo-dynamic equilibrium conditions, and kinetic information cannot be extracted.

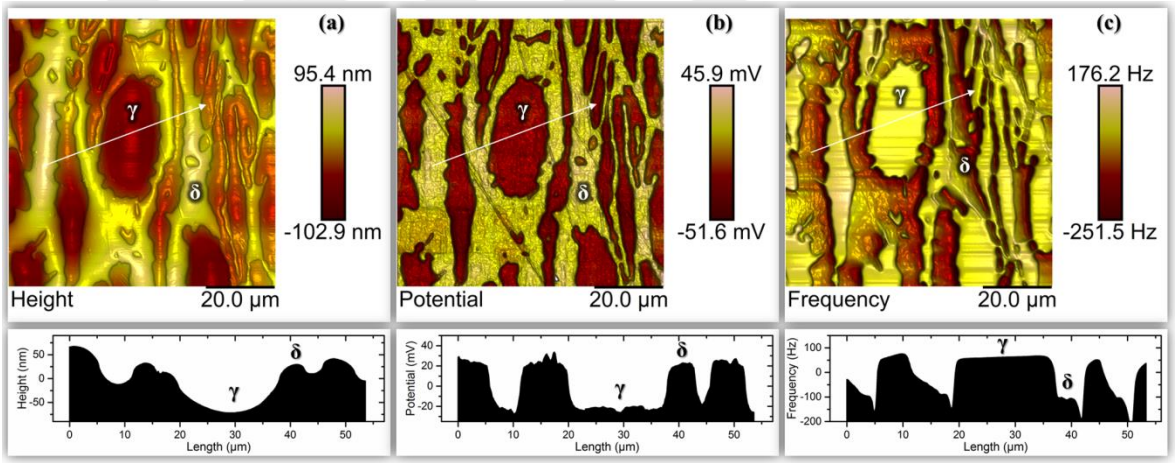

Figure 8-70: SKPFM analysis of as-received microstructure with (a) topography of a scanned area of 80 x80 µm² containing ferrite and austenite with a line profile measurement along the white arrow given below, (b) the corresponding Volta potential differences map with a line profile, and (c) correlated magnetic frequency measured over the same area (note a small off-set of the scanned area).

The ferrite showed 50-70 mV in average larger Volta potential values than the austenite indicating higher electrochemical activity. The Volta potential difference also indicated possible micro-galvanic activity between austenite and ferrite, at which the latter was expected to form the net anode while austenite the net cathode. The potential variation across ferrite and austenite interphases was smooth with only minor potential gradients. A smooth potential gradient is indicative for non-heterogeneous activity, such as selective attack. Earlier work on grade 2205 duplex stainless steel clearly demonstrated the susceptibility of

ferrite when exposed to chloride containing environment, with the introduction of plastic deformation leading to local Volta potential extremes (hot spots) [63].

A Volta potential differences map with topography to screen the 750°C aged microstructure is given in Figure 8-71(a+b). The corresponding SEM image with EBSD phase map of the same region is given in Figure 8-71(c+d). Volta potential differences over ferrite and austenite in certain regions were nearly similar, which means that the driving force for galvanic coupling between those regions is reduced. However, local Volta potential extremes were developed indicating enhanced electronic activity and galvanic coupling between net anodic and net cathodic regions.

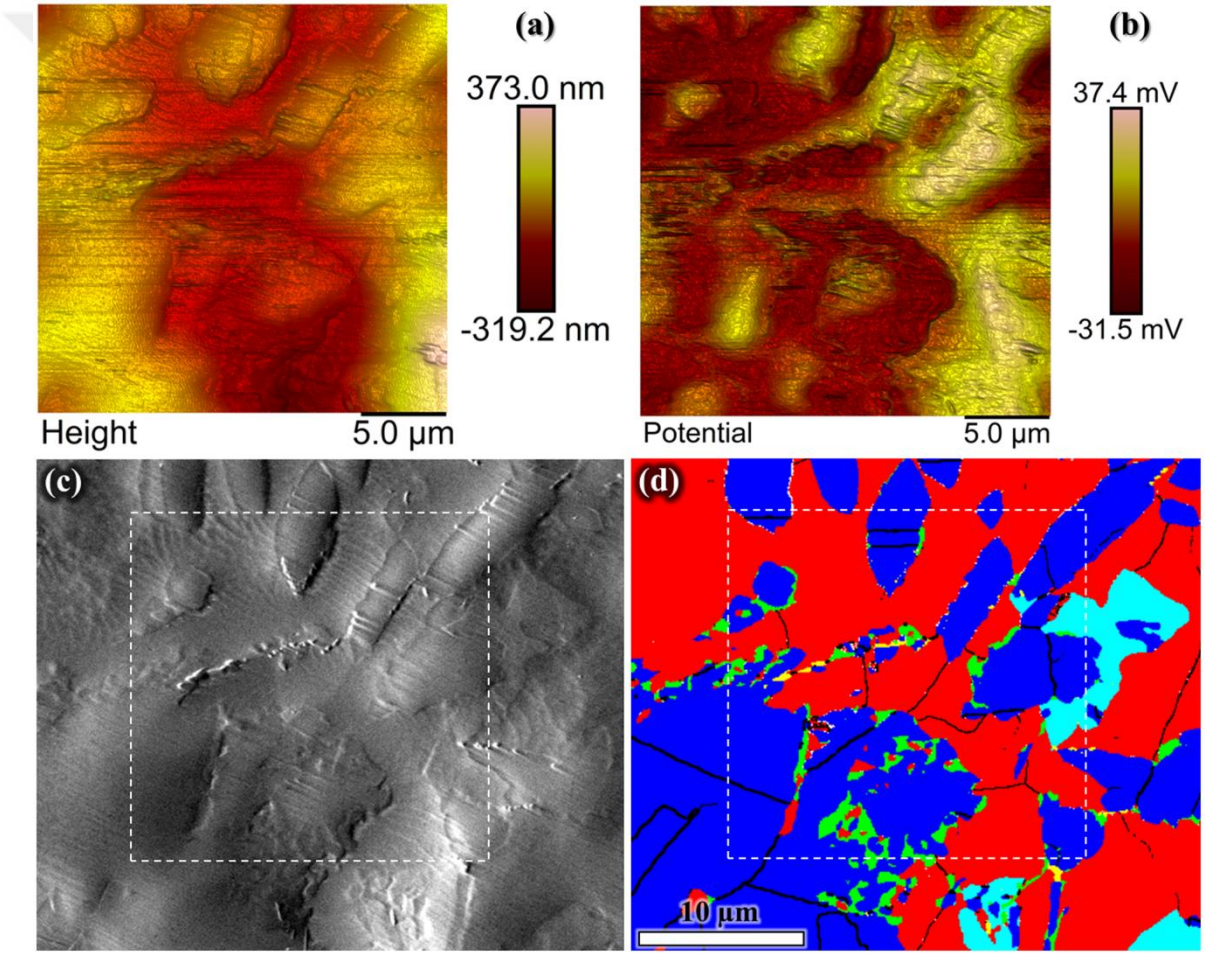

Figure 8-71: SKPFM analysis of aged microstructure with (a) topography map, (b) corresponding Volta potential map, (c) corresponding SEM micrograph in secondary electron imaging mode, and (d) corresponding EBSD phase map showing γ/γ_2 (blue), δ (red), χ-phase (green), σ-phase (aqua), Cr_2N (yellow), CrN (white), and grain/phase boundaries (black). Highlighted region in (c&d) indicate the scanned area.

The Volta potential variations within ferrite and austenite regions increased, indicating higher micro-galvanic activity within each phase. At this magnification potential differences over secondary phases could not be discerned, and the mapped area in Figure 8-71 was therefore re-scanned with higher-resolution as shown in Figure 8-72 and Figure 8-73.

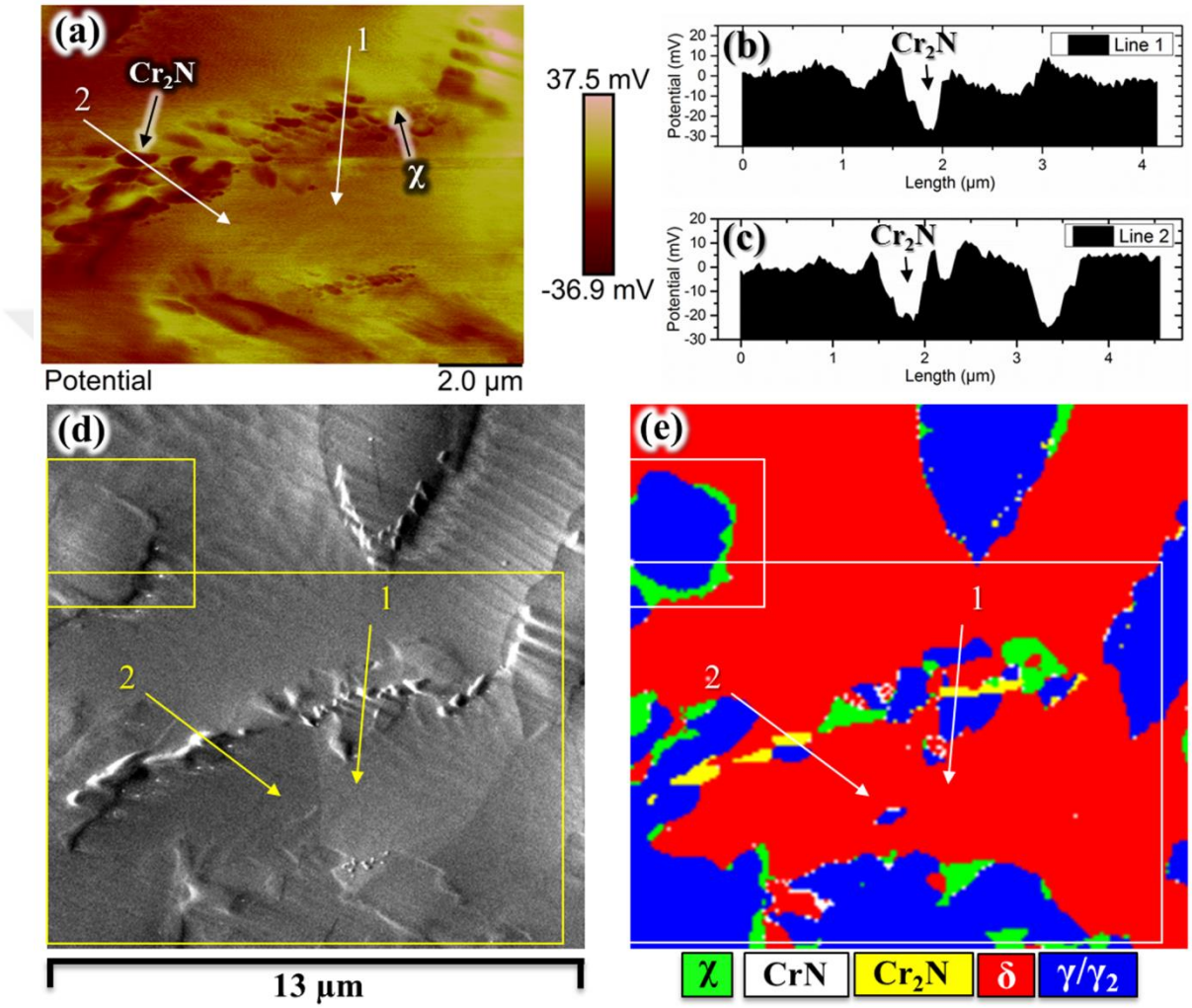

Figure 8-72: Medium-resolution SKPFM analysis of aged microstructure: (a) Volta potential map, (b+c) measured line profiles (1+2) in (a), (d) corresponding SEM image, and (e) corresponding EBSD phase map. The large highlighted area in (e) shows the SKPFM measured region in (a).

Figure 8-72 gives the Volta potential with corresponding EBSD map of an area containing intermetallic phases, showing numerous discrete regions with low and high potential variations and gradients. The line profile 1 in Figure 8-72(a+b+e) shows that Cr_2N precipitates have the lowest Volta potential followed by austenite regions, with the latter possibly secondary austenite. This indicates low electronic activity of these phases. However, large potential gradients were found surrounding Cr_2N precipitates which gives

an indication of local micro-galvanic cells with enhanced electronic coupling activity. Such large gradients adjacent to second phase precipitates are indicative of element depletion zones; hence, the adjacent regions often form local anodes. Cr_2N has been reported to contain higher Cr concentrations than CrN and χ, most likely resulting in concentration gradients during thermal treatments [11, 36]. Volta potential gradients measured adjacent to CrN and χ precipitates were far lower than those measured adjacent to Cr_2N. *Sathirachinda et al.* investigated the effect of thermally treated microstructure of grades 2205 and 2507 duplex stainless steel with SKPFM [13], measuring potential difference of 10-15 mV between γ and Cr_2N with respect to a Pt-Ir tip. The study concluded that Cr_2N have the highest practical nobility in the microstructure, which would mean net cathodic behaviour, in line with our observations.

The χ-phase showed variations of its electronic behaviour over different areas, with some regions indicating net cathodic activity, whereas others showed net anodic character as can be seen in Figure 8-72(a+e). The χ-phase at δ/γ boundaries was denoted as 'interphase/intergranular-χ' (IP-χ) and the χ-phase within ferrite labelled as 'in-ferrite/intragranular-χ' (IF-χ). The IP-χ had more net cathodic character, whilst IF-χ seemed to be net anodic, suggesting that they have different chemical composition, with the IP-χ phase probably more enriched in Cr and Mo. However, the potential gradients adjacent to IP-χ were far steeper than those observed surrounding IF-χ, indicating the presence of depletion effects.

High resolution Volta potential mapping was therefore performed on a region containing γ/γ_2, χ-phase, and CrN (Figure 8-73). Small finger-like, globular features were apparent which were indexed by EBSD as CrN precipitates and shown in Figure 8-73(e+f). The CrN particles were next to χ-phase precipitates, embedded in the ferrite. Line profile measurements across the CrN precipitates showed a potential difference of 5-10 mV higher than the surrounding ferrite phase, with the depleted areas around these precipitates indicating 5-6 mV lower potentials than the ferrite. This clearly indicated that depleted regions would behave net anodic, whilst the CrN would behave net cathodic with respect to the ferrite phase. The IP-χ in Figure 8-73 had 30-40 mV larger Volta potentials than the IF-χ shown in Figure 8-72 despite their comparable dimensions. This potential difference supported different chemical compositions of this phase. Seemingly, the cathodic character was not only limited to the χ-phase.

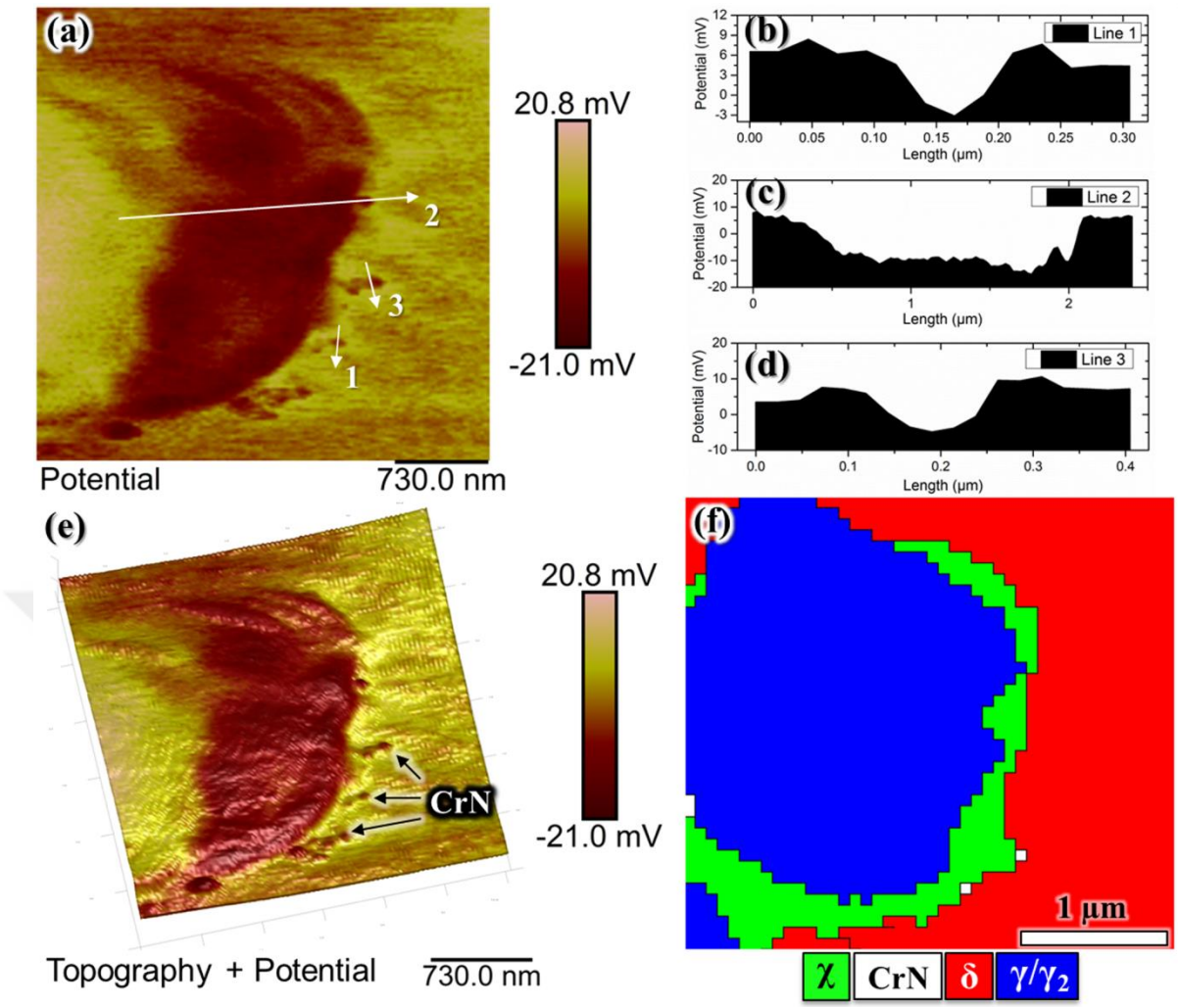

Figure 8-73: High resolution SKPFM analysis of an area containing interphase χ (IP-χ) and CrN: (a) Volta potential map, (b-d) measured line profiles (1,2,3 in (a)), (e) 3D height map overlaid with Volta potential data, and (f) corresponding EBSD map.

The potential differences measured over all crystallographic phases is summarised in Figure 8-74. The Cr_2N phase showed the largest net cathodic behaviour, together with σ and IP-χ. The IF-χ phase showed net anodic properties while the IP-χ phase was more cathodic. Therefore, both χ-phase compositions are expected to behave differently. The nobility of CrN seemed to lie in-between the matrix phases and most other secondary phases. Volta potential values of ferrite and austenite had large scatters, with ferrite showing slightly more net anodic character than austenite. The scatter is partly due to large micro-galvanic activities observed within both matrix phases.

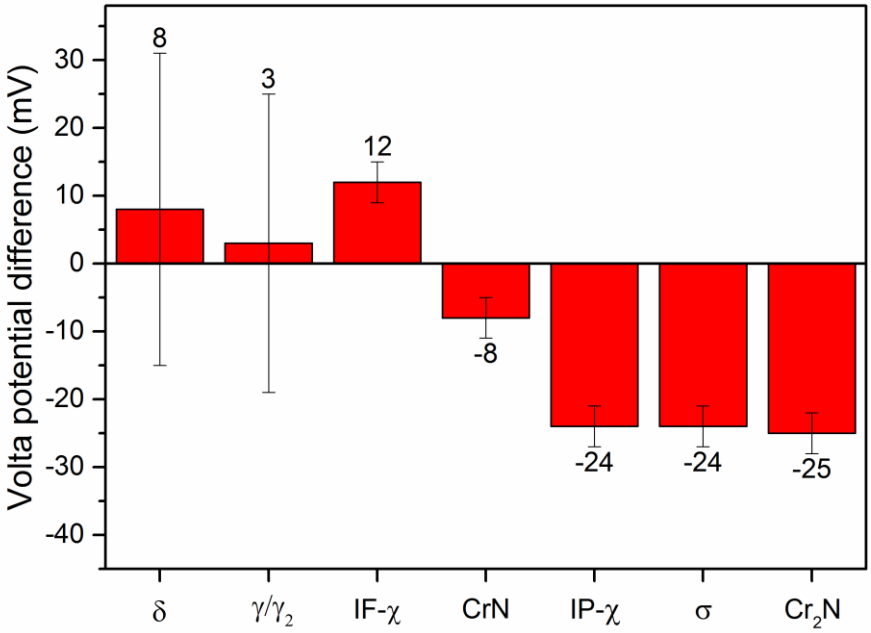

Figure 8-74: Comparison of relative Volta potential differences of all observed phases after ageing in descending order from left (ferrite) to right (Cr_2N).

8.6.4.3 Stress Corrosion Cracking Screening Tests

8.6.4.3.1 As-received Microstructure

The as-received mini-tensile specimen dosed with 1450 µg/cm² $MgCl_2$ was exposed to 50°C and 30% RH, and after removing and cleaning the sample substantial corrosion attack was observed, which can be seen in Figure 8-75(a). Primarily the ferrite was corroded under the droplet deposit with some minor corrosion observed on the austenite. The same corrosion pattern has previously been reported under similar exposure conditions [45, 63, 64], with ferrite clearly the electrochemically more active phase leading to selective dissolution [17, 18, 44, 45, 56, 64-72]. The ferrite phase is, usually, the electrochemically more active phase in 2205 duplex stainless steel due to its lower corrosion potential in contrast to the austenite in mild chloride-bearing environments, leading to micro-galvanic coupling between ferrite and austenite [66, 70, 73]. Selective corrosion of the ferrite, therefore, is often manifested as the main corrosion mechanism while the austenite is galvanically protected [17, 63, 72, 74-77].

High-resolution SEM assessment confirmed the presence of localised attack in the form of superficial sub-micrometre sized intragranular corrosion pits on the austenite, with typical

images shown in Figure 8-75(b+e). The attack on the austenite seemed to be related to slip bands and strain. The evolution of strain localisation in correlation with the development of local Volta potential extremes in austenite leading to enhanced propensity to localised corrosion with the introduction of cold deformation was earlier demonstrated [45]. Pitting corrosion on the austenite tended to suppress the selective dissolution of the ferrite. Seemingly, heterogeneous nucleation of numerous discrete corrosion pits on the austenite indicated those sites as more susceptible, possibly associated with strain localisation.

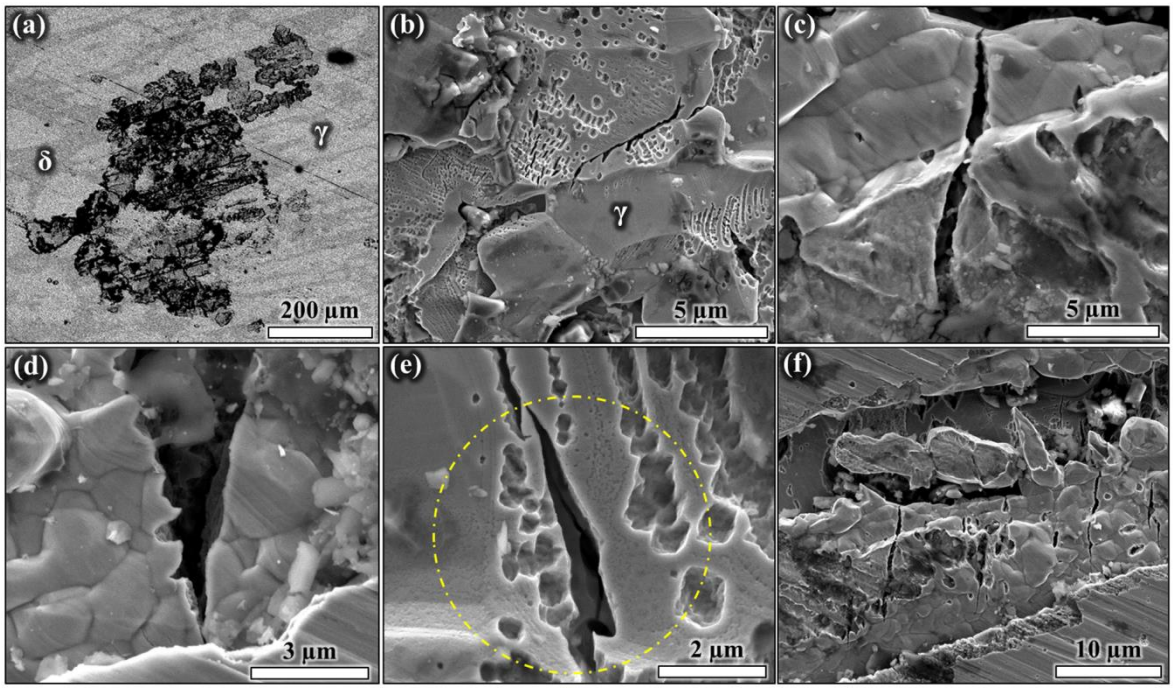

Figure 8-75: Corrosion morphology of as-received microstructure after exposure to 1450 µg/cm² $MgCl_2$ showing (a) the entire corroded area, (b) localised intra-granular corrosion attack on austenite, (c-d) stress corrosion micro-cracks on austenite, (e) multiple corrosion sites on austenite with a crack inside a crack (within the highlighted area), (f) selectively dissolved ferrite regions with multiple cracks on austenite. The stress acted along the horizontal direction.

Some stress corrosion micro-cracks were also found in the austenite, oriented perpendicular to the applied stress direction (stress acted horizontal in Figure 8-75(c,e,f)). The longest crack observed was less than 15 µm in length. Nucleation sites of cracks within existing cracks were also found, suggesting that some cracks may have stifled and stopped growing, before conditions for re-nucleating inside existing cracks were satisfied again. This is different to the classic stress corrosion cracking theory where cracks propagate with discrete steps. Figure 8-75(e) shows features related to crack nucleation inside an existing crack.

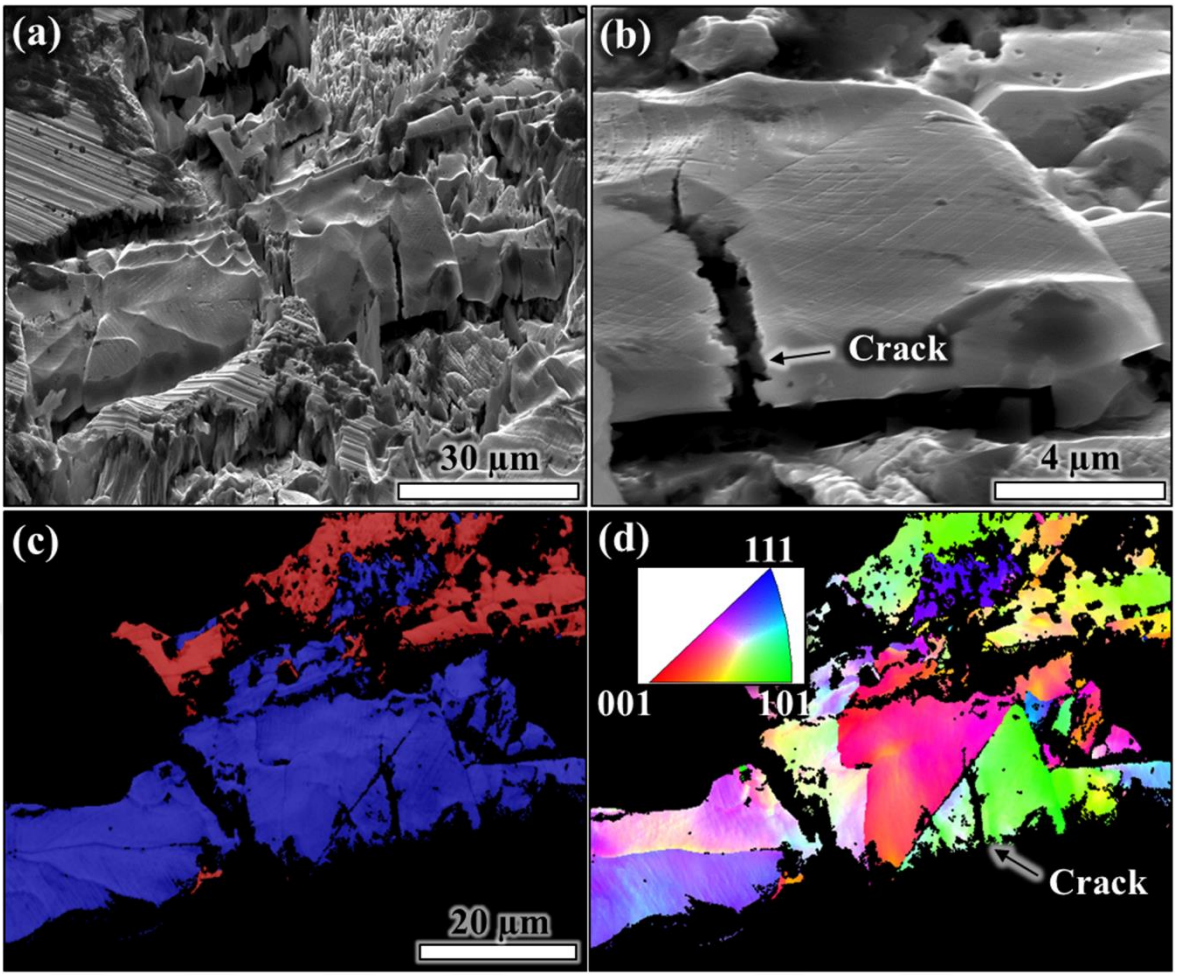

Figure 8-76: Corrosion morphology of as-received microstructure: (a) selective corrosion of ferrite (partially dissolved only) and (b) selective stress corrosion cracking of austenite with (c) corresponding EBSD phase map overlapped with band contrast map (austenite is blue and ferrite is red coloured), and (d) corresponding inverse pole figure map in x direction. Step size = 135 nm.

Retardation effects may have played an important part in crack development, for example, when the crack encounters γ/γ grain boundaries or δ/γ interphase boundaries. The stress corrosion micro-cracks observed were all transgranular in nature, and located in the austenite phase, as concluded from EBSD analysis seen in Figure 8-76. Slip planes are easily noticed from SEM images, which play an active role in crack nucleation and growth. The crack in Figure 8-76 initiated on a grain with close ⟨101⟩ orientation and grew towards the grain interior before changing its direction slightly after encountering a boundary. A difference in crack opening is also observed with the crack wide open on one side of the grain boundary, and more tightly closed on the other.

8.6.4.3.2 Heat-treated Microstructure

Figure 8-77(a) shows the specimen aged at 750°C and exposed to 14.5 µg/cm^2 chloride for 259 days. Minor corrosion attack was only observed located at interphases and on the austenite, with some attack around secondary phases. Increasing the chloride concentration resulted in more severe attack as can be seen with a deposition density of 1450 µg/cm^2 chloride (drop 3) in Figure 8-77(b). The attacked area and corroded volume of the 750°C aged sample was significantly larger than that observed on the as-received specimen exposed with equivalent deposition density of chloride in Figure 8-75(a). However, no evidence for stress corrosion micro-cracking was found in these specimens. Stress corrosion cracking can only occur when the corrosion rate and crack velocity in that corrosion system have similar order of magnitude, but when corrosion reactions advance too fast, then crack nucleation and propagation is hindered.

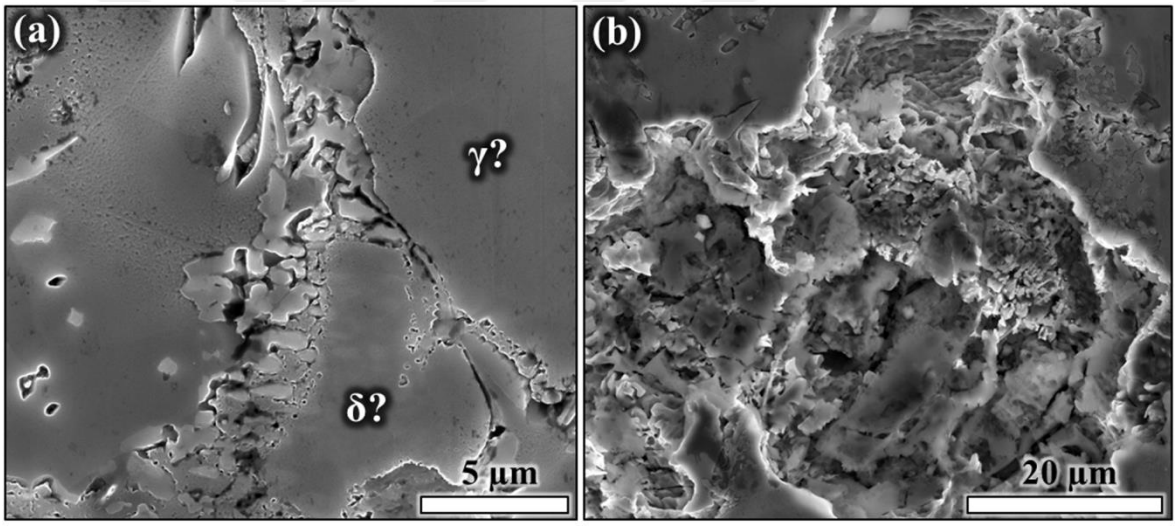

Figure 8-77: Corrosion morphology of the aged specimen with 1% elastic-plastic strain after 259 days exposure at 50°C and 30% RH: (a) minor corrosion attack under drop 1 (14.5 µg/cm²) and (b) corrosion area under drop 3 (1450 µg/cm²).

The corrosion morphology of the aged sample after exposure to 145 µg/cm² chloride (drop 2) indicated selective corrosion of the ferrite. However, high-resolution SEM analysis showed that selective corrosion of ferrite with some attack on the austenite occurred, summarised in Figure 8-78(a+b). The σ-phase often remained in corroded regions, clearly indicating its net cathodic character, whereas ferrite and austenite were attacked, indicating their more net anodic character. In Figure 8-78(b), however, secondary austenite remained unaffected after the corrosion test, indicated by the characteristic shape. A large number of

smaller, discrete precipitates can also be seen and these observations are in good agreement with the earlier Volta potential assessments, where such precipitates were measured to be net cathodic (Figure 8-74). Thus, these precipitates are assumed to be Cr_2N, χ, and possible CrN on basis of their Volta potential response and morphological appearance.

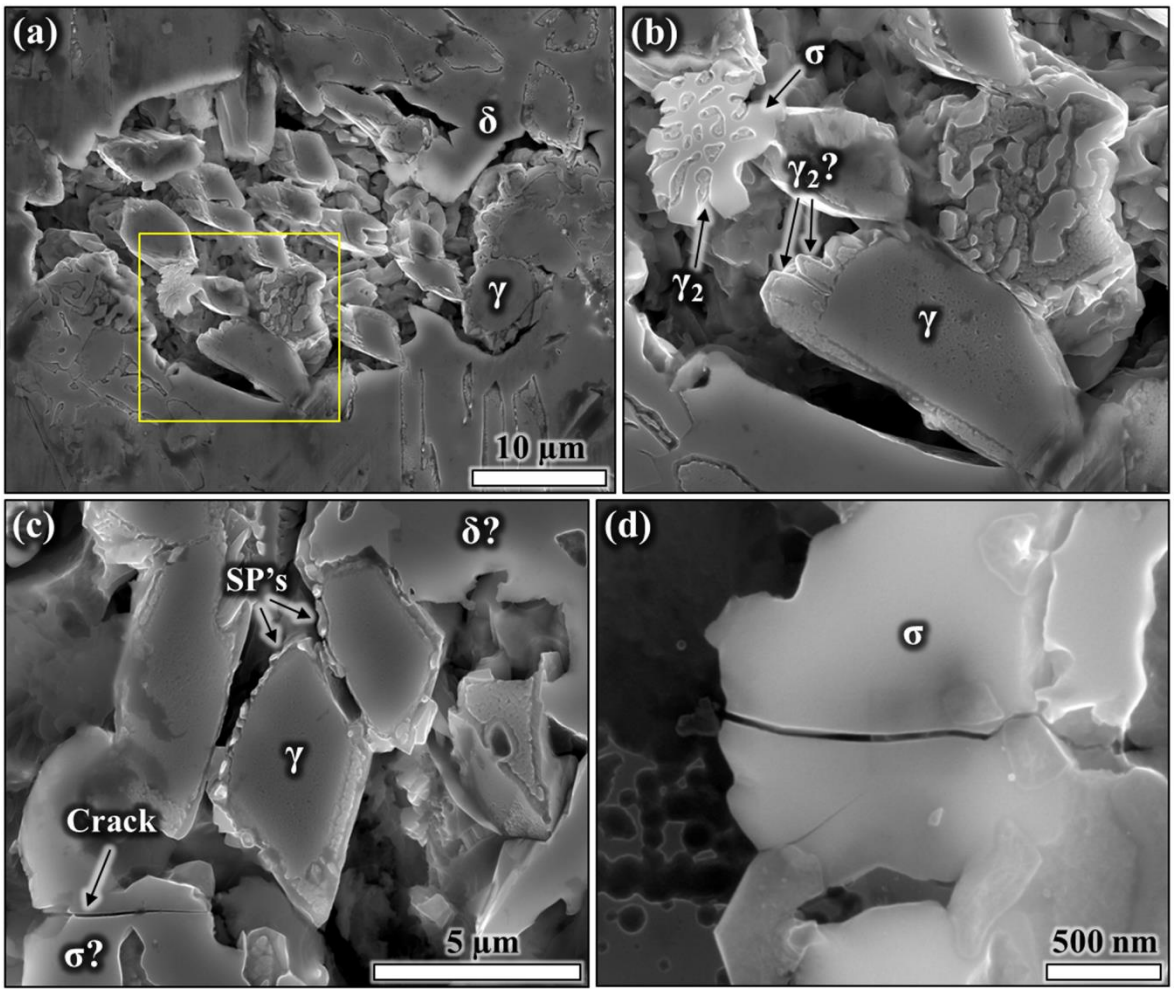

Figure 8-78: Corrosion morphology of the aged sample under drop 2 (145 µg/cm²) with (a) a corroded area, (b) higher resolution image of the highlighted box in (a), (c) selective dissolution of the ferrite with remainders of secondary phases, and cracked σ, and (d) fracture in σ phase.

A large σ-phase precipitated with a transgranular crack was also found, shown in Figure 8-78(c+d). A number of smaller cracks were also found, all located in the σ-phase indicating its brittleness and susceptibility to cracking. The presence of these cracks indicates an increased microstructure crack nucleation propensity, which was clearly enhanced by the presence of the brittle σ-phase in the microstructure.

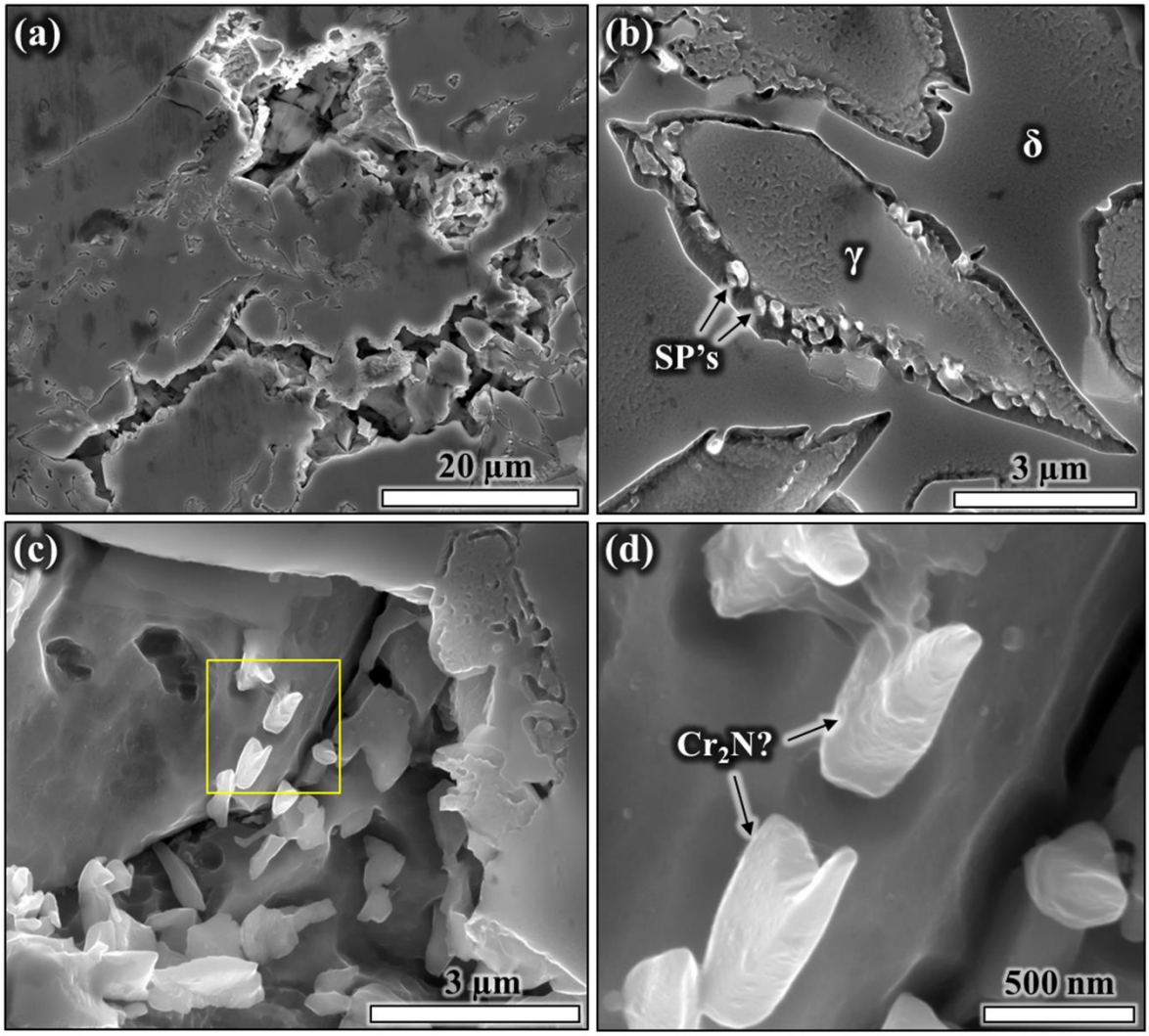

Figure 8-79: Corrosion morphology of the aged sample under drop 4 (2472 µg/cm²) with (a) selective corrosion of the ferrite, (b) selective attack along interphases with remaining secondary phases, (c+d) corrosion along interphase boundary regions with remaining secondary phases (possibly Cr_2N).

The corrosion morphology under a chloride deposition density of 2472 µg/cm² (drop 4) is shown in Figure 8-79(a). Selectively corroded ferrite regions can clearly be seen indicating the net anodic character during the corrosion process. Several corroded regions located along δ/γ interphases are also shown in Figure 8-79(b), decorated with secondary phases (SP) that seemed almost unaffected by the corrosion process, supporting their net cathodic behaviour. Their discrete shape and morphology indicated that these secondary phases are possibly Cr_2N, χ, and/or CrN (Figure 8-79(c+d)).

The same corrosion morphology as with exposure to lower chloride deposition densities was observed under the droplet containing 2856 µg/cm² chloride (drop 5), showing selective attack on the ferrite with minor attack on the austenite, as can be seen in Figure 8-80(a+b).

The most severe corrosion was observed under this droplet, due to largest deposition density, which in turn affects the corrosion potential. A large number of transgranular stress corrosion micro-cracks were observed in areas containing σ-phase and austenite.

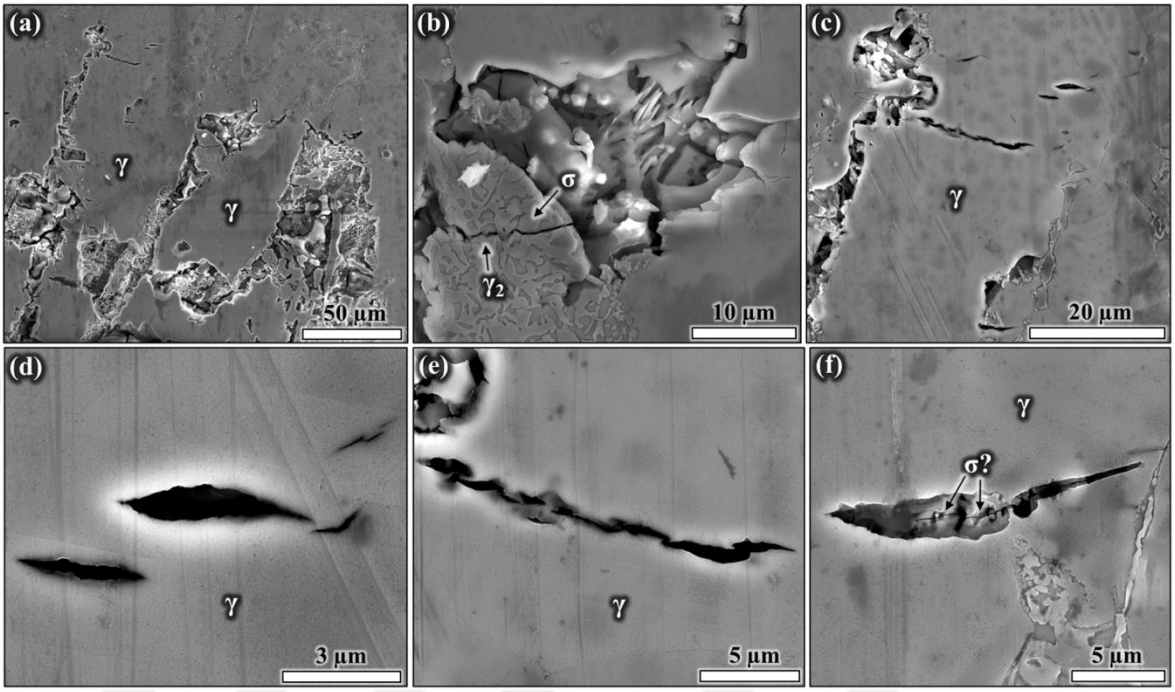

Figure 8-80: Corrosion morphology of the aged sample under drop 5 (2856 µg/cm²) with (a) selective corrosion of the ferrite and some attack on austenite, (b) transgranular cracks through an area containing σ-phase and austenite, (c-f) multiple micro-cracks nucleated within austenite.

The austenite is susceptible to stress corrosion cracking due to its critical nickel content which was determined to be in the order of 7% (see Table 8-7) [78]. The Copson-curve shows lowest time to failure, i.e. highest stress corrosion cracking susceptibility for chloride-induced stress corrosion cracking of stainless steels with nickel contents between ~7 to ~15% [78]. Stress corrosion micro-cracks were observed in regions containing secondary austenite and σ-phase as shown in Figure 8-80(b), a region eutectoidically transformed from ferrite. Secondary austenite is depleted in Cr, Mo, and N and therefore more prone to corrosion. The nickel content of secondary austenite is somewhat lower than that of primary austenite [30], and the cracking susceptibility may have been enhanced by the presence of sigma phase. Multiple stress corrosion cracking events were also seen in the primary austenite as summarised in Figure 8-80(c-f), with maximum length of cracks in the aged microstructure of up to 30-35 µm, spanning across several grains. The latter confirms stress corrosion

cracking propensity of aged sample when exposed to environment with extremely high chloride concentrations.

8.6.4.3.3 Practical Relevance

Grade 2205 duplex stainless steel in the as-received condition is typically resistant to localised corrosion and stress corrosion cracking and the material only shows propensity towards corrosion and micro-cracking with exposure to harsh environmental conditions, such as the high chloride concentrations used in Figure 8-75.

High deposition densities of chloride in high concentrations (close to deliquescence equilibrium of $MgCl_2$) led to a maximum crack length of 15 µm, which showed minor stress corrosion cracking propensity of the as-received material. Grade 2205 duplex stainless steel has superior stress corrosion cracking resistance to the most common austenitic counterpart alloys 304L and 316L which showed more severe crack developments in similar (or under less aggressive) conditions [74-76, 79-84]. The 750°C-aged microstructure, however, was clearly more susceptible to localised corrosion and stress corrosion cracking, which may have implications for welding practice of duplex stainless steels. Grade 2205 duplex stainless steel can be rendered susceptible to AISCC at a temperature of 50°C, and the calculated threshold temperature (>50°C) for AISCC in grade 2205 should re-visited under $MgCl_2$ exposure conditions [75].

8.6.5 Conclusions

The effect of 750°C ageing treatment on microstructure development using correlative EBSD and SKPFM techniques has been investigated. The crystallographic phases present were correlated to their local Volta potentials and corrosion behaviours.

1) CrN, Cr_2N, χ-, σ-, and secondary austenite (γ_2) phases precipitated in the microstructure with γ_2 and σ forming the largest secondary phases in size and fraction. The formation of σ, γ_2, and χ was allotriomorphic, with the σ-phase showing no internal grain boundaries.
2) The σ-phase and γ_2 precipitated within ferrite and at δ/γ interfaces, and χ-phase at δ/γ interfaces only, whilst CrN/Cr_2N was found at δ/γ and σ/γ_2 interfaces and δ/δ boundaries.

3) The as-received microstructure showed 50-70 mV Volta potential differences with δ acting as net anode and γ as net cathode. The Volta potential difference between δ and γ after ageing treatment decreased in certain regions, but Volta potential variations within each phase increased. Local Volta potential extremes were developed indicating enhanced corrosion susceptibility.
4) The σ-phase, Cr_2N, CrN, and inter-granular (IP) χ-phase indicated low electronic activities, i.e. expecting net cathodic behaviour, whilst the intra-granular (IF) χ-phase indicated only enhanced net anodic activity among secondary phases.
5) Selective corrosion of the ferrite was observed in the as-received and the 750°C-aged condition, with the overall corrosion propensity of secondary phases being in-line with SKPFM observations
6) Stress corrosion micro-cracks were found in the austenitic phase in the as-received and 750°C heat-treated conditions after exposure to atmospheric $MgCl_2$ electrolyte.

8.6.6 Acknowledgement

The authors acknowledge Radioactive Waste Management (RWM) (NPO004411A-EPS02) and EPSRC (EP/I036397/1) for financial support. The authors are grateful for the kind provision of Grade 2205 Duplex Stainless Steel plate by Rolled Alloys. Special thanks also to Dr Christiano Padovani, Radioactive Waste Management Ltd. for valuable discussions.

8.6.7 References

[1] C. Padovani. Overview of UK research on the durability of container materials for radioactive wastes, Corrosion Engineering, Science and Technology 49 (2014) 402-409.

[2] K.H. Lo et al. Recent developments in stainless steels, Materials Science and Engineering R 65 (2009) 39-104.

[3] Lula et al. Duplex Stainless Steels, American Society for Metals, Mars, Pennsylvania, 1983.

[4] J. Charles, S. Bernhardsson. Duplex Stainless Steels '91 - Volume 1. In: Duplex Stainless Steels '91. Beaune, Bourgogne, France: Les editions de physique, 1991.

[5] A. Redjaïmia et al. Microstructural and analytical study of heavily faulted Frank-Kasper R-phase precipitates in the ferrite of a duplex stainless steel, Journal of Materials Science 37 (2002) 4079-4091.

[6] S.-H. Byun et al. Kinetics of Cr/Mo-rich precipitates formation for 25Cr-6.9Ni-3.8Mo-0.3N super duplex stainless steel, Met. Mater. Int. 18 (2012) 201-207.

[7] H.M. Chung. Spinodal decomposition of austenite in long-term-aged duplex stainless steel. 1989. p.Medium: X; Size: Pages: 25.

[8] F.A. Garner et al. Ion-induced spinodal-like decomposition of Fe-Ni-Cr invar alloys, Nuclear Instruments and Methods in Physics Research Section B: Beam Interactions with Materials and Atoms 16 (1986) 244-250.

[9] W. Horvath et al. Microhardness and microstructure of austenite and ferrite in nitrogen alloyed duplex steels between 20 and 500°C, Materials Science and Engineering: A 256 (1998) 227-236.

[10] A.F. Padilha, P.R. Rios. Decomposition of Austenite in Austenitic Stainless Steels, ISIJ International 42 (2002) 325-327.

[11] J. Liao. Nitride Precipitation in Weld HAZs of a Duplex Stainless Steel, ISIJ International 41 (2001) 460-467.

[12] A.J. Ramirez et al. Secondary austenite and chromium nitride precipitation in simulated heat affected zones of duplex stainless steels, Science and Technology of Welding and Joining 9 (2004) 301-313.

[13] N. Sathirachinda et al. Study of nobility of chromium nitrides in isothermally aged duplex stainless steels by using SKPFM and SEM/EDS, Corrosion Science 52 (2010) 179-186.

[14] D. Bruch. Investigations on Microstructure, Mechanical Properties and Corrosion Resistance of Large Thickness Duplex Stainless Steel Forgings. Stainless Steel World. Maastricht (NL): KCI Word Publishing, 2007.

[15] D. Bruch et al. Mechanical Properties and Corrosion Resistance of Duplex Stainless Steel Forgings with Large Wall Thicknesses, La Metallurgia Italiana (2008) 1-7.

[16] J.O. Nilsson. Super duplex stainless steels, Materials Science and Technology 8 (1992) 685-700.

[17] C. Örnek, D.L. Engelberg. Effect of "475°C Embrittlement" on the Corrosion Behaviour of Grade 2205 Duplex Stainless Steel Investigated Using Local Probing Techniques. Corrosion Management. Northampton, UK: The Institute of Corrosion, 2013. p.9-11.

[18] C. Örnek et al. Effect of 475°C Embrittlement on Microstructure Development and Mechanical Properties of Grade 2205 Duplex Stainless Steel. In preparation.

[19] S.S.M. Tavares et al. 475°C Embrittlement in a duplex stainless steel UNS S31803, Materials Research 4 (2001) 237-240.

[20] C.-J. Park, H.-S. Kwon. Effects of aging at 475 °C on corrosion properties of tungsten-containing duplex stainless steels, Corrosion Science 44 (2002) 2817-2830.

[21] F. Iacoviello et al. Effect of "475 °C embrittlement" on duplex stainless steels localized corrosion resistance, Corrosion Science 47 (2005) 909-922.

[22] I. Calliari et al. Measuring secondary phases in duplex stainless steels, JOM Journal of the Minerals, Metals and Materials Society 61 (2009) 80-83.

[23] H.-S. Cho, K. Lee. Effect of cold working and isothermal aging on the precipitation of sigma phase in 2205 duplex stainless steel, Materials Characterization 75 (2013) 29-34.

[24] J.W. Elmer et al. Direct Observations of Sigma Phase Formation in Duplex Stainless Steels Using In-Situ Synchrotron X-Ray Diffraction, Metall and Mat Trans A 38 (2007) 464-475.

[25] C.-C. Hsieh, W. Wu. Overview of Intermetallic Sigma () Phase Precipitation in Stainless Steels, ISRN Metallurgy 2012 (2012) 16.

[26] J. Michalska, M. Sozańska. Qualitative and quantitative analysis of σ and χ phases in 2205 duplex stainless steel, Materials Characterization 56 (2006) 355-362.

[27] J.O. Nilsson et al. Mechanical properties, microstructural stability and kinetics of σ-phase formation in 29Cr-6Ni-2Mo-0.38N superduplex stainless steel, Metall and Mat Trans A 31 (2000) 35-45.

[28] J.-O. Nilsson, G. Chai. The physical metallurgy of duplex stainless steels. International Conference & Expo Duplex 2007. Grado, Italy: Associazone Italiana Di Metallurgia, 2007.

[29] J.-O. Nilsson, P. Liu. Aging at 400–600°C of submerged arc welds of 22Cr–3Mo–8Ni duplex stainless steel and its effect on toughness and microstructure, Materials Science and Technology 7 (1991) 853-862.

[30] A.F. Padilha et al. Chi-phase precipitation in a duplex stainless steel, Materials Characterization 60 (2009) 1214-1219.

[31] M. Pohl et al. Effect of intermetallic precipitations on the properties of duplex stainless steel, Materials Characterization 58 (2007) 65-71.

[32] H. Sieurin, R. Sandström. Sigma phase precipitation in duplex stainless steel 2205, Materials Science and Engineering 444 (2007) 271-276.

[33] J. Cui et al. Degradation of Impact Toughness due to Formation of R Phase in High Nitrogen 25Cr-7Ni-Mo Duplex Stainless Steels, ISIJ International 41 (2001) 192-195.

[34] L. Karlsson et al. Precipitation of Intermetallic Phases in 22% Cr Duplex Stainless Weld Metals - The kinetics of intermetallic phase formation in the temperature range 675°-1000°C (1247°-1832°F) and effects on mechanical properties and corrosion resistance, American Welding Society (1995).

[35] A. Redjaïmia et al. Orientation Relationships between the δ-ferrite Matrix in a Duplex Stainless Steel and its Decomposition Products: the Austenite and the χ and

R Frank-Kasper Phases. In: EMC 2008 14th European Microscopy Congress 1–5 September 2008, Aachen, Germany. Springer Berlin Heidelberg, 2008. pp. 479-480.

[36] N. Pettersson et al. Precipitation of Chromium Nitrides in the Super Duplex Stainless Steel 2507, Metall and Mat Trans A 46 (2015) 1062-1072.

[37] A.J. Ramirez et al. The relationship between chromium nitride and secondary austenite precipitation in duplex stainless steels, Metall and Mat Trans A 34 (2003) 1575-1597.

[38] J. Charles, S. Bernhardsson. Duplex Stainless Steels '91 - Volume 2. In: Duplex Stainless Steels '91. Beaune, Bourgogne, France: Les editions de physique, 1991.

[39] F.J. Humphreys. Characterisation of fine-scale microstructures by electron backscatter diffraction (EBSD), Scripta Materialia 51 (2004) 771-776.

[40] W. Li et al. Influences of tensile strain and strain rate on the electron work function of metals and alloys, Scripta Materialia 54 (2006) 921-924.

[41] W. Li, D.Y. Li. Influence of surface morphology on corrosion and electronic behavior, Acta Materialia 54 (2006) 445-452.

[42] J.O.M. Bockris et al. Modern Electrochemistry 2A. Fundamentals of Electrodics, vol. 2A. New York: Kluwer Academic Publishers, 2002. p.1-817.

[43] S. Sadewasser, T. Glatzel. Kelvin Probe Force Microscopy Measuring and Compensating Microscopy, Springer, Heidelberg, 2012.

[44] C. Örnek et al. A Corrosion Model for 475°C Embrittlement in Duplex Stainless Steel – a Comprehensive Study via Scanning Kelvin Probe Force Microscopy. Corrosion Science. Submitted.

[45] C. Örnek, D.L. Engelberg. SKPFM Measured Volta Potential Correlated with Strain Localisation in Microstructure of Cold-rolled Grade 2205 Duplex Stainless Steel, Corrosion Science 99 (2015) 164-171.

[46] N. Sathirachinda et al. Characterization of Phases in Duplex Stainless Steel by Magnetic Force Microscopy/Scanning Kelvin Probe Force Microscopy, Electrochemical and Solid-State Letters 11 (2008) C41-C45.

[47] N. Sathirachinda et al. Depletion effects at phase boundaries in 2205 duplex stainless steel characterized with SKPFM and TEM/EDS, Corrosion Science 51 (2009) 1850-1860.

[48] N. Sathirachinda et al. Scanning Kelvin probe force microscopy study of chromium nitrides in 2507 super duplex stainless steel—Implications and limitations, Electrochimica Acta 56 (2011) 1792-1798.

[49] D.B. Blücher et al. Scanning Kelvin Probe Force Microscopy: A Useful Tool for Studying Atmospheric Corrosion of MgAl Alloys In Situ, Journal of The Electrochemical Society 151 (2004) B621-B626.

[50] M. Rohwerder, F. Turcu. High-resolution Kelvin probe microscopy in corrosion science: Scanning Kelvin probe force microscopy (SKPFM) versus classical scanning Kelvin probe (SKP), Electrochimica Acta 53 (2007) 290-299.

[51] R. Wang et al. Changes of work function in different deformation stage for 2205 duplex stainless steel by SKPFM, Procedia Materials Science 3 (2014) 1736-1741.

[52] F.J. Humphreys et al. Electron backscatter diffraction of grain and subgrain structures — resolution considerations, Journal of Microscopy 195 (1999) 212-216.

[53] G.S. Frankel et al. Characterization of Corrosion Interfaces by the Scanning Kelvin Probe Force Microscopy Technique, Journal of The Electrochemical Society 148 (2001) B163-B173.

[54] M. Nonnenmacher et al. Kelvin probe force microscopy, Applied Physics Letters 58 (1991) 2921-2923.

[55] P. Marcus, F. Mansfeld. Analytical Methods in Corrosion Science and Engineering, Taylor & Francis Group, Boca Raton, FL, USA, 2006.

[56] D.L. Engelberg, C. Örnek. Probing propensity of grade 2205 duplex stainless steel towards atmospheric chloride-induced stress corrosion cracking, Corrosion Engineering, Science and Technology 49 (2014) 535-539.

[57] E.M.L.E.M. Jackson et al. Distinguishing between Chi and Sigma phases in duplex stainless steels using potentiostatic etching, Materials Characterization 31 (1993) 185-190.

[58] J.J. Shiao et al. Phase transformations in ferrite phase of a duplex stainless steel aged at 500°C, Scripta Metallurgica et Materialia 29 (1993) 1451-1456.

[59] H. Li et al. Austenite Transformation Behaviour of 2205 Duplex Stainless Steels under Hot Tensile Test, steel research international 86 (2015) 84-88.

[60] H. Liu, X. Jin. Electrochemical corrosion behavior of the laser continuous heat treatment welded joints of 2205 duplex stainless steel, J. Wuhan Univ. Technol.-Mat. Sci. Edit. 26 (2011) 1140-1147.

[61] E. Bettini et al. Study of Corrosion Behavior of a 2507 Super Duplex Stainless Steel: Influence of Quenched-in and Isothermal Nitrides, International Journal of Electrochemical Science 9 (2014) 20.

[62] J.-S. Kim et al. Mechanism of Localized Corrosion and Phase Transformation of Tube-to-Tube Sheet Welds of Hyper Duplex Stainless Steel in Acidified Chloride Environments, The Japan Institute of Metals 53 (2012) 9.

[63] C. Örnek, D.L. Engelberg. Effect of Cold Deformation Mode on Stress Corrosion Cracking Susceptibility of 2205 Duplex Stainless Steel. In preparation.

[64] C. Örnek, D.L. Engelberg. Environment-Assisted Stress Corrosion Cracking of Grade 2205 Duplex Stainless Steel Under Low-temperature Atmospheric Exposure. In preparation.

[65] N. Arnold et al. Chloridinduzierte Korrosion von Nichtrostenden Stählen in Schwimmhallen-Atmosphären Teil 1: Elektrolyt Magnesium-Chlorid (30%), Materials and Corrosion 48 (1997) 679-686.

[66] S. Aoki et al. Dissolution Behavior of α and γ Phases of a Duplex Stainless Steel in a Simulated Crevice Solution, ECS Transactions 25 (2010) 17-22.

[67] M. Femenia et al. In situ study of selective dissolution of duplex stainless steel 2205 by electrochemical scanning tunnelling microscopy, Corrosion Science 43 (2001) 1939-1951.

[68] R.F.A. Pettersson, J. Flyg. Electrochemical evaluation of pitting and crevice corrosion resistance of stainless steels in NaCl and NaBr. Stockholm, Sweden: Outokumpu, 2004.

[69] B. Deng et al. Critical pitting and repassivation temperatures for duplex stainless steel in chloride solutions, Electrochimica Acta 53 (2008) 5220-5225.

[70] S. Aoki et al. Potential Dependence of Preferential Dissolution Behavior of a Duplex Stainless Steel in Simulated Solution inside Crevice, Zairyo-to-Kankyo 60 (2011) 363-367.

[71] N. Ebrahimi et al. Correlation between critical pitting temperature and degree of sensitisation on alloy 2205 duplex stainless steel, Corrosion Science 53 (2011) 637-644.

[72] C. Örnek, D.L. Engelberg. Kelvin Probe Force Microscopy and Atmospheric Corrosion of Cold-rolled Grade 2205 Duplex Stainless Steel. Eurocorr 2014. Pisa, Italy: European Federation of Corrosion, 2014.

[73] J.-S. Lee et al. Corrosion behaviour of ferrite and austenite phases on super duplex stainless steel in a modified green-death solution, Corrosion Science 89 (2014) 111-117.

[74] T. Prosek et al. Low Temperature Stress Corrosion Cracking of Stainless Steels in the Atmosphere in Presence of Chloride Deposits. NACE corrosion conference paper no. 08484: NACE International, 2008. p.17.

[75] T. Prosek et al. Low-Temperature Stress Corrosion Cracking of Austenitic and Duplex Stainless Steels Under Chloride Deposits, Corrosion Science 70 (2014) 1052-1063.

[76] T. Prosek et al. Low-Temperature Stress Corrosion Cracking of Stainless Steels in the Atmosphere in the Presence of Chloride Deposits, Corrosion Science 65 (2009) 13.

[77] C. Örnek et al. Effect of Microstructure on Atmospheric-Induced Corrosion of Heat-treated Grade 2205 and 2507 Duplex Stainless Steels. Eurocorr 2012. Istanbul, Turkey: Dechema, 2012. p.1-10.

[78] B. Cottis et al. Shreir's Corrosion - Volume 2. Elsevier B.V., Manchester, 2010.

[79] A.B. Cook et al. Preliminary Evaluation of Digital Image Correlation for In-situ Observation of Low Temperature Atmospheric-Induced Chloride Stress Corrosion Cracking in Austenitic Stainless Steels, ECS Transactions 25 (2010) 119-132.

[80] A.B. Cook et al. Assessing the risk of under-deposit chloride-induced stress corrosion cracking in austenitic stainless steel nuclear waste containers, Corrosion Engineering, Science and Technology 49 (2014) 529-534.

[81] S.B. Lyon et al. Atmospheric corrosion of nuclear waste containers. Diamond'10 Conference Decommissioning, Immobilisation and Management of Nuclear Waste for Disposal. Manchester, UK, 2010.

[82] O.E. Albores-Silva et al. Effect of chloride deposition on stress corrosion cracking of 316L stainless steel used for intermediate level radioactive waste containers, Corrosion Engineering, Science and Technology 46 (2011) 124-128.

[83] C. Padovani et al. Corrosion control of stainless steels in indoor atmospheres – laboratory measurements under $MgCl_2$ deposits at constant relative humidity (Part 1), Corrosion 71 (2014) 292-304.

[84] C. Padovani et al. Corrosion control of stainless steels in indoor atmospheres – practical experience (Part 2), Corrosion 71 (2014) 246-266.

9 Summary

The microstructure of grade 2205 duplex stainless steel and the effect of microstructure changes on the propensity of corrosion and environmentally assisted cracking were discussed in detail. Welding and plastic deformation on real ILW containers was simulated using heat-treated and cold-deformed microstructures, and their effect on microstructure development was examined. Overall conclusions are listed in the following:

Effect of Heat Treatment on Microstructure Development and Mechanical Behaviour

- 475°C embrittlement is manifested by phase reactions limited to the ferrite and interphase boundaries, causing spinodal decomposition, R-phase precipitates with formation of secondary phases.
- Spinodal decomposition, consisting of Fe-rich α' and Cr-rich α'', were observed in ferrite with increasing amplitude as a function of ageing time.
- R-phase precipitates with disc or lenticular shape could be detected after 50 hours ageing, which grew further from ~50 nm to 200-400 nm after 255 hours of ageing.
- Macro-, micro-, and nano-indentation measurements showed hardness changes after 255 hours of ageing only, with the ferrite responsible for the increase in hardness.
- Higher yield strengths were observed with increasing degree of 475°C embrittlement, which was associated with a loss of elongation to failure.
- XRD stress measurements revealed a reduction of compressive stresses in both ferrite and austenite as a function of 475°C embrittlement, reaching a balanced microstructure after 255 hours of ageing.
- 750°C embrittlement is manifested by the formation of sigma, chi, chromium nitrides, and secondary austenite in both phases; ferrite and austenite, leading to an entirely decomposed microstructure.
- CrN, Cr_2N, χ-, σ-, and secondary austenite (γ_2) phases precipitated in the microstructure with γ_2 and σ forming the largest secondary phases in size and fraction. The formation of σ, γ_2, and χ was allotriomorphic, with the σ-phase showing no internal grain boundaries.
- The σ-phase and γ_2 precipitated within ferrite and at δ/γ interfaces, and χ-phase at δ/γ interfaces only, whilst CrN/Cr_2N was found at δ/γ and σ/γ_2 interfaces and δ/δ boundaries.

Effect of Cold Deformation on Microstructure Development

- Introduction of any mode of cold deformation caused heterogeneous strain development in the microstructure, with the austenite phase showing intense plastic strain.
- EBSD local misorientation mapping confirmed the presence of multiple heterogeneous strain hot-spots in the microstructure after introduction of any type of cold work (rolling, bending, tensile), with bending deformation showing the highest degree of strain, followed by rolling and tensile deformation.
- Strain localisation in the duplex microstructure did not necessarily lead to stress localisation; the ferrite phase was double more stressed than the austenite for low-level macroscopic strains (0.2%).
- With increasing level of cold work, the austenite enabled the ferrite to accommodate more plastic strain which led to heterogeneous strain fields within ferrite regions.
- High magnitude of strain localisation in the austenite phase was observed in highly deformed microstructure, which increased with the degree of deformation independent from the deformation mode.
- XRD stress measurements revealed substantial tensile stress development with increasing level of cold deformation, with austenite showing higher tensile stresses than ferrite after bending and rolling deformation, while ferrite shows higher stresses than austenite in tensile-deformed microstructure.

Effect of Heat Treatment on Corrosion Behaviour

- An increase in critical pitting temperature was observed for materials short-term aged up to 10 hours at 475°C showing best corrosion performance, followed by a large drop after 255 hours aging showing most severe attack.
- SKPFM Volta potential differences measured over ferrite and austenite correlated well with the observed critical pitting temperature measurements.
- The spinodal decomposed microstructure had Volta potential differences between Cr-rich α'' and Fe-rich α'phase of up to 60 mV, indicating local galvanic coupling.
- The α'' had a higher practical nobility than α' phase, and spinodal decomposition were the reason for corrosion property improvement, with other precipitates causing microstructure degradation.

- SKPFM measured element deletion zones were measured around R-phase precipitates and interface regions.
- SKPFM Volta potential measurements showed 50-70 mV differences between ferrite and austenite in the as-received condition, indicating a driving force for galvanic corrosion, whereas short-term aged microstructure, however, showed balanced Volta potential development between both phases, indicating a significant decrease or even absence of galvanic coupling, hence, enhancement of electrochemical nobility of the entire microstructure.
- The Volta potential values between ferrite and austenite converged with further ageing time and differed up to 700-800 mV after 255 hours of ageing, indicating loss of electrochemical nobility and enhanced susceptibility to corrosion.
- In as-received microstructure, selective dissolution of the ferrite was observed, whereas both ferrite and austenite were attacked in microstructure aged for 10 hours. After 255 hours ageing, ferrite was again selectively dissolved.
- Spinodal decomposition is believed to enhance the corrosion properties for ageing times up to 10 hours, with other precipitates affecting the corrosion resistance due to the formation of elemental depletion zones.
- A mechanistic model to link measured SKPFM potentials in microstructure to the overall corrosion resistance of 475°C embrittled microstructures has been introduced.
- Ageing at 750°C increases the susceptibility to localised corrosion, with the interface regions between precipitates and austenite or austenite phases being the most susceptible sites for nucleation of anodic dissolution processes.
- After ageing at 750°C, most noble phases were σ, chromium nitride (Cr_2N), and intra-granular χ, while elementally depleted zones adjacent to these phases and ferrite and austenite were most reactive and would be expected to corrode preferentially.

Effect of Cold Deformation on Corrosion Behaviour (SKPFM-EBSD)

- Selective dissolution of ferrite in as-received microstructure seemed to become compromised by localised corrosion events caused by cold working, with bending deformation showing the most severe effect, followed by tensile-strained and rolled microstructures, with austenite providing more sites for pitting corrosion than ferrite with the increasing degree of cold work.

- The introduction of 40% cold-rolling significantly reduced the Volta potential difference between ferrite and austenite, but in parallel increased the mean Volta potential difference of the entire microstructure, indicating increased electrochemical reactivity.
- Volta potential maps of the cold-rolled microstructure showed local potential hot-spots (highly active sites at confined regions) with exposure to both 38% and 86% RH environment, indicating corrosion-active sites.
- After 40% cold rolling, localised pitting corrosion in austenite and only little attack on ferrite was observed, supporting changes to the overall corrosion response of the duplex stainless steel microstructure.
- Cold deformation, in general, increased the susceptibility to localised corrosion.

Effect of Cold Deformation on Environmentally Assisted Cracking

- Large local misorientation development associated with strain was observed after bending in rolling direction (RD) and transverse direction (TD), with the latter having 2.5-times greater amplitude
- The bending process in TD affected the structure of ferrite larger than that of austenite, yielding large strain development in ferrite.
- Hardness measurements showed clear increasing behaviour with the degree of 475°C embrittlement and with U-bending processing direction, but to a higher extent of bending in TD than in RD.
- XRD stress measurements confirmed local stress development in ferrite and austenite with ageing time and bending processing, with austenite showing larger stress budgets; ferrite showed an increasing trend of stress with ageing time and austenite showed an opposite behaviour.
- The microstructure was rendered highly susceptible to corrosion and stress corrosion cracking as a function of ageing time at 475°C and bending direction, and most severe cracks were observed after bending in TD, particularly after long-term ageing (>50 hours).
- An increase of corrosion performance was observed on U-bends aged for 5 and 10 hours at 475°C for specimens bent in TD and RD, respectively.

- Good correlation was seen to exist between stress corrosion cracking performance with the overall corrosion resistance in the dependency of ageing time on all specimens bent in RD.
- Stress corrosion cracking was primarily governed by the austenite phase for all deformed microstructures pre-aged up to 50 hours at 475°C, while ferrite showed severe brittle fracture after long-term ageing (255 hours).
- Bending deformation promoted environmentally assisted cracking, with tensile deformation having slightly lower influence, whereas 20-40% cold rolling seemed to be less sufficient to promote cracking.
- The austenite phase became selectively prone to stress corrosion cracking with increasing magnitude of cold work, especially after bending and tensile deformations, whereas rolling deformation enhanced the pitting corrosion propensity only.
- The ferrite phase was less prone to environmentally assisted cracking than the austenite.
- Atmospherically induced stress corrosion cracking tests showed selective corrosion of the ferrite, whereas the austenite showed pits and micro cracks after one year exposure at 50°C, with maximum crack lengths observed in the austenite up to 15 µm.
- Atmospheric environmentally assisted cracking on as received grade 2205 has been observed under salt-laden deposit containing a mixture of $FeCl_3$:$MgCl_2$ with exposure to 50°C and 30% RH for 368 days.
- The area under the droplet was divided into different regions, revealing corrosion of both phases at the anodic center, selective dissolution and hydrogen embrittlement of the ferrite between the center and the rim, with dissolution, pitting/crevice corrosion and chloride-induced stress corrosion cracking of the austenite at the periphery of the droplet.
- Cracks in ferrite and austenite were between 10's of nm to 10's of µm long, with most cracks arrested or diverted by encountering the other phase.
- The observation of different failure morphologies as a function of location within the droplet indicated local variations of electrochemical potentials.

Effect of Heat Treatment on Environmentally Assisted Cracking Behaviour

- The as-received microstructure showed 50-70 mV Volta potential differences with δ acting as net anode and γ as net cathode. The Volta potential difference between δ and γ

after ageing treatment decreased in certain regions, but Volta potential variations within each phase increased. Local Volta potential extremes were developed indicating enhanced corrosion susceptibility.

- The σ-phase, Cr_2N, CrN, and inter-granular (IP) χ-phase indicated low electronic activities, i.e. expecting net cathodic behaviour, whilst the intra-granular (IF) χ-phase indicated only enhanced net anodic activity among secondary phases.
- Selective corrosion of the ferrite was observed in the as-received and the 750°C-aged condition, with the overall corrosion propensity of secondary phases being in-line with SKPFM observations
- Stress corrosion micro-cracks were found in the austenitic phase in the as-received and 750°C heat-treated conditions after exposure to atmospheric $MgCl_2$ electrolyte.

10 Future Work and Legacy Experiments

10.1 Legacy Experiments (in progress)

An experiment to further characterise long-term atmospheric-induced stress corrosion cracking behaviour of duplex and lean duplex stainless steel and to obtain quantitative data has been designed. Micro-tensile specimens have been exposed with low amounts of magnesium chloride (1-1000 µg/cm²) to RT/50°C and 30% RH. Duplex and lean duplex wires have been exposed to 50°C / 30% RH for more than a year and will used for XRT measurements. A manuscript draft has been developed that describes the first part of the experiment, with data from the next scan used to complete this manuscript.

Quasi In-situ Time-dependent Characterisation of Atmospheric-Induced Stress Corrosion Cracking of Duplex Stainless Steels

C. Örnek[1], F. Leonard[2,3], S. McDonald[2], P.J.Withers[2], D.L. Engelberg[1]

[1]Materials and Performance Centre & Corrosion and Protection Centre,
School of Materials, The University of Manchester,
Sackville Street, Manchester, M13 9PL, United Kingdom

[2]Manchester X-ray Imaging Facility,
School of Materials, The University of Manchester,
Sackville Street, Manchester, M13 9PL, United Kingdom

[3]BAM Federal Institute for Materials Research and Testing
Unter den Eichen 87
12205 Berlin, Germany

Abstract

Atmospheric-induced stress corrosion cracking (AISCC) of grades 2202 and 2205 duplex stainless steels was investigated using quasi in-situ x-ray computed tomography analyses. Short wire samples doped with $MgCl_2$ were exposed to 50°C/30% and the development of localised corrosion in 3D assessed, showing significantly higher corrosion rates of grade 2202 compared to the grade 2205 duplex stainless steel. Stress corrosion cracking (SCC) of grade 2205 was observed with an applied load of 550 MPa. The application of a oad around the yield point did not produce SCC in both grades 2202 and 2205. The results are discussed in the framework of prediction models for corrosion and stress corrosion cracking.

Keywords: *Duplex stainless steel; Atmospheric corrosion; Stress corrosion cracking; X-ray computed tomography*

Introduction

Duplex stainless steels (DSS) have a balanced ratio of ferrite and austenite, which provides excellent corrosion and stress corrosion cracking resistance with high yield strength to ductility ratios [1, 2]. The synergism of corrosion inhibition mechanisms in DSS is believed to be responsible for their excellent corrosion resistance [3, 4]. DSS's have become the material of choice in many critical and harsh environments.

Intermediate-level radioactive nuclear waste (ILW) is currently stored in grades 316L/304L austenitic stainless steel containers in above-ground storage facilities in the UK. Storage is anticipated for up to 300 years until a deep-underground geological disposal facility is available [5]. Grade 2205 duplex stainless steel was envisaged as a replacement option for the austenitic grades, due to its better corrosion and stress corrosion resistance [5]. Grade 2205 duplex stainless steel is now also used to manufacture ILW containers and several containers have already been manufactured in the UK [6].

The surface of the containers held in stores may experience chloride-bearing particulates from sea-salt aerosols and/or industrial pollution, which may lead to localised corrosion. Up to >30 μm/cm² of surface chloride deposition has been reported to cumulate in the Culham Warehouse within 10 years, and corrosion pits have been reported on 304L austenitic stainless steel [7]. During the manufacture of the containers bending, forming, and welding may render the material more susceptible to corrosion and AISCC. Atmospheric corrosion and atmospheric-induced stress corrosion cracking data of duplex stainless steels contaminated with low deposition densities at low temperature regimes (≤ 50°C) is not available in the literature. Quantitative assessment of the early stages of damage is required to be able to determine life-time performance of waste containers. State-of-the-art characterisation techniques such as XCT can provide unique information about location, extent, and kinetics of damage. Initial stages of localised and SCC can be visualised and quantified, providing the framework for prediction models.

In this work, lean grade 2202 and grade 2205 duplex stainless steel wires were exposed to 50°C and 30% relative humidity (RH) for up to 12 months. Time-dependent, quasi in-situ characterisation of corrosion kinetics was obtained and the effect of stress on the nucleation of SCC in these wires assessed.

Experimental

Grades 2202 and 2205 duplex stainless steel wires with respectively 500 µm and 630 µm diameter were used in this work (provided by Ugitech SA). The chemical composition of both wires is summarised in Table 10-1. The microstructure of 2202 and 2205 duplex stainless steels was analysed in both process directions, including the drawn/extruded and transverse directions. For metallographic assessment both wires were mounted in a cold mounting epoxy resin and polished to ¼ µm diamond paste polish. The wires were etched using Beraha II etchant (stem solution: 800 ml distilled water, 400 ml hydrochloric acid, and 48 g ammonium hydrogen fluoride; etch solution: 100 ml stem solution + 1 g potassium disulfite) for 10 seconds, which stains the ferrite phase. The microstructure was analysed in an FEI Quanta 650 scanning electron microscope (SEM).

Table 10-1: Chemical composition of the wire materials used

Grade	Name	C	Si	Mn	P	S	Cr	Ni	Mo	N	Cu	Fe
2205	UGI 4462	≤ 0.03	0.75	1-2	≤ 0.035	≤ 0.01	22-23	5-6	3.20	0.12-0.20	-	bal.
2202	UGI 4042	≤ 0.03	≤ 1.0	≤ 2.0	≤ 0.4	≤ 0.01	22.0-23.8	2.0-2.8	≤ 0.45	0.155	≤ 0.5	bal.

Corrosion Cell Calibration

The corrosion cells shown in Figure 10-1 were used for atmospheric-induced SCC testing. An aluminium or 304L stainless steel ring attached with a threaded steel rod was first calibrated for elastic stress and strain behaviour using an Instron 3344 testing machine. A strain gauge was placed on the outside of the ring and connected to a quarter-bridge strain gauge module, which was connected to a PC. Strain calibration and reading was operated by a LabView programme. The ring with the attached rod was then fixated in the Instron testing machine and strained in steps until deformation of the ring was recorded. This allowed determining the maximum elastic strain limit of the ring. Each strain step corresponded to a force value which was recorded by the Instron testing system.

Stress-strain measurements with different strain rates (1-10 mm/seconds) were also performed on both wires to obtain the yield point and deformation behaviour. A wire was then placed into the corrosion cell and manually strained until the yield stress was reached. A total of three in-situ cells containing grade 2202 and grade 2205 wires were set-up. The 2202 wire was strained until it yielded at 700 MPa. One of the 2205 wire was strained slightly higher than its yield point of 900 MPa, with the second 2205 wire strained to 550 MPa.

Corrosion testing

The corrosion cells were immersed into an electrolyte containing 1 M $MgCl_2$ at room temperature to contaminate the surface of the wire with $MgCl_2$. The cells were then removed and placed into a Binder KBF climatically-controlled humidity chamber which was set to 50±1°C and 30±3% relative humidity (RH). Holes on both sides of the cells allowed rapid humidity and temperature conditioning in the cell interior. The cells were taken out in certain time intervals, summarised in Figure 10-7, and assessed for corrosion and stress corrosion cracking evolution using XCT. The cells were removed on the day of scan, and transferred back to the humidity chamber on the next day. For the scans, is is assumed that the corrosion reactions have slowed down (or even stopped) since the environmental temperature did not exceed 20°C with typically far higher RH's value than the delisquesence point of $MgCl_2$ (>30%).

X-ray computed tomography scans

X-ray computed tomography (XRT) scans were performed on the Xradia Versa XRM-500 3D X-ray microscope at the Manchester X-ray Imaging Facility. The parameters used were 145 kV source voltage, 15 seconds exposure time, 4x objective lens, air source filter, 10 W source power, 2x2 binning, 1601 or 2401 projections with a 360° full angle rotation. The field of view was 984 µm giving a resolution of 1 µm (990nm). Reconstruction of the virtual slices was performed on the Xradia system; centre shift and beam hardening coefficient adjustment were performed to achieve best signal to noise quality. All reconstructed files were analysed using Avizo 8.0 software. A median filter was applied for data smoothing. The final voxel resolution was therefore around 1.5 µm, rather than the theoretical resolution. The corrosion area and volume was determined and plotted versus exposure time of the wires in the humidity chamber.

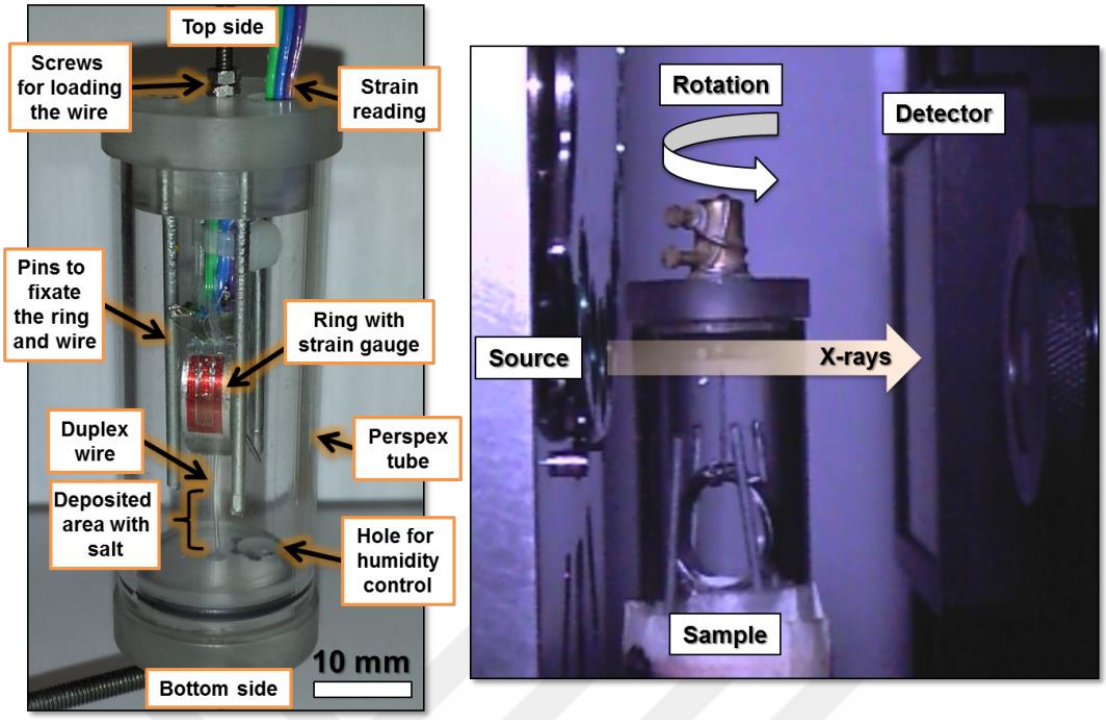

Figure 10-1: Corrosion cell (left image) and X-ray tomography measurement setup with a corrosion cell (right image)

Results and Discussion

Microstructure & Mechanical Behaviour

The microstructure of the drawn wires is shown in Figure 10-2. Both lean and conventional duplex stainless steel wires had similar microstructural appearance. Austenite and ferrite grains were elongated along the drawing direction as shown in Figure 10-2(a). The phase ratio of ferrite and austenite was approximately 50:50 and a fine grain structure was apparent.

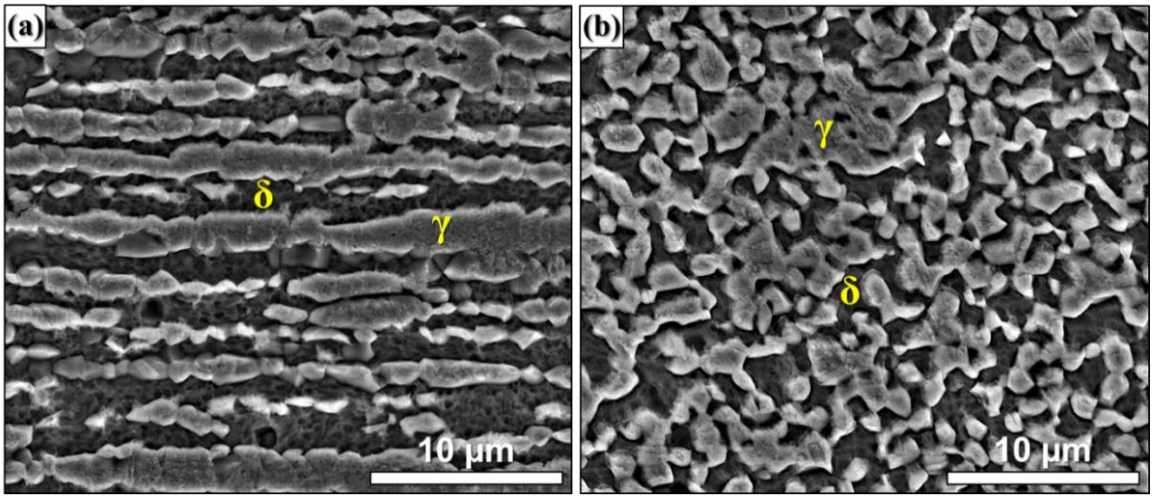

Figure 10-2: SE-SEM images showing the microstructure of 2202 and 2205 duplex stainless steel wire in (a) the extrusion direction and (b) in transverse direction.

The yield point of the wires was strain-rate independent, leading to values of 690-720 MPa and 830-880 MPa for the 2202 and 2205 wires respectively. The recorded stress-strain curves for both wires are shown in Figure 10-3. The average force required to yield the corresponding wire was taken as reference value to strain the wire in the corrosion cell.

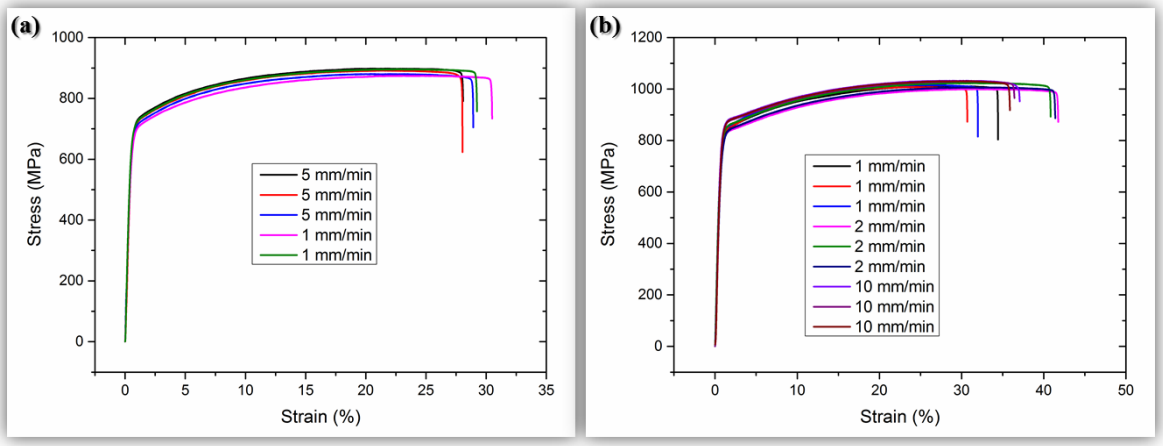

Figure 10-3: Stress-strain behaviour of (a) 2202 and (b) 2205 duplex stainless steels

Quasi in-situ corrosion monitoring

Large corrosion patches were observed on lean 2202 duplex stainless steel loaded to the yield point after 83 days of exposure at 50°C and 30% RH, as can be seen in the segmented data of Figure 10-4(a-b). Electrochemical dissolution during atmospheric corrosion seemed to spread preferentially along the wire surface rather than in depth. No clear corrosion pits with

hemispherical geometries were observed indicating a more broad corrosion attack with possible selective dissolution of ferrite or austenite. Usually, ferrite is selectively attacked in 2205 duplex stainless steel in chloride-containing environments due to its lower corrosion potential than austenite [8-13]. Similar observations have been reported to occur on lean 2101 and 2202 duplex stainless steels, anticipating the occurrence of selective attack on the ferrite [14-16]. The corrosion depth to area ratio indicated a strong re-passivation behaviour.

The attacked area of the 2202 wire significantly increased from $1.38 \cdot 10^5\ \mu m^2$ to $5.11 \cdot 10^5\ \mu m^2$ after 177 days of exposure, with the corroded volume rising from $5.59 \cdot 10^5\ \mu m^3$ to $2.4 \cdot 10^6\ \mu m^3$. This observation indicated an increase of corrosion depth to surface corrosion area ratio, causing an increase of the corrosion rate with exposure time and, as shown in Figure 10-7. The corrosion rates of duplex stainless steels are usually lower than their austenitic counterparts in most corrosive media. It has been reported that the Ni content has vital importance for pit growth and for the overall corrosion rate by decreasing the active dissolution rate of the metal [17]. Thus, larger Ni contents retard the corrosion incubation time and improve the re-passivation kinetics of the stainless steel [17]. The Ni content in 2202 duplex stainless steel is low (max. 2.8 wt.-%), and the corrosion propagation rate is therefore expected to be higher compared to the Ni-containing austenitic or higher-alloyed duplex stainless steels. Furthermore, the Mo content is also very low (max. 0.45 wt.-%) which usually improves the localised corrosion resistance of the alloy [18].

The increase of the corroded surface area indicated that the corrosion process in 2202 duplex stainless steel can extend to larger areas without the need of large net anodic current densities. Usually, large net anodic current densities are required to breakdown the passivating layer of duplex stainless steels which is accelerated by large cathode to anode ratios under thin-film electrolytes. Thus, the decrease of net cathodic to net anodic areas (actively corroded regions) would mean a decrease or, at least, a deceleration of the overall corrosion rate if the reaction takes place at the maximum cathodic current density. However, parts of the corroded surface may also re-passivate, providing an additional area fraction for the electro-chemical reaction [19]. The observed corrosion rate increased, with attack occurring along the surface as well as the depth of the 2202 wire, indicating weak re-passivation behaviour.

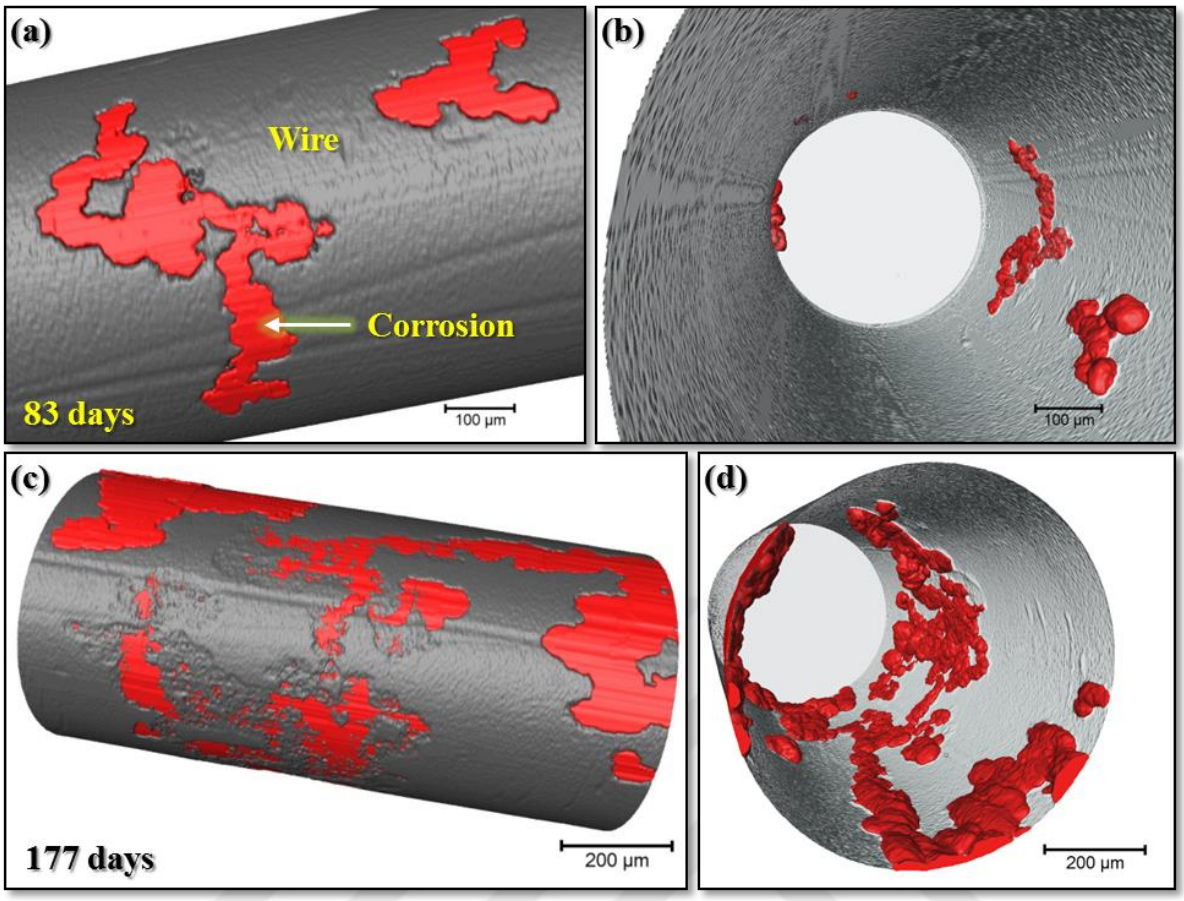

Figure 10-4: 3D visualisation of the reconstructed virtual slices of lean 2202 DSS showing (a+b) the corrosion morphology after 83 days of exposure and (c+d) after 177 days exposure

The corrosion morphology of the 2205 duplex stainless steel loaded just above the yield point after 86 days of exposure is shown in the reconstructed 3D images in Figure 10-5(a-c). Corrosion occurred along the surface with additionally the presence of several discrete corrosion pits. The corrosion process was favoured along the drawing direction, with most likely the ferrite selectively dissolved. The extent of the corrosion of 2205 duplex stainless steel was significantly lower than that of the lean 2202 duplex stainless steel, clearly showing its superior corrosion behaviour due to higher Ni and Mo contents. Interestingly, the elongated corrosion area shown in Figure 10-5(b+c) pointed towards the centre of the sample, as well as along the drawing direction, resembling an undercutting morphology.

The corrosion process seemed to have focused on the largest anodic region, which has been reported to locate at the centre of the corrosion pit, leading to a more localised corrosion pathway towards inside the wire [19]. In parallel, the corrosion process also seemed more

favoured along the processing direction of the wire, with possibly dissolved ferrite grains first at the bottom of the pit, enabling pit growth along the drawing direction of the wire.

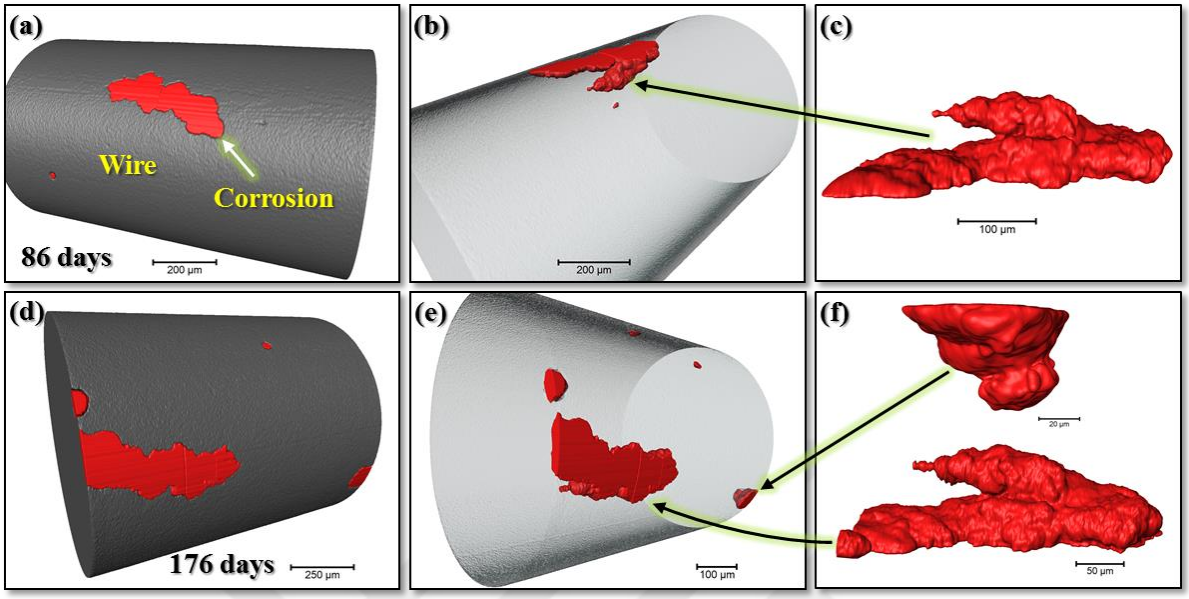

Figure 10-5: 3D visualisation of the 2205 DSS with 900 MPa applied tensile stress showing (a-c) the corrosion morphology after 86 days of exposure and (d-e) after 176 days exposure

However, pit growth towards the interior provides a more occluded pit morphology, which certainly promotes pit stability, i.e. enabling pit propagation. The observation of individual corrosion pits clearly showed stronger passive layer than its 2202 counterpart, resulting in the occurrence of corrosion pits at confined regions rather than selective dissolution. It is currently assumed that some of these pits were possibly metastable and most likely died before they could reach stable environmental conditions inside.

The area and depth of corrosion increased after 176 days of exposure, and with further exposure the rate of corrosion decelerated as can be seen in Figure 10-7. The extent of corrosion of the 2205 duplex stainless steel reached a maximum after a much shorter time, in contrast to the 2202 duplex stainless steel. For the latter, the extent of corrosion seemed to increase with longer exposure times. In the 2205 wire some new pits were found with longer exposures (Figure 10-5(d-f)).

On the 2205 duplex wire strained to 550 MPa sites of localised corrosion (pits) and atmospheric-induced stress corrosion cracks were observed shown in Figure 10-6(a). One apparent SCC site within one of the corrosion pits was seen to penetrate the wire (Figure 10-6(b-e)). This crack was located inside a pit at a side-wall highlighted in Figure 10-6(c+d).

The total length of the crack was about 80 µm, with several branches along its length, clearly indicating stress corrosion cracking.

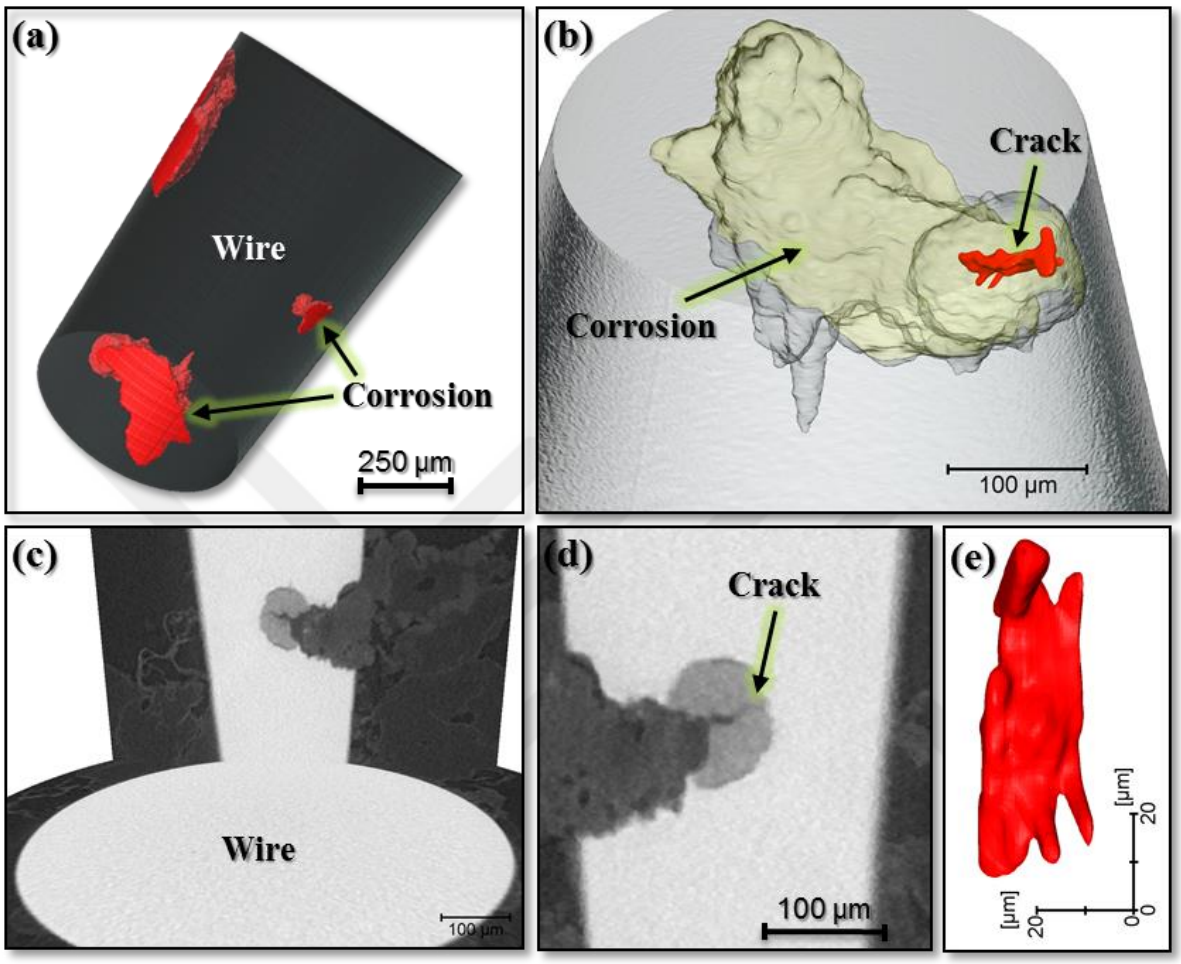

Figure 10-6: 3D visualisation of the 2205 DSS with 550 MPa applied tensile stress showing (a) the corrosion morphology after 177 days of exposure, (b) showing the largest pit in (a) with the crack segmented in red, (c+d) showing a stress corrosion crack, and (e) showing the reconstructed crack shape segmented in red.

Stress corrosion cracking can only occur when the crack velocity is higher than the corrosion rate of the alloy [20]. One explanation is that a lower corrosion rate acted on the 2205 duplex stressed to 550 MPa, compared to the 2205 wire stressed to 900 MPa since no stress corrosion cracks were observed in the latter. The same explanation may also hold true for the corrosion rate of the 2202 wire. Assumingly, fine-structured duplex stainless steels are more sensitive to applied stress or plastic deformation than coarse-grain microstructures favouring corrosion rather than stress corrosion cracking.

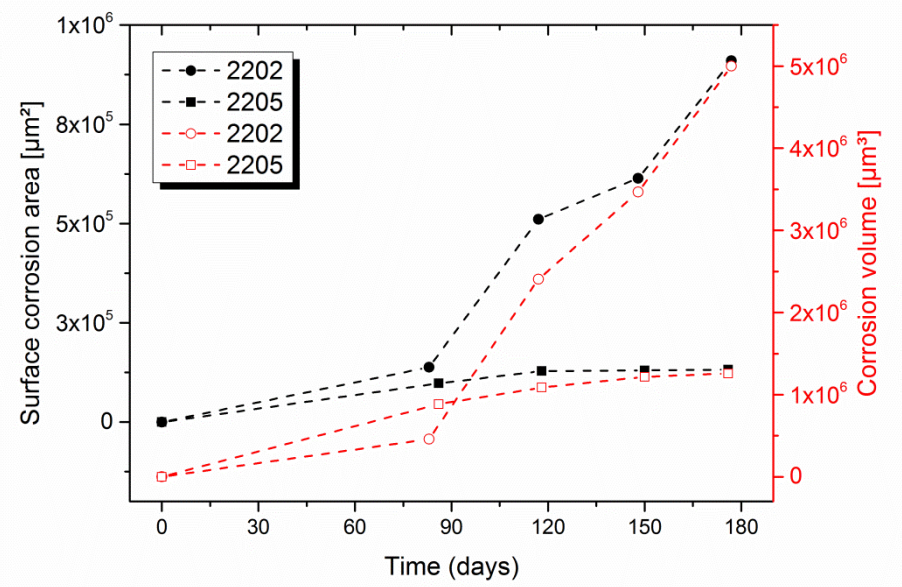

Figure 10-7: Surface corrosion area and corrosion volume of grades 2202 and 2205 DSS after exposure at 50°C and 30% RH.

9.1.1 Conclusions

Quasi in-situ time-dependent analysis of atmospheric corrosion and atmospheric-induced stress corrosion cracking led to following conclusions:

1) Lean 2202 duplex stainless steel corroded faster with higher dissolution rates than 2205 duplex stainless steel.
2) The extent of corrosion of 2205 duplex steel after 118 days of exposure at 50°C and 30% RH did not change with further exposure, whilst the extent of corrosion of the 2202 duplex wire steadily increased until 177 days of exposure.
3) No stress corrosion cracking events were observed occurring on 2202 and 2205 duplex stainless steel wires strained to their corresponding yield points, suggesting that the corrosion rate exceeded the crack propagation rate; cracking was observed on the 2205 duplex wire strained to ca. 50% of yield (550 MPa).

9.1.2 Acknowledgement

The authors acknowledge Radioactive Waste Management (RWM) (NPO004411A-EPS02) and EPSRC (EP/I036397/1) for financial support. The authors are grateful for the kind provision of Grade 2205 Duplex Stainless Steel wires by Ugitech France.

9.1.3 References

[1] J. Charles, S. Bernhardsson. Duplex Stainless Steels '91 - Volume 1. In: Charles J, Bernhardsson S, (Eds.). Duplex Stainless Steels '91, vol. 1. Beaune, Bourgogne, France: Les editions de physique, 1991.

[2] J.O. Nilsson. Super duplex stainless steels, Materials Science and Technology 8 (1992) 685-700.

[3] P. Kangas, J.M. Nicholls. Chloride-induced stress corrosion cracking of Duplex stainless steels. Models, test methods and experience, Materials and Corrosion 46 (1995) 354-365.

[4] J.-O. Nilsson, G. Chai. The physical metallurgy of duplex stainless steels. International Conference & Expo Duplex 2007. Grado, Italy: Associazone Italina Di Metallurgia - AIM, 2007.

[5] F. King. Corrosion Resistance of Austenitic and Duplex Stainless Steels in Environments Related to UK Geological Disposal. 2009.

[6] Sellafield LTD Generic 3m3 Box Design Interim Stage. Radioactive Waste Management, 2013.

[7] C. Padovani, R. Winsley, N. Smart, P. Fennell, C. Harris, K. Christie. Corrosion control of stainless steels in indoor atmospheres – practical experience (Part 2), Corrosion (2014).

[8] S. Aoki, H. Yakuwa, K. Mitsuhashi, J.i. Sakai. Dissolution Behavior of α and γ Phases of a Duplex Stainless Steel in a Simulated Crevice Solution, ECS Transactions 25 (2010) 17-22.

[9] S. Aoki, K. Ito, H. Yakuwa, M. Miyasaka, J.i. Sakai. Potential Dependence of Preferential Dissolution Behavior of a Duplex Stainless Steel in Simulated Solution inside Crevice, Zairyo-to-Kankyo 60 (2011) 363-367.

[10] S. Jae-Ho, L. Jae-Bong. Critical Pitting Temperature of 2205 Duplex Stainless Steels Using Immersion and Electrochemical Polarization Test Methods, Journal of the Korean institute of surface engineering 39 (2006) 18-24.

[11] C. Örnek, D.L. Engelberg. Kelvin Probe Force Microscopy and Atmospheric Corrosion of Cold-rolled Grade 2205 Duplex Stainless Steel. Eurocorr 2014. Pisa, Italy: European Federation of Corrosion, 2014. p.1-10.

[12] C. Örnek, D.L. Engelberg. SKPFM Measured Volta Potential Correlated with Strain Localisation in Microstructure of Cold-rolled Grade 2205 Duplex Stainless Steel, Corrosion Science (2015).

[13] C. Örnek, D.L. Engelberg. Effect of “475°C Embrittlement” on the Corrosion Behaviour of Grade 2205 Duplex Stainless Steel Investigated Using Local Probing Techniques. Corrosion Management. Northampton, UK: The Institute of Corrosion, 2013. p.9-11.

[14] L. Zhang, Y. Jiang, B. Deng, W. Zhang, J. Xu, J. Li. Effect of aging on the corrosion resistance of 2101 lean duplex stainless steel, Materials Characterization 60 (2009) 1522-1528.

[15] L. Zhang, W. Zhang, Y. Jiang, B. Deng, D. Sun, J. Li. Influence of annealing treatment on the corrosion resistance of lean duplex stainless steel 2101, Electrochimica Acta 54 (2009) 5387-5392.

[16] T. Prosek, A. Le Gac, D. Thierry, S. Le Manchet, C. Lojewski, A. Fanica, E. Johansson, C. Canderyd, F. Dupoiron, T. Snauwaert, F. Maas, B. Droesbeke. Low-Temperature Stress Corrosion Cracking of Austenitic and Duplex Stainless Steels Under Chloride Deposits, Corrosion Science 70 (2014) 1052-1063.

[17] D.J.W. Oldfield. Nickel effect: Lower rate of corrosion in stainless, Emerald Group Publishing Limited 37 (1990) 9-11.

[18] Y.C. Lu, M.B. Ives, C.R. Clayton. Synergism of alloying elements and pitting corrosion resistance of stainless steels, Corrosion Science 35 (1993) 89-96.

[19] G. Williams, N. Birbilis, N. McMurray. Controlling factors in localised corrosion morphologies observed for magnesium immersed in chloride containing electrolyte, Faraday Discussions (2015).

[20] B. Cottis, M. Graham, R. Lindsay, S. Lyon, T. Richardson, D. Scantlebury, H. Stott. Shreir's Corrosion - Volume 2. In: Cottis B, Graham M, Lindsay R, Lyon S, Richardson T, Scantlebury D, Stott H, (Eds.), vol. 1. Manchester: Elsevier B.V.,, 2010.

10.2 Further Suggestions

A comprehensive parameter analyses for the effect of stress and droplet chemistry should be made, to broaden the mechanistic understanding of EAC behaviour of grade 2205 duplex stainless steel.

Effect of Applied Stress on Atmospheric Stress Corrosion Susceptibility

The effect of the magnitude of applied stress in the elastic and elastic-plastic regime could be investigated and stress corrosion cracking engineering diagrams established. Threshold stress for the initiation of stress corrosion cracking can render useful information for life-time prediction models of the steel. Special focus should be given to crack initiation sites, crack morphology, and extent of cracking.

Analysis of Corrosion and Stress Corrosion Cracking Propagation Rates

Incubation times for corrosion and stress corrosion cracking as well as their propagation rates can be measured using correlative techniques such quasi in-situ X-ray Computed Tomography (XCT), SEM/Optical Microscopy and/or DIC. Duplex wire probes can be strained and contaminated with salt-containing electrolytes, then exposed to climatically controlled environments. The onset and progress of corrosion and stress corrosion cracking can be monitored, quasi in-situ; by screening the sample at different time intervals via X-ray CT. Synchrotron-based XCT can be performed to improve resolution, increase field of view, and acquisition time. DIC and Digital Volume Correlation (DVC) can be used to obtain stress corrosion cracking velocities.

In-situ Screening of Atmospheric Corrosion Processes and Monitoring of the Development of Local Anodic and Cathodic Sites

Tensile specimens could be exposed to salt-containing electrolytes with different deposition densities and droplet sizes containing phenolphthalein and potassium ferricyanide (Evans droplet testing) and the corrosion processes screened, in-situ, using optical and/or stereo microscopy. The region of interest (deposited area) of the specimen could be pre-characterised by optical microscopy and/or EBSD allowing allocation of corroded regions and quantification of fraction of dissolved ferrite and austenite (grains). The development of the anode and cathode can be monitored and allocated to the microstructure. Furthermore, the scanning Kelvin probe (SKP) technique can be used to measure, in-situ, Volta potential development to

assign local anodic and cathodic regions which will provide meaningful information to establish mechanistic understanding of atmospheric corrosion and stress corrosion cracking susceptibility of duplex stainless steel.

Effect of Salt Chemistry on Atmospheric Corrosion and Stress Corrosion Cracking Susceptibility

The work carried out in this thesis should be repeated by using 'real' sea-water electrolyte containing organic matter. Synthetic sea water or water from costal sites in the UK can be taken for setting up AISCC tests. EDX measurement can be carried out to map elemental distribution prior to and after the test and compare this with magnesium chloride containing droplets. The effect of pH can be studied as well to see whether the corrosion and stress corrosion susceptibility can be minimised.